Springer Series in Materials Science 173

Helmut Sitter
Claudia Draxl
Michael Ramsey *Editors*

Small Organic Molecules on Surfaces

Fundamentals and Applications

Springer

Springer Series in Materials Science

Volume 173

For further volumes:
www.springer.com/series/856

The Springer Series in Materials Science covers the complete spectrum of materials physics, including fundamental principles, physical properties, materials theory and design. Recognizing the increasing importance of materials science in future device technologies, the book titles in this series reflect the state-of-the-art in understanding and controlling the structure and properties of all important classes of materials.

Helmut Sitter • Claudia Draxl • Michael Ramsey
Editors

Small Organic Molecules on Surfaces

Fundamentals and Applications

Springer

Editors
Helmut Sitter
Semiconductor- and Solid State Physics
Johannes Kepler University Linz
Linz, Austria

Claudia Draxl
Physics Department
Humboldt Universität zu Berlin
Berlin, Germany

Michael Ramsey
Surface and Interface Physics
Institute of Physics
Karl-Franzens University Graz
Graz, Austria

ISSN 0933-033X Springer Series in Materials Science
ISBN 978-3-642-33847-2 ISBN 978-3-642-33848-9 (eBook)
DOI 10.1007/978-3-642-33848-9
Springer Heidelberg New York Dordrecht London

Library of Congress Control Number: 2013931979

© Springer-Verlag Berlin Heidelberg 2013
This work is subject to copyright. All rights are reserved by the Publisher, whether the whole or part of the material is concerned, specifically the rights of translation, reprinting, reuse of illustrations, recitation, broadcasting, reproduction on microfilms or in any other physical way, and transmission or information storage and retrieval, electronic adaptation, computer software, or by similar or dissimilar methodology now known or hereafter developed. Exempted from this legal reservation are brief excerpts in connection with reviews or scholarly analysis or material supplied specifically for the purpose of being entered and executed on a computer system, for exclusive use by the purchaser of the work. Duplication of this publication or parts thereof is permitted only under the provisions of the Copyright Law of the Publisher's location, in its current version, and permission for use must always be obtained from Springer. Permissions for use may be obtained through RightsLink at the Copyright Clearance Center. Violations are liable to prosecution under the respective Copyright Law.
The use of general descriptive names, registered names, trademarks, service marks, etc. in this publication does not imply, even in the absence of a specific statement, that such names are exempt from the relevant protective laws and regulations and therefore free for general use.
While the advice and information in this book are believed to be true and accurate at the date of publication, neither the authors nor the editors nor the publisher can accept any legal responsibility for any errors or omissions that may be made. The publisher makes no warranty, express or implied, with respect to the material contained herein.

Printed on acid-free paper

Springer is part of Springer Science+Business Media (www.springer.com)

Preface

There is an enormous world-wide effort in basic scientific research as well as in industrial development in the area of organic electronics. It is becoming increasingly clear that if devices based on organic materials are ever going to have a significant relevance beyond being a cheap replacement for inorganic semiconductors, one will need to understand interface formation, film growth, and functionality. Control of these aspects will allow the realisation of totally new device concepts exploiting the enormous flexibility inherent in organic chemistry. In the field of device-relevant semiconducting organic materials one finds many parallels with that of inorganic semiconductors. However, the versatility of organic molecules comes at the cost of higher materials complexity. This rules out the simple transfer of concepts established from inorganic semiconductor research, and makes work on organic semiconductors particularly challenging.

World-wide, investigations into organic thin films can be partitioned into three areas of focus with different aims and a mix of applied versus basic research: (1) the development and production of devices, (2) thin film characterisation, and, more recently, with the recognition of the importance of molecular level control (3) surface and interface science. As shown in this volume, linking these branches creates enormous synergies leading to a significant advance in the field of organic semiconductors.

In this review we focus on oligomeric/molecular films, as we believe that the control of molecular structures and interfaces provides highly defined systems which allows, on the one hand, the study of the basic physics and, on the other hand, to find the important parameters necessary to improve organic devices.

Even the simplest organic devices have a number of constituents whose morphology, order, and interfaces have a major influence on their properties. This book is conceived to report on the activities of the leading groups in Austria and their international collaborators, who work in the field of growth and characterisation of organic films and devices and focus on the fabrication and characterisation of highly ordered functional organic films. The wide range of expertise of the contributing groups allows the combination of different methodologies and aspects of physics, chemistry, and materials science for the design and understanding of well-defined organic structures.

Our vision is that functional organic molecules can be the basic building blocks for both low cost large area and new nano-scale devices, ranging from solar cells to chemical sensors. Because of the technological relevance and the applications that can be imagined for devices incorporating organic films it is important to understand the fundamental processes of organic film formation, the structures that are formed, their interfaces and their properties.

The scope of this book is such that it bridges the gap between fundamental research and basic applied sciences. This will contribute to new concepts and a knowledge base, which will have a direct impact in the fields of electronic, opto-electronic, and photovoltaic devices, as well as sensors and nanoscopic devices.

Berlin, Germany Claudia Draxl
Graz, Austria Michael Ramsey
Linz, Austria Helmut Sitter

Contents

Part III Electrical Properties

Part IV Optical Properties

Part V Devices

Contributors

Claudia Draxl Chair of Atomistic Modelling and Design of Materials, Montanuniversität Leoben, Leoben, Austria; Physics Department, Humboldt Universität zu Berlin, Berlin, Germany

Siegfried Bauer Department of Soft Matter Physics, Johannes Kepler University Linz, Linz, Austria

Giovanni Bongiovanni Dipartimento di Fisica, Università di Cagliari, Monserrato, (CA), Italy

Tatjana Djuric Institute of Solid State Physics, Graz University of Technology, Graz, Austria

Matthias Edler Chair of Chemistry of Polymeric Materials, University of Leoben, Leoben, Austria

Ivan I. Fishchuk Department of Theoretical Physics, Institute for Nuclear Research, National Academy of Sciences of Ukraine, Kyiv, Ukraine

Alexander J. Fleming Surface and Interface Physics, Institute of Physics, Karl-Franzens University Graz, Graz, Austria

Eric D. Głowacki Physical Chemistry, Linz Institute for Organic Solar Cells, Johannes Kepler University Linz, Linz, Austria

Thomas Griesser Chair of Chemistry of Polymeric Materials, University of Leoben, Leoben, Austria

Gerardo Hernandez-Sosa Semiconductor- and Solid State Physics, Johannes Kepler University Linz, Linz, Austria; Innovation Lab GmbH, Heidelberg, Germany

Gregor Hlawacek Physics of Interfaces and Nanomaterials, MESA+ Institute for Nanotechnology, University of Twente, Enschede, The Netherlands

Mihai Irimia-Vladu Physical Chemistry, Linz Institute for Organic Solar Cells, Johannes Kepler University Linz, Linz, Austria; Department of Soft Matter Physics, Johannes Kepler University Linz, Linz, Austria; Division of Surface Technologies and Photonics, Department of Materials, Joanneum Research Forschungsgesellschaft mbH, Weiz, Austria

Andrey Kadashchuk Department of Photoactivity, Institute of Physics, National Academy of Sciences of Ukraine, Kyiv, Ukraine; Department of Polymer and Molecular Electronics, IMEC, Leuven, Belgium

Wolfgang Kern Chair of Chemistry of Polymeric Materials, University of Leoben, Leoben, Austria

Fawad S. Khokhar Physics of Interfaces and Nanomaterials, MESA+ Institute for Nanotechnology, University of Twente, Enschede, The Netherlands

Georg Koller Surface and Interface Physics, Institute for Physics, Karl-Franzens University Graz, Graz, Austria

Andrea Mura Dipartimento di Fisica, Università di Cagliari, Monserrato, (CA), Italy

Dimitrii Nabok Chair of Atomistic Modelling and Design of Materials, Montanuniversität Leoben, Leoben, Austria; Physics Department, Humboldt Universität zu Berlin, Berlin, Germany

Martin Oehzelt Helmholtz Zentrum Berlin für Materialien und Energie GmbH, BESSY II, Berlin, Germany; Institut für Physik, Humboldt-Universität zu Berlin, Berlin, Germany

Almantas Pivrikas Physical Chemistry, Linz Institute for Organic Solar Cells, Johannes Kepler University Linz, Linz, Austria; Centre for Organic Photonics and Electronics, School of Chemistry and Molecular Biosciences, University of Queensland, Brisbane, Australia

Bene Poelsema Physics of Interfaces and Nanomaterials, MESA+ Institute for Nanotechnology, University of Twente, Enschede, The Netherlands

Peter Puschnig Chair of Atomistic Modelling and Design of Materials, Montanuniversität Leoben, Leoben, Austria; Institute of Physics, Karl-Franzens University Graz, Graz, Austria

Francesco Quochi Dipartimento di Fisica, Università di Cagliari, Monserrato, (CA), Italy

Michael G. Ramsey Surface and Interface Physics, Institute for Physics, Karl-Franzens University Graz, Graz, Austria

Roland Resel Institute of Solid State Physics, Graz University of Technology, Graz, Austria

Lorenz Romaner Chair of Atomistic Modelling and Design of Materials, Montanuniversität Leoben, Leoben, Austria

Michele Saba Dipartimento di Fisica, Università di Cagliari, Monserrato, (CA), Italy

Ingo Salzmann AG Supramolecular Systems, Department of Physics, Humboldt-Universität zu Berlin, Berlin, Germany

N. Serdar Sariciftci Physical Chemistry, Linz Institute for Organic Solar Cells, Johannes Kepler University Linz, Linz, Austria

Günther Schwabegger Semiconductor- and Solid State Physics, Johannes Kepler University Linz, Linz, Austria

Clemens Simbrunner Semiconductor- and Solid State Physics, Johannes Kepler University Linz, Linz, Austria

Helmut Sitter Semiconductor- and Solid State Physics, Johannes Kepler University Linz, Linz, Austria

Philipp Stadler Physical Chemistry, Linz Institute for Organic Solar Cells (LIOS), Johannes Kepler University of Linz, Linz, Austria

Lidong Sun Institute of Experimental Physics, Johannes-Kepler University Linz, Linz, Austria

Christian Teichert Institute of Physics, Montanuniversitaet Leoben, Leoben, Austria

Anna M. Track Surface and Interface Physics, Institute for Physics, Karl-Franzens University Graz, Graz, Austria; NXP Semiconductors Austria GmbH Styria, Gratkorn, Austria

Gregor Trimmel Institute for Chemistry and Technology of Materials, Graz University of Technology, Graz, Austria

Mujeeb Ullah Semiconductor- and Solid State Physics, Johannes Kepler University Linz, Linz, Austria; Centre for Organic Photonics & Electronics (COPE), School of Mathematics and Physics, University of Queensland, Brisbane, QLD, Australia

Raoul van Gastel Physics of Interfaces and Nanomaterials, MESA+ Institute for Nanotechnology, University of Twente, Enschede, The Netherlands

Irene Watzinger Semiconductor- and Solid State Physics, Johannes Kepler University Linz, Linz, Austria

Adolf Winkler Institute of Solid State Physics, Graz University of Technology, Graz, Austria

Harold J.W. Zandvliet Physics of Interfaces and Nanomaterials, MESA+ Institute for Nanotechnology, University of Twente, Enschede, The Netherlands

Peter Zeppenfeld Institute of Experimental Physics, Johannes-Kepler University Linz, Linz, Austria

Part I
Theory

Chapter 1
The Structure of Molecular Orbitals Investigated by Angle-Resolved Photoemission

Peter Puschnig, Georg Koller, Claudia Draxl, and Michael G. Ramsey

Abstract In this contribution, it is shown how the combination of angle-resolved photoemission spectroscopy (ARPES) with ab-initio electronic-structure calculations within the framework of density-functional theory (DFT) leads to insights into electronic and structural properties of organic molecular layers well beyond conventional density-of-sates or $E(k)$ investigations. In particular, we emphasize the rather simple, but for many cases sufficiently accurate, connection between the observed angular dependence of the photocurrent with the spatial distribution of the molecular orbital from which it is arising. After discussing the accuracy and limitations of this approach, which is based on a plane-wave approximation of the final state, three examples are presented. The first utilizes the characteristic angular pattern of the highest occupied molecular orbitals (HOMO) in a pentacene multilayer film in order to measure the molecular tilt angle in the film. In the second example, the nature of two closely spaced molecular emissions from a porphyrin thin film is unambiguously identified as HOMO and HOMO-1, and the molecule's azimuthal alignment is determined. Finally, for a monolayer of para-sexiphenyl on Cu(110), it is demonstrated how the real-space distribution of the filled LUMO and the HOMO of para-sexiphenyl can be reconstructed from the angular dependence of the photocurrent.

P. Puschnig (✉) · C. Draxl
Chair of Atomistic Modelling and Design of Materials, Montanuniversität Leoben,
Franz-Josef-Straße 18, 8700 Leoben, Austria
e-mail: peter.puschnig@uni-graz.at

Present address:
P. Puschnig
Institute of Physics, Karl-Franzens University Graz, Universitätsplatz 5, 8010 Graz, Austria

Present address:
C. Draxl
Physics Department, Humboldt Universität zu Berlin, Zum Großen Windkanal 6, 12489 Berlin,
Germany

G. Koller · M.G. Ramsey
Institute of Physics, Karl-Franzens University Graz, Universitätsplatz 5, 8010 Graz, Austria

H. Sitter et al. (eds.), *Small Organic Molecules on Surfaces*,
Springer Series in Materials Science 173, DOI 10.1007/978-3-642-33848-9_1,

1.1 Introduction

Electronic orbitals are the prime determinants of the respective compounds' chemical, electronic, and optical properties. Therefore, the knowledge of energetic positions, ordering, and spatial extent of molecular orbitals is of great interest. However, the valence bands of large conjugated molecules consist of a multitude of closely spaced molecular states, which makes their correct assignment challenging both experimentally and theoretically.

Experimentally, energy positions of molecular orbitals in organic molecular layers can be studied by ultra-violet photoemission spectroscopy (UPS) [1] or by scanning tunneling spectroscopy (STS) [2–7]. UPS has the advantage that accessible binding energies are not limited to a few electron volts from the Fermi level as in STS. However, UPS spectra of thin molecular layers on metals often show only weak and rather broad features and are, therefore, not always conclusive. Also, UPS data depend on the experimental geometry, molecular orientation, and photon energy, which further complicates the assignment of the measured peaks. Moreover, experimental techniques which are probing the *spatial* structure of individual orbitals are rare, and the interpretation of experimental data is commonly difficult and requires guidance from theory [8]. Here, scanning tunneling microscopy (STM) has proven to be a powerful technique for mapping orbital structures of rather complex molecules [2]. However, strong bonding interactions with the substrate make the interpretation of the images in terms of orbital structures problematic [9].

Angle-resolved photoelectron spectroscopy (ARPES), on the other hand, is *the* technique to study the band structure of solids by measuring the kinetic energy of the photoemitted electrons versus their angular distribution [10]. Particularly, many questions in nanophysics and interface engineering are often addressed by this experimental technique which, in combination with density-functional-theory calculations, leads to important physical insight. Recently, however, it has been shown that ARPES provides an alternative route to obtain information regarding the spatial structure of individual molecular orbitals [11–14]. By making certain assumptions about the photoemisson transition matrix element, ARPES intensity maps can also provide useful information regarding orbital structures. Specifically, it has become possible to obtain the one-dimensional wave functions of quantum-well states on nano-structured gold surfaces [13, 15], and the two-dimensional spatial electron distribution in the frontier orbitals of organic π-conjugated molecules adsorbed at metallic surfaces [12, 14].

In this contribution, we review the recent progress in measuring the spatial structure of molecular orbitals by using angle-resolved photoemission spectroscopy. By comparing measured ARPES data with simulations of the photoemission intensity based on density-functional theory, we demonstrate the strength of this method which lies in the direct and easy-to-apply connection between the measured angular dependence of the photocurrent and the Fourier transform of the molecular orbital from which electrons are emitted. First, we will give a brief account on the theoretical description which is based on the one-step model of photoemission. The implication of using a plane wave for the final state will be shown, and the limits of this approximation will be discussed. Then, three examples for molecular films consisting of highly oriented multi-layers of π-conjugated molecules down to monolayers adsorbed at metallic surfaces will be given: First, results for a pentacene multilayer film are shown for which the tilt angle of the molecules could be determined from a comparison between the ARPES data and momentum maps of the free molecule. Second, data for a monolayer of tetraphenyl porphyrine on Cu(110) demonstrate the strength of the method in identifying of molecular orbitals and determining azimuthal molecular orientations. Finally, for a monolayer of para-sexiphenyl on Cu(110) it is demonstrated how ARPES momentum maps of the former lowest unoccupied molecular orbital (LUMO) and the highest occupied molecular orbital (HOMO) are utilized to reconstruct real-space distributions of the respective orbitals.

1.2 Theory

Photoemission spectroscopy is commonly applied to study the band structure of solids by measuring the kinetic energy versus angular distribution of the photoemitted electrons. Here we show that this experimental technique can also be used to gain information on the spatial electron distribution in molecular orbitals [12]. In angle-resolved photoemission spectroscopy (ARPES), schematically depicted in Fig. 1.1, an incident photon of energy $\hbar\omega$ excites an electron from a bound initial state, described by wave function ψ_i and energy E_i, to a final electron state ψ_f with kinetic energy E_{kin}. Because energy and momentum parallel to the surface are conserved during the photoemission process, the measurement of the emitted electron's energy and momentum probes the band structure of solids. Thus, ARPES is commonly used to study band dispersions, Fermi surfaces and many-body correlations in a wide range of materials [16].

1.2.1 One-Step Model of Photoemission

A theoretical description of the angle-resolved photoelectron intensity is generally rather involved, and attempts to compute it in a quantitative manner are rather scarce. Within this work, photo-excitation is treated as a single coherent process from a molecular orbital to the final state which is referred to as the one-step model of photoemission (PE). The PE intensity $I(\theta, \phi; E_{\text{kin}})$ is given by a Fermi golden rule formula [17]

$$I(\theta, \phi; E_{\text{kin}}) \propto \sum_i \left| \langle \psi_f(\theta, \phi; E_{\text{kin}}) | \mathbf{A} \cdot \mathbf{p} | \psi_i \rangle \right|^2 \times \delta(E_i + \Phi + E_{\text{kin}} - \hbar\omega). \quad (1.1)$$

Here, the polar and azimuthal emission angles defined in Fig. 1.1 are denoted by θ and ϕ, respectively. The photocurrent I is given by a sum over all transitions from occupied initial states i described by wave functions ψ_i to the final state ψ_f

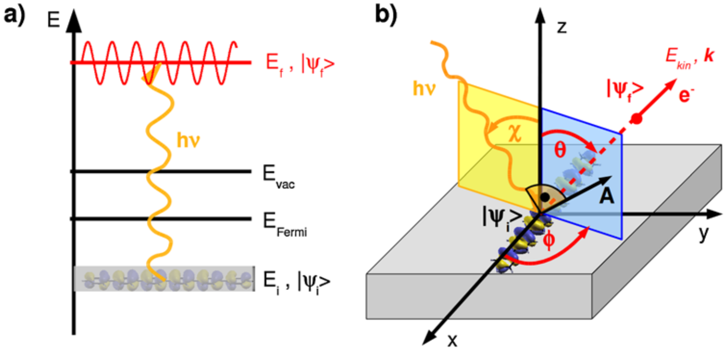

Fig. 1.1 (**a**) Schematic energy level diagram of a photoemission experiment showing the energy of the initial state, E_i, the Fermi level E_F, the vacuum level E_{vac}, and the final-state energy E_f. (**b**) In angle-resolved photoemission spectroscopy, an incident photon with energy $h\nu$ and vector potential **A** excites an electron from the initial state ψ_i to the final state ψ_f characterized by the kinetic energy E_{kin} and the momentum vector **k**. The polar and azimuthal angles θ and ϕ, respectively, define the direction of the photoemitted electron

characterized by the direction (θ, ϕ) and the kinetic energy of the emitted electron. The delta function ensures energy conservation, where Φ denotes the sample work function. The transition matrix element is given in the dipole approximation, where **p** and **A**, respectively, denote the momentum operator and the vector potential of the exciting electro-magnetic wave.

Plane-Wave Approximation

The difficult part in evaluating Eq. (1.1) is the proper treatment of the final state. In the most simple approach, it is approximated by a plane wave (PW) only characterized by the direction and wave number of the emitted electron. This has already been proposed more than 30 years ago [18] with some success in explaining the observed PE distribution from atoms and small molecules adsorbed at surfaces. Using a plane-wave approximation is appealing since the evaluation of Eq. (1.1) renders the photocurrent I_i arising from one particular initial state i proportional to the Fourier transform $\tilde{\psi}_i(\mathbf{k})$ of the initial-state wave function corrected by the polarization factor $\mathbf{A} \cdot \mathbf{k}$:

$$\left|\tilde{\psi}_i(\mathbf{k})\right| \propto \frac{\sqrt{I_i(\theta, \phi)}}{|\mathbf{A} \cdot \mathbf{k}|}. \tag{1.2}$$

Thus, if the angle-dependent photocurrent of individual initial states can be selectively measured (as it can for organic molecules where the intermolecular band dispersion is often smaller than the energetic separation of individual orbitals), a one-to-one relation between the photocurrent and the molecular orbitals in reciprocal space can be established. This allows the measurement of the absolute value of the initial-state wave function in reciprocal space and, via a subsequent Fourier transform, a reconstruction of molecular orbital densities in real space.

Limitations of the Plane-Wave Approximation

It has been observed rather early that the plane-wave final-state approximation had problems in describing the photoemission intensity of some large polyatomic molecules and/or certain experimental geometries [19, 20]. This led to the conclusion that the plane-wave final-state approximation should not be used and nourished the development of the so-called independent-atomic-center (IAC) approximation [21]. In the IAC approximation, the initial state is decomposed into atomic eigenfunctions which build up the initial molecular orbitals, while the final state is composed of scattering solutions of the atomic Schrödinger equation at the final-state energy $E_k = \frac{\hbar^2}{2m} k^2$. The transition matrix element is then given by a coherent sum over these initial and final states, respectively. Thus, the IAC expression for the photoelectron wave function A with kinetic energy E_{kin} at the detector position $\mathbf{R}$ can be written in the following form [21]:

$$A(\mathbf{R}, E_{\text{kin}}) = \sum_{\alpha} \sum_{nlm} C_{\alpha,nlm} e^{i\mathbf{k}\mathbf{R}_\alpha} \sum_{LM} M_{\alpha,nlm}^{LM}(E_{\text{kin}}) Y_{LM}(\hat{R}). \tag{1.3}$$

Here, the initial orbital $\psi_i(\mathbf{r})$ is expressed as a linear combination of atomic orbitals $\phi_{\alpha,nlm}$ centered at the position $\mathbf{R}_\alpha$, where nlm represent the principal and angular-momentum quantum numbers of the orbital and α the atomic center on which it resides:

$$\psi(\mathbf{r}) = \sum_{\alpha} \sum_{nlm} C_{\alpha,nlm} \phi_{\alpha,nlm}(\mathbf{r} - \mathbf{R}_\alpha). \tag{1.4}$$

The matrix elements $M_{\alpha,nlm}^{LM}$ in Eq. (1.3) are dipole matrix elements between the atomic wave functions $\phi_{\alpha,nlm}$ and solutions of the Schrödinger equation in an atomic potential at the energy E_{kin} and angular momentum LM.

The goal of the remaining part of this section is to shed light on the relation between the IAC and the simpler PW approach and to hint towards possible limitations of the latter. It was already noted by Grobman that expression (1.3) can be considerably simplified if the initial molecular orbital is comprised of atomic orbitals of the same chemical and orbital character. A specific example of such a situation is given by a π molecular orbital of a planar polyatomic molecule. Then the coefficients $C_{\alpha,nlm}$ are only non-zero for atomic p_z orbitals and only one term remains of the sum over nlm:

$$A(\mathbf{R}, E_{\text{kin}}) = \sum_{\alpha} C_{\alpha,2p_z} e^{i\mathbf{k}\mathbf{R}_\alpha} \sum_{LM} M_{2p_z}^{LM}(E_{\text{kin}}) Y_{LM}(\hat{R}). \tag{1.5}$$

In the above expression we have also omitted the atomic index α in the transition matrix elements since they do not depend on the position of the atom but only on the type of atomic orbital which is assumed to be $2p_z$ for all contributing atoms. Thus, the sum over the final-state angular-momentum quantum numbers LM, the atomic factor, which we abbreviate as

$$N_{2p_z}(E_{\text{kin}}, \hat{R}) = \sum_{LM} M_{2p_z}^{LM}(E_{\text{kin}}) Y_{LM}(\hat{R}), \tag{1.6}$$

can be put in front of the summation over atoms α and we are left with the simplified expression for the photoemission amplitude at the detector:

$$A(\mathbf{R}, E_{\text{kin}}) = N_{2p_z}(E_{\text{kin}}, \hat{R}) \sum_{\alpha} C_{\alpha,2p_z} e^{i\mathbf{k}\mathbf{R}_\alpha}. \tag{1.7}$$

As has been noted by Grobman [21] the term $N_{2p_z}(E_{\text{kin}}, \hat{R})$ acts only as a weakly varying envelope function while the main angular dependence of the photoemission intensity is dominated by the last term in Eq. (1.7), which is closely related to the Fourier transform of the initial molecular orbital. By taking the Fourier transform (FT) on both sides of Eq. (1.4) we see that the FT of the initial molecular orbital $\tilde{\psi}(\mathbf{k})$ can be written as

$$\tilde{\psi}(\mathbf{k}) = \tilde{\phi}_{2p_z}(\mathbf{k}) \sum_{\alpha} C_{\alpha,2p_z} e^{i\mathbf{k}\mathbf{R}_\alpha}. \tag{1.8}$$

Here, we have introduced the FT of a p_z orbital, $\tilde{\phi}_{2p_z}(\mathbf{k})$, whose angular part is simply given by the spherical harmonic, $Y_{10}(\theta, \phi) \propto \cos\theta$ [18].

Equivalence of IAC and PW Approximation

For large π conjugated molecules, the main angular dependence will be determined by the last term in Eq. (1.7). By combining Eqs. (1.7) and (1.8) we see that the IAC produces a result which is in fact very similar to the PW final-state assumption, compare Eq. (1.2), provided that the initial molecular orbital is composed of atomic orbitals of the same type as is the case for planar π conjugated molecules:

$$A(\mathbf{R}, E_{\text{kin}}) = \left(\frac{N_{2p_z}(E_{\text{kin}}, \hat{R})}{\tilde{\phi}_{2p_z}(\mathbf{k})} \right) \times \tilde{\psi}(\mathbf{k}). \tag{1.9}$$

Last but not least we note that the prefactor, $N_{2p_z}/\tilde{\psi}_{2p_z}$ can be shown to become completely independent of the emission direction (θ, ϕ) for the special case where the polarization vector $\mathbf{A}$ of the photon is exactly parallel to the emission direction $\mathbf{k}$. For this particular geometry the photoemission intensity resulting from the IAC, which is the square of $A(\mathbf{R}, E_{\text{kin}})$, reduces exactly to the intensity emerging from the plane-wave final-state assumption. This observation has already been made by Goldberg for the photoemission cross section from atoms [22]. Moreover, due to the overall weak angular dependence of the envelope factor $N_{2p_z}/\tilde{\psi}_{2p_z}$, the Fourier transform of the initial molecular orbital $\tilde{\psi}(\mathbf{k})$ continues to provide a good description of the angle-dependent PE intensity also when the direction of the polarization vector deviates from the emission direction. Hence it is expected that the difference between the PW result, Eq. (1.2), and the IAC expression, Eq. (1.8), only grows weakly with the deviation from the above mentioned condition.

Summary of Theoretical Consideration

From what was said above, the plane-wave final-state assumption can be expected to be valid if the following conditions are fulfilled: (i) π orbital emissions from large planar molecules, (ii) an experimental geometry in which the angle between the polarization vector $\mathbf{A}$ and the direction of the emitted electron $\mathbf{k}$ is rather small, and (iii) molecules consisting of many light atoms (H, C, N, O). The latter requirement is a result of the small scattering cross section of light atoms and the presence of many scattering centers expected to lead to a rather weak and structureless angular pattern [11, 23]. With these conditions satisfied, a one-to-one mapping between the PE intensity and individual molecular orbitals in reciprocal space is possible, providing a valuable tool for the investigation of organic molecular films and monolayers. This will be demonstrated with several examples in the following sections.

1.3 Photoemission Experiments

Presently, there are a number of display-type analyzers that are capable of obtaining angular-dependent photoemission intensity maps suitable for our approach [24]. Our ARPES experiments are performed at room temperature using a toroidal electron-energy analyzer described elsewhere [25] attached to the TGM-4 beamline at the synchrotron radiation facility BESSY II. This toroidal electron analyzer allows simultaneous collection of photoelectrons in a kinetic energy window of 0.8 eV over a polar angle θ range of 180° in the specular plane. Azimuthal scans are then made by rotating the sample around the surface normal in 1° steps for $>180°$ of azimuthal angle ϕ. The angular emission data are then converted to momentum $k_{\|}$ using the formula $k_{\|} = \sqrt{2m_e E_{\mathrm{kin}}/\hbar^2}\sin\theta$ [$\mathrm{\AA}^{-1}$] to create the momentum maps. The photon incidence angle is $\alpha = 40°$, and the polarization direction is always in the specular plane. A photon energy of $h\nu = 35$ eV is used throughout.

1.4 Results

In this section, we demonstrate the viability of the simple plane-wave final-state approach in conjunction with initial-state orbitals taken from density-functional theory for a number π-conjugated organic molecules. First, we present data for the

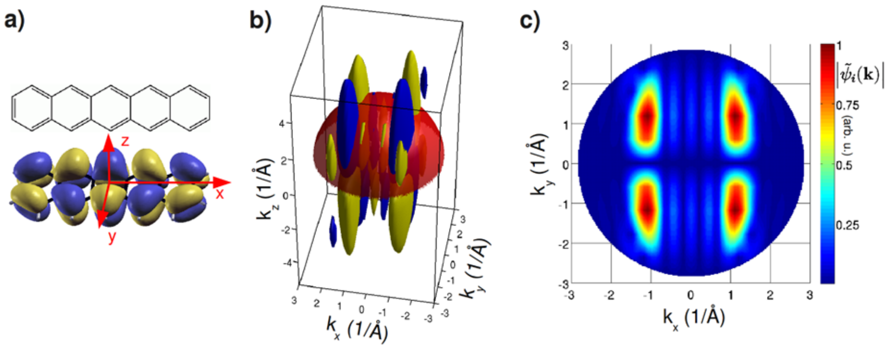

Fig. 1.2 (**a**) Chemical structure of pentacene and its highest molecular orbital (HOMO) calculated from density-functional theory. (**b**) Three-dimensional Fourier transform of the pentacene HOMO orbital, *yellow* (*blue*) showing an isosurface of a constant positive (negative) value. The *red hemisphere* illustrates a region of constant kinetic energy as explained in the text. (**c**) Absolute value of the pentacene HOMO Fourier transform on the hemisphere indicated in panel (**b**)

well-known molecular semiconductor pentacene in a multilayer thin film. Here, we focus on the emission from the HOMO and show that ARPES momentum maps—when compared to calculations—allow for a precise determination of the molecular tilt angle. As a second example, we compare ARPES momentum maps of a monolayer of tetraphenyl porphyrine with calculations of the PE intensity allowing for an identification of the HOMO and HOMO-1 and the determination of the azimuthal molecular orientation. Thirdly, we demonstrate that in certain cases the PW final-state approach enables a reconstruction of real-space orbitals. Here, we show ARPES data of a monolayer of para-sexiphenyl bonded to the Cu(110) surface. Not only are we able to reconstruct a real-space image of the HOMO but we also show that the PE intensity at the Fermi level that appears on adsorption has the orbital structure of the lowest unoccupied molecular orbital (LUMO).

1.4.1 Determination of Molecular Orientations

Pentacene is a planar aromatic molecule consisting of five linearly edge-fused phenyl rings, and has been extensively studied due to its interesting opto-electronic properties. Its electronic structure, in particular the intermolecular HOMO dispersion, has been analyzed by means of both photoemission experiments [26–28] and calculations within the framework of density-functional theory [29–31].

To illustrate the relation between the measured PE intensity and the FT of the emitting orbital, we calculate the electronic structure of an isolated pentacene molecule using DFT [32]. The resulting HOMO orbital is depicted in Fig. 1.2a, and its corresponding three-dimensional FT in Fig. 1.2b. Because the momentum maps are measured at constant binding energy, we evaluate the FT on a hemisphere of radius $k = \sqrt{(2m/\hbar^2)E_{\text{kin}}}$ (indicated in red). The value of the FT on that hemisphere

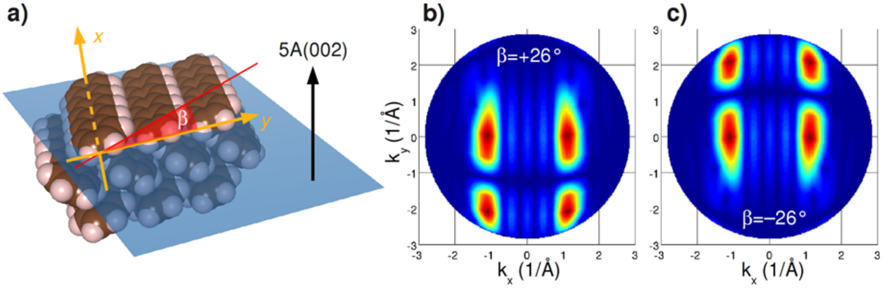

Fig. 1.3 (**a**) Geometry of the (002) plane of pentacene crystal structure exhibiting flat lying molecules with a tilt angle of $\beta = 26°$. (**b**) Simulated Fourier transform of the pentacene HOMO of a molecule with a tilt angle of $\beta = 26°$. (**c**) Same as (**b**) but for a tilt angle of $\beta = -26°$

for a kinetic energy of 29.8 eV is shown in Fig. 1.2c. We observe four main intensity maxima centered around ($k_x = 1.15,\ k_y = 1.2$) Å^{-1} and symmetrically located around the Γ point (normal emission). For emission planes parallel (perpendicular) to the long (short) molecular axis, i.e., in the xz and yz planes, respectively, a vanishing photoemission intensity is predicted. This fact is reflecting the nodal structure of the pentacene HOMO orbital.

When the molecule is vacuum deposited on the p(2x1) oxygen reconstructed Cu(110) surface, its long axis orients parallel to the oxygen rows, resulting in crystalline pentacene(022) films [33] as depicted in Fig. 1.3a. When comparing the theoretical results of Fig. 1.2 with the experimental ARPES data of a multilayer of pentacene grown on a Cu(110)-(2x1)O substrate, one has to consider the orientation of the molecules in this multilayer film. From X-ray diffraction pole-figure measurements [33], the contact plane is determined to be the (022) crystallite orientation. As visualized in Fig. 1.3, this surface termination exhibits molecules with their long axis parallel to the surface but the π face tilted out of the surface plane by an angle of $\beta = 26°$. When this tilt angle is taken into account in the calculation of the Fourier transform, the four main lobes described above are shifted in y direction. This is illustrated in Figs. 1.3b and c, which show the pentacene HOMO of a molecule with a tilt angle of $\beta = 26°$ and $\beta = -26°$, respectively.

In the multilayer film, an effective average of the two molecular orientations, $+26°$ and $-26°$, is to be expected due to the two-fold symmetry of the substrate surface. In Fig. 1.4, we therefore compute an average of the results for $\beta = 26°$ and $\beta = -26°$. Figure 1.4 also shows an experimental momentum map, at the HOMO energy of a pentacene multilayer using a toroidal electron-energy analyzer at the synchrotron radiation facility BESSY II [25]. As a function of the momentum vector parallel to the molecular axis, k_x, there is a pronounced intensity maximum of the photoemission intensity centered at 1.15 Å^{-1}, as observed previously [28]. In the momentum maps, we see that these intense features extend about ± 0.8 Å^{-1} in k_y direction, and, in addition, there are weaker intensity lobes at about the same k_x value around $k_y \approx \pm 2$ Å^{-1}. The comparison between the simulated momentum map (Fig. 1.4a) and the measurement (Fig. 1.4b) is very satisfying. In particular, the

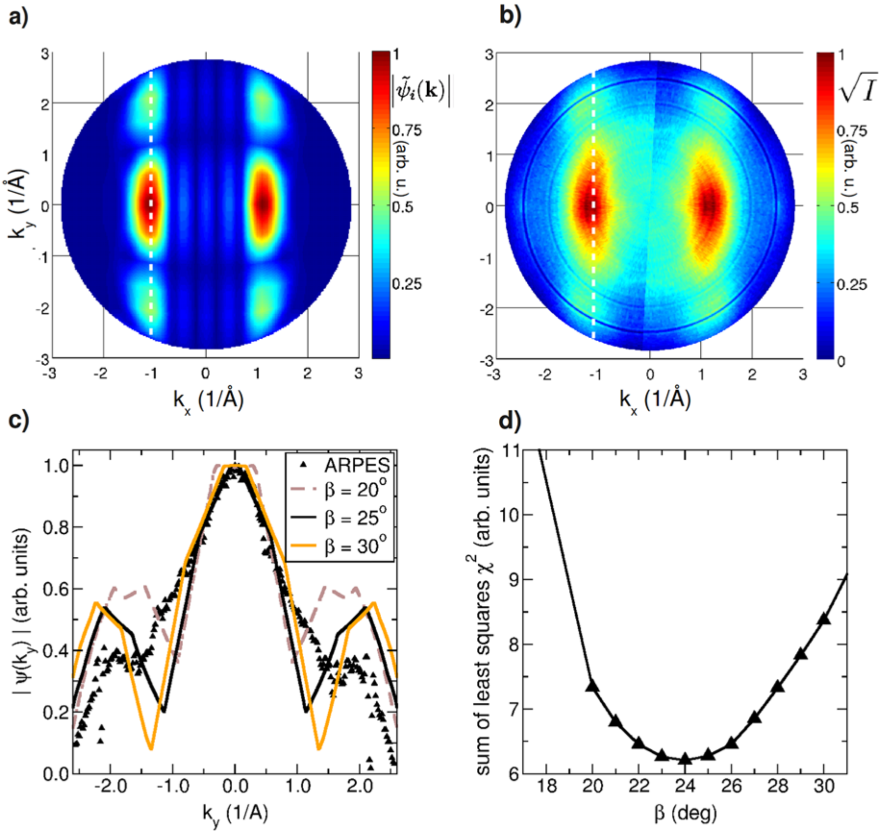

Fig. 1.4 (**a**) The sum of the data shown in Figs. 1.3b and c corresponding to the experimental situation where both tilts will be present. (**b**) Experimental photoemission intensity at a constant binding energy corresponding to the pentacene HOMO from the multilayer of pentacene as described in the text. (**c**) Experimental (*symbols*) vs. theoretical (*lines*) line scans at $k_x = -1.1$ Å as indicated by the *white dashed line* in (**a**) and (**b**). Simulations for three different tilt angles β are shown, 20° (*brown*, *dashed*), 25° (*black*, *solid*), 30° (*orange*). (**d**) Difference between experiment and simulation expressed as the sum of squared differences versus pentacene tilt angle β

maxima at the $k_y = 0$ line are clearly found to originate from the tilt angle of the molecules. Both the strong maxima at $k_y = 0$ and the weak peaks at $k_y = 2$ Å^{-1} result from the out-of-plane tilt angle of the pentacene molecules. Clearly, the FT approach describes the PE intensity well and therefore allows molecular orientations to be determined.

In order to emphasize the sensitivity of the PE intensity on the tilt angle we show a line scan along k_y at constant $k_x = -1.1$ Å as indicated by the white dashed line in Fig. 1.4a. These plots are shown in Fig. 1.4c where we compare the experimental line scan (symbols) with our simulated PE intensity for three different tilt angles β of the pentacene molecule. Clearly, the simulation result for $\beta = 25°$ is in better agreement with the measurement than the computations for 20° and 30°, respectively. In particular, the peak position of the maxima around $k_y \approx \pm 2\ \text{Å}^{-1}$ are shifted to lower (higher) values by decreasing (increasing) the tilt angle. But also the shape of the main feature centered around $k_y = 0$ is reproduced better by the simulation for $\beta = 25°$. To quantify the quality of the simulations for various tilt angles β we also show the sum of the squared differences between the experimental line scans and the simulated ones in Fig. 1.4d. The curve shows a minimum at $\beta = 24°$ which is very close to the value of 26° obtained from X-ray pole-figure measurements on these pentacene multilayer films [33] and assuming the bulk structure from Mattheus and co-workers [34]. Thus, we estimate the accuracy of the ARPES approach to determine molecular tilt angles better than 5°. Compared to alternative methods, such as NEXAFS, the ARPES approach has the added advantage that rather than giving an average orientation, multiple orientations are immediately apparent and can be resolved. Moreover, ARPES works at low photon energies, minimizing damage to the sample, and does not require a tunable photon source.

1.4.2 Identification of Molecular Orbitals

In this section, it is demonstrated how ARPES momentum maps can be utilized to identify molecular states of organic molecules adsorbed on metallic surfaces beyond a simple comparison of calculated orbital energies with energy-distribution curves measured by UPS. As an example, we choose porphyrines which are of interest as versatile materials for organic electronics due to their tendency to form π–π stacked layers. In particular, thin films of tetraphenyl porphyrin, $C_{44}H_{30}N_4$, (H_2TPP) deposited on the oxygen reconstructed Cu(110)-(2x1)O surface have been shown to produce well-ordered, epitaxially aligned porphyrin thin films [35].

As can be seen from Fig. 1.5a, H_2TPP molecules consists of a highly conjugated porphyrin skeleton (macrocycle) in which two hydrogen atoms are attached to two out of four nitrogen atoms sitting in the center of the molecule. The macrocycle is surrounded by four phenyl rings which are tilted out of the porphyrin plane. Figure 1.5 shows the optimized geometry of an isolated H_2TPP molecule as obtained from DFT by using a generalized gradient approximation [36] for exchange-correlation effects together with a density-of-states plot (b) and orbital pictures of the HOMO (c) and HOMO-1 (d). At the GGA-DFT level, the two highest occupied orbitals, the HOMO and HOMO-1, are separated by 0.4 eV followed by two closely spaced states at about 1 eV binding energy. The LUMO is separated from the HOMO by a GGA-DFT gap of about 1.7 eV. Focusing on the HOMO and HOMO-1, we observe distinct nodal patterns which should also be reflected in the respective momentum maps thereby allowing for a clear distinction of these two orbitals. For instance, the HOMO is both symmetric about the xz plane and about the yz plane, while the HOMO-1 is anti-symmetric about these two planes, i.e., exhibits nodal planes in the xz and yz planes.

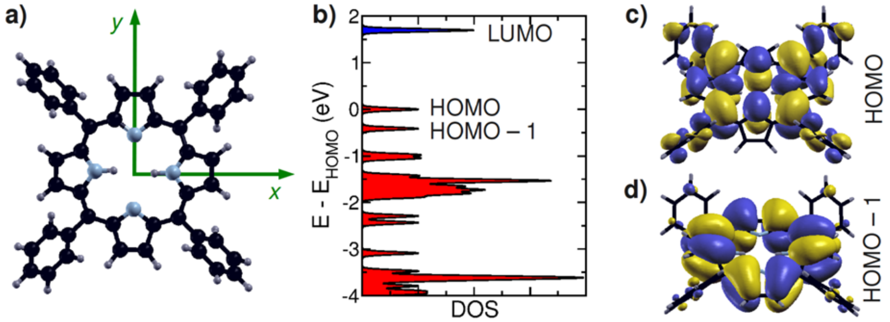

Fig. 1.5 (**a**) Chemical structure of tetraphenyl porphyrine with two hydrogen atoms saturating the bonds at the center of the molecule (H_2TPP). (**b**) Density of states of an isolated H_2TPP molecule as obtained from density-functional theory and a generalized gradient approximation for the exchange-correlation potential. (**c**) and (**d**) are corresponding orbital pictures of the HOMO and HOMO-1 separated by 0.4 eV

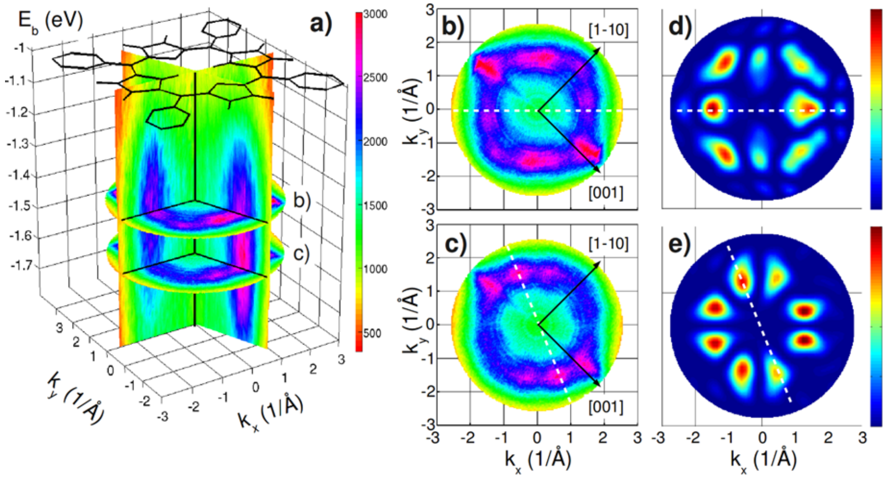

Fig. 1.6 (**a**) Experimental photoemission intensity (*color coded*) of a H_2TPP film as a function of binding energy E_b and momenta k_x and k_y, respectively. Two 'horizontal' sections at constant binding energies, -1.38 and -1.55 eV, as well as two 'vertical' sections at $k_y = 0$ and at an angle of $-22°$ from k_x are shown. Panels (**b**) and (**c**) display those constant binding energy momentum maps corresponding to $E_b = -1.38$ and -1.55 eV, respectively. Panels (**d**) and (**e**) are simulated momentum maps corresponding the H_2TPP HOMO and HOMO-1, respectively

In Fig. 1.6, ARPES data of a thin film of H_2TPP on Cu(110)-(2x1)O with a nominal thickness of 6 Å are compared to simulated momentum maps of the isolated molecule. By using 35 eV photons and the toroidal electron-energy analyzer at BESSY II, an energy window from about -1.0 to -1.8 eV below the Fermi level has been scanned. Further, by collecting electrons with a polar angle span from -70 to $+70°$ and by azimuthally rotating the sample around 180°, a comprehensive data

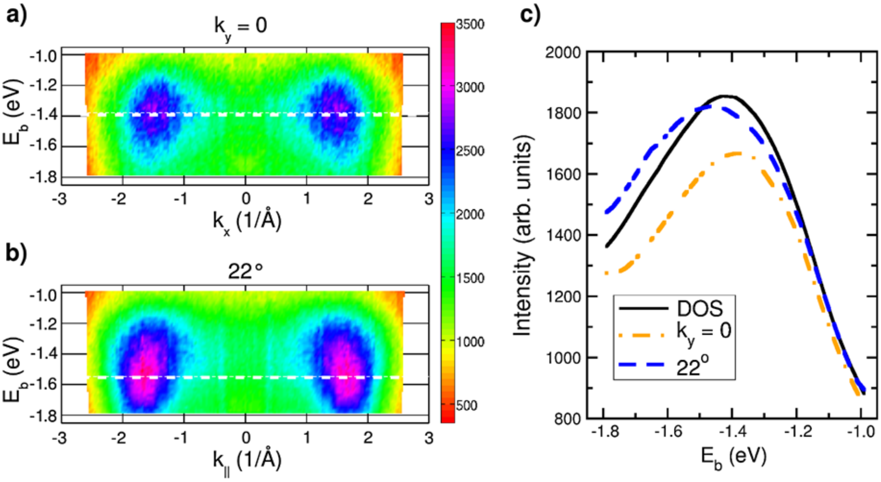

Fig. 1.7 (**a**) Band map of a H_2TPP film in the xz emission plane. (**b**) Same as (**a**) but for an emission plane rotated by $-22°$ with respect to the yz plane as indicated by the 'vertical' sections through the three-dimensional data cube shown in Fig. 1.6. (**c**) Energy-distribution curves (EDC) integrated over the whole k_x–k_y plane (*black line*) as well as for the emission planes shown in (**b**) and (**c**), respectively

set of the photoemission intensity, I, as a function of binding energy E_b and parallel momenta components k_x and k_y has been measured. These ARPES data are visualized in Fig. 1.6a in which the intensity is color-coded and several sections through the data are shown. On the one hand, two 'vertical' sections show the energy and polar angle distribution of the photocurrent for fixed azimuths of the emission plane. These tomographic sections are displayed separately in Fig. 1.7 and are discussed in more detail below. On the other hand, Fig. 1.6a also features two 'horizontal' sections at constant binding energies (CBE), namely at $E_b = -1.38$ and -1.55 eV. For clarity, these CBE momentum maps are also displayed in panels (b) and (c) of Fig. 1.6, respectively. Although quite close in energy, i.e., only 170 meV, the azimuthal intensity distribution appears different. While the map at -1.55 eV exhibits minima along the $k_x = 0$ and $k_y = 0$ directions, the intensity along these directions has clearly increased for the momentum map at -1.38 eV. This is indicative of the distinct symmetries and nodal patterns of the HOMO-1 and HOMO of H_2TPP mentioned earlier.

Indeed, the calculated momentum maps of the isolated molecule's HOMO and HOMO-1 displayed in panels (d) and (e) of Fig. 1.6 also reflect the orbitals' symmetry and their nodal patterns. In addition, also the (k_x, k_y) positions of the intensity maxima can be compared to the measured maps.[1] This comparison lets us conclude that the HOMO of the adsorbed H_2TPP is centered at an energy of -1.38 eV

---

[1] Note that the intensity maxima close to the substrate's [001] direction are due to a measurement artifact, i.e., a reflection of the primary photon beam into the detector.

whereas its HOMO-1 has a peak at a binding energy of -1.55 eV. It is also evident from the 'vertical' sections in Fig. 1.6a that the HOMO and HOMO-1 resonances are observed over several tenth of an eV and are, therefore, overlapping in energy. Hence, both momentum maps at -1.38 and -1.55 eV show contributions from both HOMO and HOMO-1 and the symmetry and nodal patterns cannot be seen as clearly as in the computed, pure maps. But how could we separate these two orbital resonances and assign to them the above mentioned binding energies?

The key are those 'vertical' sections through $I(E_b, k_x, k_y)$ which can be chosen in such a way as to highlight characteristic features of the respective molecular orbitals. For instance, the HOMO is expected to have maxima along k_x as indicated by the white dashed line in panel (b), while the HOMO-1 has a nodal plane in this direction. Therefore, ARPES scans along this azimuth project out contributions of the HOMO. Similarly, the HOMO-1 has intensity maxima for an emission plane rotated by 22° with respect to the k_y axis (dashed line in panel (c)), while the HOMO has almost vanishing intensity along this azimuth. Hence, this azimuth serves as a fingerprint for the HOMO-1. As can be seen from Fig. 1.6a, this allowed us to assign the energies of -1.38 eV and -1.55 eV to the center of the HOMO and HOMO-1 emissions and determine their energy width to be about 0.5 eV. For clarity, the ARPES band maps at the above mentioned azimuthal directions are also reproduced in Fig. 1.7. Panel (c) of this figure also shows the corresponding energy-distribution curves (EDC) integrated over all polar angles, i.e. parallel momentum values, along the k_x axis (red line) and the 22° azimuth with respect to the k_y axis (blue line). Also, these EDCs exhibit different energy peak positions allowing the HOMO and HOMO-1 to be separated. In contrast, an EDC integrated over the full polar and azimuthal angle dependence, i.e., integrated over the k_x–k_y plane (black line), yields a broad and featureless peak with no possibility to discern the contributions from the two involved orbitals. In summary, the characteristic (k_x, k_y)-dependences of molecular emissions allows their energy position and width to be determined beyond the limit of energy resolution. Our data also show that emission planes not carefully chosen may emphasize or suppress particular molecular orbitals due to selection rules inevitably involved in any photoemission process.

We conclude this section by discussing the azimuthal alignment of the H_2TPP molecules with respect to the Cu(110)-(2x1)O substrate. Tacitly, we have been assuming throughout this section that the molecule's (x, y) coordinate frame is rotated by 45° with respect to the principal substrate directions as already indicated in Fig. 1.6 and visualized more clearly in Fig. 1.8. Indeed, there is evidence for such an alignment from X-ray diffraction pole-figure measurements of 370 Å thick film of H_2TPP/Cu(110)-(2x1)O [35]. For these thicker films, the X-ray diffraction showed the $(5\overline{1}\overline{0}3)$ net plane of the triclinic H_2TPP polymorph crystal structure to be parallel to the substrate surface. In this plane, the porphyrin macrocycle is almost parallel to the substrate surface. Moreover, the epitaxial relationships revealed that the molecules are oriented such that the central hydrogens attached to the nitrogen atoms are pointing towards a 45° direction with respect to the [001] substrate axis [35] as also indicated in Fig. 1.8. In addition to this evidence derived from a 370 Å thick film, also the ARPES data for the 6 Å film reveal the identical alignment. As can be seen from Fig. 1.6, the chosen azimuthal orientation maximizes the

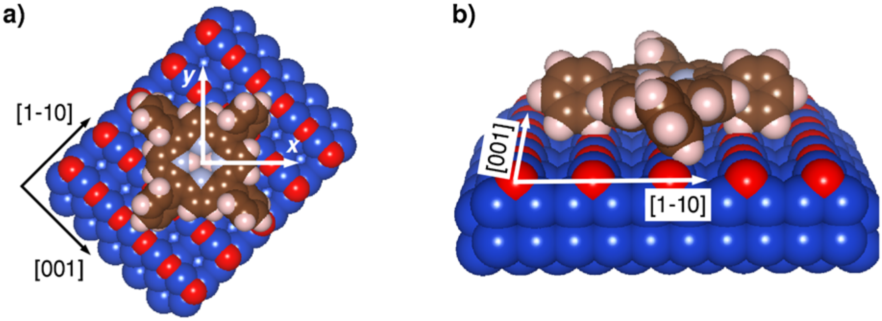

Fig. 1.8 Top (**a**) and side view (**b**) showing the azimuthal alignment of H_2TPP adsorbed on the Cu(110)-(2x1)O substrate. The substrate's [001], i.e., the oxygen row direction, and [1-10] directions are indicated as well as the (x, y) coordinate frame of the molecule which is rotated by 45° about the substrate's principal axes. Copper atoms are colored *dark blue*, oxygens *red*, carbons *dark brown*, nitrogens *light blue*, and hydrogens *light brown*

agreement with the calculated momentum maps for both the HOMO and HOMO-1. Thus, ARPES maps do not only allow molecular emissions to be identified but also enable azimuthal alignments of extremely thin films, down to monolayers, to be determined.

1.4.3 Reconstruction of Molecular Orbitals in Real Space

We continue by demonstrating the viability of the plane-wave approach for both reciprocal space mapping as well as real-space reconstructions of relatively complicated molecular orbitals. Here, we show that this approach allows reconstruction of the orbitals of para-sexiphenyl bonded to the Cu(110) surface. Not only are we able to reconstruct a real-space image of the HOMO but we also show that the PE intensity at the Fermi level that appears on adsorption has the orbital structure of the lowest unoccupied molecular orbital (LUMO).

When deposited on a Cu(110) substrate, sexiphenyl (6P) molecules align with their long molecular axes parallel to the [1-10] azimuth of Cu(110) [37], i.e., parallel to the copper rows and, upon saturation, form a well-ordered monolayer. A structural motif of this adlayer together with the underlying Cu(110) substrate is displayed in Fig. 1.9a. Here, we show the primitive surface unit cell of the saturated adlayer indicated by the blue arrows. This structure has been deduced from both low energy electron diffraction [38] and the STM in Fig. 1.9b. This typical room temperature STM image of a saturated monolayer of sexiphenyl on Cu(110) was obtained with a bias voltage 0.19 V.

In Fig. 1.9c, we show the angle-dependent photoemission of the sexiphenyl monolayer adsorbed on Cu(110) with the emission plane parallel to the long molecular axis. Comparison with equivalent photoemission data for the clean Cu(110) surface identifies the two features indicated by the red arrows as stemming from

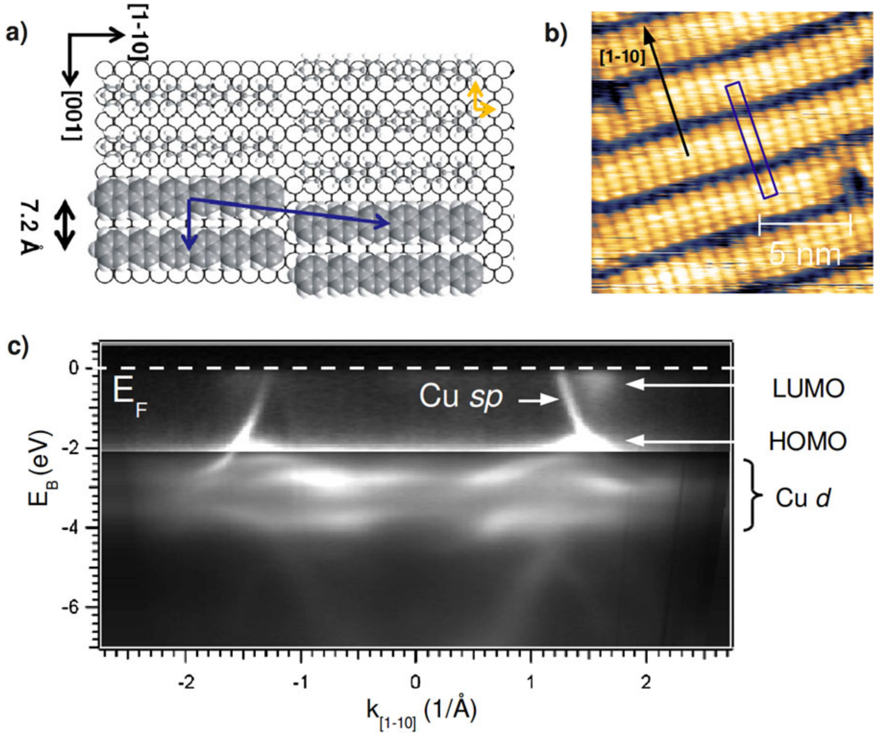

Fig. 1.9 (**a**) Schematic representation of the para-sexiphenyl (6P) monolayer on the Cu(110) surface. The long molecular axis is oriented parallel to the [1-10] direction of the Cu(110) surface, the primitive surface unit cell of the adlayer is indicated by *blue arrows*. (**b**) STM image of the 6P monolayer on the Cu(110) surface. The substrate [1-10] direction is indicated by the *arrow*, and the equivalent centered surface unit cell [c(2x22)] of the 6P adlayer is marked as the *blue rectangle*. (**c**) Angle-resolved photoemission intensity from the 6P monolayer on Cu(110) with an emission plane parallel to the long molecular axis. The *dashed line* indicates the Fermi level and *arrows* point at features that we identify as originating from the sexiphenyl HOMO and LUMO. Between 0 and −2 eV, the *intensity scale* has been magnified for clarity

molecule. The state slightly below the Fermi level is tentatively attributed to the partially filled LUMO, while the newly appearing emission with a binding energy of 1.9 eV is likely due to the sexiphenyl HOMO. The fact that the peaks are at positions in k_x direction which reflect the main spatial periodicity of the sexiphenyl HOMO [39] and LUMO, respectively, is already the first indication for this assignment.

A proof of this assignment can be given by measuring k_x–k_y momentum maps at the constant binding energies corresponding to these features appearing upon adsorption, i.e., at 0.3 and 1.9 eV below the Fermi level. Momentum maps at these two binding energies are shown in Fig. 1.10 and compared to the calculated FTs of the HOMO and LUMO from an isolated 6P molecule (Figs. 1.10c and d). The main characteristics, maxima at $k_x^{\mathrm{HOMO}} \approx \pm 1.45\ \text{Å}^{-1}$ reflecting the spatial periodicity set

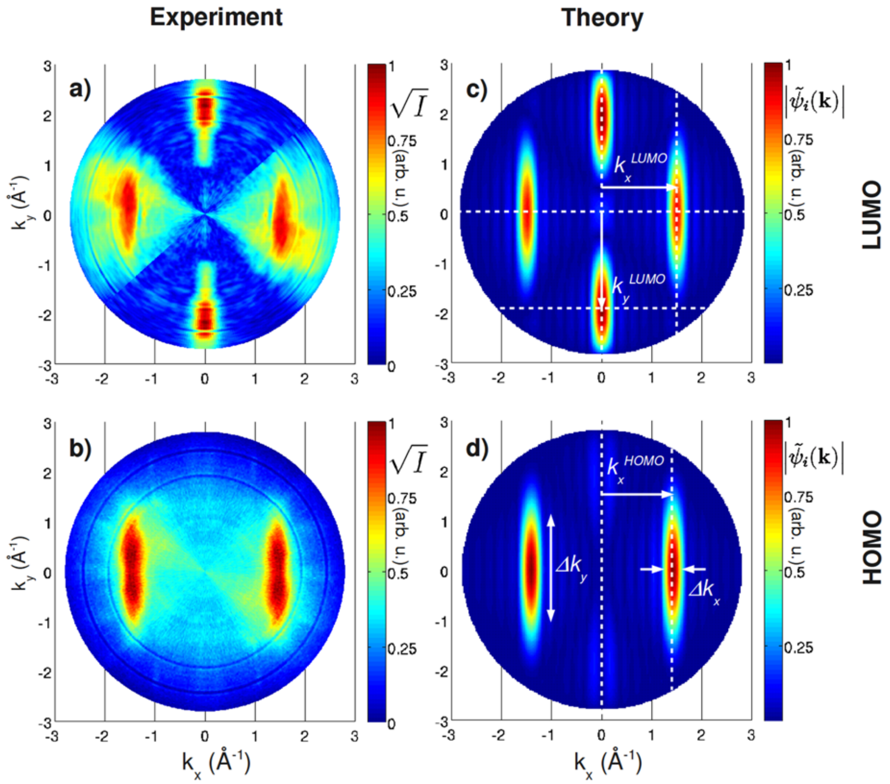

Fig. 1.10 Measured photoemission intensities (*left column*) compared to calculated Fourier transforms (*right column*). (**a**) Photoemission momentum map (square root of the intensity) from a 6P of sexiphenyl on Cu(110) at a binding energy of 0.3 eV corresponding to the 6P LUMO. (**b**) Same as in (**a**) but for a binding energy of 1.9 eV corresponding to the 6P HOMO. (**c**) Absolute value of the Fourier transform of the 6P LUMO calculated for an isolated molecule within DFT. (**d**) Same as in (**c**) but for the sexiphenyl HOMO. Characteristic features in the computed Fourier transforms are indicated by the *white arrows* as described in the text

by the length of one phenyl ring ($2\pi/k_x^{\mathrm{HOMO}} \approx 4.3$ Å) [39], are observed in the data as well as in the calculation. Also, the width Δk_x, which is inversely proportional to the length of the molecule, appears consistent in the PE data. The same holds for the extension in y direction, Δk_y, which is related to the width of a phenyl ring. We take these findings as strong evidence that the molecular feature observed at a binding energy of 1.9 eV can indeed be attributed to the sexiphenyl HOMO and, moreover, that its character is preserved even in a strongly interacting monolayer on a metal surface. In a similar manner, we are able to unambiguously assign the intensity close to the Fermi level to an emission from the filled LUMO (Fig. 1.10a and c). This emission thus indicates electron transfer from the metal into the former LUMO of the isolated molecule: as was the case for the HOMO, the nodal structure of the LUMO is found to be preserved on adsorption. Thus, we see that PE momentum

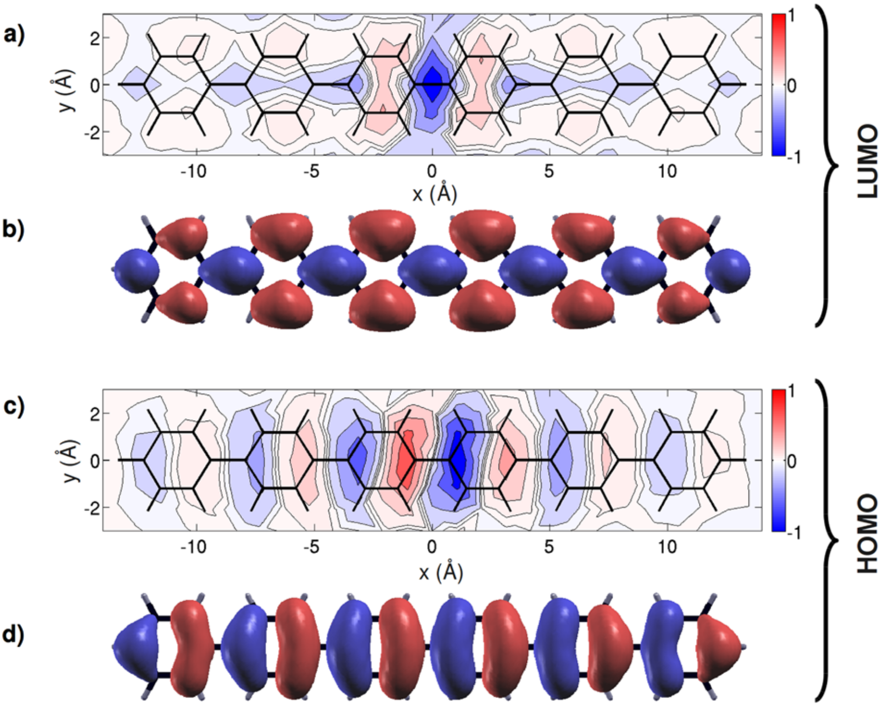

Fig. 1.11 Molecular orbitals reconstructed from photoemission data compared to DFT orbitals. (**a**) The 6P LUMO reconstructed from the PE momentum map at a binding energy of 0.3 eV. (**b**) LUMO of an isolated 6P molecule from DFT. (**c**) The HOMO of sexiphenyl reconstructed from the momentum map at a binding energy of 1.9 eV. (**d**) LUMO of an isolated 6P molecule from DFT. Experimentally determined orbitals are displayed as density plots where *red* (*blue*) *colors* indicate positive (negative) values isolines are added for clarity. The DFT orbitals are represented as isosurface plots using the same color code. The molecular backbone is indicated by *black lines*

maps provide fingerprints of molecular states allowing for their unique identification even in cases where there is a rather strong bonding interaction.

The ability to reproduce the PE momentum maps with Fourier transforms of the initial-state wave functions encouraged us to reconstruct real-space images of the molecular orbital densities from the experimental photoemission data. According to Eq. (1.2) we take the square root of the PE data and divide it by the polarization factor $|\mathbf{A} \cdot \mathbf{k}| \propto |\sin\theta \cos\chi - \cos\theta \sin\chi|$. Restricting the data to positive k_x values and considering the incidence angle $\chi = -40°$ of the p-polarized photons, this function has a maximum for a take-off angle $\theta = 50°$ and a minimum value of 0.64 at normal emission. Before performing the inverse FT of the processed PE data we mirror the data to the negative k_x plane and change their sign (or leave it unchanged) according to the parity of the wave function which is even (odd) for the HOMO (LUMO). By the latter procedure we restore phase information on the wave function to facilitate the comparison with calculated orbitals. The inverse Fourier transforms of the PE data for the adsorbed sexiphenyl HOMO and LUMO are compared with the DFT calculated orbitals of the isolated molecule in Fig. 1.11. Spatial periodicities and nodal structure are well-conserved across theory and experiment. Because the resolution Δx in the reconstructed images is inversely proportional to the plane-wave cut-off k_{max} (thus $\Delta x = \pi / k_{\mathrm{max}}$), kinetic energies of around 30 eV as used in our experiments lead to $\Delta x \approx 1$ Å.

Compared to the DFT orbitals, both the HOMO and LUMO electron densities obtained from photoemission are more weighted around the center of the molecule, a distinction we tentatively attribute to the interaction with the Cu surface. Indeed, in sexiphenyl charge transfer salts the local distortions and the transferred electrons are located around the center of the molecule [40]. Furthermore, although STM images typically do not match molecular orbital images exactly, an STM image of a monolayer of sexiphenyl adsorbed on Cu(110) does show an electron density distribution that is weighted towards the center of the molecules (Fig. 1.9). Nonetheless, we feel that improvements in the PE signal-to-background ratio are necessary before any strong conclusions can be reached concerning the extent of orbital distortion introduced by the metal surface.

1.5 Conclusion

We have demonstrated that the simple relation between the photoemission intensity and the Fourier transform of the molecular orbital can be a valuable tool for the investigation of organic molecular films and their interfaces with metallic surfaces. We envision a wide applicability of the presented approach for studying the valence-band electronic structure of organic molecular films, particularly with the latest generation of angular-resolved display-type electron spectrometers. This may not only lead to a renaissance of angle-resolved photoemission spectroscopy in the field of organic electronics, but it also provides stringent tests for further development of accurate electronic-structure calculations.

Acknowledgements We acknowledge financial support from the Austrian Science Fund (FWF), projects S97-04, S97-14, P21330-N20, and P23190-N16. We further acknowledge the Helmholtz-Zentrum Berlin - Electron storage ring BESSY II for provision of synchrotron radiation at beamline U125/2-SGM and in particular thank Dr. Christian Schüssler-Langeheine for assistance. We would also like to thank Prof. Falko P. Netzer and Prof. Thomas Seyller for discussions. The research leading to these results has received funding from the European Community's Seventh Framework Programme (FP7/2007-2013) under grant agreement number 226716.

References

1. N. Ueno, S. Kera, Prog. Surf. Sci. **83**, 490 (2008)
2. J. Repp, G. Meyer, S.M. Stojkovic, A. Gourdon, C. Joachim, Phys. Rev. Lett. **94**, 026803 (2005)
3. A. Kraft, R. Temirov, S.K.M. Henze, S. Soubatch, M. Rohlfing, F.S. Tautz, Phys. Rev. B **74**, 041402(R) (2006)

4. R. Temirov, S. Soubatch, A. Luican, F.S. Tautz, Nature **444**, 350 (2006). doi:10.1038/nature05270
5. J. Kröger, H. Jensen, R. Berndt, R. Rurali, N. Lorente, Chem. Phys. Lett. **438**, 249 (2007)
6. I. Torrente, K. Franke, J. Pascual, J. Phys. Condens. Matter **20**, 184001 (2008)
7. S. Soubatch, C. Weiss, R. Temirov, F. Tautz, Phys. Rev. Lett. **102**, 177405 (2009)
8. W.H.E. Schwarz, Angew. Chem., Int. Ed. Engl. **45**, 1508 (2006). doi:10.1002/anie.200501333
9. R. Temirov, S. Soubatch, O. Neucheva, A.C. Lassise, F.S. Tautz, New J. Phys. **10**, 053012 (2008). doi:10.1088/1367-2630/10/5/053012
10. S. Hüfner, *Photoelectron Spectroscopy* (Springer, Berlin, 2003)
11. S. Kera, S. Tanaka, H. Yamane, D. Yoshimura, K. Okudaira, K. Seki, N. Ueno, Chem. Phys. **325**, 113 (2006). doi:10.1016/j.chemphys.2005.10.023
12. P. Puschnig, S. Berkebile, A.J. Fleming, G. Koller, K. Emtsev, T. Seyller, J.D. Riley, C. Ambrosch-Draxl, F.P. Netzer, M.G. Ramsey, Science **326**, 702 (2009). doi:10.1126/science.1176105
13. F. Himpsel, J. Electron Spectrosc. Relat. Phenom. **183**, 114 (2011). doi:10.1016/j.elspec.2010.03.007
14. J. Ziroff, F. Forster, A. Schöll, P. Puschnig, F. Reinert, Phys. Rev. Lett. **104**(23), 233004 (2010). doi:10.1103/PhysRevLett.104.233004
15. J.E. Ortega, S. Speller, A.R. Bachmann, A. Mascaraque, E.G. Michel, A. Närmann, A. Mugarza, A. Rubio, F.J. Himpsel, Phys. Rev. Lett. **84**(26), 6110 (2000). doi:10.1103/PhysRevLett.84.6110
16. A. Damascelli, Phys. Scr. T **109**, 61 (2004)
17. P.J. Feibelman, D.E. Eastman, Phys. Rev. B **10**, 4932 (1974)
18. J.W. Gadzuk, Phys. Rev. B **10**, 5030 (1974). doi:10.1103/PhysRevB.10.5030
19. T. Permien, R. Engelhardt, C.A. Feldmann, E.E. Koch, Chem. Phys. Lett. **98**, 527 (1983)
20. N.V. Richardson, Chem. Phys. Lett. **102**, 390 (1983)
21. W.D. Grobman, Phys. Rev. B **17**, 4573 (1978). doi:10.1103/PhysRevB.17.4573
22. S.M. Goldberg, C.S. Fadley, S. Kono, Solid State Commun. **28**, 459 (1978)
23. E.L. Shirley, L.J. Terminello, A. Santoni, F.J. Himpsel, Phys. Rev. B **51**, 13614 (1995)
24. H. Daimon, F. Matsui, Prog. Surf. Sci. **81**, 367 (2006)
25. L. Broekman, A. Tadich, E. Huwald, J. Riley, R. Leckey, T. Seyller, K. Emtsev, L. Ley, J. Electron Spectrosc. Relat. Phenom. **144–147**, 1001 (2005). doi:10.1016/j.elspec.2005.01.022
26. N. Koch, A. Vollmer, I. Salzmann, B. Nickel, H. Weiss, J.P. Rabe, Phys. Rev. Lett. **96**, 156803 (2006). doi:10.1103/PhysRevLett.96.156803
27. H. Kakuta, T. Hirahara, I. Matsuda, T. Nagao, S. Hasegawa, N. Ueno, K. Sakamoto, Phys. Rev. Lett. **98**, 247601 (2007). doi:10.1103/PhysRevLett.98.247601
28. S. Berkebile, P. Puschnig, G. Koller, M. Oehzelt, F.P. Netzer, C. Ambrosch-Draxl, M.G. Ramsey, Phys. Rev. B **77**, 115312 (2008)
29. M.L. Tiago, J.E. Northrup, S.G. Louie, Phys. Rev. B **67**, 115212 (2003)
30. K. Hummer, C. Ambrosch-Draxl, Phys. Rev. B **72**, 205205 (2005)
31. D. Nabok, P. Puschnig, C. Ambrosch-Draxl, O. Werzer, R. Resel, D.M. Smilgies, Phys. Rev. B **76**, 235322 (2007). doi:10.1103/PhysRevB.76.235322
32. X. Gonze, J.M. Beuken, R. Caracas, F. Detraux, M. Fuchs, G.-M. Rignanese, L. Sindic, M. Verstraete, G. Zerah, F. Jollet, M. Torrent, A. Roy, M. Mikami, P. Ghosez, J.Y. Raty, D.C. Allan, Comput. Mater. Sci. **25**, 478 (2002)
33. M. Koini, T. Haber, O. Werzer, S. Berkebile, G. Koller, M. Oehzelt, M. Ramsey, R. Resel, Thin Solid Films **517**, 483 (2008). doi:10.1016/j.tsf.2008.06.053
34. C.C. Mattheus, A.B. Dros, J.B.A. Meetsma, J.L. de Boer, T.T.M. Palstra, Acta Crystalogr. C **57**, 939 (2001)
35. T. Djuric, T. Ules, S. Gusenleitner, N. Kayunkid, H. Plank, G. Hlawacek, C. Teichert, M. Brinkmann, M.G. Ramsey, R. Resel, Phys. Chem. Chem. Phys. (2011, submitted)
36. J.P. Perdew, K. Burke, M. Ernzerhof, Phys. Rev. Lett. **77**, 3865 (1996)
37. M. Oehzelt, L. Grill, S. Berkebile, G. Koller, F.P. Netzer, M.G. Ramsey, Chem. Phys. Chem. **8**, 1707 (2007). doi:10.1002/cphc.200700357

38. S. Berkebile, T. Ules, P. Puschnig, L. Romaner, G. Koller, A.J. Fleming, K. Emtsev, T. Seyller, C. Ambrosch-Draxl, F.P. Netzer, M.G. Ramsey, Phys. Chem. Chem. Phys. **13**, 3604 (2011). doi:10.1039/C0CP01458C
39. G. Koller, S. Berkebile, M. Oehzelt, P. Puschnig, C. Ambrosch-Draxl, F.P. Netzer, M.G. Ramsey, Science **317**, 351 (2007). doi:10.1126/science.1143239
40. M.G. Ramsey, M. Schatzmayr, S. Stafström, F.F.P. Netzer, Europhys. Lett. **28**, 85 (1994)

Part II
Growth Model and Interfaces

Chapter 2
Pre-nucleation and Growth of Self-assembling Organic Molecule Crystals

Alexander J. Fleming and Michael G. Ramsey

Abstract The self-assembly of the prototypical organic molecule sexiphenyl (6P) into ordered molecular crystals is examined on two different types of surface. It is shown that new measurements taken during the pre-nucleation deposition period using Photoemission Electron Microscopy (PEEM) can explain the different preferred orientations of the molecular crystals observed for each substrate. The strength of molecule-substrate interaction (adjusted by using two different substrates: metal Cu (110) and oxide-covered metal Cu (110) $2 \times 1 - \mathrm{O}$ surfaces) is shown to determine the final molecular crystal orientation ((20-3) needles and (21-3) crosses, respectively). Measurements of molecular diffusion anisotropy and temperature dependence using PEEM are presented that support the finding that, in both cases, the preferred critical nuclei orientation is (20-3) and that only post-nucleation processes that occur exclusively in the case of 6P deposited on the Cu (110) substrate, lead to a change to the (21-3) orientation. Nucleation energies measured using PEEM show, in both cases, a nearly identical value of 950 meV. This confirms that the two structures observed, needles and crosses, both start from identical (20-3) critical nuclei; and it is the latter that is caused by nuclei continuing to grow in the presence of a molecular reconstructed layer in the post-nucleation deposition period.

Self-assembly is a general term used to describe the growth of ordered structures which emerge over time from a disordered reservoir/collection of building blocks (molecules) [1]. For the organic electronics industry it promises to be the most efficient way to achieve bottom-up construction—as inferred from the plurality of self-assembled complex molecular structures that are ubiquitous in nature. A major hurdle though is that the degree of control demonstrated by nature, however desirable, still remains poorly understood. Our approach to improve our understanding is to distil the complexity of natural self-assembly processes into controllable model systems that can be investigated in the laboratory [2]. A good approach, such as

---

A.J. Fleming (✉) · M.G. Ramsey
Surface and Interface Physics, Institute of Physics, Karl-Franzens University Graz,
Universitätsplatz 5, 8010 Graz, Austria
e-mail: sandy_fleming@yahoo.com

H. Sitter et al. (eds.), *Small Organic Molecules on Surfaces*,
Springer Series in Materials Science 173, DOI 10.1007/978-3-642-33848-9_2,

depositing synthetic molecules on atomically clean metal crystal surfaces in ultra-high-vacuum, sets a well defined environment for experimentation. A careful choice of molecule and substrate can ensure that a good yield of identical self-assembled structures of a single type form on the surface is obtained. This is desirable, since it reduces the number of possible mechanisms that must be examined and it demonstrates that the self-assembly process, although unknown, is at least under control. In this chapter, growth of a proto typical linear conjugated molecule on two different surfaces is presented. Many interesting dynamic phenomena are highlighted that explain the growth at different stages of the self-assembly process.

Numerous studies conducted on sexiphenyl (6P) to date, such as electronic band formation [3, 4] and doping [5, 6], have demonstrated that this molecule is exceptionally well suited to be a text book example of organic molecule phenomenology in the condensed phase. Our focus recently has been to comprehensively explain growth phenomena of 6P [7]. Having accrued many years of experience preparing high quality single crystals of 6P on surfaces for various electron spectroscopy [8, 9] and surface probe techniques [10, 11], we have with our detailed in-situ growth study by photoemission electron microscopy (PEEM), systematically examined the three growth processes: pre-nucleation, nucleation and 3D growth [12]. The process of molecular crystal growth can be observed by various techniques after nucleation has begun, however, our emphasis here will be to highlight the crucial events that occur prior to nucleation and their importance in determining final crystal morphologies. PEEM has been used previously to observe the growth of pentacene [13] on SiO_2, chloroaluminium phthalocyanine on MoS_2 film [14], anthracence on Si(111) [15], PTCDA on Ag (111) [16] and to study the dynamic CO oxidation on platinum [17] and other dynamic processes [18].

Anisotropic properties of surfaces and molecules are of particular interest in the development of low-dimensional molecular nanostructures. Needles are a common type of nanostructure that is routinely observed when anisotropic molecules are deposited on anisotropic surfaces. For instance 6P deposited on TiO2 (110) [19], Mica [20], Cu (110) and Cu (110) $2 \times 1 - O$ [7, 10] will self-assemble into nanoneedles. Furthermore, in terms of the self-assembly sequence of events, the choice of an anisotropic molecule/substrate combination permits the decoupling of the description of molecular interactions into two separate directions: (a) parallel direction and (b) perpendicular direction to the atomic surface corrugation. Although this decoupling will be shown to facilitate our understanding of the assembly process, the extended and linear shape of 6P molecules interacting with an anisotropic surface means that a standard hard-sphere atomistic approximation [21] is really not applicable. Likewise, classical nucleation theory, an effective tool in predicting growth behaviour, does not deal with the underlying kinetic mechanisms of growth [22]. Therefore, for our interpretation, we rely on trends observed from our data and some well founded assumptions of nucleation theory to propose and/or exclude possible growth mechanisms. This is aided by the fact that fully grown 6P nanostructures, identical to those presented here, have previously been characterised in terms of their geometric and electronic structure, through various static techniques such as NEXAFS [4], STM [10], RDS [23, 24] and ARUPS [8].

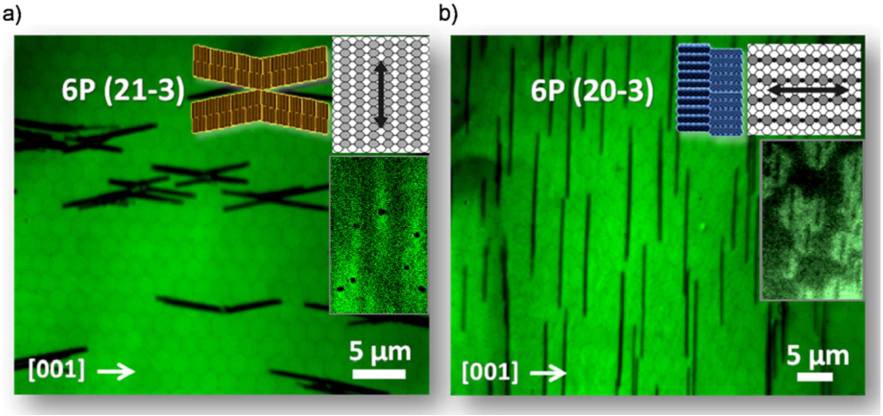

Fig. 2.1 PEEM image of two types of 6P self-assembled nanostructure that forms when 6P is deposited on (**a**) Cu (110) and (**b**) Cu (110) 2 × 1 – O surfaces. Typical heights of the nanostructures are in the range 50–500 nm. *Insets*: top view of crystalline structure of the nanostructures grown and top view of the Cu (110) and Cu (110) 2 × 1 – O substrates with *arrows* indicating surface corrugation direction (both surfaces are anisotropic and the surface corrugations are orthogonally oriented with respect to the other). PEEM images of nucleation induced dewetting demonstrate the different anisotropies of the surfaces

When 6P (also known as hexaphenyl and p6P) molecules are deposited on Cu (110) and Cu (110) 2 × 1 – O surfaces, two different 6P nanostructures form as shown in Fig. 2.1(a) and (b), respectively. The differences in structure are due to changes to the surface by the formation of the 2 × 1 – O reconstruction. These changes lead to a rotation of the molecular long axis by 90° and dissimilar dewetting phenomena as shown in the insets of Fig. 2.1(a) and (b). As with many weakly bound organic crystals of short chain-like molecules, 6P readily nucleates into an energetically stable herring-bone crystalline structure. When 6P nucleates on a surface, a combination of kinetics and energetics determines which plane of the molecular herring-bone crystal contacts the substrate surface. In Fig. 2.2, several relevant crystal contact planes of a 6P crystal are given. It is important to note that the molecular orientation with respect to the crystal plane can be described as tilted, flat, or combinations of tilted and flat. When 6P is deposited on weakly interacting anisotropic substrates (Cu (110) 2 × 1 – O, TiO_2 and organic crystals) a tilted wetting layer covers the surface [4, 7, 8, 11]. On top of this tilted wetting layer all subsequent molecules arrange into crystals with the (20-3) plane contacting the wetting layer. On the other hand, when 6P is deposited on stronger interacting substrates [10, 23] (Cu (110) and Al (111)) a flat-lying wetting layer covers the surface). On top of this wetting layer crystals grow with alternate layers arranged in tilted/flat/tilted intralayer orientations. This corresponds to the (21-3) or (-629) crystal plane contacting the flat-lying wetting layer. Henceforth 6P nanostructures are described as (21-3) crystals on Cu (110) and (20-3) crystals on Cu (110) 2 × 1 – O.

Highly ordered and aligned molecular crystallites form when 6P molecules are deposited on Cu (110) and Cu (110) 2 × 1 – O. Templating of the first molecular

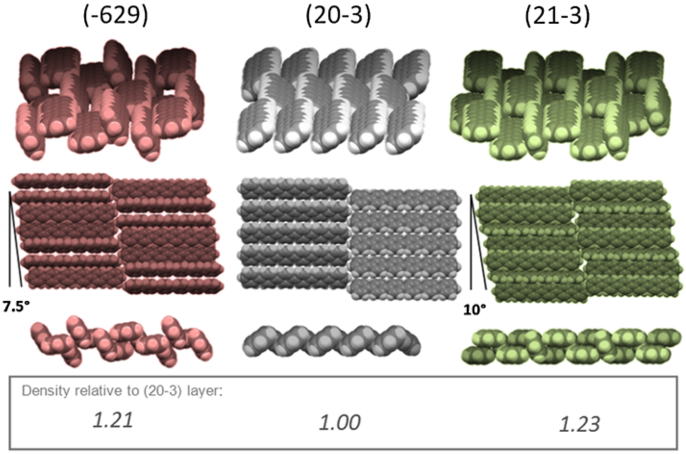

Fig. 2.2 Stereoscopic, top and side views of some commonly observed 6P crystallite orientations where the molecular axes are parallel to the substrate: crystal planes (-629), (20-3) and (21-3) of the 6P herring-bone crystal. The surface densities required for *full-coverage* for each plane relative to the (20-3) crystal plane are given in italics

layer by the metal surface corrugation into an ordered and aligned layer, leads to anisotropic surface diffusion of molecules and anisotropic crystallite growth. Shown in Fig. 2.1 are typical examples of the different nanostructures that form when 6P is deposited Cu (110) and Cu (110) at 140 °C. Straight (20-3) needles form when 6P is deposited on Cu (110) 2 × 1 – O, whereas crossed (21-3) needles form when 6P is deposited on Cu (110). It is the binding/sticking anisotropy of linear 6P molecules which results in a preferred co-facial stacking. Hence upon stacking, crystallites grow perpendicular to the molecular orientation within the molecular crystal [11]. As will be shown later, this growth direction is also perpendicular to the fastest molecular diffusion direction.

It will also be shown that although the deposition of 6P on both substrates results in entirely different molecular crystal orientation growth ((20-3) versus (21-3)) during the post-nucleation deposition period, during the time defined by the pre-nucleation deposition period there are some remarkable similarities. These include the gradual filling of meta-stable layers to a similar density of tilted molecules followed by the formation, in *both cases*, of (20-3) critical nuclei. Although this may seem counter-intuitive, it is only after nucleation that differences start to become apparent.

2.1 Experimental Methodology

The experiments were performed in a custom-designed, combined Omicron VT-AFM/scanning tunnelling microscopy (STM)-PEEM UHV instrument with a base pressure $< 2 \times 10^{-10}$ mbar. The Cu (110) crystal was cleaned in five steps, namely

(a) flashing of the crystal to above the desorption temperature of 6P (>220 °C) to reduce the amount of 6P on the crystal before sputtering, (b) Ar^+ sputtering (10 μA, 1.5 kV, 45 min) followed by (c) annealing for 5 min at 500 °C (d) cooling in oxygen partial pressure at 5×10^{-7} mbar for 5 min and (e) flashing to 500 °C. Several cycles of the cleaning steps (b) through to (e) were performed with the final cleaning cycle omitting (d) and (e). These cleaning steps result in a Cu (110) surface. To form the $2 \times 1 - O$ reconstruction 50 L of O_2 are dosed in the chamber at 2×10^{-7} mbar. Following cleaning, the sample was transferred, via a magnetically coupled transfer rod, to the PEEM.

The molecular evaporator, mounted in-situ and facing the sample holder of the PEEM, consists of a Knudsen type effusion cell resistively heated by current supplied to a filament by a constant-current source. The 6P in powder form, supplied by TCI chemicals (Japan) and introduced previously into the Knudsen cell, is degassed thoroughly by extended heating just below the sublimation temperature of 6P. The first few 6P films deposited are not used for measurements. There is no quartz thickness monitor available due to space restrictions so no instantaneous deposition rate monitoring is possible. However, the constant-current supply allows the heating of the evaporator to be stabilised to a given temperature, which when combined with the accurate photoemission intensity versus time curves (see results) allows for an accurate a posteriori calculation of the stabilised deposition rate. Typical deposition rates of molecules are between 0.25 to 1 ML min^{-1}. However, it will be shown that the deposition rate does not influence the layer filling in the time-scales explored during deposition. Unless otherwise stated, the molecular evaporator shutter is open throughout the entire deposition. After nucleation, and once dewetting is complete, the shutter is opened and closed periodically to probe molecular surface diffusion.

PEEM measurements were carried out using a FOCUS/Omicron PEEM instrument in high magnification mode using a Mercury HBO 103W/2 discharge lamp (maximum of $h\nu = 4.9$ eV) for illumination at angle of incidence of 25°. For the molecule/substrate combination used here the image contrast in PEEM makes use of laterally distributed local workfunction differences that result in varying yields of photoelectrons. In threshold mode, the ionisation potential of 6P (6.12 eV) is too large for the Hg lamp excitation source (4.9 eV) thus no photoemission is observed from 6P. However, the workfunction of the metal substrate is less than 4.9 eV, therefore photoemission from the metal surface is observed. Depositing 6P (a dielectric) on to the metal substrate reduces the surface dipole component of the metal surface workfunction and hence the photoemission intensity increases. However, once the first monolayer is complete no more changes to the surface dipole of the metal occur so any further molecules deposited do not change the workfunction but instead attenuate the photoemission originating from the metal. The attenuation is due to inelastic scattering of photoelectrons by 6P molecules (the electronic bandgap is ~ 3.9 eV). An aperture size of 50 μm together with a fully open iris gave the optimal resolution for images with a pre-calibrated (in-house) field-of-view of 20–70 μm. Extractor voltages of 10.5–13.5 kV were employed, with a sample-extractor distance of 1.8 mm. No adverse effects, such as decomposition or desorption, arising from the UV light or high electric field were observed for 6P on Cu (110). Photoelectron intensities plotted in the results section were acquired directly from intensity averaged areas of the PEEM images. Area-averaging of the intensity works well up to the point when dark structures form on the surface (nucleation). Once dark structures start growing, area-averaging the intensity to determine the surface molecular density will become distorted by the coverage of three-dimensional dark structures. At 140 °C the ratio of dark structures to bright area is small; therefore the error introduced is also small. A video camera exposure time of 500 ms at an acquisition rate of 2 Hz was found to be adequate to monitor dynamic processes on the surface. In-situ sample heating was achieved by indirect heating with a filament following a pre-determined and calibrated temperature-time curve.

To observe dynamic changes in surface molecular density during the pre-nucleation deposition period, some post-processing of PEEM images is required. First all PEEM images of a video sequence are normalised to the average intensity of the first image (clean surface before deposition) and batch processed to produce a difference image sequence with respect to the first image. Furthermore, any contrast enhancement observed can be quantised by batch processing PEEM image sequence to determine the intensity r.m.s. deviation for each image and plot it versus deposition time.

2.2 PEEM Photoemission Intensity Time Plots

Typical area-averaged photoemission intensity versus time plots which correspond to 6P deposited on (a) Cu (110) $2 \times 1 - \mathrm{O}$ and (b) Cu (110) are given in Fig. 2.3. Both plots undergo a similar general trend which involves (1) a sharp rise in intensity, (2) a maximum with a subsequent decrease in intensity (this decrease is more prolonged for 6P on Cu (110) since more molecules must be deposited), and (3) upon reaching a critical deposited amount, a sharp cusp followed by a constant gentle rise in intensity thereafter. The transition from increasing to decreasing photoemission intensity upon completion of the first layer is a general characteristic of photoemission obtained in the threshold regime.

To facilitate comparison, the photoemission intensity curves, shown in Fig. 2.3, are double normalised to the maximum intensity and to one complete monolayer as explained in more detail in Fleming et al. [7]. To facilitate interpretation of the double normalised plots, the inset in Fig. 2.3 is a plot of the same data where the normalised photoemission intensity is plotted versus the total surface density of molecules deposited. This better illustrates how more material must be deposited to form a *tilted* first layer on Cu (110) $2 \times 1 - \mathrm{O}$ compared to a *flat-lying* first layer on Cu (110). A noticeable difference between the evolution of the photoemission intensity for 6P on Cu (110) and 6P on Cu (110) $2 \times 1 - \mathrm{O}$ up to 1 ML deposited material, is the presence of a rearrangement kink at ~ 0.2 ML in the double normalised plot for 6P deposited on Cu (110) $2 \times 1 - \mathrm{O}$. A kink describes a sudden change in the rate of intensity increase/decrease with deposition time. Thus during the initial deposition of 6P on Cu (110) $2 \times 1 - \mathrm{O}$, PEEM correctly indicates that the dilute layer undergoes a rearrangement from flat-lying to tilted 6P orientation

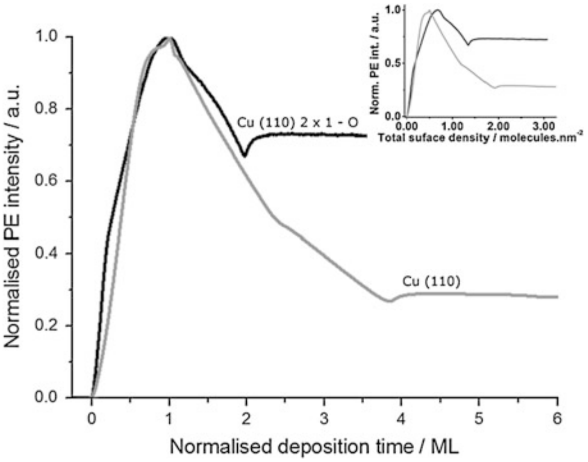

Fig. 2.3 Normalised area-averaged photoemission intensity versus normalised time for 6P deposited on Cu (110) 2 × 1 – O at 140 °C (*black line*) and on Cu (110) at 125 °C (*grey line*). *Inset*: Same data re-plotted with normalised intensity as a function of total surface molecular density

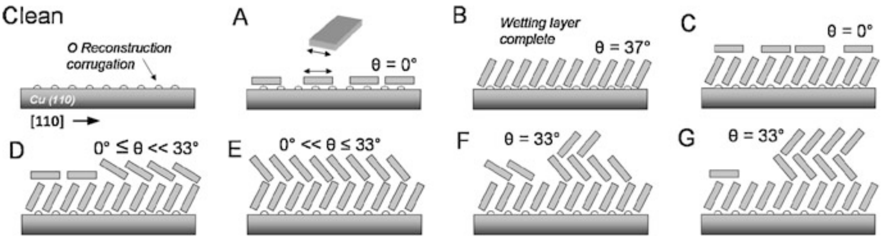

Fig. 2.4 Schematic diagram of 6P molecular layers on Cu (110) 2 × 1 – O during the pre-nucleation deposition period illustrating (molecular end-on view only) the various orientations and packing changes that explain the shape of the photoelectron intensity versus normalised time plot. The short axis of the 6P molecule is illustrated by a *double-headed arrow*. Critical nucleation begins at F. The packing angle θ is the angle between the molecular short axis and the surface. The O induced corrugated surface reconstruction is indicated by showing the end atoms of extended O *rows* (which run into and out of the printed page in the [001] crystal direction). Distance between adjacent rows is 5.1 Å

(Fig. 2.4 A and B). This agrees with the observation, from STM [8] and LEED, that the 6P wetting layer molecules are tilted at an angle of 37° with respect to the surface. It can therefore be deduced from the monotonic intensity increase during the initial deposition of 6P on Cu (110) (i.e. without a rearrangement kink between 0 ML and 1 ML) that molecules in the wetting layer remain flat-lying (Fig. 2.5 a) throughout first layer formation. This is supported by STM [10] and valence-band photoemission [3, 8] of the wetting layer, which shows that the wetting layer consists of flat-lying 6P molecules strongly bound to the surface. Thus, unlike with Cu (110) 2 × 1 – O, no change in tilt is observed nor expected for the first layer deposition.

During second layer filling, on the other hand, photoemission intensity decrease of both systems are not monotonic. The rearrangement kinks, observed at ~ 1.2 ML for 6P deposited on Cu (110) 2 × 1 – O and at ~ 1.1 ML for 6P deposited on

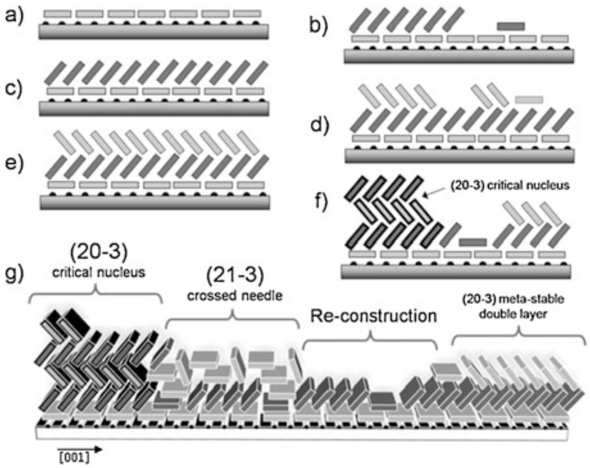

Fig. 2.5 Schematic of the filling scheme for 50–125 °C for 6P deposited on Cu (110). (**a**) Wetting layer completion (first layer). (**b**) Condensation at steps of incomplete second layer. Molecules diffuse flat then join subcritical (20-3) tilted second layer that extends over the terraces from the steps. (**c**) Completion of second layer for 50–125 °C. The interaction with the wetting layer beneath prevents critical nucleation from occurring. (**d**) Partial condensation at steps by incomplete third layer due to coupling with tilted second layer to form a double meta-stable layer. (**e**)–(**f**) Critical surface density reached when a third layer can spontaneously form large enough nuclei that no longer require kinetic stabilisation and are thus energetically stable. This leads to dewetting of the double layer of tilted molecules surrounding the critical nucleus. (**g**) Sketch showing the dewetting induced spontaneous reconstruction of the double tilted layer into channels that include flat lying molecules. These channels, visible in Fig. 2.7(a), run in to and out of the page. The effect of the reconstruction is to force molecules to assemble into (21-3) layers rather than continue with (20-3)

Cu (110) indicate that rearrangements of dilute second layer molecules occur. The implication is that for both systems the second layers are initially filled with flat-lying molecules which, at a certain surface density, tilt to eventually form a densely packed layer of tilted molecules (Fig. 2.4 C, D and E, and Fig. 2.5(b) and (c)). This filling process is temperature independent for 6P deposited on Cu (110) $2 \times 1 - \mathrm{O}$ and it proceeds until a maximum surface density is reached (when the tilt angle of the second layer reaches $\sim 33°$). At this maximum surface density, critical nucleation occurs, followed by growth and concomitant dewetting (Fig. 2.4 F).

For 6P on Cu (110) on the other hand, neither nucleation nor dewetting occurs during second layer filling. Instead layer filling continues uninterrupted up to $\sim$ 3.8 ML. However, there is a significant kink at 2.4 ML. This is not a rearrangement kink as described above, rather it indicates when a layer is completed and next layer filling commences. The surface density of a full-coverage 6P *tilted* layer (at 33°) is a factor ~ 1.4 greater than the density of a full-coverage *flat-lying* layer (at 0°). Hence the 1.4 factor difference in the density between a flat-lying and a tilted layer should be taken into account when interpreting the time evolution of the averaged area photoemission intensity for coverages > 1 ML in the double normalised plot. This means that the *normalised* time required to fill identical tilted layers will be 1.4 ML for 6P deposited on Cu (110) and 1.0 ML for 6P deposited on Cu (110) 2 × 1 – O. As can be seen from the plot, there is a kink in the intensity evolution at ~ 2.4 ML. This kink at 2.4 ML indicates that a second layer, composed of tilted molecules, is completed (Fig. 2.5(c) and (d)). More significantly, the important result from this quantitative analysis is that both *second* layers, on Cu (110) 2 × 1 – O and on Cu (110), have the same density (as can also be seen in the inset Fig. 2.3).

On Cu (110), once the tilted second layer is complete a subsequent third layer begins to fill for 6P deposited on Cu (110). This layer, in common with the second layer, also has a rearrangement kink located at ~ 2.5 ML which indicates a change from flat-lying to tilted orientation (Fig. 2.5(d) and (e)). As can be seen in Fig. 2.3, third layer filling continues until a critical density is reached and spontaneous nucleation occurs (Fig. 2.5(f)). For 6P deposited on Cu (110), the critical surface density is reached at 3.8 ML (normalised time) which corresponds to two completed tilted 6P layers (1.4 ML + 1.4 ML) deposited on top of a flat-lying first layer (1 ML). Thus critical nucleation occurs at the point in time when the third layer is just completed. Similarly, for 6P deposited on Cu (110) 2 × 1 – O, critical nucleation begins when the second layer is just completed at ~ 2 ML. Note that the second and third layers on Cu (110) and the second layer on Cu (110) 2 × 1 – O, all have the same density. This will be shown later to be the deciding factor that determines what crystal structure critical nuclei have.

To summarise, comparison of area-averaged photoemission intensity versus deposition time curves for both substrates indicates that more 6P must be deposited on Cu (110) to initiate critical nuclei formation. 6P deposited on Cu (110) 2 × 1 – O fills two layers with tilted-lying-down molecules: the first layer is a permanent tilted wetting layer and the second is a tilted layer. This second layer is meta-stable since it dewets upon critical nucleation. On the other hand, 6P deposited on Cu (110) fills three layers: the first is a flat-lying permanent wetting layer and the second/third layers together form a tilted-lying-down double layer. This double layer will be also shown to be meta-stable since it partially dewets upon critical nucleation to form a permanent second layer reconstruction. Interestingly, the photoemission intensity curves also show that at 125 °C all tilted layers on any of the systems have approximately the same density.

2.3 Nucleation Mechanism of 6P on Cu (110) 2 x 1 – O

Below the critical density, second layer molecules are in a 2D liquid state with randomly staggered intermolecular overlaps such as in a smectic phase, and hence have little or no long-range order along the [001] direction (they only have orientation order due to the anisotropy of the molecule and substrate). As more molecules are deposited the second layer becomes denser by packing molecules closer together with a smaller spacing S by increasing the average tilt angle θ (Fig. 2.4 C, D and E). The sliding displacement along the short axis of the molecule as θ increases in turn leads to a greater intermolecular π-orbital overlap which leads to stronger intermolecular binding. Nevertheless, the actual intermolecular binding between the molecules is also determined by the lateral overlap along the long axis of the molecule. The total intermolecular overlap area α is given by $\alpha = L(W - (T/\tan\theta))$, if $\sin\theta > T/W$, where L is the length, W is the short axis width and T is the thickness, of the molecule. Statistically, certain regions in the layer will have molecules in preferred arrangements with a greater overall overlap. For 6P on Cu (110) $2 \times 1 - \mathrm{O}$, regions with the strongest molecular binding are eclipsed with $\theta = 33°$. This is the required alignment for a 2D sheet of the (20-3) crystal plane. As discussed earlier a larger θ and hence α does not necessarily guarantee stability since the interaction with the first layer surface corrugation will also play a role.

For any given tilt angle any regions where molecules have an optimal long axis overlap will survive longer as a nucleus (the binding energy is high hence the rate of de-binding is low). Therefore, as the tilt angle of bound molecules increases so does their lifetime as a bound entity increase. This lifetime is crucial for the next step that involves all the molecules that surround a nucleus that are still in a 2D liquid state. Molecules loosely bound to other molecules in regions surrounding the longer lifetime nucleus have smaller intermolecular π-orbital overlaps and are therefore weaker bound, have much shorter lifetimes as bound entities and as a consequence are very mobile (as demonstrated by the fast dewetting of the second layer once critical nuclei form).

An important outcome of molecules crystallising into strongly bound 2D nuclei is that bound molecules are less able to move independently from each other and hence are immobile. This means that surrounding molecules experience less collisions from molecules bound in the nucleus. Therefore, as soon as a more strongly bound long-lifetime (and hence meta-stable) 2D nucleus forms, suddenly all surrounding molecules experience a net diffusion driving force pushing them towards the nucleus along the corrugation grooves in the [001] direction (Fig. 2.4 F). A much smaller contribution will arise from the perpendicular direction [110] due to the fact that if molecules move into the third layer from this direction the space left behind it will be partially filled by molecules from a 2D nucleus by reducing θ. The effect will be to severely reduce the lifetime of 2D nuclei.

The net force on molecules results from the thermal motion of unbound molecules giving rise to a biased random walk towards the nucleus, hence the net driving force will be larger for high surface densities and high temperatures. If this driving force is sufficient, given the mobility of 6P molecules, to move enough molecules on top of the 2D critical nucleus during the lifetime of the 2D critical nucleus, then a stable 3D nucleus will form. It is this driving force that explains how a large enough number of molecules can move into the third layer, in a fast dewetting process, to create a high enough third layer density for molecules to arrange into the bulk structure (with $\theta = 33°$) as shown in the insets of Fig. 2.1 and in Fig. 2.7. It is therefore evident that in the two step process of forming bulk-type 3D needles, the first required step is the formation of a 2D critical nucleus to act as a stable platform. The net driving force that pushes molecules to climb on top of the 2D critical nucleus and form a stable 3D nucleus is a diffusion process that results from the non-equilibrium surface density gradient at the interface of the nucleus and the surrounding 2D liquid as soon as crystallisation begins. As the dewetting proceeds the net driving force will keep decreasing in tandem with the 2D liquid layer density decrease. The shape of the 3D nucleus will also play a role since the more layers a molecule must climb above to crystallise the slower the process will be (the mobility of the molecules on the steps and terraces up to the upper most layer may be much slower).

2.4 Nucleation Mechanism of 6P on Cu (110)

The comparison of 6P depositions on two substrates with differently bound wetting layers reveals that there are several pre-nucleation mechanisms that determine the nucleation process. At 50–125 °C deposition temperature range of 6P deposited on Cu (110) produces (20-3) critical nuclei and 6P deposited on Cu (110) $2 \times 1 - \mathrm{O}$ produces (20-3) critical nuclei at all temperatures. In both cases, critical nucleation occurs after filling two layers with tilted molecules that are meta-stable where each layer has a density approximately equal to the density of a (20-3) crystal plane. However, 6P deposition on Cu (110) is temperature dependent [12] whereas deposition on Cu (110) $2 \times 1 - \mathrm{O}$ is not. The reason is that when 6P is deposited on Cu (110) $2 \times 1 - \mathrm{O}$ there is only one dominant orientation for molecules—a tilted orientation whereby molecules are bound to the layer. However, for 6P deposited on Cu (110), there are two different orientations, with equivalent binding energies, that molecules in the second layer can adopt—tilted or flat-lying orientation. In the meta-stable double layer, molecules can either tilt to bind with other tilted molecules or equivalently lie flat to bind with the flat-lying wetting layer (for example Fig. 2.5(b)). This mixture of orientations is confirmed by the observation, by STM, of channels consisting of a mixture of molecular orientations in the energetically stable post-nucleation reconstructed layer (Fig. 2.8(b)). The binding energies of both orientations will be roughly the same since the molecules are bound to other molecules by their aromatic plane in both cases. This means that for 6P deposited on Cu (110) these two molecular orientations are in continuous competition during layer filling and hence temperature dependence is observed. The relative rate at which vacancies in the second layer are occupied with flat-lying molecules, or flat-lying molecules tilt and join the tilted layer, is given by the difference in chemical potential between the two states. Since both states have similar binding energies, it is the surface density of available molecules that determines the chemical potential for each state.

As evidenced by the rearrangement of both the third and second layer into a single reconstructed layer during dewetting (Fig. 2.8(b)), molecules in second and third layers only exist as two tilted layers because of the kinetic stabilisation enabled by the high surface density of 6P molecules. This confirms that for 6P deposited on Cu (110) the dynamic behaviours of the two tilted layers (second and third layers) are coupled to each other in the form of a meta-stable double layer. On the other hand, for 6P deposited on Cu (110) $2 \times 1 - \mathrm{O}$ the tilted layers (first and second layers) are not dynamically coupled since the wetting layer is energetically stabilised by the interaction with the Cu (110) 2 × 1 – O reconstruction. This means that when 6P is deposited on Cu (110) 2 × 1 – O only the tilted second layer behaves dynamically.

These factors play a significant role in determining at what total surface density critical nucleation begins. It is important to ask the question: why does nucleation of 6P on Cu (110) not begin earlier, say during second or third layer filling? As explained in the next section, condensation at steps forces molecules to adopt a much higher local surface density compared to when molecules are evenly distributed over the surface (as with 6P deposited on Cu (110) 2 × 1 – O), surely nucleation could begin during second layer deposition? Answering these questions leads one to examine the very nature of the nucleation process. As described earlier, the post-dewetting reconstruction offers us a glimpse into what the preferred structure to assemble on a flat-lying wetting layer is. During layer filling, 6P molecules will always try to reach this energetically stable structure, but high temperatures will tend to encourage flat-lying molecules in the second layer to de-bind and tilt, and the presence of an ever increasing amount of molecules will quickly fill the gap left behind with tilted molecules. This process, given that both tilted layers are dynamically coupled, is repeated during third layer filling via molecules rearranging together with molecules in the second layer beneath. It should be noted that (20-3) meta-stable layers are kinetically stabilised by a continuous filling of holes that appear in the layers [12]. Averaged over a long time, at 50–125 °C, there are no holes and this is illustrated in Fig. 2.5.

It is this competition between tilted and flat orientation for 6P deposited on Cu (110) that prevents subcritical nuclei from growing in size within the layer, since any gaps opened up by molecules climbing on top of subcritical nuclei will be filled by a neighbouring molecule that will lie flat. It is the stability of flat lying molecules, offered ultimately by the flat-lying wetting layer, which disrupts the growth of subcritical (20-3) nuclei and shortens their lifetime. It is only when complete coverage is reached on the third layer that there is no rearrangement space for any gaps to be stabilised by flat-lying molecules (the layer is fully kinetically stabilised with tilted molecules) and this allows subcritical (20-3) nuclei to grow, uninterrupted, to be large enough to become an energetically stable nuclei. Thus in order for critical nucleation to begin, the system has to effectively decouple the layer undergoing critical nucleation (meta-stable third layer) from the flat-lying (first) layer by having a layer of molecules between them (meta-stable second layer) acting as a buffer. At higher temperatures 140–150 °C this process is repeated except that more molecules are required to initiate critical nucleation. This is due to the continuous process of hole creation and hole filling, leaving a net density of holes in the layer as molecules climb to higher layers.

Upon critical nucleation, spontaneously induced dewetting reduces the surface density (as molecules diffuse and attach to the nuclei) which in turn reduces the kinetic stabilisation of the second and third layers. The interaction with the flat-lying wetting layer once again plays a role as it promotes an energetically stable reconstruction that includes flat and tilted molecules (the holes are permanently filled with flat-lying molecules). It is because of the similarity of the reconstruction structure to the (21-3) and (-629) crystal planes that ultimately crossed needles assemble around the initial (20-3) critical nucleus.

2.5 6P Condensation at Steps During Pre-nucleation Deposition Period for 6P on Cu (110)

In-situ real-time monitoring by PEEM enables surface density re-distributions to be monitored during pre-nucleation and post-nucleation deposition periods. The difference image sequence shown in Fig. 2.6 A–F for 6P deposited on Cu (110) reveals large changes in PEEM image contrast which indicate that 6P re-distributes on the surface during the pre-nucleation deposition period. The contrast enhancement observed, quantised by batch processing, is plotted versus normalised deposition time and displayed in tandem with the corresponding photoemission intensity curve in Fig. 2.6(b). Large variations in image contrast for the different layers are explained by variations in molecule to surface interactions during this pre-nucleation deposition period. The surface on which molecules diffuse and condense changes depending on which layers are completed. This explains the varying behaviour as a function of deposition time in Fig. 2.6(b). For deposition times < 1 ML 6P molecules diffuse on Cu (110) whereas > 1 ML 6P molecules diffuse on either flat-lying (first layer) or a tilted layer (second and third layer) of 6P. No 6P condensation at steps is observed when deposited on Cu (110) $2 \times 1 - \mathrm{O}$.

Examining Fig. 2.6(b) to compare the spatial r.m.s intensity versus the area-averaged photoemission intensity plots reveals some trends. Namely, spatial r.m.s intensity minima observed at 1 ML, 2.4 ML and 3.8 ML, coincide in time with the completion of each successive layer: first, second and third layer, respectively (these are indicated by B, D and F, respectively, in Fig. 2.6). Reciprocally, spatial r.m.s intensity maxima coincide, with the exception of the first layer, with the point in deposition time when a layer is exactly half filled (indicated by C and E in Fig. 2.6). Thus when the condensation at steps reaches 50 % coverage of terraces the contrast observed is maximised, whereas 50 % coverage with no condensation at steps, whereby molecules are distributed *homogeneously* over the surface results in no contrast enhancement. Likewise 100 % coverage of terraces (completed layers) results in no contrast enhancement, but serves to confirm that the normalised deposition times for layer completion (1 ML, 2.4 ML and 3.8 ML), extrapolated from the area-averaged photoemission intensity curves in Fig. 2.3 are correct. The reasons why condensation at steps varies during deposition is explained next.

For depositions times ≤ 1 ML 6P molecules interact strongly with the metal surface when 6P is deposited on Cu (110) and thus adopt a flat-lying orientation. This strong binding interaction with the surface prevents a strong binding interaction between molecules (there is a minimal *inter*-molecular orbital overlap in the flat-lying configuration) so no preferred condensation at steps is observed. This is illustrated in Fig. 2.6 A. On the other hand, 6P molecules filling the second layer on Cu (110) do not interact with the metal surface and instead experience weaker van der Waals

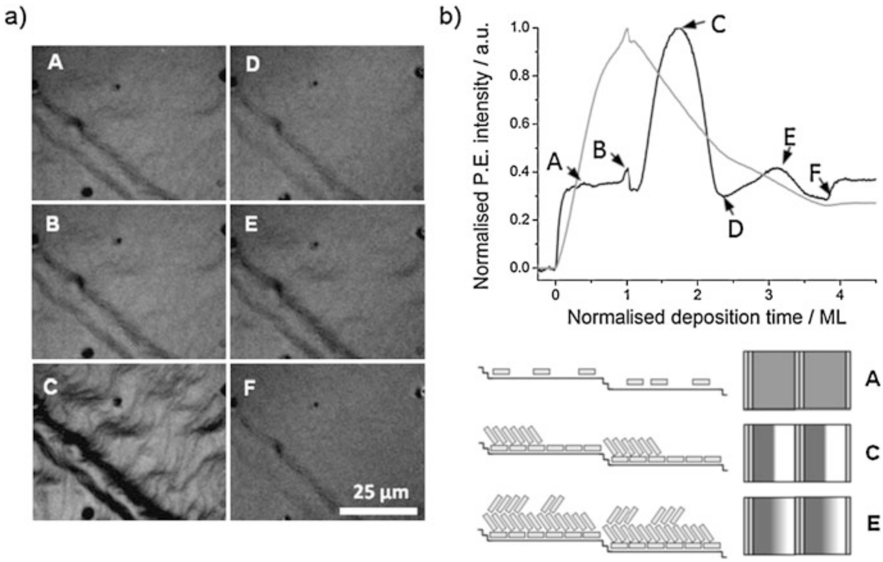

Fig. 2.6 (**a**) Difference image sequence (*A* to *F*) for 6P deposited on Cu (110) that illustrates the contrast enhancement provided by 6P condensation at steps during second layer and third layer deposition. (**b**) Combined plot of area-averaged photoemission intensity for 6P on Cu (110) deposited at 125 °C (*grey*) and corresponding area-calculated r.m.s. intensity deviation plotted versus normalised deposition time in monolayers (*black*). Note that (*A* to *F*) correspond to the image sequence. (**c**) Schematic diagram of condensation at steps starting from the bottom of the step (condensation starting from top of step is also possible but not drawn) for *A*, *C* and *E*

interactions with flat-lying molecules from the first layer. It is this relative weakness which allows molecules to re-orient into a tilted orientation. The process of tilting is kinetically driven in the presence of a high surface density of molecules. Since condensed and tilted 6P molecules on top of the flat-lying layer present a hydrogen terminated surface towards the aromatic plane of the first layer, as shown in Fig. 2.6 C, the intra-layer intermolecular overlap of the second layer is comparatively greater and hence the van der Waals interaction *within* the second layer will dominate. It is important to note that the flat-lying layer also presents a relatively small surface topology corrugation compared to the bare substrate. This combination facilitates the 6P condensation at steps process since second layer molecules will diffuse on terraces and collect at stronger binding sites such as steps. It should be noted that condensation at steps does not produce a bulk type crystal arrangement (in fact the layers are meta-stable), but it is nevertheless energetically favourable during the pre-nucleation deposition period to condense.

From Fig. 2.6 it is clear that third layer condensation at steps produces a weaker contrast enhancement than the second layer. Although condensed molecules in the third layer also present a hydrogen terminated surface to the second layer, the matching surface topology (they can adopt a 1:1 commensurate spacing) to the second layer hydrogen termination results in molecules condensing anywhere on the terraces including at step edges. Thus this more sympathetic interaction leads to only a partial condensation at steps for the third layer. It should be noted that due to the differential layer photoemission attenuation, the maximum contrast enhancement from the third layer condensation at steps will be half that of the contrast enhancement of the second layer. Apart from confirming some of the conclusions garnered from photoemission intensity curves, the agreement between the positions of r.m.s. minima and layer completion kinks indicates that at 125 °C the layer filling mode, in the pre-nucleation deposition time, is layer-by-layer.

2.6 Spontaneous Dewetting During Post-nucleation Deposition Period

Thus far, it has been shown that comparisons between the intensity evolution of 6P on Cu (110) $2 \times 1 - \mathrm{O}$ and 6P on Cu (110) allows pre-nucleation layer filling mechanisms to be established. The post-nucleation deposition period can also be studied. When 6P is deposited on Cu (110) $2 \times 1 - \mathrm{O}$, second layer molecules form a meta-stable layer that spontaneously dewets at a critical density to form 6P (20-3) 3D needles [7]. No condensation at steps is observed during deposition of the second layer, since in this case the layer is in a homogeneous liquid state up until a critical surface density is reached at ~ 1.95 ML. At this critical density, (20-3) nuclei form and spontaneous dewetting of the layer to form 3D nuclei proceeds. As described above, the deposition timeline for 6P deposited on Cu (110) is different—layer filling continues up to 3.8 ML (one flat and two tilted layers); upon when spontaneous nucleation induced dewetting occurs. It will be shown later that, unlike with 6P deposited on Cu (110) $2 \times 1 - \mathrm{O}$, the (20-3) critical nuclei formed when 6P is deposited on Cu (110) do not determine the final structure of the nanostructures that grow. This is because the process of dewetting leads to a molecular layer reconstruction, of areas surrounding critical nuclei, which changes the favourable crystal structure to self-assemble from (20-3) to (21-3) for temperatures > RT.

Shown in Fig. 2.7(a) and (b), are post-nucleation PEEM images, taken shortly after nucleation has begun, of 6P deposited on Cu (110) and Cu (110) $2 \times 1 - \mathrm{O}$, respectively. In both cases, 6P crystals that form are darker in PEEM than the surrounding area. This is due to their 3D structure of multiple 6P layers which, in total, attenuate secondary photoelectrons very strongly. Notice that areas immediately surrounding nuclei are brighter than the rest of the image. These bright areas indicate regions of low surface density where molecules have dewetted the surface by diffused away (in the presence of a concentration gradient) to nuclei. The shape of these low surface density regions is determined by how anisotropically 6P diffuses on the surface. As can be seen in Fig. 2.7(a), the elongated bright areas are clear evidence of anisotropic diffusion during the process of nucleation induced spontaneous dewetting. In Fig. 2.7(b) the elongation is not as pronounced, however, in both cases the direction of fastest dewetting is perpendicular to the fastest growth direction of the nanostructures that form and is parallel to the surface corrugation that templated

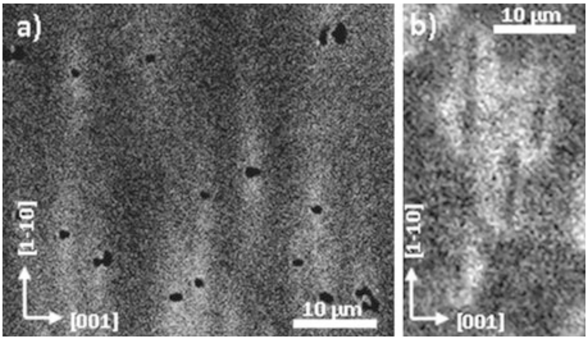

Fig. 2.7 Anisotropic dewetting of 6P from (**a**) meta-stable second and third layer of 6P on Cu (110) to form crossed needles and (**b**) meta-stable second layer of 6P on Cu (110) 2 × 1 – O to form needles. Areas with lower surface density of 6P molecules appear bright since there is less attenuation of the photoemission from the Cu (110) 2 × 1 – O or Cu (110) surface beneath. The fastest diffusion direction is along the Cu (110) 2 × 1 – O or Cu (110) surface corrugations. Note that in both cases the permanent first layers never dewet

the wetting layer (shown in Fig. 2.1). In Fig. 2.7, the dewetting process occurs on a much larger length scale for 6P on Cu (110). It is *highly* anisotropic ($>$ 10:1) and produces long thin streaks in the [1-10] direction that grow wider in tandem with the length increase of the nanostructures. It is also important to note that the boundary of the dewetted region is sharp in the [001] direction and smeared out in the direction parallel to the fast diffusion direction [1-10]. 6P deposited on Cu (110) 2 × 1 – O, on the other hand, produces a less anisotropic (roughly 4:1) spontaneous nucleation dewetting bright area with sharp boundaries in all directions. This is because during dewetting 6P molecules diffuse on an un-reconstructed tilted molecular layer which weakly confines molecules into anisotropic diffusion. On the other hand, it will be shown later that the high anisotropy observed during dewetting on Cu (110) is due to molecules diffusing on a reconstructed molecular layer that channels molecules towards the nuclei.

2.7 PEEM Measurement of Diffusion Anisotropy

It is possible to study this molecular diffusion process once the whole surface reconstruction is completed (roughly double the time required for nucleation to begin). A simple way to probe molecular diffusion on the reconstructed surface is to close the shutter of the molecular evaporator and examine the time evolution of photoemission intensity that accompanies the reduction in the surface density of 6P molecules in areas between needles. Once the shutter is closed the equilibrium surface density of molecules re-adjusts to a lower value since the rate of molecules leaving the surface to join the 3D needles remains high, the rate of molecules leaving the crossed needles to join the surface remains low and the number of molecules

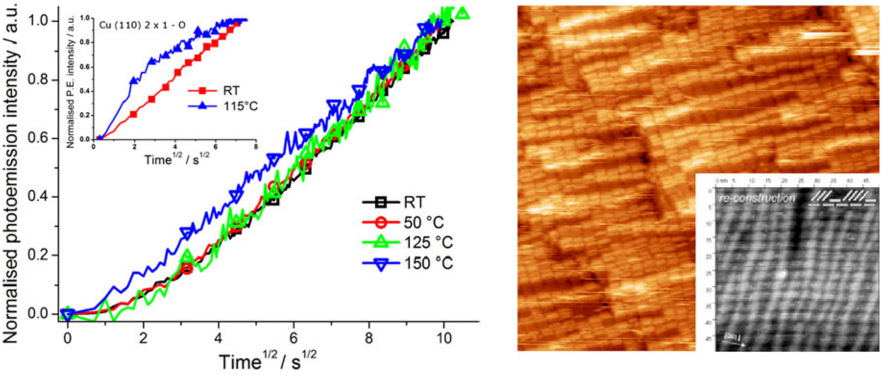

Fig. 2.8 (**a**) Multi-plot of photoemission intensity versus square-root-time, acquired after 6P nucleation on Cu (110) and dewetting is complete. Measured from the time the molecular beam shutter is closed. *Insert*: equivalent plot for 6P on Cu (110) 2 × 1 – O. (**b**) Reconstructed layer of 4 ML 6P on Cu (110) imaged by LT-STM at 5 K. *Inset*: RT STM of similar surface

arriving at the surface from the evaporator is now zero. Eventually a new equilibrium surface density in the areas between needles will be reached where the number of molecules leaving the needle to diffuse in the surrounding area will equal the number of molecules leaving the surrounding area to join the needle.

The resultant increase in photoemission intensity (since there is a depletion of molecules attenuating) is plotted in Fig. 2.8. To test whether the molecular diffusion is anisotropic the photoemission intensity is plotted against square-root-time and compared to the inverse [7] of the one-dimensional diffusion [22] equation $\rho(x,t) = (\rho_0/2)(\pi Dt)^{-1/2}\exp(-x^2/4Dt)$ where ρ_0 is the initial surface density, D is the diffusion coefficient, x is the position along a 1-D ordinate and all other symbols have their usual meaning. A straight line indicates that the system diffuses one dimensionally. Certain considerations must be taken into account. For instance, the photoemission intensity changes are measured when there are crossed needles on the surface. Since the whole image is used to acquire the average intensity changes, the effect of dark needles remaining constantly dark while the surface between the needles undergoes rapid changes in intensity must be accounted for. When the intensity for the one-dimensional diffusion equation is integrated and averaged over a finite length (e.g. the distance between needles) a distinctive concave curve prior to the onset of the linear regime as is observed in Fig. 2.8. The larger distance between crossed needles at 150 °C produces a straighter plot.

The fact that a linear response is observed for all four temperature ranges explored indicates that molecular diffusion is anisotropic at all deposition temperatures from RT to 150 °C. This confirms that at all deposition temperatures a reconstruction occurs that produces channels such as those in Fig. 2.8(b) on Cu (110) but not Cu (110) 2 × 1 – O. Comparisons to similar diffusion measurements of 6P diffusing on a (20-3) type wetting layer for 6P deposited on Cu (110) 2 × 1 – O (see inset Fig. 2.8) suggest that if, hypothetically, the (20-3) type meta-stable double layer did *not* undergo a reconstruction and remained intact, a pseudo 2-D diffusion would be observed at high temperatures. This is not observed. It is interesting to note that since the total number of molecules of the meta-stable double layer (the second and third layers) exceeds the number required to form a single reconstructed layer (the post-dewetting permanent second layer), the reconstruction cannot proceed unless excess molecules are removed from the surface via large scale mass transport to growing nuclei. This reduction in surface density shifts the equilibrium away from kinetic stabilisation of the meta-stable double layer and towards a single reconstructed layer that is energetically stable. The energetic stability comes from partial interaction of the reconstructed layer with flat-lying molecules of the underlying wetting layer. During the pre-nucleation deposition period, the surface free energy of the first/second layer interface is large due to the weak interaction between aromatic planes of first layer molecules and hydrogen atoms of the 6P tilted layer. The reconstruction is therefore an attempt, by incorporating flat molecules, to reduce the surface free energy of this interface. This is the layer measured by STM. The exact ratio of flat-lying to tilted molecules of the reconstructed layer is most likely temperature dependent (as is the rate at which molecules re-tilt). However, the important aspect of the reconstruction, in relation to the formation of (-629) and (21-3) crossed needles, is that the reconstruction has a mixture of flat and tilted molecules in a similar fashion to (-629) and (21-3) layers (see Fig. 2.2). It is for this reason that crossed needles (21-3) grow when 6P is deposited on Cu (110) and straight (20-3) needles grow when 6P is deposited Cu (110) $2 \times 1 - \mathrm{O}$, even though both involve an intermediate step where (20-3) layers form and (20-3) critical nuclei crystallise.

2.8 Direct Evidence of the Formation of (20-3) Critical Nuclei on Cu (110)

More compelling evidence of the intermediate (20-3) layers and (20-3) critical nuclei formation for 6P deposited Cu (110) can be found in PEEM images in Fig. 2.9. Comparison of the meta-stable layer densities on Cu (110) with 6P deposited on Cu (110) $2 \times 1 - \mathrm{O}$ strongly suggests that critical nuclei that form will also be (20-3) type. This would appear to be counter-intuitive because (21-3) crossed needles are observed post-nucleation. However, as has been shown by the anisotropy of diffusion and from STM, as soon as dewetting occurs areas surrounding critical nuclei in the [110] direction reconstruct into a layer containing flat and tilted molecules. The outcome of this process is that as soon as critical nuclei (20-3) grow larger and begin to self-assemble over reconstructed areas that now surround nuclei, the favourable structure to assemble changes from (20-3) to (21-3). Strong evidence that supports the formation of critical (20-3) nuclei is provided by the occasional (20-3) needle that happens to grow quicker than the reconstruction wave proceeds outwards. Some examples are given in Fig. 2.9. This is possible because (20-3) needles grow perpendicular to the spontaneous nucleation fastest dewetting direction. Some examples of (20-3) needles are also observed at 140–150 °C. As can be seen in Fig. 2.9, at lower temperature (115 °C), curvy needles grow because the rate of needle growth is comparable to the rate at which the reconstruction wave advances away from the critical

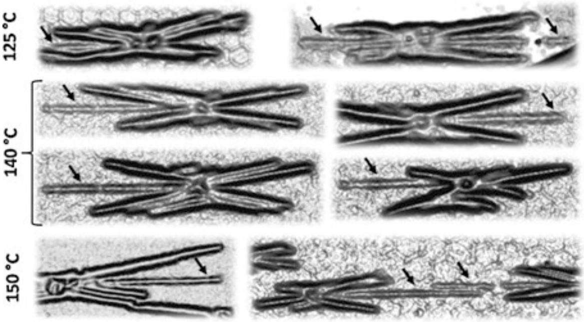

Fig. 2.9 PEEM images, treated by applying an edge-detect filter (gradient algorithm) to enhance weak features, clearly show several instances of straight needles (indicated by *arrows*) emerging from crossed needles. Straight needles are (20-3) needles that grew out of (20-3) critical nuclei ahead of the advancing surface reconstruction wave. The reconstruction wave changes two meta-stable (20-3) type layers into a single reconstructed layer. Hence the straight (20-3) needles are generally longer than crossed needles. Notice that all (20-3) straight needles point directly to the central intersection of crossed needles where critical nucleation began. Many crossed needles appear to have a missing centre which would correlate well with an original (20-3) critical nucleus sacrificially Ostwald ripening to surrounding (21-3) needles

(20-3) nucleus. This leads to needles growing on top of partially reconstructed areas which will be a mixture of (20-3) type and flat/tilted reconstructed layers; and hence some crossed needles straighten out in the [001] direction as they begin to grow on un-reconstructed (20-3) type regions. As can be seen in Fig. 2.9, the fastest (i.e. longest) growing needle (excluding the fast growing (20-3) needles) is always the needle that is most likely to curve or kink. From inspection of many PEEM images of crossed needles grown at this temperature, the direction of curviness is also always towards the midline (in the [001] direction) of a given crossed needle. This direction of curviness confirms that the reconstruction wave starts at the centre of the crossed needles (where the critical nucleus is located). This is further confirmed by the fact that all fast growing (20-3) needles point towards the centre of crossed needles. This is in fact a fingerprint of the original critical nucleus being (20-3) type.

At 140–150 °C crossed needles have no curviness, since at these higher temperatures molecular rearrangements, required for reconstruction, proceed much quicker than crossed needles grow. Thus crossed needles never cross the reconstruction wave travelling boundary and thus remain straight. Another feature of crossed needles that becomes more apparent at higher temperatures is the hole that appears at the intersection point of crossed needles. It is highly probable that this is a hole created by (20-3) critical nuclei sacrificially Oswald ripening the crossed needles. Since (20-3) critical nuclei have a crystalline structure that in the presence of flat and tilted molecules of the reconstruction is inherently less energetically stable than the surrounding (21-3) crossed needles (as evidenced by the reconstruction during dewetting), eventually molecules forming (20-3) critical nuclei detach and diffuse to (21-3) needles and leave behind a hole.

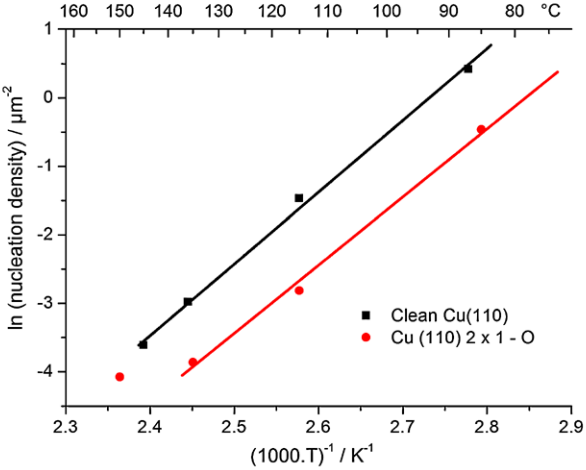

Fig. 2.10 Arrhenius plot of the natural log of the nucleation rate per unit area versus $1/T$. The slope of the plot is used to determine the nucleation energy for 6P on each surface. Note the general similarity in slope for both systems studied. This is further confirmation that the formation of (20-3) critical nuclei is common to both

2.9 Nucleation Densities of (20-3) Critical Nuclei on Cu (110) and Cu (110) 2 x 1 – O

When the rate of nucleation, which is proportional to the number of nuclei per unit area, plotted in the form of an Arrhenius plot, allows the nucleation energy to be determined, for a particular substrate/molecule combination, from the slope of the plot. However, the term nucleation energy is slightly misleading since many activation energies and binding energies determine the final rate of nucleation. The positive slope of the plots in Fig. 2.10 indicates that at higher temperatures fewer nucleation sites form. It is important to note that nucleation sites are formed when a critical surface density of molecules is reached. It is at this point that kinetically stabilised subcritical nuclei become energetically stable via dynamic processes that positions molecules into static arrangements such as energetically stable crystalline structures. The process of kinetic stabilisation is controlled by the rate at which molecules join subcritical nuclei—which would appear to be controlled by activation barriers associated with diffusion. However, high layer densities required for 6P to nucleate suggests that molecules spend more time bound to other molecules in the form of small subcritical nuclei. Hence, intermolecular binding energies will therefore determine the rates at which molecules de-bind from subcritical nuclei which will in turn affect (a) the lifetime of subcritical nuclei and (b) the rate at which molecules become available to diffuse to other subcritical nuclei. Conversely, when the critical surface density is low, such as with nucleation from a 2D gas phase, molecules spend a greater proportion of time diffusing rather than binding/de-binding.

The nucleation rate data presented in Fig. 2.10 demonstrate that the nucleation energy for both 6P deposited on Cu (110) and Cu (110) $2 \times 1 - O$ in the temperature range $85 < T < 150$ °C are nearly identical at ~ 950 meV. The nucleation rates for depositions < 85 °C are too high for 6P on Cu (110) to be accurately assessed. The near identical nucleation energy does strongly confirm that critical nuclei formed on both substrates are (20-3) 6P crystallites. The molecular binding energy of 6P molecules in bulk-type arrangement was measured [7] to be 2.1 eV from PEEM measurements of desorption of 6P molecules from needles grown on Cu (110) 2 × 1 – O. Since the nucleation energy is a combination of binding energies and activation barriers, the maximum total activation energy for the nucleation of 6P deposited on Cu (110) and Cu (110) 2 × 1 – O surfaces is 1.15 eV.

2.10 Conclusions

Nucleation is only the last part of a convoluted series of events in which many spontaneous molecular rearrangements occur. These events reveal a fluid and dynamic picture of the pre-nucleation deposition period. Furthermore, the self-assembly process has been shown to involve intermediary structures that depend on the substrate in some form or another for stability, hence their meta-stability. Some can be very stable indeed, such as the molecular reconstruction layer on Cu (110) that temporarily forms during second layer filling and to which the system returns during the post-nucleation dewetting process.

As has been shown, at the point of critical nucleation, facets which comprise (20-3) nuclei become the new preferred surfaces for molecules to attach to and hence the role of the substrate as a template for nuclei becomes less dominant. However, an interesting case occurs on Cu (110) where after the formation of (20-3) nuclei and spontaneous dewetting, there are two competing long-lifetime structures: the (20-3) nuclei and the molecular layer reconstruction surrounding it. In the absence of a reconstructed layer, (20-3) nuclei on Cu (110) would survive a long time, but instead the reconstruction and molecules attaching to facets of (20-3) nuclei cooperate to produce (21-3) needles.

To summarise, the conclusions that can be drawn from the comparison of the nucleation of 6P on Cu (110) 2 × 1 – O and 6P on Cu (110) are:

(a) On an anisotropic substrate whereby 6P molecules align with their long axis parallel to the surface, the densest arrangement of molecules in a layer is of a (20-3) type. Therefore this is the preferred arrangement of 6P molecules in layer that is kinetically stabilised.
(b) The geometric and energetic strength of interaction between layers decides whether large scale molecular re-distributions, such as condensation at steps, will occur. It will also decide whether kinetically stabilised layers are in an oriented liquid state or, such as with 6P deposited on Cu (110), in a more crystalline state.
(c) The creation of (20-3) critical nuclei requires a double layer of (20-3) type form, with at least one layer being kinetically stabilised. Once a critical density is reached energetically stable (20-3) critical nuclei will form.
(d) The first layer of 6P molecules, oriented by the choice of metal or metal oxide substrate, ultimately determines what crystal structure the nanostructures will have. There may be intermediate steps that will determine the rate of nucleation but ultimately the dynamic interaction of the meta-stable layer with the wetting layer will decide how the nanostructures will continue growing.

Since most growth studies are not performed in-vitro or real-time, but rather in a step-by-step fashion with sequential growth and measurements, the results obtained may vary significantly. With this PEEM study of a prototypical organic molecule, it is hoped that the dynamics of molecular crystal growth will become more appreciated and understood, and that the door may open to controlling nano-structured growth.

Acknowledgements Supported by the Austrian Science Foundation (FWF) through the NFN: Interface Controlled And Functionalised Organic Films.

References

1. G.M. Whitesides, B. Grzybowski, Science **295**, 2418 (2002)
2. W.J. Blau, A.J. Fleming, Science **304**, 1457 (2004)
3. P. Puschnig, S. Berkebile, A.J. Fleming, G. Koller, K. Emtsev, T. Seyller, J.D. Riley, C. Ambrosch-Draxl, F.P. Netzer, M.G. Ramsey, Science **326**, 702–705 (2009)
4. G. Koller, S. Berkebile, J. Ivanco, F.P. Netzer, M.G. Ramsey, Surf. Sci. **601**, 5683 (2007)
5. M.G. Ramsey, D. Steinmüller, F.P. Netzer, Synth. Metals **54**, 209 (1993)
6. M.G. Ramsey, M. Schatzmayr, S. Stafströmand, F.P. Netzer, Euro. Phys. Letts. **28**, 85 (1994)
7. A.J. Fleming, F.P. Netzer, M.G. Ramsey, J. Phys: Condens. Matter **21**, 445003 (2009)
8. G. Koller, S. Berkebile, M. Oehzelt, P. Puschnig, C. Ambrosch-Draxl, F.P. Netzer, M.G. Ramsey, Science **317**, 351 (2007)
9. S. Berkebile, G. Koller, P. Puschnig, C. Ambrosch-Draxl, F.P. Netzer, M.G. Ramsey, Appl. Phys. A-Mater. Sci. Procc. **95**, 101–105 (2009)
10. M. Oehzelt, L. Grill, S. Berkebile, G. Koller, F.P. Netzer, M.G. Ramsey, Chem. Phys. Chem. **8**, 1707 (2007)
11. S. Berkebile, G. Koller, G. Hlawacek, C. Teichert, F.P. Netzer, M.G. Ramsey, Surf. Sci. **600**, 313 (2006)
12. A.J. Fleming, S. Berkebile, T. Ules, M.G. Ramsey, Phys. Chem. Chem. Phys. **13**, 4693 (2011)
13. F.-J. Meyer zu Heringdorf, M.C. Reuter, R.M. Tromp, Nature **412**, 517 (2001)
14. H. Yasufuku, M. Okumura, S. Kera, K.K. Okudaira, Y. Harada, N. Ueno, J. Elec. Spec. and Rel. Phen. **114–116**, 1025 (2001)
15. N.M. Buckanie, F.-J. Meyer zu Heringdorf, Surf. Sci. **601**, 1701 (2007)
16. H. Marchetto, U. Groh, T. Schmidt, R. Fink, H.-J. Freund, E. Umbach, Chem. Phys. **325**, 178 (2006)
17. H.H. Rotermund, S. Nettesheim, A. von Oertzen, G. Ertl, Surf. Sci. **275**, 645 (1992)
18. H.H. Rotermund, Surf. Sci. **283**, 87 (1993)
19. J. Ivanco, T. Haber, J.R. Krenn, F.P. Netzer, R. Resel, R.M. G, Surf. Sci. **601**, 178 (2007)
20. F. Balzer, H.-G. Rubahn, Surf. Sci. **507**, 588 (2002)
21. Z. Zhang, L.M. G, Science **276**, 377 (1997)
22. K.A. Jackson, *Kinetic Processes* (Wiley/VCH, Weinheim, 2004), p. 188
23. J. Ivanco, F.P. Netzer, M.G. Ramsey, Org. Elec. **8**, 545–551 (2007)
24. L. Sun, G. Weidlinger, M. Denk, R. Denk, M. Hohage, P. Zeppenfeld, Phys. Chem. Chem. Phys. **12**, 14706–14709 (2010)

Chapter 3
Organic–Organic Heteroepitaxy—The Method of Choice to Tune Optical Emission of Organic Nano-fibers?

Clemens Simbrunner, Gerardo Hernandez-Sosa, Martin Oehzelt, Roland Resel, Francesco Quochi, Dimitrii Nabok, Tatjana Djuric, Lorenz Romaner, Peter Puschnig, Claudia Draxl, Ingo Salzmann, Günther Schwabegger, Irene Watzinger, Michele Saba, Andrea Mura, Giovanni Bongiovanni, and Helmut Sitter

Abstract In this chapter the potential of Organic–Organic heteroepitaxy is discussed concerning the ability to provide efficient color tuning of organic nano-fibers deposited on muscovite mica substrates. The first part is focused on the epitaxial growth of rod-like molecules on sheet silicates which has been analyzed by de-

---

C. Simbrunner (✉) · G. Hernandez-Sosa · G. Schwabegger · I. Watzinger · H. Sitter
Semiconductor- and Solid State Physics, Johannes Kepler University Linz, Altenbergerstraße 69, 4040 Linz, Austria
e-mail: Clemens.Simbrunner@jku.at

Present address:
G. Hernandez-Sosa
Innovation Lab GmbH, Speyerer Straße 4, 69115 Heidelberg, Germany

M. Oehzelt
Helmholtz Zentrum Berlin für Materialien und Energie GmbH, BESSY II, Albert-Einstein-Strasse 15, 12489 Berlin, Germany

M. Oehzelt
Institut für Physik, Humboldt-Universität zu Berlin, Newtonstrasse 15, 12489 Berlin, Germany

R. Resel · T. Djuric
Institute of Solid State Physics, Graz University of Technology, Petersgasse 16, 8010 Graz, Austria

F. Quochi · M. Saba · A. Mura · G. Bongiovanni
Dipartimento di Fisica, Universita di Cagliari, 09042 Monserato, Italy

D. Nabok · L. Romaner · P. Puschnig · C. Draxl
Chair of Atomistic Modelling and Design of Materials, Montanuniversität Leoben, Franz-Josef-Straße 18, 8700 Leoben, Austria

H. Sitter et al. (eds.), *Small Organic Molecules on Surfaces*,
Springer Series in Materials Science 173, DOI 10.1007/978-3-642-33848-9_3,

positing p-6P and 6T using hot-wall epitaxy. It is demonstrated that substituting para-phenylenes by other molecules for efficient color tuning is not trivial leading in the general case to multidirectional nano-fibers. The presented growth model is based on detailed analysis using XRD pole-figure measurements, atomic force microscopy and force-field simulations. In the second part it is demonstrated that organic–organic heteroepitaxy provides a proper method for efficient color tuning of organic nano-fibers. It is shown that using p-6P nano-fiber templates can be used as fundament for the epitaxial growth of 6T crystallites. The formed 6T crystallites adopt the molecular and morphological orientation of the p-6P layer beneath and provide highly polarized emission in the blue, green, and red spectral range.

3.1 Introduction

During the last years a clear trend towards organic electronics could be recognized within the scientific community. The huge spectrum of organic molecules available by chemical synthesis [1] and adequate for the implementation of electronic, photonic and optoelectronic devices, combined with cheap and easy processing and the ability to manufacture devices on flexible substrates opens niches not occupied by anorganic semiconductors [2]. Moreover using organic molecules instead of inorganic compounds in order to fabricate nanostructures, coincides with higher luminescence efficiency at the same material density, more flexible spectroscopic properties and easier processing since controlled, self-assembled growth can be implemented [3].

Consequently a lot effort has been undertaken to study the growth of thiophenes and phenylenes on various substrates [3–10], motivated by the discussed advantages and especially due to their high affinity to form highly crystalline organic nano-needles [7, 11, 12]. Nevertheless it turned out that oligo-p-phenylenes in combination with muscovite mica as substrate represent a prominent and outstanding material combination, forming a stable molecular building block [13, 14]. In

---

Present address:
D. Nabok
Physics Department, Humboldt Universität zu Berlin, Zum Großen Windkanal 6, 12489 Berlin, Germany

P. Puschnig
Institute of Physics, Karl-Franzens University Graz, Universitätsplatz 5, 8010 Graz, Austria

C. Draxl
Physics Department, Humboldt Universität zu Berlin, Zum Großen Windkanal 6, 12489 Berlin, Germany

I. Salzmann
AG Supramolecular Systems, Department of Physics, Humboldt-Universität zu Berlin, Brook-Taylor-Straße 6, 12489 Berlin, Germany

that sense it has been demonstrated that their ability for generating long, parallel-aligned nano-fibers provides a proper fundament for several applications e.g. wave-guiding and lasing [15–17]. Motivated by this promising criterion the growth of para-hexaphenyl (p-6P) on muscovite mica has been investigated intensely by several groups [4, 5, 12, 18] and as a consequence the discussed material system is well understood concerning morphological, structural, and optical properties.

Nevertheless, the variety of physical properties covered by oligo-p-phenylenes is quite narrow and the optical emission spectrum shifts with decreasing number of phenyl rings from the blue to the UV [20]. As a result it becomes difficult to tune the optical properties of p-6P nano-fibers [7] leading to a lot of efforts to substitute oligo-p-phenylenes by other molecules. Among the huge variety of possible organic molecules, thiophenes and phenylenes are most promising building blocks for the nano-fibers because of their photonic and electronic properties as well as their thermal stability [21]. As a consequence, beside the growth of para-phenylene oligomers—thiophenes [7, 21], thiophene/phenylene co-oligomers [21, 22], and functionalized para-phenylene molecules [6, 14, 23, 24] have been deposited on muscovite mica.

Thiophenes represent an important and well-known class of rod-like molecules for fabrication of active layers providing highly efficient electrical, structural and opto-electrical properties [25, 26]. Most prominent representatives within this group of molecules are α-quaterthiophene (4T) and α-sexithiophene (6T), providing intense green and orange luminescence [7]. By depositing 6T and 4T on muscovite mica, needle-like structures can be obtained [7], but it has to be stated that two main differences of thiophene- in comparison to phenylene-needles are observed: On the one hand, beside needle formation flat islands are formed on muscovite mica (001) showing weak fluorescence which gives a first hint for the formation of upright standing molecules [7, 27]. On the other hand, needle formation shows a lower macroscopic anisotropy as compared to p-6P, which is caused by a needle formation in multiple directions [7, 21] and consequently polarized fluorescence of the nano-fibers is significantly hampered.

A similarly complex behavior is found for thiophene/phenylene co-oligomers [21]. In particular, the growth of 5,5′-di-4-biphenylyl-2,2′-bithiophene (PPTTPP)—also known as BP2T [28, 29] and 4,4′-di(2,2′-bithienyl)-biphenyl (TTPPTT) on muscovite mica has already been studied [21, 22].

Another approach to control the morphology and the luminescence of nano-fibers is provided by chemical functionalizing the organic molecules [24]. Nevertheless, it is rather difficult to modify para-phenylenes because of their low solubility, which even decreases with increasing chain length of the molecules. A generic concept has been developed to access a wider range of molecules on the basis of a functionalized para-quaterphenylene (p-4P) unit [30] which represents a compromise between solubility and critical chain length being the key for mutually parallel needle alignment. In particular, functional groups (e.g. methoxy, chloro, cyano, amino, dimethylamino and benzylamino) are attached on the two para-positions of the p-4P unit which allows to synthesize two different molecular classes—symmetrically [14, 24] and non-symmetrically [6, 30, 31] substituted oligomers. It has been demonstrated

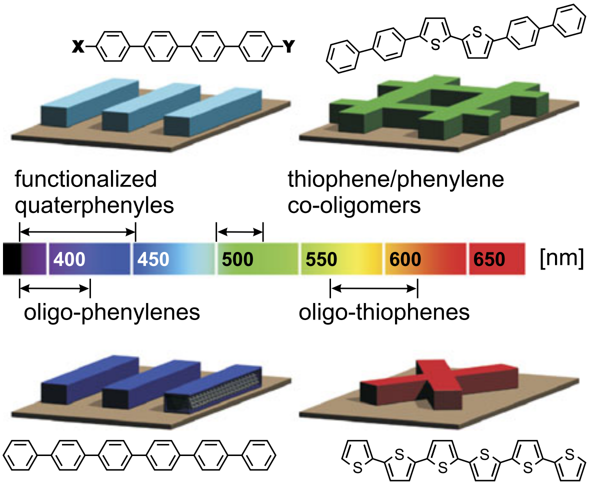

Fig. 3.1 Observed needle orientations on muscovite mica with respect to the fluorescence emission wavelength [19]. Whereas for oligo-phenylenes and functionalized phenylenes parallel needle formation has been observed, oligothiophenes and thiophene/phenylene oligomers are characterized by x-shaped or rhombical morphology

that functionalized p-4P oligomers form well-defined fiber-like nanostructures upon vapor deposition on muscovite mica [6] and consequently it can be stated that the suggested strategy represents up to now the most promising approach in order to achieve macroscopically highly ordered parallel organic nano-needles (beside the well-known para-phenylenes). This fact has been underlined by the demonstration of optical devices, such as frequency doublers [31]. Furthermore, the integration of non-symmetric molecules within organic nano-fibers represents an interesting, novel aspect for optical applications, as is expected from theory that they feature second-order non-linear optical activity [6]. The degree of freedom with functionalized quaterphenylenes is quite narrow, in particular concerning their optical response. All molecules investigated so far, emit in the blue spectral range (from 383 nm to 452 nm) [6] which restricts the potential for optical applications.

A graphical summary of the present state of research is shown in Fig. 3.1, indicating by arrows the main optical emission range of thiophene/phenylene co-oligomers in the green [22], of thiophenes in the green to orange [7], of functionalized quaterphenylenes in the blue (383–452 nm) [6] and of para-phenylenes in the UV to blue spectral range [20]. The macroscopic degree of order is sketched as graphical model visualizing parallel (phenylenes, functionalized quaterphenylenes), rhombic (thiophene/phenylene co-oligomers) and x-shaped (thiophenes) needle formation.

Based on these observations several criteria can be defined which have to be fulfilled to achieve long nano-fibers providing highly polarized emission:

- *Parallel molecular alignment* In order to achieve a maximum degree of anisotropy, rod-like molecules have to be aligned parallel to each other. Only in that way it becomes possible to make use of the single molecular polarized emission/absorption on an macroscopic scale being essential for device applications.
- *Parallel formation of nano-fibers* plays an essential role to obtain large single-crystalline nanostructures. As observed for thiophenes and thiophene/phenylene co-oligomers non-parallel growth of nano-fibers inevitable leads to an increased

probability that nano-fibers which originate from different nucleation centers cross each other. Consequently effective lateral needle growth is significantly hampered leading to shorter structures.

- *High crystal quality* In order to reduce parasitic processes within the organic crystallites high crystal quality represents an inevitable prerequisite for optical applications.
- *Tunable fiber cross section* As lasing of organic nano-fibers can only be obtained by efficient waveguiding within the crystallites, the achievable fiber cross section represents a crucial issue in particular for shifting the lasing emission to longer wavelength.

3.2 Sheet Silicate Substrates

In order to investigate and in particular to understand the epitaxial growth on mica surfaces a detailed knowledge about the substrate surface morphology, geometry and composition seems inevitable. Substrate surfaces for evaporation of organic molecules and force-field simulations in the presented work are all representatives of the phyllosilicate group. The nomenclature of this mineral group is strongly connected to its crystal structure and in further consequence to its physical, mechanical, and structural properties. In particular all phyllosilicates are built up in a sheet like structure which is expressed by the Greek word *phyllon* which can be translated by *leaf* [32] rooting in another often used nomenclature, namely sheet silicates. The crystal structure of sheet silicates can be assembled by two elementary units which are represented by tetrahedral and octahedral cation–anion bonds, depicted in Fig. 3.2a.

In the case of the tetrahedral unit Si or Al atoms form the center of a tetrahedra surrounded by four oxygen atoms (three basal and one apical oxygen). Single tetrahedra are linked together by means of the basal oxygen atoms resulting in the formation of a two dimensional hexagonal mesh. Analogous considerations hold true for the formation of the octahedral sheet.

Based on these two units phyllosilicates can be divided into two subclasses namely 1:1 or 2:1 layer types. In the case of 1:1 layers one octahedral sheet is bound to a single tetrahedral one whereas in the 2:1 layer type one octahedral sheet is sandwiched between two tetrahedral units. In both cases sheets are aligned parallel to the $\{001\}$ netplanes of the bulk crystal and apical oxygens of the tetrahedra are shared with the octahedral sheet. Consequently each tetrahedra points with its apical oxygen to the octahedral layer whereas the basal atoms form a horizontal plane as indicated in Fig. 3.2b for a 2:1 layered structure, which is described below in more detail.

A partial cation substitution of Al^{3+} instead of Si^{4+} in the tetrahedral layer crucially influences the crystal stacking in phyllosilicates due to the generation of uncompensated charges within the layers. Pyrophyllite and talc belong to the not substituted phyllosilicates and consequently provide charge neutrality, whereas micas

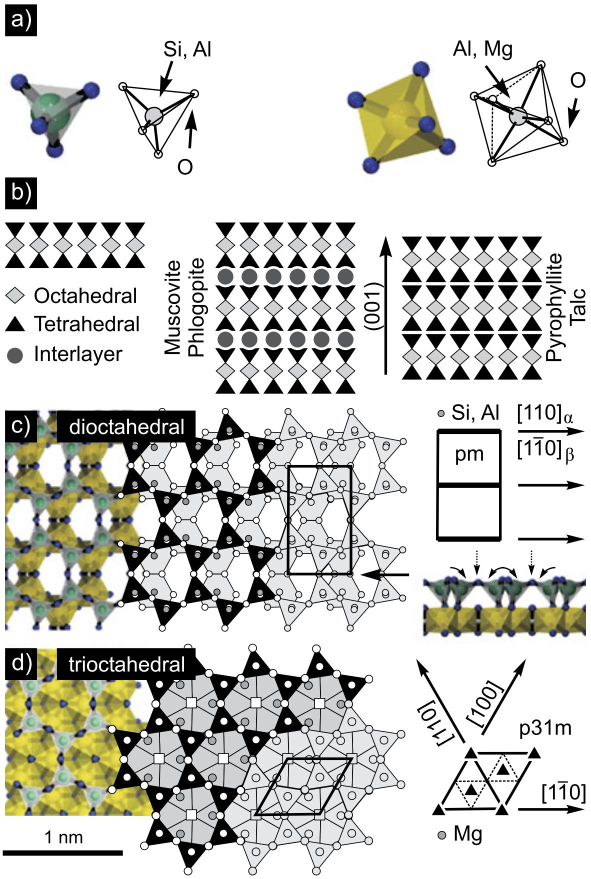

Fig. 3.2 (**a**) Elementary units of sheet silicates: tetrahedra (*left*) and octahedra (*right*) are built up by Si, Mg or Al atoms surrounded by oxygens. (**b**) Sheet like structure of 2:1 phyllosilicates defined by octahedral units sandwiched between tetrahedra. The crystal formation of muscovite and phlogopite is depicted beside showing a potassium interlayer holding the single sheets together. Contrary pyrophyllite and talc do not show such an interlayer. (**c**) Top view onto a {001} surface of a dioctahedral phyllosilicate (muscovite). As indicated by the *pm* space group beside, surface symmetry is showing mirror axes parallel to the surface grooves, indicated by a *solid arrow*. A side view along the grooved direction is sketched beside showing the tilted tetrahedral units. (**d**) Contrary trioctahedral phyllosilicate surfaces provide *p31m* symmetry, characterized by three mirror axes and three-fold symmetry

(e.g. muscovite, phlogopite) show an Al:Si ratio of 1:3 which leads to an uncompensated negative charge within the tetrahedral layers. By the addition of a cation interlayer sheet in the crystal structure the charge deficiency has to be balanced. In the case of muscovite and phlogopite this interlayer is provided by K^+ ions housed in quasi hexagonal cavities formed by the O^{2-} anions of the opposite tetrahedral sheets. Figure 3.2b sketches the stacking of 2:1 layer phyllosilicates with cation interlayers (e.g. muscovite, phlogopite) binding the single sheets together. Contrary pyrophyllite and talc stack without additional interlayers and consequently the binding between the two neighboring tetrahedral sheets depends exclusively on van der Waals bonds only [32].

Furthermore the presence of a potassium interlayer in micas is finally responsible for their perfect cleavage along {001} net planes as the electrostatic linkage represents the weak point in the crystal structure. The higher stability of cation–anion bonds within the octahedral and tetrahedral layers results in a quasi atomically flat surface being not only suitable for AFM studies [33–35] but also provides a perfect substrate surface for organic crystal growth [12, 36–38] and molecular adsorption [39–41].

It is important that the linkage between tetrahedral and octahedral sheets results in structural deformations (due to changing of bond angles and length) accompanied by a symmetry reduction of the bound tetrahedral–octahedral unit. In particular the hexagonal symmetry of individual tetrahedral and octohedral layers is reduced to at least 3-fold ditrigonal symmetry of the resulting units due to a tilt of the tetrahedra with a rotation axis normal to their basal plane [42]. The octahedral sheet is formed by octahedra which are linked together by sharing their six vertices. This can be provided when either each anion is bound to three cations (trioctahedral, see Fig. 3.2d) or to two cations leaving the third site vacant (dioctahedral, see Fig. 3.2c) [32]. As dioctahedral and trioctahedral sheets do not undergo identical deformations [32], the surface properties strongly differ between these two groups and in particular the symmetry of the cleavage plane crucially depends on the structural configuration of the octahedral layer, therefore we have to distinguish between dioctahedral and trioctahedral phyllosilicates.

3.2.1 Dioctahedral Phyllosilicates (Muscovite Mica, Pyrophyllite)

Dioctahedral phyllosilicates are characterized by a vacant octahedral site as indicated in Fig. 3.2c, sketching a top view on a dioctahedral phyllosilicate surface (e.g. muscovite mica surface when cleaved at the potassium interlayer). In particular a significant elongation of vacant octahedron edges can be recognized, caused by the absence of the cation in the center reducing attractive forces on the surrounding anions [32]. Thus the linkage between the tetrahedral sheet and a dioctahedral sheet requires an additional rotation of the tetrahedra around axes in the basal planes becoming visible by the shifted apical oxygen atoms (white circles) out of the centered cation (gray circle). The resulting tilt not only reduces the symmetry of the surface unit cell, but additionally causes also a surface corrugation of about 0.2 Å [42]. The situation is indicated in the inset of Fig. 3.2c representing a side view along the groove direction. Solid arrows indicate the rotational tilt of the tetrahedra whereas the dashed arrow marks the resulting groove which are caused by lowered oxygen atoms. At this point it has to be stressed that this corrugation originates from the interlinkage between octahedral and tetrahedral sheets and is not caused by a surface reconstruction due to cleaving. Hence the surface morphology of different dioctahedral phyllosilicates cleaved at the tetrahedral sheet provide analogous behavior and surface symmetry. In particular, the mirror symmetry of the surface unit cell is conserved for dioctahedral phyllosilicates in one axis that coincides with the direction of the present surface grooves and the resulting geometry of the surface unit cell can be described by the 2D-space group *pm* [43] as indicated in Fig. 3.2c.

As already discussed, muscovite mica and pyrophyllite, both representatives of dioctahedral phyllosilicates group, mainly differ due to their different cation substitution ratios and the resulting stacking sequence (see Fig. 3.2b). The octahedral layers in both materials provide analogous structural properties, 25 % of the Si^{4+} atoms within the tetrahedral layers of muscovite mica are substituted by Al^{3+}. Consequently the tetrahedral mesh can be formed by (i) Si–O–Si, (ii) Si–O–Al or (iii) Al–O–Al bonds, where the third possibility can be excluded based on electrostatic considerations (Löwenstein's rule) [44, 45]. As an experimental analysis based on X-ray diffraction exhibits serious difficulties due to the similarity of atomic scattering factors of Al and Si [45], information about two and three dimensional ordering is mainly based on computational models (e.g. Monte Carlo simulations) [44, 46] in combination with experimental data deduced by nuclear magnetic resonance (NMR) [45, 47].

A detailed look at the crystal properties of muscovite mica (Fig. 3.2b) reveals that the bulk unit cell includes two tetrahedral–octahedral–tetrahedral sheet units (compare Table 3.1). Interestingly both sheets provide an angular twist of 120° relative to each other leading to an alternating stacking sequence of type $\alpha\beta\alpha\beta$ along (001) crystal orientation. Whereas α planes provide their symmetry axis (and consequently grooved direction) in $[110]_M$ direction, the β planes show mirror symmetry along $[1\overline{1}0]_M$ [12]. Consequently, the mirror symmetry of the muscovite Mica surface unit cell has been indicated in Fig. 3.2c by two crystallographic directions, $[110]_\alpha$ and $[1\overline{1}0]_\beta$, respectively. Therefore it becomes evident that the presence of cleavage steps causes the presence of two different surface domains when switching from α to β planes and vice versa [12].

3.2.2 Trioctahedral Phyllosilicates (Phlogopite Mica, Talc)

Whereas the presence of vacant sites in dioctahedral systems favors deformation effects, such processes do not occur in trioctahedral–tetrahedral sheets [32]. Figure 3.2d depicts a top view of a trioctahedral phyllosilicate surface (phlogopite mica surface when cleaved at the potassium interlayer) providing a detailed model of the tetrahedral and octahedral layers. The hexagonal symmetry of the tetrahedral sheet is lost due to a rotation of the tetrahedra units around the axes perpendicular to the basal plane [32] resulting in a ditrigonal symmetry. Nevertheless the distortion of the octahedral and tetrahedral units in comparison with dioctahedral phyllosilicates (e.g. muscovite mica) is significantly reduced [32] resulting in a highly symmetric surface unit cell which is indicated by solid lines in Fig. 3.2d. A closer look to the atomic positions reveals a 3-fold symmetry with three mirror axes resulting in a *p31m* 2D-space group [43].

In analogy to dioctahedral phyllosilicates phlogopite mica and talc mainly differ due to their different cation substitution ratios and the resulting stacking sequence. As the surface morphology and symmetry are mainly determined by the formation of the octahedral layer both phyllosilicates show comparable surface morphology and symmetry.

In comparison to muscovite mica the crystal unit cell of phlogopite mica consists of only one tetrahedral–octahedral–tetrahedral sheet and consequently high symmetry directions can be defined uniquely as indicated by dashed–dotted arrows pointing in $[110]_P$, $[100]_P$ and $[1\bar{1}0]_P$ crystallographic directions, which means that all cleavage planes show the same surface symmetry.

Table 3.1 summarizes the discussed properties for phlogopite, muscovite, talc and pyrophyllite including its bulk unit cell parameters taken from literature [48–52].

3.2.3 Freshly Cleaved Mica Surfaces

Although the structural and crystallographic properties of phlogopite and muscovite seem conclusive and well understood, a detailed analysis of the morphological and structural properties of a freshly cleaved mica surface poses a demanding challenge. The following paragraph is only focused on the matters of fact playing a major role for the experimental procedures and computer simulations applied within this article.

In particular it has to be stated that the conditions during the cleaving procedure predominate the surface conditions and in further consequence certainly effect further growth experiments. In particular it has been demonstrated by Low Energy Electron Diffraction (LEED) that cleaving mica in ultra high vacuum conditions (UHV) leads to charging effects accompanied by triangular shaped diffraction patterns which are attributed to surface dipole fields [53, 54]. Complementary atomic force microscopy (AFM) investigations found UHV cleaved mica surfaces to be highly charged, effectively prohibiting AFM imaging of any reasonable resolution [55]. It is reported that exposure to air for a couple of minutes significantly reduces the charging effects [55] and in particular it is stressed that triangular shaped LEED pattern are never observed for mica substrates cleaved in air at atmospheric pressure [18, 54]. All these observations are in agreement with experiments providing chemical sensitivity, e.g. secondary-ion mass spectrometry (SIMS) and Auger electron spectroscopy (AES). In particular clear signals originating from carbon compounds have been detected on air cleaved mica by complementary techniques [18, 56, 57]. Interestingly it was found that an additional adsorption component is necessary to bind gaseous carbon compounds which is assumed to be provided by water [56]. In summary all these observations hint that a chemical reaction of residual surface potassium ions with carbonaceous gases and water [34, 55] takes place on air cleaved mica, which significantly forces the neutralization of uncompensated charges (potassium ions) in an irreversible way [54].

Table 3.1 Lattice parameters of trioctahedral and dioctahedral phyllosilicates

Material	Octahedral type/cation	Tetrahedral Al:Si ratio	Interlayer	a [Å]	b [Å]	c [Å]	α [°]	β [°]	γ [°]
Phlogopite	tri-oct./Mg	1:3	K^+	5.3158	9.2036	10.3100	90.00	99.891	90.00 [48]
Talc	tri-oct./Mg	only Si	none	5.26	9.10	18.81	90.00	100	90.00 [49]
				5.290	9.173	9.460	90.46	98.68	90.09 [51]
Muscovite	di-oct./Al	1:3	K^+	5.1988	9.0266	20.1058	90.00	95.782	90.00 [50]
Pyrophyllite	di-oct./Al	only Si	none	5.14	8.9	18.55	90.00	99.55	90.00 [49]
				5.160	8.966	9.347	91.18	100.46	89.64 [52]

Furthermore morphological and symmetrical properties of the mica surfaces are strongly related to the structural formation of the octahedral layers. In particular the vacant sites within dioctahedral systems are mainly responsible for the symmetry breaking and structural deformations [32]. The consistent picture is further substantiated by the comparison between experimentally deduced bulk crystal structures of muscovite [50] and phlogopite [48], showing the presence of parallel surface corrugations only within the dioctahedral muscovite mica. Additionally reported AFM measurements [33] on air-cleaved muscovite clearly reveal the presence of such grooves that break the 3-fold symmetry of the surface unit cell. Contrary AFM images reported from phlogopite mica surfaces show quasi hexagonal symmetry as expected by geometrical considerations (compare Fig. 3.2) [32].

In summary it can be justified that the surface morphology dominates the molecule-surface interactions during the deposition process whereas electrostatic forces due to Al–Si substitution and uncompensated potassium ions play a minor role when cleaving the mica substrate in air.

3.3 Epitaxial Growth of Rod-Like Molecules on Sheet Silicates

In order to discuss the epitaxial growth on sheet silicate substrates we have selected two representative rod-like molecules, namely p-6P and 6T. Both molecules are already intensively investigated and it has been demonstrated that they can be successfully used for organic device applications [58–60].

3.3.1 Para-Hexaphenyl

As depicted in Fig. 3.3a each p-6P molecule consists of six phenyl rings linked together in a chain like structure. Organic p-6P crystallites provide a large energy gap (3.1 eV) between highest occupied molecular orbital and lowest unoccupied molecular orbital, excellent optical properties including photoluminescence with high quantum yield and outstanding structural properties. These properties provide a proper fundament for optoelectronic devices which further explains that p-6P based organic light-emitting devices were among the first candidates applied for blue emission [58, 59].

During the last years the epitaxial growth of p-6P has been analyzed extensively on several substrates by optical, crystallographic and morphological methods. In that sense also the crystal formation on muscovite mica has been studied in detail and it has been found that p-6P tends to crystallize in its β-structure [61] which represents the equilibrium bulk structure [12]. Figure 3.3b indicates the β-structure primitive unit cell which consists of two p-6P molecules packed in herringbone fashion. Depending on the chosen substrate temperature it has been shown that p-6P crystallizes either with its $(11\bar{1})$ or $(11\bar{2})$ crystal planes parallel to the muscovite mica substrate surface [12]. As the dominating fraction of p-6P crystallites

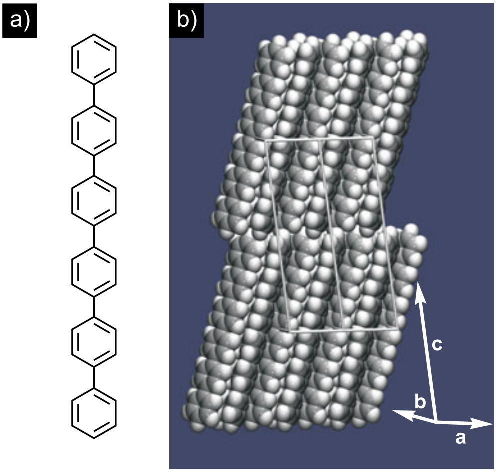

Fig. 3.3 (**a**) Molecular representation of the p-6P molecule, characterized by six phenyl rings linked together. (**b**) Primitive monoclinic lattice of p-6P β-structure representing the equilibrium bulk structure ($a = 8.091$ Å, $b = 5.568$ Å, $c = 26.241$ Å and $\beta = 98.17°$) [61]

are characterized by a $(11\overline{1})$ contact plane further discussion is focused only on this orientation.

To analyze the epitaxial growth of p-6P on sheet silicate substrates a series of samples has been prepared by hot-wall epitaxy (HWE). The growth time was chosen to 40 min and the substrate temperature has been kept constant at 90 °C during the deposition procedure while the source and wall ovens were kept at 240 °C and 260 °C, respectively. As substrates two different types of mica have been chosen, namely muscovite mica and phlogopite mica. In order to verify the morphological properties of the grown nanostructures atomic force microscopy (AFM) images have been acquired. In the case of muscovite mica highly parallel needle formation can be observed providing nanostructures which are several micrometers long (see Fig. 3.4a). To analyze the azimuthal alignment and consequently the epitaxial relationships between the organic crystallites and the mica substrates in detailed XRD pole-figure measurements have been performed. The measured pole figure for the $(11\overline{1})$ diffraction peaks are shown in Fig. 3.4c. For a direct comparison with the geometry of the muscovite mica substrate surface, the mirror axis for a β-cleavage plane [12] is indicated in the pole figure by a solid line along $[1\overline{1}0]_M$ crystallographic direction. Diffraction peaks which can be attributed to organic p-6P crystallites are indicated by arrows. Strikingly organic diffraction peaks observed in the upper and lower hemispheres of the polar plot can be nicely correlated with each other by a mirror operation along the $[1\overline{1}0]_M$ direction. So it is demonstrated that the expected mirror symmetry of the substrate surface is nicely adopted by the organic crystallites. Thus, the measurement can be well explained by the presence of four crystal orientations, which have in common the mirror symmetry originating from the substrate and a 2-fold symmetry due to the geometry of the p6P molecule. For each p-6P crystallite a unique long needle axis (LNA) can be defined by the orientation of its $[1\overline{1}0]$ crystallographic direction [12]. The resulting orientations are indicated in the left part of Fig. 3.4b, following the geometric considerations already discussed. As AFM measurements provide direct access to the azimuthal

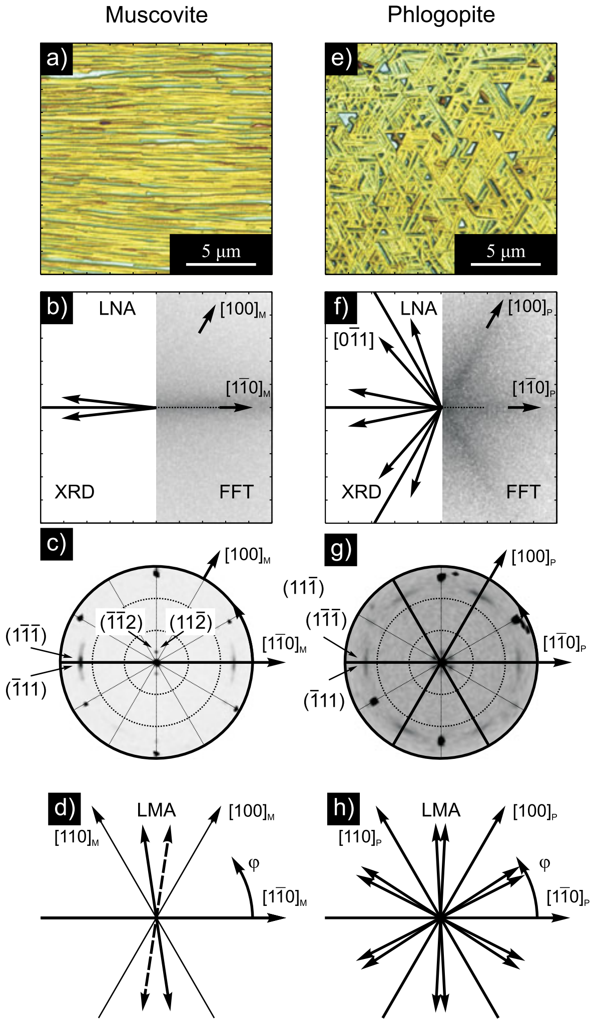

Fig. 3.4 AFM images of para-hexaphenyl (p-6P) nano-needles grown on muscovite (**a**) and phlogopite (**e**) mica. Azimuthal alignment of the long needle axis (LNA) deduced by XRD pole-figure measurements (*left*) and AFM-FFT analysis (*right*) for p-6P deposited on muscovite (**b**)/phlogopite (**f**) substrates. XRD pole-figure measurement performed at a scattering angle of 29.5° with an acceptance angle of ±1° performed on p-6P crystals on muscovite (**c**) and phlogopite (**g**) mica. Azimuthal alignment of the long molecular axis (LMA) deduced by XRD pole-figure measurements (**d**, **h**)

distribution of the LNAs, the calculated FFT pattern of Fig. 3.4a is presented in the right part of Fig. 3.4b providing excellent agreement with crystallographic analysis. As indicated in Fig. 3.3b p-6P molecules are aligned quasi parallel with their long molecular axis (LMA) within the crystal unit cell. Consequently each organic crystallite can be correlated with a unique LMA providing information about the alignment of the p-6P molecules relative to the substrate surface. As indicated in Fig. 3.4d p-6P molecules align nearly normal to the mirror axis of the muscovite mica substrate.

In order to analyze the influence of di- and trioctahedral mica substrates on the organic needle formation, analogue analysis has been applied to p-6P films deposited on phlogopite mica. As indicated by the AFM image depicted in Fig. 3.4e the higher substrate surface symmetry of phlogopite mica is directly reflected by the orientation of the LNA. Whereas muscovite mica shows only one dominant LNA, p-6P deposited on phlogopite mica is characterized by triangular structures resulting from the three-fold symmetry of the substrate surface. Due to crossing of the individual p-6P crystallites nano-fibers become much shorter in length as compared with the same growth conditions on muscovite mica substrates. Again FFT analysis of the AFM images has been performed and is depicted in the right part of Fig. 3.4f showing three streaks separated by 60°. In order to analyze the epitaxial relationship of organic crystallites and the substrate XRD pole-figure measurements have been performed and are reported in Fig. 3.4g. To provide direct comparison with the muscovite mica substrate, XRD pole-figure measurements have been performed with unchanged conditions choosing an scattering angle of 29.5° with an acceptance angle of ±1°. Strikingly the XRD pattern observed on muscovite mica are also reflected for the trioctahedral mica substrate. This observation is consistent with specular XRD diffraction spectra which show analogue configuration concerning the contact plane of p-6P nano-needles on both substrates, namely a dominating formation of p-6P crystallites characterized by a parallel $(11\overline{1})$ crystal plane to the substrate surface. Moreover azimuthal alignment of p-6P crystallites varies only marginally between both substrates due to a similar configuration of the tetrahedral layer determining the interface between substrate and organic crystallites. Nevertheless higher symmetry of the phlogopite mica substrate is clearly reflected by a three-fold symmetry of the pole figure. As expected also the azimuthal alignment of the LNA, which is indicated in the left part of Fig. 3.4, reflects this geometry. Again nice correlation with AFM-FFT analysis being sensitive to morphology can be observed. The orientation of the LMA is depicted in Fig. 3.4h reporting a preferred molecular orientation along the $[310]_P$, $[3\overline{1}0]_P$ and $[010]_P$ crystallographic directions of phlogopite mica.

3.3.2 Sexithiophene

α-Sexithiophene, a conjugated oligomer consisting of six thiophene units linked at alpha position (see Fig. 3.5a), is one of the most promising materials for organic-based electronic devices, primarily, organic field-effect transistors (OFETs) [60, 62, 63]. Concerning its crystallization the appearance of polymorphism is observed leading to two different crystal configurations [64]. Whereas 6T crystallites grown from the vapor phase pack with four molecules (low-temperature—LT—phase, sketched in Fig. 3.5b) [65] those grown from the melt are characterized by two molecules per unit cell (high temperature—HT phase) [66]. Whereas p-6P emits in the blue spectral range, the emission of 6T is significantly red shifted leading to orange-red fluorescence when optically excited [62, 63].

All these properties imply that 6T represents a promising candidate to study the epitaxial growth on sheet silicates. Again, two different kind of mica substrates have

Fig. 3.5 (**a**) Molecular structure of sexithiophene (6T) providing six thiophene units linked together at alpha position. (**b**) Primitive monoclinic lattice of the 6T low-temperature phase

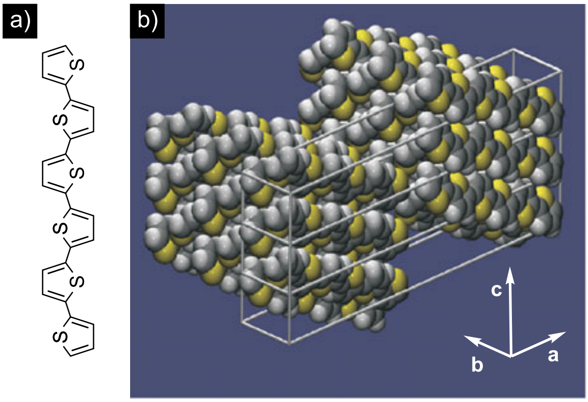

been used to study the epitaxial growth of 6T by HWE. After cleaving the mica substrates in air, they have been transferred to the HWE chamber working at $9 \cdot 10^{-6}$ mbar. After a thermal treatment of the substrate at 90 °C, the sample has been transferred in vacuum conditions to the 6T HWE oven. Subsequently 6T has been deposited for 90 min, keeping a substrate temperature of 90 °C. The source material has been evaporated at 190 °C and the wall was heated to 220 °C.

To analyze sample morphology optical microscope images have been taken and are reported in Fig. 3.6a. Comparable to p-6P organic nano-needles become visible on the muscovite mica substrate. Nevertheless, anisotropy is significantly lowered which becomes visible by multiple azimuthal orientations. In order to analyze the angular distribution of the organic nano-needles in more detail, FFT analysis has been applied to the optical microscope image and is reported in the right part of Fig. 3.6b. A closer look to the depicted pattern reveals four sharp streaks, each representing a distinct needle orientation. The obtained crystal orientation has been analyzed in more detail by XRD pole-figure measurements which are reported in Fig. 3.6c. In particular, the orientations of 6T $(\bar{2}11)$ netplanes were probed to determine the azimuthal alignment of the organic crystallites. As indicated in Fig. 3.6c by black arrows, XRD pattern reveal eight diffraction spots which underline a defined azimuthal order of the 6T crystallites. This pattern can be explained by a packing of 6T molecules in the so-called low-temperature phase [65] and a parallel orientation of the $\{\bar{4}11\}$ planes to the muscovite mica $(001)_M$ substrate surface. The diffraction spots in Fig. 3.6c again clearly reflect the geometry of the muscovite mica surface unit cell. Analogous to the analysis reported for p-6P the orientation of the LNA and LMA has been deduced from the experimental data. Whereas the LNA of the 6T crystallites can be deduced by their $[0\bar{1}1]$ crystallographic orientation, the angular orientation of the LMA is concluded by the molecular alignment within the crystal unit cell. As indicated in the left part of Fig. 3.6b XRD experiments provide excellent agreement with morphological investigations, indicating four distinct needle orientations. Contrary the LMA, as reported in Fig. 3.6d, are aligned along two orientations which are defined by the $[110]_M$ and $[100]_M$ crystallographic directions of the muscovite mica substrate. Moreover, the diffraction spots in Fig. 3.6c

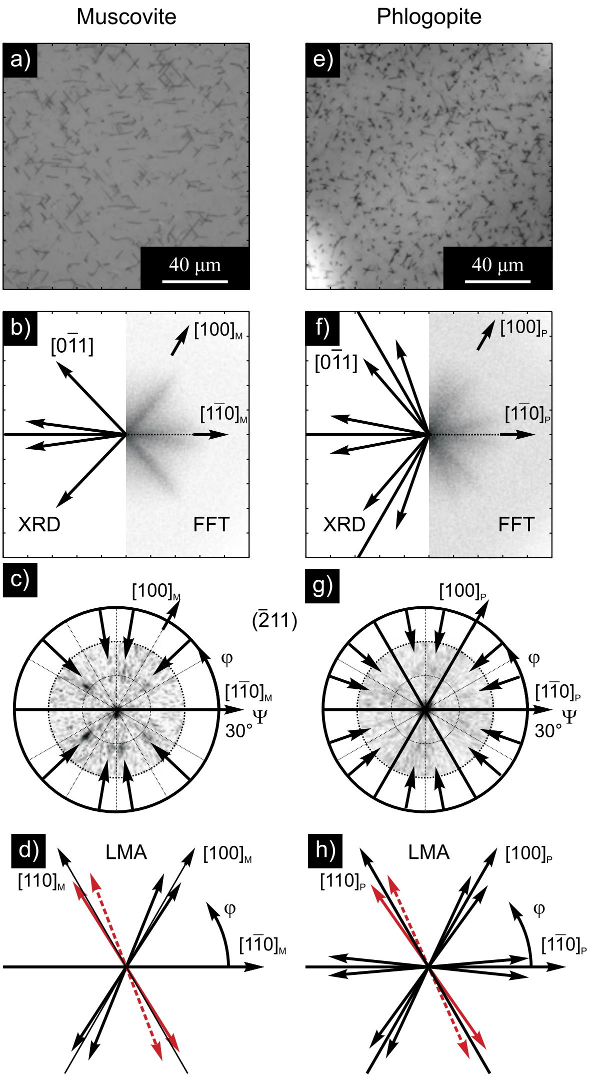

Fig. 3.6 Optical microscope image of 6T nano-needles deposited on muscovite (**a**) and phlogopite mica (**e**). The angular configuration of the long needle axes (LNA) deduced by XRD (*left*) and AFM-FFT (*right*) analysis for 6T crystallites deposited on muscovite (**b**)/phlogopite (**f**) mica. XRD pole-figure measurements of the $\{\bar{2}11\}$ diffraction peaks, *arrows* indicate azimuthal position of the $\{\bar{2}11\}$ poles. Results for sexithiophene crystals deposited on (**c**) muscovite mica and (**g**) phlogopite mica are presented. (**c**)–(**h**) Orientation of the 6T long molecular axis (LMA) deduced from the corresponding XRD pole-figure measurements depicted above

clearly reflect the geometry of the muscovite mica surface unit cell. This becomes evident by the presence of a mirror symmetry along the $[110]_M$ direction, implying crystal growth on a α terminated muscovite mica substrate [12].

To compare the crystal growth on tri- and dioctahedral mica substrates, comparable investigations have been applied to nano-needles which have been deposited on phlogopite mica. As expected film morphology is dominated by nano-needles which are oriented along multiple directions (Fig. 3.6a). Whereas the microscope image indicates quasi random azimuthal order, the calculated FFT pattern, which is reported in the right part of Fig. 3.6b clearly reveals distinct azimuthal orientations. As already demonstrated for p-6P crystallites the deduced FFT pattern nicely reflects the symmetry of the substrate surface unit cell. In particular three-fold and mirror symmetry along $[100]_P$, $[1\overline{1}0]_P$ and $[\overline{1}10]_P$ crystallographic orientations of phlogopite mica becomes visible. As expected also XRD pole-figure measurements, which are reported in Fig. 3.6b reflect these observations. Again, black arrows indicate the azimuthal angle where $\overline{2}11$ diffraction spots are observed. The XRD pattern can be explained by a packing of 6T molecules in the low-temperature phase [65] and a parallel orientation of the $\{\overline{4}11\}$ planes to the phlogopite mica $(001)_P$ substrate surface. As observed for p-6P the crystal orientation on phlogopite mica nearly follows the trend observed for muscovite mica substrates. In particular, the orientations of LMA and LNA observed for muscovite mica are quasi conserved and are accompanied by further possible configurations due to three-fold symmetry of the substrate surface unit cell. As indicated in Fig. 3.6b crystallographic analysis nicely correlates with morphological investigations provided by optical microscopy. The angular orientation of the LMA is depicted in Fig. 3.6h showing an alignment along the high symmetry orientations of the phlogopite mica substrate.

For the sake of completeness it has to be mentioned that beside the discussed needle formation additionally island like structures are observed on both kind of mica substrates. These entities can be related to 6T crystallites which are characterized by a (100) contact plane and are consequently formed by quasi standing 6T molecules on the substrate surface. Interestingly, also these crystallites provide a distinct azimuthal orientation which follows substrate surface symmetry and can be explained by a distinct relationship to 6T crystallites forming the organic nanoneedles. More details concerning the epitaxial growth of 6T on mica substrates can be found elsewhere [27].

3.3.3 *Growth Model of Rod-Like Molecules on Sheet Silicates*

In order to understand the discussed experimental observations in more detail Fig. 3.7 sketches a growth model which can explain the epitaxial growth on sheet silicates.

1. *Molecular Adsorption* In the initial phase of organic crystal growth single rod-like molecules align flat lying on the substrate surface. It can be expected that for each molecule type there exists an energetically preferred azimuthal orientation which leads to distinct azimuthal orientation of the LMA. In order to verify this statement force-field simulations have been performed on tri- and dioctahedral sheet silicate substrates, namely talc and pyrophyllite [19]. As discussed extensively pyrophyllite and muscovite mica mainly differ concerning the Al–Si substitution of the tetrahedral layer, whereas their substrate surface geometry is comparable. Consequently the influence of electric fields originating from the mica substrate can be excluded whereas just the effect of surface corrugation is considered by the force-field calculations. By minimizing the adsorption energy for each angle ϕ the optimal adsorption position of an isolated organic molecule

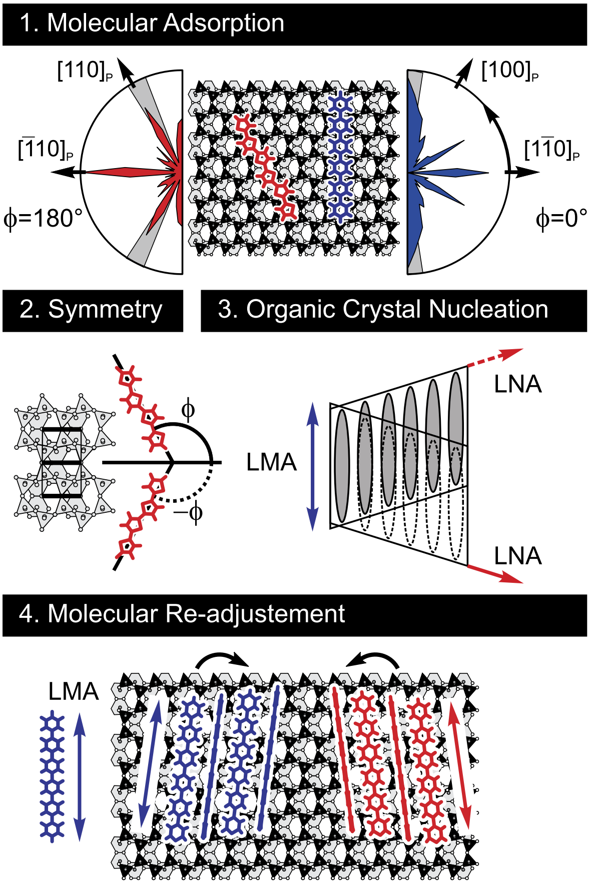

Fig. 3.7 Graphical overview demonstrating the epitaxial growth of rod-like molecules on sheet silicates. In the initial stage (**1**) the interaction between single molecules and the substrate surface plays a major role. Depending on the molecules different angular alignment can be expected representing an energetically favorable configuration. In a further step (**2**) substrate surface geometry and in particular mirror symmetry leads to multiple orientations which are energetically equivalent. Molecular configuration within the unit cell of the organic crystallite leads to the formation of multiple needle orientations (**3**) nucleating at the molecule adsorption sites. With growing crystal size molecule–molecule interactions within the organic crystallite become dominant and can further lead to slight angular realignment (**4**) on the substrate surface

on top of such a substrate can be determined. In that way each azimuthal molecular orientation can be correlated with an adsorption energy which is defined as the difference between the energies of the isolated subsystems and the energy of the combined system, i.e., the molecule and the substrate. Therefore, maxima in the E_{ad} vs. ϕ curve evidence the favorable adsorption geometries. Figure 3.7(1) presents the obtained results as a polar diagram for 6T (left) and p-6P (right) molecules. As both molecules provide two-fold symmetry full polar plots can be deduced by a 180° rotation. As expected also simulations nicely reflect the symmetry of the di-octahedral substrate. To compare simulations with experimental results gray areas indicate the orientation of the LMA deduced by XRD pole-figure measurements. As indicated by the red curve in the left part of Fig. 3.7(1) simulations for 6T molecules reveal three local maxima (90°, 120°, 180°) which represent energetically preferable molecular adsorption geometries. Out of these configurations, the intermediate, but not the strongest, peak is in accordance with experiment. This small discrepancy can be explained by the usage of empirical potentials which in some cases may yield the wrong energetic ordering of competing structure solutions [67]. In the case of p-6P which is presented on the right side of Fig. 3.7(1) simulations provide perfect agreement with experimental data. Strikingly, the global maxima located at $\phi = 90°$ perfectly overlaps with experimental findings. The corresponding molecular adsorption site on the pyrophyllite surface is indicated in the center of Fig. 3.7(1) showing two different adsorption angles for 6T and p-6P molecules.

2. *Substrate Surface Symmetry* Due to substrate surface geometry, each adsorption site has a mirrored energetically equivalent adsorption site on the surface as indicated in Fig. 3.7(2). This energetically equivalence results statistically in an equally appearance of these adsorption sites and furthermore in nucleation on these sites. This expectation can be nicely confirmed by XRD pole-figure measurements which directly proof mirror symmetry of the organic crystallites. As a consequence of this finding it has to be stated that maximized anisotropy of organic crystallites can only be provided when molecules align parallel or normal to the substrate surface mirror axis. Exactly this situation holds true for p-6P whereas 6T molecules are accompanied by a twin configuration leading to X-shaped needle formation.
3. *Organic Crystal Nucleation* As the density of molecules on the surface increases, needles start to nucleate from a single molecule. Due to clustering of molecules the crystal structure of the respective bulk phase is adopted. There are, in principle, two possible growth directions. This is visualized in Fig. 3.7(3) by the solid and dashed ovals representing the rod-like molecules. The molecules in one needle are turned upside down (mirrored) with respect to the molecules in the other needle. Consequently each molecular adsorption site leads to the formation of two needle directions. In general, this will not lead to two energetically equivalent geometries. As these two orientations are further doubled due to the substrate surface mirror symmetry the existence of four needle orientations can be expected in the general case.
4. *Molecular/Crystal Re-adjustment* During needle growth molecule–molecule interactions will become more and more important. This will cause a slight readjustment of the LMA in the order of a few degrees to obtain a better lattice match with the substrate [12, 68]. This adjustment can be assumed to be different for the two needle-growth directions. As indicated in Fig. 3.6d and Fig. 3.6h XRD pole-figure measurements indicate a slight splitting of the LMA which has been verified also by force-field calculations [19].

Summarizing the discussed growth model it has to be stated that parallel needle formation, as in the case of p-6P and functionalized quaterphenylenes, can be only achieved in outstanding molecular systems. In particular two main criteria have to be fulfilled:

- The long molecular axis of the chosen molecule has to be aligned parallel or normal to the mirror axis of the muscovite mica substrate. Only in these configurations the mirrored adsorption site coincides with its twin position.

- The molecular configuration within the unit cell of the organic crystallite crucially influences the expected splitting of organic nano-needles. An optimized configuration can be expected if the surface unit cell of the organic crystallite provides an rectangular shape which would theoretically lead to only one needle orientation per molecular adsorption site.

Based on these findings it has to be stated that substitution of p-6P molecules by other species in order to achieve an efficient color shift of organic nano-fibers grown on muscovite mica is not trivial and it can be expected that only a small group of molecules can fulfill the inevitable conditions. In further consequence other solutions have to be found to achieve parallel molecular alignment being an essential requisite for polarized emission.

3.4 Organic Hetero-epitaxy of Nano-fibers

In recent years, heteroepitaxy of organic–organic nanostructures has been demonstrated as a valuable technique to explore the full potential of organic semiconductors for optoelectronic applications. Crystalline and highly ordered heterostructures with different morphology and molecular orientations can be realized by heteroepitaxy starting from conjugated oligomers, aimed at tailoring their optical properties and transport characteristics [69–73].

Whereas the deposition of organic molecules directly on muscovite mica seems not very promising in order to obtain highly anisotropic nano-fibers, organic heteroepitaxy could provide a proper tool to achieve the desired goal. The principal idea is sketched in Fig. 3.8 and proposes the organic crystal growth on top of p-6P fiber templates. As material couple for heteroepitaxy p-6P and 6T seem compatible due to their rod-like configuration and comparable chain length. Moreover it has already been demonstrated that molecular orientation can be influenced by organic heteroepitaxy of p-6P/6T [72, 73].

In order to verify if organic–organic heteroepitaxy can be successfully implemented on organic nano-fibers, samples have been fabricated on muscovite mica (001) substrates by using HWE. Immediately after cleaving, the mica substrates were transferred via a load lock to the growth chamber, providing two separated HWE reactors equipped with p-6P and 6T source material. The optimized evaporation temperature for p-6P is given at 240 °C (190 °C), leading to a nominal growth rate of 3 nm/min (4.5 nm/min). In order to avoid temperature gradients during growth and to reduce adsorbed species on the surface, the substrate has been preheated at 120 °C for 30 min. The chosen temperature is kept constant during the whole growth procedure. After depositing p-6P for 40 min ($\approx$120 nm fiber height), the sample is automatically transferred in high vacuum conditions to the 6T source

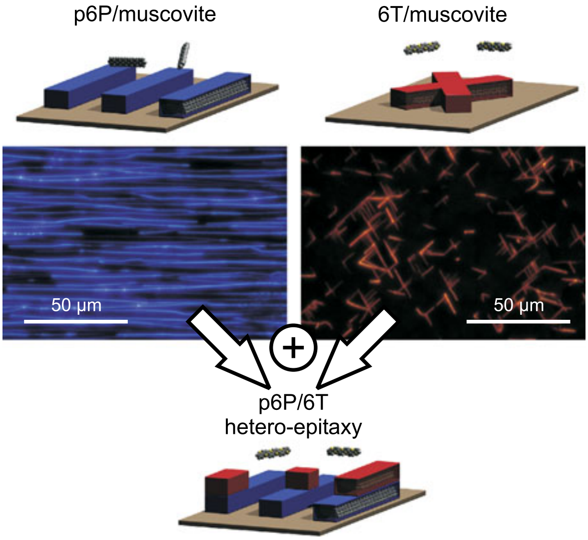

Fig. 3.8 Deep-blue-emitting highly oriented p-6P nano-fibers (*left*) and red-orange 6T fibers (*right*) grown on muscovite mica. Schematic representations of multilayer fibers are provided above, with crystalline p-6P represented by *blue sticks*, and crystalline 6T as *red sticks*. The schematic below sketches the desired behavior when using organic–organic heteroepitaxy. The usage of p-6P template needles should force a realignment of 6T crystallites

oven. Subsequently, 6T has been deposited for 1 s up to 90 min (≈405 nm). The nominal layer thickness is defined as average fiber height.

In a first step heterostructures grown with nominally 120 nm p-6P and 400 nm 6T layer thickness have been investigated by AFM. As indicated in Fig. 3.9a film morphology of the pure p-6P needle template seems to be conserved becoming visible by nicely parallel oriented nano-fibers. A closer look to the AFM image indicates the presence of two different needle morphologies which becomes obvious by excerpting a cross-sectional view as indicated in Fig. 3.9b. Interestingly, needles with two characteristic height levels are formed on the muscovite mica substrate. Moreover, the height histogram of the AFM image (Fig. 3.9b) underlines this observation showing three peaks which can be attributed to the bare muscovite mica substrate (A), the p-6P template needles (B) and p-6P needles which have been overgrown by 6T crystallites. Corresponding regions are indicated also in the AFM image and in the depicted cross section. Moreover needle shape of both needle structures seem to differ significantly as indicated in Fig. 3.9b. Whereas lower needles provide a nearly rectangular shape of their cross section, which is expected for p-6P crystallites [30], organic–organic heterostructures are characterized by a triangular rounded silhouette already hinting a different growth morphology.

For a more detailed analysis XRD pole-figure measurements have been performed providing information about crystal phase, contact plane and azimuthal orientation. In particular, the azimuthal orientation of $(\bar{2}11)$ of 6T ($q = 1.34$ Å) has been analyzed in detail and is reported in Fig. 3.9c. Experiments reveal two significant spots located symmetrically aligned around the [110] direction of muscovite mica and are consequently characteristic for a single fiber domain deposited on an α-cleavage plane [12]. A more detailed analysis of the pole figure (see the inset) allows to resolve additional distinct diffraction peaks originating from the $\{\bar{2}11\}$ netplanes of 6T as well as from the $\bar{1}11$ netplanes of p-6P. The observed diffraction

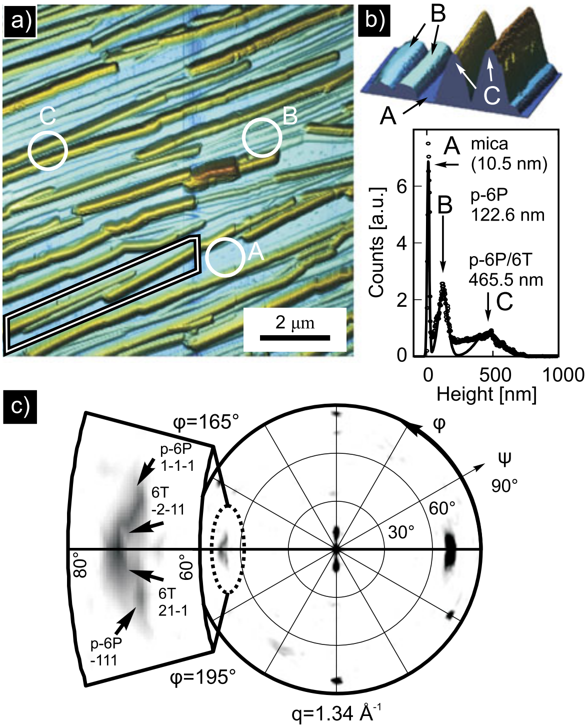

Fig. 3.9 (**a**) AFM image of the heteroepitaxial sample structure showing parallel aligned nano-fibers. (**b**) Height histogram of AFM image showing three peaks originating from the bare mica substrate, visible between the fiber structures (A), the p-6P fibers (B), and the overgrown 6T/p-6P fibers (C). Corresponding regions are marked in (**a**). (**c**) XRD pole-figure measurement ($q = 1.34$ Å) providing information about the azimuthal orientation of the p-6P and 6T crystals relative to the muscovite mica substrate. The *inset* depicts a zoom of the pole figure, indicating the presence of p-6P and 6T crystallites

pattern can be described by four crystallites of each molecular species representing a two-fold symmetry with an additional mirror axis around the [110] direction of muscovite mica. Whereas p-6P crystallites provide a $(\bar{1}11)$ contact plane 6T crystallites are oriented parallel with their $\{\bar{4}11\}$ netplanes to the muscovite mica surface. Interestingly an analogous configuration concerning the contact plane has also been observed for 6T nano-fibers directly deposited on bare muscovite mica substrates. Nevertheless their pole-figure pattern significantly differ underlining a changed azimuthal orientation due to organic–organic heteroepitaxy.

Based on pole-figure measurements it is possible to deduce a real space model of the crystal and molecular orientations (Fig. 3.10a). The crystal stack on the left side demonstrates the molecular orientation of p-6P (gray) molecules in one crystallite, and the white arrow points in the $[1\bar{1}0]$ direction of the p-6P stack, defining the resulting LNA [12]. On top of the organic template, 6T molecules (yellow atoms represent sulfur) are indicated, packed in the low-temperature herringbone structure and characterized by a $(\bar{4}11)$ contact plane parallel to the substrate surface. A more detailed inspection of the p-6P/6T interface (shown in the inset of Fig. 3.10a) resolves the expected herringbone package providing nearly perfect adoption of 6T to p-6P layers. To aid the reader, the mirrored crystallite is reduced to two single molecules and the corresponding LNA that has an angle of 6° with respect to the [110] direction of muscovite mica. As a consequence of these orientations, both LMAs are parallel to each other and have an angle of 83° with respect to the high symmetry

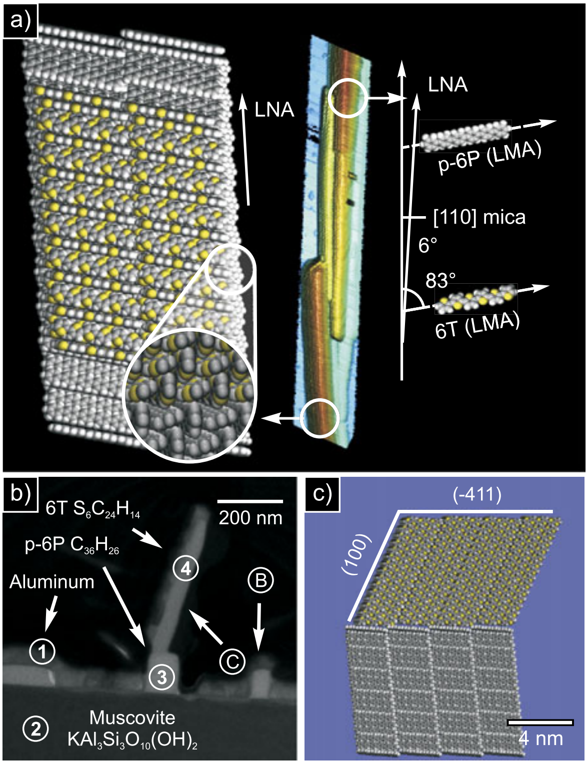

Fig. 3.10 (**a**) Simulation of the molecular alignment within the nano-fibers concluded from the XRD pole-figure measurements. The angle between the long needle axis (LNA), the long molecular axis (LMA), and the mica [110] direction is indicated in the mirrored crystal model on the *right*. The *inset* indicates the herringbone structure of p-6P and 6T at the crystal interface. (**b**) TEM cross section of p-6P/6T heterostructure, indicating the deposited aluminum layer (1), muscovite mica substrate (2), p-6P template region (3), and 6T crystallite (4). (**c**) Simulated view along LNA of p-6P templates showing the expected angular alignment of 6T low energy (100) plane

axis of muscovite mica. A splitting of the LNA around the [110] direction of muscovite mica due to mirror symmetry can be further outlined by the morphological arrangement of two single nano-fibers seen in the center of the plot (Fig. 3.10a). The magnification is taken from a 10 × 10 µm AFM image, and its origin is indicated by a white polygon in Fig. 3.9a.

In order to further clarify the epitaxial overgrowth of p-6P nano-fibers by 6T crystallites, transmission electron microscopy (TEM) analysis has been conducted, providing a nanoscopic view on the structural properties. Before preparing TEM slides, samples have been covered with a 25 nm thick aluminum (Al) layer for protection purposes, becoming visible by an enclosing cover layer, indicated in Fig. 3.10b by region 1. Furthermore, the muscovite mica substrate can be clearly determined by a sharp contrast and is indicated by region 2. Structures characteristic for the two different fiber types are labeled B and C. In particular, rectangular appearance of fiber-type B in combination with a correlation in height justifies the direct comparison with AFM analysis. Strikingly, fiber structures of type C are characterized by a tilted entity on top of a rectangular fiber basement, emphasizing the difference in shape already observed by AFM analysis. In order to understand the observed behavior, molecular stacking has been modeled based on structural investigations determined by XRD pole-figure measurements. The obtained result is indicated in Fig. 3.10c, providing a cross-sectional view along the fiber directions and consequently com-

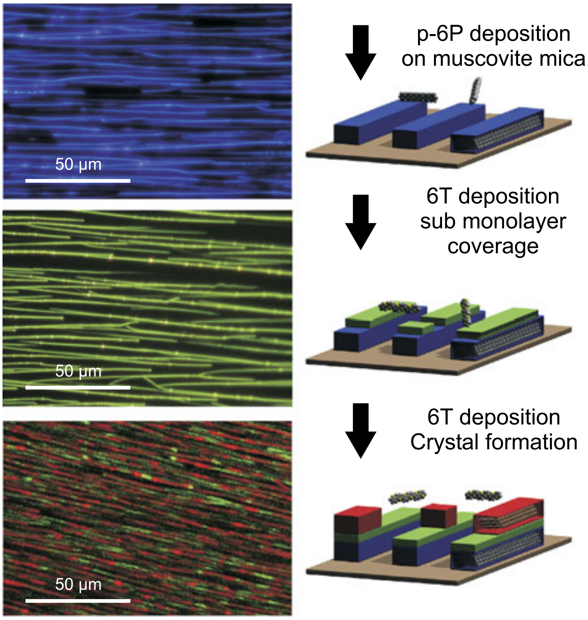

Fig. 3.11 Fluorescence microscopy images of p-6P/6T heterostructures at different 6T layer thickness. Whereas pure p-6P fibers which are used as templates provide deep-blue emission (*top*) the evaporation of 6T with nominally sub monolayer coverage provides green emission under UV excitation (*center*). With increasing 6T deposition time 6T crystallites are formed on top of the needle structures which provide red emission

parable with TEM analysis. The lower part of the image indicates a single p-6P crystallite characterized by a horizontal alignment of its $\{\bar{1}11\}$ netplanes. On the contrary, $\{\bar{4}11\}$ netplanes of the overgrown 6T crystallite are aligned horizontally, fulfilling structural alignment deduced by XRD. The presented model stack directly reveals a different stacking of 6T and p-6P crystallites along the growth direction, which can be explained by the different tilt of low index planes, namely, $(001)_{p-6P}$ and $(100)_{6T}$, providing the lowest surface energy. Whereas p-6P low index plane is more or less oriented vertically, the low energy facet of 6T is remarkably tilted and astonishingly provides excellent agreement with experimental data (demonstrated in Fig. 3.10b).

In summary structural and morphological investigations have demonstrated that organic–organic heteroepitaxy can be successfully implemented on nano-fibers. Whereas 6T crystallites deposited directly on muscovite mica substrates are characterized by X-shaped morphology, organic–organic heteroepitaxy provides a proper method to force a realignment of the crystallites. Moreover, TEM analysis has demonstrated that a sharp organic–organic interface can be achieved underlining a well-defined epitaxial relationship between both organic crystallites. As shown by XRD pole-figure measurements the LMA of 6T molecules adopt the highly parallel ordered arrangement of p-6P molecules in the template crystallite which promises highly polarized emission of p-6P as well as 6T crystallites.

For the optical characterization of the p-6P/6T heterostructures in a first step fluorescence microscopy has been applied on various samples providing a first hint concerning the emission properties. Interestingly emission properties strongly depend on the deposited thickness of 6T layers and consequently Fig. 3.11 summarizes the obtained results for the three representative configurations. In a first step p-6P template structures have been investigated under UV excitation providing deep-blue emission (top). In a next step 6T has been deposited on top of a p-6P needle template with nominally submonolayer coverages. As indicated in Fig. 3.11 (center), green-emitting fibers are obtained. The emission spectrum is dominated by that of the 6T molecules deposited on top of the p-6P fibers while blue fluorescence of p-6P is significantly quenched. For increasing 6T coverage, the red-orange fluorescence band typical of 6T polycrystalline films appears, suggesting that crystal nucleation occurs on top of the fibers. The emission intensity of the new band is much weaker than that of a submonolayer film grown on p-6P fibers, whereas it is comparable to that of a pure 6T/muscovite mica film of polyoriented crystalline fibers. Scanning probe fluorescence images collected in different spectral bands are indicated in Fig. 3.11 (bottom) and make it possible to map the distributions of green-emitting 6T molecules and 6T crystals along the 6P template fibers. Fluorescence intensity measured through a green band-pass filter shows quite a homogeneous distribution of green-emitting molecules, whereas fluorescence imaging through a red-transmitting filter proves that 6T crystals are superimposed to the templating fibers and form fibers themselves. Consequently optics underlines the drawn picture based on structural and morphological investigations.

For a deeper understanding concerning the optical anisotropy, molecular orientation and long-range order of the p-6P/6T heteroepitaxial films, samples have been investigated by combined fluorescence spectroscopy and fluorescence polarization averaged over sample areas as large as 500 μm^2. The emission spectrum of the films can be decomposed in its three components arising from crystalline p-6P, 6T interfacial layers and crystalline 6T, which emit in the blue, green and red, respectively. The three components are singled out from the emission spectrum by measuring pure p-6P films, p-6P/6T films with short 6T deposition times, and pure 6T films on muscovite mica (dashed lines in Fig. 3.12a). It is noteworthy that the spectrum of green-emitting, submonolayer 6T aggregates (Fig. 3.12a) is considerably blueshifted with respect to that of 6T crystals and only slightly redshifted from that of noninteracting molecules [74]. This is reminiscent of what has been reported for submonolayer films of lying 6T molecules deposited on silicon dioxide, which could be understood as an effect of J-type aggregation [75]. In our case, J-type aggregation would in fact explain the very intense emission of the interfacial 6T material. A linear superposition of the three reference spectra fits well to the emission spectrum, hinting to the potential ability of tuning fiber chromaticity across the entire visible spectrum by selecting proper p-6P and 6T layer thicknesses. Polarization-resolved measurements can then be used to determine molecular orientation of each material phase within the fibers. The polar plot (Fig. 3.12b) of fitted spectral weights versus polarization angle clearly shows that emission dipoles of crystalline p-6P, interfacial 6T and crystalline 6T are fairly well aligned along the same direction, i.e., perpendicular to the fibers' axis (at 0° angle). Strong polarization anisotropy is demonstrated by the high (up to 9 dB) ratios obtained between fluorescence intensity maxima and minima vs. angle, thereby revealing a high orientational order of the fibers' constituent material phases.

Fig. 3.12 (**a**) Fluorescence spectra of a film with nominally 400 nm 6T fiber thickness, acquired at 0° (long fiber axis) and 90° polarization angle. The *blue*, *green*, and *red dashed lines* represent the fitted contribution of blue (p-6P), green (interfacial 6T submonolayer), and red (crystalline 6T) components. (**b**) Polar plot of the p-6P and 6T material phases' fluorescence intensity versus polarization angle. (**c**) Contribution of crystalline p-6P to the single spectra, representing a magnification of section (**b**) for better visibility (*solid lines* represent a $\cos^2$ fit to the experimental data)

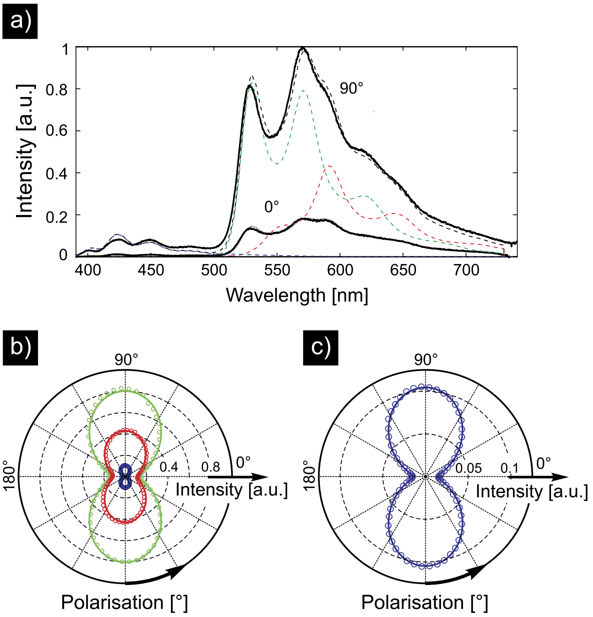

Overall, structural, morphological and optical investigations provide a consistent picture concerning the epitaxial growth of p-6P/6T heterostructures. It is demonstrated that organic–organic heteroepitaxy provides the ability to drive the growth of highly oriented 6T fibers on p-6P fiber templates. In particular it is demonstrated that organic–organic heteroepitaxy can force the molecules to lie parallel to each other. Moreover structural investigations underline a sharp organic–organic interface determined by parallel orientated 6T molecules on top of the p-6P needle template. Optical spectroscopy underlines that at low 6T coverage the interface exhibits uniformly distributed submonolayer aggregates made of co-oriented molecules that are determinant for the green fiber emission color. With increasing 6T layer thickness red emission of nucleated 6T crystals contributes to the emission spectrum which is also observed by fluorescence microscopy investigations. It is found that green-emitting 6T phase can be efficiently sensitized by p-6P molecules via energy transfer. Moreover, the green emission band provides a more intense emission as compared to the red crystalline 6T phase.

3.5 Summary

In order to deduce a model explaining the epitaxial growth of rod-like molecules on sheet silicate substrates detailed crystallographic and morphological analysis has been conducted. As model system 6T and p-6P molecules have been chosen. Whereas both molecules crystallize in nano-fibers, p-6P provides much higher anisotropy due to a nearly perfect parallel alignment of its crystallites. Based on experimental data a growth model has been presented which is further underlined by force-field simulations. It is shown that in the general case the formation of poly-oriented nano-fibers can be expected when choosing muscovite mica as substrate surface. Parallel needles can only be obtained when the rod-like molecules align parallel or perpendicular to the mirror axis-direction of the mica substrate surface unit cell in combination with a rectangular surface unit cell of the molecules. In all other configurations an energetically equivalent adsorption site will lead to non-parallel molecular alignment and multiple needle directions. Consequently para-phenylenes in combination with muscovite mica are characterized as an outstanding material system fulfilling all conditions for optimized optical and morphological anisotropy. In further consequence it has to be stated that efficient color tuning of organic nano aggregates grown on muscovite mica seems strongly limited to a small group of molecules.

In order to overcome this natural limitation the organic–organic epitaxial growth of 6T on top of p-6P needle templates has been investigated. It is demonstrated by morphological, structural and optical investigations that organic heteroepitaxy can be successfully applied to achieve a higher molecular and morphological order. In particular it is demonstrated by XRD pole-figure measurements and polarization dependent optics that 6T molecules adopt the azimuthal order of the p-6P template. It is shown that the p-6P/6T material couple provides a sharp organic–organic interface and that 6T crystallization takes place dominantly on top of the p-6P template needles. Moreover, optical spectroscopy reveals two different 6T phases emitting in the green and orange-red spectral range. The intense green light emission originates from a thin 6T interface layer and the red emission can be attributed to 6T crystallites which have nucleated on top of the p-6P nano-fibers.

In summary all these observations underline that organic–organic heteroepitaxy seems to be the key to overcome the limitations of muscovite mica substrate surface geometry. It has been demonstrated that the spectral emission of organic nano-fibers can easily be tuned from the blue via the green to the red spectral range simply by choosing a second molecular species. Moreover, it can be expected that organic–organic heteroepitaxy can force highly molecular ordering in other material systems further enlarging the emission properties of organic nano-fibers being essential to become more flexible concerning the fabrication of optoelectronic devices based on organic nano-fibers.

References

1. Y. Shirota, H. Kageyama, Charge carrier transporting molecular materials and their applications in devices. Chem. Rev. **107**, 953 (2007)
2. S.R. Forrest, The path to ubiquitous and low-cost organic electronic appliances on plastic. Nature **428**, 911 (2004)
3. F. Balzer, H.-G. Rubahn, Growth control and optics of organic nanoaggregates. Adv. Funct. Mater. **15**(1), 17 (2005)

4. F. Balzer, H.-G. Rubahn, Dipole-assisted self-assembly of light-emitting p-np needles on mica. Appl. Phys. Lett. **79**, 3860–3862 (2001)
5. A. Andreev, G. Matt, C. Brabec, H. Sitter, D. Badt, N.S. Sariciftci, Highly anisotropically self-assembled structures of para-sexiphenyl grown by hot-wall epitaxy. Adv. Mater. **12**, 629–633 (2000)
6. M. Schiek, F. Balzer, K. Al-Shamery, A. Lützen, H.-G. Rubahn, Light-emitting organic nanoaggregates from functionalized p-quaterphenylenes. Soft Matter **4**, 277–285 (2008)
7. L. Kankate, F. Balzer, H. Niehus, H.-G. Rubahn, Organic nanofibers from thiophene oligomers. Thin Solid Films **518**, 130–137 (2009)
8. F. Balzer, H.-G. Rubahn, Chain-length dependent para-phenylene film- and needle-growth on dielectrics. Surf. Sci. **548**, 170–182 (2004)
9. H. Yanagi, T. Ohara, T. Morikawa, Self-waveguided gain-narrowing of blue light emission from epitaxially oriented p-sexiphenyl crystals. Adv. Mater. **13**(19), 1452 (2001)
10. G. Koller, S. Berkebile, J.R. Krenn, G. Tzvetkov, G. Hlawacek, O. Lengyel, F.P. Netzer, C. Teichert, R. Resel, M.G. Ramsey, Oriented sexiphenyl single crystal nanoneedles on TiO2(110). Adv. Mater. **16**, 2159 (2004)
11. R. Resel, Crystallographic studies on hexaphenyl thin films—a review. Thin Solid Films **433**, 1–11 (2003)
12. R. Resel, T. Haber, O. Lengyel, H. Sitter, F. Balzer, H.-G. Rubahn, Origins for epitaxial order of sexiphenyl crystals on muscovite (001). Surf. Interface Anal. **41**, 764–770 (2009)
13. M. Schiek, F. Balzer, K. Al-Shamery, A. Lützen, H.-G. Rubahn, Light-emitting organic nanoaggregates from functionalized p-quaterphenylenes. Soft Matter **4**, 277–285 (2007)
14. M. Schiek, A. Lützen, K. Al-Shamery, F. Balzer, H.-G. Rubahn, Nanofibers from methoxy functionalized para-phenylene molecules. Surf. Sci. **600**, 4030 (2006)
15. F. Quochi, Random lasers based on organic epitaxial nanofibers. J. Opt. **12**(2), 024003 (2010)
16. F. Quochi, A. Andreev, F. Cordella, R. Orru, A. Mura, G. Bongiovanni, H. Hoppe, H. Sitter, N.S. Saricifci, Low-threshold blue lasing in epitaxially grown para-sexiphenyl nanofibers. J. Lumin. **112**(1), 321 (2005)
17. F. Balzer, V. Bordo, A. Simonsen, H.-G. Rubahn, Optical waveguiding in individual nanometer-scale organic fibers. Phys. Rev. B **67**, 115408 (2003)
18. P. Frank, G. Hlawacek, O. Lengyel, A. Satka, C. Teichert, R. Resel, A. Winkler, Influence of surface temperature and surface modifications on the initial layer growth of para-hexaphenyl on mica (001). Surf. Sci. **601**, 2152 (2007)
19. C. Simbrunner, D. Nabok, G. Hernandez-Sosa, M. Oehzelt, T. Djuric, R. Resel, L. Romaner, P. Puschnig, C. Ambrosch-Draxl, I. Salzmann, G. Schwabegger, I. Watzinger, H. Sitter, Epitaxy of organic nano-fibers on sheet silicates—a growth model based on experiments and simulations. J. Am. Chem. Soc. **133**, 3056–3062 (2011)
20. C. Ambrosch-Draxl, P. Puschnig, R. Resel, G. Leising, Electronic properties of ppp-oligomers investigated from first-principles. Synth. Met. **101**, 673 (1999)
21. F. Balzer, M. Schiek, H.-G. Rubahn, K. Al-Shamery, A. Lützen, Surface bound organic nanowires. J. Vac. Sci. Technol. B **26**(4), 1619–1623 (2008)
22. M. Schiek, F. Balzer, K. Al-Shamery, A. Lützen, H.-G. Rubahn, Nanoaggregates from thiophene/phenylene co-oligomers. J. Phys. Chem. **113**, 9601–9608 (2009)
23. M. Schiek, A. Lützen, R. Koch, K. Al-Shamery, F. Balzer, R. Frese, H.-G. Rubahn, Nanofibers from functionalized para-phenylene molecules. Appl. Phys. Lett. **86**, 153107 (2005)
24. M. Schiek, A. Lützen, K. Al-Shamery, F. Balzer, H.-G. Rubahn, Organic nanofibers from chloride functionalized p-quaterphenylenes. Cryst. Growth Des. **7**, 229–233 (2007)
25. T. Mori, Molecular materials for organic field-effect transistors. J. Phys. Condens. Matter **20**, 184010 (2008)
26. J. Ivanco, T. Haber, J.R. Krenn, F.P. Netzer, R. Resel, M.G. Ramsey, Sexithiophene films on ordered and disordered TiO2(110) surfaces: electronic, structural and morphological properties. Surf. Sci. **601**, 178–187 (2007)
27. C. Simbrunner, G. Hernandez-Sosa, M. Oehzelt, T. Djuric, I. Salzmann, M. Brinkmann, G. Schwabegger, I. Watzinger, H. Sitter, R. Resel, Epitaxial growth of sexithiophene on mica

surfaces. Phys. Rev. B **83**, 115443 (2011)
28. H. Yanagi, T. Morikawa, S. Hotta, K. Yase, Epitaxial growth of thiophene/p-phenylene co-oligomers for highly polarized light-emitting crystals. Adv. Mater. **13**(5), 313 (2001)
29. Y. Yoshida, N. Tanigaki, K. Yase, S. Hotta, Color-tunable highly polarized emission from uniaxially aligned thin films of thiophene/phenylene co-oligomers. Adv. Mater. **12**(21), 1587 (2000)
30. M. Schiek, F. Balzer, K. Al-Shamery, J.R. Brewer, A. Lützen, H.-G. Rubahn, Organic molecular nanotechnology. Small **4**, 176–181 (2008)
31. J. Brewer, M. Schiek, A. Ltzen, K. Al-Shamery, H.-G. Rubahn, Nanofiber frequency doublers. Nano Lett. **6**(12), 2656–2659 (2006)
32. A. Meunier, *Clays* (Springer, Berlin, 2005)
33. Y. Kuwahara, Comparison of the surface structure of the tetrahedral sheets of muscovite and phlogopite by AFM. Phys. Chem. Miner. **28**, 1–8 (2001)
34. F. Ostendorf, C. Schmitz, S. Hirth, A. Kühnle, J.J. Kolodziej, M. Reichling, Evidence for potassium carbonate crystallites on air-cleaved mica surfaces. Langmuir **25**(18), 10764 (2009)
35. Y. Kuwahara, Muscovite surface structure imaged by fluid contact mode AFM. Phys. Chem. Miner. **26**, 198 (1999)
36. L. Kankate, F. Balzer, H. Niehus, H.-G. Rubahn, From clusters to fibers: parameters for discontinuous para-hexaphenylene thin film growth. J. Chem. Phys. **128**, 084709 (2008)
37. G. Hernandez-Sosa, C. Simbrunner, H. Sitter, Growth and optical properties of α-sexithiopene doped para-sexiphenyl nanofibers. Appl. Phys. Lett. **95**, 013306 (2009)
38. F. Balzer, M. Schiek, A. Lützen, H.-G. Rubahn, Self-organized growth of organic thiophene-phenylene nanowires on silicate surfaces. Chem. Mater. **21**, 4759–4767 (2009)
39. C. Xia, X. Fan, J. Locklin, R.C. Advincula, A. Gies, W. Nonidez, Characterization, supermolecular assembly and nanostructures of thiophene dendrimers. J. Am. Chem. Soc. **126**(28), 8735 (2004)
40. I. Díez-Peŕez, M. Luna, F. Teherán, D.F. Ogletree, F. Sanz, M. Salmeron, Interaction of water with self-assembled monolayers of alkylsilanes on mica. Langmuir **20**, 1284 (2004)
41. N. Gunari, M. Schmidt, A. Janshoff, Persistence length of cylindrical brush molecules measured by atomic force microscopy. Macromolecules **39**, 2219 (2006)
42. W.F. Bleam, Electrostatic potential at the basal (001) surface of talc and pyrophyllite as related to tetrahedral sheet distortions. Clays Clay Miner. **38**(5), 522 (1990)
43. H. Wondratschek, U. Müller, *International Tables for Crystallography* (Springer, Berlin, 2009)
44. E.J. Palin, M.T. Dove, S.A.T. Redfern, A. Bosenick, C.I. Sainz-Diaz, M.C. Warren, Computational study of tetrahedral Al–Si ordering in muscovite. Phys. Chem. Miner. **28**, 534 (2001)
45. C.P. Herrero, J. Sanz, J.M. Serratosa, Si, Al distribution in micas: analysis by high-resolution 29Si NMR spectroscopy. J. Phys. C **18**, 13 (1985)
46. M.C. Warren, M.T. Dove, E.R. Myers, A. Bosenick, E.J. Palin, C.I. Sainz-Diaz, B.S. Guiton, S.A.T. Redfern, Monte Carlo methods for the study of cation ordering in minerals. Mineral. Mag. **65**(2), 221 (2001)
47. A.R. González-Elipe, J.P. Espinós, G. Munuera, J. Sanz, J.M. Serratosa, Bonding state characterization of constituent elements in phyllosilicate minerals by XPS and NMR. J. Phys. Chem. **92**, 3471 (1988)
48. G.J. Redhammer, G. Roth, Single-crystal structure refinements and crystal chemistry of synthetic trioctahedral micas $KM_3(Al,Si)_4O_{10}(OH)_2$, where M = Ni, Mg, Co, Fe, Al. Am. Mineral. **87**, 1464 (2002)
49. J.W. Gruner, The crystal structures of talc and pyrophyllite. Z. Kristallogr. **55**, 412 (1934)
50. S.M. Richardson, J.W. Richardson, Crystal structure of a pink muscovite from Archer's post, Kenya. Am. Mineral. **67**, 69 (1982)
51. B. Perdikatsis, H. Burzlaff, Strukturverfeinerung am talk. Z. Kristallogr. **156**, 177 (1981)
52. J.H. Lee, S. Guggenheim, Single crystal X-ray refinement of pyrophyllite-1tc. Am. Mineral. **66**, 350 (1981)

53. K. Müller, C.C. Chang, Low energy electron diffraction observations of electric dipoles on mica surfaces. Surf. Sci. **8**, 455 (1968)
54. K. Müller, C.C. Chang, Electric dipoles on clean mica surfaces. Surf. Sci. **14**, 39 (1969)
55. F. Ostendorf, C. Schmitz, S. Hirth, A. Kühnle, J.J. Kolodziej, M. Reichling, How flat is an air-cleaved mica surface. Nanotechnology **19**, 305705 (2008)
56. H. Poppa, A.G. Elliot, The surface composition of mica substrates. Surf. Sci. **24**, 149 (1971)
57. M.G. Dowsett, R.M. King, E.H.C. Parker, Evaluation of impurity and contamination levels on mica surfaces using ssims. J. Vac. Sci. Technol. **14**(2), 711 (1977)
58. G. Kranzelbinder, F. Meghdadi, S. Tasch, G. Leising, L. Fasoli, M. Sampietro, Transient electroluminescence in para-hexaphenyl based multilayer device. Synth. Met. **102**, 1073 (1999)
59. S. Tasch, C. Brandstätter, F. Meghdadi, G. Leising, G. Froyer, L. Athouel, Red-green-blue light emission from a thin film electroluminescence device based on parahexaphenyl. Adv. Mater. **9**(7), 33 (1997)
60. G. Horowitz, F. Garnier, A. Yassar, R. Hajlaoui, F. Kouki, Fet with a sexithiophene single crystal. Adv. Mater. **8**(1), 52 (1996)
61. K.N. Baker, A.V. Fratini, T. Resch, H.C. Knachel, W.W. Adams, E.P. Socci, B.L. Farmer Polymer **34**, 1571 (1993)
62. G. Horowitz, F. Kouki, A.E. Kassmi, P. Valat, V. Wintgens, F. Garnier, Structure-dependent fluorescence in sexithiophene single crystals. Adv. Mater. **11**, 234 (1999)
63. M.A. Loi, E.D. Como, F. Dinelli, M. Murgia, R. Zamboni, F. Biscarini, M. Muccini, Supramolecular organization in ultra-thin films of α-sexithiophene on silicon dioxide. Nat. Mater. **4**, 81 (2005)
64. L. Antolini, G. Horowitz, F. Kouki, F. Garnier, Polymorphism in oligothiophenes with an even number of thiophene subunits. Adv. Mater. **10**, 382 (1998)
65. G. Horowitz, B. Bachet, A. Yassar, P. Lang, F. Demanze, J.-L. Fave, F. Garnier, Growth and characterization of sexithiophene single crystals. Chem. Mater. **7**, 1337–1341 (1995)
66. T. Siegrist, R.M. Fleming, R.C. Haddon, R.A. Laudise, A.J. Lovinger, H.E. Katz, P. Bridenbaugh, D.D. Davis, The crystal structure of the high-temperature polymorph of a-hexathienyl (a-6t/ht). J. Mater. Res. **10**, 2170–2173 (1995)
67. R.G.D. Valle, E. Venuti, A. Brillante, A. Girlando, Do computed crystal structures of nonpolar molecules depend on the electrostatic interactions? The case of tetracene. J. Phys. Chem. A **112**, 1085–1089 (2008)
68. T. Haber, S. Muellegger, A. Winkler, R. Resel, Temperature-induced epitaxial growth modes of para-sexiphenyl on Au(111). Phys. Rev. B **74**, 045419 (2006)
69. C. Simbrunner, F. Quochi, G. Hernandez-Sosa, M. Oehzelt, R. Resel, G. Hesser, M. Arndt, M. Saba, A. Mura, G. Bongiovanni, H. Sitter, Organic–organic heteroepitaxy of red-, green-, and blue-emitting nanofibers. ACS Nano **4**, 6244 (2010)
70. S.C.B. Mannsfeld, K. Leo, T. Fritz, Phys. Rev. Lett. **94**, 561041 (2005)
71. S. Timpanaro, A. Sassella, A. Borghesi, W. Porzio, P. Fontaine, M. Goldmann, Adv. Mater. **13**, 127 (2001)
72. M. Oehzelt, G. Koller, J. Ivanco, S. Berkebile, T. Haber, R. Resel, F.P. Netzer, M.G. Ramsey, Organic heteroepitaxy: p-sexiphenyl on uniaxially oriented α-sexithiophene. Adv. Mater. **18**, 2466 (2006)
73. G. Koller, S. Berkebile, J.R. Krenn, F.P. Netzer, M. Oehzelt, T. Haber, R. Resel, M.G. Ramsey, Heteroepitaxy of organic–organic nanostructures. Nano Lett. **6**(6), 1207 (2006)
74. R.S. Becker, J.S. de Melo, A.L. Macuanita, F. Elisei, Comprehensive evaluation of the absorption, photophysical, energy transfer, structural, and theoretical properties of α-oligothiophenes with one to seven rings. J. Phys. Chem. **100**, 18683 (1996)
75. E.D. Como, M.A. Loi, M. Murgia, R. Zamboni, M. Muccini, J-aggregation in α-sexithiophene submonolayer films on silicon dioxide. J. Am. Chem. Soc. **128**, 4277 (2006)

Chapter 4
Ehrlich-Schwoebel Barriers and Island Nucleation in Organic Thin-Film Growth

Christian Teichert, Gregor Hlawacek, Adolf Winkler, Peter Puschnig, and Claudia Draxl

Abstract In inorganic epitaxy, intra- and interlayer surface diffusion processes—which are significantly influencing island nucleation and morphology evolution when growing under conditions far from equilibrium—are well understood. Using the rod-like organic molecule para-hexaphenyl, it is demonstrated that experimental and theoretical concepts developed to reveal the underlying atomic diffusion processes for inorganic systems can be applied to understand the growth of crystalline organic films. Here, we focus on the one hand on the determination of step-edge barriers, so-called Ehrlich-Schwoebel barriers, resulting in terraced growth mounds. On the other hand, we explore the island nucleation applying various approaches developed for inorganic systems. Compared to atomic systems, the anisotropy and complexity of the molecular building blocks yield a richer spectrum of diffusion processes resulting in novel phenomena as, e.g., level-dependent step-edge barriers for interlayer diffusion and peculiarities in the size of the critical nucleus.

C. Teichert (✉)
Institute of Physics, Montanuniversitaet Leoben, Franz-Josef-Straße 18, 8700 Leoben, Austria
e-mail: teichert@unileoben.ac.at

G. Hlawacek
Physics of Interfaces and Nanomaterials, MESA+ Institute for Nanotechnology,
University of Twente, PO Box 217, 7500AE Enschede, The Netherlands

A. Winkler
Institute of Solid State Physics, Graz University of Technology, Petersgasse 16, 8010 Graz,
Austria

P. Puschnig · C. Draxl
Chair of Atomistic Modelling and Design of Materials, Montanuniversitaet Leoben,
Franz-Josef-Straße 18, 8700 Leoben, Austria

P. Puschnig
Institute of Physics, Karl-Franzens University Graz, Universitätsplatz 5, 8010 Graz, Austria

C. Draxl
Physics Department, Humboldt Universität zu Berlin, Zum Großen Windkanal 6, 12489 Berlin,
Germany

H. Sitter et al. (eds.), *Small Organic Molecules on Surfaces*,
Springer Series in Materials Science 173, DOI 10.1007/978-3-642-33848-9_4,

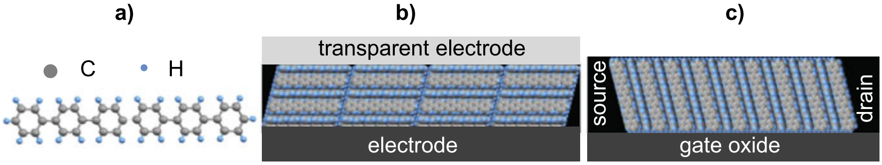

Fig. 4.1 (**a**) Scheme of para-hexaphenyl ($C_{36}H_{26}$), (**b**) desired molecular orientation for OLEDs or organic solar cells, (**c**) arrangement of 6P for an OFET application

4.1 Introduction

In the field of organic electronics, there are ongoing efforts to determine structure-property relations between organic films and the resulting electronic properties with the aim of optimizing the performance of devices like organic light-emitting diodes (OLEDs), organic solar cells, and organic field effect transistors (OFETs) [1]. In particular films composed of small, rod-like molecules like oligoacenes, oligophenylenes, and oligothiophenes grow in a crystalline fashion. To utilize these films in electronic and optoelectronic devices, the molecular orientation with respect to the substrate is crucial as is demonstrated in Fig. 4.1 for the model molecule para-hexaphenyl (6P). 6P ($C_{36}H_{26}$) is a rodlike, π-conjugated molecule composed of six phenyl rings with a length of 2.7 nm (Fig. 4.1(a)). It forms a monoclinic lattice with $a = 0.8091$ nm, $b = 0.5565$ nm, $c = 2.624$ nm, and $\beta = 98.17°$, with a herringbone stacking of the molecules [2]. For OLED or solar cell applications, growth of the molecules should preferably occur in a lying fashion. This allows for the charge carrier transport—which is perpendicular to the molecule's long axis—between the electrodes as is illustrated in Fig. 4.1(b). For OFETs, growth of standing molecules is desired on the gate oxide between source and drain (Fig. 4.1(c)).

In fact, both molecular orientations of 6P can be obtained, even on the same substrate. Figure 4.2 summarizes the growth morphologies of 6P on muscovite mica recorded by atomic-force microscopy (AFM). On a clean mica surface (Fig. 4.2(a)), the growth morphology at 330 K substrate temperature is dominated by well oriented chains of crystallites which are forming on a wetting layer obeying Stranski-Krastanov growth mode [3]. The same morphology is observed when the film is grown by hot-wall epitaxy [4]. In both cases, the preexisting crystallites most probably self-organize into chains via a strain-induced interplay with the wetting layer [5]. The crystallites as well as the wetting layer are composed of lying molecules as has been demonstrated by x-ray pole-figure measurements [4]. In fact, a layer-by-layer growth up to at least four layers of 6P has been obtained by using graphene as a substrate (see Chap. 5). The orientation of the 6P molecules changes to an upright position if the mica substrate is modified as is demonstrated in Figs. 4.2(b,c). On a mica substrate which has been preheated to an elevated temperature of 770 K (causing partial damage of the mica crystallography), the film is characterized by two-dimensional (2D) islands of about 2.5 nm height (Fig. 4.2(b)). Taking

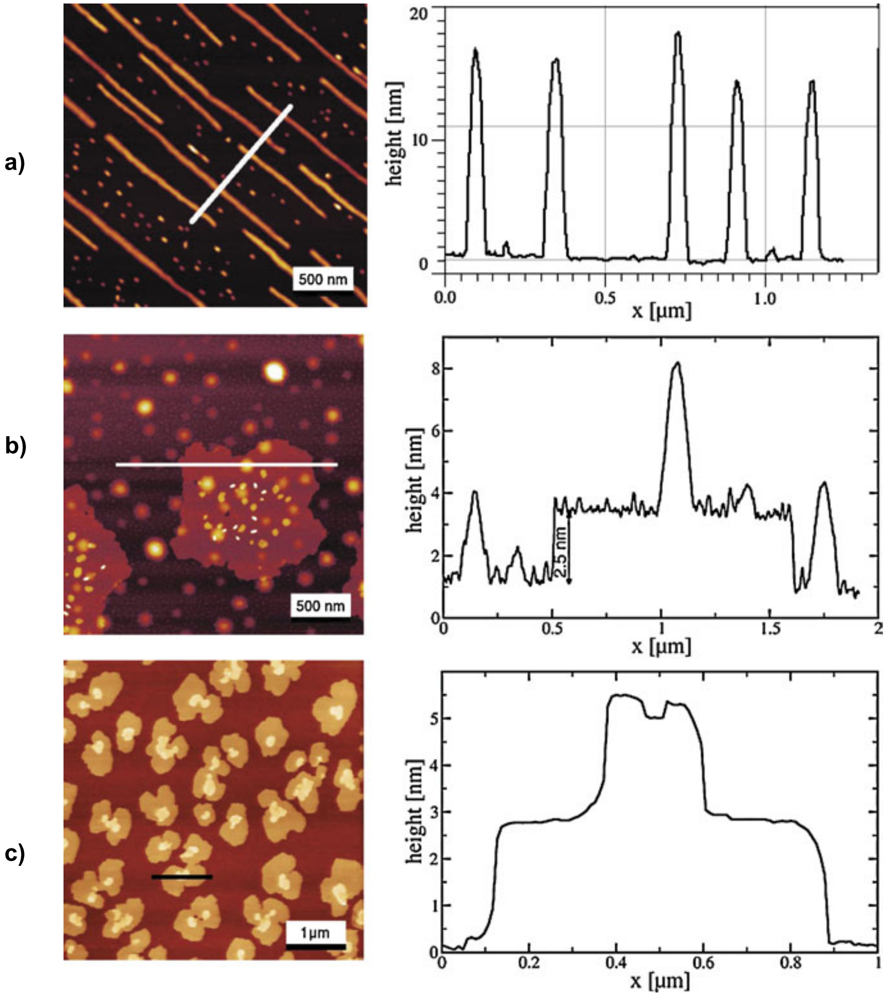

Fig. 4.2 AFM images (*left*) and corresponding cross sections (*right*) of 6P growth on mica substrates. (**a**) 1 nm thick 6P film grown at room temperature on clean mica(001). (**b**) 1.3 nm thick 6P film deposited at room temperature on mica preheated to 770 K. The round structures are attributed to subsurface water bubbles in the mica [6]. (**c**) 1 nm thick 6P film grown on carbon covered mica (001) at 330 K. (After Refs. [3] (**a**, **c**) and [6] (**b**))

into account the 17° tilt of the molecules in the bulk (see Fig. 4.1(c)), this indicates the presence of (almost) upright-standing molecules [6]. Islands of upright-standing molecules are also obtained if carbon is pre-adsorbed on the mica(001) substrate (Fig. 4.2(c)). Thermal desorption spectroscopy (TDS) proved that for sufficiently high C coverage no lying molecules exist [3]. In the latter example, second-layer islands have already been formed prior to the completion of the first layer.

To understand the observed growth morphologies, not only the thermodynamics—resulting in the well known classification into layer-by-layer growth, Stranski-Krastanov growth, and 3D island growth [7]—have to be considered. Of similar importance are the kinetics at the particular growth conditions which might hinder important diffusion processes resulting in severe deviations from equilibrium morphologies. For inorganic epitaxy of metal films, growth kinetics have been analyzed in the past decades in very much detail [8]. The same is true for the case of homogeneous island nucleation [9]. Using the growth of 6P on mica substrates, we will demonstrate in this chapter that procedures developed for inorganic epitaxy (dealing mostly with atoms as building blocks) can be applied for organic thin-film growth to reveal the underlying molecular intra- and interlayer diffusion processes. The first part of the chapter deals with the determination of the so-called Ehrlich-Schwoebel barrier (ESB) [10, 11] which results in terraced mounds rather than layer-by-layer growth. We will demonstrate that in organic thin films level-dependent ESBs can occur [12]. In the second half, several procedures will be applied to determine the critical nucleus size for 6P island nucleation on amorphous mica [13] and silicon oxide [14] substrates. In each case, the experimental findings are supported by simulations. It is this combination which reveals new phenomena due to the complexity and anisotropy of the molecular building blocks.

4.2 Experimental

For all the examples presented in this chapter, organic molecular beam epitaxy (OMBE) under ultra-high vacuum (UHV) conditions has been employed using Knudsen cells. The 6P deposition rate was controlled by a quartz microbalance. The muscovite mica(001) surface was prepared by cleaving a mica sheet with the help of adhesive tape and immediately installed into the UHV system. Deposition occurred either on this clean substrate or on a further treated mica as is described below. For the deposition on silicon oxides, native oxide covered Si(001) substrates were used which have been cleaned in UHV by annealing at 780 K. AFM in tapping mode has been performed under ambient conditions to characterize the resulting film morphology. To study the azimuthal orientation of standing molecules, novel transverse shear microscopy (TSM) operating in contact mode [15, 16] has been employed.

4.3 Step-Edge Barriers in Organic Thin-Film Growth

In this section we will first demonstrate how the step-edge barrier in organic thin-film growth can be determined experimentally and theoretically by analyzing morphologies of terraced growth mounds. In the second part, the ESB will be derived from morphologies in the early growth stage which is dominated by first-layer islands.

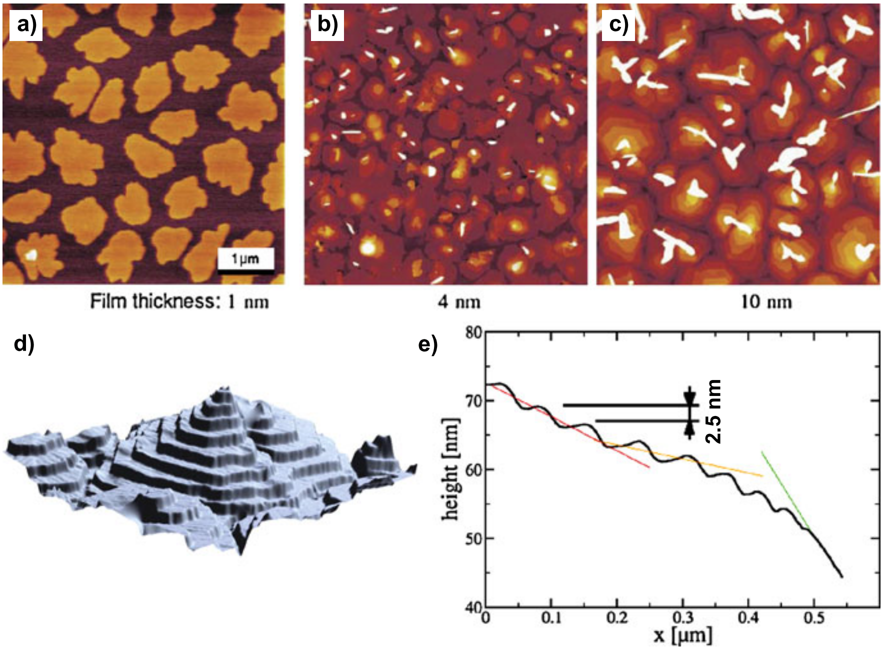

Fig. 4.3 (**a**)–(**c**) Morphological evolution of 6P thin films grown at room temperature and an evaporation rate of 0.3 nm/min on ion-bombarded mica for film thicknesses ranging from 1 nm to 10 nm (z scale: 5, 35, and 50 nm, respectively). (**d**) 3D AFM image of a typical mature growth mound (1.5 µm × 1.5 µm × 25 nm). (**e**) Representative cross section of a mature mound showing terrace heights of about 2.5 nm and varying local slopes. (Partly adapted from [12])

4.3.1 Formation of Terraced Growth Mounds

In comparison to the procedures described in Figs. 4.2(b,c), there is, in fact, a more reproducible possibility to allow for the growth of upright-standing 6P molecules on modified mica. In this case, the mica substrate was bombarded in UHV by 500 eV Ar^+ ions just until the ordered low-energy electron diffraction pattern disappeared avoiding any surface roughening [3, 12]. The resulting growth morphologies as a function of coverage are presented in Fig. 4.3. In the early growth stage, irregularly shaped islands appear on this smooth, amorphized mica surface (Fig. 4.3(a)). With increasing film thickness, terraced growth mounds with hexagonally shaped bases are observed (Fig. 4.3(b–d)). The height of the individual terraces (see Fig. 4.3(e)) is again about 2.5 nm, indicating almost upright-standing molecules. It should be noted that the bright features which form at higher thickness (see Fig. 4.3(c)) are small crystallite chains composed of lying molecules. As can be seen in the mound cross section presented in Fig. 4.3(e), the local slopes of the mounds are steeper at their bases and their tops compared to the intermediate levels.

Similarly, mound formation is observed for 6P growth on amorphous silicon oxide as can be seen in Fig. 4.4. In this case, the mound base is irregularly shaped and

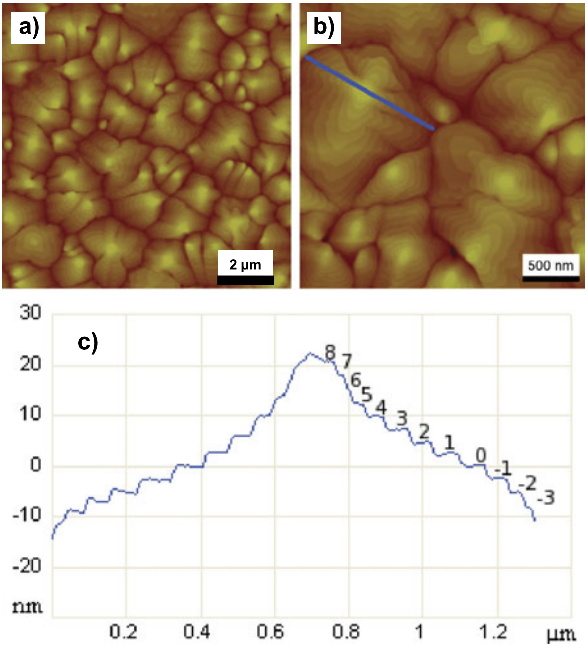

Fig. 4.4 Morphology of a 50 nm 6P film grown on SiO_2 at 150 °C and a rate of 2.4 nm/min. (**a**) 10 μm × 10 μm and (**b**) 2.5 μm × 2.5 μm AFM images (z-scale 50 nm). (**c**) Cross-section along the line marked in (**b**) revealing 12 different terrace levels, each 2.5 nm high

features composed of lying molecules are rarely occurring [17]. Again, the characteristic mound cross section is observed with 2.5 nm terrace heights due to standing 6P molecules.

Mound formation has also been observed for thin films of other organic molecules [18–20], but how can we explain it? In fact, in inorganic epitaxy such growth features are known for decades as the consequence of an active barrier for interlayer diffusion across step edges. Direct evidence came from Ehrlich and Hudda, who found in field ion microscopy experiments that tungsten adatoms diffusing on a W(111) terrace are reflected at a descending step edge rather than crossing this step edge [10]. As is demonstrated in Fig. 4.5(a), this was addressed to an increased barrier for adatom hopping across the step edge compared to the barrier E_D for adatom diffusion on the terrace [10, 11, 21]. This phenomenon can be explained simply by the fact that the adatom hopping across the step edge has to overcome an energetically disfavored location of less nearest neighbors. The difference between E_D and the step-edge barrier is nowadays called Ehrlich-Schwoebel barrier (ESB or E_{ES}). The reflected adatom will diffuse on the original terrace until it will meet with other adatoms to nucleate a new island before the first monolayer (ML) is completed. Repeated 2D nucleation of islands of monatomic thickness will result in terraced growth mounds [22] as has been revealed decades ago by transmission electron microscopy utilizing so-called gold decoration technique where subsequently deposited gold decorates the step edges in the Ag film (see Fig. 4.5(b)). Nowadays, modern scanning probe technique yields access to the 3D shape of such growth mounds with superior resolution as is shown in Figs. 4.5(c, d) for Pt/Pt(111) ho-

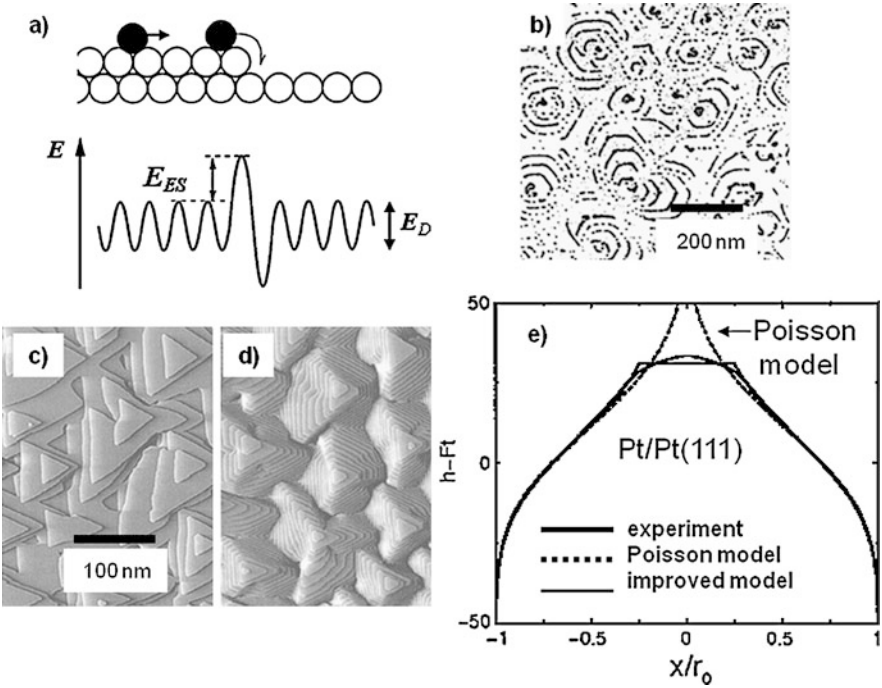

Fig. 4.5 Formation of terraced mounds due to the Ehrlich-Schwoebel barrier. (**a**) Schematic side view of an adatom diffusing on a terrace and approaching a descending step edge. The *lower panel* illustrates the corresponding potential energy landscape (adapted from [8]). (**b**) Transmission electron microscopy of a gold decorated 5 ML thick silver film deposited on Ag(111) at room temperature (after [22] with permission). (**c**, **d**) Scanning tunneling microscopy image of Pt/Pt(111) homoepitaxy at 440 K and a growth rate of 0.007 ML/s: 3 ML (**c**) and 12 ML (**d**) (adapted from [8] with permission). (**e**) Comparison of the averaged mound shape of a 130 ML Pt/Pt(111) film with the Poisson distribution of the layer coverage (adapted from [8] with permission)

moepitaxy [23]. It has to be pointed out here that in the case of complete absence of interlayer mass transport, i.e., in the case of such a high ESB which is under the experimental conditions not to be overcome by the diffusing adatoms, the surface fractions in the individual layers $f(n,h)$ follow a Poisson distribution as has been pointed out in the 1970s by Seah [24]

$$f(n,h) = e^{-h}\frac{h^n}{n!} \tag{1}$$

where n denotes the layer number and h is coverage in ML. As is demonstrated in Fig. 4.5(e), the average shape of the Pt mounds follows the Poisson model at the base and at the intermediate levels quite well with some deviations at the top of the mounds. A further characteristic of an active ESB is the formation of deep trenches between the mounds also seen in Figs. 4.3–4.5. Since these trenches ideally never close, their formation has been referred to as the Zeno effect [25].

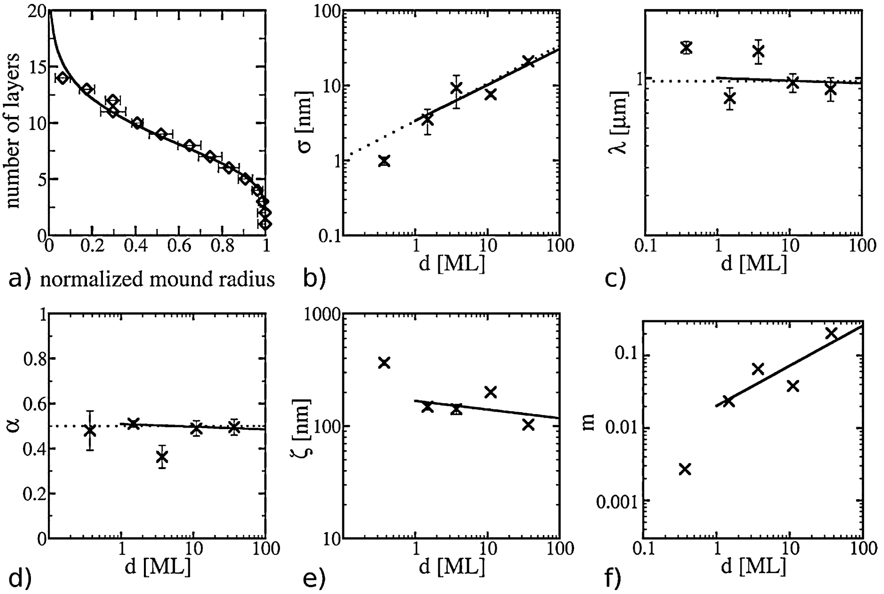

Fig. 4.6 Evolution of roughness parameters and mound characteristics for 6P thin films grown at room temperature and with an evaporation rate of 0.3 nm/min on ion-bombarded mica as a function of film thickness d. (**a**) Normalized averaged cross section of five representative mounds in the 30 nm thick film. (**b**) RMS roughness σ, the power-law fit (*solid line*) reveals a growth exponent $\beta = 0.49$. (**c**) Evolution of the average mound separation λ, the power-law fit corresponds to an exponent of -0.01 (*solid line*). (**d**) Hurst parameter α, (**e**) lateral correlation length ξ, and (**f**) local mound slope m, the power-law fit corresponds to an exponent of 0.55 (*solid line*). All *solid lines* in (**b**–**f**) correspond to fits where the first data point was omitted. (Adapted from [12])

In inorganic epitaxy, procedures have been developed to prove the existence of an ESB from the evolution of roughness parameters like root mean square (RMS) roughness σ, lateral correlation length ξ, and roughness exponent or Hurst parameter α as well as mound separation λ and local mound slope m [8, 23, 26]. Such quantitative morphology parameters are easy to extract from scanning probe microscopy experiments like scanning tunneling microscopy and atomic-force microscopy (which yield a matrix $z(x_i, y_i)$) via calculation of the height-height correlation function [27, 28]

$$C(\boldsymbol{r}) = \big\langle \big[z(\boldsymbol{r}_o + \boldsymbol{r}) - \langle z\rangle\big]\big[z(\boldsymbol{r}_o) - \langle z\rangle\big]\big\rangle; \tag{2}$$

where $\langle\ldots\rangle$ means the average over all possible pairs in the matrix that are separated by $\boldsymbol{r}$. The z values that are taken into account in Eq. (2) are the deviations from the average height $\langle z\rangle$. For 6P on ion-bombarded mica, the above-mentioned parameters have been presented in Fig. 4.6 for coverages ranging from about 0.4 ML to 40 ML (of standing 6P molecules), i.e., from 1–100 nm thickness. In addition, Fig. 4.6(a) shows the normalized, averaged cross section of five mounds found in the 30 nm thick film. The latter has been calculated by transforming the layer coverages into circular discs [23]. As it is obvious, also in the case of 6P mounds the cumulative Poisson distribution fits quite well the changing slope of the mound cross section (Fig. 4.6(a)) indicating negligible interlayer mass transport. The evolution of σ follows—for film thicknesses d above 2 ML—almost exactly a $\sqrt{d}$ behavior which is expected for a scaling law in the absence of interlayer mass transport (Fig. 4.6(b)). The mound separation (Fig. 4.6(c)) has been determined by fitting the height-height correlation function with a form suitable for mounded surfaces [29]

$$C(r) = \sigma^2 \exp\bigl[-\bigl(|r|/\xi\bigr)^{2\alpha}\bigr] \cos(2\pi r/\lambda). \tag{3}$$

The mound separation remains unchanged after the first-layer nucleation has stopped; all mass transport between individual mounds is suppressed, and no coalescence or ripening of the mounds occurs indicating the presence of the Zeno effect. The corresponding data obtained for α and ξ are shown in Figs. 4.6(d, e). The local slope (for which we assume $m \propto \sigma/\xi$ in the limit of $\xi \ll \lambda$ [27, 29]) increases with increasing film thickness as $m \propto d^{0.5}$ [17], also in agreement with the Zeno effect (Fig. 4.6(f)). We have to emphasize that all exponents mentioned have been determined by omitting the first data point for submonolayer growth. As will be shown in Sect. 4.3.2, for the first-layer islands indeed interlayer mass transport takes place.

In the following it is elaborated how the height of the ESB, E_{ES}, can be determined using again morphology parameters as input. Based on the scheme presented in Fig. 4.5(a), the interlayer jump ν' rate can be rewritten as

$$\nu' = \nu e^{-E_{ES}/(k_B T)} \tag{4}$$

with the jump rate for adatom diffusion ν

$$\nu \propto e^{-E_D/(k_B T)} \tag{5}$$

and k_B and T Boltzmann's constant and substrate temperature, respectively. Following a method successfully applied for Pt/Pt(111), the interlayer jump rate ν' can be estimated from the top-terrace diameter ℓ and the flux F [26]:

$$\ell \propto \left(\frac{\nu'}{F}\right)^{1/5}. \tag{6}$$

In the presence of an ESB, which is large enough to effectively suppress interlayer mass transport, the mound separation λ is related to the nucleation density N [9]:[1]

$$\frac{1}{\lambda} \propto N^{\frac{1}{2}} \propto \left(\frac{F}{\nu}\right)^{\frac{i}{2(i+2)}} \tag{7}$$

because the initial nuclei density determines the final density of the growth mounds (no coarsening). Here, i denotes the size of the critical island (see Sect. 4.4). Assuming at this point that the critical nucleus size is just 1, i.e., two molecules are forming already a stable island, the exponent in Eq. (7) is 1/6. With the known

---

[1] Note that Eq. (3) in Ref. [12] is incorrect.

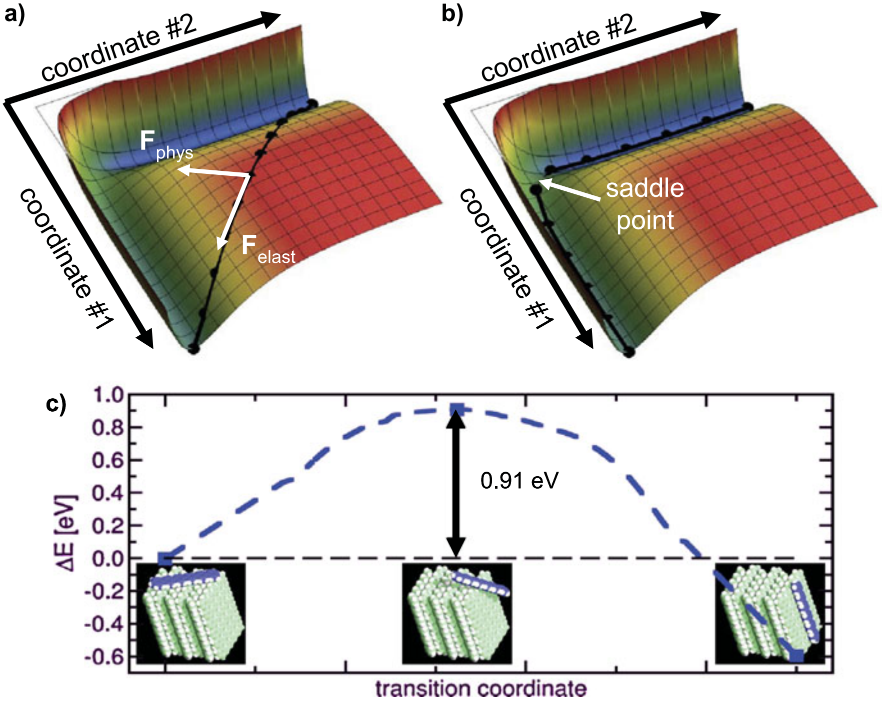

Fig. 4.7 (**a**, **b**) Illustration of the search for the saddle point energy following the nudged elastic band method for just two coordinates. (**c**) Energies associated with the transition path of a stiff 6P molecule across the step edge of 17° tilted standing 6P molecules. *Inserts* show snapshots of the corresponding molecule position

growth parameters (F, T) and experimentally determined values for ℓ and λ, one can calculate E_{ES} using Eqs. (4), (6), and (7). With $\lambda = 1$ μm (see Fig. 4.6(c)) and top-terrace diameters of 40 nm ± 20 nm determined from AFM cross sections we obtain for the ESB a value of $E_{ES} = (0.67 \pm 0.04)$ eV for 6P mounds composed of upright molecules [12].

To cross-check the experimental value, we calculated—in the framework of transition state theory (TST)—the step-edge barrier, i.e., the difference between the saddle point energy and the initial energy of the potential energy surface of the diffusing 6P molecule. For the search of the saddle point, the nudged elastic band (NEB) method [30] is adopted as is demonstrated in Fig. 4.7 for a two-dimensional potential energy surface. Within the NEB method, the minimum energy path, which contains the saddle point, is found by solving the equation of motion for a number of configurations (black dots) which in addition to the physical force F_{phys} determined by the gradients on the potential energy surface also feel an elastic force F_{elast}. Due to the large number of degrees of freedom, the structural degrees of freedom were reduced by treating the 6P molecule as rigid body, i.e., three translational plus three rotational degrees of freedom. In addition bending of the molecule was allowed. Thus, the transition state search was performed in this seven-dimensional configuration space. The large size of the required simulation cell and the structural degrees of freedom preclude an ab initio approach, instead we used empirical potentials as has been done in the first theoretical approach to determine the ESB in organic thin-film growth [31]. Here, total-energy and force calculations for the step-edge diffusion of 6P on the 6P(001) surface are performed using the GULP simulation program [32] applying an empirical force-field approach based on Brenner's bond order potentials [33] where the intramolecular forces are modeled by a second-generation potential energy function for solid carbon and hydrocarbon. This potential allows for covalent bond breaking and forming with associated changes in atomic hybridization within a classical potential. Intermolecular forces are treated by a Lennard-Jones potential for which we obtain a cohesive energy of bulk 6P of 2.77 eV per molecule in good agreement with the ab initio value of 2.82 eV when using the van der Waals density functional [34].

For the diffusion of a lying molecule on a 6P(001) terrace, a diffusion barrier E_D of 22 meV has been calculated. The binding energy of a 6P molecule lying almost flat on top of an existing island of upright-standing molecules is computed to be -1.29 eV. Figure 4.7(c) shows the resulting energetics of the transition path of a lying 6P molecule diffusing with its long molecular axis perpendicular to the step edge not allowing for bending of the molecule. For this case, an overall potential barrier of 0.91 eV is obtained to overcome the step edge. Thus, the resulting ESB has a value of 0.89 eV, which is in fact much higher than the experimentally determined value. A much better agreement is obtained when allowing the molecule to bend when crossing the step edge which is vividly demonstrated in Fig. 4.8 [12]. The bending of the molecule allows for maintaining interaction with the underlying 6P molecules (lower curve in Fig. 4.8(a)) as is demonstrated in the presented snapshots (Figs. 4.8(a–g)). However, the bending of the 6P molecule costs energy which is calculated by first-principles density functional calculation (see below) and is indicated by vertical bars in Fig. 4.8(a). Nevertheless, maintaining of the intermolecular interaction by far overcompensates the energy needed to bend the 6P molecule resulting in a significant reduction of the ESB. The obtained E_{ES} of 0.61 eV is in good agreement with the experimental value. Also, we have to note that there is a shift of the transition coordinate of the saddle point. Once, one phenyl ring has "crawled" across the edge, the saddle point is already reached. There is no further barrier to reach the final position at the terrace edge (i.e., on a 6P(100) edge) with -1.87 eV binding energy.

In summary, for the case of terraced growth mounds in 6P films on ion-bombarded mica surfaces, we were able to determine experimentally the ESB in good agreement with results of TST calculations [12]. The latter also revealed that—in contrast to atomic systems—the conformation of the molecules plays a role. The obtained value of about 0.65 eV is obviously so high that it cannot be overcome in the reality of the actual growth conditions. This is in agreement with the observed Poisson distribution and the Zeno effect which are due to the absence of interlayer mass transport.

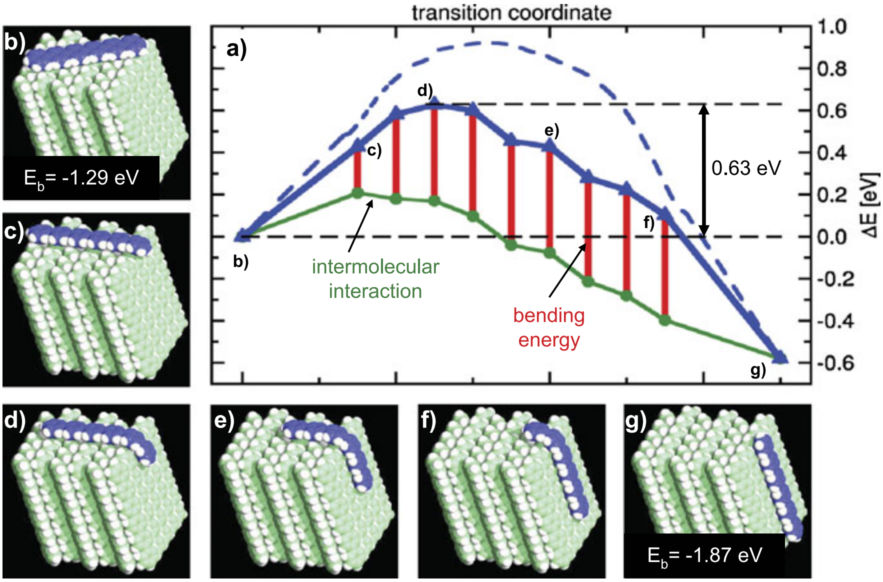

Fig. 4.8 (**a**) Energies associated with the transition path for diffusion of a 6P molecule over a step edge, resulting in a total activation barrier of 0.63 eV. The energy values are given with respect to the initial binding energy of −1.29 eV (**b**). The *thick solid line* indicates the total binding energy of the diffusing molecule, which is composed of the attractive intermolecular interaction (*lower curve*) and the positive bending energy (*bars*). The *dashed curve* shows for comparison again the energies associated with a rigid 6P molecule. *Labels* (**b**) to (**g**) correspond to situations illustrated in the snapshots of the transition path presented in (**b**) to (**g**). Situation shown in (**d**) corresponds to the configuration at the transition state. (Adapted from [12])

4.3.2 Level-Dependent Ehrlich-Schwoebel Barriers

In the following, the early growth stage of 6P growth on ion-bombarded mica is inspected in more detail. In fact, when comparing the layer distributions extracted from the 1 nm and 4 nm thick films (Fig. 4.3(a, b)) with the expected ones according to the cumulative Poisson distribution as is presented in Table 4.1, we observe a clear deviation. In particular for the 1 nm film, where the Poisson model predicts 5 % second-layer coverage and still detectable amounts of 6P in the third layer we hardly observe a second-layer island. Obviously, in this early growth stage there is significant interlayer mass transport resulting in a morphology close to a two-level system like it is characteristic for layer-by-layer growth. This experimental evidence hints to a reduced ESB for the first-layer 6P islands. In fact, there is also a procedure available to determine the ESB for the early growth stage from second-layer islands [35] which has again been first applied to metal homoepitaxy [28]. The number fraction of first-layer islands $f(R)$ with size R that have nucleated a second-layer island on top is

$$f(R) = 1 - e^{-\left(\frac{R}{R_c}\right)^{3i+4}}. \tag{8}$$

Table 4.1 Measured 6P coverages (in percentage of a ML) of the individual layers in comparison to the ones expected according to the cumulative Poisson distribution for the 1 nm and 4 nm thick films

Layer	1 nm 6P film measured (%)	1 nm 6P film expected (%)	4 nm 6P film measured (%)	4 nm 6P film expected (%)
1	50.0 ± 2.0	30.9	94.5 ± 4.0	75.5
2	0.1 ± 0.01	5.3	84.2 ± 3.0	41.8
3	0.000	0.6	26.5 ± 1.0	16.9
4	0.000	0.005	9.3 ± 0.5	4.6

Assuming here again a critical nucleus size of $i = 1$, the critical island radius for second-layer nucleation R_c is

$$R_c = \left(\frac{7\nu'}{2\alpha_s^4 F N} \right)^{1/7} \tag{9}$$

which depends on the interlayer jump rate ν', the known growth rate and the nucleation density. The shape parameter $\alpha_s = A/C^2$ is the ratio between island area A and square of the island circumference C. Both, R_c and α_s can be determined from the AFM images (see inset in Fig. 4.9(a)). With R_c of about 400 nm and using Eq. (4), a value for the ESB active in the first layer of 0.26 eV is obtained which is considerably lower than the obtained value for the mature mounds. In metal epitaxy, it has been shown that impurities preferentially decorating the step edges can influence the ESB [36]. Also the roughness of the island edges can account for an increased interlayer mass transport [37]. There, the reason is the dependence of the ESB on the local morphology. Step edges barriers can be even smaller than the activation energy E_D for adatom diffusion [38], which results even in a negative ESB [39].

What is the reason for the reduction of the ESB in the first layer in our case? Important information can be extracted from a careful analysis of the island heights in the early growth stage as is demonstrated in Fig. 4.9. AFM cross sections of the 1 nm 6P film (Fig. 4.9(a)) clearly show that the island height is only 2.05 nm ± 0.1 nm. Inspecting the height histogram of the 4 nm film (Fig. 4.9(b)), we find that also in the initial mounds the terrace height is only gradually approaching the height expected from the 6P bulk structure. This change in terrace height can be explained by a variation in tilt angle of the molecules in the first layers. This situation is schematically illustrated in Fig. 4.9(c). According to the measured height, the first-layer molecules are tilted by 43° with respect to the surface normal. This tilt angle gradually decreases until it reaches the value of 17° for the bulk arrangement in the fourth terrace of the mounds. Such a gradual change of tilt angle is in fact not unusual in organic thin-film growth as can be seen in Fig. 4.9(d) for the growth of copper phthalocyanine on highly ordered pyrolytic graphite (HOPG) [40]. There, metastable atom electron spectroscopy and ultraviolet photoelectron spectroscopy revealed a gradual change in orientation from molecules lying flat on the substrate to increasingly tilted ones in subsequent layers.

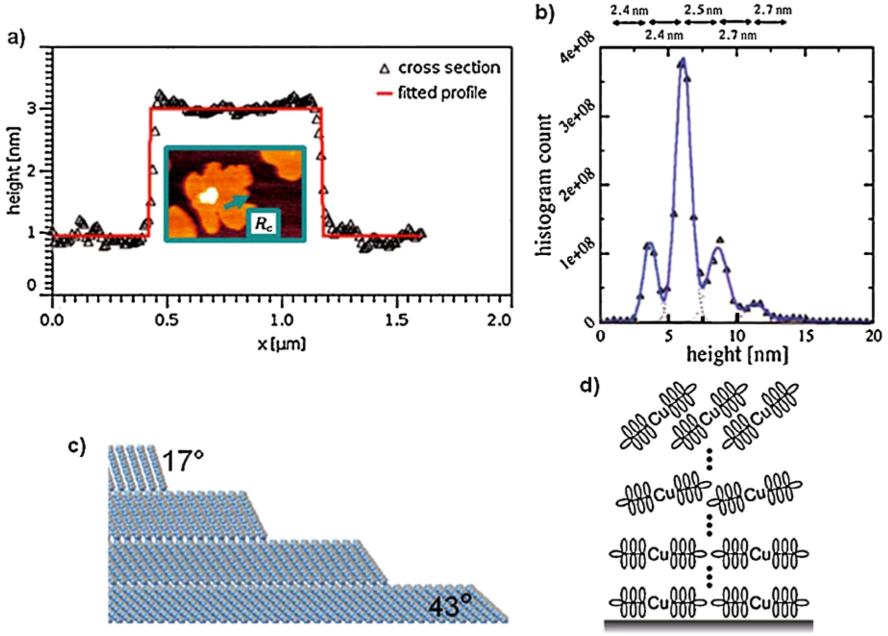

Fig. 4.9 (**a**) AFM cross section through one of the islands of the 1 nm film. The fitted height is 2.05 ± 0.1 nm. The *inset* illustrates the determination of the critical radius for second-layer nucleation. (**b**) Height analysis of a 5 µm × 5 µm AFM image of the 4 nm thick 6P film. The peaks originate from the uncovered part of each terrace. The height values indicated have been obtained by fitting the individual peaks using Gaussians. (**c**) Schematic view of the molecular tilt angle in the first four layers. (**d**) Scheme of the transition from lying copper phthalocyanine molecules on HOPG to tilted ones (adapted from [40] with permission)

Taking the higher tilt of the molecules in the first-layer islands into account, one can calculate the ESB again in the framework of TST as is presented in Fig. 4.10(a). As it is obvious from the snapshots presented in Figs. 4.10(b–g), to maintain the intermolecular contact the diffusing molecule has to bend less at the 43° tilted step edge which should cost less energy. Indeed, the bending energy of an isolated 6P molecule decreases significantly with bending angle as is shown in Fig. 4.10(h). To reduce the number of structural degrees of freedom for the transition state search, we describe the bending of the molecule by a smooth function parameterized by the overall bending angle as given in the inset of Fig. 4.10(h). Assuming a given total bending angle we find the total bending energy as calculated from density functional theory (DFT) to vary only by roughly 2–3 % when shifting the center of the bending from an interring-bond to the center of a phenyl ring. These DFT calculations have been performed using the ABINIT package which is a plane-wave-based implementation of density functional theory for periodic systems [41]. Exchange and correlation effects were treated with the generalized gradient approximation (GGA) using the parameterization of Perdew, Burke, and Ernzerhof [42]. The all-electron

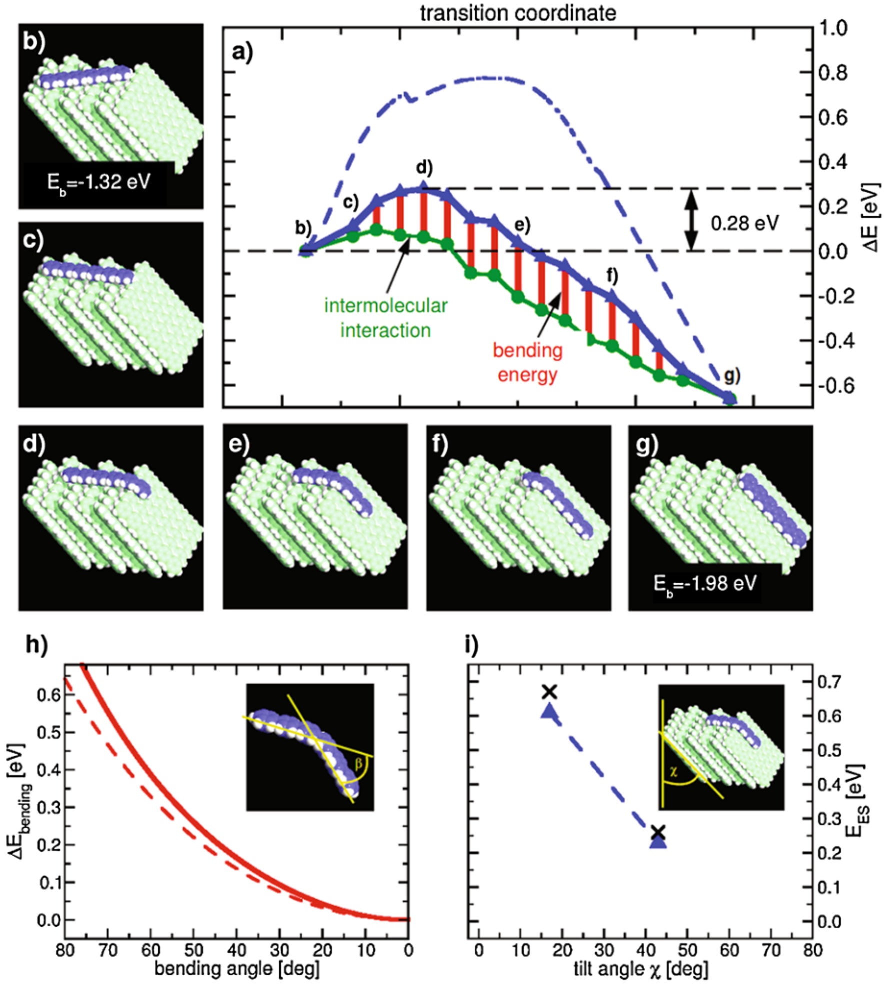

Fig. 4.10 (**a**) Energies associated with the transition path at the initial growth stages corresponding to a 43° tilted 6P terrace. The *blue solid line* refers to the total binding energy of the diffusing molecule which is comprised of the attractive intermolecular interaction (*green*) and the positive bending energy (*red bars*). The *blue dashed line* shows the energies obtained assuming a rigid 6P molecule. (**h**) Energy required for bending a single 6P molecule as a function of bending angle. The *thick red line* is a result of ab initio density functional theory calculations; the *dashed line* follows from Brenner's bond order potentials. (**i**) Value of the ESB versus tilt angle of the 6P(001) surface. Experimental values are indicated by *black crosses*, and theoretical values by *blue triangles*. (Adapted from [12])

potentials are replaced by extended norm-conserving, highly transferable Troullier-Martins pseudo potentials [43] using a plane-wave cut-off of 30 Ryd.

With this input we find the total energy barrier for a 6P molecule descending the first-layer island to be 0.27 eV. Taking the slightly increased activation en-

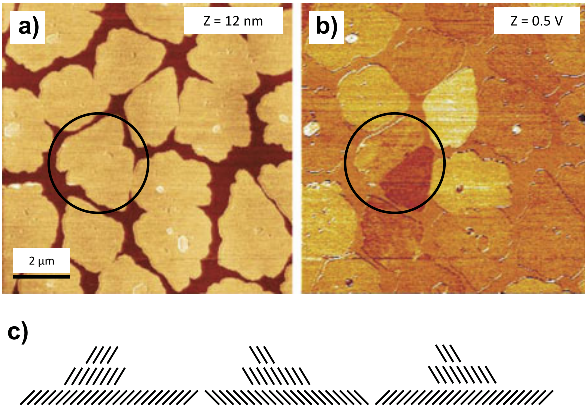

Fig. 4.11 (**a**, **b**) 10 mm × 10 µm AFM and corresponding TSM image of a 0.6 ML 6P film grown on ion-bombarded mica. The *circles* mark two islands with different azimuthal orientation of the molecules which have merged at a rather early stage as revealed by TSM. (**c**) Scheme of the resulting final film morphology in side view presentation

ergy of $E_D = 50$ meV for molecule diffusion on the terrace composed of the tilted molecules into account an ESB of $E_{ES} = 0.22$ eV is obtained in surprisingly good agreement with the value determined from the experiment. This reduced value of the ESB is obviously so small that it can be overcome under the growth conditions applied. We also have to note here that a similar bending—as is required for this interlayer diffusion process—has indeed been observed by scanning tunneling microscopy for 6P molecules bending across surface corrugations [44].

The discovered level dependence of the ESB due to the change in molecular tilt is a novel phenomenon which is the direct consequence of the anisotropy and complexity of the building blocks in organic thin-film growth. A layer-dependent ESB has also been reported for di-indenoperylene growth on SiO_2 where mound formation sets in only after completion of the first two layers [45]. Such a phenomenon is certainly useful in designing desired growth morphologies. In fact, we have shown recently that the first layer of 43° tilted 6P molecules almost closes [13]. Figure 4.11 shows AFM and TSM results for a 0.6 ML thick 6P film grown at room temperature on ion-bombarded mica. The morphology (Fig. 4.11(a)) looks layer-by-layer like; most of the 2D islands have coalesced already and only a few second-layer islands are found. The TSM image which is sensitive to the azimuthal orientation of the tilted molecules [15] reveals several remarkable observations. First, within an irregularly shaped island we find only one azimuthal orientation, i.e., we can consider such an island as a 2D 6P crystallite for which the azimuthal orientation of the 43° tilted molecules remains unchanged upon growth. This allows for identifying whether a large island is a result of coalescence event as can be seen in the area encircled in Figs. 4.11(a–b). Second, the azimuthal orientations are random, and we find by sample rotation that there is no preferential azimuth as it is indeed expected for an amorphous substrate. This fact is in agreement with the observation of a random azimuthal orientation of the mature hexagonal mounds (compare to Fig. 4.3(c)). Third—and this needs further investigation—we see that the second-layer islands not necessarily continue the azimuthal orientation of the first layer. The findings are summarized in Fig. 4.11(c). The reduced ESB in the first layer results in an almost closed film of standing molecules with a tilt angle of about 45°, and there is hope to even improve this situation, e.g., by choosing a slightly higher growth temperature. On this first layer, mounds do form because of an increased ESB as a consequence of the change in molecular tilt. These mounds will not coalesce in our case because of the Zeno effect as described above. The resulting morphology looks very similar to that of the Stranski-Krastanov growth mode [7] where 3D crystallites do form on a wetting layer, however, we have to emphasize that here kinetics, in particular the discovered level-dependent ESB, are the driving force.

As it has been found previously for metal systems, the ESB depends on the step orientation and the step roughness [38], i.e., there can be a broad spectrum of step-edge barriers depending on the island shape. So, there are still a lot of details to explore by simulations. Also, possible exchange processes at step edges [46] might play a role for interlayer diffusion. Further, the way how the 6P molecule approaches the step edge will determine the details of the diffusion mechanism. Goose et al. also have performed a computational study on the Ehrlich-Schwoebel barriers for several small organic molecules including 6P [47]. In contrast to our approach using the NEB method to search for the minimum energy path across the step edge, they employed a trajectory search algorithm which is able to sample a larger portion of the available configuration space. Their method has the advantage that the many internal degrees of freedom accessible to 6P can be probed including molecular torsion. In contrast to our minimum energy path, they observe that 6P has a tendency to orient parallel to the step edge during descent. As a result, they find a "log roll" mechanism with only a slight bending but increased torsion angles with an overall lower energy barrier for step edge descent. However, this mechanism should be less dependent on the level number.

4.4 Island Nucleation in Organic Thin-Film Growth

The morphology of a thin-film is essentially determined by the very first steps of film formation, the nucleation of two- or three-dimensional islands. The number of generated islands per surface area will define the coarseness of a film. And—as we have seen above—the size of the critical island i is an important input parameter to reveal the ESB from mound morphologies. In this section we will first review atomistic nucleation theory [9] and present the results for i obtained from rate-dependent growth experiments for our model system, 6P on ion-bombarded mica. Thereafter, we will compare the findings with the results of scaling theories for island-size and capture-zone distributions. Finally we will discuss the issue of the molecular orientation within the critical island.

4.4.1 Atomistic Nucleation Theory and Desorption Rate Dependence of Film Formation

The classical mean-field nucleation theory for atoms starts from rate equations for the island densities N_s of islands with size s. If the monomers (adatoms) are the only mobile species, then the islands of size s change their size solely by incorporation or removal of monomers, with the monomer density N_1. The net rate Γ_s, which is the rate to form islands of size $s+1$, is then given by [8, 9]

$$\Gamma_s = \sigma_s D N_1 N_s - \gamma_{s+1} N_{s+1} \tag{10}$$

where σ_s is the capture number and γ_s is the rate at which monomers detach from an island of size s. D is the surface diffusion coefficient for the monomers. In this context it is assumed that no desorption of monomers can take place. This scenario is called *complete condensation* limit. The change of the monomer density is given by the deposition flux F and by the removal rate of the monomers due to dimer formation or the incorporation of monomers into an island of size s:

$$\frac{dN_1}{dt} = F - 2\Gamma_1 - \sum_{s\geq 2} \Gamma_s. \tag{11}$$

The change of the island densities with size s is given by $dN_s/dt = \Gamma_{s-1} - \Gamma_s$. There are too many parameters to solve this set of differential equations. To circumvent this problem one defines a critical island size i. One assumes that above this critical size the islands become stable, i.e., the detachment rate γ becomes zero. Then the change of the stable island density N is given by

$$\frac{dN}{dt} = \sigma_i D N_1 N_i. \tag{12}$$

Since under equilibrium conditions the unstable clusters should be in equilibrium with the monomers, the Walton relation [48] holds for these clusters:

$$\frac{N_s}{N_0} = \left(\frac{N_1}{N_0}\right)^s e^{E_s/kT}. \tag{13}$$

Here N_0 is the number of surface sites and E_s the binding energy of an island with size s. This yields for the nucleation rate of supercritical islands:

$$\frac{dN}{dt} = \sigma_i D N_1 N_0 \left(\frac{N_1}{N_0}\right)^i e^{E_i/kT}. \tag{14}$$

With the assumption of the critical island size Eq. (11) changes to

$$\frac{dN_1}{dt} = F - \sigma_i D N_1 N_i - \bar{\sigma} D N_1 N \tag{15}$$

where an average capture number $\bar{\sigma}$ was assumed for the different stable islands. For a detailed discussion of capture numbers σ_i and $\bar{\sigma}$ the reader is referred to the literature [9]. It turns out that these quantities are weakly varying functions of the coverage Θ and the critical island size i, and will be summarized in the factor

$\eta(\Theta, i)$. The solution of the coupled differential equations Eqs. (14), (15) leads to two temporal regimes. At early time, when the two terms at the right hand side of Eq. (15) are negligible, the number of monomers increases proportional to the total coverage $\Theta = Ft/N_0$, and the number of stable islands increases proportional to Θ^{i+2}. This is the so-called "nucleation regime". When the coverage becomes larger, the last term in Eq. (15) becomes larger too until it balances the deposition flux. In this case, the monomer density and the total island density N are nearly constant. In this so-called "steady state nucleation regime" (aggregation regime), the monomer density N_1 is correlated with the island density by $N_1 \approx F/(\bar{\sigma} DN)$. Inserting this relationship into Eq. (14) and integrating by separation of variables yields the classical equation of nucleation theory [9]:

$$\frac{N}{N_0} = \eta(\Theta, i)\left(\frac{F}{DN_0^2}\right)^{\frac{i}{i+2}} e^{E_i/(i+2)kT}. \tag{16}$$

Using the surface diffusion rate equation for a square lattice

$$D = \frac{\nu_0}{4N_0} e^{-E_D/kT} \tag{17}$$

where ν_0 is the pre-exponential factor for diffusion, this finally yields

$$\frac{N}{N_0} = \eta(\Theta, i)\left(\frac{4F}{\nu_0 N_0}\right)^{\frac{i}{i+2}} \exp\left(\frac{iE_D + E_i}{(i+2)kT}\right). \tag{18}$$

Equation (18) relates the number of all stable islands in the aggregation regime, independent of their size, with the experimental parameters temperature and deposition rate. This relationship is, in addition to the system parameters E_i and E_D, solely defined by the critical island size i.

Thus, a plot of $\ln N$ vs. $\ln F$ for constant substrate temperature and coverage allows the determination of the critical cluster size i from the slope $\alpha_R = i/(i+2)$ and the intercept with the y-axis yields information on the energies involved.

A prerequisite for the application of Eq. (18) to determine the critical island size i is that the system is in the aggregation regime, i.e., where the number of islands is nearly constant and only the size of the islands increases with coverage. Figure 4.12 shows AFM images for different 6P coverages in the early growth stage, prepared at room temperature with an evaporation rate of 0.02 ML/min on ion-bombarded mica [13]. In Fig. 4.12(e), the island number density is shown as obtained from evaluating the AFM images for the individual coverages. Until a coverage of 0.2 ML, there is an increase in island density (nucleation regime), whereas for 0.98 ML coverage (Fig. 4.12(d)) strong island coalescence (as already discussed previously) is observed. Thus we can conclude that the aggregation regime with constant island number is between about 0.2 ML and 0.6 ML.

Figure 4.13 shows now the AFM results of the nucleation regime (0.25 ML) for 6P deposited at room temperature with deposition rates varying between 0.02 and 0.5 ML/min. The plot of $\ln N$ vs. $\ln F$ is presented in Fig. 4.13(e). The data can be well approximated by a straight line, where a slope α_R of 0.55 ± 0.05 is obtained, which yields a critical island size of $i = 2.5 \pm 0.5$. A further evaluation of

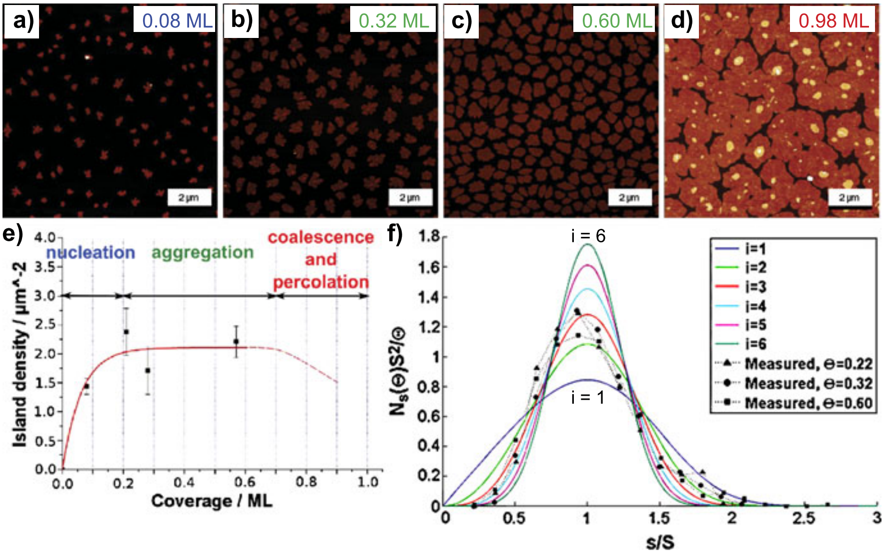

Fig. 4.12 (**a**–**d**) 10 μm × 10 μm AFM images of 6P deposited on amorphous mica at room temperature with a rate of 0.02 ML/min for the coverages indicated (z scale: 5 nm in (**a**)–(**c**), 10 nm in (**d**)). (**e**) Island density as a function of coverage. (**f**) Scaled island-size distribution for three different coverages in the aggregation regime and comparison with scaling functions for $i = 1, \ldots, 6$. (Partly adapted from [13])

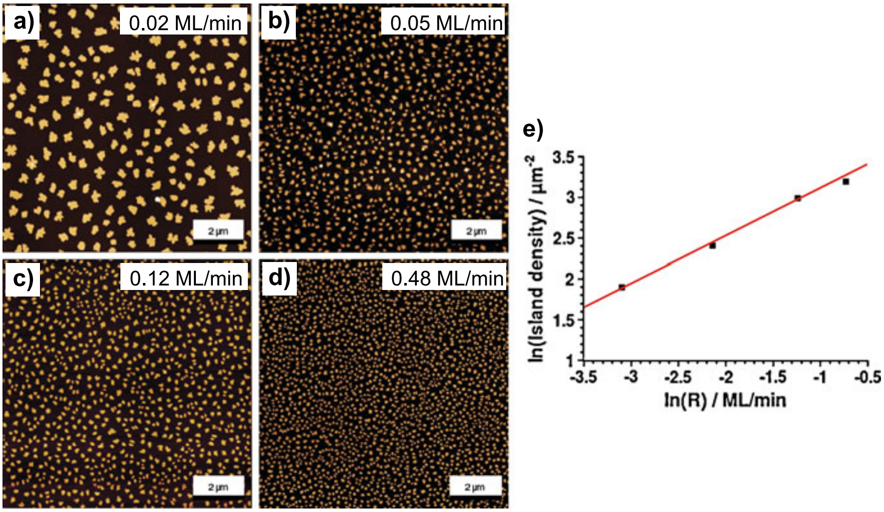

Fig. 4.13 10 μm × 10 μm AFM images of 0.25 ML 6P deposited on amorphous mica at room temperature with varying rates as indicated in the images (z scale: 5 nm). (**e**) Resulting island density as a function of growth rate. (Adapted from [13])

the temperature dependence of the island density yields a pre-exponential factor for diffusion of the 6P monomers on the amorphous mica surface of $2 \times 10^{17}\ \mathrm{s}^{-1}$ [13].

4.4.2 Scaling Theories for the Island-Size Distribution and the Capture-Zone Distribution

In the following it is described how one can determine the critical island size without performing a rate-dependent growth experiment. According to the dynamic scaling assumption [49], the scaled island-size distribution $f_i(s/S)$ in the aggregation regime should be independent of the coverage Θ and the mean island size S and only be a function of the critical island size i [50]:

$$f_i(s/S) = N_s(\Theta) S^2/\Theta \tag{19}$$

with s being the island size and S the average island size. Amar and Family [54] proposed an analytical expression for the scaled island-size distribution in the form

$$f_i(u) = C_i u^i \exp\bigl(-i a_i u^{1/a_i}\bigr) \tag{20}$$

with $u = s/S$ and C_i, a_i being defined by implicit geometrical equations:

$$\frac{\Gamma[(i+2)a_i]}{\Gamma[(i+1)a_i]} = (i a_i)^{a_i} \quad \text{and} \quad C_i = (i a_i)^{(i+1)a_i}/a_i \Gamma\bigl[(i+1)a_i\bigr]. \tag{21}$$

In Fig. 4.12(f) the scaled island-size distribution functions for various i ($i = 1$–6), according to Eq. (20), are compiled. In addition, experimentally obtained scaled distribution functions for 6P on amorphous mica are shown for three different coverages in the aggregation regime ($\Theta = 0.22$ ML, 0.32 ML, 0.60 ML). One can see that indeed all distributions collapse in one scaled distribution. A least squares fit yields the best agreement with a critical island size of $i = 3 \pm 1$ [13].

Pimpinelli and Einstein [52] have recently proposed an alternative method, based on an earlier work by Mulheran and Blackman [53], where the critical island size can be derived from the capture-zone distribution. By capture zone one understands the region of the substrate from which monomers are more likely to diffuse to this particular island than to any other in the system. The capture zones can be roughly correlated with Voronoi polygons. It is assumed that the capture-zone distribution P can be described by a simple expression based on the generalized Wigner surmise, i.e., being the product of a power-law rise and a Gaussian decay:

$$P_\beta(s) = a_\beta s^\beta \exp\bigl(-b_\beta s^2\bigr). \tag{22}$$

Here, $\beta = i + 2$ [54, 55], $s = v/V$, with v: Voronoi polygon size, V: mean value of v, a_β and b_β are constants fixed by normalization and unit-mean conditions [55]:

$$a_\beta = 2\Gamma\left(\frac{\beta+2}{2}\right)^{\beta+1} \Big/ \Gamma\left(\frac{\beta+1}{2}\right)^{\beta+2} \quad \text{and} \quad b_\beta = \left[\Gamma\left(\frac{\beta+2}{2}\right) \Big/ \Gamma\left(\frac{\beta+1}{2}\right)\right]^2. \tag{23}$$

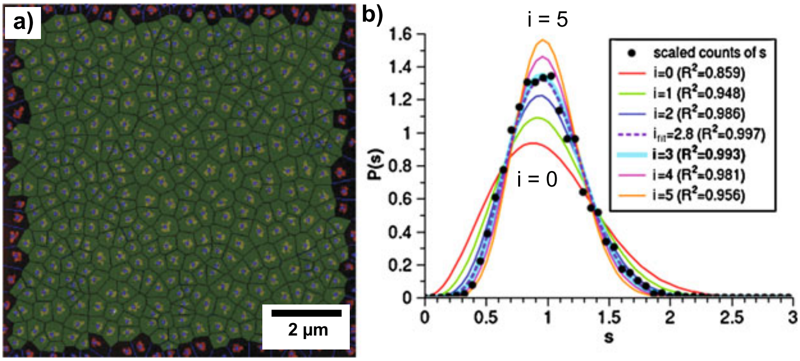

Fig. 4.14 (**a**) 10 µm × 10 µm AFM image of 0.19 ML 6P deposited on amorphous mica at room temperature with a rate of 0.04 ML/min. The overlaid Voronoi tessellation omits islands at the image rim. (**b**) Distribution of capture zones as shown in (**a**), and comparison with the scaling functions, according to Eq. (22). (After [13])

The results of the capture-zone scaling applied to our model system, deposition of 6P at room temperature on ion-bombarded mica are summarized in Fig. 4.14. From the Voronoi tessellation (Fig. 4.14(a)), the experimentally obtained capture-zone distribution is obtained. In Fig. 4.14(b), this is plotted together with the calculated functions, according to Eq. (22) for i ranging from 0 to 5. The optimum number of bins for the histograms were derived from the Scott model [56]. The value of $i_{\text{fit}} = 2.8$ was estimated from a direct fit using the method of least squares with the Levenberg-Marquardt algorithm [13].

In summary, by applying nucleation theory and two different scaling approaches, a critical island size of $i = 2$ to 3 was obtained for the room-temperature growth of 6P on ion-bombarded mica. Before we want to discuss this result, we summarize in Fig. 4.15 the results for 6P growth on amorphous SiO_2 at room temperature [14]. As it can be seen in Fig. 4.15(c), analysis of the capture-zone distribution results in a critical nucleus size of $i = 1$ whereas the island-size distribution reveals a best fit for $i = 2$.

4.4.3 Discussion of the Critical Island Size and Molecular Orientation

The nucleation of 6P on amorphous mica can be successfully described by the classical nucleation theory, at least for the given experimental conditions of room-temperature growth and a deposition rate in the range of 0.04–0.5 ML/min. The critical island size as obtained by three different evaluation methods, the rate-dependent island density, the island-size distribution, and the capture-zone distribution is in the range between 2 and 3 molecules. In fact, the actual critical island size must not necessarily be an integer value. This situation would only result if indeed all

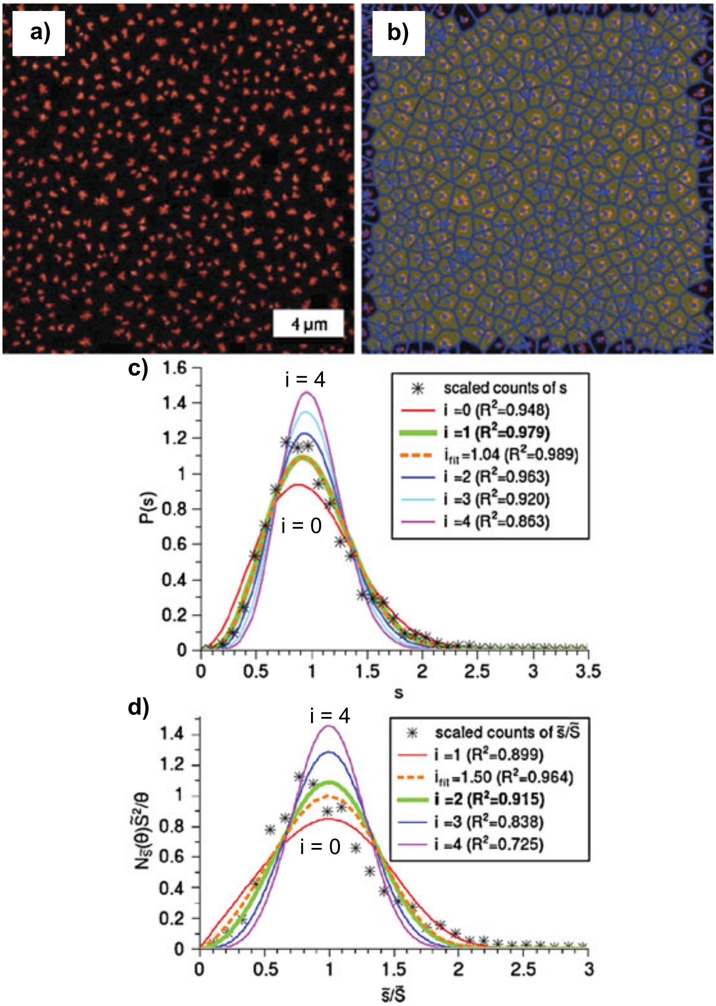

Fig. 4.15 (**a**) 20 μm × 20 μm AFM of 6P grown at room temperature on SiO_2 (z scale: 5 nm) and (**b**) image masked with the calculated Voronoi polygons. (**c**) Capture-zone histogram obtained from analysis of about 2700 capture-zone areas. Capture-zone distributions for several values of i are plotted for comparison. The *dashed line* is a least square fit to the data of the histogram. The *thick line* marks the selected i. (**d**) Island-size histogram obtained from the same data set of about 2700 islands analyzed by the model of Family and Amar [51] and compared with fits for several i. The *dashed line* is a least square fit to the data of the histogram. The *thick line* marks the selected i. (Adapted from [14])

islands with size larger than i would be totally stable. However, it has been pointed out previously that rather a continuous transition from unstable to stable islands will exist [57]. This means that always a finite detachment rate from the island edges exists which, however, decreases considerably with increasing island size. In addition to that, different arrangements of the monomers in the "supercritical" island might be of different stability. Such a scenario will definitely be more pronounced in the case of rod-like molecules than of point-like atoms, and might explain the observed non-integer critical island size of about 2.5 ± 0.5. With other words, both, trimer ($i = 2$) and tetramer ($i = 3$) nuclei of 6P molecules are of similar stability. Actually, this situation is not implausible. Compared to the clustering of single atoms, where a trimer is a quite well-defined entity, a trimer of lying rod-like entities can have a variety of different conformations. Thus, one can imagine that a special arrangement of three 6P molecules is already stable, whereas for another arrangement four molecules are necessary to form a stable island [13]. Thus, we encounter here again peculiarities that are the consequence of anisotropy of the building blocks and their interaction.

A further important question arises whether the critical nuclei consists of molecules still lying on the substrate as the single diffusing molecules do or if it is are already composed of standing molecules. To answer this question, we have calculated the binding energy $E(n)$ of an island containing n 6P molecules using the force-field approach. Here, $E(n)$ is defined as the energy difference between the n-molecule cluster adsorbed on the substrate compared to the energy of n adsorbed, but well-separated, lying 6P molecules. For the calculation we have modeled the substrate surface by the (001) plane of a 6P crystal because the atomic structure of the actually used, ion-bombarded mica surface is not known, precluding a force-field simulation of the 6P deposition on this substrate. We expect our simulation results, concerning the cluster shapes of standing and lying islands, to be rather insensitive to the exact nature of the substrate/molecule interaction as long as it remains in the weakly interacting regime resulting in standing molecules. The results of our calculations are presented in Fig. 4.16 which shows $E(n)$ for clusters composed of 1 to 20 molecules together with the energetically favorable arrangement for both standing and lying conformations. For the lying clusters, an offset along the long molecular axis between adjacent molecules is observed which is caused by the π–π interaction of the aromatic molecules. The lattice mismatch with the substrate results in the fact that only a maximum of four molecules exhibit this offset in the same direction. For the standing islands, the molecular packing systematically approaches the bulk-like herringbone structure with increasing island size. It can be seen that for $n < 4$, the standing configuration is energetically unstable. For cluster sizes between 4 and 14, standing molecules are energetically less favorable compared to those composed of lying molecules, however, they would be at least metastable with respect to isolated, adsorbed molecules. Only above $n = 14$ do the clusters of standing molecules become more favorable. However, the location of crossover of both curves in Fig. 4.16(a) certainly depends on the molecule/substrate interaction. Qualitatively, a stronger substrate/molecule interaction will energetically favor "lying clusters" due to the larger adsorption energy of lying molecules compared to standing ones. On the other hand, a weaker substrate/molecule interaction will favor islands composed of standing molecules due to their lower surface energy. With other words, tuning the strength of the substrate/molecule interaction will result in a relative shift of the binding energy curves for the standing and lying clusters, respectively. Thus, the crossover could be at a somewhat different cluster size for 6P on

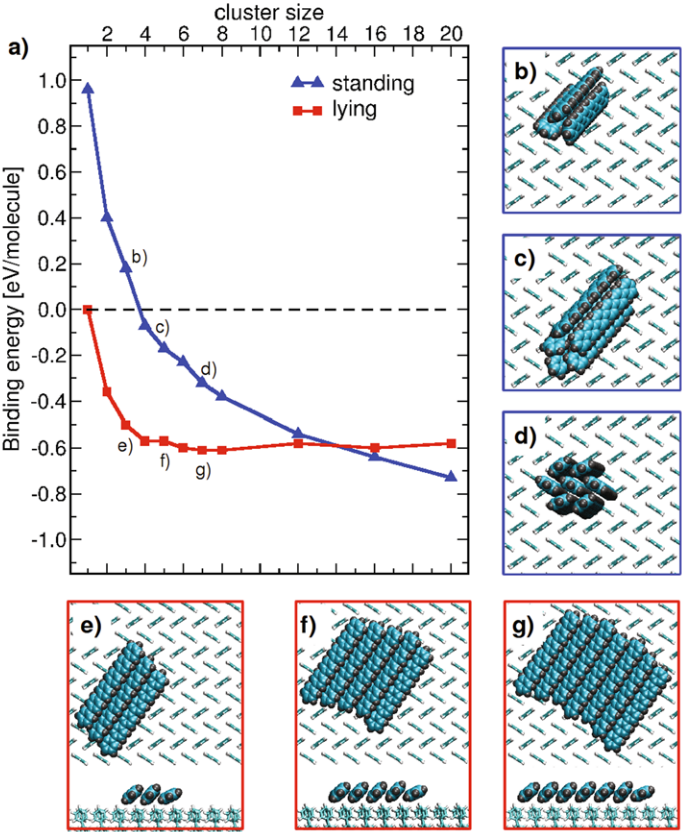

Fig. 4.16 (**a**) 6P cluster binding energy on a 6P(001) plane as a function of cluster size for clusters with standing and lying molecules, respectively. (**b–d**) Conformation of minimum energy clusters composed of 3, 4, and 7 standing molecules. (**e–g**) Conformation of clusters composed of 3, 5, and 7 lying molecules. (Adapted from [13])

the amorphized mica surface. Nevertheless, from the results presented in Fig. 4.16, we have to conclude that the critical islands ($n = 2, 3$) are still composed of lying molecules [12]. Only after further island growth do the molecules rotate into the standing configuration. How this change proceeds in detail is not clear, and only further studies—possibly by molecular dynamic simulations can elucidate this process.

At this point we want to comment on the problem that we have used $i = 1$ in the formalisms to extract E_{ES} from both, the mound morphologies and second-layer island formation in Sect. 4.3, although there is strong evidence for a larger critical nucleus size. For values of i larger than 1, the formalisms used in Sects. 4.3.1 and 4.3.2 become difficult. The usually unknown dimer dissociation time τ_{dis} introduces a further timescale into the problem (in addition to the adatom residence time τ, the adatom traversal time τ_r, and to the time between adatom deposition events).

The balance between these different times changes the nucleation probability in a non-linear way. It turns out that due to the uncertainty of τ_{dis}, the problem can be generalized only for a limited number of situations [26]. However, the case of $i = 1$ can always be treated as a lower limit for the step-edge barrier.

4.5 Summary and Outlook

Using the growth of standing oligophenyl (6P) molecules on amorphous substrates like ion-bombarded mica or SiO_2 as a model system, we have demonstrated that procedures that have developed in inorganic epitaxy quite a while ago can be successfully applied to extract quantitative data on step-edge barriers. This so-called Ehrlich-Schwoebel barrier is responsible for the formation of terraced growth mounds composed of standing molecules as has been found in several organic thin-film systems [3, 6, 12, 18–20, 45, 58, 59]. In combination with transition state theory calculations it could be revealed that the complexity and anisotropy of the molecules can result in a change in the molecular conformation during the inter-layer mass transport like molecular bending or twisting. This effect, in conjunction with a gradual change of the molecular orientation in the different levels, can result in the novel phenomenon of level-dependent step-edge barriers which seems to be quite common in organic thin-film growth [12, 45].

With respect to intralayer diffusion processes, we focused on the determination of the critical island size for which again procedures developed for inorganic growth like classical atomistic nucleation theory and scaling approaches for island-size and capture-zone distributions have been applied. Here, the anisotropy of the organic building blocks can result in situations where the critical island size is not a single integer number because there can exist differently sized clusters of molecules having similar binding energy due to different configurations.

We want to emphasize that detailed studies of molecular diffusion processes just started recently and there are still a lot of open questions. With respect to inter-layer diffusion, we have to name phenomena as morphology-dependent ESBs and collective diffusion processes like exchange processes. With respect to island nucleation, one has to consider that the capture probability at low temperatures will no longer be independent of the orientation of the individually approaching molecules and will most probably be much smaller than unity which is referred to rotational hindering [60, 61]. This effect of steric constraints for island formation might be the reason that the nucleation theory fails at low substrate temperatures as we observed for 6P on ion-bombarded mica [13]. A further field of both, experimental and theoretical studies will certainly be the intralayer diffusion of molecules along island rims or terrace edges since these processes are determining the 2D shape of islands or growth mounds. For instance, the transition from irregularly shaped ramified islands to hexagonal terraces of the mature growth mounds (see Fig. 4.3) via the formation of elongated hexagonal second-layer islands (see Fig. 4.11) waits to be explored. Here, one will benefit again from efforts in inorganic epitaxy where such complex questions have been addressed by combination of atomistic models and Kinetic Monte Carlo simulations [62].

Although the degrees of freedom are much larger in organic growth systems compared to atomic, inorganic epitaxy, we are confident that one will acquire with time a similar understanding of the underlying dynamics and growth kinetics to finally be able to tune growth morphologies with respect to desired device applications in organic electronics as has been mentioned in the introduction of this chapter.

Acknowledgements We wish to thank P. Frank, O. Lengyel, S. Lorbek, D. Nabok, T. Potocar, R. Resel, Q. Shen, and L. Tumbek for sample preparation and contributions to the measurements. This work was financially supported by the Austrian Science Fund (FWF) under Projects No. P19197, S9707, and S9714.

References

1. K. Al-Shamery, H.-G. Rubahn, H. Sitter (eds.), *Organic Nanostructures for Next Generation Devices*. Springer Series in Materials Science, vol. 101 (Springer, Berlin, 2008)
2. K.N. Baker, A.V. Fratini, T. Resch, H.C. Knachel, W.W. Adams, E.P. Socci, B.L. Farmer, Polymer **34**, 1571 (1993)
3. P. Frank, G. Hlawacek, O. Lengyel, A. Satka, C. Teichert, R. Resel, A. Winkler, Surf. Sci. **601**, 2152 (2007)
4. H. Plank, R. Resel, H. Sitter, A. Andreev, N.S. Sariciftci, G. Hlawacek, C. Teichert, A. Thierry, B. Lotz, Thin Solid Films **443**, 108 (2003)
5. C. Teichert, G. Hlawacek, A. Andreev, H. Sitter, P. Frank, A. Winkler, N.S. Sariciftci, Appl. Phys. A **82**, 665 (2006)
6. G. Hlawacek, Q. Shen, C. Teichert, R. Resel, D. Smilgies, Surf. Sci. **601**, 2584 (2007)
7. E. Bauer, Z. Kristallogr. **110**, 372–395 (1958)
8. T. Michely, J. Krug, *Islands, Mounds and Atoms*. Springer Series in Surface Science, vol. 42 (Springer, Berlin, Heidelberg, 2004)
9. J.A. Venables, G.D.T. Spiller, M. Hanbücken, Rep. Prog. Phys. **47**, 399 (1984)
10. G. Ehrlich, F. Hudda, J. Chem. Phys. **44**, 1039 (1966)
11. R.L. Schwoebel, E.J. Shipsey, J. Appl. Phys. **37**, 3682 (1966)
12. G. Hlawacek, P. Puschnig, P. Frank, A. Winkler, C. Ambrosch-Draxl, C. Teichert, Science **321**, 108 (2008)
13. T. Potocar, S. Lorbek, D. Nabok, Q. Shen, L. Tumbek, G. Hlawacek, P. Puschnig, C. Ambrosch-Draxl, C. Teichert, A. Winkler, Phys. Rev. B **83**, 075423 (2011)
14. S. Lorbek, G. Hlawacek, C. Teichert, Eur. Phys. J. Appl. Phys. **55**, 23902 (2011)
15. K. Puntambekar, J. Dong, G. Haugstad, C.D. Frisbie, Adv. Funct. Mater. **16**, 879 (2006)
16. J. Zhang, J.P. Rabe, N. Koch, Adv. Mater. **20**, 3254 (2008)
17. G. Hlawacek Ph.D. Thesis, Montanuniversität Leoben, Leoben (2007)
18. F.-J. Meyer zu Heringdorf, M. Reuter, R. Tromp, Nature **412**, 517 (2001)
19. L. Kilian, E. Umbach, M. Sokolowski, Surf. Sci. **573**, 359 (2004)
20. S. Zorba, Y. Shapir, Y. Gao, Phys. Rev. B **74**, 245410 (2006)
21. M. Klaua, Rost Krist. **11**, 65 (1975)
22. K. Meinel, M. Klaua, H. Bethge, J. Cryst. Growth **89**, 447 (1988)
23. M. Kalff, P. Šmilauer, G. Comsa, T. Michely, Surf. Sci. **426**, L447 (1999)
24. M.P. Seah, Surf. Sci. **32**, 703 (1972)
25. I. Elkinani, J. Villain, Solid State Commun. **87**, 105 (1993)
26. J. Krug, P. Politi, T. Michely, Phys. Rev. B **61**, 14037 (2000)

27. Y. Zhao, G.-C. Wang, T.-M. Lu, *Characterization of Amorphous and Crystalline Rough Surface: Principles and Applications*. Experimental Methods in the Physical Sciences, vol. 37 (Academic Press, New York, 2001)
28. C. Teichert, Phys. Rep. **365**, 335 (2002)
29. Y.-P. Zhao, H.-N. Yang, G.-C. Wang, T.-M. Lu, Phys. Rev. B **57**, 1922 (1998)
30. G. Henkelman, H. Jonsson, J. Chem. Phys. **113**, 9978 (2000)
31. M. Fendrich, J. Krug, Phys. Rev. B **76**, 121302 (2007)
32. J.D. Gale, A.L. Rohl, Mol. Simul. **29**, 291 (2003)
33. D.W. Brenner, O.A. Shenderova, J.A. Harrison, S.J. Stuart, B. Ni, S.B. Sinnott, J. Phys. Condens. Matter **14**, 783 (2002)
34. D. Nabok, P. Puschnig, C. Ambrosch-Draxl, Phys. Rev. B **77**, 245316 (2008)
35. J. Rottler, P. Maass, Phys. Rev. Lett. **83**, 3490 (1999)
36. S. Esch, M. Hohage, T. Michely, G. Comsa, Phys. Rev. Lett. **72**, 518 (1994)
37. R. Kunkel, B. Poelsema, L.K. Verheij, G. Comsa, Phys. Rev. Lett. **65**, 733 (1990)
38. C. Teichert, C. Ammer, M. Klaua, Phys. Status Solidi A **146**, 223 (1994)
39. J.G. Amar, F. Family, Phys. Rev. B **54**, 14071 (1996)
40. H. Yamane, Y. Yabuuchi, H. Fukagawa, S. Kera, K.K. Okudaira, N. Ueno, J. Appl. Phys. **99**, 093705 (2006)
41. X. Gonze, J.M. Beuken, R. Caracas, F. Detraux, M. Fuchs, G.M. Rignanese, L. Sindic, M. Verstraete, G. Zerah, F. Jollet, M. Torrent, A. Roy, M. Mikami, P. Ghosez, J.Y. Raty, D.C. Allan, Comput. Mater. Sci. **25**, 478 (2002)
42. J.P. Perdew, K. Burke, M. Ernzerhof, Phys. Rev. Lett. **77**, 3865 (1996)
43. N. Troullier, J.L. Martins, Phys. Rev. B **43**, 1993 (1991)
44. G. Koller, S. Surnev, M. Ramsey, F. Netzer, Surf. Sci. **559**, L187 (2004)
45. X.N. Zhang, E. Barrena, D. Goswami, D.G. de Oteyza, C. Weis, H. Dosch, Phys. Rev. Lett. **103**, 136101 (2009)
46. B. Yu, M. Scheffler, Phys. Rev. B **55**, 13916 (1997)
47. J.E. Goose, E.L. First, P. Clancy, Phys. Rev. B **81**, 205310 (2010)
48. D. Walton, J. Chem. Phys. **37**, 2182 (1962)
49. T. Vicsek, F. Family, Phys. Rev. Lett. **52**, 1669 (1984)
50. J.G. Amar, F. Family, P.M. Lam, Phys. Rev. B **50**, 8781 (1994)
51. J.G. Amar, F. Family, Phys. Rev. Lett. **74**, 2066 (1995)
52. A. Pimpinelli, T.L. Einstein, Phys. Rev. Lett. **99**, 226102 (2007)
53. P.A. Mulheran, J.A. Blackman, Phys. Rev. B **53**, 10261 (1996)
54. A. Pimpinelli, T.L. Einstein, Phys. Rev. Lett. **104**, 149602 (2010)
55. M. Li, Y. Han, J.W. Evans, Phys. Rev. Lett. **104**, 149601 (2010)
56. D.W. Scott, Biometrica **66**, 605 (1979)
57. C. Ratsch, A. Zangwill, P. Šmilauer, D.D. Vvedensky, Phys. Rev. Lett. **72**, 3194 (1994)
58. R. Ruiz, D. Choudhary, B. Nickel, T. Toccoli, K.C. Chang, A.C. Mayer, P. Clancy, J.M. Blakely, R.L. Headrick, S. Iannotta, G.G. Malliaras, Chem. Mater. **16**, 4497 (2004)
59. E. Gomar-Nadal, B.R. Conrad, W.G. Cullen, E.A. Williams, J. Phys. Chem. C **112**, 5646 (2008)
60. M. Beutl, M. Riedler, K.D. Rendulic, Chem. Phys. Lett. **247**, 249 (1995)
61. W.A. Dino, H. Kasai, A. Okiji, Prog. Surf. Sci. **63**, 63 (2000)
62. J.W. Evans, P.A. Thiel, M.C. Bartelt, Surf. Sci. Rep. **61**, 1 (2006)

Chapter 5
In-situ Observation of Organic Thin Film Growth on Graphene

Gregor Hlawacek, Fawad S. Khokhar, Raoul van Gastel,
Harold J.W. Zandvliet, Bene Poelsema, and Christian Teichert

Abstract In-situ monitoring is highly convenient for obtaining profound insight into growth processes. In particular, real time imaging during film formation allows an unambiguous identification of growth modes such as Frank van der Merwe Layer-by-Layer, Stranski–Krastanov or Vollmer–Weber island growth. Here, we discuss the benefits of using Low Energy Electron Microscopy (LEEM) as a tool for the application relevant deposition of para-Sexiphenyl on graphene and Ir$\{111\}$ substrates. Changes in the growth mode can be identified and interpreted with ease directly from the real time LEEM observations. Examples of all three principal growth modes will be discussed together with a state of the art structure determination. The presented system is a prime candidate for the possible fabrication of thin organic light emitting diodes. It combines an optically active organic semiconductor with the transparent, flexible, and conductive electrode material graphene.

5.1 Introduction

The growth of organic thin films is gaining more attention as the possible benefits become clear. This is due to a number of applications, in particular organic semiconductor displays, used in modern cell phones, television sets, and computer screens. However, many more applications including organic semiconductor-based sensor arrays, lighting, and solar cells will hit the market soon. In addition to this active use of organic thin films many passive applications in coating technology and biotechnology are envisioned. All these new applications require a precise engineering of thin film morphology and other physical properties, often on the nanometer

---

G. Hlawacek (✉) · F.S. Khokhar · R. van Gastel · H.J.W. Zandvliet · B. Poelsema
Physics of Interfaces and Nanomaterials, MESA+ Institute for Nanotechnology, University of Twente, PO Box 217, 7500AE Enschede, The Netherlands
e-mail: g.hlawacek@utwente.nl

C. Teichert
Institute of Physics, Montanuniversitaet Leoben, Franz Josef Str. 18, 8700 Leoben, Austria

H. Sitter et al. (eds.), *Small Organic Molecules on Surfaces*,
Springer Series in Materials Science 173, DOI 10.1007/978-3-642-33848-9_5,

scale. This can only be achieved once a fundamental understanding of the underlying growth mechanisms has been established.

The property that distinguishes most organic materials from nearly all classic metals and inorganic semiconductors, is the fact that the building blocks of the latter two can be considered as zero dimensional particles. Atoms are the building blocks and diffusing entity of nearly all inorganic systems. An atom diffusing on the surface of a substrate and approaching an ad-island has no orientational preferences that would influence the adsorption into the step edge. This is different for nearly all organic species of interest. Their higher dimensionality tends to lead to highly directional diffusion and large variations in the sticking coefficient. The combination of the two often leads to a highly anisotropic growth [1, 2]. For many cases this is undesirable as implementation of integrated electronic devices, sensors, and solar cells requires large area homogeneous thin films. The typical rod or plate like shape of conjugated molecules used for organic semiconductor thin films results in many small deviations from the classically expected behavior. To understand the resulting growth mechanism it is often advantageous to use model molecules like para-sexiphenyl or pentacene which exhibit the shape effects in a very pronounced way. For example, in the case of diffusion over a step edge it was demonstrated that not only a high step edge barrier exists [3], but that it is also influenced by the stiffness of the molecular backbone and its anisotropy [4]. Furthermore, changes in molecular tilt angle—something which is impossible for a zero dimensional atom—leads to a level dependence of the step edge barrier [3, 5]. A more elaborate discussion can be found in Chap. 4. A practical consequence of the higher dimensionality of the building blocks manifests itself in crystallography. There, the notation {lmn} describes a set of planes that are equivalent to (lmn) by the symmetry of the lattice. Ir(111) and Ir{111} can be considered equivalent notations as there is no way of separating the (111) plane from e.g. the $(\bar{1}1\bar{1})$-plane. Both notations—() and { }—are often used when strictly speaking only one of them would be correct. This can not be done for organic systems. The plate- or rod-like molecules make many, if not all, planes in the set of {lmn} non-equivalent.

The fundamental growth processes that occur on the surface of a substrate are best studied using in-situ real time methods to monitor the growth process. At the same time the method of choice needs to provide the required resolution laterally, vertically, and temporally. Usually a compromise is found that allows to keep all three requirements in a good balance. One such method is Low Energy Electron Microscopy (LEEM) [6] and its variant Photo Electron Emission Microscopy (PEEM). LEEM in particular is capable of visualizing surface details with lateral resolution as good as 2 nm [7]. At the same time several different contrast mechanisms [8] can be exploited to reveal different layers and even measure their thickness. All this can be done with a time resolution smaller than one second. This is sufficient for many diffusion related processes, provided deposition rates can be kept low. PEEM on the other hand while inferior in resolution allows the direct qualitative assignment of work functions.

Many other techniques—used in thin film growth—perform better in one or another aspect, but it is the unique combination of in-situ, real time and real space that makes LEEM/PEEM such a valuable technique. Scanning Tunneling Microscopy (STM) for one, has unparalleled spatial resolution. However, the real time capabilities of the technique are limited and are currently under intense development [9–11]. The biggest drawback of STM is the extremely small field of view. Once nucleation is finished the mesoscopic growth processes and the formation of thin layers that cover several μm are of prime interest.

Here, we describe an in depth study of growth processes in organic thin films on different surfaces on the mesoscale. We will highlight the benefits of real time observation that allows us to reveal new insights that can be used with other—post deposition—techniques to quickly identify mechanisms active during the growth of the observed surface structures.

5.2 Experimental

5.2.1 Low Energy Electron Microscopy

The Low Energy Electron Microscope (LEEM) [6, 8, 12] has been developed in the 1980s and since than it has been a viable surface science tool. It utilizes a cathode lens to decelerate high energy electrons with typical energy of 20 keV to a few eV (start voltage) just in front of the specimen. These slow electrons than interact with the sample surface. The energy of the electrons impinging on the sample surface is below the energy of the minimum of the mean free path in the universal curve of electrons in penetrating matter. A good surface sensitivity is guaranteed as the electrons will not be able to penetrate deeply into the material.

The typical resolution achieved with state of the art LEEM is of the order of a few nanometers, but can be as good as 2 nm [7]. Several contrast mechanisms are at work simultaneously when imaging with a LEEM. The two important ones for the presented work are based on structural differences and on work function differences. Contrast can usually be enhanced by optimizing the start voltage of the impinging electrons. However, care has to be taken not to influence the growth process via material modification or local charge build up by the electron beam. This is important in this context since conjugated molecules must be considered as fragile objects. To avoid any unwanted impact on the molecules, start voltages below the bandgap of 6P (3.1 eV) have been used.

One big advantage of a typical LEEM instrument is the possibility to do spatially resolved Low Energy Electron Diffraction (LEED). With the help of an illumination aperture these diffractions patterns can be acquired from individual areas of interest. In the current case an aperture with a projected diameter of 1.4 μm has been used to obtain structural information on individual features on the surface. Obviously, typical energies will exceed the bandgap of 6P substantially. As a result diffraction patterns—in particular from thin layers—disappear with in a few seconds. The obtained μLEED patterns therefore contain a significant diffuse background and are susceptible to peak broadening. Besides the issues mentioned here, it has been shown that SPA-LEED [13] can be used for the structural characterization of organic semiconductor thin films [14].

5.2.2 Metal Supported Graphene

Graphene [15], one of the most exciting materials today, is investigated by many groups because of its unique electronic properties. The particular interest here is related to the fact that it is a transparent, flexible and highly conductive electrode material [16, 17]. It is the ideal substrate for organic semiconductor applications [18, 19]. Next to the original exfoliation method [15] and the growth from carbides [20, 21] the metal route [22] has been demonstrated to be a viable route to obtain single layer graphene. Besides many single crystalline materials also the growth on cheaper Ni [23] and Cu [24] foils has been mastered recently.

The case of graphene on Ir$\{111\}$ [25] is of special interest for two reasons. First, it has been shown that graphene films on Ir$\{111\}$ have a very weak coupling to the substrate and can be considered extremely close in the relevant electronic properties to free standing graphene films [26]. Second graphene flakes can be grown with selected orientation with millimeter size [27, 28]—a prerequisite for device fabrication.

Here, several μm large graphene flakes have been grown on Ir$\{111\}$ by thermal decomposition of ethylene gas [25, 27, 29].

5.2.3 Para-Sexiphenyl

Para-Sexiphenyl (6P) is a model molecule of particular interest to investigate diffusion of non-zero dimensional particles. It consists of 6 phenyl rings connected by single bonds in a linear fashion. Due to steric hindering between the hydrogen atoms the molecule is twisted in the gasphase. However, when incorporated in a crystal the energy gain is larger than the activation energy for turning all the rings into a planar configuration [30]. At room temperature, 6P crystallizes in the space group $P2_1/c$ with lattice constants $a = 26.241$ Å, $b = 5.568$ Å, $c = 8.091$ Å, and a monoclinic angle $\beta = 98.17°$ [31]. The unit cell holds two molecules which are rotated with respect to each other, leading to a herringbone motif. Throughout the text 6P molecules are drawn rigid and planar for clarity of the drawings. However, one has to keep in mind that 6P is not rigid at finite temperatures and, in particular, one can assume that the planarity is lifted at the surface of the crystal. As a consequence the two differently rotated molecules in the unit cell do not show up separately in diffraction patterns because their already similar molecular form factors are smeared out by thermal motion.

The molecule has a large anisotropy and three different sides can be differentiated. The small side of the molecule is terminated by a single hydrogen atom. Compared to the other two, approach via this side has an extremely low sticking coefficient [1, 2]. This can be seen in nearly all 6P growth experiments on a mesoscopic scale by the fact that one dimensional fibers are the dominant morphology [32–34]. These 1D chains and needles have the molecules aligned perpendicular to their long axis, as the growth rate for the direction along the long molecular axis—connected via the small side of the molecule—is very small. The two long sides form the herringbone motif via a quadrupole interaction in the bulk. They are different as the one (edge side) is again terminated by hydrogen, while the other (flat side) carries the large π orbital—the preferred binding site.

Sublimation purified 6P has been evaporated from a Knudsen cell. Any low boiling point contaminations were removed prior to deposition by thoroughly outgassing the source material over several hours.

5.3 Graphene

5.3.1 Layer-by-Layer Growth

Real Space Observation of Layer-by-Layer Growth

On graphene the Layer-by-Layer (LbL) growth mode can be achieved [35] by carefully influencing the mobility of the diffusing molecules and the nucleation probability in the following way:

1. Lowering the sample temperature, thus reducing the thermal energy of the diffusing 6P molecules.
2. Lowering the deposition rate, and consequently ensuring a low supersaturation of the 2D gas phase.

A subtle interplay between thermodynamic and kinetic growth factors is the base of this counterintuitive finding. As we will show later 1. effectively reduces the tendency of 6P to form 3D crystallites. The resulting reduced mobility of the diffusing entities prevents uphill diffusion. In this way, it is ensured that molecules that reach an island get incorporated into the island edge instead of climbing on top of the island. The proper inclusion into the terrace edge eventually requires a detachment of the molecule back in to the 2D gas phase. However, in any case, time will be required for the molecule to diffuse along the terrace edge to an available kink position. This time is available to the molecule as the number of diffusing entities reaching the step edge is kept low due to 2. The low deposition rate also keeps the number of nuclei low so that large domains can form despite the low sample temperature.

Figure 5.1 shows a sequence of LEEM images recorded during the deposition of 6P on graphene at 240 K. The graphene flake and the first initial islands are shown

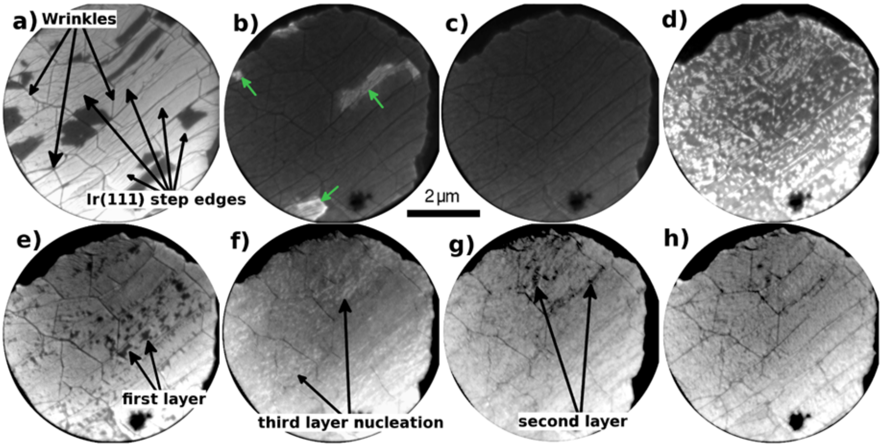

Fig. 5.1 Layer-by-Layer growth of 6P on graphene. The above sequence of LEEM images shows the formation of the first three molecular layers on graphene during the 6P deposition at a sample temperature of 240 K. (**a**, $t = 134$ s) Initial 6P islands form. Wrinkles in the graphene and steps in the underlying Ir{111} surface are indicated by *arrows*. (**b**, $t = 1514$ s) The initial islands have formed a closed layer. After 400 s of 6P deposition a second darker contrast appeared within the islands. Areas where the initial islands are visible are marked by *arrows*. (**c**, $t = 1698$ s) The first layer of 6P molecules is fully closed. Wrinkles are still visible as thin lines. (**d**, $t = 2107$ s) The second layer (bright) nucleates at random positions. (**e**, $t = 2901$ s) The second layer is nearly closed. Uncovered areas of the first monolayer are indicated. (**f**, $t = 3467$ s) Nucleation of the third layer (bright islands) is observed. (**g**, $t = 4429$ s) Only a few small areas are left still showing the second layer. (**h**, $t = 5723$ s) Another cycle begins with the nucleation of the fourth layer. The field of view is 6 μm in all images. The *dark spot in the lower part of the images* is a defect in the micro channel plate of the LEEM. The gray scale of all images has been adjusted for optimum contrast. Reprinted with permission from [35]. Copyright 2011 American Chemical Society

in Fig. 5.1(a). The straight thick and curved thin lines are the result of wrinkles in the graphene [36, 37] and steps in the underlying Ir{111} surface, respectively. The islands grow over the steps, but they do not cross the much higher wrinkles. As the islands grow after approximately 400 s of 6P deposition, a second, darker contrast becomes visible in the center of the islands. After 1514 s the first layer closes completely (Fig. 5.1(b)) and shortly after that at a deposition time of 1698 s also the second darker contrast closes and covers the whole surface (Fig. 5.1(c)). Next, the formation of bright islands is observed (Fig. 5.1(d)). These islands coalesce and form a uniform contrast over the entire surface (Fig. 5.1(e)). This cycle repeats with the formation of another set of bright islands (Fig. 5.1(f)) that coalesce, later yielding a uniform contrast (Fig. 5.1(g)). Figure 5.1(h) shows the start of the next cycle.

Figure 5.2 displays the times when a uniform contrast has been observed by LEEM. Ignoring the first data point—which corresponds to the closing of the initial layer—we can extract a growth rate of 2.7 ML/h from the remaining points. The LbL growth was therefore followed for four complete monolayers. The term

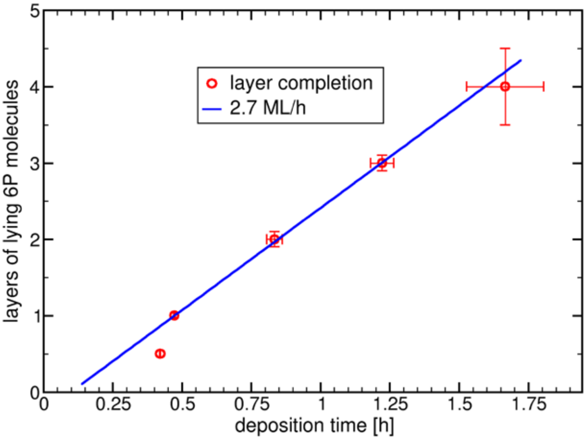

Fig. 5.2 6P layer completion times. The data points indicate times when a uniform contrast has been observed in the LEEM. All but the first data point are found on a straight line corresponding to a growth rate of 2.7 ML/h. Adapted with permission from [35]. Copyright 2011 American Chemical Society

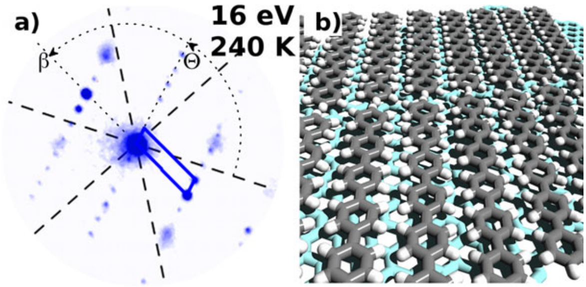

Fig. 5.3 (**a**) μLEED pattern obtained at 240 K and with a start voltage of 16 eV. The size of the unit cell is: $a = 28.1$ Å and $b = 6.0$ Å, with $\beta = 79°$ and $\Theta = 79°$. (*Thick dashed lines* indicate the [1000] graphene direction.) (**b**) Proposed structure of the initial layer. (Planar molecules are used for clarity.) Adapted with permission from [35]. Copyright 2011 American Chemical Society

monolayer is used here for a closed molecular layer with the final complete layer structure.

Structure of the First Monolayer

Next, we discuss the structural evolution of the first 6P monolayer on graphene and the related consequences for the mesoscopic behavior of the islands. The LEED pattern obtained from the initial islands (see Fig. 5.1(a)) is presented in Fig. 5.3(a). This single domain μLEED pattern has been obtained using an aperture with a projected diameter of 1.4 μm. The indicated unit cell has the following dimensions: $a = 28.1$ Å and $b = 6.0$ Å, with $\beta = 79°$ and $\Theta = 79°$. We assign one flat lying molecule to this unit cell. Consequently, we obtain the structure displayed in Fig. 5.3(b). The matrix notation of this loosely packed open structure is $\begin{bmatrix} 8.7 & 13.0 \\ -1.3 & 1.5 \end{bmatrix}$. It should be pointed out that this initial layer structure is different from the one that has been observed for 6P on highly ordered pyrolytic graphite (HOPG) [38]. On HOPG the 6P molecules are aligned with the $[1\bar{1}00]$ armchair direction of graphite. In the present case the long axis (LA) of the 6P molecules is parallel to the $[01\bar{2}0]$ direction of graphene. The short axis (SA) is 3° off the $[\bar{2}0\bar{1}0]$ direction. This corresponds to a rotation of the 6P film by 11° with respect to the 6P on graphite case. Before we discuss the further growth of the 6P thin films on graphene we discuss this peculiar difference to graphite in a little more detail and the potential consequences for 6P growth on graphene.

Unfortunately, little is known about the growth of 6P on graphene. Recent results obtained for benzene—the sixth fraction of 6P—reveal a net Mullikin charge transfer of 0.03 e from the molecule to the graphene [39]. Furthermore, the binding energy of benzene on graphene is roughly two thirds ($E_b = 0.24$ eV) of the one for graphite ($E_b = 0.35$ eV) [40], resulting in a weaker binding of the molecules to the graphene substrate. To obtain an estimate for the corresponding values of 6P one can simply multiply the binding energies by six and arrive at the right order of magnitude.

Further insight can be gained by performing total energy calculations for the different configurations to obtain the binding energy. For this purpose a single 6P molecule has been placed on a large piece of single layer (3130 carbon atoms) or double layer graphene (6260 carbon atoms). The latter case is used as a simple model for graphite. The molecular modeling software Avogadro [41] together with a variant [42] of the Tripos-5.2 [43, 44] force field has been used. All four configurations of interest have been allowed to relax until the change between two successive steps was less than a fraction of 10^{-8} of the total energy. These energies were subtracted from the sum of the total energies of the molecule and the substrate, and then compared against each other. The comparison of the values shows that the case of $6P_{LA}||(01\bar{2}0)$ is favored by roughly 300 meV on graphene over $6P_{LA}||(1\bar{1}00)$. On graphite the opposite is true and $6P_{LA}||(1\bar{1}00)$ is energetically advantageous by about 100 meV over $6P_{LA}||(01\bar{2}0)$. In fact, precisely this orientation ($6P_{LA}||(1\bar{1}00)$) has been reported by for ultra thin layers of 6P on HOPG [38]. The calculation results for 6P on graphene corroborate the observed $6P_{LA}||(01\bar{2}0)$ orientation observed for the growth on Ir$\{111\}$ supported graphene flakes. However, not only the structure of this first layer is of high interest. Also the particular way the islands form and move on the graphene surface requires some attention.

Figure 5.4 shows three consecutive images of 6P islands on graphene during the formation of the initial layer (see Fig. 5.1(a)). Figure 5.4(a) shows the initial situation. An island has nucleated next to a wrinkle (in the upper right corner) and grown to a size of roughly 50000 nm^2. It has an aspect ratio (AR) of 1:1.9. One second later the same island (Fig. 5.4(b)) has elongated (AR 1:3) and grown in size (projected area: 55000 nm^2). The island is about to detach from the wrinkle that helped nucleating the island. One second later the center of mass of the island has moved 280 nm to a new position away from the wrinkle (Fig. 5.4(c)). During this time the island continued to grow (projected area: 61000 nm^2) and obtained a more rounded shape again (AR: 1:2.3).

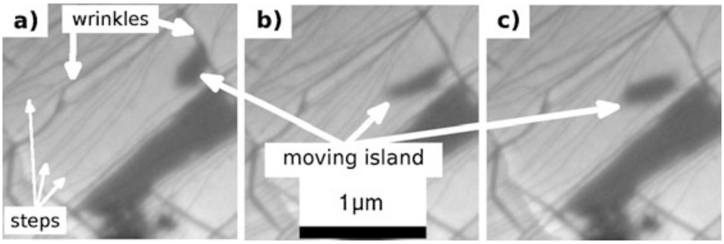

Fig. 5.4 Sequence of three LEEM images recorded at an interval of one second, showing the mobility of the 6P islands (*dark patches*) on graphene. A few wrinkles in the graphene and steps in the underlying Ir{111} surface are marked. The marked island once it reaches a critical size starts to move further away from the wrinkle. The entire sequence covers two seconds. Reprinted from [45], with permission

Careful analysis of many islands showed that the 6P islands nucleate next to wrinkles or at wrinkle crossings. The islands do not nucleate on top of the wrinkles. It has been shown in the past that highly curved areas of graphene—like the wrinkles—are unfavorable for the deposition of organic molecules [46]. However, the 6P islands do nucleate in close vicinity of the wrinkles. This behavior will be discussed next.

The wrinkles are a result of the different thermal expansion coefficients of graphene and iridium [36]. When the sample is cooled down from the graphene forming temperature, the thermal stress is released by the formation of wrinkles in the graphene. This relief is most effective in areas close to the formed wrinkles. In areas further away from the wrinkle the graphene is still bonded in its original way to the iridium and compressive strain will remain. It is well known that for metallic systems diffusion is easier on compressively strained areas [47–49]. Assuming a similar behavior for the current system leads to a higher diffusion rate further away from the wrinkles. As a consequence, the nucleation rate further away from the wrinkles will be lower compared to areas close to the wrinkles, where the rate of diffusion is smaller. The observed island mobility and the fact that we can obtain single domain LEED patterns over areas of at least 1.4 μm (the size of the field limiting aperture) requires a high edge diffusion mobility of 6P on graphene—even at low temperatures. Therefore, even though the islands nucleate next to the wrinkles they are not bound to stay there as they grow in size. Additionally, the 6P edge diffusion mobility enables them to freely change their shape. At least two possible mechanisms can be put forward to explain this behavior.

First, an argument based on strain that builds up in the island during growth will be used to explain the island movement. The balance between the size and shape of a 6P island and the total strain energy it holds is one of the possible driving forces [50, 51]. As the island grows, tensile strain in the island will increase. This stress results partially from the peculiar structure of the initial islands. The exclusive face-on arrangement of the molecules in the initial low density phase is different from the favorable bulk arrangement of alternating face-on/edge-on molecules (the herringbone motif). The second contribution arises from the mismatch between the phenyl ring spacing in the molecule and the graphene ring spacing. Depending on the balance between the step free energy and the stress, this can result in a shape transition of the island [52]. However, in the present case of 6P on graphene a second pathway of releasing the strain exists. As discussed above, the graphene flakes are subject to a strain gradient. Depending on the local environment, larger islands can therefore become more stable further away from the wrinkle—a more compressively strained area. On compressively strained graphene the molecules as well as the phenyl rings can relax into a closer packing, thereby reducing the tensile strain in the island.

The second argument is based on changes in the electronic structure. The electronic structure of graphene changes under the influence of the underlying Ir$\{111\}$ surface and the strain field created by the epitaxial mismatch between the two [26]. Therefore, different electronic properties are to be found in areas adjacent to the wrinkles and further away in areas with higher compressive strain. Unfortunately little is known about the precise electronic structure of graphene on Ir$\{111\}$. However, based on theoretical studies of benzene on graphene [39] a slight charge transfer is to be expected from the molecule to the graphene. Most likely both mechanisms are active simultaneously, but based on the currently available data we have no means of distinguishing between the two.

Next we would like to take a look at the proposed diffusion process in a more quantitative way. When the island shown in Fig. 5.4 has moved, an area of 55000 $\mu\mathrm{m}^2$ has been cleared from 6P molecules. The unit cell has a size of 1.56 nm^2 and contains one molecule [35]. Assuming that the observed changes are achieved by edge diffusion, we can estimate that roughly 35000 6P molecules have to move from the back to the front of the island. The distance they have to cover is 400 nm. Taking the graphene lattice constant (2.46 Å) as an estimate for the smallest possible step the molecules can do, a total of $\nu = 2.9 \times 10^7$ hops are necessary. This is an upper limit of hops for a directed sequential movement of the molecules along the rim of the island. The activation barrier E_A can then be calculated from

$$\nu = \nu_0 \mathrm{e}^{\frac{-E_A}{kT}} \tag{5.1}$$

where ν_0 is the attempt frequency, k the Boltzmann constant and $T = 240$ K for the described situation. Using the standard value of $\nu_0 = 1 \times 10^{13}\ \mathrm{s}^{-1}$, an activation barrier of $E_A = 0.26$ eV is obtained [45]. In the past higher attempt frequencies around $1 \times 10^{19}\ \mathrm{s}^{-1}$ for desorption have been reported experimentally [53–56] and theoretically [57–59] for many organic molecules including 6P. For 6P in particular, values as high as $\nu_0 = 5.6 \times 10^{25}\ \mathrm{s}^{-1}$ have been reported. Furthermore, a recent study of 6P on modified mica shows that the pre-exponential factor for surface diffusion is also increased by four orders of magnitude to $2 \times 10^{17}\ \mathrm{s}^{-1}$ [60]. Using above value of $\nu_0 = 5.6 \times 10^{25}\ \mathrm{s}^{-1}$ we calculate the upper bound for the activation barrier to be of the order of 0.87 eV. However, using the more realistic value of $\nu_0 = 2 \times 10^{17}\ \mathrm{s}^{-1}$—obtained explicitly for surface diffusion—we arrive at a value $E_A = 0.47$ eV for the activation barrier. For completeness we want

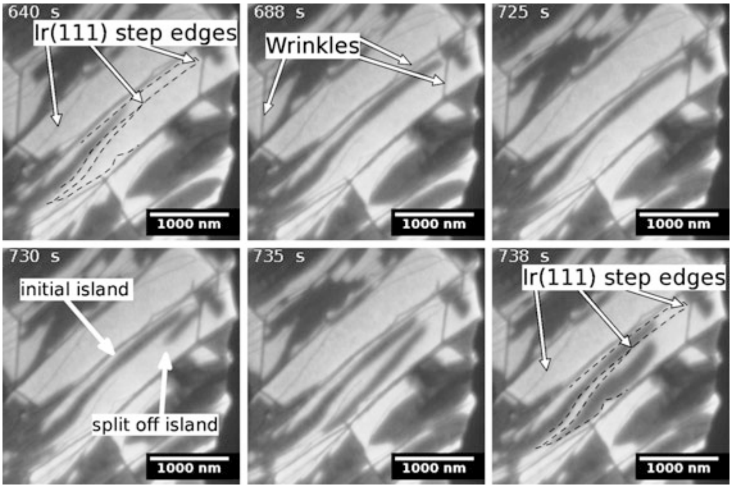

Fig. 5.5 Sequence of LEEM images recorded during the deposition of 6P on graphene at 240 K. A narrow island (*dark patches*) which is confined between two steps caused by the underlying Ir slowly grows and finally fills the area enclosed by the steps (deposition time from 640 s to 688 s). 32 s later the island overcomes the step and spills out onto the adjacent graphene covered Ir{111} terrace (725 s of deposition). As the island on the new terrace grows in size (730 s of deposition) it moves away from the low strain area next to wrinkle (735 s of 6P deposition). After reaching an area where the strain mismatch between the big 6P island and graphene is reduced it starts to fill the entire area by reducing its aspect ratio (738 s of deposition). Please be aware of the non-uniform time step between the images. Some wrinkles and Ir{111} step edges are marked by *arrows* and *dashed lines* to guide the eye. Reprinted from [45], with permission

to point out that an alternative explanation for the observed high mobility exists. Schunack et al. reported an anomalous amount of long jumps in the surface diffusion of large organic molecules [61]. Both effects—changes in the apparent attempt frequency and heaped occurrence of long jumps—can explain the observed high mobility.

Processes as illustrated in Fig. 5.4 are always observed to be confined to an area enclosed by wrinkles. Often, the path of the islands is also confined by steps in the underlying Ir. The increased curvature of the graphene sheet at the position of the Ir{111} step poses a small but noticeable obstacle to the growth of the 6P islands. However, the effect is smaller than that due to the wrinkles. Figure 5.5 depicts an island that is first overcoming a step edge, then splits in two and finally moves across the graphene flake. Initially the island grows in size without crossing the surrounding steps until 720 s of 6P deposition. It then suddenly crosses the small end of the step enclosed area and spills out on the next graphene covered terrace. There, it quickly grows in size covering the area next to the wrinkle. As in the above situation, when a certain size is reached, it detaches from the wrinkle (island size: 117400 nm^2; AR: 1:10) and for this case also separates from the initial island. It continues to grow (final island size: 300000 nm^2; maximum AR: 1:13), while the center of mass moves 810 nm across the surface. After reaching an area where the

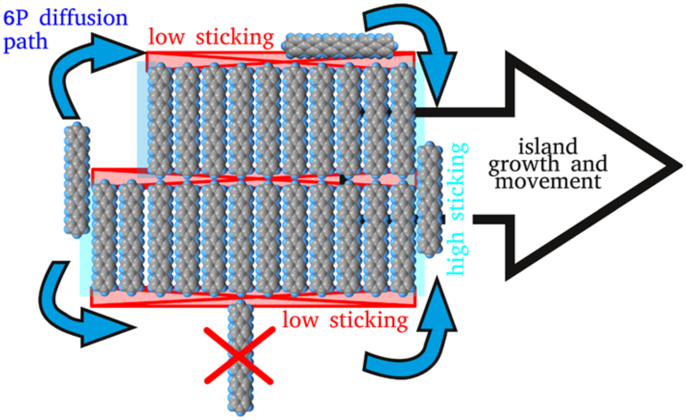

Fig. 5.6 Sketch of a 6P island and the possible diffusion path's and preferred sites of attachment. Para-Sexiphenyl molecules are detaching from the left side of the island and move towards the right side. This results in an overall movement of the island to the right side. Top and bottom facets are exclusively terminated by hydrogen atoms and represent low sticking facets. The left and right edge of the island have a large sticking probability due to the large π–π overlap of the electronic system which is possible there. Reprinted from [45], with permission

mismatch between the 6P island and the strained graphene becomes small enough, the shape transition is also reversed leading to a lower AR of 1:6.

For the second part of the island movement we estimate a total number of 137700 6P molecules to move over a five second period. The distance and therefore the number of required hops is higher (8130 hops) and we estimated the jump frequency to be $\nu = 22.3 \times 10^7\ \mathrm{s}^{-1}$. Using the most realistic value of $\nu_0 = 2 \times 10^{17}\ \mathrm{s}^{-1}$ we obtain $E_A = 0.43$ eV. This result is in good agreement with the above mentioned value.

An advantage of the in-situ real time observation of growth processes using LEEM is that we can directly deduce the real space orientation of the molecules. This can be achieved by monitoring the shape evolution and movements of the 6P islands. This information is complementary to the exact molecular structure obtained by LEED. A sketch of a 6P island is shown in Fig. 5.6. Molecules detaching from the left side of the island diffuse along the rim of the island towards the right side. This process could be triggered by a strain field—like in the present case. As the molecules move along the top or bottom edge of the sketched island they experience a low sticking probability. The purely hydrogen terminated edge is not favorable for incorporating molecules in the proper crystallographic orientation determined by the remainder of the island. The situation is different for the right (and left) facet of the island. Here, the π-systems of the newly arriving molecules and the ones forming the edge can interact over the full length of the molecule. This results in a high sticking probability. A consequence of this behavior are the well known 3D fibers that are frequently observed for the growth of rod like molecules and in particular for 6P [32, 33]. For the initial 6P islands on graphene this leads to an anisotropic growth and movement of the whole island. In turn, we can deduce

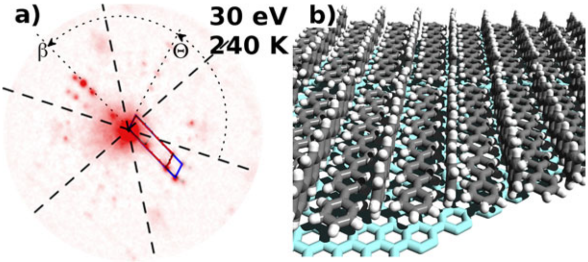

Fig. 5.7 (**a**) μLEED pattern obtained from the first full monolayer at 240 K and with a start voltage of 30 eV. *Dashed lines* indicate the [1000] direction of graphene. (Unit cell are given in the text.) (**b**) Proposed molecular structure of the first full monolayer. Adapted with permission from [35]. Copyright 2011 American Chemical Society

the molecular orientation with respect to the real space shape and orientation of the island directly from our real time observations.

The speed at which the islands change their shape and move over the graphene substrate is related to the low density structure of 6P in these islands. Once the film gets thicker, a second darker contrast starts to appear in the center of the islands (see Fig. 5.1 and Sect. 5.3.1). At the same time islands exhibiting this darker contrast stop moving across the surface. We will discuss the structural changes during further thin film growth in the following paragraphs.

A LEED pattern obtained from the full first monolayer (Fig. 5.1(c)) is presented in Fig. 5.7(a). Two unit cells can be identified in the pattern. The blue unit cell is identical to the one discussed above and originates from parts of the surface still covered only by the initial layer. However, a second (red) slightly bigger unit cell can be identified. The size of this cell is $a = 28.1$ Å, and $b = 7.5$ Å with $\beta = 69°$, and $\Theta = 79°$. The matrix notation is $\left[\begin{smallmatrix} 8.7 & 13.0 \\ -1.7 & 1.9 \end{smallmatrix}\right]$. As more material is deposited, this unit cell has to accommodate the additional molecules. The only way to do this in an energetically favorable way is through an alternating face-on/edge-on configuration, as shown in Fig. 5.7(b). To achieve this (i) additional molecules will squeeze in between the face-on molecules already there from the initial layer and (ii) some of the face-on molecules will have to cant up into the edge-on configuration. Although this requires a massive rearrangement of molecules the positive effect on the energy balance is high as this film obtains a structure that is very similar to the bulk structure of 6P. The surface unit cell of the similar $(1\overline{1}\overline{1})$ plane in 6P is $a = 26.4$ Å, and $b = 9.8$ Å with $\beta = 82.2°$ [31]. A similar structure and growth mechanism has been found for the growth of 6P on Au{111} [55]. In this detailed LEED and TDS study an initial layer of flat lying molecules has been found. With increasing coverage this structure is transformed into an face-on/edge-on arrangement similar to the one described here.

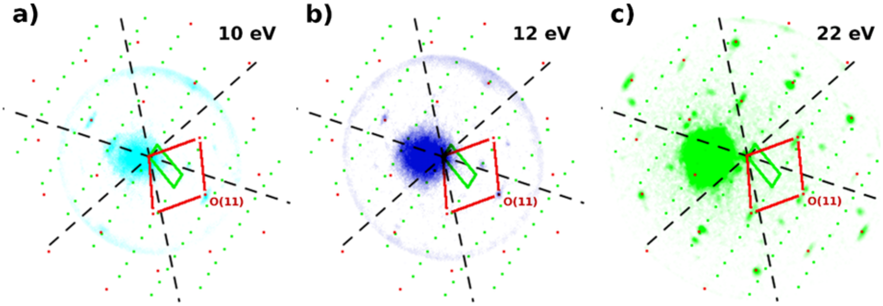

Fig. 5.8 μLEED analysis of four layers of 6P on graphene grown in LbL mode. LEED patterns recorded at (**a**) 10 eV, (**b**) 12 eV, and (**c**) 22 eV are displayed. The unit cell of the layer stack and of the adlayer are indicated by *green* and *red lines* and *dots*, respectively. *Dashed lines* indicate the graphene [1000] zig-zag directions

5.3.2 Structure of the Thicker Layer

As we have seen in Sect. 5.3.1 and Fig. 5.1 the growth continues in a Layer-by-Layer-like fashion. Next, we will discuss the structure and growth mechanism of these additional layers.

Figure 5.8 shows μLEED patterns recorded at various energies. Although the patterns contain at least two different rotational domains, two main features can be easily identified. A weak set of spots visible particularly in Fig. 5.8(a) originate from a unit cell, the size of which is $a = 26.9$ Å, $b = 9.2$ Å, with $\beta = 74°$ and $\Theta = 77°$. The unit cell and its continuation over the whole pattern are indicated by green lines and dots. This unit cell is again in good agreement with the unit cell of the $(1\overline{1}\overline{1})$ plane in 6P which size is $a = 26.4$ Å, and $b = 9.8$ Å with $\beta = 82.2°$ [31]. This weak diffraction pattern comes from the *bulk* of the underlying four layers of 6P. Similar to the first full monolayer, this unit cell with a size of 236.7 Å^2 contains two molecules. However, the LEED pattern is clearly dominated by another, stronger set of diffraction spots, indicated by red lines and dots. The unit cell has a size of $a = 6.8$ Å, $b = 6.4$ Å, with $\beta = 75°$ and $\Theta = 141°$. By comparing Figs. 5.8(a)–(c), one can see that the spots belonging to this part of the diffraction pattern change with varying energy. This is illustrated in Fig. 5.9, where the change in spot profile for the O(11) spot is shown. In Fig. 5.9(a) the profile at 10 eV is shown. The central spot has two pronounced shoulders along the $(1\overline{1})$ direction. Increasing the start voltage to 12 eV and 14 eV these shoulders disappear with the higher electron energy (Fig. 5.9(b) and (c)). A further increase of the electron energy to 22 eV results in a clearly split spot. Only a minute central spot at the O(11) position is left. The distance between the two peaks of the O(11) spot at 22 eV corresponds to 28.7 Å. Such behavior has been explained already 1982 by M. Henzler as the result of a particular form of surface roughness. Figure 5.10 shows three principal combinations of basic defects that will result in some kind of spot splitting. An in depth review of spot profile analysis can also be found in Ref. [63]. Figure 5.10(b) corresponds to the current situation. Depending on energy

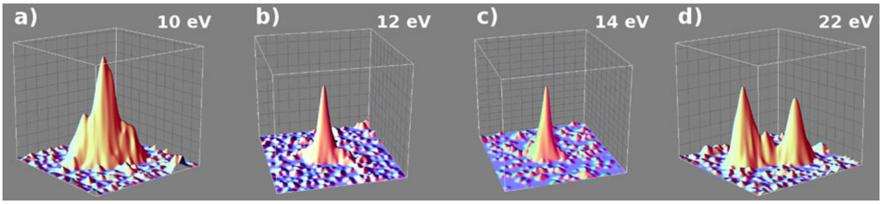

Fig. 5.9 Spot profiles of the O(11) spot (see Fig. 5.8) for different energies. The shape of the spot evolves from a central peak with a broad shoulder to a single peak at O(11) position back to a split spot with two clearly peaks and a minute central peak. The shoulders or satellite peaks appear along the O($1\bar{1}$) direction

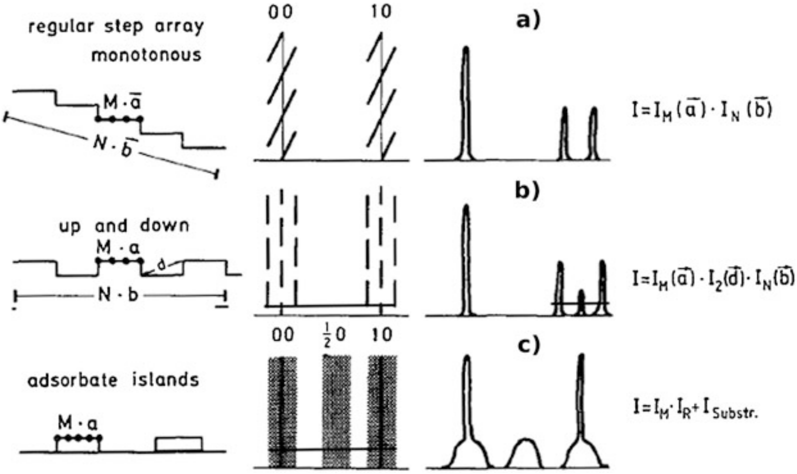

Fig. 5.10 Combination of basic defect structures. (**a**) Monotonous regular step array; (**b**) regular step array in two layers; (**c**) random distribution of identical islands. Reprinted from [62], with permission from Elsevier

the spot profile will either be a single peak or a double peak structure when the diffraction rod splits into a double rod for the out-of-phase condition. The separation of the spots in reciprocal space is related to the lateral size of the islands. For spot splitting due to a regular step train, the odd and even spots should show opposed behavior. Looking at the LEED patterns displayed in Fig. 5.8 we can indeed observe that different spots belonging to the same pattern have a different appearance. In Fig. 5.11 3D representations of the O(01), O(02), O(11), and O(22) spot profiles recorded at 22 eV are displayed. While the odd spots show the typical split spot appearance, the even spots are formed by a single peak only. The necessary array of islands in a two layer system is provided by the 6P molecules that form an adlayer.

The measured diffraction pattern is a result of scattering from the individual phenyl rings that comprise the molecule. The molecule in turn leaves its footprint in the form of spot splitting in the diffraction pattern. The spacing between the two split

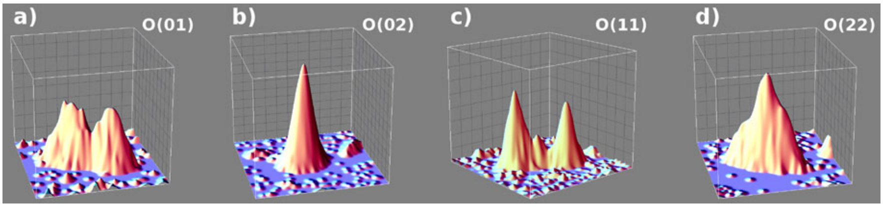

Fig. 5.11 Spot profiles of the O(01), O(02), O(11), and O(22) spots at 22 eV (compare to Fig. 5.8(c)). While even numbered spots show a clear split spot behavior the odd spots are formed by a single peak only

spots corresponds to the length of the molecule. If the position of the phenyl rings is fixed, we can deduce the 6P unit cell for this adlayer to be $a = 29.2$ Å, $b = 6.3$ Å, with $\beta = 75°$ and $\Theta = 0°$. In this case Θ is measured with respect to the long axis of the molecules in the underlying 6P layers. Similar to the initial layer, this unit cell with a size of 162.7 Å^2 contains only a single lying molecule. From the fact that the angle Θ is zero, it is clear that the molecules in this layer are aligned parallel to the molecules in the underlying layers. Although the unit cell is smaller, the density of this layer is reduced compared to the underlying layers because it contains only a single molecule per unit cell. As a result we can estimate that for the nominal coverage of 4.35 ML at which this patterns were recorded, the adlayer covers 50 % of the surface. Although only a limited data set is available, more information can be extracted from the spot profile analysis.

From the energy dependence of the spot splitting we can calculate the adlayer thickness. Using

$$2d = n\lambda \tag{5.2a}$$

$$2d = \left(n + \frac{1}{2}\right)\lambda \tag{5.2b}$$

for the in phase condition (5.2a) and the out-of-phase condition (5.2b) and energies of 14 eV and 22 eV, respectively, for the wavelength λ, we calculate a value of $n = 2$ (1.97) [64]. The distance d between the adlayer and the upper most *bulk* layer is than $d = 3.3$ Å. This value for d is smaller than the bulk distance between two $(1\overline{1}\overline{1})$ layers of 4.6 Å [31]. However, the adlayer contains no edge-on molecules. Assuming that the width of the molecules is 4 Å and the thickness of the backbone is around 1 Å, the molecules can get closer to the underlying layer by about 1.5 Å. This rough estimate is in good agreement with the measured difference of 1.3 Å.

Combining all the information we obtained, we can propose a final model for the 6P thin film growth on metal supported graphene. The model of the final structure is depicted in Fig. 5.12.

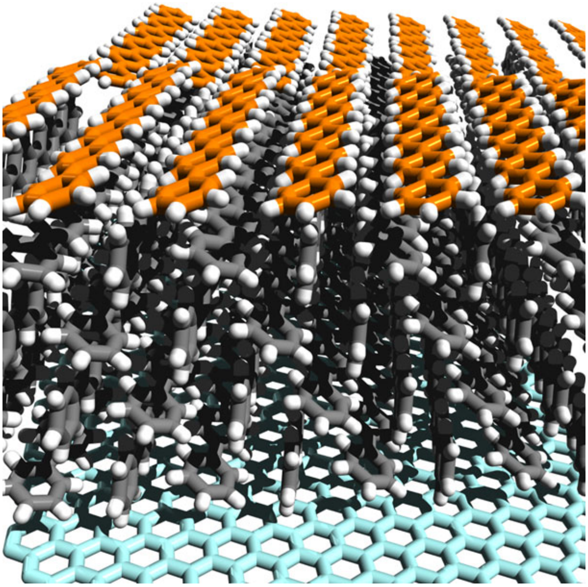

Fig. 5.12 Proposed structure of 6P on metal supported graphene. Four layers of bulk-like 6P with their $(1\bar{1}\bar{1})$ plane parallel to the substrate are shown. The top most layer is formed exclusively from lying molecules. The carbon atoms are color coded for clarity with respect to their affiliation: Graphene: *light blue*, bulk-like 6P: *gray*, and adlayer: *orange*. Reprinted with permission from [35]. Copyright 2011 American Chemical Society

The Layer-by-layer growth of this structure proceeds in the following way [35].

1. The growth of this structure starts with the formation of 6P islands exhibiting an open structure formed by flat lying molecules only. The metastable nature of this structure and the high—edge diffusion—mobility of 6P on graphene (activation barrier $E_A = 0.45$ eV) allow the formation of large single domain islands. The number of defects and the resulting domain size is—in a lower limit—only controlled by the size of the defect free graphene areas.
2. With increasing coverage the adlayer transforms into a more bulk-like configuration. Additional 6P molecules are inserted in an edge-on configuration resulting in a stable configuration for the layer. Island diffusion comes to a halt for this molecular arrangement which is similar to the one observed in the bulk $(1\bar{1}\bar{1})$ plane.
3. Every successive layer starts with the nucleation of small islands formed exclusively by face-on molecules. With increasing coverage this structure is transformed into the final bulk-like structure comprising alternating edge-on and face-on molecules.

The Layer-by-Layer growth mode is ensured by the fact that the next layer can only nucleate once the current layer has obtained a bulk-like structure. It is understandable that molecules arriving on top of the initial islands—which possess the

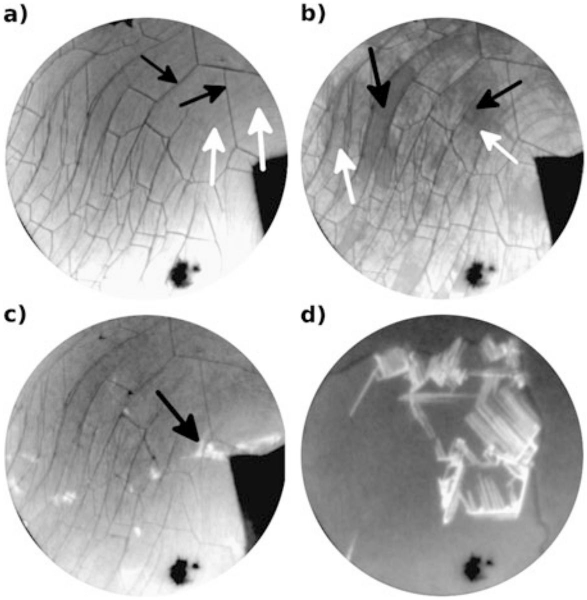

Fig. 5.13 LEEM images of 6P deposition at 320 K. Electron energy: 2.7 eV (**a**)–(**c**), 3.7 eV (**d**). FOV 6 µm (**a**)–(**c**), 4 µm (**d**). (**a**, $t = 0$ s) Single graphene flake prior to 6P deposition. Graphene wrinkles (*black arrow*) and steps in the Ir{111} surface (*white arrow*) are marked. (**b**, $t = 813$ s) A wetting layer has formed on the graphene flake. Both the initial layer (*white arrow*) and the final monolayer (*black arrows*) can be seen. (**c**, $t = 1268$ s) Formation of 3D crystallites. (**d**, $t = 2149$ s) The crystallites continue to grow and form parallel needles. All times are with respect to the begin of the 6P deposition. Reprinted from [65], with permission from Elsevier

open structure formed by face-on molecules only—will either be incorporated as an edge-on molecule or diffuse off the island, but do not nucleate a new layer on top of the metastable structure beneath.

5.3.3 Stranski–Krastanov Growth

In this section we will review the consequences of raising the deposition temperature. We will discuss the change from Layer-by-Layer growth to the Stranski–Krastanov (SK) growth mode in the temperature range from 320 K to 352 K. At higher temperatures the increased mobility prevents the growth of 6P structures on graphene supported flakes completely.

In Fig. 5.13 a sequence of LEEM images illustrates the growth behavior of 6P on metal supported graphene flakes at 320 K. A single graphene flake is shown prior to deposition in Fig. 5.13(a). Formation of 6P structures starts with the growth of a wetting layer. Similar to the observations at lower temperatures, first a medium gray layer starts to grow. Shortly after that the growth of a second darker contrast starts

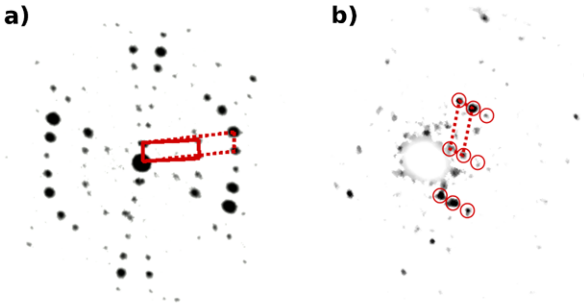

Fig. 5.14 (**a**) µLEED pattern obtained from the wetting layer. Unit cells of the initial (*dashed line*) and final (*solid line*) layer are indicated. (**b**) µLEED pattern obtained from an area on the graphene flake covered by 6P needles. The unit cell is marked by *red circles* and *dashed lines*. Adapted from [65], with permission from Elsevier

within the medium gray areas. After 813 s of deposition (see Fig. 5.13) the flake is partly covered by the initial layer (medium gray, white arrows) and the darker final monolayer (black arrows). µLEED has been used to resolve the structure of this layer. Two unit cells are found. The bigger one (indicated by a solid red line in Fig. 5.14(a)) has a size of $a = 8.3$ Å, $b = 27.8$ Å and $\beta = 70°$, while the smaller one has the following dimensions: $a = 5.2$ Å, $b = 27.8$ Å with $\beta = 72°$.

This growth behavior and the size of the unit cells is comparable to what has been described for the begin of the low temperature (LT) growth in Sects. 5.3.1 and 5.3.2. Although the exact size of the unit cell is slightly different from what has been found at LT, the structural models from the above sections are still valid. It is important to remember that this is a commensurate organic layer. The unit cell is practically unchanged over a range of at least 80 K. However, the smallest derived matrix notations ($\begin{bmatrix} 8.6 & 12.8 \\ -1.3 & 1.2 \end{bmatrix}$… initial layer, $\begin{bmatrix} 8.6 & 12.8 \\ -1.9 & 2.0 \end{bmatrix}$… final layer) do not necessarily describe the structure accurately. Keeping in mind the accuracy of the initial measurements of 5 % a detailed analysis allows to identify this as a coincidence type II quasiepitaxial relationship [66]. In fact a 5×10 superstructure allows the molecules to relax slightly into preferred adsorption sites without deviating substantially from the crystal structure [65]. Like in the LT experiments, no other morphological features appear before the first wetting layer is completed.

However, different from what we have seen for the growth of 6P at LT, dramatic changes in the growth processes are observed once the wetting layer is completed. Instead of the formation of small islands all over the surface of the wetting layer, we observed the formation of very bright structures near the wrinkles (Fig. 5.13(c)). With ongoing deposition these small crystallites grow in one dimension and form comb-like structures of 6P fibers. This is a well known growth phenomenon often observed for 6P [34, 67–69]. The needles nucleate either on defects (cracks in the wetting layer along the wrinkles) or at other needles. Again µLEED is used to resolve the structure of the needles. The unit cell with a size $a = 9.5$ Å, $b = 26.9$ Å and $\beta = 69°$ is marked with a dashed line in Fig. 5.14(b). Red circles are used to mark some of the other spots belonging to the pattern. This unit cell is similar to what is found for the wetting layer and very close to the unit cell of the $(1\bar{1}\bar{1})$ plane of bulk 6P [31]. Similar to the structural model depicted in Fig. 5.12, molecules in the needles have a herringbone arrangement.

Further increasing the deposition temperature to 350 K results in no substantial changes in the growth behavior. The size of the unit cells (initial layer and wetting layer) obtained by µLEED are identical to the ones observed at 320 K. After the initial two step formation of the wetting layer, needles nucleate next to the wrinkles. Needles formed at higher temperature are fewer in number but longer [68]. These needles represent the most common form of 6P growth structure. They have been observed on a variety of substrates including but not limited to gold [70], muscovite [71], TiO_2 [69], para-Sexiphenyl [3], and KCl [72]. A limited number of contact planes is found including the $(1\bar{1}\bar{1})$, $(20\bar{3})$, and $(21\bar{3})$. The common property of all these needles is that the molecules are always oriented roughly perpendicular to the long needle axis (see also Fig. 5.6 and the corresponding discussion). The unit cell measured for the needles is closer to the 6P surface unit cell than the one measured in the thick layer at LT. The enhanced mobility of the molecules at elevated temperatures enables the SK growth mode. Compared to the LbL growth mode—where the interaction with the substrate plays an important role—stress relaxation is more efficient in SK mode. Hence, we observe the switch to the SK mode as soon as the mobility of the molecules is sufficient for uphill diffusion and consequently the formation of 3D structures.

The growth of 6P on metal supported graphene flakes at moderate temperatures between 320 K and 352 K can be summarized by the following four steps [65].

1. An initial layer of only flat lying molecules is formed on the graphene surface. This layer nucleates next to the wrinkles.
2. When a critical coverage is reached, the initial layer transforms into a bulk-like layer (Fig. 5.13(b)). The molecules obtain an alternating face-on/edge-on configuration similar to the $6P(1\bar{1}\bar{1})$ plane.
3. 6P fibers nucleate on top of the wetting layer (Fig. 5.13(c)). This nucleation occurs at the edge of the wetting layer next to the wrinkles.
4. Parallel bundles of needles grow away from the wrinkles (Fig. 5.13(d)). The needles have the same $(1\bar{1}\bar{1})$ orientation as the underlying wetting layer. Their azimuthal orientation reflects the azimuthal orientation of the molecules in the wetting layer.

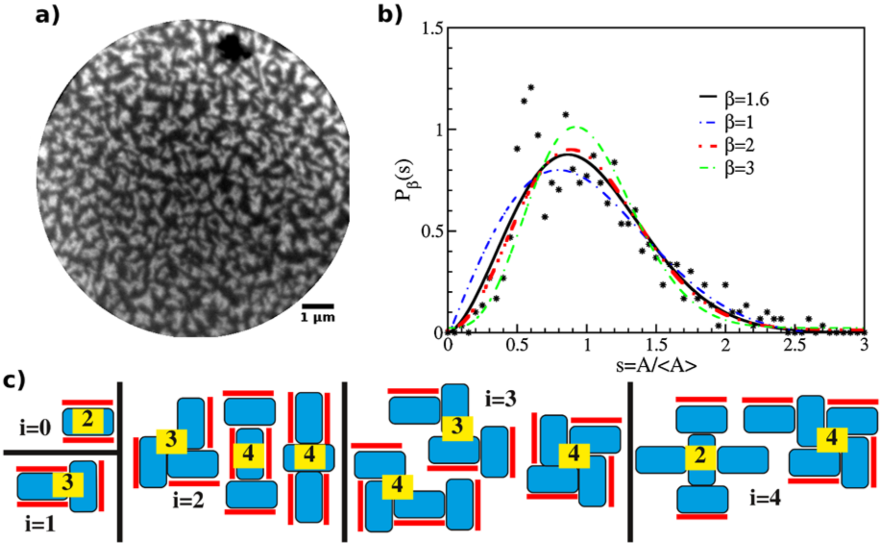

Fig. 5.15 (**a**) LEEM image (FOV: 10 µm) of an area far away from graphene flakes. After 6P deposition the area is covered by small 6P islands. (**b**) Capture zone distribution for 6P grown on Ir{111} for a growth temperature of 240 K. The best fit (*solid line*) to the data (*stars*) and three functions for the GWS are displayed. (**c**) Proposed configurations of the critical 6P nucleus. Molecular arrangements for $i^* = 0$ to $i^* = 4$ are sketched. Upright standing 6P molecules are depicted as rectangles with an aspect ratio based on the Van der Waals dimensions of 6P. Fully exposed π-systems are indicated by a *red line*. Partially covered π-systems are not considered. The number of exposed π-systems is given in the center of the arrangement. Configurations with i^* equals 0 and 4 show the smallest number of exposed π-systems. Reprinted from [45], with permission

5.4 Iridium{111}

As before, this section of 6P growth on the bare Ir{111} surface, is divided into two subsections in which we will explore the different growth modes.

5.4.1 Island Growth

Deposition at Low Temperatures

Para-Sexiphenyl has been deposited at 240 K onto the bare iridium surface between the graphene flakes. As soon as deposition starts the Ir{111} surface gets covered by a structureless 6P layer, resulting in a darkening of the Ir{111} surface in LEEM. Such an area—free of graphene flakes—is covered by small 6P islands after deposition (Fig. 5.15(a)). From µLEED measurements we obtain a typical intermolecular distance of 4.4 Å. This distance corresponds to the distance between the center molecule and the corner of the 6P(100) plane in bulk 6P. The total amount of deposited 6P is 4.35 ML of flat lying molecules. Due to the higher areal density of the (100) plane this corresponds to 0.8 ML of upright standing molecules. However, the coverage that is obtained from the LEEM analysis is only 0.5 ML. This discrepancy is rooted in the Ehrlich–Schwoebel barrier that is active in the growth of films formed by upright standing molecules [3]. For a high barrier—as has been observed for the growth of 6P—*Poisson shaped* mounds, i.e. the visible layer fractions are Poisson distributed, are the result. Although we do not know the precise barrier for the 6P on Ir{111} system, we will assume *Poisson shaped* mounds for the moment. As a result part of the molecules will form small second layer islands on top of the first layer. The expected coverage for the first layer is then 55 % for a nominal film thickness of 0.8 ML. This corresponds to 0.44 ML, which is slightly smaller than the measured coverage. However, 0.44 ML is only correct for an indefinitely high barrier. A finite but still high barrier as is observed for the growth of upright standing 6P thin films will result in deviation towards higher first layer coverages [3, 4]. In addition, it has been observed that the step edge barrier in organic thin films increases with film thickness. The first layers often have a substantially lower step edge barrier [3, 5].

Several interesting quantities can be extracted from LEEM images like the one above. To ensure a good statistical representation of the surface all values are averaged over at least 3–5 different images recorded in separate areas of the sample. The nucleation density N_s for 6P on Ir{111} at 240 K is 7.2 μm^2. Information on the critical nucleus can be obtained by using the capture zone distribution. Voronoi tessellation of the images allows to obtain the size A of the capture zone around each island [73, 74]. The obtained values of A can be used in the distribution function of the general Wigner Seitz surmise (GWS) as proposed by Pimpinelli and Einstein in Ref. [75]:

$$P_\beta(s) = a_\beta s^\beta e^{-b_\beta s^2}, \tag{5.3}$$

with

$$a_\beta = \frac{2\Gamma\left(\frac{\beta+2}{2}\right)^{\beta+1}}{\Gamma\left(\frac{\beta+1}{2}\right)^{\beta+2}} \quad \text{and} \quad b_\beta = \left[\frac{\Gamma\left(\frac{\beta+2}{2}\right)}{\Gamma\left(\frac{\beta+1}{2}\right)}\right]^2 \tag{5.4}$$

being constant given by the normalization and unit-mean conditions, respectively.[1] The fluctuating variable is given by $s = A/\langle A\rangle$. The only fit parameter in (5.3) $\beta = i^* + 2$ [76] allows us to extract the size of the critical nucleus i^*.

The capture zone distribution for 6P islands on Ir{111} grown at 240 K is shown in Fig. 5.15(b). The best fit of the GWS distribution to the data is obtained for $\beta = 1.6$ and GWS distributions for $\beta = 1$, 2, and 3 are added to the graph. The so obtained i^* value of 0 requires further discussion. A critical nucleus size of zero means that a single molecule on the surface would be immobile and spontaneous

---

[1] The Γ-function is an extension of the factorial function to real and complex numbers. However, the argument is shifted down by 1. For positive integer values of n: $\Gamma(n) = (n-1)!$.

nucleation proportional to the ad-molecule density should be observed. Care has to be taken in interpreting this result, since the above calculation is strictly speaking only valid for homogeneous nucleation. However, a critical nucleus size of zero can be explained in terms of heterogeneous or defect nucleation [77, 78]. An abrupt transition from $i^* = 0$ to $i^* = 3$ is observed for the Pd/MgO system. G. Haas et al. explain this transition by the presence of defects which act as traps. This and additional geometric effects will stabilize $i^* = 3$ [79]. The situation here is similar, as both effects play a role for the growth of 6P on Ir$\{111\}$.

It is important to keep in mind that in our particular case the Ir$\{111\}$ surface is not clean or defect free. The above experiment was not performed on a properly prepared Ir$\{111\}$ surface in the spirit of a surface science experiment. Prior to 6P deposition, graphene flakes were grown and carbon residues, maybe in the form of small graphene flakes that are not visible at the selected magnifications, will cover the surface between the big flakes. This is corroborated by the fact that we observe upright standing molecules on a metal surface. It has been shown in the past that on a clean metal surface 6P adopts a flat lying configuration [80, 81]. Furthermore, on a contaminated—in particular carbon contaminated—metal surface the molecules will reorient themselves and adopt an upright standing configuration [82, 83]. The sensitivity of rod-like molecules to defects is very high. For pentacene, calculations predict that a single dangling bond can force the molecules into an upright orientation on a surface where they would obtain a flat lying configuration otherwise [84].

As we have stated above, geometrical effects also play an important role in stabilizing the critical nucleus. In addition to the parameters that will define the size of the critical nucleus in terms of thermodynamic and kinetic driving forces, two other contributions are of special interest here:

1. Getting the molecules in the nucleus as close as possible to the bulk herringbone arrangement.
2. Minimization of the number of complete π-systems exposed to the outside.

Possible configurations of nuclei with $i^* = 0$ to $i^* = 4$ are sketched in Fig. 5.15(c). Configurations with a critical nucleus size of zero and four have a minimum number of only two fully exposed π-systems. These results are also in good agreement with recent DFT calculations that among other things predict a smallest stable nucleus size of 4 ($i^* = 3$) for a defect free substrate [60]. On a more realistic surface with many defects and sites that allow for heteronucleation—like in the present case—the defect binding energy can be sufficiently high to suppress the homogeneous nuclei with $i^* = 1$ to 3. Only at much higher temperatures small clusters trapped at defects will break up and homogeneous nucleation with $i^* = 4$ should become effective. The changes in film morphology after increasing the deposition temperature will be discussed next.

6P Deposition at Moderate Temperatures

Para-Sexiphenyl deposition at 320 K onto the Ir$\{111\}$ surface leads to large ramified islands. Two such irregularly shaped islands are visible in the LEEM image shown

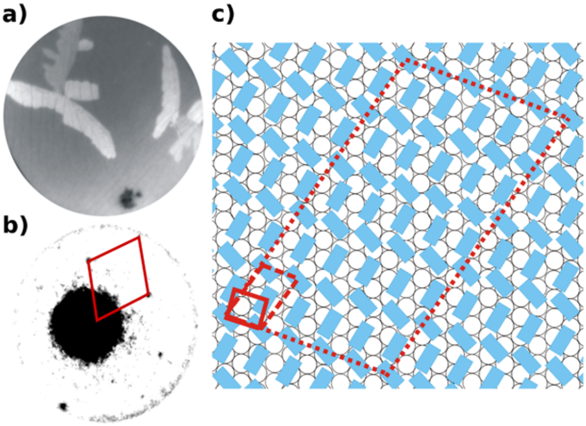

Fig. 5.16 (**a**) Ramified 6P islands on Ir{111}. Different crystallographic orientations lead to different gray levels in the individual branches. (FOV: 15 μm; 320 K) (**b**) μLEED pattern (19.4 eV) obtained from one of the arms, revealing a single domain LEED pattern. The NN cell is marked by a *red line*. (**c**) Proposed 6P structure; NN cell, unit cell, and super structure (*solid*, *dashed*, and *dotted*) are indicated. Adapted from [65], with permission from Elsevier

in Fig. 5.16(a). The nucleation density has become so small that a statistically sound evaluation of the critical nucleus size is impossible. However, the small number and large size of the quiet irregularly shaped islands clearly indicates a dramatic change in the growth process. We possibly witness the expected transition from defect triggered nucleation at low temperatures to homogeneous nucleation with $i^* = 4$ or higher at elevated temperatures. However, no definite nucleus size can be provided at this point. It has been shown theoretically that for homogeneous nucleation of 6P on 6P, although upright standing nuclei with $i^* = 3$ are stable, flat lying nuclei are energetically preferred. Only for nuclei larger than 14 molecules is an upright standing configuration energetically preferred [60].

Figure 5.16(b) shows a μLEED pattern obtained from a single arm of such a ramified island. The angle between the vectors is $\beta = 108°$. The size of the indicated cell is 5.0 Å by 5.0 Å. This corresponds to the nearest neighbor (NN) distance between upright standing molecules (solid line in Fig. 5.16(c)). The molecular form factors of the two differently rotated molecules within the 6P(100) plane cannot be distinguished because they are similar. The actual unit cell vectors for 6P on Ir{111} grown at 320 K are 5.0 Å by 9.1 Å at an angle $\beta = 105°$ with $\Theta = 25°$ (dashed line in Fig. 5.16(c)). Following the arguments in Sect. 5.3.3 the structure is described best by a coincidence type II quasiepitaxial relationship [66] and a 5×5 superstructure with a matrix notation of $\left[\begin{smallmatrix} 19 & 8 \\ -2 & 8 \end{smallmatrix}\right]$.

It is remarkable that the LEED patterns obtained from individual branches are all single domain. However, these patterns are rotated with respect to each other. A closer inspection of the irregularly shaped islands reveals that indeed the individual arms show a uniform contrast while there are slight differences between the arms of a single island. For the picture presented in Fig. 5.16(a) this has been made visible

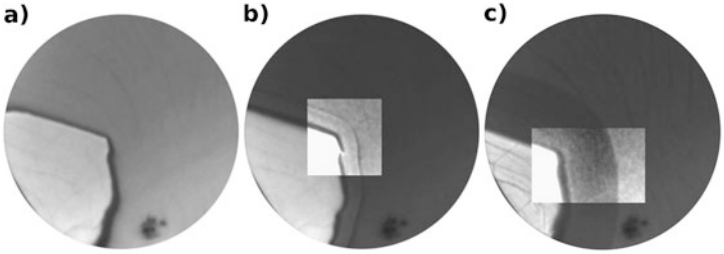

Fig. 5.17 Sequence of 6 µ FOV LEEM images (electron energy 2.7 eV) recorded during the deposition of 6P at 405 K. (**a**, $t = 0$ s) A part of a single graphene flake on Ir{111} prior to deposition of 6P. (**b**, $t = 831$ s) A 6P layer is nucleated by the graphene flake and starts to grow. The contrast enhanced center of the image clearly shows the boarder between the 6P layer and the 2D gas phase on Ir{111}. (**c**, $t = 1391$ s) The 6P layer has extended further away from the flake. The *center of the image* has been contrast enhanced to increase legibility. Graphene: *bright*; 6P layer: *black*; 6P 2D gas phase: *dark gray*. Adapted from [65], with permission from Elsevier

by using a slight off normal incidence of the electron beam. As a result, the different azimuthal crystal orientations of the arms will yield different intensities—similar to a dark field image.

A further increase of the growth temperature to 352 K changes the nucleation behavior of the 6P islands on Ir{111} once again. Para-Sexiphenyl islands on Ir{111} are now nucleated exclusively at the rim of the graphene flakes [65].

5.4.2 Step Flow Growth

A further increase of the deposition temperature to 405 K activates an entirely new growth mode. A step-flow-like growth of 6P on Ir{111} is observed at these high temperatures. Figure 5.17 shows a sequence of LEEM images (electron energy 2.7 eV) recorded during the deposition of 6P at 405 K. Figure 5.17(a) shows a part of a graphene flake prior to 6P deposition. Steps and wrinkles are visible on the flake as dark lines. The dark contrast around the flake is an artifact. It results from the work function difference between graphene and the Ir{111} surface [85]. Figure 5.17(b) shows the same sample area after 813 s of 6P deposition. As 6P deposition begins the Ir{111} surface becomes dark due to the 2D gas phase of 6P molecules on the surface. However, the brightness of the graphene flake remains unchanged during 6P deposition, indicating an extremely low ad-molecule density. A third, slightly darker contrast appeared next to the graphene flake and is slowly extending outward further away from the flake. With increasing coverage this layer continues to grow (Fig. 5.17(c)). Please note that the contrast on the graphene flake has not changed and that wrinkles in the graphene and steps in the underlying Ir{111} are still clearly visible.

µLEED measurements on graphene and far away from the flakes show clean graphene and a large diffuse secondary electron contribution, respectively. This confirms the above observation that no significant structures grow on the graphene flake

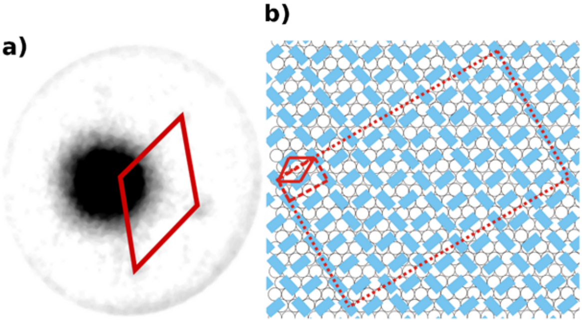

Fig. 5.18 Structural analysis of the 6P layer on Ir{111} formed at 405 K. (**a**) µLEED pattern obtained from the 6P layer next to the flake. Six broad and extremely weak spots are found using an electron energy of 25.6 eV. The NN cell is indicated with a *red rhombus*. (**b**) Corresponding structural model. NN cell, unit cell, and superstructure are indicated by *solid*, *dashed*, and *dotted lines*, respectively. Adapted from [65], with permission from Elsevier

itself. For the areas far away the dominant diffuse background is an indication that the Ir{111} surface is covered by a 2D gas phase of 6P molecules. Figure 5.18(a) shows the µLEED pattern obtained from the wide dark band next to the flakes. A weak pattern of six diffuse spots can be seen. This is attributed to scattering from the nearest neighbor cell in a plane similar to the 6P(100) plane. The size of the NN cell is 5.0 Å by 5.0 Å with an angle β of 120° (solid line in Fig. 5.18(b)). Although similar to the NN cell found at moderate temperatures, the angle between the cell vectors is clearly dictated by the Ir{111} substrate. This is made possible by the lower molecule–molecule interaction at this elevated temperature. The geometry of the resulting unit cell (8.7 Å by 5.0 Å and $\beta = 90°$, dashed line in Fig. 5.18(b)) deviates from the 6P bulk (100) plane (8.091 Å by 5.568 Å and $\beta = 90°$ [31]). The unit cell vectors are compressed along the short and stretched along the long axis, indicating a larger tilt angle of the molecules. Changes to the molecular tilt angle for the first layer have been observed already earlier [3]. However, the benefit of this distortion becomes evident when looking at the resulting matrix notation $\begin{bmatrix} 1.9 & 3.7 \\ 1.9 & 0 \end{bmatrix}$. As can also be seen from the NN cell angle, the molecules are lined up with the underlying Ir{111} surface atoms. However, a 6 × 6 superstructure will allow all molecules to reach well coordinated positions by minimal deviations from the unit cell position. The resulting quasiepitaxial coincidence type II relationship [66] has a matrix notation of $\begin{bmatrix} 11 & 22 \\ 11 & 0 \end{bmatrix}$. In the non-metallic 6P on TiO_2 system [1, 2, 86] a wetting layer of flat lying molecules has been found, below the upright standing molecules [87]. However, we see no evidence for such a growth behavior in this system.

5.5 Summary

The growth of thin films of conjugated molecules is still a relatively young field. Many of the established models and routines can be applied but not all of them fit precisely to the particular needs which arise from the higher dimensionality of the building blocks. In-situ real time and real space observation of growth processes allows the unambiguous identification of growth modes and the underlying physical principles. In addition, by combing a real space method with a local probe for structural resolution, LEEM is an extremely powerful tool that is well suited for this purpose.

μLEED allowed to unambiguously resolve the molecular ordering in the grown para-Sexiphenyl thin films. Although 6P thin films—in particular on graphene—are extremely fragile, this could be done from the submonolayer regime to higher coverages using state-of-the-art spot profile analysis. The use of this method allowed us to not only resolve the structure, but also to shed light on the details of the Layer-by-Layer growth process it self.

We could prove that it is in principle possible to obtain the basic real space orientation of the molecules directly from real space observations, without the use of reciprocal space methods. By observing the shape, shape transition and movement of (monolayer) islands, it is possible to deduct the molecular orientation in real space on a per island base.

The growth modes in the 6P on graphene system can be selected by carefully adjusting diffusion parameters. At low temperatures the mobility of the lying molecules is small enough to prevent uphill diffusion. However, the metastable crystal structure of the initial submonolayer islands allows them to adapt to local strain fields by moving and adjusting their shape. As a consequence, single crystalline domains of several μm in size are formed. With increasing film thickness the crystal structure gets denser and the lying molecules arrange in a herringbone motif. This stable structure effectively hinders island diffusion. This can be understood by considering that this structure is more bulk-like and individual molecules are more strongly bound to the crystal. A repetition of this process ultimately leads to the desired Layer-by-Layer growth. Increasing the mobility of the molecules allows them to form 3D structures and the well known Stranski–Krastanov growth of 6P fibers sets in at moderate deposition temperatures.

Growth of 6P on Ir{111} reveals an interesting defect driven nucleation process at low temperatures. At low temperatures, defects on Ir{111} trigger nucleation and formation of ramified islands formed by upright standing molecules. Increasing the deposition temperature results in a sudden increase to a stable nucleus formed by five molecules. We explain this by a geometrically driven minimization of the number of fully exposed π-systems. At even higher temperatures the high mobility suppresses any growth on the graphene but leads to a step-flow-like growth on Ir{111}. This growth behavior starts at the edges of the large graphene flakes.

Similar as for the LbL growth at LT on graphene, forcing 6P to deviate from the bulk crystal structure allows the growth of smooth layers. On graphene the open metastable layer formed at the beginning of each layer formation cycle suppresses nucleation in the next layer. For the high temperature growth on Ir{111}, an increase of the angle between the b and c unit cell vectors allows the growth of a smooth layer of upright standing 6P. The non-bulk structure of the first layer hinders nucleation of the next layer.

Although the controlled growth of uniform and smooth films of upright standing molecules seems to be difficult due to the existence of a high Ehrlich–Schwoebel barrier in many organic systems, this is not necessarily true for flat lying molecules. However, by using in-situ real time and real space characterization techniques we have been able to show that eventually smooth growth of upright standing films can be achieved through the utilization of heterogeneous nucleation. In principle the use of surfactants (carbon residues on the surface in the present case) could also help to overcome the issues with upright standing molecules.

References

1. G. Hlawacek, C. Teichert, A.Y. Andreev, H. Sitter, S. Berkebile, G. Koller, M. Ramsey, R. Resel, Self-organization of para-Sexiphenyl on crystalline substrates. Phys. Status Solidi A **202**(12), 2376–2385 (2005). doi:10.1002/pssa.200521173. http://dx.doi.org/10.1002/pssa.200521173
2. S. Berkebile, G. Koller, G. Hlawacek, C. Teichert, F.P. Netzer, M.G. Ramsey, Diffusion versus sticking anisotropy: anisotropic growth of organic molecular films. Surf. Sci. **600**(24), 313–317 (2006). doi:10.1016/j.susc.2006.06.044
3. G. Hlawacek, P. Puschnig, P. Frank, A. Winkler, C. Ambrosch-Draxl, C. Teichert, Characterization of step-edge barriers in organic thin-film growth. Science **321**(5885), 108–111 (2008). doi:10.1126/science.1159455. http://dx.doi.org/10.1126/science.1159455
4. J.E. Goose, E.L. First, P. Clancy, Nature of step-edge barriers for small organic molecules. Phys. Rev. B **81**(20), 205310 (2010). doi:10.1103/PhysRevB.81.205310. http://dx.doi.org/10.1103/PhysRevB.81.205310
5. X. Zhang, E. Barrena, D. Goswami, D.G. de Oteyza, C. Weis, H. Dosch, Evidence for a layer-dependent Ehrlich–Schwöbel barrier in organic thin film growth. Phys. Rev. Lett. **103**(13), 136101 (2009). doi:10.1103/PhysRevLett.103.136101. http://dx.doi.org/10.1103/PhysRevLett.103.136101
6. E. Bauer, Low energy electron microscopy. Rep. Prog. Phys. **57**(9), 895 (1994). doi:10.1088/0034-4885/57/9/002. http://dx.doi.org/10.1088/0034-4885/57/9/002
7. R.M. Tromp, J.B. Hannon, A.W. Ellis, W. Wan, A. Berghaus, O. Schaff, A new aberration-corrected, energy-filtered LEEM/PEEM instrument. I. Principles and design. Ultramicroscopy **110**(7), 852–861 (2010). doi:10.1016/j.ultramic.2010.03.005. http://dx.doi.org/10.1016/j.ultramic.2010.03.005
8. E. Bauer, LEEM basics. Surf. Rev. Lett. **5**(6), 1275–1286 (1998)
9. M.J. Rost, L. Crama, P. Schakel, E. van Tol, G.B.E.M. van Velzen Williams, C.F. Overgauw, H.T. Horst, H. Dekker, B. Okhuijsen, M. Seynen, A. Vijftigschild, P. Han, A.J. Katan, K. Schoots, R. Schumm, W. van Loo, T.H. Oosterkamp, J.W.M. Frenken, Scanning probe microscopes go video rate and beyond. Rev. Sci. Instrum. **76**(5), 053710 (2005). doi:10.1063/1.1915288. http://dx.doi.org/10.1063/1.1915288
10. F. Esch, C. Dri, A. Spessot, C. Africh, G. Cautero, D. Giuressi, R. Sergo, R. Tommasini, G. Comelli, The FAST module: an add-on unit for driving commercial scanning probe microscopes at video rate and beyond. Rev. Sci. Instrum. **82**(5), 053702 (2011). doi:10.1063/1.3585984. http://dx.doi.org/10.1063/1.3585984
11. Q. Li, Q. Lu, Atomic resolution ultrafast scanning tunneling microscope with scan rate breaking the resonant frequency of a quartz tuning fork resonator. Rev. Sci. Instrum. **82**(5), 053705 (2011). doi:10.1063/1.3585200. http://dx.doi.org/10.1063/1.3585200
12. W. Telieps, E. Bauer, An analytical reflection and emission UHV surface electron microscope. Ultramicroscopy **17**(1), 57–65 (1985)

13. U. Scheithauer, G. Meyer, M. Henzler, A new LEED instrument for quantitative spot profile analysis. Surf. Sci. **178**(1–3), 441–451 (1986). doi:10.1016/0039-6028(86)90321-3. http://dx.doi.org/10.1016/0039-6028(86)90321-3
14. L. Kilian, E. Umbach, M. Sokolowski, Molecular beam epitaxy of organic films investigated by high resolution low energy electron diffraction (SPA-LEED): 3,4,9,10-perylenetetracarboxylicacid-dianhydride (PTCDA) on Ag(111). Surf. Sci. **573**(3), 359–378 (2004). doi:10.1016/j.susc.2004.10.004. http://dx.doi.org/10.1016/j.susc.2004.10.004
15. K.S. Novoselov, A.K. Geim, S.V. Morozov, D. Jiang, Y. Zhang, S.V. Dubonos, I.V. Grigorieva, A.A. Firsov, Electric field effect in atomically thin carbon films. Science **306**(5696), 666–669 (2004). doi:10.1126/science.1102896. http://dx.doi.org/10.1126/science.1102896
16. T.J. Echtermeyer, M.C. Lemme, M. Baus, B.N. Szafranek, A.K. Geim, H. Kurz, Nonvolatile switching in graphene field-effect devices. IEEE Electron Device Lett. **29**(8), 952–954 (2008)
17. A.K. Geim, K.S. Novoselov, The rise of graphene. Nat. Mater. **6**(3), 183–191 (2007). doi:10.1038/nmat1849. http://dx.doi.org/10.1038/nmat1849
18. Q.H. Wang, M.C. Hersam, Room-temperature molecular-resolution characterization of self-assembled organic monolayers on epitaxial graphene. Nat. Chem. **1**(3), 206–211 (2009)
19. P. Lauffer, K.V. Emtsev, R. Graupner, T. Seyller, L. Ley, Molecular and electronic structure of PTCDA on bilayer graphene on SiC(0001) studied with scanning tunneling microscopy. Phys. Status Solidi B **245**(10), 2064–2067 (2008)
20. I. Forbeaux, J.M. Themlin, J.M. Debever, Heteroepitaxial graphite on $6h-\mathrm{SiC}(0001)$: interface formation through conduction-band electronic structure. Phys. Rev. B **58**(24), 16396–16406 (1998). doi:10.1103/PhysRevB.58.16396. http://dx.doi.org/10.1103/PhysRevB.58.16396
21. T. Ohta, A. Bostwick, T. Seyller, K. Horn, E. Rotenberg, Controlling the electronic structure of bilayer graphene. Science **313**(5789), 951–954 (2006). doi:10.1126/science.1130681. http://dx.doi.org/10.1126/science.1130681
22. J. Wintterlin, M.L. Bocquet, Graphene on metal surfaces. Surf. Sci. **603**(10–12), 1841–1852 (2009). doi:10.1016/j.susc.2008.08.037. http://dx.doi.org/10.1016/j.susc.2008.08.037
23. A. Reina, X. Jia, J. Ho, D. Nezich, H. Son, V. Bulovic, M.S. Dresselhaus, J. Kong, Large area, few-layer graphene films on arbitrary substrates by chemical vapor deposition. Nano Lett. **9**(1), 30–35 (2008). doi:10.1021/nl801827v. http://dx.doi.org/10.1021/nl801827v
24. X. Li, W. Cai, J. An, S. Kim, J. Nah, D. Yang, R. Piner, A. Velamakanni, I. Jung, E. Tutuc, S.K. Banerjee, L. Colombo, R.S. Ruoff, Large-area synthesis of high-quality and uniform graphene films on copper foils. Science **324**(5932), 1312–1314 (2009). doi:10.1126/science.1171245. http://dx.doi.org/10.1126/science.1171245
25. A.T. N'Diaye, J. Coraux, T.N. Plasa, C. Busse, T. Michely, Structure of epitaxial graphene on Ir(111). New J. Phys. **10**(4), 043033 (2008). doi:10.1088/1367-2630/10/4/043033. http://dx.doi.org/10.1088/1367-2630/10/4/043033
26. I. Pletikosić, M. Kralj, P. Pervan, R. Brako, J. Coraux, A.T. N'Diaye, C. Busse, T. Michely, Dirac cones and minigaps for graphene on Ir(111). Phys. Rev. Lett. **102**(5), 056808 (2009). doi:10.1103/PhysRevLett.102.056808. http://dx.doi.org/10.1103/PhysRevLett.102.056808
27. R. van Gastel, A.T. N'Diaye, D. Wall, J. Coraux, C. Busse, N.M. Buckanie, F.J. Meyer zu Heringdorf, M. Horn von Hoegen, T. Michely, B. Poelsema, Selecting a single orientation for millimeter sized graphene sheets. Appl. Phys. Lett. **95**(12), 121901 (2009). doi:10.1063/1.3225554. http://link.aip.org/link/?APL/95/121901/1
28. H. Hattab, A.T. N'Diaye, D. Wall, G. Jnawali, J. Coraux, C. Busse, R. van Gastel, B. Poelsema, T. Michely, M. zu Heringdorf, M.H. von Hoegen, Growth temperature dependent graphene alignment on Ir(111). Appl. Phys. Lett. **98**(14), 141903 (2011). doi:10.1063/1.3548546. http://dx.doi.org/10.1063/1.3548546

29. J. Coraux, A.T. N'Diaye, C. Busse, T. Michely, Structural coherency of graphene on Ir(111). Nano Lett. **8**(2), 565–570 (2008)
30. S. Guha, W. Graupner, R. Resel, M. Chandrasekhar, H.R. Chandrasekhar, R. Glaser, G. Leising, Planarity of para-hexaphenyl. Phys. Rev. Lett. **82**(18), 3625–3628 (1999)
31. K. Baker, A. Fratini, T. Resch, H. Knachel, W. Adams, E. Socci, B. Farmer, Crystal structures, phase transitions and energy calculations of poly(p-phenylene) oligomers. Polymer **34**(8), 1571–1587 (1993). doi:10.1016/0032-3861(93)90313-Y. http://dx.doi.org/10.1016/0032-3861(93)90313-Y
32. F. Balzer, V.G. Bordo, A.C. Simonsen, H.G. Rubahn, Optical waveguiding in individual nanometer-scale organic fibers. Phys. Rev. B **67**(11), 1154081 (2003)
33. H. Plank, R. Resel, H. Sitter, A. Andreev, N.S. Sariciftci, G. Hlawacek, C. Teichert, A. Thierry, B. Lotz, Molecular alignments in sexiphenyl thin films epitaxially grown on muscovite. Thin Solid Films **443**(1–2), 108–114 (2003). doi:10.1016/S0040-6090(03)01021-6. http://dx.doi.org/10.1016/S0040-6090(03)01021-6
34. C. Teichert, G. Hlawacek, A.Y. Andreev, H. Sitter, P. Frank, A. Winkler, N.S. Sariciftci, Spontaneous rearrangement of para-Sexiphenyl crystallites into nano-fibers. Appl. Phys. A **82**(4), 665–669 (2006). doi:10.1007/s00339-005-3450-7. http://dx.doi.org/10.1007/s00339-005-3450-7
35. G. Hlawacek, F.S. Khokhar, R. van Gastel, B. Poelsema, C. Teichert, Smooth growth of organic semiconductor films on graphene for high-efficiency electronics. Nano Lett. **11**(2), 333–337 (2011). doi:10.1021/nl103739n. http://dx.doi.org/10.1021/nl103739n
36. A.T. N'Diaye, R. van Gastel, A.J. Martínez-Galera, J. Coraux, H. Hattab, D. Wall, F.J. Meyer zu Heringdorf, M. Horn von Hoegen, J.M. Gómez-Rodríguez, B. Poelsema, C. Busse, T. Michely, In situ observation of stress relaxation in epitaxial graphene. New J. Phys. **11**(11), 113056 (2009). doi:10.1088/1367-2630/11/11/113056. http://dx.doi.org/10.1088/1367-2630/11/11/113056
37. E. Loginova, S. Nie, K. Thürmer, N.C. Bartelt, K.F. McCarty, Defects of graphene on Ir(111): rotational domains and ridges. Phys. Rev. B **80**(8), 085430 (2009)
38. Z.H. Wang, K. Kanai, K. Iketaki, Y. Ouchi, K. Seki, Epitaxial growth of p-sexiphenyl film on highly oriented pyrolytic graphite surface studied by scanning tunneling microscopy. Thin Solid Films **516**(9), 2711–2715 (2008)
39. Y.-H. Zhang, K.-G. Zhou, K.-F. Xie, J. Zeng, H.-L. Zhang, Y. Peng, Tuning the electronic structure and transport properties of graphene by noncovalent functionalization: effects of organic donor, acceptor and metal atoms. Nanotechnology **21**(6), 065201 (2010). doi:10.1088/0957-4484/21/6/065201. http://dx.doi.org/10.1088/0957-4484/21/6/065201
40. A.J. Fisher, P.E. Blöchl, Adsorption and scanning-tunneling-microscope imaging of benzene on graphite and mos_2. Phys. Rev. Lett. **70**(21), 3263–3266 (1993). doi:10.1103/PhysRevLett.70.3263. http://dx.doi.org/10.1103/PhysRevLett.70.3263
41. Avogadro, 2010. http://avogadro.openmolecules.net
42. *OBForceFieldGhemical*, 2010. http://openbabel.org/wiki/OBForceFieldGhemical
43. M. Clark, R.D. Cramer, N. Van Opdenbosch, Validation of the general purpose tripos 5.2 force field. J. Comput. Chem. **10**(8), 982–1012 (1989). doi:10.1002/jcc.540100804. http://dx.doi.org/10.1002/jcc.540100804
44. T. Hassinen, M. Peräkylä, New energy terms for reduced protein models implemented in an off-lattice force field. J. Comput. Chem. **22**(12), 1229–1242 (2001). doi:10.1002/jcc.1080. http://dx.doi.org/10.1002/jcc.1080
45. G. Hlawacek, F.S. Khokhar, R. van Gastel, C. Teichert, B. Poelsema, Diffusion and submonolayer growth of para-Sexiphenyl on Ir(111) and Ir(111)-supported graphene. IBM J. Res. Dev. **55**(4), 15 (2011). doi:10.1147/JRD.2011.2160303. http://dx.doi.org/10.1147/JRD.2011.2160303
46. F. Tournus, J.C. Charlier, Ab initio study of benzene adsorption on carbon nanotubes. Phys. Rev. B **71**(16), 165421 (2005). doi:10.1103/PhysRevB.71.165421. http://dx.doi.org/10.1103/PhysRevB.71.165421

47. M. Gsell, P. Jakob, D. Menzel, Effect of substrate strain on adsorption. Science **280**(5364), 717–720 (1998)
48. M. Schroeder, D.E. Wolf, Diffusion on strained surfaces. Surf. Sci. **375**(1) (1997). doi:10.1016/S0039-6028(96)01250-2
49. H. Brune, K. Bromann, H. Röder, K. Kern, J. Jacobsen, P. Stoltze, K. Jacobsen, J. Norskov, Effect of strain on surface diffusion and nucleation. Phys. Rev. B **52**(20), 14380–14383 (1995)
50. V.S. Stepanyuk, D.I. Bazhanov, W. Hergert, J. Kirschner, Strain and adatom motion on mesoscopic islands. Phys. Rev. B **63**(15), 1534061 (2001)
51. J. Tersoff, R.M. Tromp, Shape transition in growth of strained islands: spontaneous formation of quantum wires. Phys. Rev. Lett. **70**(18), 2782–2785 (1993)
52. H.J.W. Zandvliet, R. van Gastel, Bistability in the shape transition of strained islands. Phys. Rev. Lett. **99**(13), 136103 (2007)
53. K.R. Paserba, A.J. Gellman, Kinetics and energetics of oligomer desorption from surfaces. Phys. Rev. Lett. **86**(19), 4338–4341 (2001). doi:10.1103/PhysRevLett.86.4338. http://dx.doi.org/10.1103/PhysRevLett.86.4338
54. P. Frank, T. Djuric, M. Koini, I. Salzmann, R. Rieger, K. Müllen, R. Resel, N. Koch, A. Winkler, Layer growth, thermal stability, and desorption behavior of hexaaza-triphenylene-hexacarbonitrile on Ag(111). J. Phys. Chem. C **114**(14), 6650–6657 (2010). doi:10.1021/jp100704v. http://dx.doi.org/10.1021/jp100704v
55. S. Müllegger, A. Winkler, Hexaphenyl thin films on clean and carbon covered Au(111) studied with TDS and LEED. Surf. Sci. **600**(6), 1290–1299 (2006). doi:10.1016/j.susc.2006.01.018. http://dx.doi.org/10.1016/j.susc.2006.01.018
56. S.L. Tait, Z. Dohnálek, C.T. Campbell, B.D. Kay, n-alkanes on MgO(100). II. Chain length dependence of kinetic desorption parameters for small n-alkanes. J. Chem. Phys. **122**(16), 164708 (2005). doi:10.1063/1.1883630. http://dx.doi.org/10.1063/1.1883630
57. K.E. Becker, K.A. Fichthorn, Accelerated molecular dynamics simulation of the thermal desorption of n-alkanes from the basal plane of graphite. J. Chem. Phys. **125**(18), 184706 (2006). doi:10.1063/1.2364894. http://dx.doi.org/10.1063/1.2364894
58. K.A. Fichthorn, R.A. Miron, Thermal desorption of large molecules from solid surfaces. Phys. Rev. Lett. **89**(19), 196103 (2002). doi:10.1103/PhysRevLett.89.196103. http://dx.doi.org/10.1103/PhysRevLett.89.196103
59. K. Fichthorn, K. Becker, R. Miron, Molecular simulation of temperature-programmed desorption. Catal. Today **123**(1–4), 71–76 (2007). doi:10.1016/j.cattod.2006.12.003. http://dx.doi.org/10.1016/j.cattod.2006.12.003
60. T. Potocar, S. Lorbek, D. Nabok, Q. Shen, L. Tumbek, G. Hlawacek, P. Puschnig, C.A. Draxl, C. Teichert, A. Winkler, Initial stages of a para-hexaphenyl film growth on amorphous mica. Phys. Rev. B **83**(7), 075423 (2011). doi:10.1103/PhysRevB.83.075423. http://dx.doi.org/10.1103/PhysRevB.83.075423
61. M. Schunack, T.R. Linderoth, F. Rosei, E. Laegsgaard, I. Stensgaard, F. Besenbacher, Long jumps in the surface diffusion of large molecules. Phys. Rev. Lett. **88**(15), 156102 (2002). doi:10.1103/PhysRevLett.88.156102. http://dx.doi.org/10.1103/PhysRevLett.88.156102
62. M. Henzler, LEED studies of surface imperfections. Appl. Surf. Sci. **11–12**, 450–469 (1982). doi:10.1016/0378-5963(82)90092-7. http://dx.doi.org/10.1016/0378-5963(82)90092-7
63. M. Horn-von Hoegen, Growth of semiconductor layers studied by spot profile analysing low energy electron diffraction—Part II. Z. Kristallogr. **214**(11), 684–721 (1999)
64. M. Henzler, LEED-investigation of step arrays on cleaved germanium (111) surfaces. Surf. Sci. **19**(1), 159–171 (1970)
65. F.S. Khokhar, G. Hlawacek, R. van Gastel, H.J.W. Zandvliet, C. Teichert, B. Poelsema, The influence of substrate temperature on growth of para-Sexiphenyl thin films on Ir111 supported graphene studied by Leem. Surf. Sci. **606**(3–4), 475–480 (2012). doi:10.1016/j.susc.2011.11.012. http://dx.doi.org/10.1016/j.susc.2011.11.012
66. D.E. Hooks, T. Fritz, M.D. Ward, Epitaxy and molecular organization on solid substrates. Adv. Mater. **13**(4), 227–241 (2001). doi:10.1002/1521-4095(200102)13:4%3C227::AID-

ADMA227%3E3.0.CO;2-P. http://dx.doi.org/10.1002/1521-4095(200102)13:4%3C227::AID-ADMA227%3E3.0.CO;2-P

67. G. Hlawacek, C. Teichert, S. Müllegger, R. Resel, A. Winkler, Pattern formation in para-quaterphenyl film growth on gold substrates. Synth. Met. **146**(3), 383–386 (2004)
68. F. Balzer, H.G. Rubahn, Chain-length dependent para-phenylene film- and needle-growth on dielectrics. Surf. Sci. **548**(1–3), 170–182 (2004)
69. G. Koller, S. Berkebile, J.R. Krenn, G. Tzvetkov, G. Hlawacek, O. Lengyel, F.P. Netzer, C. Teichert, R. Resel, M.G. Ramsey, Oriented sexiphenyl single crystal nanoneedles on TiO2 (110). Adv. Mater. **16**(23–24), 2159–2162 (2004). doi:10.1002/adma.200400276. http://dx.doi.org/10.1002/adma.200400276
70. S. Müllegger, G. Hlawacek, T. Haber, P. Frank, C. Teichert, R. Resel, A. Winkler, The influence of substrate temperature on the structure and morphology of sexiphenyl thin films on Au(111). Appl. Phys. A **87**(1), 103–111 (2007). doi:10.1007/s00339-006-3845-0. http://dx.doi.org/10.1007/s00339-006-3845-0
71. R. Resel, Crystallographic studies on hexaphenyl thin films — a review. Thin Solid Films **433**, 1–11 (2003)
72. A. Andreev, T. Haber, D.M. Smilgies, R. Resel, H. Sitter, N.S. Sariciftci, L. Valek, Morphology and growth kinetics of organic thin films deposited by hot wall epitaxy on KCl substrates. J. Cryst. Growth **275**(1–2), 2037–2042 (2005)
73. P.A. Mulheran, J.A. Blackman, Capture zones and scaling in homogeneous thin-film growth. Phys. Rev. B **53**(15), 10261–10267 (1996). doi:10.1103/PhysRevB.53.10261. http://dx.doi.org/10.1103/PhysRevB.53.10261
74. M. Brinkmann, S. Graff, F. Biscarini, Mechanism of nonrandom pattern formation of polar-conjugated molecules in a partial wetting regime. Phys. Rev. B **66**(16), 165430 (2002). doi:10.1103/PhysRevB.66.165430. http://dx.doi.org/10.1103/PhysRevB.66.165430
75. A. Pimpinelli, T.L. Einstein, Capture-zone scaling in island nucleation: universal fluctuation behavior. Phys. Rev. Lett. **99**(22), 226102 (2007)
76. A. Pimpinelli, T.L. Einstein, Pimpinelli and Einstein reply:. Phys. Rev. Lett. **104**(14), 149602 (2010). doi:10.1103/PhysRevLett.104.149602. http://dx.doi.org/10.1103/PhysRevLett.104.149602
77. D.D. Chambliss, K.E. Johnson, Nucleation with a critical cluster size of zero: submonolayer Fe inclusions in Cu(100). Phys. Rev. B **50**(7), 5012–5015 (1994). doi:10.1103/PhysRevB.50.5012. http://dx.doi.org/10.1103/PhysRevB.50.5012
78. G. Rosenfeld, R. Servaty, C. Teichert, B. Poelsema, G. Comsa, Layer-by-layer growth of Ag on Ag(111) induced by enhanced nucleation: a model study for surfactant-mediated growth. Phys. Rev. Lett. **71**(6), 895–898 (1993). doi:10.1103/PhysRevLett.71.895. http://dx.doi.org/10.1103/PhysRevLett.71.895
79. G. Haas, A. Menck, H. Brune, J.V. Barth, J.A. Venables, K. Kern, Nucleation and growth of supported clusters at defect sites: Pd/MgO(001). Phys. Rev. B **61**(16), 11105–11108 (2000). doi:10.1103/PhysRevB.61.11105. http://dx.doi.org/10.1103/PhysRevB.61.11105
80. B. Winter, J. Ivanco, F.P. Netzer, M.G. Ramsey, Ordered mono- and multilayer films of sexiphenyl on Al(111): a LEED investigation. Thin Solid Films **433**(1–2), 269–273 (2003)
81. H. Oji, E. Ito, M. Furuta, K. Kajikawa, H. Ishii, Y. Ouchi, K. Seki, p-Sexiphenyl/metal interfaces studied by photoemission and metastable atom electron spectroscopy. J. Electron Spectrosc. Relat. Phenom. **101–103**, 517–521 (1999). doi:10.1016/S0368-2048(98)00485-X. http://dx.doi.org/10.1016/S0368-2048(98)00485-X
82. S. Müllegger, A. Winkler, The influence of carbon on the adsorption/desorption kinetics and monolayer formation of quaterphenyl on Au(111). Surf. Sci. **574**(2–3), 322–330 (2005). doi:10.1016/j.susc.2004.10.044. http://dx.doi.org/10.1016/j.susc.2004.10.044
83. P. Frank, G. Hlawacek, O. Lengyel, A. Satka, C. Teichert, R. Resel, A. Winkler, Influence of surface temperature and surface modifications on the initial layer growth of para-hexaphenyl on mica (0 0 1). Surf. Sci. **601**(10), 2152–2160 (2007)

84. L. Tsetseris, S.T. Pantelides, Atomic-scale mechanisms of selective adsorption and dimerization of pentacene on Si surfaces. Appl. Phys. Lett. **87**(23), 233109 (2005). doi:10.1063/1.2139989. http://link.aip.org/link/?APL/87/233109/1
85. F. Schertz, D. Kutnyakhov, S. Schuppler, P. Nagel, S. Nepijko, G. Schönhense, Measurement of object height in emission electron microscopy. Appl. Phys. A **102**(2), 253–258 (2011). doi:10.1007/s00339-010-5998-0. http://dx.doi.org/10.1007/s00339-010-5998-0
86. R. Resel, M. Oehzelt, O. Lengyel, T. Haber, T. Schulli, A. Thierry, G. Hlawacek, C. Teichert, S. Berkebile, G. Koller, The epitaxial sexiphenyl (001) monolayer on TiO2(110): a grazing incidence X-ray diffraction study. Surf. Sci. **600**(19), 4645–4649 (2006). doi:10.1016/j.susc.2006.07.021. http://dx.doi.org/10.1016/j.susc.2006.07.021
87. L. Sun, S. Berkebile, G. Weidlinger, G. Koller, M. Hohage, F.P. Netzer, M.G. Ramsey, P. Zeppenfeld, Revealing the buried interface: para-Sexiphenyl thin films grown on TiO2(110). Phys. Chem. Chem. Phys. **12**(13), 3141–3144 (2010). doi:10.1039/b922285e. http://dx.doi.org/10.1039/b922285e

Chapter 6
Tuning Organic Electronics via Photoreactive Thin Organic Films

Matthias Edler, Thomas Griesser, Gregor Trimmel, and Wolfgang Kern

Abstract The present chapter deals with photoreactive thin films and describes processes to tune both surface and material properties by means of UV-irradiation. Selected applications of these materials as UV tunable interfaces in organic electronics are demonstrated. Two examples of photoreactive polymers together with the underlying photochemistry are presented. Polymers bearing aryl ester groups or N-arylamide units in their side-chain undergo the photo-Fries reaction under UV-light which yields hydroxyketone and aminoketone units as photoproducts, respectively. The reaction results in a change in surface polarity, which is accompanied by a significant increase in refractive index (Δn up to $+0.10$). Another example is given with polymers bearing ortho-nitrobenzyl ester units in their side chain. UV-irradiation causes the scission of the ester unit and the formation of polar carboxylic acids. Employing these photosensitive polymers as interfacial layers between the organic semiconductor and the gate dielectric, the characteristics of OTFTs such as carrier mobility and threshold voltage can be varied over a wide range. Moreover, the epitaxial growth of organic semiconductors (para-sexiphenyl and pentacene) on these surfaces can be influenced by photochemical adjustment of surface polarity. Proceeding from thin polymer layers to molecular layers, several examples for photoreactive mono- and oligolayers on metals and oxidic surfaces are presented. These layers, containing aryl ester units for example, were modified by UV illumination and post-exposure derivatization. Lithographic patterns in molecular layers were characterized with friction force microscopy.

M. Edler (✉) · T. Griesser · W. Kern
Chair of Chemistry of Polymeric Materials, University of Leoben, Otto-Glöckel Strasse 2,
8700 Leoben, Austria
e-mail: Matthias.Edler@unileoben.ac.at

G. Trimmel
Institute for Chemistry and Technology of Materials, Graz University of Technology,
Stremayrgasse 9, 8010 Graz, Austria

H. Sitter et al. (eds.), *Small Organic Molecules on Surfaces*,
Springer Series in Materials Science 173, DOI 10.1007/978-3-642-33848-9_6,

6.1 Introduction

Photochemical reactions in polymers and in thin molecular layers (or even self-assembled monolayers (SAMs) are a convenient way to tune the materials properties over a wide range with the possibility to pattern the material. In principle, photolithography will give a two-dimensional pattern of the surface and in some cases the bulk material below. However, by using two-photon absorption techniques even three dimensional modifications within a bulk polymer film are possible. In addition, standard photolithography is a well established technology used in the semiconductor industry and micro systems technology and thus new photochemical reactions or methods can be easily implemented in today's industrial processes. The state-of-the-art processes already allow a lateral resolution below 100 nm using excimer laser and deep-UV-lithography. Using experimental methods such as scanning near-field lithography, even a lateral resolution below 20 nm has already been achieved using SAMs on gold surfaces in special material combinations [1, 2].

The technological interest in the application of photoreactive materials in organic electronic devices has therefore seen a strong increase during the last decades and is today an active area of science. Specifically, materials that operate at deep UV-wavelengths and simultaneously offer the advantage of a well defined photochemistry are of technological interest.

Depending on the application and technology, different types of photochemical reaction are used for mono- and oligolayers of organic molecules and for thin polymeric films. These include photochemical degradation, radiation induced cross-linking and photochemically induced polymerization using the properties of high energy radiation to create radicals, with or without an additional radical initiator. Alternatively, photoreactions with a defined reaction pathway can be used, generating new defined chemical species. Examples are photochromic spiropyrans, fulgides or azobenzenes for reversible transformations and ortho-nitrobenzyl esters, benzyl thiocyanates, or aromatic esters for irreversible reactions.

In this chapter we demonstrate the versatility of photoreactive thin layers using polymeric films and 2D layers of bifunctional molecules bearing photoreactive ester groups, capable of undergoing the photo-Fries reaction or a photocleavage reaction. These layers can be applied as UV-patternable interfacial layers in organic devices to improve the performance of the device characteristics. Furthermore, upon irradiation with UV-light surface properties such as wettability, conductivity, adhesion and optical parameters can be modified. A schematic overview of the discussed possibilities in thin polymeric films is shown in Fig. 6.1.

Starting from a homogeneous photoreactive polymer film, illumination with UV or visible light changes the molecular structure of the photoreactive groups and thus the properties of the material (i). The most interesting properties include the refractive index, surface polarity and chemical reactivity, as well as conductivity. Changes in the refractive index are of substantial interest in optical data storage, waveguides and optical gratings (see Sect. 6.3.1). In addition, a change usually occurring in

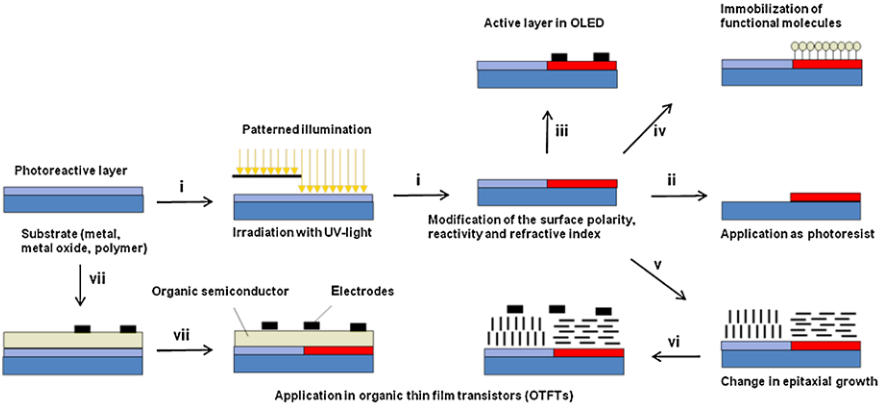

Fig. 6.1 Field of application for photoreactive organic thin films

the solubility of these polymers renders the application as photoresist materials (ii). In the case of a suitable photoreactive conductive polymer, such materials can be directly used for patterned organic devices, i.e. for organic light-emitting devices (OLEDs) (iii, see Sect. 6.5.2). Applying photolithographic techniques a patterned modulation of materials properties can be achieved. In the current examples presented the reactivity of the surface is always enhanced and therefore activated, e.g. for the immobilization of functional molecules, including dyes, nanoparticles and biomolecules (iv).

The change in surface polarity can be used to influence the growth of small organic molecules (e.g. para-sexiphenyl (PSP), pentacene) by vapor deposition (PVD) [3, 4]. Differences in the wetting behavior of these molecules induce changes of the growth conditions leading to differences in the crystal morphology and/or crystal size (v). Based on the influence of the crystal structure and morphology on the electrical and optical bulk parameters, a tuning of organic light-emitting diodes (OLED) or organic thin-film transistors (OTFTs) (vi) is possible.

Potential applications are the use of such layers as dielectric layer or additional interfacial layers in OTFTs. In this case, the performance of the OTFT is strongly dependent on the doping situation at the interface between the gate oxide and the organic semiconductor [5]. A modification of the electronic properties at this interface therefore has an enormous influence on the transistor characteristics. However, to exclude other effects stemming from different growing behavior (vide supra), it may be necessary to illuminate the assembled device (vii, Sect. 6.5.1)

The main part of this chapter deals with the application of thin photoreactive polymer layers. A further step comprises the transfer of the concept of photo patterning from polymer surfaces to very thin layers of bifunctional molecules, or better still self-assembled monolayers (SAMs). Self-assembled monolayers (SAMs) are highly ordered and oriented monomolecular layers of bifunctional organic molecules that assemble spontaneously on suitable solid surfaces. These ultra-thin layers consisting of bifunctional molecules should allow a better resolution down to the nanometer regime, as diffuse scattering within the polymer layer can be neglected. In the final section, we will show first results on photoreactive SAMs with aromatic esters capable of undergoing the photo-Fries reaction.

6.2 Examples of Photoreactions

Among the variety of photoreactions which are known to proceed in organic polymers and/or self-assembled monolayers, we focus on two photoreactions which have been the centre of our interest over the last five years. Firstly the photoreaction of aromatic esters, the photo-Fries rearrangement is presented, followed by the photocleavage of ortho-nitrobenzyl esters. Both of these reactions have a high change in surface polarity as well as the chemical reactivity being induced by the photoreaction.

6.2.1 Photo-Fries Rearrangement of Aromatic Esters and Amides

The chemical Fries reaction was discovered by Fries and Fink in 1908 [6]. In the presence of aluminium chloride as Lewis acid a rearrangement of aromatic ester groups occurs and consequently ortho- and para-hydroxyketones are formed. The light induced Fries reaction was first mentioned in the 1960s. Anderson and Reese [7] discovered that upon irradiation with UV-light aryl esters can be transformed into hydroxyketones. Unlike the chemical Fries reaction a radical mechanism [8] is the base of the photo-Fries rearrangement (cf. Fig. 6.2). In addition to aromatic esters, aromatic amides also show this photoisomerization reaction leading to ortho- and para- aminoketones as photoproducts.

The accepted mechanism for the photo-Fries reaction of phenyl esters, introduced by Lochbrunner et al. [9], is shown in Fig. 6.2. The photolysis reaction mainly proceeds from an excited singlet (S1) state (π–π^* transition). Via crossing with the π–σ^* state, the C–O bond in the ester group is elongated. Consequently, the C–O bond cleaves and free radicals are formed. In the solvent cage the photogenerated radicals can recombine to the starting compound or ortho- and/or para-isomers of cyclohexadienone are generated as “cage product” via an acyl shift. Tautomerism then gives hydroxyketones. The “escape product” of the geminate radical pair is mainly phenol, which is formed by H abstraction from the solvent.

Compared to the photoreaction of low-molecular weight esters, the yield of photoproduct in polymeric layers is significantly lower. This is caused by the higher absorption behavior of the generated hydroxyketones, forming a blocking layer for the UV light. Consequently, this kind of filter effect inhibits a further photoconversion of ester groups and degradation of the product.

The formation of the ortho product is favored in highly viscous solvents or solid matrices. The reaction mechanism shows that the limited mobility of the acyl radicals hinders high yields of the para product in contrast to the preferred attachment on the ortho position. In addition phenol as side product is formed [8].

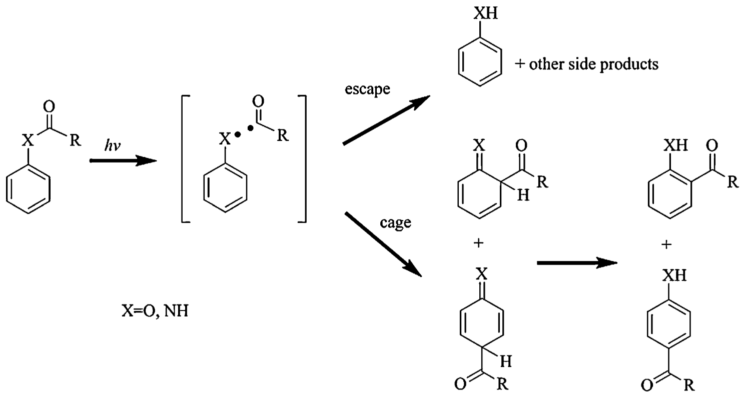

Fig. 6.2 Reaction scheme of the photo-Fries rearrangement

6.2.2 Photoreaction of ortho-Nitrobenzyl Ester

The o-nitrobenzyl group is well known to provide a photocleavable protection for hydroxyl compounds, such as alcohols and carboxylic acids [10]. In 1901 Ciamician and Silber discovered that upon irradiation with UV-light 2-nitrobenzylaldehyde undergoes an intramolecular conversion to nitrosobenzoic acid [11]. In 1966, Barltrop et al. [12] introduced o-nitrobenzyl moieties as photolabile protecting groups, which can be cleaved upon UV-irradiation and consequently release the functional group. The deprotection of the ester groups and formation of the carboxylic acid is a photo acid generating (PAG) process. Therefore, nitrobenzyl ester groups are formed as PAG groups.

An accepted mechanism for the photochemical deprotection is based on Norrish-type II reactions [13]. Upon irradiation with UV-light an n–π transition occurs. The excited singlet state is transferred into a triplet state and the nitro group abstracts a proton from the methylene carbon in the γ-H position. An acinitro intermediate is formed and resonance stabilized by a five-membered ring intermediate which rapidly decomposes to an aldehyde and a carboxylic acid [14]. The reaction of these photolabile compounds is shown in Fig. 6.3.

6.3 Tuning of Material Parameters

Photolithographic patterning of polymers selectively induces changes of material properties in the irradiated area and is useful in a variety of applications: e.g. a difference in solubility for photoresists, refractive index modulation for optical data storage, waveguides, gratings or distributed feedback lasers, the chemical reactivity for site-selective immobilization and electroless plating of metals. In the following, examples of photoinduced changes of the properties and post-modification reactions as well as applications are shown for polymers investigated during the last years in our group [15–21].

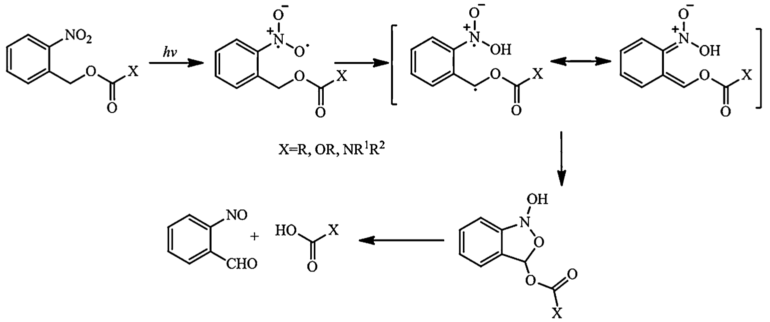

Fig. 6.3 Reaction scheme of the ortho-nitrobenzyl ester cleavage upon irradiation with UV-light

6.3.1 Refractive Index Changes Induced by the Photo-Fries Rearrangement and Related Photoreactions

Polymeric materials with tunable refractive index are of interest for applications related to optical communication (e.g. polymeric waveguides, optical switches) [22] and data storage devices [23]. Besides well established data storage devices (e.g. CD, DVD, and blue-ray discs) holographic and two-photon recording processes offer incomparably high storage densities [24].

A large number of photoreactive polymers with tuneable refractive index have therefore been developed and introduced over the last few years. A commonly used technology is based on the photobleaching process of dye-doped polymers which results in required refractive index changes Δn for optical devices in the order of 10^{-3}. Photochromic dyes which bleach upon UV-irradiation are dispersed in thermoplastic polymeric matrices, e.g. polymethylmethacrylate (PMMA), polystyrene and polyethylene [25]. Alternatively, photoinduced refractive index modification can also be achieved with photosensitive polymers, in which the dye units are covalently attached to the polymer backbone. These polymers have the advantage that a high chromophore concentration can be incorporated into the polymer system without crystallization, phase separation, or the formation of concentration gradients. In addition, these systems are expected to be more stable over time than the dye-doped systems due to the covalent immobilization of the chromophores [26]. Besides these photochromic materials, other approaches are based on photopolymerisable acrylate resins and polymers with photoreactive side groups, e.g. cinnamate units which undergo a [2 + 2] cyclodimerization [27].

Recently, we have shown that the photo-Fries reaction of phenyl esters and N-arylamides in polymeric materials induces very high refractive index changes compared to other polymer-based systems. The observed large increase in refractive index stems from the difference in the chemical structure of the phenyl ester (before illumination) and the hydroxyketone (after illumination). Furthermore, the change in refractive index is proportional to the conversion of the starting compound, which allows a selective adjustment of the refractive index by the irradiation

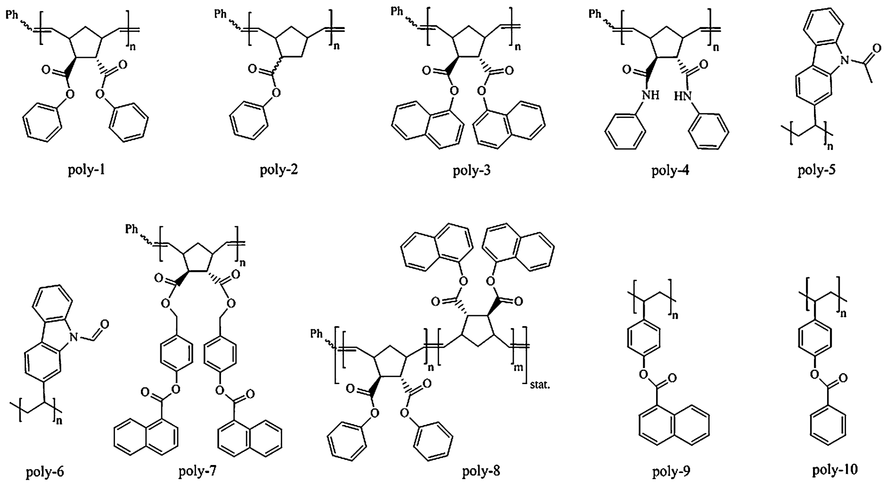

Fig. 6.4 Overview of various photoreactive polymers applied for refractive index modulation

dose. Figure 6.4 provides examples of photoreactive polymers exhibiting high refractive index changes. The polymers have been either prepared using ring opening metathesis polymerization or radical polymerization, with, the polymer backbone consisting of a polynorbornene main chain or a polyvinyl chain. This has, however, only a minor effect on the photochemistry, whereas the photoreactions used are based on functional groups. Hence, the conversion efficiency, the wavelength of illumination and the photochemistry itself can be influenced. The basic motif for polymers that undergo the photo-Fries rearrangement is shown in poly-1 and poly-2. Both polymers are easily accessible and possess a suitable aryl ester unit which can be excited with UV-light up to 270 nm. Using instead the naphthyl ester, the photo-Fries reaction can be induced with UV-light up to 320 nm (poly-3). However, in these polymers, the yield of the photo-Fries reaction is rather low. By using fully aromatic esters, as realized in the structures poly-7, poly-9 and poly-10, the yield of the ortho- and para-hydroxyketone can be increased. Furthermore, photoreactive aryl amides (poly-4 and poly-5) are an alternative for materials with high refractive index changes, but with a difference in the reaction products (hydroxyl groups versus amino groups). Instead of a photo-Fries reaction, the formic acid amide (poly-6) shows a photodecarbonylation with almost 100 % yield (extrusion of C≡O).

The main features of the photo-Fries reaction are exemplarily illustrated using poly(endo,exo-diphenyl bicyclo[2.2.1]hept-5-ene-2,3-dicarboxylic acid, diphenyl ester) [20] (poly-1) in Fig. 6.5. To avoid photooxidative side reactions, illumination with UV-light of 254 nm was carried out under inert atmosphere. The change of the chemical structure in poly-1 causes a significant change in the UV-Vis spectrum. As depicted in Fig. 6.5, the phenyl groups absorb UV-light at a wavelength $\lambda \sim 280$ nm (π–π^* transitions). The ester shows characteristic absorption near $\lambda \sim 190$ nm (C=O group, π–π^* transitions) and 270 nm (n–π^* transitions). Illumination with

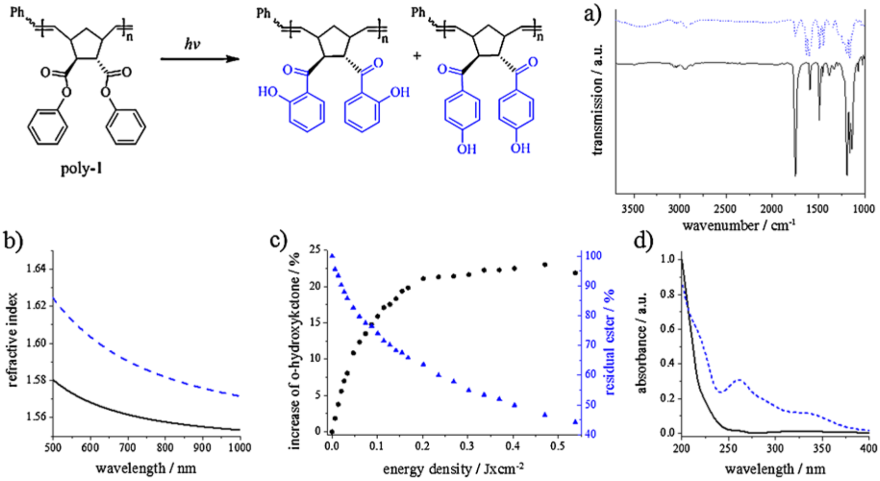

Fig. 6.5 FT-IR spectra (**a**), Cauchy Fit of the dispersion of the refractive index (**b**), progress in photo-Fries rearrangement (**c**) and UV VIS spectra (**d**) of a film of poly-1 before (*solid line*, *black*) and after (*dotted line*, *blue*) illumination with UV-light of 254 nm (energy density $E = 0.5\ \mathrm{J\,cm^{-2}}$)

monochromatic UV-light (254 nm, energy density $E = 0.5\ \mathrm{J\,cm^{-2}}$) causes the formation of two new absorbance maxima at $\lambda \sim 260$ nm and $\lambda \sim 330$ nm, which reveal the generation of aromatic hydroxyketone units [20]. The FT-IR spectra display the depletion of the ester peaks at 1745 $\mathrm{cm^{-1}}$ (C=O stretch) and 1197 $\mathrm{cm^{-1}}$ (asym. C–O–C stretch) accompanied by the formation of bands at 3400 $\mathrm{cm^{-1}}$ for the O–H stretching of the hydroxyl group and 1632 $\mathrm{cm^{-1}}$ which can be attributed to the formation of an ortho-hydroxyketone. Furthermore, a weak signal emerges at 1670 $\mathrm{cm^{-1}}$. This signal describes the formation of para-hydroxyketone groups. In addition, the evaluation of the FT-IR spectra provided an estimate of the yield of the photo-Fries products. A comparison of the intensity of the ester carbonyl peak (1763 $\mathrm{cm^{-1}}$) in non-irradiated poly-1 and the ortho-hydroxyketone carbonyl peak (1641 $\mathrm{cm^{-1}}$) showed that the yield of ketone in poly-1 is approximately 25 % after 10 min of irradiation ($E = 0.5\ \mathrm{J\,cm^{-2}}$), while approximately 45 % of the ester units remain unchanged. Ellipsometric measurements were performed for the determination of refractive index modulation. For poly-1 a significant change of up to $\Delta n = 0.05$ was obtained.

The observed difference in refractive index is directly proportional to the yield of photoproduct and can significantly be attributed to the progress of photoreactions. Figure 6.5 shows the optimal illumination time and thus the refractive index modulation can be exactly tuned. In Table 6.1 the refractive index changes which can be obtained for the polymers presented in Fig. 6.4 are summarized.

All the investigated polymers show high refractive index changes in the range of $\Delta n = +0.01$ (for poly-5 and poly-9) up to an astonishing value of $\Delta n = +0.10$ in poly-4. Usually, the refractive index variations in the range from 0.003 to 0.03

Table 6.1 Refractive index changes (Δn) and photoconversion upon UV-irradiation in polymers bearing aryl ester and amide units

Polymer		Change in refractive index ($\Delta n_{(x)}$)	Formation of hydroxyketone [%]	Literature
Poly(endo,exo-diphenyl bicyclo[2.2.1]hept-5-ene-2,3-dicarboxylate)	poly-1	$+0.049_{(450)}$	24	[20]
Poly(endo,exo-phenyl bicyclo[2.2.1]hept-5-ene-2-carboxylate)	poly-2	$+0.042_{(450)}$	21	[20]
Poly(endo,exo-dinaphthyl bicyclo[2.2.1]hept-5-ene-2,3-dicarboxylate)	poly-3	$+0.048_{(589)}$	27	[17]
Poly(endo,exo-N,N′-diphenyl bicyclo[2.2.1]hept-5-ene-2,3-dicarboxamide)	poly-4	$+0.100_{(450)}$	n.d.	[21]
Poly(1-(2-vinyl-9H-carbazol-9-yl)ethanone)	poly-5	$+0.010_{(650)}$	n.d.	[15]
Poly(2-vinyl-9H-carbazole-9-carbaldehyde)	poly-6	$+0.038_{(650)}$	n.d.	[15]
Poly(endo,exo-di(benzyl-4-oxycarbonyl-naphthalen-1-yl) bicyclo-[2.2.1]-hept-5-ene-2,3-dicarboxylate)	poly-7	$+0.043_{(370)}$	37	[18]
Poly(endo,exo-diphenyl bicyclo[2.2.1]hept-5-ene-2,3-dicarboxylate-co-endo,exo-di(1-naphthyl) bicyclo[2.2.1]hept-5-ene-2,3-dicarboxylate)]	poly-8	$+0.036_{(589)}$	n.d.	[17]
Poly(4-vinylphenyl 1-naphthoate)	poly-9	$+0.010_{(600)}$	45	[16]
Poly(4-vinylphenyl benzoate)	poly-10	$+0.036_{(600)}$	45	[16]

n.d.: Formation of photoproduct not determined
$\Delta n_{(x)}$: refractive index change determined at defined wavelength

are already considered to be high and a refractive index change of approx. 0.005 is enough for many optical applications e.g. waveguiding [28].

The change of the refractive index is based on the difference in the chemical structure before and after illumination. Comparing polymers poly-1, poly-2 and poly-3, all of them convert an aliphatic carboxylic acid aryl ester into a hydroxyarylketone. In all cases a similar and relatively high refractive index change (Δn between 0.042 and 0.049) could be observed, despite the conversion to the hydroxyketone is in all cases being rather low. Furthermore, a slight contribution to the increase in refractive index can stem from photo-crosslinking, observed as a side reaction in these polymers and is expected due to a slight reduction in volume [29].

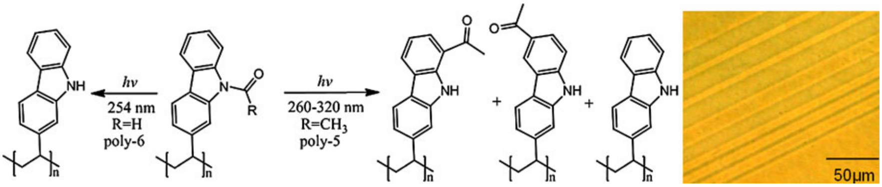

Fig. 6.6 Photodecarbonylation of poly-6 and photo-Fries rearrangement of poly-5 [15]; pattern in poly-5

Changing from phenyl esters in poly-1 and poly-2 to naphthyl ester units in poly-3 allows the use of wavelengths above 300 nm for the photoreactions with similar results for the refractive index change.

In this context, copolymers bearing both chromophores phenyl and naphthyl esters are interesting materials as realized with poly-8. A selective excitation of the naphthyl ester is achieved with UV-light > 300 nm whilst both phenyl and naphthyl ester units are converted by using UV-light < 270 nm. This allows a finer tuning of the refractive index and a double writing methodology.

The conversion of the ester units in the fully aromatic ester systems—in poly-9 bearing naphthyl ester groups and in poly-10 bearing phenyl ester is comparably high for polymeric materials resulting in up to 45 % hydroxyketone formation (see Table 6.1). However, the refractive index change for poly-9 is relatively low ($\Delta n = 0.011$), while poly-10 yielded in $\Delta n = 0.036$ compared to the aliphatic carboxyl acid aryl esters (poly-1, poly-2 and poly-3).

The highest refractive index changes—$\Delta n = +0.10$ at 450 nm—obtained in polymers have been realized in poly-4, the arylamide-based system.

Poly-5 and poly-6 are a special class of materials based on carbazol polymers [15]. The photochemical reaction in poly-5 is a partial photo-Fries reaction analogous to the reaction in aryl amides (poly-4). Photodecarbonylations occur to a lesser extent than common side reactions of the photo-Fries reaction (escape product). A refractive index modulation of $\Delta n = 0.01$ was obtained in poly-5. However, the higher refractive index change in poly-6 ($\Delta n = 0.03$) is based on the quantitative photodecarbonylation to poly(2-vinyl-9H-carbazole). This can be attributed to the low-stability of the formyl radical which is formed upon UV exposure. Moreover, this photoisomerization reaction can be achieved by two-photon excitation as shown in the optical phase contrast image in Fig. 6.6. Well separated lines have been realized.

6.3.2 Tuning the Chemical Reactivity

In addition to the change of the refractive index UV-irradiation achieves a significant change in chemical reactivity. The enhancement is caused by the formation of aromatic o-and p- hydroxyketones. Via combination of photolithographic techniques and selective immobilization, patterned functionalized surfaces can be obtained.

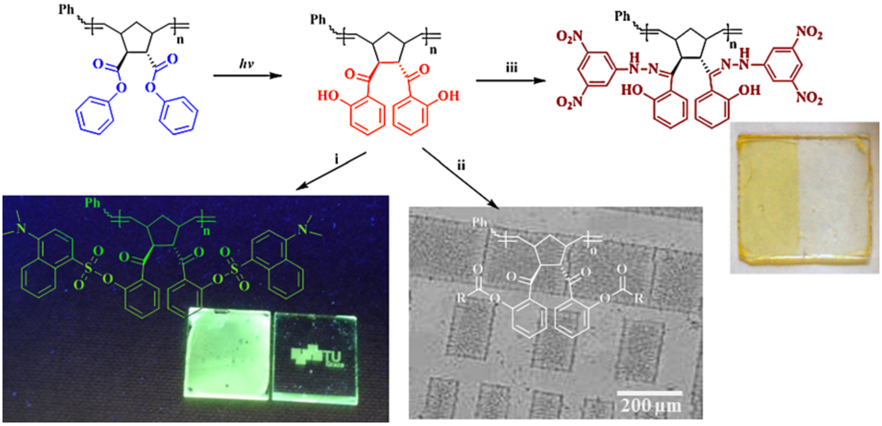

Fig. 6.7 Subsequent post-exposure reactions with dansyl chloride (i), acetyl chloride (ii) and 2,4-dinitrophenylhydrazine hydrochloride (iii) [19]

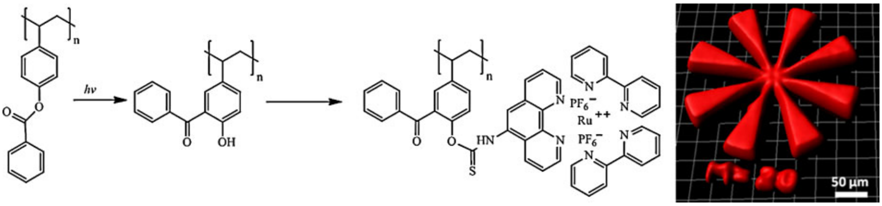

Fig. 6.8 Derivatization reactions of poly-10 and post-modification of patterned polymeric layer with $Ru(bpy)_2(phen\text{-}5\text{-}NCS)(PF_6)_2$ (*red*) [16]. Reproduced with permission from The Royal Society of Chemistry

Using poly-1 as an example several possibilities of post-modification reactions are shown in Fig. 6.7.

The hydroxyl groups can react with acid chlorides to give the corresponding ester. For the immobilization of fluorescent dyes, the illuminated films were immersed in a solution of dansyl chloride (i) and both flood and patterned functionalization of the thin polymer film were realized. Another approach for the immobilization of molecules on the irradiated areas of the poly-1 surface is the reaction of hydroxyl groups with acetyl chloride and the presence of CH_2Cl_2 (ii). The latter reagent is additionally added to cause a swelling of the polymer film, enabling a derivatization throughout the whole layer. Another functionalization is based on the reaction of the ortho-, para-photoproduct with hydrazine derivatives such as 2,4-dinitrophenylhydrazine hydrochloride resulting in the corresponding hydrazones (iii). A selective change in color indicated the effective post-exposure reaction of the layer of poly-1 [19].

A further functionalization using poly-10 [16] is shown in Fig. 6.8. The post-modification reaction was performed in a solution of $Ru(bpy)_2(phen\text{-}5\text{-}NCS)(PF_6)_2$ in acetonitrile. The photogenerated hydroxyl groups react readily with the isothio-

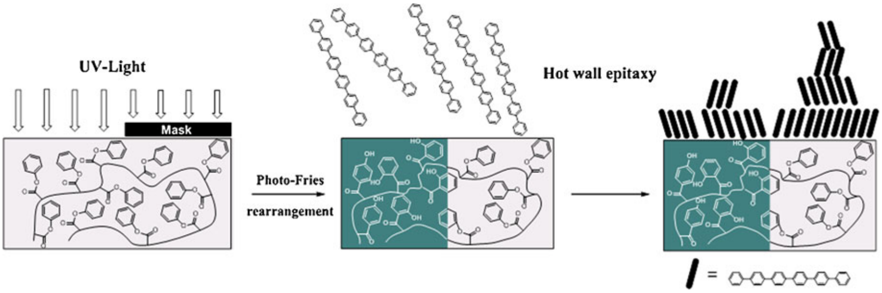

Fig. 6.9 UV illumination of a film of poly-1 through a mask and subsequent, growth of PSP performed by hot wall epitaxy [4]

cyanate groups of the red fluorescent dye. Confocal fluorescence microscopy indicates that the immobilization of the fluorescence dyes proceeds through the whole polymeric layer, as depicted in Fig. 6.8. The immobilized dye was excited with UV-light of 488 nm wavelength.

6.4 Influence on Epitaxial Growth of Small Molecules

Electroluminescence and charge carrier mobility, crucial electrical and optical characteristics of organic semiconducting layers largely depend on crystal structure, crystallite size and morphology. This can be strongly influenced by the interaction of the molecules with the substrate and the surface energy of the substrate plays a major role.

Again, using the photochemistry of poly-1, the growth of para-sexiphenyl (PSP, $C_{36}H_{26}$) on the pristine polymer substrates has been compared to the growth on an illuminated polymer surface at different temperatures. PSP is an interesting semiconductor for electroactive layer in OLED displays. The photoluminescence of PSP is thereby dependent on the morphology and crystal structure [30]. The concept is depicted in Fig. 6.9. The change in surface polarity induced by the photo-Fries reaction is expected to influence the growth morphology of PSP. Hot wall epitaxy as deposition method was chosen, because it enables organic molecules to adjust in the most suitable arrangement before fitting in the crystal lattice [31]. Prior to each growth experiment, one half of the substrate was illuminated (the other half covered) allowing the comparison of the growth conditions on the different surfaces, keeping all other parameters constant.

The change in surface energy was first studied by contact angle measurements. Due to the illumination of the poly-1 the surface tension decreases from 43.4 mJ m^{-2} to 40.6 mJ m^{-2}. However, this slight difference already has an enormous influence on the obtained crystal morphology. In Fig. 6.10, the AFM images of samples prepared at two different temperatures and with different deposition times prove in all cases a significant difference in the crystal size and shape of PSP. In

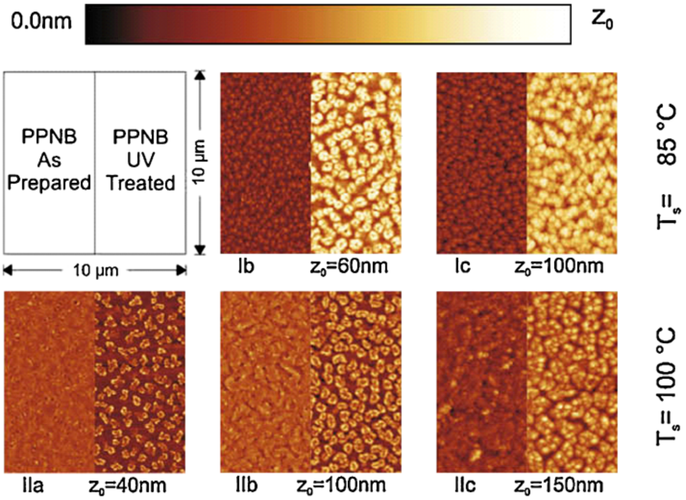

Fig. 6.10 AFM images of PSP deposited via different substrate temperatures and deposition times on variably illuminated poly-1 (PPNB). Reprinted from [4], Copyright (2009), with permission from Elsevier

the non-illuminated region the film seems to be more homogeneous. Increasing the deposition time, a lateral expansion of single islands can be observed. This behavior is based on the change in surface polarity via UV-irradiation. An additional increase in temperature coincides with the increase in structure size. A change in polarity of amorphous polymer films of poly-1 significantly influences the growth of PSP film deposited by hot wall epitaxy. Treating substrates by UV as a prestructuring process therefore enables new perspectives for the fabrication of devices.

6.5 Applications of Photoreactive Polymer Layers in Organic Electronics

6.5.1 Tuning the Characteristics of Organic Thin-Film Transistors (OTFTs)

Since the first publication of organic field effect transistors (OFETs) in 1986 [32] the research area of organic field effect transistors has grown steadily. The advantages of low cost fabrication and large area coverage represent an interesting alternative to conventional inorganic semiconductors based on silicon technology. The field of potential application is manifold and OFETs are used as electrical switches, low cost sensors [33] and memory cards [34]. Organic thin-film transistors (OTFTs), a special kind of OFETs, are three terminal devices. In Fig. 6.11 the schematic view of a top contact OTFT is presented. The three electrodes are referred to as gate, source

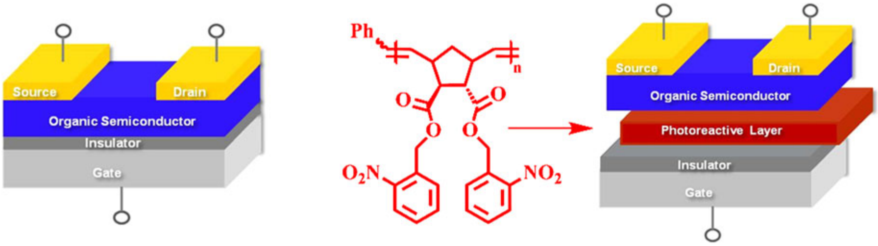

Fig. 6.11 Set up of a standard OTFT and set up of an OTFT with additional photoreactive layer

and drain electrode. Additionally, as gate dielectric (insulator) thermally grown SiO_x on a highly doped silicon wafer (gate electrode) is applied. The organic semiconductor layer normally consists of highly conjugated small molecules or polymers such as pentacene [35], rubrene, poly(9,9-dioctylfluorene-*co*-bithiophene) [36], and poly(3-hexylthiophene) (P3HT) [37].

Recent studies have shown that the performance of organic thin-film transistors (OTFTs) is to a large extent governed by the properties of the interface between the organic semiconductor and the gate dielectric [38]. One commonly applied scheme for tuning those interface characteristics is the use of organo-silane-based thin layers and self-assembled monolayers (SAMs) [39, 40], covalently linked to the gate dielectric. A photoreactive interfacial layer is inserted between the gate dielectric and the organic semiconductor in the OTFT set up. In the following we show two approaches on how to control two of the most crucial device parameters—the charge carrier mobility (μ) and the threshold voltage (V_{Th}). The main goal for most applications is the maximization of mobility [41], whereas the reproducible tuning of the threshold voltage (V_{Th}) over a broad range is desired, e.g. for inverter applications in integrated circuits.

Photochemical Control of the Carrier Mobility in Pentacene-Based Organic Thin-Film Transistors

In this study we use a thin layer of the photoreactive polymer poly(*endo*,*exo*-di(2-nitrobenzyl)bicyclo[2.2.1]hept-5-ene-2,3-dicarboxylate) (poly-11) [42]. The formation of carboxylic acid groups upon illumination as shown in Fig. 6.12 has the same effect as shown for the photo-Fries reaction. Due to the polar and protic acid groups the surface polarity increases dependent on the illumination time. To influence the growth of pentacene, a thin layer of poly-11 is spin cast on top of the SiO_2 gate dielectric. The chemical composition of the poly-11 surface can be tuned upon irradiation with UV-light, see Fig. 6.12.

The photoreaction was investigated by FTIR spectroscopy. The signal of the ester group at 1744 cm^{-1} and the nitro peaks at 1526 cm^{-1} and 1343 cm^{-1} decreased significantly after 1200 s of illumination, whereas a new signal at 1706 cm^{-1}—attributed to the photogenerated carboxylic acid group—emerges. The photoconversion of the photoreactive layer leads to a change of surface energy from 47.4 mJ/m^2

Fig. 6.12 FT-IR spectrum of poly-11 prior to (*blue*) and after illumination (*red*)

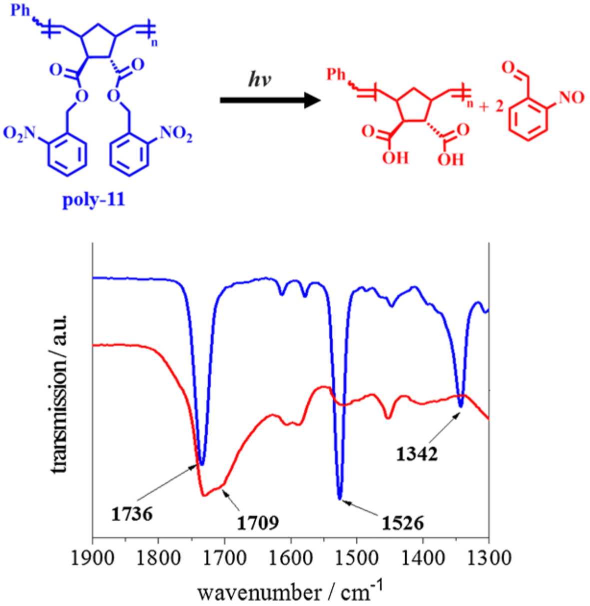

Fig. 6.13 AFM images of the pentacene surface on poly-11 after different illumination times. Reprinted with permission from [42] Copyright (2010), American Institute of Physics

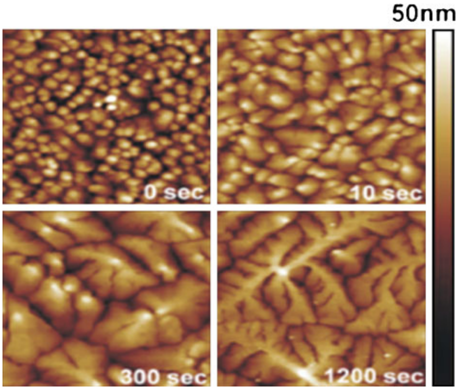

to 42.0 mJ/m^2 and a similar trend is observed in the case of poly-1 [3]. Figure 6.13 shows AFM images of the grown pentacence crystals depending on the illumination time of the substrate (0 s, 10 s, 300 s, 1200 s). Pentacene growth on unexposed poly-11 causes high nucleation density with average grain sizes of 0.2 µm while after 1200 s of illumination dendritic growth occurs. Furthermore, a linear relationship between the mobility and the grain size is observed, shown in Fig. 6.14. This results in an increase in the charge carrier mobility in the OTFT by approximately one order of magnitude (from 0.06 to 0.7 cm^2/V s) and is in accordance with literature reports on the linear relationship of the carrier mobility with grain size [43, 44]. Therefore, influencing the morphology and the grain size, allows the control of the effective field effect mobility in OTFTs.

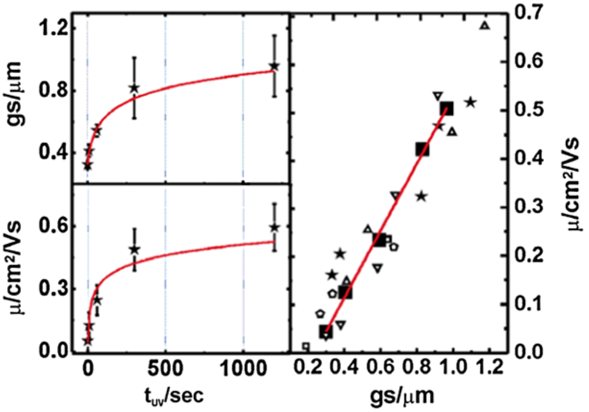

Fig. 6.14 *Top left*: Average grain size as a function of illumination time. *Bottom left*: OTFT mobility as a function of illumination time. *Right*: OTFT mobility as a function of grain size. The *large squares* denote the average values for 0, 10, 60, 300, and 1200 s UV exposure times. Reprinted with permission from [42] Copyright (2010), American Institute of Physics

Tuning the Threshold Voltage in Organic Thin-Film Transistors by Local Channel Doping Using Photoreactive Interfacial Layers

Over the years, a wide range of methods has been applied to tune threshold voltages, including the application of oxygen plasma [45] and UV ozone treatments [46] to generate charged surface states at the dielectric semiconductor interface of an organic gate dielectric (parylene). V_{Th} is also shifted to more positive values by inserting a polarizable layer into the dielectric [47]. However, drawbacks including mechanisms and the operation with high “programming” voltages to tune V_{Th} are poorly understood. By insertion of self-assembled monolayers [35] or chemically reactive thin layers [48] local channel doping and dedoping processes using acid groups and bases are realized. A local patterning, important for the realization of integrated electronic circuits, is, however, not obtainable. With the insertion of a thin poly-11 layer, acid groups are generated upon UV-irradiation and photochemical patterning is easily accomplished. In addition, the threshold voltage can be exactly controlled. The subsequent deprotonation of the acidic groups in the device due to the reaction with the organic semiconductor results in the formation of a space-charge region at the interface. A shift of V_{Th} is explained by the compensation of the formed conjugated bases by mobile holes. This has been shown by drift diffusion-based modelling [49].

Figure 6.15 shows that the threshold voltage is tuned by short time illumination. The shape of the curves is similar and during this short illumination the slopes and furthermore the mobility remains constant. Simultaneously, with an increased channel doping the drain current in the output characteristics rises and the hysteresis remains small ($\Delta VG = 2$ V at $I_D = 0.10$ mA).

Photolithographic patterns and interfacial doping processes enable the local control of V_{Th} and thus, the possibility to define if a transistor works in depletion or enhancement mode. Due to the application of photoreactive layers in a set up, integrated circuits such as depletion-load inverters are easily fabricated. The set up of a depletion-load inverter consists of an enhancement mode driven transistor and a depletion mode load transistor using only p-type OTFTs. The load transistor works

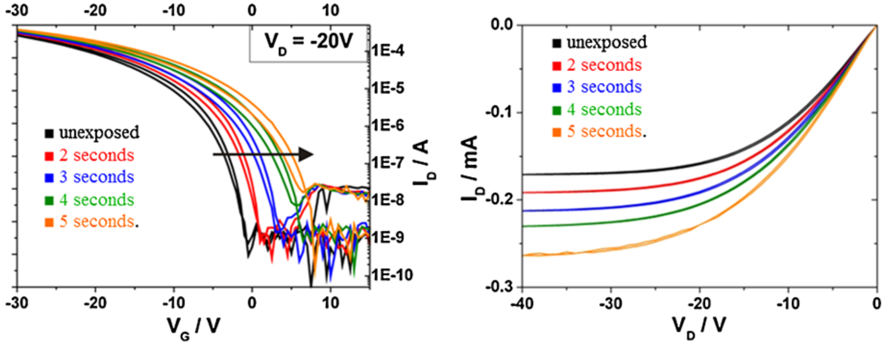

Fig. 6.15 Transfer characteristics at $V_D = -20$ V of one series of pentacene/poly-11 OTFTs and output characteristics for a representative series of poly-11 OTFTs varying illumination times. The *arrow* indicates an increase of illumination time [5]. Copyright Wiley-VCH Verlag GmbH & Co. KGaA. Reproduced with permission

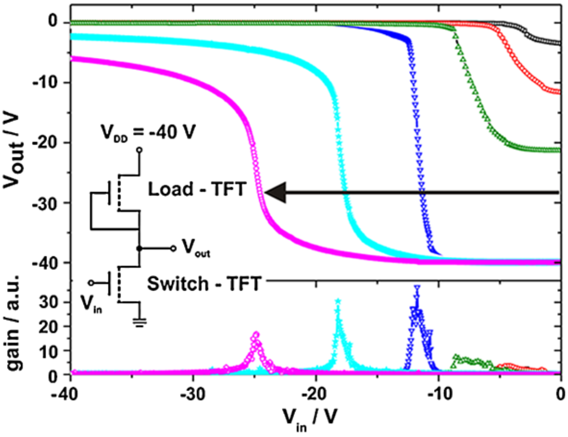

Fig. 6.16 Inverter characteristics with short time illuminated load-TFTs (for 0, 1, 2, 3, 4 and 5 seconds); the trend for increasing illumination times is shown by the *arrow*; *bottom*: the corresponding gains of the inverters; *inset*: wiring diagram of a depletion-load inverter [5]. Copyright Wiley-VCH Verlag GmbH & Co. KGaA. Reproduced with permission

in depletion mode and has a positive threshold voltage. The transistor is turned “on” due to the fact that it is already switched on at zero gate base bias. The switch TFT working in enhancement mode is normally an off transistor with a negative V_{Th}.

Both the switch and the load transistor in the inverter are equipped with a photoreactive layer. While the switch transistor remains non-illuminated, the load transistor was illuminated in 1 s steps. By increasing illumination time the load transistor shifts and the inverter characteristic improves significantly. After a 3 s illumination time a maximum gain of 40, based on the optimum value of V_{Th} for the load transistor with respect to the switch transistor (see Fig. 6.16).

With the application of photoreactive layers in OTFTs we demonstrated that device characteristics such as mobility and threshold voltage can be easily tuned and adjusted. Furthermore, the fabrication method presented offers the possibility for the production of monolithical circuits by UV-lithography.

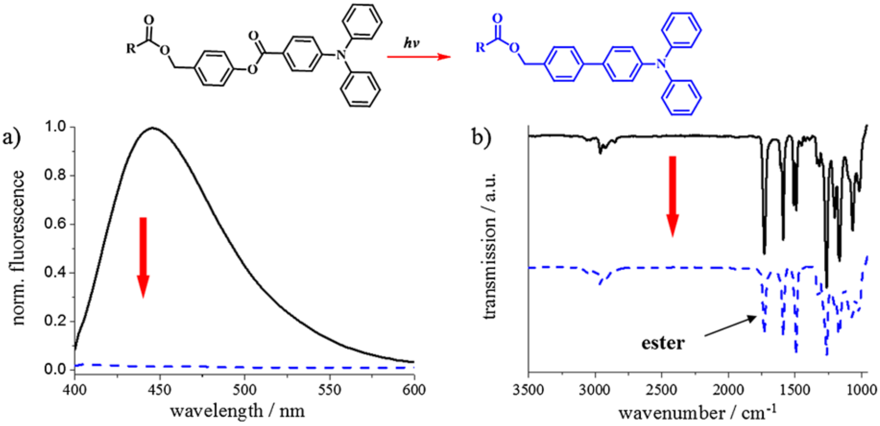

Fig. 6.17 Photoluminescence spectra (**a**) and FT-IR spectra (**b**) of poly-12 before (*solid line*) and after illumination with 254 nm (irradiation dose (1.35 J/cm^2) for 120 min (*dashed line*) [53]

6.5.2 Application of Photoreactive Polymeric Layers in OLEDs

Organic light-emitting diodes (OLEDs) represent a widely used application method in today's display technology. In general, the basic OLED set up consists of a film of fluorescent organic material, embedded between two electrodes: a transparent conducting anode and a metallic cathode [50, 51].

As soon as an appropriate bias is applied to the device, holes are injected from the anode and electrons from the cathode. The occurring recombination between holes and electrons results in electroluminescence. With the application of a photoreactive organic layer, patterned OLEDs with structured fluorescent surfaces can be obtained. As an example poly-(endo,exo-bis(4-(4-(diphenylamino)benzoyloxy) benzyl)-bicyclo[2.2.1]hept-5-ene-2,3-dicarboxylate) (poly-12) combines two main aspects: the photochemistry of aryl esters, and the fluorescence properties of derivatives of 4-(diphenylamino)benzoic acid.

4-(Diphenylamino)benzoic acid derivative consists of a diphenylamino group as a donor component and the ester group as acceptor and thus the polymer exhibits blue photo- and electroluminescence [52]. The photosensitivity of the aryl esters modifies the chemical composition of the functional side groups (chromophores) and therefore the emission characteristics of the polymeric layer. When the polymeric layer of poly-12 [53] is irradiated with UV-light in the wavelength range over 300 nm no photoreaction can be detected. However, by irradiation with deep UV (254 nm) the occurrence of the blue fluorescence bleaches slowly and finally vanishes (Fig. 6.17).

The results of the FTIR spectroscopy indicate that the reduction of the ester bands at 1730 cm^{-1}, 1263 cm^{-1}, and 1170 cm^{-1} by approx. 50 % show that a significant fraction of the ester units is transformed during the irradiation. However, no new peak, attributable to the formation of hydroxyketones, is detectable. Instead of

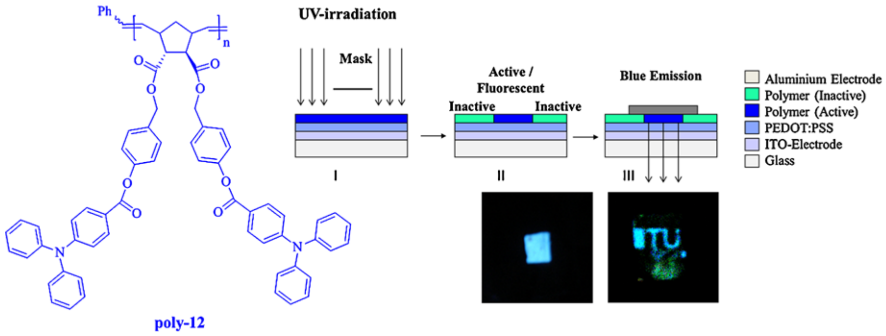

Fig. 6.18 Set up of the patterned organic light-emitting diode (OLED) applied [53]

the expected photo-Fries rearrangement, a decarboxylation reaction occurs as competing reaction in the photochemistry of aromatic esters [54]. The loss of carbon dioxide leads to a destruction of the push-pull chromophore and thus blue fluorescence disappears. Consequently, the polymer is qualified for the development of photolithographically patterned fluorescent films.

For the realization of a patterned OLED we investigated the efficiency of our material as light emitter. A simple OLED set up (see Fig. 6.18) was fabricated based on an indium-tin oxide (ITO) coated glass substrate. On the transparent ITO electrode a stack of poly(3,4-ethylene-dioxythiophene)-poly(styrene-4-sulfonate) (PEDOT–PSS) acts as electron injection layer, covered by poly-12 as emissive material. On top of the OLED aluminium as electrode material was deposited. The OLED with poly-12 as active layer was photostructured by means of UV-irradiation at a wavelength of 254 nm. When operated at 18 V bias, the blue electroluminescence of the patterned device was observed.

6.6 Photoreactive Self-assembled Monolayers

The functionalization of inorganic surfaces by self-assembled monolayers (SAMs) is a widely applied and important technique for the fabrication of nanostructured and hierarchically organized materials. With the transfer of photoreactive groups from polymeric media to very thin layers of bifunctional molecules, forming self-assembled monolayers (SAMs), high optical resolutions for photo structuring should be obtained. By utilization of a scanning near-field optical microscope (SNOM) a resolution of 9 nm [55] has been obtained in self-assembled organic thiol monolayers on microcrystalline gold surfaces. The surface properties can be tailored via the head group over a wide range from apolar to polar, or from acidic to basic groups and from non-reactive to reactive groups [56]. In this context, SAMs with photoreactive headgroups offer the advantage that the surface properties can easily be changed by photolithography with the above mentioned excellent lateral resolution.

Fig. 6.19 Overview of the bifunctional molecules undergoing the photo-Fries reaction upon illumination with UV-light

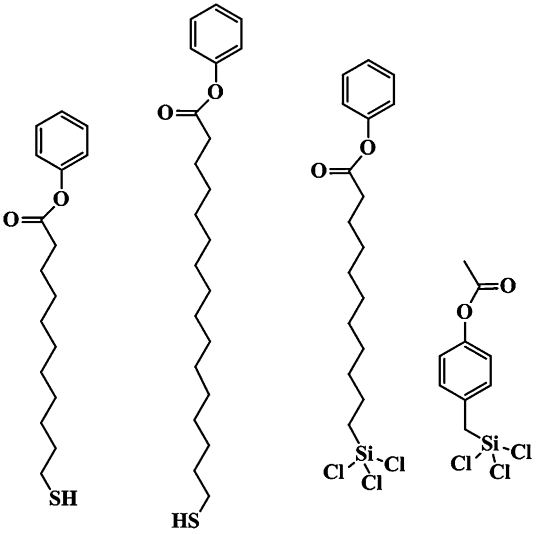

SAM-1 **SAM-2** **SAM-3** **SAM-4**

We have therefore combined two of the most common anchor-group substrate combinations: thiols on gold and trichlorosilanes on SiOx surfaces, both with photoreactive aryl ester groups. Four bifunctional molecules (as depicted in Fig. 6.19) have been investigated. The surface modification and patterning is exemplarily shown for the thiol-Au surfaces using SAM-1 and SAM-2. Similar reactions are performed on silicon/SiOx surfaces using SAM-3 and SAM-4 [57].

The phenyl ester groups photoisomerize and hydroxyketones are formed upon irradiation with UV-light ($\lambda = 254$ nm). The formation of polar hydroxyl groups additionally leads to a change in the surface tension of the SAMs. In a next step the photogenerated hydroxyl groups which are more reactive than the corresponding ester can react with several compounds. For SAM-1 the post-modification with perfluorobutyryl chloride is presented, while the illuminated SAM-2 molecules are derivatized with adipoyl chloride and ethylenediamine in a subsequent post-modification step. This post-exposure modification led to a significant change in wetting behavior and surface energy.

In Fig. 6.20 the reaction scheme of the bifunctional molecule SAM-1 with perfluorobutyryl chloride is presented. For this modification reaction, one half of the substrate was exposed to UV-light while the other half was covered with a chromium mask. The whole substrate was then exposed to the modification reagent.

An increase in contact angles both for water (from 88° to 91°) and for CH_2I_2 (from 23° to 32°) can be determined during formation of SAM-1, indicating a reduced overall surface tension caused by the chemisorption of the molecules. After the irradiation the contact angle of water decreases to 78° whereas the contact angle of CH_2I_2 only slightly increases to 35°. The surface tension is slightly enhanced, accompanied by higher polarity, caused by the polar hydroxyl groups formed by

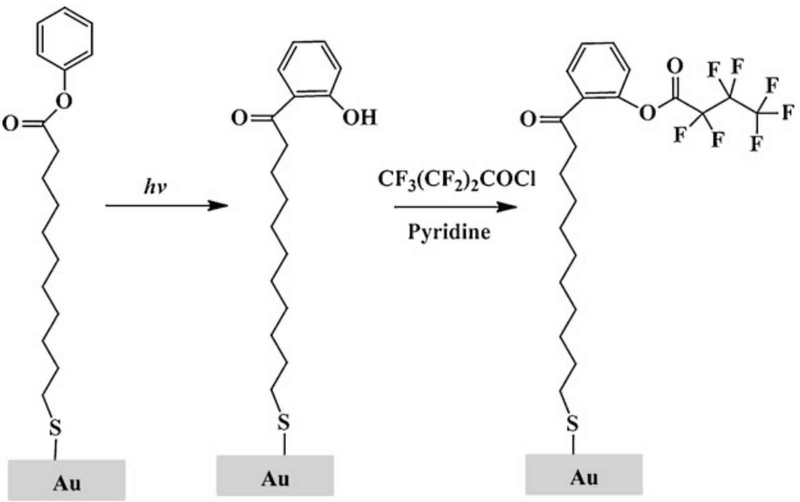

Fig. 6.20 Irradiation of SAM-1 and post exposure reaction of the formed hydroxyketone with perfluorobutyryl chloride

Fig. 6.21 XPS analysis of the self-assembled monolayer (SAM) of the not illuminated thiol layer (*solid line*) and after illumination and postmodification reaction with perfluorobutyryl chloride (*dashed line*)

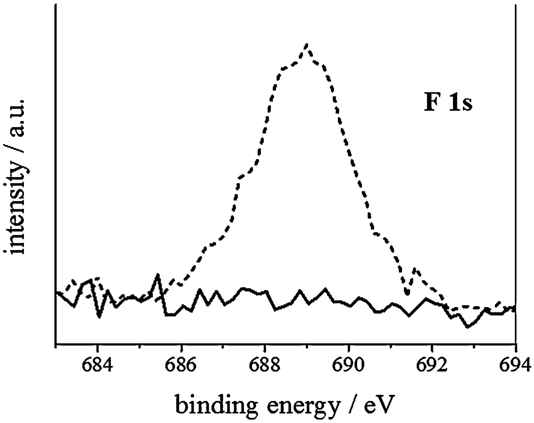

the photoreaction. After treatment with perfluorobutyryl chloride, both contact angles rise to values of 94° and 52°, respectively (Table 6.2). These characteristics are based on the hydrophobic and oleophobic properties of fluorocarbons. Investigations performed with XPS-spectroscopy indicate the SAM formation as the corresponding carbon, sulfur and oxygen signals were found. The XPS spectra hardly change due to the photo-Fries reaction, as no change of the chemical composition occurs. However, after the post-modification reaction with perfluorobutyryl chloride, only the illuminated part of the sample shows an intense signal in the F1s region (Fig. 6.21). This clearly indicates that selective surface chemistry is occurring and lithographic patterning are possible.

Table 6.2 Contact angle (θ) and surface tension (γ); γ^D: disperse part, γ^P: polar part; Surface polarity = 100 (γ^P/γ)) of SAM layer prior to and after illumination and after post-modification respectively

Substrate	θ H_2O [°]	θ CH_2I_2 [°]	γ [mJ/m^2]	γ^D [mJ/m^2]	γ^P [mJ/m^2]	Surface polarity [%]
Gold	88	23	47.5	47.8	0.7	1.5
SAM-1	91	32	43.8	43.4	0.4	0.9
SAM-1 illuminated	78	35	45.8	42.2	3.7	8.1
SAM-1 modified	94	52	34.2	33.1	1.1	3.2

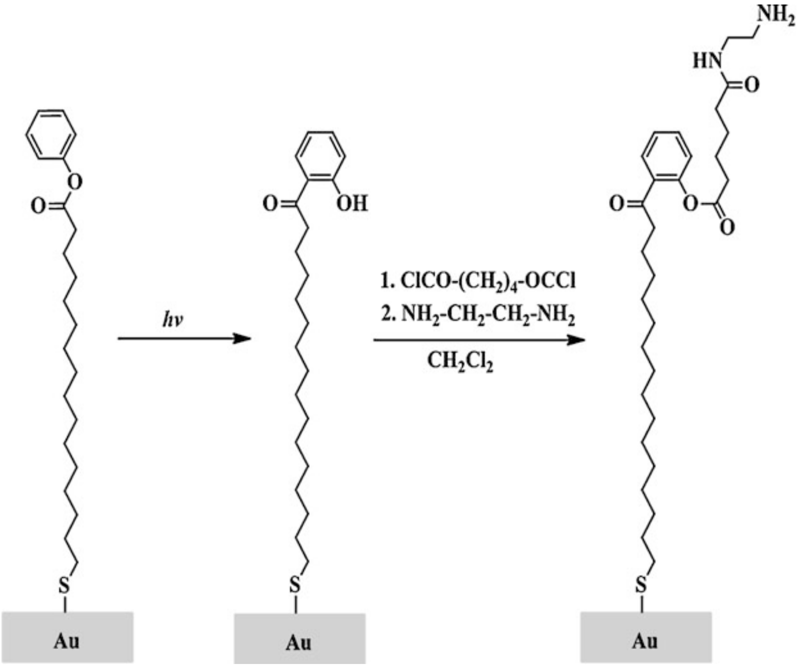

Fig. 6.22 Irradiation of SAM-2 and post exposure reaction of the formed hydroxyketone with adipoyl chloride and ethylenediamine

Furthermore, the photoreaction in the monolayer SAM-2 as well as the selective post-modification reaction with adipoyl chloride and ethylenediamine was investigated by contact angle and XPS measurements. The overall reaction scheme is depicted in Fig. 6.22. After illumination the contact angle of water decreased significantly from 90° to 67°. As a result of the derivatization with adipoyl chloride and ethylenediamine, the contact angle decreased further to 38°. Thus, the attachment of the polar compounds induces a fundamental change of the surface properties. The XPS results reveal a selective post-modification. Again, half of the substrate was exposed to UV-light and post-modified while the non-illuminated part remained un-

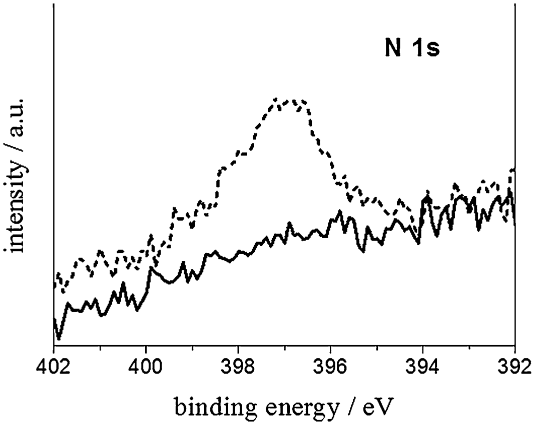

Fig. 6.23 XPS analysis of the self-assembled monolayer (SAM) (*solid line*) and after illumination and postmodification reaction with adipoyl chloride and ethylenediamine (*dashed line*)

affected. A clear increase of the nitrogen signal (N1s), see Fig. 6.23, proves the derivatization reaction.

A further step is related to the micro and nano structuring of a SAM-2 layer. Patterned functionalized surfaces were prepared by two different photolithographic methods: the use of a contact mask (chromium on SiO_2) and scanning near-field photolithography, using a near-field scanning optical microscope with a wavelength of 244 nm [58].

After the photopatterning, again the same post-exposure modification was applied to develop a highly hydrophilic surface in the illuminated areas and to enhance the contrast between modified and unmodified regions of the patterned samples. Friction force microscopy, where a tip substrate interaction leads to a twisting cantilever indicating the friction of the substrate, was performed. As depicted in Fig. 6.24 and Fig. 6.25 the areas which have undergone the photo-Fries reaction and were derivatized with the amine compound appear dark and the non-illuminated areas appear bright. A high overall contrast between both regions was obtained.

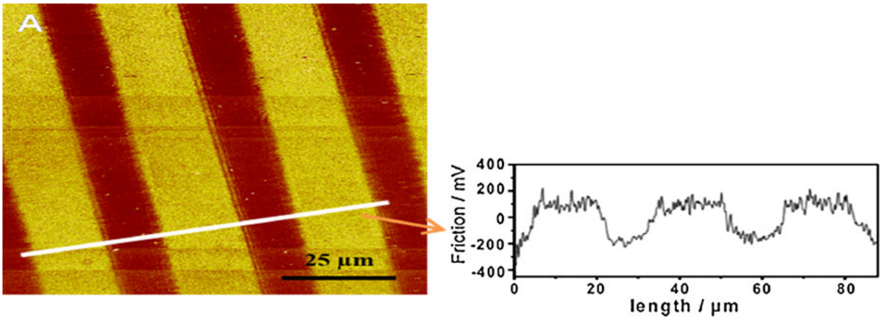

Fig. 6.24 Friction force microscopy image and section analysis of photostructured and selectively derivatized SAM-2 layer. Reprinted with permission from [58]. Copyright (2008) American Chemical Society

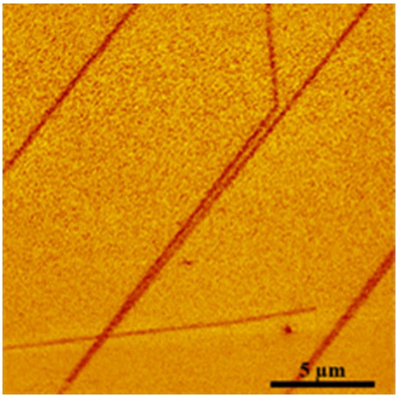

Fig. 6.25 Friction force microscopy image of SNOM structured and selectively derivatized SAM-2 layer Reprinted with permission from [58]. Copyright (2008) American Chemical Society

6.7 Summary

In this book chapter it has been demonstrated that both thin films of photoreactive polymers and molecular layers bearing UV-reactive groups can be applied to modulate material and surface properties over a wide range.

Considering the well-known photo-Fries reaction, which transforms (non-polar) aryl esters and N-arylamides to hydroxyketones and aminoketones, the surface properties (polarity, wettability) as well as bulk properties such as the chemical reactivity and the refractive index can be tuned over a wide range. It has been shown that in thin polymeric layers this peculiar photoreaction causes very large changes in refractive index (Δn up to $+0.10$), which can be applied for optoelectronic elements such as waveguides. Using these polymers as substrates for the growth of conductive molecular layers such as para-sexiphenyl (PSP), the grain size and the morphology of the grown PSP layer can be modulated by UV-irradiation of the substrate, and the characteristics of organic thin-film transistors can be adjusted. The chemical reactivity of the photogenerated groups (hydroxy and amino moieties) paves the way for a variety of post-exposure modifications of the irradiated zones of the surface, and patterns with almost any property profile are accessible using such methods.

In a similar way, the photoscission of nitrobenzyl esters yields carboxylic acids which are both highly polar and chemically reactive. By employing appropriate derivatization reactions, esters and amides are obtained, and the surface properties can be further shifted to enhanced hydrophilicity or hxdrophobicity. The photoassisted generation of acidic groups has been utilized to modulate the characteristics, e.g. carrier mobility and threshold voltage, of organic thin-film transistors (OTFTs). This effect can be attributed to the formation of space charges at the interface. Moreover, the epitaxial growth of pentacence on layers of these polymers differs with respect to grain size and morphology, which provides a way to modulate the carrier mobility in OTFTs by UV pretreatment of the substrate.

Proceeding from polymeric layers to molecular layers, more sophisticated techniques are required both for the preparation and for the characterization. Various anchoring groups both for metals and oxidic surfaces are available (e.g. thiols, silanes and phosphonates), and especially for silanes the layer thickness (mono- to oligolayers) strongly depends on the process conditions.

It has been demonstrated that selected photochemical reactions, amongst them the photo-Fries rearrangement, can be achieved in molecular layers. Using the concept of UV-reactive molecular layers, virtually any surface chemistry can be realized by appropriate post-exposure derivatization. These photosensitive molecular layers can be applied to numerous inorganic surfaces without changing topographic features, and render the modulation of surface polarity, wettability and reactivity possible. Applications in the field of electronic organic devices are currently being investigated by our group.

As for all photoreactions, photolithographic techniques such as contact and projection lithography allow to create gradients and patterns in molecular layers with a resolution line the submicron and even nanometer range. Friction force microscopy has proven to be of exceptional value to detect chemical transformations in molecular layers.

References

1. G.J. Leggett, Chem. Soc. Rev. **35**, 1150–1161 (2006)
2. S. Sun, G.J. Leggett, Nano Lett. **7**, 3753–3758 (2007)
3. P. Ribič, V. Kalihari, C. Frisbie, G. Bratina, Phys. Rev. B **80**, 115307 (2009)
4. G. Hernandez-Sosa, C. Simbrunner, T. Höfler, A. Moser, O. Werzer, B. Kunert, G. Trimmel, W. Kern, R. Resel, H. Sitter, Org. Electron. **10**, 326–332 (2009)
5. M. Marchl, M. Edler, A. Haase, A. Fian, G. Trimmel, T. Griesser, E. Zojer, B. Stadlober, Adv. Mater. **22**, 5361–5365 (2010)
6. K. Fries, G. Finck, Chem. Ber. **41**, 4271–4284 (1908)
7. J.C. Anderson, C.B. Reese, Proc. Chem. Soc. (1960), p. 217
8. C.E. Kalmus, D.M. Hercules, J. Am. Chem. Soc. **96**, 449–456 (1974)
9. S. Lochbrunner, M. Zissler, J. Piel, E. Riedle, A. Spiegel, T. Bach, J. Chem. Phys. **120**, 11634 (2004)
10. H. Barzynski, D. Sänger, Angew. Makromol. Chem. **93**, 131–141 (1981)
11. G. Ciamician, P. Silber, Chem. Ber. **34**, 2040–2046 (1901)
12. J.A. Barltrop, P.J. Plant, P. Schofield, Chem. Commun. (London) 822 (1966)
13. C.H. Bamford, R.G.W. Norrish, J. Mater. Chem. 1504–1511 (1934)
14. C.G. Bochet, J. Chem. Soc., Perkin Trans. **1**, 125–142 (2002)
15. T. Griesser, A. Wolfberger, M. Edler, M. Belzik, G. Jakopic, G. Trimmel, W. Kern, J. Polym. Sci., Part A, Polym. Chem. **48**, 3507–3514 (2010)
16. T. Köpplmayr, M. Cardinale, G. Jakopic, G. Trimmel, W. Kern, T. Griesser, J. Mater. Chem. **21**, 2965 (2011)
17. T. Griesser, T. Höfler, G. Jakopic, M. Belzik, W. Kern, G. Trimmel, J. Math. Chem. **19**, 4557–4565 (2009)
18. T. Höfler, T. Grießer, M. Gruber, G. Jakopic, G. Trimmel, W. Kern, Macromol. Chem. Phys. **209**, 488–498 (2008)
19. T. Griesser, T. Höfler, S. Temmel, W. Kern, G. Trimmel, Chem. Mater. **19**, 3011–3017 (2007)
20. T. Höfler, T. Grießer, X. Gstrein, G. Trimmel, G. Jakopic, W. Kern, Polymer **48**, 1930–1939 (2007)
21. T. Griesser, J. Kuhlmann, M. Wieser, W. Kern, G. Trimmel, Macromolecules **42**, 725–731 (2009)
22. H.G. Unger, *Planar Optical Waveguides and Fibres* (Clarendon, Oxford, 1993)

23. R.A. Lessard, R. Changkakoti, G. Manivannan, Processes in Photoreactive Polymers (New York, 1995), pp. 305–367
24. T.D. Milster, Y. Zhang, Mater. Res. Soc. Bull. **31**, 318–323 (2006)
25. R.S. Moshrefzadeh, D.K. Misemer, M.D. Radcliffe, C.V. Francis, S.K. Mohapatra, Appl. Phys. Lett. **62**, 16 (1993)
26. A. Natansohn, P. Rochon, C. Barrett, A. Hay, Chem. Mater. **7**, 1612–1615 (1995)
27. H.J. Coufal, D. Psaltis, G.T. Sincerbox, A.M. Glass, M.J. Cardillo, *Springer Ser. Opt. Sci.*, vol. 76 (2000)
28. I. Assaid, D. Bosc, I. Hardy, J. Phys. Chem. B **108**, 2801–2806 (2004)
29. M. Shirai, W. Ma, M. Tsunooka, Eur. Polym. J. **29**, 913–918 (1993)
30. D. Stifter, H. Sitter, Appl. Phys. Lett. **66**, 679 (1995)
31. A. Andreev, G. Matt, C.J. Brabec, H. Sitter, D. Badt, H. Seyringer, N.S. Sariciftci, Adv. Mater. **12**, 629–633 (2000)
32. A. Tsumura, H. Koezuka, T. Ando, Appl. Phys. Lett. **49**, 1210 (1986)
33. T. Someya, T. Sekitani, S. Iba, Y. Kato, H. Kawaguchi, T. Sakurai, Proc. Natl. Acad. Sci. USA **101**, 9966–9970 (2004)
34. B. Crone, A. Dodabalapur, Y.Y. Lin, R.W. Filas, Z. Bao, A. LaDuca, R. Sarpeshkar, H.E. Katz, W. Li, Nature **403**, 521–523 (2000)
35. S. Kobayashi, T. Nishikawa, T. Takenobu, S. Mori, T. Shimoda, T. Mitani, H. Shimotani, N. Yoshimoto, S. Ogawa, Y. Iwasa, Nat. Mater. **3**, 317–322 (2004)
36. A. Salleo, M.L. Chabinyc, M.S. Yang, R.A. Street, Appl. Phys. Lett. **81**, 4383 (2002)
37. B.H. Hamadani, D.A. Corley, J.W. Ciszek, J.M. Tour, D. Natelson, Nano Lett. **6**, 1303–1306 (2006)
38. L.L. Chua, J. Zaumseil, J.F. Chang, E.C.W. Ou, P.K.H. Ho, H. Sirringhaus, R.H. Friend, Nature **434**, 194–199 (2005)
39. H. Klauk, U. Zschieschang, J. Pflaum, M. Halik, Nature **445**, 745–748 (2007)
40. C. Huang, H.E. Katz, J.E. West, Langmuir **23**, 13223–13231 (2007)
41. G. Horowitz, Adv. Mater. **10**, 365–377 (1998)
42. M. Marchl, A.W. Golubkov, M. Edler, T. Griesser, P. Pacher, A. Haase, B. Stadlober, M.R. Belegratis, G. Trimmel, E. Zojer, Appl. Phys. Lett. **96**, 213303 (2010)
43. Di Carlo, F. Piacenza, A. Bolognesi, B. Stadlober, H. Maresch, Appl. Phys. Lett. **86**, 263501 (2005)
44. S.D. Wang, T. Miyadera, T. Minari, Y. Aoyagi, K. Tsukagoshi, Appl. Phys. Lett. **93**, 043311 (2008)
45. A. Wang, I. Kymissis, V. Bulović, A.I. Akinwande, in *Electron Devices Meeting*, (IEEE Press, New York, 2004), pp. 381–384
46. A. Wang, I. Kymissis, V. Bulović, A.I. Akinwande, Appl. Phys. Lett. **89**, 112109 (2006)
47. H. Sakai, K. Konno, H. Murata, Appl. Phys. Lett. **94**, 073304 (2009)
48. P. Pacher, A. Lex, V. Proschek, H. Etschmaier, E. Tchernychova, M. Sezen, U. Scherf, W. Grogger, G. Trimmel, C. Slugovc, E. Zojer, Adv. Mater. **20**, 3143–3148 (2008)
49. S.K. Possanner, K. Zojer, P. Pacher, E. Zojer, F. Schürrer, Adv. Funct. Mater. **19**, 958–967 (2009)
50. K. Müllen, U. Scherf, *Organic Light Emitting Devices* (Wiley/VCH, Weinheim, 2005)
51. E.J. Cho, F.V. Bright, Anal. Chem. **73**, 3289–3293 (2001)
52. Z. Chen, Z. Zhang, T. Zhao, F. Bai, Y. Zhang, Z. Wang, Spectrochim. Acta, Part A, Mol. Biomol. Spectrosc. **57**, 419–422 (2001)
53. T. Griesser, T. Rath, H. Stecher, R. Saf, W. Kern, G. Trimmel, Chem. Mon. **138**, 269–276 (2007)
54. G. Weiquiang, D.J. Abdallah, R.G. Weiss, J. Photochem. Photobiol. A, Chem. **139**, 79–87 (2001)
55. M. Montague, R.E. Ducker, K.S.L. Chong, R.J. Manning, F.J.M. Rutten, M.C. Davies, G.J. Leggett, Langmuir **23**, 7328–7337 (2007)

56. S. Flink, F.C.J.M. van Veggel, D.N. Reinhoudt, J. Phys. Org. Chem. **14**, 407–415 (2001)
57. T. Höfler, A.M. Track, P. Pacher, Q. Shen, H.G. Flesch, G. Hlawacek, G. Koller, M.G. Ramsey, R. Schennach, R. Resel, Mater. Chem. Phys. **119**, 287–293 (2010)
58. T. Griesser, J. Adams, J. Wappel, W. Kern, G.J. Leggett, G. Trimmel, Langmuir **24**, 12420–12425 (2008)

Part III
Electrical Properties

Chapter 7
Effective Medium Approximation Theory Description of Charge-Carrier Transport in Organic Field-Effect Transistors

Ivan I. Fishchuk and Andrey Kadashchuk

Abstract In spite of a large amount of work having been done on the description of the charge-carrier transport in organic materials for last decades, the processes that determine charge transport in real organic electronic devices are still not completely understood, but their comprehension is definitely the key for designing materials with improved properties and, thereby, for a further increase in the performance of the devices. In this review, we will present an overview of the current achievements regarding theoretical description of the charge transport in disordered organic semiconductors with emphasis to charge transport behaviors at large carrier concentrations as realized in organic field-effect transistors (OFETs). A particular focus is given to the Effective Medium Approximation (EMA) analytical method, which was applied to describe the carrier-concentration-, electric-field- and temperature-dependent charge transport in organic materials that are used as active layers in OFET devices. In particular, we show that the establishment of the Meyer-Neldel rule (MNR) is a characteristic signature of hopping charge transport in a random system with variable carrier concentration irrespective of their polaronic character. The EMA model provides compact analytical relations which can be readily used for the evaluation of the energetic disorder parameter in organic semiconductor layers from experimentally accessible data on temperature dependent mobility in the OFET devices. The EMA theory is found to be in good agreement with previous computer simulations results and has been applied to describe recent experimental measurements of the temperature dependent electron mobility in a C_{60}-based OFET for different carrier concentrations and different lateral (source-drain) electric fields.

I.I. Fishchuk
Department of Theoretical Physics, Institute for Nuclear Research, National Academy of Sciences of Ukraine, Prospekt Nauki 47, 03680 Kyiv, Ukraine

A. Kadashchuk (✉)
Department of Photoactivity, Institute of Physics, National Academy of Sciences of Ukraine, Prospekt Nauki 46, 03028 Kyiv, Ukraine
e-mail: kadash@iop.kiev.ua

A. Kadashchuk
Department of Polymer and Molecular Electronics, IMEC, Kapeldreef 75, 3001 Leuven, Belgium

H. Sitter et al. (eds.), *Small Organic Molecules on Surfaces*,
Springer Series in Materials Science 173, DOI 10.1007/978-3-642-33848-9_7,

Finally, we compare our theory with alternative models suggested before to explain the MNR behavior for the charge transport in organic semiconductors.

7.1 Introduction

Organic semiconductor films offer a huge potential for the emerging flexible large-area electronics because they allow for low-cost device fabrication and a low-temperature processing of semiconductor layers compatible with flexible plastic substrates [1, 2]. In typical amorphous or polycrystalline organic films the charge carriers move much more slowly than in perfect molecular crystals because they hop among localized states that are distributed in space and energy. The charge-carrier mobility, μ, is thus a critical parameter for the operating speed of a device, notably, in an organic field-effect transistor (OFET). Therefore, apart from the endeavor to optimize the structure-property relations of organic functional layers, it is of paramount importance to improve the understanding of *conceptual premises* of the electrical transport mechanisms in realistic organic electronic devices.

It is believed that charge-carrier transport in disordered organic semiconductors occurs via incoherent thermally activated hopping [3–6] within a manifold of states commonly described by a Gaussian density-of-states (DOS) distribution of energetic width σ. Charge-carrier transport studies in such materials have most often been described for the last two decades within the framework of the Gaussian Disorder formalism, originally suggested by Bässler and coworkers [3]. Recently the formalism was further advanced to account for the charge-carrier concentration effects [7–12], and one should distinguish charge transport regimes at *small* and *high* carrier concentrations that can be realized in the same organic material. A notorious feature of a Gaussian-shaped DOS is that at *small carrier concentrations*, when charge carriers are non-interacting, the majority of equilibrated carriers mostly occupy weakly filled states well above the Fermi level. In this case, the equilibrium occupational DOS (ODOS) is also a Gaussian with width σ, but off-set from the center of the intrinsic DOS by an energy $\varepsilon_{\mathrm{eq}} = -\sigma^2/k_B T$. The charge transport in this case is controlled by carrier jumps from states around the energy level $\varepsilon_{\mathrm{eq}}$ to the so-called effective transport energy level ε_t (described below). Therefore at *low carrier concentration* the position of the Fermi level in case of an empty DOS is irrelevant for the charge-carrier mobility [3, 12]. This case is typically realized in Time-of-Flight (ToF) experiments to measure charge-carrier mobility in the bulk of organic semiconducting films [3, 4].

However, the conditions described above are no longer true at *high carrier concentrations* when the deep tail states of the DOS are completely filled by charge carriers and the Fermi level rises above the mean quasi-equilibrium energy level $\varepsilon_{\mathrm{eq}}$ [8–13]. At sufficiently high carrier densities (as in an organic thin-film transistor (OTFT) where the current is confined to a very thin conductive layer near the interface with the gate dielectric, and in chemically doped organic semiconductors) carrier jumps from the Fermi level dominate the charge-carrier transport giving rise to an Arrhenius-type $\ln(\mu) \propto T^{-1}$ temperature dependence of the mobility [12, 13] with a virtually constant (yet dependent on carrier concentration) activation energy. It was found that charge-carrier mobility in the same material can differ up to three orders of magnitude depending on whether the mobility is measured in a diode or OFET device geometry [7, 8, 10]. This demonstrates that the concentration dependence of the mobility must be taken into account to describe the charge transport in realistic organic electronic devices. The latter transport regime has recently been described within so-called Extended Gaussian Disorder Model (EGDM) using numerical computer simulations by Pasveer and Coehoorn [8, 9], which predicts an increase of the μ with increasing both charge-carrier concentration and electric field. This model was also corroborated by analytic theories which were first formulated for a zero-field limit [10–12] and recently extended for arbitrary electric fields [14, 15].

The disorder formalism was also invoked to explain the electric-field dependence of the charge-carrier mobility conventionally, as observed in disordered organic semiconducting materials. In contrast to perfect organic single crystals where the charge carrier mobilities are normally electric-field independent at room temperature [16, 17], in disordered organic semiconductors μ increases with electric field typically in a Poole-Frenkel (PF) fashion, $\ln \mu \propto F^{1/2}$ [3, 4], which is a consequence of charge hopping within the DOS distribution. The applied electric field tilts the DOS and thus lowers the average barrier height for energetic uphill jumps in the field direction. The initial Gaussian Disorder model (GDM) [3] predicts the $\ln \mu \propto F^{1/2}$ dependence yet for a rather high electric field only [3]. Subsequent work [18, 19] showed that by introducing spatial correlation of the energies of transport sites, experimentally observed PF-type dependence at lower fields is recovered. The electric-field dependence of μ is also predicted by the EGDM for a large charge-carrier concentration transport regime [20, 21].

In a number of experimental studies [22–24] it was commonly observed that charge-carrier mobility in OFET devices shows Arrhenius-type $\mu(T)$ temperature dependences which intersect at a given finite temperature T_0 when measured at different gate voltages (V_G), thus suggesting that the Meyer-Neldel rule (MNR) [25] is obeyed. The MNR is an empirical relation [25], originally derived from chemical kinetics, and describes the fact that enthalpy and entropy of a chemical reaction are proportional. More generally, it states that in a thermally activated process an increase of the activation energy E_a is partially compensated by an increase of the prefactor:

$$\mu = \mu_0 \exp\left(-\frac{E_a}{k_B T}\right) \tag{7.1}$$

where E_a is the activation energy, T is the absolute temperature, k_B is the Boltzmann constant. It is empirically found that the prefactor μ_0 increases exponentially with E_a:

$$\mu_0 = \mu_{\text{const}} \exp\left(\frac{E_a}{k_B T_{MN}}\right) \tag{7.2}$$

where μ_{const} is a constant prefactor and T_{MN} is the so-called Meyer-Neldel temperature. A combination of Eq. (7.1) and (7.2) gives the general form:

$$\mu = \mu_{\text{const}} \exp\left[-E_a\left(\frac{1}{k_B T} - \frac{1}{k_B T_{MN}}\right)\right]. \tag{7.3}$$

Equation (7.3) shows the MNR relation between the OFET charge-carrier mobility μ and the activation energy "E_a" which is, in the case of OFET measurements, gate voltage dependent. Equation (7.3) implies an isokinetic temperature $T = T_{MN}$ determined by the Meyer-Neldel energy $E_{MN} = k_B T_{MN}$, at which charge-carrier mobility values coincide in one value.

The aim of the present chapter is to review the current achievements regarding theoretical description of the charge-carrier transport in disordered organic semiconductors with particular attention on charge-carrier transport behavior at large carrier concentration as realized in organic field-effect transistors. Our consideration is focused on Effective Medium Approximation (EMA) analytic theory, which was applied to describe the charge-carrier concentration-, electric-field- and temperature-dependent charge-carrier transport in organic materials that are used as active layers in OFET devices. In particular, we show that the establishment of the Meyer-Neldel rule is a characteristic signature of hopping transport in a random system with variable charge-carrier concentration irrespective of their polaronic character. Finally we compare our theory with alternative models suggested before to explain the MNR for the charge-carrier transport in OFETs.

7.2 EMA Approach to Hopping Charge Transport at Large Charge-Carrier Concentrations

7.2.1 General EMA Theory Formulation

Recently Fishchuk et al. [14, 15] formulated an analytic theory which is able to describe the drift charge-carrier mobility in a disordered organic solid as a function of *carrier concentration*, *temperature*, and applied *electric field*, and is based on the EMA method using the concept of effective transport energy. A key point of this model compared to the previous EMA treatment [11, 12] is that it is extended for *arbitrary electric fields* and is able to describe consistently both the carrier-density and field dependences of charge-carrier mobility. Another important modification of the previous EMA formalism [15] is using the method of configurational averaging of hopping *transition times.* Initially suggested for zero-field and low-carrier concentration limits according to Ref. [26], it has been now generalized to calculate the drift mobility at finite electric field and for the high-carrier concentration transport regime.

Within this approach a disordered organic system is replaced by an effective three-dimensional (3D) manifold of localized sites with an average intersite distance $a = N^{-1/3}$, where N is the density of the localized states. The theory considers an energetically disordered organic system of localized states characterized by the DOS distribution $g(\varepsilon)$ in the framework of the EGDM [8, 11] which accounts for the dependence of the charge-carrier mobility on the relative carrier concentration n/N, where n is the density of charge carriers. Positional disorder is neglected.

In general, the effective drift hopping mobility μ_e in a random 3D hopping transport system under an applied electric field can be obtained as

$$\mu_e = ak_0 \frac{W_e^+ - W_e^-}{F} \tag{7.4}$$

where W_e^+ and W_e^- describe the effective jump rates along and opposite to the electric-field direction, respectively, for an arbitrary electric field $\mathbf{F} = \{F, 0, 0\}$. An additional coefficient k_0 emerges in Eq. (7.2) to include the generalized Einstein equation, as recently suggested by Tessler [27], relating the mobility and diffusion coefficient at arbitrary carrier concentration. This coefficient is essential at large carrier concentrations, while in the case of vanishing carrier density $k_0 \to 1$. Within the average-hopping-times method [26], the effective jump rates W_e^+ and W_e^- can be calculated using the effective transport energy ε_t level as

$$W_e^{\pm} = \langle \tau_{12}^{\pm} \rangle^{-1}, \quad \langle \tau_{12}^{\pm} \rangle = \frac{\int_{-\infty}^{\varepsilon_t} P(\varepsilon) \{W_{12}^{\pm}(\varepsilon_t, \varepsilon)\}^{-1} \, \mathrm{d}\varepsilon}{\int_{-\infty}^{\varepsilon_t} P(\varepsilon) \, \mathrm{d}\varepsilon}, \tag{7.5}$$

where W_{12}^+ and W_{21}^- are effective jump rates between two neighboring localized sites along- and opposite- to the electric-field direction, respectively. We use the Miller-Abrahams (MA) jump rate [28]

$$W_{12}^{\pm}(\varepsilon_t, \varepsilon) = W_0 \exp\left[-\frac{|\varepsilon_t - \varepsilon \mp eaF| + (\varepsilon_t - \varepsilon \mp eaF)}{2k_B T} \right] \tag{7.6}$$

to describe an elementary charge transfer under an applied eclectic field between sites with energy ε and ε_t being defined in the limit of zero field. Here $W_0 = \nu_0 \exp(-2r_t/b)$, where ν_0 is the attempt-to-escape frequency, r_t is the jump distance below the effective transport energy ε_t, and b is the localization radius of the charged site.

As was shown in [26, 29, 30], the major contribution to the drift time is determined by the upward hops of carriers from states located below the transport energy to the state ε_t. Therefore, configurational averaging of the hopping transition times in Eq. (7.5) has to be done over the energy distribution of empty localized states, viz. by using the function

$$P(\varepsilon) = g(\varepsilon)\left[1 - f(\varepsilon, \varepsilon_F)\right], \tag{7.7}$$

where $f(\varepsilon, \varepsilon_F)$ is given by the Fermi-Dirac statistics,

$$f(\varepsilon, \varepsilon_F) = \frac{1}{1 + \exp\left(\frac{\varepsilon - \varepsilon_F}{k_B T}\right)}. \tag{7.8}$$

The Fermi level ε_F position can be determined from the following transcendental equation for the carrier concentration n:

$$n = \int_{-\infty}^{\infty} \mathrm{d}\varepsilon g(\varepsilon) f(\varepsilon, \varepsilon_F). \tag{7.9}$$

The coefficient k_0 (cf. Eq. (7.4)) in this case is determined as

$$k_0 = 1 - \frac{\int_{-\infty}^{\infty} \mathrm{d}\varepsilon\, g(\varepsilon) f^2(\varepsilon, \varepsilon_F)}{\int_{-\infty}^{\infty} \mathrm{d}\varepsilon\, g(\varepsilon) f(\varepsilon, \varepsilon_F)}. \tag{7.10}$$

The DOS distribution $g(\varepsilon)$ is assumed be a Gaussian with width σ, which is generally accepted to be appropriate for disordered organic media

$$g(\varepsilon) = \frac{N}{\sigma\sqrt{2\pi}} \exp\left[-\frac{1}{2}\left(\frac{\varepsilon}{\sigma}\right)^2\right], \quad -\infty < \varepsilon < \infty. \tag{7.11}$$

A combination of Eq. (7.4) with Eqs. (7.5)–(7.10), and (7.11) gives the effective charge-carrier mobility μ_e as

$$\mu_e = \mu_0 k_0 \left(\frac{r}{a}\right)^2 \exp\left(-2\frac{r_t}{b}\right) \frac{(Y_e^+)^{-1} - (Y_e^-)^{-1}}{f}, \tag{7.12}$$

where

$$Y_e^{\pm} = \frac{\int_{-\infty}^{x_t} \mathrm{d}t\, \frac{\exp\{-\frac{t^2}{2} + \frac{1}{2}[|x_t - t \mp f| + (x_t - t \mp f)]x\}}{1 + \exp[-(t - x_F)x]}}{\int_{-\infty}^{x_t} \mathrm{d}t\, \frac{\exp\{-\frac{t^2}{2}\}}{1 + \exp[-(t - x_F)x]}}. \tag{7.13}$$

Here

$$Y_e^{\pm} = \frac{W_e^{\pm}}{W_0}, \quad f = \frac{eaF}{\sigma}, \quad x = \frac{\sigma}{k_B T}, \quad x_F = \frac{\varepsilon_F}{\sigma}, \quad x_t = \frac{\varepsilon_t}{\sigma}, \quad \mu_0 = \frac{ea^2 \nu_0}{\sigma}. \tag{7.14}$$

The concept of effective transport energy has been proved to be especially efficient for calculating the carrier mobility in disordered materials [29–31]. The effective transport energy ε_t in this method does not depend on the applied electric field F and hence for a Gaussian DOS distribution can be determined from the transcendental equation derived for zero-field mobility [11]

$$\frac{1}{\sqrt{2\pi}} \frac{\exp\left(-\frac{1}{2}x_t^2\right)}{1 + \exp[-(x_t - x_F)x]} \left\{\frac{1}{\sqrt{2\pi}} \int_{-\infty}^{x_t} \mathrm{d}t \frac{\exp\left(-\frac{1}{2}t^2\right)}{1 + \exp[-(t - x_F)x]}\right\}^{-\frac{4}{3}} = \frac{3}{2}\left(\frac{4\pi}{3B}\right)^{\frac{1}{3}} x \frac{b}{a}. \tag{7.15}$$

Here, the parameter $B = 2.7$ has been determined according to percolation criteria [31]. The factor r_t is calculated by

$$r_t = a\left\{\frac{4\pi}{3B} \frac{1}{\sqrt{2\pi}} \int_{-\infty}^{x_t} \mathrm{d}t \frac{\exp\left(-\frac{1}{2}t^2\right)}{1 + \exp[-(t - x_F)x]}\right\}^{-\frac{1}{3}}. \tag{7.16}$$

It should be noted that percolative effects have been considered in Ref. [31] not-rigorously in that the consideration was limited to the renormalization solely of the factor r_t. Since r_t and ε_t are quantities interrelated by definition, the accounting for the percolative effects must be done for the transport energy ε_t as well. A combination of Eqs. (7.15) and (7.16) takes this duly into account.

7.2.2 *Spatial Energy Correlations*

Energy correlations in organic disordered solids imply slowly varying static spatial fluctuation in the potential energy landscape and can arise due to charge-dipole [19] or charge-quadrupole interactions or fluctuations (inhomogeneity) in electronic polarization energy, resulting from molecular density fluctuations in an organic material due to microscopic regions that are under compression or dilation [32]. The energy correlation effects were mostly used to describe a $\ln\mu \propto \sqrt{F}$ Poole-Frenkel-type field dependence of charge-carrier mobility, typically observed in ToF measurements. The EGDM was originally suggested for energy *uncorrelated* systems and therefore it predicts a specific $\ln\mu \propto F$ field dependence [8, 9] that is in variance to available experimental data featuring a $\ln\mu \propto \sqrt{F}$ behavior in the experimentally accessible range of electric fields.

On the other hand, it is well established that a PF-type field dependence of the charge-carrier mobility can be reproduced over an extended interval of electric fields when some kind of correlated disorder is taken into account in the framework of the Correlated Disorder model (CDM) [19] or the Extended Correlated Disorder model (ECDM) [20, 21]. Conventional non-correlated disorder models ignoring the energy correlation effects, i.e. assuming that site energies are distributed independently, predict the PF-law only in a very narrow range of high electric fields ($F > 3 \times 10^5$ V/cm) [3]. Therefore, accounting for the energy correlation effects is necessary for an adequate description of the Poole-Frankel-type of charge-carrier mobility dependence on electric fields, as experimentally observed down to moderate electric fields. This aspect is especially relevant in the case of the OFET mobility measurements, because in this configuration measurements are done at rather *low lateral electric fields* owing to typically large transistor channel length used in OFET devices, if compared to other organic electronic devices, e.g. in sandwich-type diodes.

Generally, accounting for the energy correlated disorder effects could hardly be treated rigorously analytically, although it might be solved by numerical computer simulations [19, 20]. Therefore in our analytical treatment [15] we have used some key ingredients from the numerical simulations studies performed before within the CDM [19, 20] for a low carrier-concentration limit. The authors of this reference have shown [19, 20] that the size of an "energetic valley" (cluster) comprising many localized sites, scales algebraically with the depth of fluctuations. As suggested before [33], by using the simulations results of Parris et al. [34], one could account for the energy correlation effects by substituting the parameters $x = \sigma/k_BT$ and $f = eaF/\sigma$ (for non-correlated disordered system) by $x_c = \sigma_c/k_BT$ and $f_c = h_c\sqrt{x_c/2}$, respectively, where $h_c = \sqrt{eaF/\sigma_c}$. The presence of energy correlations results also in some flattening of the local potential energy landscape within larger scale energetic structures. Therefore the width of the so-called correlated DOS, σ_c, has to be somewhat smaller than the initial σ-value featuring in the non-correlated GDM approximation. Coehoorn and coworkers [20] have shown that one can use $\sigma_c \cong 0.83\sigma$ due to the charge-carrier mobility under the presence of the energy correlations. In the limit of zero field and zero charge carrier density the charge-carrier mobility follows a $\mu_e \propto \exp(-0.29x^2)$ temperature dependence instead of that $\mu_e \propto \exp(-0.44x^2)$ inherent for the GDM.

Another important consequence of the energy correlation effects on the field dependence of the charge-carrier mobility $\mu(F)$ at *high* carrier concentrations relevant for OFET operation has been recently demonstrated by Bouhassoune et al. [20] and Novikov [21]. Based on their computer simulations, they found that the typical size of the jump length governing the charge-carrier mobility, does not depend only on electric field *but also on carrier concentration*. The typical jump length within ECDM was found to decrease with increasing carrier concentration. This leads to a decrease of the slope S of the electric-field dependence of the charge-carrier mobility $\ln\mu$ vs $S \times \sqrt{F}$ compared to the slope S_0 in the case of zero-concentration limit $n/N \to 0$, as $S = S_0(1 - n/N)^m$, provided that the energy correlations have been taken into account. For a non-correlated disordered system within the EGDM the slope remains the same upon varying carrier concentration [21]. This effect can be accounted [15] by the following expressions for the temperature dependence of S_0 and m: $S_0 = -5.42 + 2.995(\sigma/k_BT) - 0.115(\sigma/k_BT)^2$ and $m = -9.69 + 10.81(\sigma/k_BT) - 0.905(\sigma/k_BT)^2$. In the range $2.0 < \sigma/k_KT < 5.0$ the calculated parameter S_0 perfectly agrees with the relevant slope $S_1 = 0.78[(\sigma/k_BT)^{3/2} - 2]$ obtained by numerical computer simulations [16] for the small-carrier-concentration limit.

Coulomb interactions between charge carriers might start to play an essential role at large carrier concentrations [21, 35], which is not accounted for in the present theoretical description [15]. The recent Monte-Carlo simulations by Zhou et al. [35] have, however, demonstrated that the effect of Coulomb interactions is not significant if the carrier density is below $n/N < 10^{-2}$. In accordance with that, charge-mobility computer simulations (accounting for Coulomb interactions) by Novikov [21] show that for charge-carrier concentrations $n/N \le 10^{-1}$ the charge-carrier mobility increases with increasing n/N exactly in the same manner as in the case of non-interacting carriers (cf. Ref. [8]). Since our theoretical model does not go beyond the charge-carrier density limit given above, the present consideration disregards the Coulombic interaction effects.

Thus, the charge-carrier mobility in disordered organic semiconductors can be calculated by Eq. (7.12)–(7.16) obtained within the EGDM approximation with accounting for energy correlation effects by substituting parameters σ, f by σ_c, f_c, respectively, as described above.

7.3 Calculations of the Charge-Carrier Concentration and the Electric-Field Dependences of the Charge Mobility

7.3.1 Dependence of the Charge Mobility on Carrier Concentration

In the following the EMA theory, formulated in the Sect. 7.2, will be used to calculate the charge-carrier mobility in organic semiconductor materials as a function of

Fig. 7.1
Carrier-concentration dependence of the charge-carrier mobility in an organic disordered material calculated by Eq. (7.17) at different temperatures at the zero electric-field limit (*solid curves*) using the transport energy concept [14]. Numerical results from Ref. [8] obtained for the same parameters are given by *symbols*

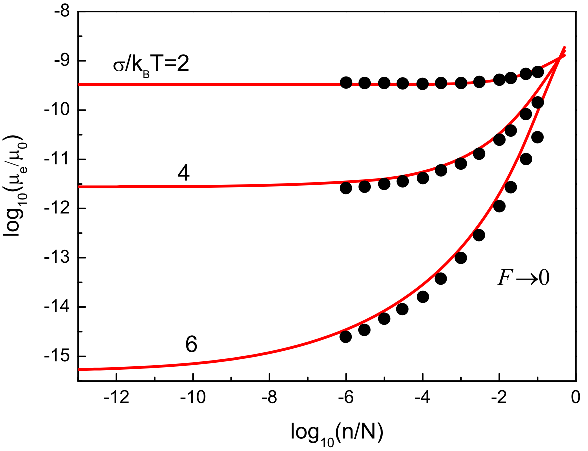

carrier concentration, applied *electric field* and *temperature*. The best verification of an analytical theory is a direct comparison with computer simulation results as the simulation actually solves the model as it stands while a real experiment can include processes not accounted for. Relevant computer simulations of the charge-carrier transport in a random organic solid have been reported in Ref. [8], assuming an energy *uncorrelated system* and neglecting variable hopping range transitions. In this approximation Eq. (7.12), obtained within the above described analytical EMA model, transforms to

$$\mu_e = \mu_0 k_0 \exp\left(-2\frac{a}{b}\right)\frac{Y_e^+ - Y_e^-}{f}, \tag{7.17}$$

where the values $Y_e^\pm$ are given by Eq. (7.13). To employ Eq. (7.17) for calculating the charge-carrier mobility one has to define the effective transport energy level x_t. Recently Fishchuk et al. [11] found that this level is given by the relation $x_t = -x/18$ (cf. Eqs. (7.15), (7.16)), which is valid for a broad range of charge carrier densities relevant for practical applications (except for extremely high densities) and the Miller-Abrahams jump rate.

Charge-carrier concentration dependences of the charge-carrier mobility μ_e calculated by Eq. (7.17) at zero-field limit ($F \to 0$) for different temperatures are presented in Fig. 7.1. The results of numerical simulations of the charge-carrier mobility by Pasveer et al. [8] for a system with an equivalent set of parameters are given by symbols in Fig. 7.1 for comparison. It is gratifying that the present EMA theory provides an excellent quantitative agreement with previous numerical simulation data for the charge-carrier mobility. The presented results are similar to calculations presented in Ref. [11] although they are obtained by a different calculation method. The presented EMA model describes also very well the results on concentration dependence of the electron mobility measured in C_{60} films presented in Fig. 8.7 in Chap. 8.

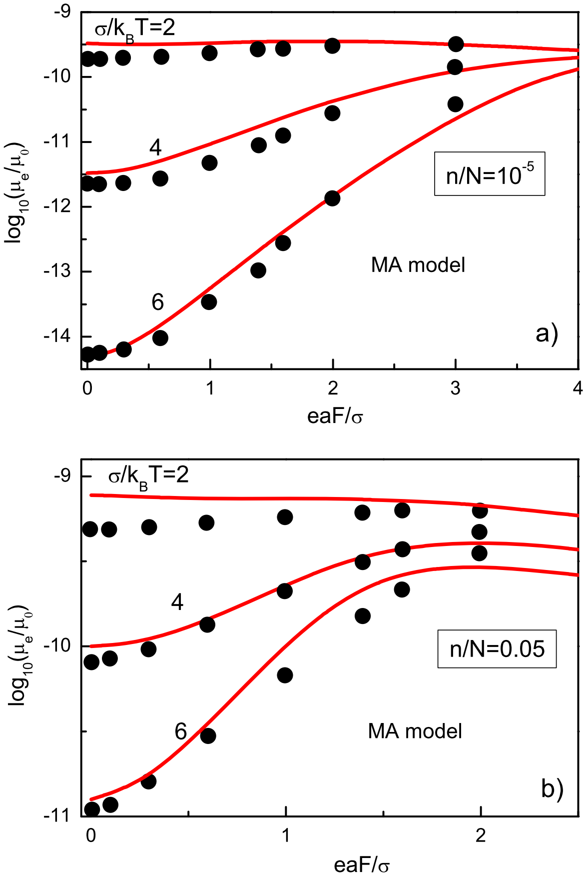

Fig. 7.2 (**a**) Electric-field dependences of the drift charge mobility calculated by Eq. (7.17) in *an energy uncorrelated* disordered system at various temperatures for relatively small $n/N = 10^{-5}$ and (**b**) large carrier concentration $n/N = 0.05$ (**b**) (*solid curves*) using the transport energy concept [14]. Numerical results from Ref. [8] for the same parameters are given by *symbols* for comparison

Thus, for energy *uncorrelated* hopping transport systems, calculations of the charge-carrier mobility by the present EMA theory are in excellent agreement with the relevant numerical computer simulation data.

7.3.2 Dependence of the Charge-Carrier Mobility on Electric Field

The approximated Eq. (7.17) can also be used to calculate the electric-field dependence of the charge-carrier mobility in *an energy uncorrelated* disordered system [14] and results could be compared which recent computer simulations [8] performed on the same system. Figure 7.2a shows the electric-field dependences of the charge-carrier mobility μ_e (solid curves) calculated by Eq. (7.17) at different temperatures for *relatively small* carrier concentration $n/N = 10^{-5}$, which is typically realized at OLED device operation. These dependences differ little from that obtained for a vanishing charge-carrier concentration ($n/N \to 0$). The field dependence of μ_e for *relatively large* carrier concentration $n/N = 0.05$, which is typically

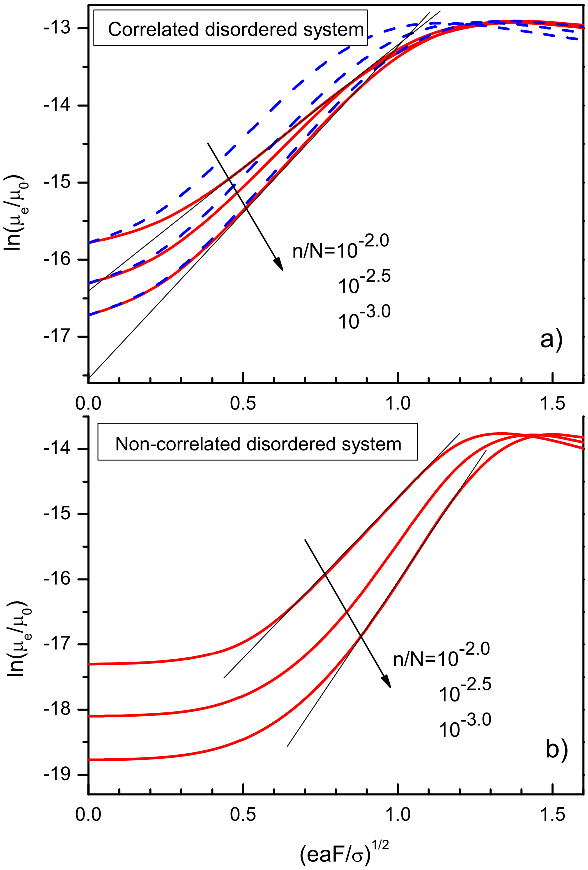

Fig. 7.3 (**a**) Poole-Frenkel plots of electric-field dependences of the effective charge-carrier mobility $\ln(\mu_e/\mu_0)$ calculated by Eqs. (7.12)–(7.16) for an *energy-correlated* organic disordered system for several carrier concentrations ($n/N = 10^{-3.0},\ 10^{-2.5}$, and $10^{-2.0}$) at $a/b = 5$, and $\sigma/k_BT = 5$ with accounting (see text) for the carrier concentration dependence of the jump length (*solid curves*) and ignoring the latter effect (*dashed curves*) [15]; (**b**) electric-field dependence of charge-carrier mobility calculated for a *non-correlated* disordered system

realized in a conductive channel of an OFET, calculated at different temperatures by Eq. (7.17) are depicted in Fig. 7.2b (solid lines). Symbols in Figs. 7.2a and 7.2b show results of the relevant recent computer simulations of Pasveer et al. [8] for comparison with the present theory [14] and one can see a good quantitative agreement between the EMA theory predictions and the numerical results for the same material parameters. One might note a slight decrease of the calculated mobility with increasing electric field at large temperatures (upper curves in Figs. 7.2a and 7.2b) while the numerical simulations show a slightly increasing/saturating mobility (symbols). This seemingly has no physical meaning and is due to a limitation of the present theoretical treatment at small σ/k_BT values at which the transport energy approximation becomes less accurate.

The electric-field dependences of the charge-carrier mobility $\mu(F)$ in *energy-correlated* organic disordered system can be calculated by the modified EMA theory described in Ref. [15] with accounting for the energy correlation effects as suggested in Sect. 7.2.2. The corresponding EMA calculation results are depicted in Fig. 7.3a in $\ln\mu \propto \sqrt{F}$ representation. The curves (solid lines) were calculated

Fig. 7.4 Poole-Frenkel plots of electric-field dependences of the effective charge-carrier mobility $\ln(\mu_e/\mu_0)$ in an organic disordered system calculated by Eqs. (7.12)–(7.16) at different temperatures with accounting for *energy correlations* for two carrier concentrations: $n/N = 10^{-1.5}$ (*upper branch*) and 10^{-5} (*lower branch*). $a/b = 5$

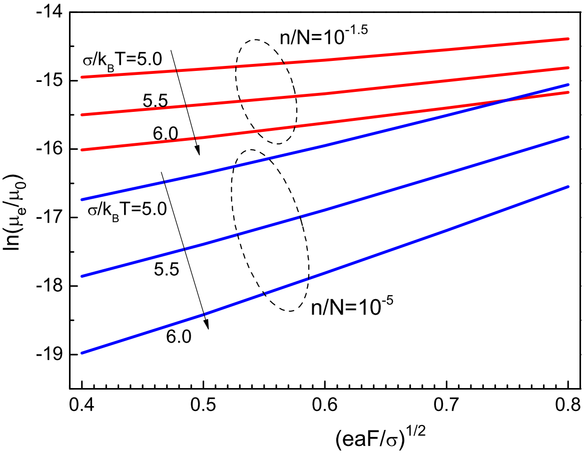

by Eqs. (7.12)–(7.16) for *different carrier concentrations* relevant to OFET operation, taking into account the dependence of the jump length on carrier concentration according to Ref. [20]. The same dependences were also calculated by ignoring the latter effect and are given for comparison (Fig. 7.3a, dashed curves). As one can see, the Poole-Frenkel field dependences are well reproducible in the range $0.4 < (eaF/\sigma)^{1/2} < 1.0$ for the considered charge-carrier concentrations and feature a clear decrease in the slope of the curves with increasing carrier concentration (Fig. 7.3a, solid lines), whereas the slope remains virtually the same if the carrier concentration dependence of the jump length is ignored (dashed curves in Fig. 7.3a). These analytically calculated dependences agree well with the relevant computer simulation results of Ref. [21]. Assuming representative material parameters for a disordered solid, viz. $\sigma = 0.07$ eV and $a = 1.4$ nm, one obtains a corresponding electric field range 8×10^4 V/cm $< F < 5 \times 10^6$ V/cm for which the PF-type field dependence is valid (shown by straight lines in Fig. 7.3a).

Figure 7.3b shows the electric-field dependences of the charge-carrier mobility, calculated with the same parameters as in Fig. 7.3a, but for an energy *non-correlated* organic disordered system. As one can see from Fig. 7.3b, a $\ln \mu \propto \sqrt{F}$ dependence (straight lines in Fig. 7.3b) is revealed for such a system but only within a narrower range of strong electric fields, consistent with previous computer simulations by Bässler and coauthors [3]. In the present study we used a representative ratio $a/b = 5$ for organic disordered semiconductors, which has extensively been employed before in Monte-Carlo simulations studies of the charge-carrier transport [3].

The electric-field dependences of the charge-carrier mobility calculated by Eqs. (7.12)–(7.16) for an *energy-correlated* system at different temperatures for a relatively small carrier density, $n/N = 10^{-5}$ and a very high carrier-density, $n/N = 10^{-1.5}$ are shown in Fig. 7.4. As one can see, a $\ln \mu \propto \sqrt{F}$ dependence of the charge-carrier mobility has been revealed at both carrier concentration regimes. It is basically similar to the Poole-Frenkel field dependences conventionally observed in the limit of low carrier concentrations, i.e. in time-of-flight (ToF) mobility measurements.

7.3.3 Concept of Strong Local Fields in Inhomogeneous Materials

In order to verify predictions of the present EMA theory, we compared the results of our analytical calculations with experimental results on charge-carrier mobility in a C_{60}-based OFET [36, 37]. Details of the experimental measurements are described in Chap. 8. First of all one has to rationalize the observed Poole-Frenkel field dependence of the OFET mobility upon applied lateral electric field as demonstrated by experimental measurements of the charge mobility as a function of the source-drain voltage (V_{SD}) (see Fig. 8.10 in Chap. 8).

Although the present analytic model [15], as well as previous computer simulation studies [20], does predict a PF-type dependence for the FET mobility, the major problem is that the experimentally observed field dependences are usually beyond the field range where the PF-law is predicted. Note that the established hopping transport models predict that μ should saturate at electric fields $F \leq 10^4$ V/cm [15, 20, 21]. Here we should emphasize that the average lateral electric field in OFET devices is usually relatively small, being of the order of 10^3 V/cm due to normally long transistor channels, while a Poole-Frenkel ($\ln(\mu_e) \propto \sqrt{F}$) dependence is predicted to occur at much higher fields—around $F \approx 10^5$ V/cm. Therefore neither available analytical theories nor computer simulations are able to reproduce the experimental observations even when the energy correlation effects are taken into account. To solve the puzzle, we propose that in multiple-grain organic films the OFET mobility is controlled not by the lateral field averaged over the transistor channel (as conventionally assumed), but rather by the much stronger effective local electric fields generated in such inhomogeneous media. The presence of strong local fields confined to grain boundaries was recently demonstrated by studying the surface electrostatic potential distributions along the transistor channel by scanning Kelvin probe measurements (SKPM) during OFET device operation in a polycrystalline organic semiconductor layer [38].

The strong inhomogeneity of lateral electric field in the conductive channel can be rationalized in terms of electrostatic screening due to different local conductivities within grains and at grain boundaries (GB). GBs are known to limit charge-carrier transport in polycrystalline films by establishing major potential barriers [39–41] between their more ordered domains. In such case the OFET conductive channel can be considered as a series of resistors whose resistance is controlled by the "microscopic" charge-carrier mobility. In the off-state the lateral field is homogeneous because the dielectric constant is virtually isotropic. However, upon applying a gate voltage to a channel with GB, charges start to accumulate in the channel, and instantaneously the density of accumulated charge carriers within an individual grain is redistributed along the *external* lateral-field (source to drain) direction: at one side of the grain it generates a locally increased charge concentration, and at the other side a reduced (or close to locally "depleted") charge density. This creates an *internal* lateral electric field within the individual grain which compensates the applied external field. This "charge-redistribution" effect stems from the *mobile* (not trapped) holes inside grains induced by the gate voltage (V_G), therefore termed here a charge *accumulation* (rather than trapping) process at the grain boundary. This

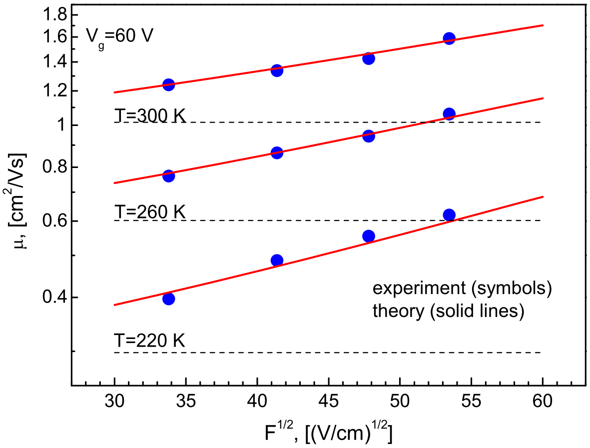

Fig. 7.5 Experimental (*symbols*) lateral-field dependence of the charge-carrier mobility measured in C_{60}-based OFETs at different temperatures [15] and theoretical fitting by Eqs. (7.12)–(7.16) (*solid lines*) with accounting for energy correlations and using the following set of parameters: $\sigma = 0.07$ eV; $a/b = 5$; $a = 1.4$ nm; $n/N = 0.05$ and $q = 256$. *Dashed curves* were calculated at $q = 1$, i.e. assuming a homogeneous lateral electric field

effect generates a high local electric field between the grains (i.e. at the GB), while the electric field inside the grains is screened. This would translate into an inhomogeneity of the lateral electric field. As long as the spatial extension of GB is much smaller than the average size of more ordered grains, the local fields could be much stronger than the average applied field.

The concept of inhomogeneous local fields can describe *quantitatively* the experimentally observed lateral-field dependence of the OFET mobility in C_{60}-based OFET devices by the extended EMA model as just these fields should be used in Eqs. (7.12)–(7.16) instead of the average one [15]. The barrier heights due to GB are subject to distribution over the film, therefore taking into account a huge variety of percolative passes present between the long source and drain electrodes, the charge transport on average could be considered as that occurring in an effectively random disordered system even though charge carriers may experience just a few crossings over GB in a particular percolative pass. Since the actual ratio between local field at the GB and the averaged field is not amenable to analytical treatment, we will introduce a phenomenological field magnification parameter $q \gg 1$ as a fitting parameter. Evidently the employment of the parameter q just results in a renormalization of the electric field F used in our calculations.

Figure 7.5 shows the lateral electric-field dependence of the OFET mobility $\log_{10}(\mu) \propto \sqrt{F}$ (symbols) measured [15] at different temperatures in C_{60} film and the theoretical values calculated with Eqs. (7.12)–(7.16) (solid lines) using $q = 256$. The presented results prove that the OFET mobility features a Poole-Frenkel-type dependence on lateral electric field in the range of very low electric fields of the order of $\sim 10^3$ V/cm (instead of $\sim 10^5$ V/cm predicted by previous studies) generated by the applied source-drain voltage (V_{SD}) over the conductive channel (length

35 µm) of the OFET device. The dashed curves in Fig. 7.5 were calculated assuming a homogeneous lateral electric field in the transistor channel and, as one can see, no electric-field dependence is expected within the range of such low electric fields. This justifies the critical role of strong local fields for the theoretical description of the electric-field dependence of the charge-carrier mobility in OFET structures.

7.4 Calculations of Temperature Dependence of the Charge-Carrier Mobility: Influence of Carrier Concentration and Electric Field

Temperature dependence of the hopping charge-carrier mobility is of particular interest as it bears on the fundamental nature of hopping charge transport in disordered organic semiconductors. In this section, using the above EMA analytical formalism we consider thoroughly the temperature dependence of the charge-carrier mobility in disordered organic solids at large carrier concentration transport regime relevant in organic field-effect transistors.

7.4.1 The Influence of the Carrier Concentration on $\mu(T)$ in Zero Electric-Field Limit (Meyer-Neldel Compensation Rule)

The effective drift mobility μ_e for any jump rate model can be calculated in zero-field limit using the generalized Einstein equation, which can be written as suggested recently by Tessler [27]

$$\mu_e = ek_0 r_t^2 W_e / k_B T, \tag{7.18}$$

where

$$W_e = \langle W_{12} \rangle. \tag{7.19}$$

To calculate W_e for arbitrary carrier-concentration n ($n < N$) one should account for a many-particle nature of the charge-carrier transport process by a proper choice of the energy distribution functions for starting- and target- states: $P(\varepsilon_1)$ and $Q(\varepsilon_2)$ function, respectively. For the intrinsic Gaussian DOS distribution $g(\varepsilon)$, the normalized $P(\varepsilon_1)$ distribution can be presented as

$$P(\varepsilon_1) = \frac{g(\varepsilon_1) f(\varepsilon_1, \varepsilon_F)}{\int_{-\infty}^{\infty} \mathrm{d}\varepsilon g(\varepsilon) f(\varepsilon, \varepsilon_F)}, \tag{7.20}$$

and the normalized $Q(\varepsilon_2)$ distribution as

$$Q(\varepsilon_2) = \frac{g(\varepsilon_2)[1 - f(\varepsilon_2, \varepsilon_F)]}{\int_{-\infty}^{\infty} \mathrm{d}\varepsilon g(\varepsilon)[1 - f(\varepsilon, \varepsilon_F)]}. \tag{7.21}$$

The effective drift mobility Eq. (7.18) at arbitrary concentration of charge carriers can also be calculated by employing the concept of the *effective transport energy*

ε_t which depends on temperature and carrier concentration. The effective transport energy level implies the energy of a target site to which most of localized carriers make thermally activated jumps and which does not depend on the energy of a starting state ε_1 when $\varepsilon_1 < \varepsilon_t$. This approach accounts for changing the jump distance with changing temperature in the two-site transitions. By employing this concept Eq. (7.22) reduces to

$$Q(\varepsilon_2) = \delta(\varepsilon_2 - \varepsilon_t). \tag{7.22}$$

Substituting Eqs. (7.6) at zero electrical field, (7.20) and (7.22) into Eq. (7.19), for the Miller-Abrahams jump rate model one obtains for an arbitrary carrier density

$$W_e = \frac{\int_{-\infty}^{\varepsilon_t} \mathrm{d}\varepsilon\, W(\varepsilon, \varepsilon_t) g(\varepsilon) f(\varepsilon, \varepsilon_F)}{\int_{-\infty}^{\varepsilon_t} \mathrm{d}\varepsilon\, g(\varepsilon) f(\varepsilon, \varepsilon_F)}, \tag{7.23}$$

where

$$W(\varepsilon, \varepsilon_t) = \nu_0 \exp\left(-2\frac{r_t}{b}\right) \exp\left(-\frac{\varepsilon_t - \varepsilon}{k_B T}\right), \tag{7.24}$$

here $r_t = r(\varepsilon_t)$ is the jump distance at and below the transport energy level ε_t. In Eq. (7.23) and further, only hopping transitions to the transport energy level from the states below the ε_t have been taken into account at the configuration averaging. Then Eq. (7.19) for the effective Miller-Abrahams jump rate can be rewritten as

$$W_e = \nu_0 \exp\left(-2\frac{r_t}{b}\right) \exp\left(-\frac{\varepsilon_t}{k_B T}\right) \frac{\int_{-\infty}^{\varepsilon_t} \mathrm{d}\varepsilon \exp\left(\frac{\varepsilon}{k_B T}\right) g(\varepsilon) f(\varepsilon, \varepsilon_F)}{\int_{-\infty}^{\varepsilon_t} \mathrm{d}\varepsilon\, g(\varepsilon) f(\varepsilon, \varepsilon_F)}. \tag{7.25}$$

Then one obtains the effective charge mobility

$$\mu_e = \mu_0 x k_0 \left(\frac{r_t}{a}\right)^2 \exp\left(-2\frac{r_t}{b}\right) \exp(-x x_t) \frac{\int_{-\infty}^{x_t} \mathrm{d}t \frac{\exp(-\frac{1}{2}t^2 + xt)}{1+\exp[x(t-x_F)]}}{\int_{-\infty}^{x_t} \mathrm{d}t \frac{\exp(-\frac{1}{2}t^2)}{1+\exp[x(t-x_F)]}}. \tag{7.26}$$

It should be noted that the effective transport energy concept is justified for a considerable degree of the energetic disorder, i.e. Eq. (7.15) is valid only at $\sigma/k_B T > 1$.

Here we limit our consideration of the charge-carrier transport to a region of relatively high temperatures only. For low temperature, charge-carrier transport is discussed in Ref. [12]. Figure 7.6a (thick curves) shows the calculated temperature dependences of the charge-carrier mobility, plotted in a $\ln(\mu_e/\mu_0)$ vs. $\sigma/k_B T$ representation for different charge-carrier concentrations assuming $a/b = 10$. The calculations are restricted to a temperature regime defined by $\sigma/k_B T \geq 3$. The Arrhenius-type of the $\mu(T)$ dependence indicates that the ODOS is virtually temperature independent. This is quite in contrast to the case of $n/N \to 0$ characterized by the non-Arrhenius-type temperature dependence $\ln(\mu_e/\mu_0) \propto (\sigma/k_B T)^2$, since in such a case charge-carrier transport is dominated by hopping from the equilibrium occupational DOS distribution which is temperature dependent as discussed in the introduction.

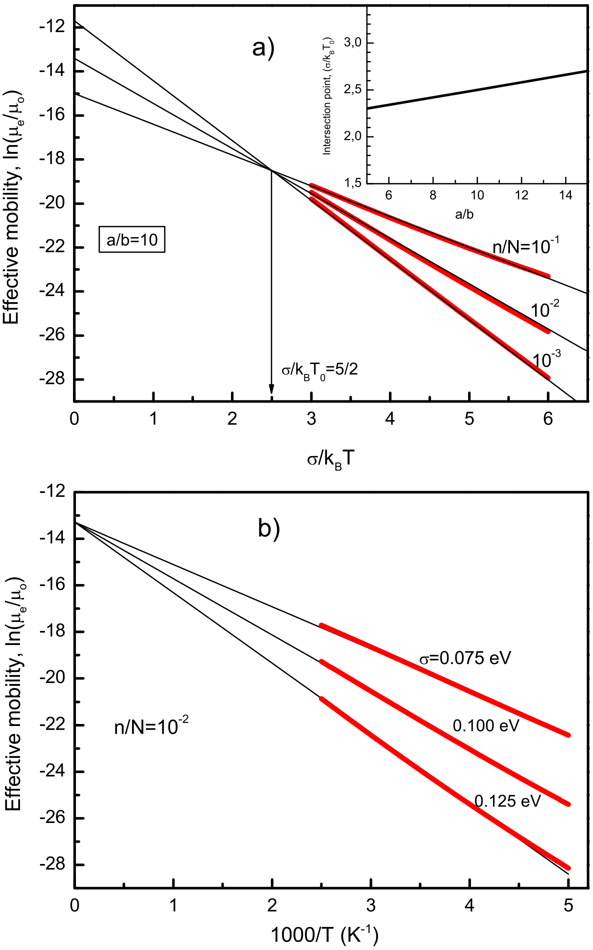

Fig. 7.6 (**a**) Dependence of effective charge mobility $\ln(\mu_e/\mu_0)$ on σ/k_BT at *different carrier concentrations* calculated by Eq. (7.26) (*red thick curves*) at $\sigma/k_BT \geq 3$ and $a/b = 10$. *Thin lines* present the approximation dependences calculated by approximated Eq. (7.28). The *inset* shows the intersection point σ/k_BT_0 vs. a/b ratio. (**b**) $\ln(\mu_e/\mu_0)$ vs. $1/T$ dependences at *different width of the DOS*, σ, calculated by Eq. (7.26) (*red thick curves*) at constant $n/N = 10^{-2}$ and $a/b = 10$. *Thin lines* present the approximation dependences calculated by approximated Eq. (7.28)

A remarkable result is that if one would—hypothetically—extend the above calculations to higher temperatures the asymptotes (thin lines) would intersect at finite temperature $T_0 \cong 2\sigma/5k_B$. Note that the Effective Medium approximation approach [11] does not allow us to present the results in closed analytic form. However, the calculated results including their (hypothetical) extension towards infinite T can be parametrized in terms of an approximate analytical equation for the charge-carrier mobility μ_e as a function of σ/k_BT, a/b, and n/N,

$$\begin{aligned}\mu_e = \mu_0 \exp\left[-2\frac{a}{b} + \frac{1}{2}\left(\frac{a}{b} - 7\right)\right] \\ \times \exp\left\{-\left[\frac{3}{40}\frac{a}{b} - \frac{1}{15}\frac{a}{b}\log_{10}\left(\frac{n}{N}\right)\right]\left(\frac{\sigma}{k_BT} - y_0\right)\right\},\end{aligned} \tag{7.27}$$

where $y_0 = 21/10 + (1/25)(a/b)$. It is appropriate for $8 < a/b < 12$ and for $10^{-3} \leq n/N \leq 10^{-1}$ which is relevant for OFET operation. The inset in Fig. 7.6a proves that the isokinetic temperature T_0, at which the $\ln(\mu) \propto T^{-1}$ graphs intersect, depends rather weakly on a/b. Rewriting Eq. (7.27) yields [12]

$$\mu_e = \mu_0 \exp\left[-2\frac{a}{b} + \frac{1}{2}\left(\frac{a}{b} - 7\right)\right] \exp\left[-E_a\left(\frac{1}{k_B T} - \frac{1}{k_B T_0}\right)\right], \tag{7.28}$$

where

$$E_a = \left[\frac{3}{40}\frac{a}{b} - \frac{1}{15}\frac{a}{b}\log_{10}\left(\frac{n}{N}\right)\right]\sigma; \qquad T_0 = \frac{E_{MN}}{k_B} = \frac{\sigma}{k_B y_0}. \tag{7.29}$$

It turns out that Eq. (7.28) can be extended to lower carrier concentrations, $10^{-5} \leq n/N < 10^{-3}$, if E_a is substituted by $E'_a = 0.85 E_a$.

As one can note, Eq. (7.28) is nothing else than the conventional Meyer-Neldel relation (cf. Eq. (7.3)), which has been verified by experiments on several OFET devices [22–24]. A certain compensation effect is evident from Eq. (7.28) that is the essence of the Meyer-Neldel rule. The prefactor of the charge-carrier mobility is a product of parameter μ_0 and the temperature independent exponential term in Eq. (7.28). Let us rewrite Eq. (7.28) as

$$\mu_e = \mu_{00} \exp\left(-\frac{E_a}{k_B T}\right), \tag{7.30}$$

where

$$\mu_{00} = \mu_0 \exp\left[-2\frac{a}{b} + \frac{1}{2}\left(\frac{a}{b} - 7\right) + \frac{E_a}{k_B T_0}\right]. \tag{7.31}$$

Then one can obtain

$$\ln\left(\frac{\mu_{00}}{\mu_0}\right) = -2\frac{a}{b} + \frac{1}{2}\left(\frac{a}{b} - 7\right) + \frac{E_a}{k_B T_0}. \tag{7.32}$$

Equation (7.32) relates the prefactor μ_{00} with the activation energy E_a, namely predicts a linear relationship between $\ln \mu_{00}$ and E_a exactly as suggested by the Meyer-Neldel rule.

If one assumes $\sigma = 0.1$ eV and $a/b = 10$, a typical value for organic disordered materials, then Meyer-Neldel energy $E_{MN} = k_B T_0 = 0.04$ eV is obtained, the value which indeed has been typically observed in many relevant experiments. The activation energy E_a (Eq. (7.29)) is temperature independent, varies linearly with σ and decreases with increasing charge-carrier concentration due to the shift of the Fermi level [11, 22] towards the effective transport energy level. An important consequence of the presented theoretical model is that it provides compact analytical relations (viz. Eqs. (7.28) and (7.29)) which can be readily used to evaluate material parameters like the effective carrier concentration from experimentally accessible data on temperature dependence of the mobility measured in organic semiconductor-based devices [12]. The width of the DOS $\sigma = 5E_{MN}/2$ can be obtained from the experimentally determined quantity E_{MN} assuming a typical value

$a/b = 10$, and Eq. (7.29) yields an estimate for the effective carrier concentration n/N from experimentally measured E_a at vanishing lateral electric field.

Interestingly, the structure of Eq. (7.28) predicts that if one extends a family of $\ln(\mu)$ vs. T^{-1} graphs calculated at variable E_a, i.e. by changing the active organic semiconductor layer, yet constant carrier concentration, to $T \to \infty$, they would intersect at $T \to \infty$ and not at a finite T_0 as MNR would imply. Figure 7.6b shows temperature dependences of the effective mobility calculated by Eqs. (7.26) (thick lines) and approximated Eq. (7.28) (thin lines) for different energetic disorder parameter σ, yet constant carrier concentration $n/N = 10^{-2}$ and $a/b = 10$. These calculations are restricted to moderately high temperatures. As is evident from Fig. 7.6b, the calculated temperature dependences in this case *do not show* any MNR compensation effect and intersect at infinite temperature. This is in disagreement with the conventional MNR that predicts a correlation between prefactor rate and activation energy regardless of how the change of E_a is accomplished, i.e. by either changing the width of the DOS itself or changing the degree of state filling.

7.4.2 The Influence of the Electric Field on $\mu(T)$

Let us consider first the electric field effect on $\mu(T)$ in the small-carrier-concentration transport regime. The charge-carrier mobility at low carrier concentration is conventionally measured by the ToF technique which has been applied extensively to study charge-carrier transport in disordered organic solids, for instance, in vapor-deposited molecular glasses [3, 4]. A small charge-carrier concentration is required in the ToF method to avoid any space charge inside the sample and, hence, a field redistribution, which can distort the ToF signal. To limit space charge effects it has become common practice to limit the number of migrating charge carriers to 5 % of the capacitor charge, i.e. ca. 10^{10} charge carriers/cm^2 in an electric field of 10^5 V/cm, equivalent to a concentration of $n = 10^{13}$ cm^{-3} in a 10 μm thick sample. Taking $N \approx 10^{22}$ cm^{-3} as a representative value for molecular glasses, one gets a relative carrier concentration of $n/N \approx 10^{-9}$. At such a carrier concentration the charge-carrier mobilitycharge-carrier mobility is independent on carrier concentration, because the Boltzmann statistic dominates the hopping transport; that is the reason why it is called the "small-carrier-concentration limit".

Figure 7.7a presents the temperature dependences of the charge-carrier mobility calculated by Eq. (7.12) with accounting for energy correlation effects at $n/N = 10^{-9}$ for different electric fields. As one could expect, the temperature dependences are nice straight lines in $\ln(\mu) \propto T^{-2}$ representation, which agrees with a number of previous theoretical and computer simulation data, as well as with ToF experiments [3, 4, 6]. The temperature dependences intersect at infinite temperature as suggested by the GDM [3], and no Meyer-Neldel rule (or Gill-type) behavior is observed. If one, hypothetically, re-plots these data in simple Arrhenius coordinates $\ln(\mu) \propto T^{-1}$ then, as one can see from Fig. 7.7b: (i) the calculated T-dependences are no longer perfect straight lines, and (ii) their formal extrapolation to higher temperatures shows an apparent intersect at some intermediate temperature T^*. It is

Fig. 7.7 (**a**) Temperature dependences of the charge-carrier mobility $\ln(\mu_e) \propto 1/T^2$ calculated by Eq. (7.12) for an energy correlated system at low carrier concentration $n/N = 10^{-9}$ parametric in electric fields and at $a/b = 5$; (**b**) the same data re-plotted in Arrhenius ($\ln(\mu_e) \propto 1/T$) representation

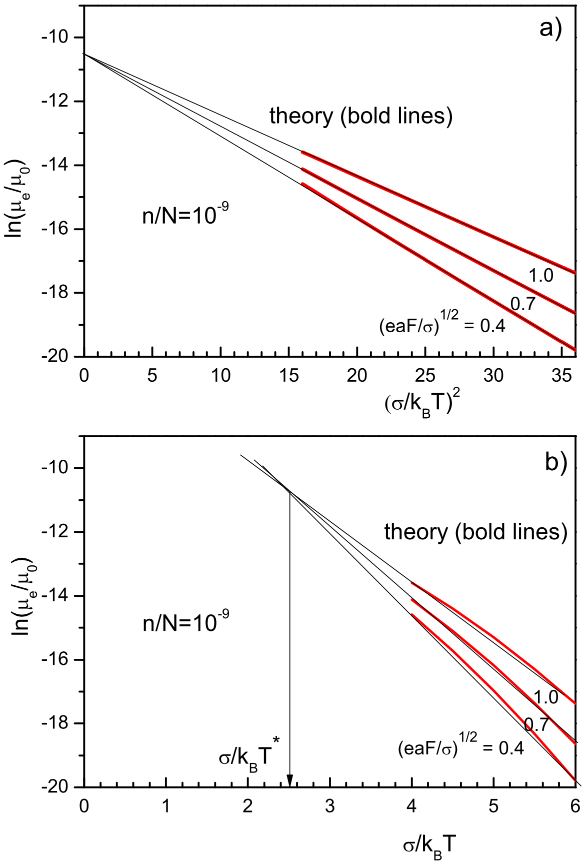

clear that the latter is just a simple consequence of *improper* $\ln(\mu) \propto T^{-1}$ representation of the data, which in reality feature a functionally different temperature dependence. Thus, as was already stated long ago [4], the Gill relation is not appropriate for the description of the ToF mobility data.

Meyer-Neldel Effect at Finite Electric Field

Hereafter we consider the transport regime of large carrier concentrations, which is typically realized in operating OFET devices. The temperature dependence of the charge-carrier mobility at large carrier densities differs from that for the low concentration limit. (i) It obeys an Arrhenius-type dependence as discussed already in literature [13, 14], and (ii) while in the low-carrier-density limit the slope of $\mu(T)$ depends on the electric field only, at large carrier densities it depends not only on the electric field but also on the carrier concentration.

Figure 7.8 (bold curves) depicts the temperature dependences of the charge-carrier mobility calculated by Eq. (7.12) at a *finite* constant electric field taking

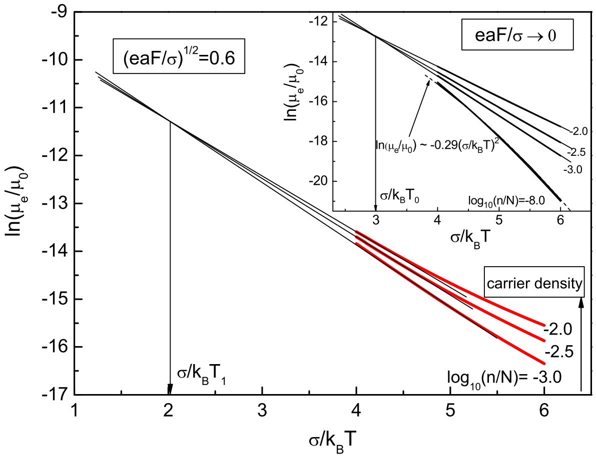

Fig. 7.8 Effective charge-carrier mobility $\ln(\mu_e/\mu_0)$ vs. σ/k_BT calculated by Eq. (7.12) at finite electric field ($(eaF/\sigma)^{1/2} = 0.6$) for different effective carrier concentrations (*bold curves*) [15] with accounting for energy correlations and $a/b = 5$. *Inset*: $\ln(\mu_e/\mu_0)$ versus σ/k_BT calculated at vanishing electric field ($F \to 0$) for different effective carrier concentrations (*bold curves*) with accounting for energy correlations

into account the energy correlations for several large carrier concentrations relevant for OFET operation [15]. The calculated curves are virtually straight lines in Arrhenius representation and their asymptotes, due to an extension to higher temperatures (given by thin lines in Fig. 7.8), intersect at some finite temperature T_1 featuring, thus, a MNR-type behavior.

Temperature dependences of the charge-carrier mobility for *vanishing electric field* ($F \to 0$) calculated by Eq. (7.12) taking into account the energy correlations at different carrier concentrations are shown in the inset in Fig. 7.8 for comparison. As one can see, the asymptotes to the calculated dependences at high carrier concentrations ($n/N = 10^{-3} \ldots 10^{-2}$) can be linearly extrapolated to higher temperatures and intersect at finite temperature T_0 demonstrating thus a MNR effect. These results agree well with our previous calculations of the temperature dependent charge-carrier mobility [12] parametric in carrier concentration using an EMA theory developed *solely* for zero-electric field and for a non-correlated energy disordered system. This verifies that the present extended EMA model at vanishing electric field provides virtually the same results regarding the MNR effect for $\mu(T)$ upon varying the charge-carrier concentration as the model described before [12]. At a very low carrier concentration, $n/N = 10^{-8}$, the calculated temperature dependence of the charge-carrier mobility can be perfectly fitted by the relation $\ln(\mu_e) \propto -0.29(\sigma/k_BT)^2$ (inset in Fig. 7.8, dashed curve) which was obtained before from computer simulation studies [34], which supports the adequateness of the present analytical theory. Thus, accounting for energy correlations does result in a notably weaker temperature dependence of the charge-carrier mobility as compared

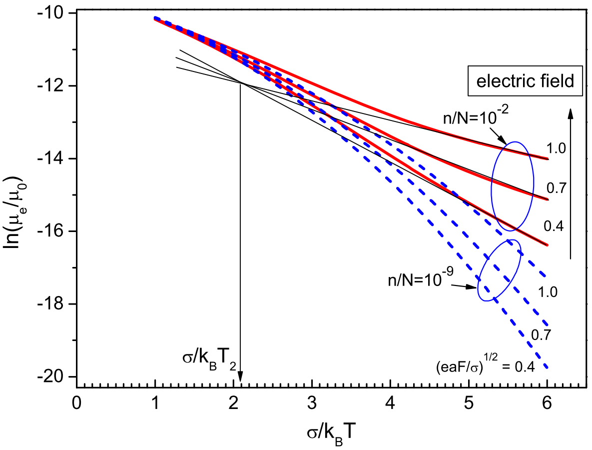

Fig. 7.9 Effective charge-carrier mobility $\ln(\mu_e/\mu_0)$ versus σ/k_BT calculated by Eq. (7.12) parametric in electric fields for two different carrier concentrations $n/N = 10^{-9}$ and 10^{-2} (*dashed and bold curves*, respectively) at $a/b = 5$ in an energy correlated hopping system [15]. The *thin straight lines* show extrapolation of the calculated dependences at $n/N = 10^{-2}$ to higher temperatures

to that for non-correlated systems, notably for the charge-carrier mobility at vanishing electric field.

Gill Effect upon Varying the Electric Field

Temperature dependences of the charge-carrier mobility parametric in electric fields calculated by Eq. (7.12) are plotted in Fig. 7.9 for two different carrier concentrations: $n/N = 10^{-9}$ (dashed curves, lower branch) and 10^{-2} (bold curves, upper branch). These dependences were calculated within the present EMA model over a broad temperature range up to very high temperatures not accessible for experiments. As one can see from Fig. 7.9, at large carrier concentration asymptotes to the calculated $\ln(\mu) \propto T^{-1}$ dependences extrapolated to higher temperatures (thin straight lines) intersect at finite temperature T_2 implying that the MNR-type behavior *upon varying the electric field* (also called in the literature the Gill effect, empirically found long ago [49]) is reproduced over a range of moderate temperatures. These EMA calculation results are in good agreement with recent experimental observation of the Gill effect in C_{60}-based OFET devices [36] (see also Fig. 8.13 in Chap. 8). No Gill-type behavior occurs for very low carrier concentration, ($n/N = 10^{-9}$) (Fig. 7.9), because the charge-carrier mobility in this regime does not follow $\ln(\mu) \propto T^{-1}$ dependence as was discussed above.

At very high temperatures the calculated charge carrier mobilities merge into the same value independent of electric field and carrier concentration (Fig. 7.9). This means that, according to the present treatment, there is no finite critical temperature above which the mobility would feature negative field dependence as follows from the empirical Gill equation. The reason for such $\mu(T)$ dependences is that at higher temperatures the average energy ε_m of the equilibrium occupational density-of-states (ODOS), which derives from $\varepsilon_m = \int_{-\infty}^{\infty} d\varepsilon \varepsilon g(\varepsilon) n(\varepsilon, \varepsilon_F) / \int_{-\infty}^{\infty} d\varepsilon g(\varepsilon) n(\varepsilon, \varepsilon_F)$, is no longer approached to the T-independent Fermi level ε_F, but is determined by the T-dependent shift of $\varepsilon_m \rightarrow$

$\varepsilon_0 = -\sigma^2/k_B T$ towards the transport energy [12] and, concomitantly, towards the center of the DOS.

The electric-field dependence of the charge-carrier mobility is consistent with the reasoning described above. Under the applied field the average equilibrium energy ε_m increases and, as a consequence, the charge-carrier mobility determined by jumps from ε_m to ε_t should also increase with increasing electric field. At high carrier concentrations the EGDM formalism predicts a lowering of the barrier height for carrier jumps, because ε_m increases not only as a result of an increase of the carrier density but also due to an increase of the applied electric field (lateral field in the case of an OFET).

7.5 The Influence of Electric Field on Meyer-Neldel Temperature and the Influence of Charge Carrier Concentration on Gill Temperature

For the sake of convenience, we discriminate between the isokinetic temperatures resulting from intersection of $\ln(\mu) \propto T^{-1}$ upon *varying carrier concentration* and that upon *varying applied electric field* and call them *Meyer-Neldel* (denoted as T_1) and *Gill* (denoted as T_2) temperature, respectively. Recent experimental studies [15, 37] have revealed (Fig. 8.15 in Chap. 8) that the Meyer-Neldel temperature and Gill temperature are not constant but depend on the electric field F and on charge-carrier concentration n/N, respectively. This effect can be well reproduced within the present extended EMA model [15] provided that the carrier concentration dependence of the jump length is taken into account according to Ref. [20] as described in Sect. 7.2.2. The latter is responsible for changing the slope of the field dependences of the OFET mobility with increasing carrier concentration shown in Fig. 7.3a. Figure 7.10a (solid curves) shows the MN-temperature T_1 versus applied electric field calculated within the present model. Apparently, the MN-temperature shifts to lower values with increasing F. The field dependence of T_1 can be parameterized as follows [15]:

$$\frac{k_B T_1}{\sigma} = 0.5 + 0.029\frac{eaF}{\sigma} - 0.039\left(\frac{eaF}{\sigma}\right)^2. \tag{7.33}$$

If the carrier concentration dependence of the jump length is ignored (cf. dashed lines in Fig. 7.3a) the $k_B T_1/\sigma$ quantity demonstrates just a very weak field dependence as given by the dashed curve 2 in Fig. 7.10a. Virtually no field dependence was found for $k_B T_1/\sigma$ calculated for an energy non-correlated disordered system and $k_B T_1/\sigma \cong 0.42$ (dashed curve 3 in Fig. 7.10a). Thus, we conclude that the change of the MN-temperature T_1 upon applied electric field results from the presence of energy correlation effects, namely, due to the decrease of the typical jump length with increasing carrier concentration.

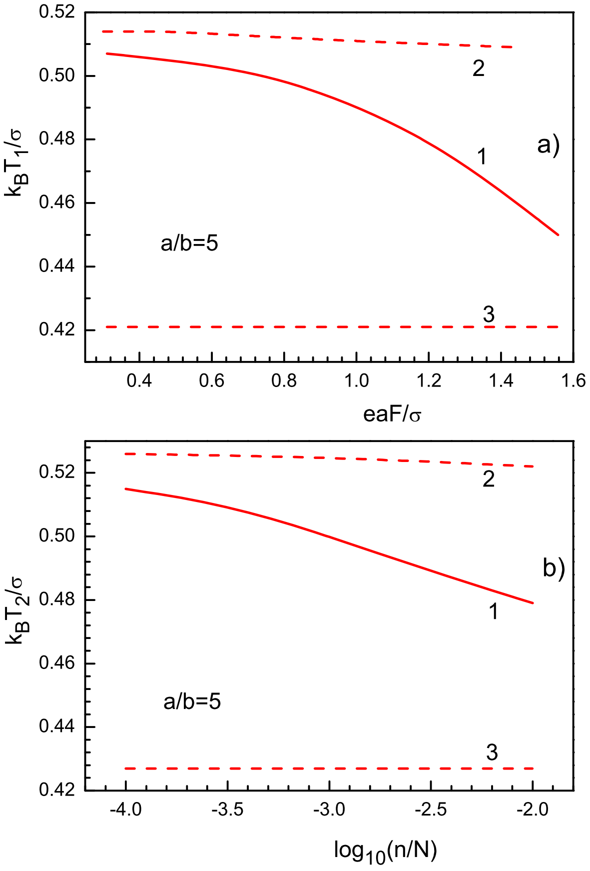

Fig. 7.10 Calculated dependence of MN-temperature T_1 (**a**) on electric field, and the dependence of Gill temperature T_2 on carrier concentration (**b**) for an energy correlated disordered hopping system [15]. The same dependences calculated upon ignoring the carrier concentration dependence of the jump length (*dashed curves 2*) and upon ignoring any energy correlation effects (*dashed curves 3*). See text for details

Along this line, the Gill temperature T_2 tends to decrease with increasing carrier concentration n/N (Fig. 7.10, solid curve 1). This carrier density dependence of T_2 can be well approximated by

$$\frac{k_B T_2}{\sigma} = 0.416 - 0.037 \log_{10}\left(\frac{n}{N}\right) - 0.0031\left[\log_{10}\left(\frac{n}{N}\right)\right]^2. \qquad (7.34)$$

We found that $k_B T_2/\sigma$ shows a very weak concentration dependence (dashed curve 2 in Fig. 7.10b) if the carrier concentration dependence of the typical jump length is ignored. If energy correlations are absent, the Gill temperature is virtually independent on carrier concentration and reaches the constant value $k_B T_2/\sigma \cong 0.43$ (Fig. 7.10b, dashed curve 3). Both $k_B T_1/\sigma \cong 0.42$ and $k_B T_2/\sigma \cong 0.43$ values obtained for an energy uncorrelated system are slightly smaller than that obtained when energy correlations are taken into account because the formers ignore the decrease of σ due to the presence of the energy correlations. It should be pointed out that the above calculated dependences for T_1 and T_2 are only relevant to the range of electric fields where the Poole-Frenkel-type field dependence holds.

The results of the above calculated charge-carrier mobility in the high-carrier-concentration limit can be used to estimate the energetic disorder parameter σ from experimental data basically by two different methods:

(1) Equation (7.33) allows calculating the parameter σ using the experimentally measured Meyer-Neldel temperature T_1 ($E_{MN} = k_B T_1$) at a given electric field F (within the field interval where a PF-type dependence is obeyed) according to the following relation:

$$\sigma = E_{MN} A \left(1 + \sqrt{1 + \left(\frac{eaF}{E_{MN}} \right)^2 \frac{0.078}{A^2}} \right), \quad A = 1 - 0.029 \frac{eaF}{E_{MN}}. \tag{7.35}$$

The present extended theoretical model [15] yields $E_{MN}/\sigma \cong 0.33$ for zero-field mobility. Previous theoretical treatment limited to the zero-field case [12], which disregarded the energy correlations and percolation effects, yielded a somewhat different ratio: $E_{MN}/\sigma \cong 0.40$.

(2) In its turn, the experimentally measured Gill temperature T_2 ($E_G = k_B T_2$) at a given high carrier concentration n/N (being determined by a gate voltage (V_G) in an OFET) can also be used to calculate σ by Eq. (7.34), which yields

$$\sigma = \frac{E_G}{0.416 - 0.037 \log_{10}\left(\frac{n}{N}\right) - 0.0031 \left[\log_{10}\left(\frac{n}{N}\right)\right]^2}. \tag{7.36}$$

To use Eq. (7.36) one has, however, to know the effective carrier concentration in a thin conductive channel of an OFET, which demonstrates a highly non-uniform distribution—strongly decreasing from the semiconductor/insulator interface into the bulk [42].

Thus, the first of the above-mentioned methods seems to be more appropriate for estimating the energetic disorder parameter σ from experimental data. A big advantage of the present extended theoretical model is that it *does not require an extrapolation* of experimental data to zero electric field. It allows fitting of experimental data, obtained at a given (not too low) electric field, in order to evaluate material parameters of organic semiconductors.

Finally, we should note that the above consideration suggests that the MN and Gill energies are inherently interrelated in disordered organic semiconductors. Indeed, combining Eqs. (7.33) and (7.34) one obtains

$$\frac{E_G}{E_{MN}} \equiv \frac{T_1}{T_2} = \frac{0.416 - 0.037z - 0.0031z^2}{0.5 + 0.029h - 0.039h^2}, \tag{7.37}$$

where $z = \log_{10}(n/N)$ and $h = eaF/\sigma$, for $-4 \le z \le -2$ and $0.3 \le h \le 1.6$. Figure 7.11 presents a 3D plot of the ratio E_G/E_{MN} upon carrier concentrations and applied electric fields calculated by Eq. (7.37).

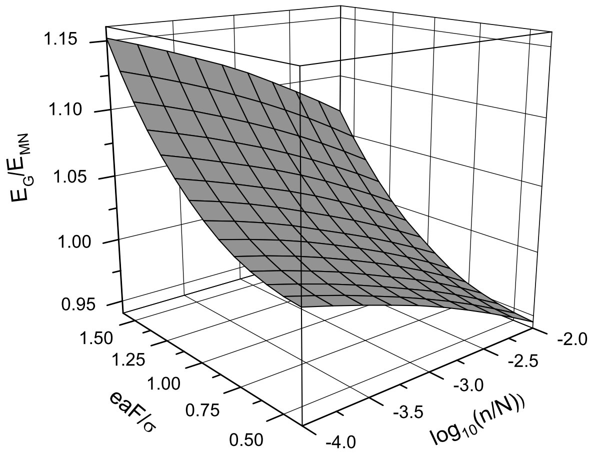

Fig. 7.11 Ratio of E_G/E_{MN} calculated by Eq. (7.37) for different electric fields and carrier concentrations [15]

It is important to note that according to the presented EMA model the MN- and Gill-energies are interrelated but they are not identically equal—as can be seen from Fig. 7.11, E_{MN} and E_G values coincide only at certain electric fields and carrier concentrations.

7.6 Concluding Remarks on the Comparison of Different Models for the MNR in OFETs

In this chapter we have demonstrated that the establishment of the MNR is a characteristic signature of conventional hopping charge transport in a disordered organic system with variable carrier concentration and can be rationalized within the recently suggested analytic EMA theory [11, 12, 15] based on disorder formalism, which was applied to describe the observed MNR behavior in C_{60}-based OFETs as shown in Chap. 8. The presented theoretical model premised a Gaussian DOS distribution and Miller-Abrahams jump rate, and it ignores polaronic effects. It attributes the MNR behavior to disorder and predicts that the MNR energy E_{MN} in organic semiconductors is directly related to the width of the Gaussian DOS, σ, providing thus a method for evaluating the amount of energetic disorder in the material. An important experimental verification of the suggested model is that the MNR behavior for the OFET mobility is clearly observed in C_{60} films (see Chap. 8), i.e. in a system where polaron effects are negligible due to a very weak electron–phonon coupling found for this material [43], which is shown to be inversely proportional to the number of π-bonded atoms [43]. Indeed, C_{60} single crystals are normally characterized by a virtually temperature independent mobility [44], whereas polaron transport (Holstein polaron model) does require an activation energy equal to the half of the polaron binding energy [45]. Thus polaron formation does not necessarily need to be involved to rationalize the MNR phenomenon.

Let us compare the presented EMA model by Fishchuk et al. [12, 15] with alternative models suggested before to explain the MNR phenomenon in different systems. The so-called multiexcitation entropy (MEE) model by Yelon and Movaghar [46, 47] was conventionally used to explain the Meyer-Neldel rule for thermally activated processes in general and it predicts a correlation between the prefactor rate and the activation energy E_a *regardless of how the change of* E_a *is accomplished.* The latter is in clear disagreement with the experimental observation that the MNR effect for the temperature dependences of the charge-carrier mobility in C_{60} films arises upon varying the carrier concentration, but not regarding varying the width of the DOS (cf. Figs. 8.11 and 8.19a in Chap. 8). As is demonstrated in Fig. 7.6b, the EMA calculated temperature dependences in the latter case do not show any MNR compensation effect and intersect at the infinite temperature [12]. This implies that for the OFET charge mobility there is in fact no genuine correlation between the prefactor and the Arrhenius factor that arises from activated jumps, and therefore the *MNR phenomenon in these materials is an apparent rather than true one*, exactly as predicted by the EMA theory of Fishchuk et al. [12]. Another drawback of the above MEE model is that it is not able to rationalize both the experimentally observed electric-field dependence of the Meyer-Neldel temperature as well as the carrier concentration dependence of the Gill temperature, because these models predict that MN and Gill temperatures are the same, in contradiction to experimental results shown in Figs. 8.15a and 8.15b Chap. 8. On the other hand, the suggested disorder-based EMA model can explain the phenomena mentioned above (Fig. 7.11) and provides a qualitative fit of experimental data (solid lines in Figs. 8.15a and 8.15b Chap. 8). Further, the shift in the Mayer-Neldel energy was found to clearly correlate with energetic disorder in C_{60} films grown at different growth conditions, which is in excellent agreement with the predictions of the above EMA theory (cf. Fig. 8.18 in Chap. 8). In contrast, the MEE model by Yelon and Movaghar [46, 47] neglects the inherent energetic disorder in these materials and therefore cannot rationalize the observed significant change in the MNR energy with changing film morphology. Besides, this model is unable to account for the carrier concentration effects on charge mobility.

Moreover, the MEE model predicts that the exponential increase of the prefactor with increasing activation energy (to provide MNR behavior) can only occur at large values of the activation energies $E_a \sim 1$ eV [46]. In this case the Debye energy $\hbar\omega_D \ll E_a$, so the thermal activation process can only occur via multiphonon excitations, which results in an exponential increase of the number of different activation paths and consequently in an exponential increase of the prefactor with increasing E_a. This can be interpreted also in terms of increasing entropy S, i.e. $S \propto E_a$. For two-site approximation in Refs. [46, 47] with a fixed difference in site energies $\varepsilon_2 - \varepsilon_1 = E_a$ the MNR behavior arises as a result of multiphonon activated transitions, while no such a behavior is expected for single phonon transitions. In the latter case there is just a single activation path that cannot lead to an exponential increase of the prefactor, which implies that the MNR effect is not expected for the Miller-Abrahams transport in the framework of the MEE model suggested before [46, 47]. On the other hand, the activation energies of the charge mobility in C_{60}-based OFETs are found to be considerably smaller (a few tens of eV) than that required by the MEE model, which in combination with negligible polaron effects in this material justifies the Miller-Abrahams jump rate approximation. The puzzle can be solved if one accounts for disorder effects and considers a random system with a Gaussian DOS distribution of site energies where a charge carrier experiences a large number of hops between sites with *different energies* before it reaches a collecting electrode. This is just the hopping transport within a manifold of localized states distributed in energy, which gives rise to the MNR effect for the Miller-Abrahams hopping transport regime as recovered by analytical EMA calculations [12] and also confirmed by computer simulations [8]. In this case an increase of E_a can also be associated with increasing entropy S, so that from $\mu_1 = \mu_0 \exp(S/k_B)$ [47] it follows that the entropy is given by $S = E_a/T_0$ and it depends on the energetic disorder parameter σ, as $E_a \propto \sigma$ according to Eq. (7.29). Experimental data on E_a and T_0 can provide an estimate for the entropy S and for its dependence on charge-carrier concentration (gate voltage). With increasing charge-carrier concentration the part of the DOS between Fermi level and the effective transport energy level becomes more narrow, which is equivalent to some ordering of the system and consequently to reducing entropy.

Finally, it should be noted that recently Emin [48] advanced an adiabatic polaron model that considers carrier-induced softening of the vibrations upon electron motion and includes the Fröhlich long-range polaron approach, and showed that this conditions bring up the MNR and Poole-Frenkel-type behavior for the charge mobility. Although this model recovers the above behaviors as good as the Fishchuk theory [12, 15], it seems to be irrelevant for the charge-carrier transport in C_{60}-based OFETs due to its contradictions and/or fails to explain a number of other essential experimental observations listed here.

1. As the Emin model ignores energy disorder, it clearly fails to explain the dependence of the charge-carrier mobility on carrier concentration (on V_G) in OFETs because the activation energy of the charge mobility is assumed to be determined solely by polaron formation and no tail state filling is expected within this approach. There is no charge-carrier concentration factor in this model.
2. For the above reason the MNR effect in OFETs *regarding changing the gate voltage* cannot be reproduced at all by the Emin model, because the model does not predict the dependence of the activation energy on V_G. In fact, the Emin model was suggested for the ToF mobility, i.e. for a very low carrier concentration transport regime.
3. Emin's theory predicts that the characteristic Meyer-Neldel temperature $T_{MN} \equiv t/k_B$ is determined by the electron-transfer energy t. Therefore, to rationalize an experimentally observed strong decrease of T_{MN} from 408 K to 250 K in C_{60}-films grown at substrate temperatures T_{sub} increasing from room temperature to $T_{\text{sub}} = 250$ °C, one has to assume a strong increase of average intermolecular distances in such C_{60} films because the Emin model relates the change in parameter t to the change of intermolecular distance in material. This would imply considerably less dense C_{60} films grown at $T_{\text{sub}} = 250$ °C compared to

those grown at room temperature, which sounds highly unrealistic especially because such films are known to have better crystallinity and should be better packed.

4. The Fröhlich polaron approach implemented in Emin's model requires a polar medium that is difficult to justify for C_{60}-based OFET structures with nonpolar BCB dielectric layers.
5. The Emin model explains neither a weakening of the Poole-Frenkel field dependence in the same material at larger carrier concentration, which was clearly observed by comparing OFET and CELIV charge carrier mobilities (see Fig. 7.8a), nor the electric-field dependence of T_{MN} experimentally found in C_{60}-based OFET (Fig. 7.11a).
6. Finally, the Emin model fails to explain why the charge mobility in C_{60} crystals is temperature independent [44] and thus featuring no MNR effect, while the temperature dependent charge-carrier transport is typically observed in deposited thin C_{60} films. Ignoring the energy disorder in Emin model should result in identical charge transport properties in both cases, which is in clear contradiction to experiment.

Therefore we have to conclude that the Emin model is not appropriate to describe the presented experimental results on the charge-carrier transport in C_{60} films. The temperature dependent charge-carrier mobility measured at different carrier concentrations and electric fields in C_{60} films of different morphology can be consistently described within the EMA theory of Fishchuk et al. [12, 15, 50] based solely on disorder arguments without necessity to invoke polaron formation. Nevertheless, we want to emphasize that our approach does not exclude polaron formation in organic solids at all; the polaron effects are certainly present and might be readily incorporated into the present Gaussian disorder model via employing the polaron jump rate and the MNR behavior retains.

Acknowledgements The research was supported by the ÖAD Project UA 10/2011, by the European Projects POLARIC (FP7-247978), by the State Agency on Science, Innovations and Informatization of Ukraine under the project No. M/283-2011, by the Science & Technology Center in Ukraine under the contract No. 5258, and by the NAS of Ukraine via the program of fundamental research on nanophysics (project No. 1/10-H-23K). The authors gratefully acknowledge valuable collaboration with Prof. N.S. Sariciftci, Prof. H. Sitter, Prof. J. Genoe, Prof. P. Heremans, and Prof. H. Bässler.

References

1. H. Klauk, *Organic Electronics: Materials, Manufacturing and Applications* (Wiley/VCH, Weinheim, 2006)
2. M. Berggren, D. Nilsson, N.D. Robinson, Nat. Mater. **6**, 3–5 (2007)
3. H. Bässler, Phys. Status Solidi, B Basic Res. **175**, 15 (1993)
4. P.M. Borsenberger, D.S. Weiss, *Organic Photoreceptors for Xerography* (Dekker, New York, 1998)
5. P.W.M. Blom, M.C.J.M. Vissenberg, Mater. Sci. Eng. **27**, 53 (2000)

6. V.I. Arkhipov, I.I. Fishchuk, A. Kadashchuk, H. Bässler, in *Semiconducting Polymers: Chemistry, Physics and Engineering*, ed. by G. Hadziioannou, G. Malliaras, 2nd edn. (Wiley/VCH, Weinheim, 2007)
7. C. Tanase, E.J. Meijer, P.W.M. Blom, D.M. deLeeuw, Phys. Rev. Lett. **91**, 216601 (2003)
8. W.F. Pasveer, J. Cottaar, C. Tanase, R. Coehoorn, P.A. Bobbert, P.W.M. Blom, D.M. de Leeuw, M.A.J. Michels, Phys. Rev. Lett. **94**, 206601 (2005)
9. R. Coehoorn, W.F. Pasveer, P.A. Bobbert, M.A.J. Michels, Phys. Rev. B **72**, 155206 (2005)
10. V.I. Arkhipov, P. Heremans, E.V. Emelianova, G.J. Adriaenssens, H. Bässler, J. Phys. Condens. Matter **14**, 9899–9911 (2002)
11. I.I. Fishchuk, V.I. Arkhipov, A. Kadashchuk, P. Heremans, H. Bässler, Phys. Rev. B **76**, 045210 (2007)
12. I.I. Fishchuk, A.K. Kadashchuk, J. Genoe, M. Ullah, H. Sitter, T.B. Singh, N.S. Sariciftci, H. Bässler, Phys. Rev. B **81**, 045202 (2010)
13. N.I. Craciun, J. Wildeman, P.W.M. Blom, Phys. Rev. Lett. **100**, 056601 (2008)
14. I.I. Fishchuk, A. Kadashchuk, V.N. Poroshin, H. Bässler, Philos. Mag. **90**, 1229 (2010)
15. I.I. Fishchuk, A. Kadashchuk, M. Ullah, H. Sitter, A. Pivrikas, J. Genoe, H. Bässler, Phys. Rev. B **86**, 045207 (2012)
16. W. Warta, N. Karl, Phys. Rev. B **32**, 1172 (1985)
17. W. Warta, R. Stehle, N. Karl, Appl. Phys. A, Solids Surf. A **36**, 163–170 (1985)
18. Y.N. Gartstein, E.M. Conwell, Chem. Phys. Lett. **245**, 351–358 (1995)
19. S.V. Novikov, D.H. Dunlap, V.M. Kenkre, P.E. Parris, A.V. Vannikov, Phys. Rev. Lett. **81**, 4472 (1998)
20. M. Bouhassoune, S.L.M. van Mensfoort, P.A. Bobbert, R. Coehoorn, Org. Electron. **10**, 437 (2009)
21. S.V. Novikov, Phys. Status Solidi C **5**, 740 (2008)
22. E.J. Meijer, E.J. Meijer, M. Matters, P.T. Herwig, D.M. de Leeuw, T.M. Klapwijk, Appl. Phys. Lett. **76**, 3433 (2000)
23. E.J. Meijer Ph.D. thesis. Technical University of Delft (2003)
24. J. Paloheimo, H. Isotalo, Synth. Met. **55**, 3185 (1993)
25. W. Meyer, H. Neldel, Z. Tech. Phys. **18**, 588 (1937)
26. S.D. Baranovskii, H. Cordes, F. Hensel, G. Leising, Phys. Rev. B **62**, 7934 (2000)
27. Y. Roichman, N. Tessler, Appl. Phys. Lett. **80**, 1948 (2002)
28. A. Miller, E. Abrahams, Phys. Rev. **120**, 745 (1960)
29. V.I. Arkhipov, P. Heremans, E.V. Emelianova, G.J. Adriaensses, H. Bässler, Appl. Phys. Lett. **82**, 3245 (2003)
30. V.I. Arkhipov, E.V. Emelianova, P. Heremans, H. Bässler, Phys. Rev. B **72**, 235202 (2005)
31. O. Rubel, S.D. Baranovskii, P. Thomas, S. Yamasaki, Phys. Rev. B **69**, 0.14206 (2004)
32. S.V. Rakhmanova, E.M. Conwell, Appl. Phys. Lett. **76**, 3822 (2000)
33. I.I. Fishchuk, D. Hertel, H. Bässler, A.K. Kadashchuk, Phys. Rev. B **65**, 125201 (2002)
34. P.E. Parris, D.H. Dunlap, V.M. Kenkre, Phys. Status Solidi, B **218**, 47 (2000)
35. J. Zhou, Y.C. Zhou, J.M. Zhou, C.Q. Wu, X.M. Ding, X.Y. Hou, Phys. Rev. B **75**, 153201 (2007)
36. A. Pivrikas, M. Ullah, H. Sitter, N.S. Sariciftci, Appl. Phys. Lett. **98**, 092114 (2011)
37. M. Ullah, A. Pivrikas, I.I. Fishchuk, A. Kadashchuk, P. Stadler, C. Simbrunner, N.S. Sariciftci, H. Sitter, Appl. Phys. Lett. **98**, 223301 (2011)
38. X. Li, A. Kadashchuk, I.I. Fishchuk, W.T.T. Smaal, G. Gelinck, D.J. Broer, J. Genoe, P. Heremans, H. Bässler, Phys. Rev. Lett. **108**, 066601 (2012)
39. L.C. Teague, B.H. Hamadani, O.D. Jurchescu, S. Subramanian, J.E. Anthony, T.N. Jackson, C.A. Richter, D.J. Gundlach, J.G. Kushmerick, Adv. Mater. **20**, 4513–4516 (2008)
40. G. Horowitz, M.E. Hajlaoui, R. Hajlaoui, J. Appl. Phys. **87**, 4456 (2000)
41. L.G. Kaake, P.F. Barbara, X.-Y. Zhu, J. Phys. Chem. Lett. **1**, 628–635 (2010)
42. C. Tanase, E.J. Meijer, P.W.M. Blom, D.M. de Leeuw, Org. Electron. **4**, 33 (2003)
43. A. Devos, M. Lannoo, Phys. Rev. B **58**, 8236 (1998)
44. E. Frankevich, Y. Maruyama, H. Ogata, Chem. Phys. Lett. **214**, 39 (1993)

45. D. Emin, Phys. Rev. B **46**, 9419 (1992)
46. A. Yelon, B. Movaghar, Phys. Rev. Lett. **65**, 618 (1990)
47. A. Yelon, B. Movaghar, R.S. Crandall, Rep. Prog. Phys. **69**, 1145 (2006)
48. D. Emin, Phys. Rev. Lett. **100**, 166602 (2008)
49. W.G. Gill, J. Appl. Phys. **43**, 5033 (1972)
50. M. Ullah, I.I. Fishchuk, A.K. Kadashchuk, P. Stadler, A. Pivrikas, C. Simbrunner, V.N. Poroshin, N.S. Sariciftci, H. Sitter, Appl. Phys. Lett. **96**, 213306 (2010)

Chapter 8
Charge Transport in Organic Diodes and OFETs: A Comparison

Mujeeb Ullah, Almantas Pivrikas, N. Sedar Sariciftci, and Helmut Sitter

Abstract Charge carrier mobility can be measured in the bulk of fullerene films using the Charge Extraction by Linearly Increasing Voltage (CELIV) technique and at the interface with insulators using Organic Field-Effect Transistors (OFET). Time-resolved non-equilibrium electron mobility and relaxation of photo-generated charge carriers are measured using photo-CELIV. Electric field, carrier concentration and temperature dependences of the electron mobility, measured using both methods, are compared. The electron mobility is at least two orders of magnitude higher than for hole transport in the C_{60} films prepared by thermal evaporation. More than one order of magnitude higher charge carrier mobility values are measured in OFET configuration due to high charge carrier concentrations at the quasi 2D transport near the dielectric interface. The Meyer-Neldel Rule is observed in both the bulk of the fullerene films and in the transistor channel at the interface. Meyer-Neldel energy $E_{\mathrm{MN}} = 35$ meV is observed in both device structures but the charge carrier mobility is much higher in OFETs. The Meyer-Neldel energy, which is interpreted as disorder parameter, is the same in both device geometries, which suggests that the level of disorder is similar in the bulk of fullerene films and at the interface with insulators. The over one order of magnitude higher electron mo-

---

M. Ullah · H. Sitter
Semiconductor- and Solid State Physics, Johannes Kepler University Linz, Altenbergerstr. 69, 4040 Linz, Austria

M. Ullah (✉)
Centre for Organic Photonics & Electronics (COPE), School of Mathematics and Physics, University of Queensland, St Lucia Campus, Brisbane, QLD 4072, Australia
e-mail: Mujeeb.Ullah@uq.edu.au

A. Pivrikas · N.S. Sariciftci
Physical Chemistry, Linz Institute for Organic Solar Cells, Johannes Kepler University Linz, Altenbergerstraße 69, 4040 Linz, Austria

Present address:
A. Pivrikas
Centre for Organic Photonics and Electronics, School of Chemistry and Biosciences, University of Queensland, St. Lucia Campus, Brisbane, QLD 4072, Australia

H. Sitter et al. (eds.), *Small Organic Molecules on Surfaces*,
Springer Series in Materials Science 173, DOI 10.1007/978-3-642-33848-9_8,

bility in OFETs in comparison to diodes is explained by the much higher carrier concentrations in the channel compared to transport in the bulk.

8.1 Introduction

The charge carrier transport mechanism has been the subject of intensive research for some years and it is fundamentally important for understanding the electronic phenomena in organic semiconductor devices [1–8]. In crystalline inorganic semiconductors, the presence of periodic long-range order of strongly coupled (covalent) atoms results in delocalized energy bands separated by a forbidden energy gap. The charge carrier transport proceeds within extended states and is mainly dependent on scattering events and on the effective mass of electrons or holes. In contrast, organic semiconductors are weakly bound, where the molecules are held together by Van der Waals and London forces (dipole–dipole interaction) [9]. The absence of translational symmetry with a three-dimensional periodic lattice in disordered films results in a random distribution of potential wells yielding a distribution of Density of States (*DOS*). Shallow localized states (band-tail states) are considered to be due to the positional disorder, whereas deep localized states can occur due to topological or chemical defects or impurities. The concept of band conduction does generally not apply and charge carrier transport is described within the interplay of extended (delocalized) and localized states [10].

The important parameter describing charge carrier transport is charge carrier mobility. Although the electric field (E), temperature (T) and carrier concentration (n) dependence of the charge carrier mobility (μ) in organic electronic devices particularly in diodes and organic field-effect transistors (OFETs) has been reported [12–25], the charge transport mechanisms in these organic devices are still not fully understood. Observations from thermally activated behavior [11, 17] to temperature independent transport [18, 19] are reported. It is difficult to obtain an accurate picture of the nature of the transport due to large variations in the experimental data on even nominally the same samples [18, 20]. Studies of mobility are explained in terms of multiple trapping [26], hopping [27] and Coulomb blockade [23] as described in more detail in Chap. 7.

The Meyer-Neldel Rule (MNR) is a commonly observed phenomenon in organic films [26]. This empirical rule can occur in any situation where Arrhenius-type temperature dependent behavior exists [28, 29]. The Arrhenius relation for charge carrier mobility as described above gives a characteristic temperature named as Meyer-Neldel temperature, usually converted to the Meyer-Neldel energy. Most recently, Fishchuk et al. [30, 31] have formulated an analytical theory based on the Effective Medium Approximation (EMA) to describe the Meyer-Neldel rule for the OFET mobility of charge carriers irrespective of their polaronic character by employing the conventional hopping transport concept for a disordered system with a Gaussian DOS distribution and Miller-Abrahams jump rates (see Chap. 7).

An important prediction of the suggested theory is that the Meyer-Neldel energy (E_{MN}) in organic semiconductors is directly related to the width of the Gaussian

DOS, σ, thus providing a new method for the evaluation of the amount of energetic disorder in the material. Another prediction of the theory is that the MNR effect of the charge carrier mobility arises upon varying the carrier concentration, but not regarding varying the width of the DOS, σ [31]. The Fishchuk model was originally developed for zero electric fields. Later, this model was further developed considering arbitrary electric fields which allows to describe the lateral field (F) dependence of the E_{MN}. This dependence can be parameterized as described in detail in Chap. 7 in Eqs. (7.33)–(7.35).

Among the n-type organic semiconductors, C_{60}, with a symmetric structure and a low ionization potential ($\sim$3.4 eV) shows the highest charge carrier mobility 0.6–6 $\mathrm{cm^2/Vs}$ [32–34], which makes it an attractive material for applications. In this chapter a systematic investigation on the electric field, carrier concentration, film morphology and temperature dependence of charge carrier mobility in C_{60}-based diodes and OFETs is presented and discussed according to the Meyer-Neldel formalism.

8.2 Experimental Details and Sample Configuration

Non-equilibrium, time-resolved charge carrier transport studies in disordered organic semiconductors are challenging due to time-dependent charge carrier mobility. Low charge carrier mobility ($\mu < 1\ \mathrm{cm^2\,V^{-1}\,s^{-1}}$), pronounced trapping, dispersive transport and a significant amount of thermally generated carriers make standard methods like Hall effect, Time-of-flight (TOF) or space charge limited current injection inapplicable [33, 34]. However, CELIV and OFET measurements allow one to experimentally measure the charge carrier mobility in fullerene (C_{60}) films. The non-equilibrium time-resolved transport of photo-generated charge carriers is studied using photo-CELIV, whereas steady state transport is measured in OFETs.

Usually a large discrepancy between the bulk and the interface mobility values is observed, which is attributed to the difference in charge carrier concentration and to the difference of the DOS at the interface and in the volume of the film [35, 36]. Therefore, charge carrier mobility, which characterizes the charge transport in the material, depends on the device geometry which must be taken into consideration when presenting mobility data.

OFETs are three terminal devices with the structure given in Fig. 8.1b, where the charge carrier transport proceeds between the source and drain electrodes at the interface of the semiconductor and insulator. Charge carriers are distributed within a few nanometer thick channel in the semiconductor film of the OFET structure and the transport occurs parallel to the interface [37, 38]. The gate voltage applied to the gate electrode below the insulator induces the charge carriers in the channel. It has been shown that the charge carrier transport is strongly dependent on the insulator material and the interface treatment [38, 39].

In the CELIV experiment a triangular-shaped increasing voltage pulse is applied to a C_{60} film in diode geometry (see Fig. 8.1a) with injection preventing (blocking)

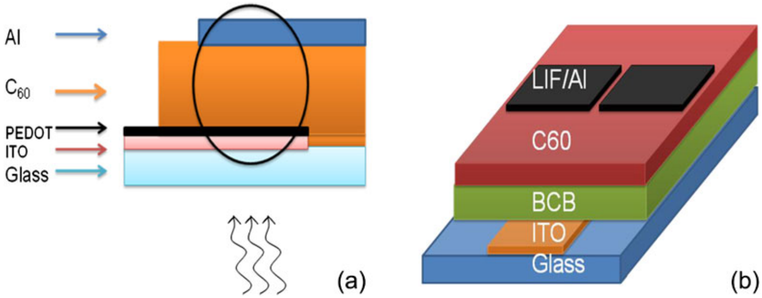

Fig. 8.1 Schematic illustration of (**a**) diode structure (for CELIV) and (**b**) OFET structures used to comparatively study the charge carrier transport in the bulk of a C_{60} film and at the interface with the gate insulator (BCB)

contacts. The mobile charge carriers are photo-generated with short laser pulses and are extracted by an applied increasing electric field. By changing the delay time (t_{del}) between the laser pulse and the applied voltage pulse, or by changing the laser intensity, the charge carrier mobility is measured as a function of carrier concentration directly from the current transients [40]. Thick fullerene films (≈1–5 μm) were grown on ITO/glass substrates using physical vapor deposition to fabricate diode structures with measurable transition times. The temperature dependence of the charge carrier mobility was measured in a cryostat under vacuum to prevent the oxidation and film degradation. CELIV could only be performed down to 240 K because a peel off of the thick C_{60} films occurred below this temperature.

OFET devices were fabricated using BCB as gate dielectric on ITO/glass substrates. Aluminum contacts were evaporated in a vacuum below 10^{-6} mbar. The transistor channel length was 35 μm, width 2 mm and for concentration calculations we assumed a channel thickness at the interface of 10 nm (where most of the charge carriers are accumulated). Details of device fabrication steps were reported previously [32, 41]. The completed devices were loaded in an Oxford cryostat under nitrogen atmosphere inside a glove box to avoid exposure to ambient condition. All the measurements were carried out at 10^{-6} mbar vacuum and the temperature was changed from 300 K to 80 K for OFET measurements. The measurements were conducted with a small temperature step of 10 K, with a time delay of 1 hour so that the devices became thermally stabilized. The transistor characteristics were recorded by Agilent 2000 SMU.

8.3 Evaluation of Charge Carrier Mobility

CELIV and OFET measurements are used to experimentally measure the charge carrier mobility in fullerene (C_{60}) films. The non-equilibrium time-resolved transport of photo-generated charge carriers is studied using photo-CELIV, whereas steady state transport is measured in OFET structures.

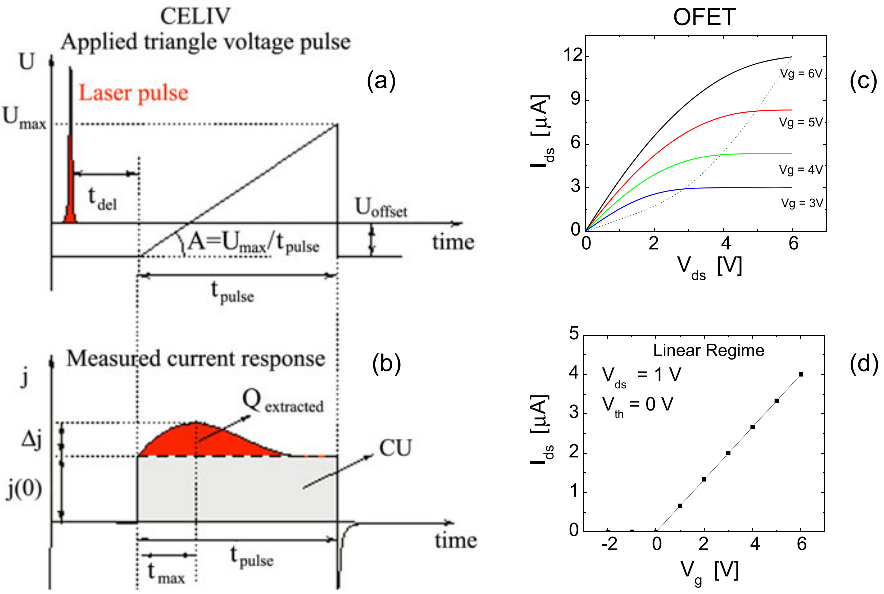

Fig. 8.2 Schematic time dependence (**a**) and (**b**) current transients for CELIV measurements. OFET output (**c**) and transfer curves (**d**) used to experimentally measure the charge carrier mobility

Figure 8.1 shows schematic sample configurations used for (a) CELIV and (b) OFET measurements. The data evaluation from CELIV measurements is well described in the literature [44, 45]. The charge carrier mobility was investigated as a function of the following parameters: (a) sample temperature, controlled by a cryostat, (b) electric field, by changing the maximum voltage ($V_{\max}$) in CELIV or the source-drain voltage (V_d) in OFET, (c) charge carrier concentration, by changing the delay time (t_{del}) in CELIV and the gate voltage (V_g) in OFET.

8.3.1 *Charge Carrier Mobility Measurements by Charge Extraction by Linearly Increasing Voltage*

CELIV allows measurement of the charge carrier mobility and concentration from current transients directly and independently. Moreover, time, concentration, electric field and temperature dependent effects on charge carrier mobility can be studied in films with rather dispersive charge transport, where other methods (e.g. Time-of-Flight) are inapplicable due to the required experimental conditions [45–48]. Schematic time dependence of the applied triangle rising voltage pulse and the current transient response are shown in Fig. 8.2a and b, respectively.

A linearly increasing voltage pulse with the slope $A = U_{\max}/t_{\text{pulse}}$ is applied to the sample to extract the equilibrium charge carriers. The charge carriers inside the film can also be photo-generated by a light pulse (sometimes called photo-CELIV technique). Then, the photo-generated charge carriers are extracted by the linearly increasing voltage pulse after some delay time t_{del}. At the beginning of the CELIV current transient a capacitive current step $j(0)$ is seen (Fig. 8.2b). The following current increase Δj is related to the injection current caused by the charge carriers transported in the film. The current continues to increase as the voltage increases until the charge carriers are extracted from the film and the current drops down to the capacitive step level. In practice, if the duration of the applied triangle voltage pulse t_{pulse} is not long enough, then there might be some carriers left in the film and the current will end at a higher level than the capacitive step. The charge carrier mobility is estimated from the extraction maximum [45–51]. We have

$$\mu = K\frac{d^2}{At_{\mathrm{max}}^2}, \tag{8.1}$$

where d is the film thickness, $K = 2/3$ for $\alpha d \ll 1$ (where α is the light absorption coefficient from Beer-Lambert's law) and $K = 2$ for surface photo-generation $(\alpha d \gg 1)$. The charge carrier concentration ($n = Q_{\mathrm{extracted}}/e$) is estimated from the integrated extraction current with respect to time. Since the electrical field in CELIV experiments is not a constant value but is ramping with time, the field at which the charge carrier mobility is measured is estimated from At_{max}/d (electric field at maximum extraction point t_{max}).

8.3.2 Charge Carrier Mobility Measurements by Organic Field-Effect Transistor

Figure 8.2c and d show a typical output characteristics of an OFET device at different gate voltages and corresponding transfer characteristics in the linear regime $(V_g \gg V_d)$. In the linear regime, the applied gate field is much larger than the in-plane drift field, which results in an approximately uniform density of charge carriers in the active channel. Under these conditions I_d increases linearly with V_g and is approximately described by Eq. (8.2):

$$I_d|_{V_d \ll V_g.} = \frac{W}{L}\mu_{\mathrm{FE}} C_i V_d (V_g - V_{th}) \tag{8.2}$$

where L is the channel length, W is the channel width, C_i is the capacitance per unit area of the insulating layer, V_{th} is the threshold voltage, and μ_{FE} is the field-effect mobility.

By plotting I_d versus V_g at low V_d and evaluating the slope of this plot, μ_{FE} can be calculated using Eq. (8.2). Similarly μ_{FE} can also be determined in the saturation regime $(V_d \geq V_g)$, but due to pinch off in the channel, the mobility calculated in the saturated regime is not an option to study the charge carrier transport in FET devices, because it is deduced from an inhomogeneous distribution of the charge carriers in the conductive channel of the OFET.

By fitting the plots of transfer curves, the field-effect mobility as a function of gate voltage can be calculated. One can calculate the charge carrier concentration as a function of V_g from the charge accumulated at the semiconductor/insulator interface by increasing V_g across the dielectric in a metal-insulator-semiconductor (MIS) capacitor.

The V_g or carrier concentration dependence of the field-effect mobility is explained by the charge concentration effect at the insulator-semiconductor interface [52, 53].

In these experiments, a low V_d (2, 4, 6 8, 10 V) compared to a high V_g (60 V) was used to study the source-drain electric field dependence of the field-effect mobility in order to stay in the linear regime.

8.4 Type of Mobile Charge Carriers in C_{60} films

In order to determine the dominant type of mobile carriers in the studied C_{60} films, CELIV and OFET measurements were performed to see both types of charge carriers. To compare the electron and hole mobility by CELIV, on one hand, thick fullerene films were illuminated either from the aluminum or ITO side, keeping the same applied voltage polarity [54, 55] and on the other hand, by shining the LASER pulse on the ITO electrode and changing the applied voltage polarity. In that way, either electron or hole transport can be measured in the films where the light absorption depth is much smaller than the film thickness (surface photo-generation). Figure 8.3a shows a typical CELIV transient for electron and hole transport. The extraction current is seen only for electron transport, whereas for hole transport the CELIV transients are indistinguishable from the dark response concluding that the electron mobility is much higher (>100 times) compared to the hole mobility.

The electric current response for electron transport resembles a typical CELIV transient. At the initial time ($t = 0$), the capacitive current step is seen in the transient due to an RC circuit response to an applied triangle-shaped voltage pulse. Proceeding further in time, the capacitive (displacement) charging current for dark transients is slightly increasing with time due to a time-dependent polarization (change in dielectric constant due to diffusion of charges) or due to non-perfect blocking electrodes. When laser light is used to photo-generate charge carriers the conductivity (extraction) current is seen as a “mountain” superimposed onto this capacitive charging current. Initially the extraction current is increasing due to an increase of the applied voltage and carrier drift velocity. At a certain point, when the mobile charge carrier concentration starts to decrease due to the carrier arrival at the electrode, the extraction current starts to diminish forming an extraction maximum. The extraction current further decreases to approach the dark capacitive current.

The OFET transfer curve, shown in Fig. 8.3b, shows no significant hole injection into the channel when negative voltage is applied to the gate. Strong electron current is observed under positive gate bias. Therefore, both CELIV and OFET experiments confirm that electron mobility is much higher than hole mobility in fullerene films.

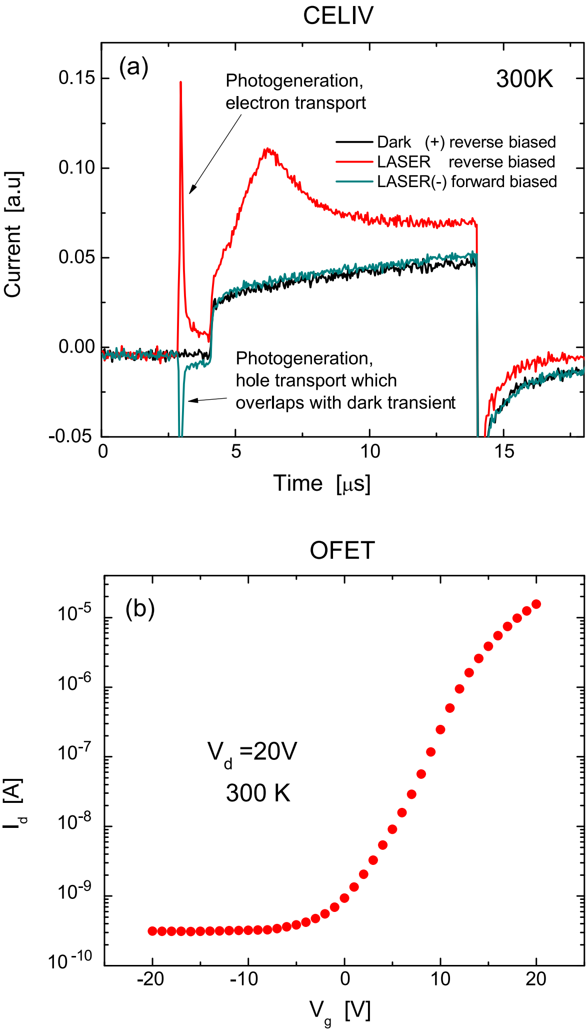

Fig. 8.3 (**a**) CELIV transients and (**b**) OFET transfer curve showing that the electron mobility is at least 100 times larger than hole mobility in C_{60}

8.5 Charge Carrier Concentration Dependence of Electron Mobility

Since the charge carrier mobility is also strongly dependent on the charge carrier concentration, we have measured the charge carrier mobility as a function of carrier concentration at various temperatures using CELIV and OFET techniques.

We have changed systematically in our CELIV experiments the delay time t_{del} between the laser pulse and the extracting voltage pulses to vary the carrier concentration during extraction. Figure 8.4 shows CELIV transients for different t_{del}. On the other hand, the gate voltage (V_g) and the geometry of OFET structures defines the charge carrier concentration in the channel. Figure 8.5 shows OFET output

Fig. 8.4 CELIV current transients at various delay times t_{del} at 300 K

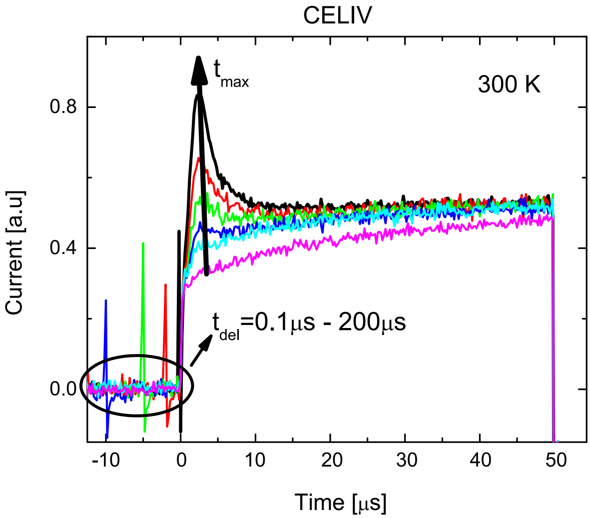

Fig. 8.5 OFET output curves for different gate voltages at 300 K

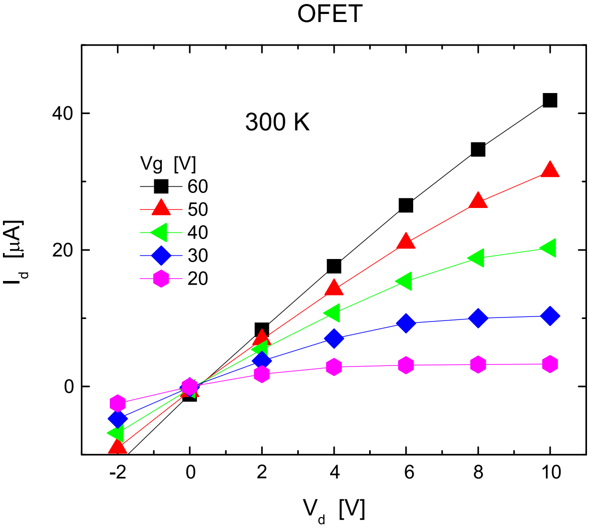

curves at 300 K for different gate voltages. The charge carrier mobility is calculated using Eq. (8.2) from the OFET transfer curves.

The charge carrier concentration was calculated as a function of V_g assuming a 10 nm thick conductive channel in the C_{60} film at the semiconductor/insulator interface:

$$n = C_i V_g \frac{1}{ed} \tag{8.3}$$

Fig. 8.6 (**a**) Non-equilibrium time-dependent electron mobility and (**b**) charge carrier concentration decay in C_{60} films shown at various temperatures as measured by CELIV

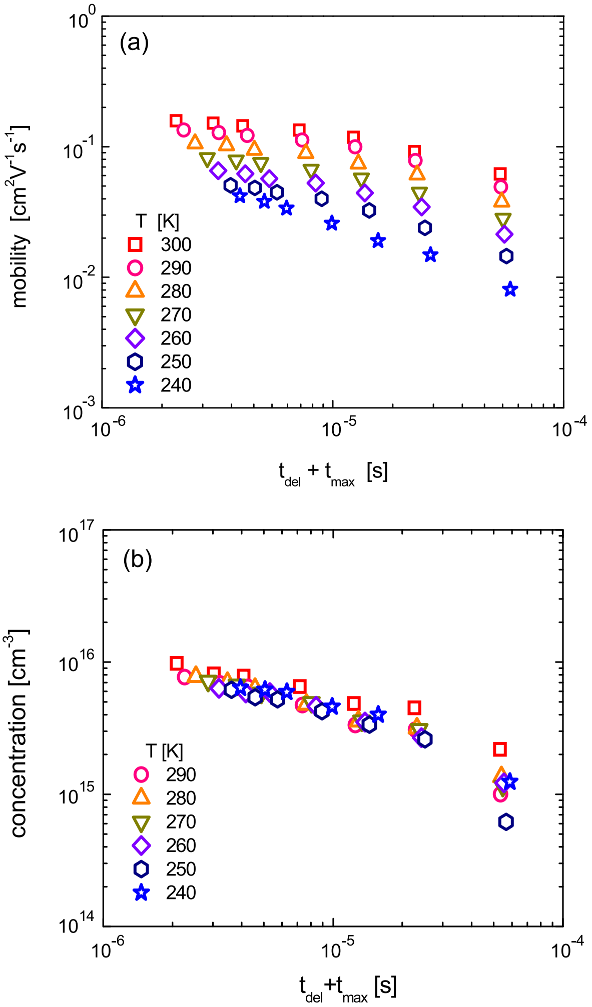

where e is the elementary charge, C_i is the geometric capacitance of the device with a 35 μm channel length and 2 mm channel width and d is the thickness of the dielectric materials.

This set of OFET-based experiments was repeated at different temperatures, which gave the carrier concentration dependence of the charge carrier mobility for different temperatures as summarized in Fig. 8.7.

In CELIV measurements, performed at longer delay times, charge carriers have more time to relax prior to extraction. Because the carrier extraction is not instantaneous and $t_{\max}$ is comparable to the short delay times, the time used at which the carrier mobility was estimated is $(t_{\mathrm{del}} + t_{\max})$ [55].

The charge carrier mobility was calculated using Eq. (8.1) and its dependence upon time is plotted in Fig. 8.6a for different sample temperatures. The charge

Fig. 8.7 Concentration dependent electron mobility in C_{60} films measured from CELIV and OFET. Concentration is plotted on logarithmic scale with a break

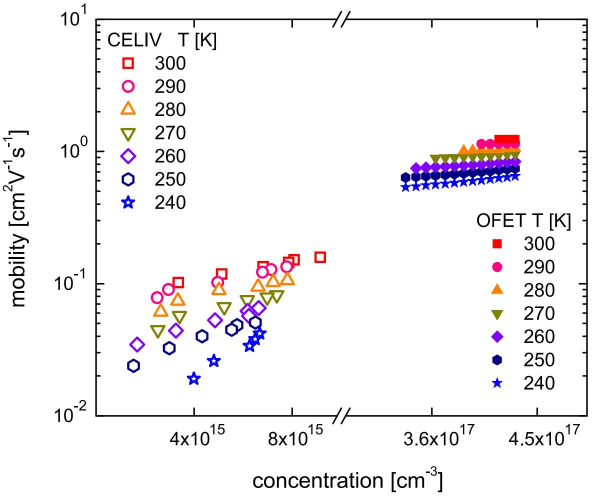

carrier mobility decreases as a function of time due to the relaxation phenomena of photo-generated charge carriers (thermalization) within the DOS to deeper states [55]. This behavior is usually observed in disordered semiconductors showing the existence of dispersive transport. However, in C_{60} layers the charge transport is weakly dispersive especially at room temperature, therefore only a weak charge carrier mobility dependence on time is seen. At low temperatures the carrier mobility follows a stronger time dependence compared to higher temperatures as expected in case of temperature activated transport.

By integrating the extraction current (dark current subtracted) of the CELIV transient over time, we calculated the amount of extracted charge which is proportional to the charge carrier concentration in the film [55]. The time-resolved decay of charge carrier concentration was measured and is plotted in Fig. 8.6b. Charge carrier concentration during CELIV experiments is similar at all temperatures allowing an estimation of the charge carrier mobility as a function of concentration at all measured temperatures.

The charge carrier mobilities as a function of carrier concentration measured at different temperatures from CELIV and OFET are compared in Fig. 8.7.

Much lower charge carrier mobility values and a stronger concentration dependence are seen in the bulk of the film deduced from CELIV, since the carrier concentrations are significantly lower. A weak dependence of carrier mobility on concentration, as observed in OFETs, is attributed to the trap filling effect at high carrier concentrations which increases the effective transport energy in the *DOS* to higher values. This allows charge carriers to reach higher energy states where the mobility is larger and less dependent on carrier concentration due to a higher density of available states.

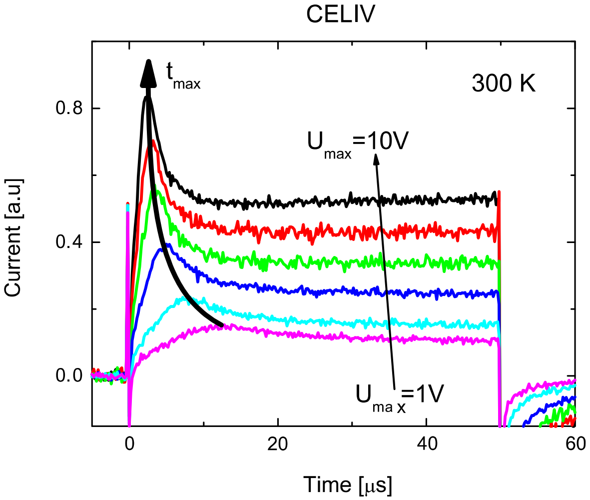

Fig. 8.8 Electric field dependent CELIV transients at 300 K. *Thick arrow* marks the extraction maximum $t_{\max}$ for each CELIV transient

8.6 Electric Field Dependence of Electron Mobility

It is well known that the mobility of charge carriers typically increase with electric field according to a $\ln \mu \propto F^{1/2}$ law, called "Poole-Frenkel" (PF)-type dependence, though the Poole–Frenkel description itself is strictly not applicable to organic semiconductors [42].

In CELIV measurements, the applied electric field can be increased by increasing the maximum voltage at the end of ramp. In OFET measurements the electric field in the direction of current can be controlled by the applied source-drain voltage. Figure 8.8 shows CELIV transients and Fig. 8.9 shows OFET output characteristics for different external applied voltages (electric fields) at 300 K.

The CELIV transients in Fig. 8.8 are similar to those shown in Fig. 8.3a. Different slopes for the increasing voltage and higher maximum voltages were applied, whereas the delay time between the laser pulse and the extracting voltage pulse was fixed at $t_{\text{del}} = 0.1$ μs. The extraction maximum $t_{\max}$ shifts towards a shorter time at higher applied voltages, as predicted by drift mobility definition. The extraction peak becomes less sharp at lower temperatures due to a more pronounced dispersive transport [40, 43–47]. Since the electric field is changing during the carrier extraction in CELIV experiments, the electric field value is taken at the point of maximum extraction from which the charge carrier mobility is calculated as well. The same experiment was repeated at different temperatures. The charge carrier mobilities are calculated using Eq. (8.1) and are plotted for different sample temperatures in Fig. 8.10 as a function of the electric field.

Figure 8.9 shows the OFET transfer curves in the linear operating regime of the transistor $V_g \gg V_d$ to avoid the complex charge carrier distribution in the channel at voltages above the pinch-off point. Again this set of experiment was repeated at different temperatures.

Fig. 8.9 OFET transfer curves for different source-drain voltages (V_d) at 300 K

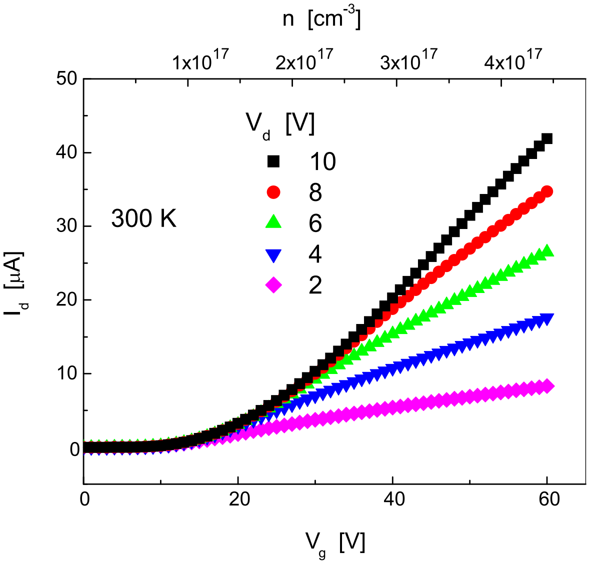

The charge carrier mobility was calculated using Eq. (8.2) at different V_d (V_g = 60 V) and at various temperatures. The results are shown in Fig. 8.10 together with the data obtained from CELIV measurements. The electric field between the source and drain electrodes in the OFET channel is of the same magnitude as the electric field between anode and cathode in the diode structures.

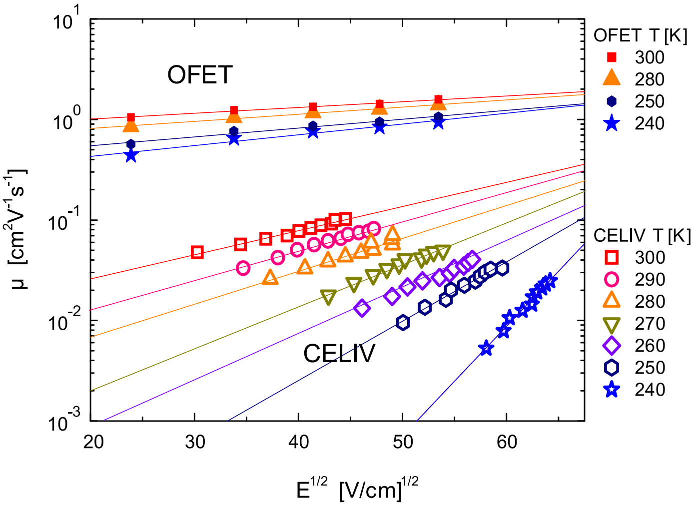

Fig. 8.10 Poole-Frenkel plot of electron mobility in C_{60} at various temperatures measured from CELIV and OFET

It was shown in the past that the charge carrier mobility measured from CELIV is in good agreement with values measured by TOF [54, 55].

A lower charge carrier mobility as well as a stronger electric field dependence were found for CELIV measurements in comparison to those obtained from OFET measurements. Since the electric field range is similar in both experiments, the difference in mobility has its origin in the charge carrier concentrations which are very different. Over an order of magnitude smaller carrier concentration is present in the bulk of the film in CELIV experiment compared to the conductive channel in OFET measurements. At low concentrations the charge carrier distribution occupies states with lower energies which results in a lower mobility and a stronger electric field dependence.

It is important to note that a non-equilibrium mobility of photo-generated charge carriers is measured from CELIV, therefore high charge carrier mobility values are not expected in the time scale of the experiment (in the order of microseconds), since the charge carriers had enough time to relax to the deeper states of DOS distribution which results in lower mobility values [38].

8.7 Temperature Dependence of Charge Carrier Mobility

A detailed theoretical discussion of the temperature dependence of charge carrier mobility is given in Chap. 7. We present here the experimental results and the evaluation based on the previously discussed theory.

8.7.1 Meyer-Neldel Rule

Figure 8.11a and b show the Arrhenius-type of charge carrier mobility replotted from Fig. 8.7 at different concentrations for CELIV and OFET experiments, respectively. By increasing the delay time between the LASER pulse and the extraction voltage ramp in CELIV, the carrier concentration was reduced, while in OFET measurements the carrier concentration was increased by increasing the gate voltage, V_g. In both experiments the carrier mobility follows an Arrhenius type of temperature dependence. A common intersection point of extrapolated data lines allows evaluating the Meyer-Neldel parameters. The MNR temperature obtained from CELIV is $T_{\mathrm{MN}} = 400$ K and from OFET is $T_{\mathrm{MN}} = 408$ K which in both cases corresponds approximately to $E_{\mathrm{MN}} = 35$ meV. The MNR mobility prefactors Eq. (8.2) are $\mu_{\mathrm{MN}} = 0.4\ \mathrm{cm}^2\,\mathrm{V}^{-1}\,\mathrm{s}^{-1}$ from CELIV and $\mu_{\mathrm{MN}} = 4\ \mathrm{cm}^2\,\mathrm{V}^{-1}\,\mathrm{s}^{-1}$ from OFET. The mobility prefactor is higher in OFET measurements due to a higher carrier mobility at the interface. The obtained values are in good agreement with the results obtained in similar C_{60} devices in the past [26, 32, 33, 40].

Since the Meyer-Neldel energy E_{MN} is directly correlated with the film quality and the width of the DOS in which charge transport occurs [31, 48], similar MNR

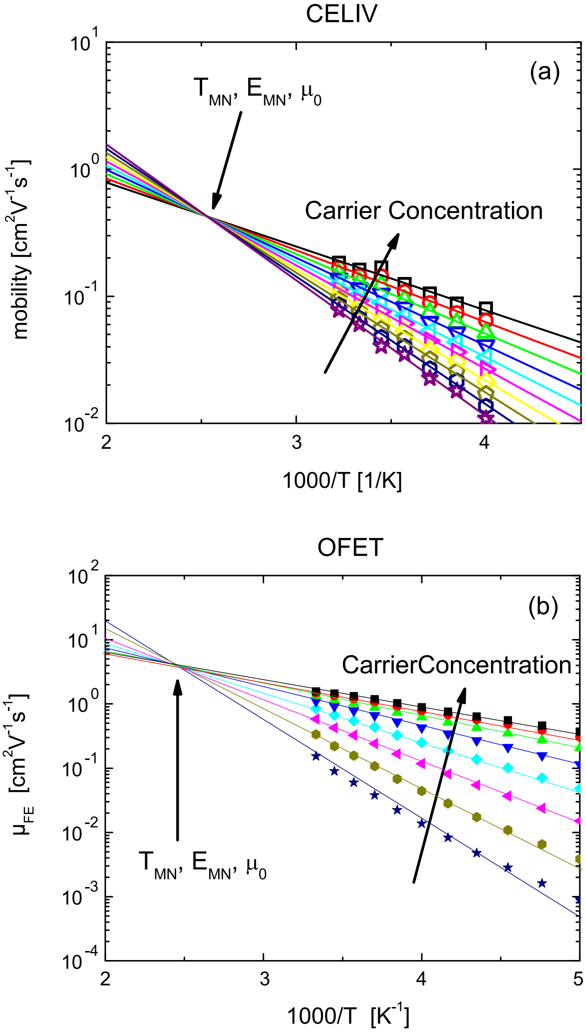

Fig. 8.11 Arrhenius plots of temperature dependent electron mobility at various concentrations measured using (**a**) CELIV and (**b**) OFETs. Meyer-Neldel parameters from CELIV: $T_{MN} = 406$ K, $E_{MN} = 35$ meV, $\mu_{MN} = 0.4$ cm^2 V^{-1} s^{-1}; from OFET: $T_{MN} = 408$ K, $E_{MN} = 35$ meV, $\mu_{MN} = 4$ cm^2 V^{-1} s^{-1}

energies obtained from CELIV and OFET suggest that the charge carriers experience a similar energetic landscape during transport in the bulk of the film and at the interface in the studied devices. The absence of dipoles at the interface of fullerene and BCB forms a beneficial interface allowing high charge carrier mobility values to be reached.

The lines of the best fit, shown for each carrier concentration in Fig. 8.11a and b, allowed calculation of an activation energy from the slope, as well as a mobility prefactor μ_0 from the extrapolation to infinite temperature.

Figure 8.12 shows the mobility prefactor μ_0 as a function of activation energy. Similar slopes of lines of best fit in Fig. 8.12, representing the Meyer-Neldel energy (E_{MN}), show well matching E_{MN} in both the bulk of the film and at the interface.

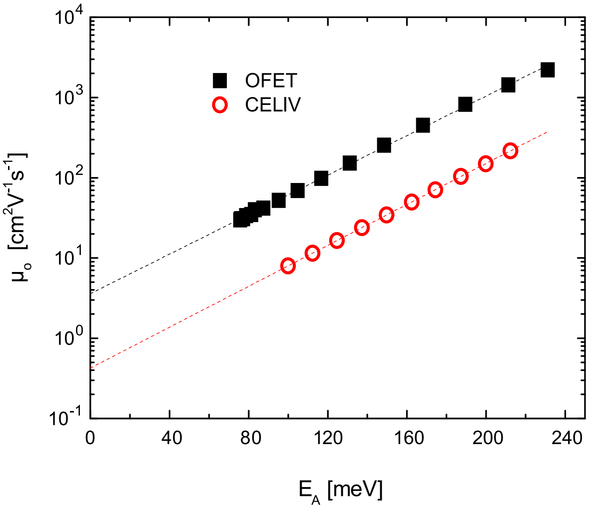

Fig. 8.12 Mobility prefactor μ_0 dependence on activation energy E_A empirically found from extrapolation of experimental results, for CELIV and OFET experiments

The extrapolation of the lines of best fit in Fig. 8.12 gives the Meyer-Neldel mobility. The Meyer-Neldel mobility (μ_{MN}) is one order of magnitude higher in the OFETs compared to the transport in the bulk materials as measured from CELIV. Equal MN energies ($E_{\mathrm{MN}} = 35$ meV) obtained from both CELIV and OFET experiments, suggest that the charge carrier transport proceeds within similar energetic and positional landscape so that a similar amount of energy is required to reach a concentration and temperature independent mobility. However, the difference in μ_{MN} shows that the carrier mobility is strongly dependent on carrier concentration regardless of the Meyer-Neldel energy.

8.7.2 Gill's Law

The electron mobility obtained from CELIV and OFET measurements are shown in Fig. 8.10 as a function of the applied electric field at different temperatures. More than one order of magnitude higher electron mobility values are observed in OFETs. It is important to note that the charge carrier concentration differs by more than one order of magnitude in both experiments due to the two dimensional nature of the carrier concentration distribution in the channel of the transistor. In CELIV the concentration range is between 2×10^{15}–8×10^{15} cm^3, whereas in OFET the range is 2×10^{17}–5×10^{17} cm^3. It was tried to experimentally limit the large concentration difference by lowering the gate voltage but still working in the linear regime of OFETs. In CELIV experiments, the carrier concentration is limited by the charge stored on the electrodes CV (capacitance times voltage) due to Langevin type of bimolecular carrier recombination at high concentrations in fullerenes.

As can be seen from Fig. 8.10, the electric field dependence increases at lower temperatures. The extrapolated mobility data converge to an electric field, where

Fig. 8.13 Arrhenius plots of electron mobility at various electric fields. Gill's temperature T_{Gill} is shown for both types of device

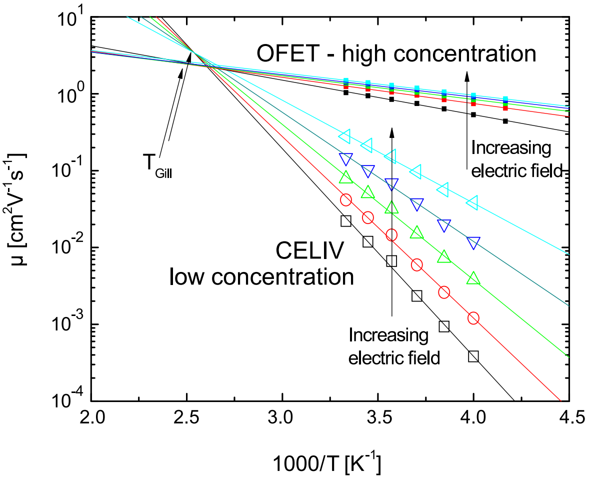

the carrier mobility becomes temperature independent, $F_{\text{CELIV}} = 9.2$ kV/cm and $F_{\text{OFET}} = 9.4$ kV/cm.

In order to demonstrate Gill's law, the charge carrier mobility data from Fig. 8.10 are replotted as Arrhenius plots in Fig. 8.13. Important observations are: (a) the data follow an Arrhenius-type temperature dependence (in contrast to low carrier concentration regime, i.e. *TOF* measurements, where $1/T^2$ temperature dependence is usually seen and explained by Bässler model); (b) the activation energy is field dependent (decreasing with increasing field) and (c) the extrapolated data intersect at T_{Gill}.

The isokinetic point (T_{Gill}) shows the energy $E_{\text{Gill}} = kT_{\text{Gill}}$ required for electric field independent carrier mobility. The corresponding Gill's energies are $E_{\text{CELIV}} =$ 34 meV and $E_{\text{OFET}} = 34$ meV. The experimentally observed E_{Gill} corresponds well to the Meyer-Neldel energy $E_{\text{MN}} = 35$ meV as described above in fullerene films [39]. A good match between the values shows the similarities between the Gill law and Meyer-Neldel rule and indicates that the level of disorder in diodes and OFETs is very similar.

In agreement with studies in the past, the activation energy follows a square-root dependence on the electric field in diodes within the range of experimental error [43–45]. As described above, in comparison to diode structures, a much lower activation energy is required in OFETs, due to a much larger charge carrier concentration present in the channel of field-effect transistor. Field and temperature activated charge transport through the manifold of DOS distribution of localized states below a certain mobility edge can explain the presence of both convergence points, where mobility becomes independent on temperature (Poole-Frenkel plot) and electric field (Arrhenius plot).

In conclusion, it is shown that the electron mobility follows a Poole-Frenkel-type electric field dependence in fullerene diodes and field-effect transistors. A comparison of charge carrier mobility in both types of device reveals that electron mobility is much higher in OFETs where the charge carrier density in the channel is much

Fig. 8.14 Arrhenius activation energy measured in OFETs as a function of applied electric field at different charge carrier concentrations

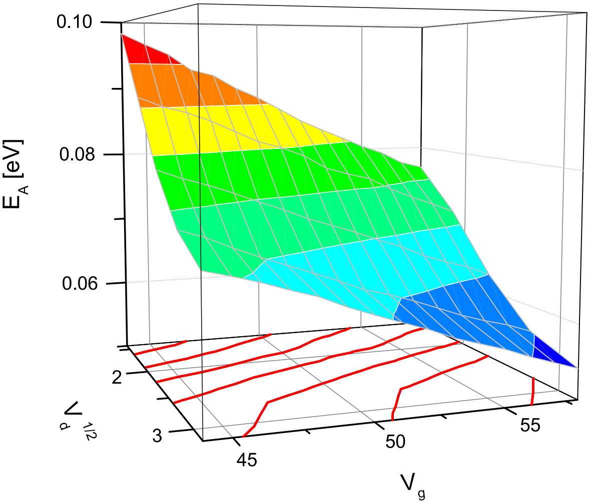

higher. Gill's law is observed in both types of device showing that the activation energy for electron transport is larger at lower applied fields. Larger activation energy is required in diodes at lower carrier concentrations in comparison to OFETs. Gill's energy value in both devices $E_{\mathrm{Gill}} = 34$ meV is in good agreement with Meyer-Neldel energy $E_{\mathrm{MN}} = 35$ meV observed in the past.

The activation energy decreases with increasing electric field in the film, which can be explained by the fact that the electric field lowers the average barrier height for energetic uphill jumps in the field direction [31]. Figure 8.14, obtained by a combination of experimental data from Figs. 8.11 and 8.13, shows a Poole-Frenkel-type behavior of the activation energy which decreases approximately linearly with the square root of the source-drain voltage for different carrier concentrations.

8.7.3 *Electric Field and Carrier Concentration Dependence of Meyer-Neldel Energy and Gill Energy, Respectively*

The Meyer-Neldel energy $E_{\mathrm{MN}} = k_B T_{\mathrm{MN}}$, as determined from temperature dependences of OFET mobility upon varying carrier concentration in the C_{60}-based OFET, is shown in Fig. 8.15a (symbols) as a function of the applied lateral electric field (E_d) [46]. Figure 8.15b shows the dependence of the Gill energy $E_{\mathrm{Gill}} = k_B T_2$, as determined from temperature dependences of the FET mobility upon varying lateral electric field in the same device, on the applied gate voltage V_g (i.e. on carrier concentration n/N). The theoretical model given in Sect. 7.5, Chap. 7, describes reasonably well these experimental data. The dependence of E_{MN} on the applied electric field as well as dependence of E_{Gill} on the charge carrier concentration can be well fitted using the same set of parameters; the calculated values are shown by a solid curve in Fig. 8.15a and b.

Fig. 8.15 Experimentally determined (**a**) MN-energy (*symbols*) versus the applied lateral electric field and (**b**) Gill energy $E_{\mathrm{Gill}} = k_B T_2$ as a function of used gate voltage V_g. Fitting by Fishchuk's model (*solid lines*)

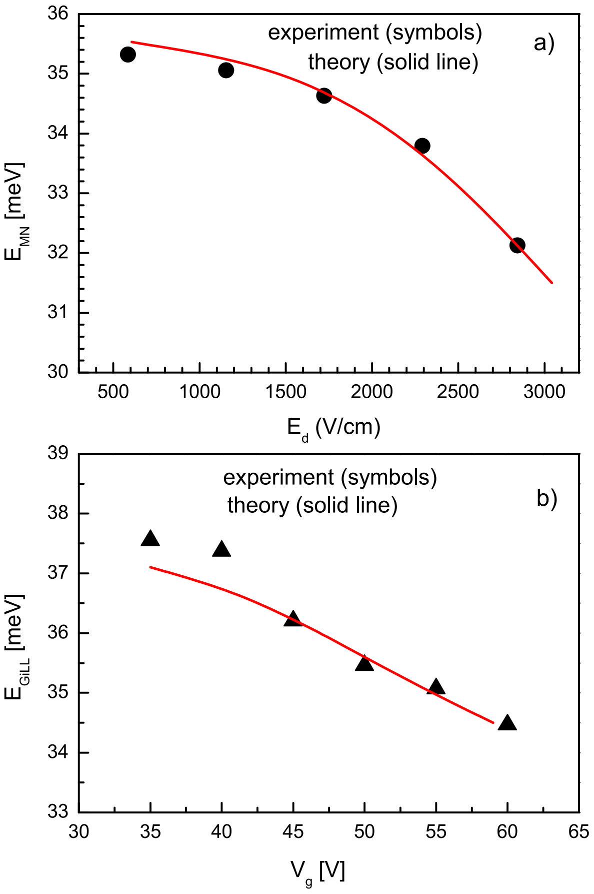

However, the effects observed in Fig. 8.15a and b can only be fitted provided that energy correlation effects are taken into account as described in Chap. 7. Therefore we consider these findings as an experimental proof for the presence of energy correlations in an organic semiconductor: Meyer-Neldel and Gill energy are expected to depend on the lateral electric field and on carrier concentration, respectively.

8.8 Grain Size Dependence of Charge Carrier Mobility and Meyer-Neldel Energy

A systematic experimental study was performed to investigate the interrelation between the energetic disorder and the MNR energy as derived from the temperature dependent FET mobilities in C_{60} films grown at different conditions resulting in dif-

Fig. 8.16 Schematic cross-section of OFET structures (**a**). AFM images of C_{60} films grown by flush evaporation at room temperature (**b**) and by Hot-Wall Epitaxy at a substrate temperature of 130 °C (**c**) and 250 °C (**d**)

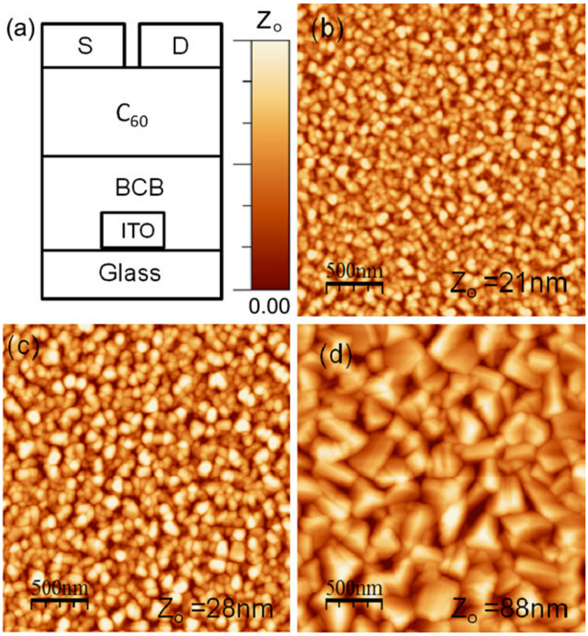

ferent film morphologies. The top-contact bottom-gate OFET devices, as schematically shown in Fig. 8.1b and in cross-section in Fig. 8.16a, were fabricated on ITO covered glass substrates using divinyltetramethyldisiloxane-bis(benzocyclobutane) (BCB) as gate-insulating layer.

The thin C_{60} films were deposited at different substrate temperatures using standard flush evaporation or the Hot-Wall Epitaxy (HWE) technique [56–58]. As one can see from Fig. 8.16b–d the film morphology depends quite considerably on the growth conditions—increasing the substrate temperature (T_{sub}) results in larger grain size of the C_{60} films. The smallest grains were obtained in films grown by conventional thermal evaporation without substrate heating (Fig. 8.16b), and the largest ones in films grown by HWE technique at $T_{\text{sub}} = 250$ °C.

The XRD measurements also confirm the increasing crystallinity in the C_{60} films with increasing substrate temperature as shown in Fig. 8.17. Finally LiF/Al top contacts were evaporated in high vacuum. The completed devices were loaded for electrical characterization in an Oxford cryostat inside the glove box. The temperature was changed in the range from 320 K to 80 K with steps of 20 K. The field-effect mobility μ_{FE} of the C_{60}-based OFET has been determined in the linear regime of the I_d–V_g characteristics (at low source-drain voltage $V_d = 2$ V). The applied source-gate electric field in this regime was much larger than the in-plane source-drain field, which resulted in an approximately uniform density of charge carriers in the conductive channel.

Figure 8.18a and b (symbols) show the field-effect mobility μ_{FE} as a function of inverse temperature at different gate voltages V_g obtained for C_{60} films grown by HWE at substrate temperature $T_{\text{sub}} = 130$ °C and 250 °C, respectively. It is ev-

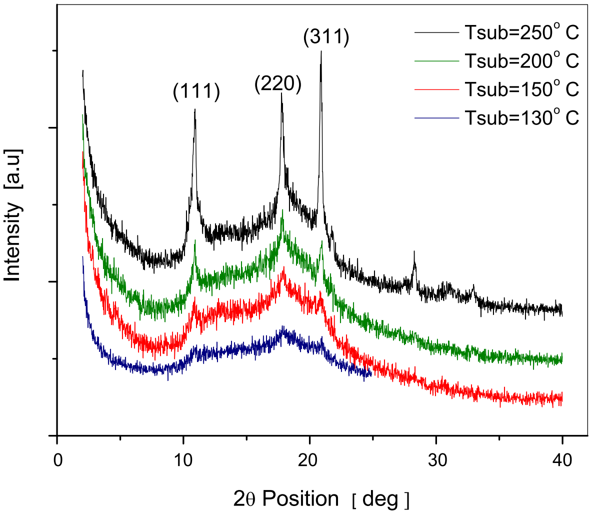

Fig. 8.17 XRD ω-2θ scans for C_{60} films grown by HWE on BCB at different substrate temperatures

ident that the extrapolation of these graphs intersect at the isokinetic temperature $T_0 = 351$ K and 250 K for the films grown at 130 °C and 250 °C, respectively, thus clearly demonstrating an MNR-type behavior. This yields corresponding MNR energies of $E_{\mathrm{MN}} = 30.2$ and 21.5 meV. The MNR effect has been described above in Sect. 8.7 for the flush evaporated C_{60} film which was deposited at room temperature [40] (Fig. 8.16b), which featured also a clear MNR-type behavior resulting in $E_{\mathrm{MN}} = 34$ meV for this highly disordered film. Using Eq. (7.29) from Chap. 7 for each T_{MN}, determined from experiment, the corresponding width of the DOS, $\sigma = 88$ meV, 75.5 meV, and 54 meV can be obtained for films grown at room temperature, 130 °C, and 250 °C, respectively.

Figure 8.19a shows the mobility data as a function of inverse temperature for the two samples with two different morphologies as described above, but for the same gate voltage, V_g, which means for the same effective carrier concentration. Due to the different degree of disorder the activation energies are different. But most striking is the fact that extrapolating the data does not intersect at a finite temperature and consequently shows no MNR effect. This experimental finding can be well fitted by the EMA theory [31] (Fig. 8.19a, bold curves) using the same σ-parameters as derived from Fig. 8.16a and b. This provides an additional cross-check for the validity of the suggested theoretical model. As predicted by the theory, extrapolations of these temperature dependences (thin solid lines in Fig. 8.19a intersect at infinite temperature in accordance with Eqs. (7.3), Chap. 7.

Figure 8.19b summarizes the mobility data at room temperature, together with the width σ of the Gaussian DOS as a function of the grain size of the C_{60} layers, deduced from AFM pictures. It can be clearly seen that with increasing grain size the degree of disorder decreases and the mobility increases. The reduced E_a for the C_{60} film grown at higher substrate temperature is direct evidence for the reduced energetic disorder in this film.

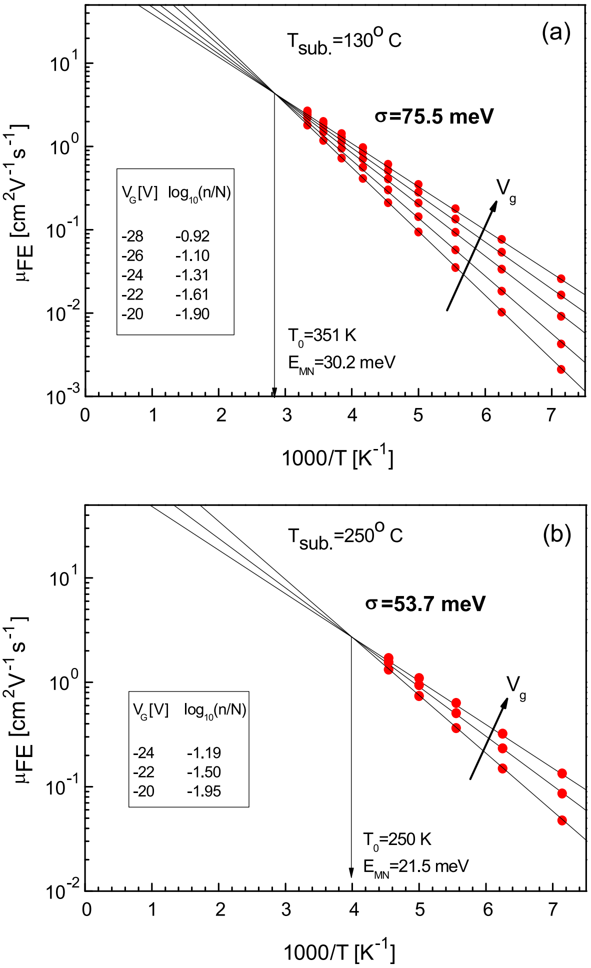

Fig. 8.18 Temperature dependence of the FET mobility measured at different V_g in C_{60} films grown by HWE at (**a**) $T_{\mathrm{sub}} = 130$ °C and (**b**) 250 °C (*symbols*) and results of their fitting with theoretical description (Chap. 7) (*solid lines*). The isokinetic temperature T_0 is indicated by an *arrow*

It is worth noting that $E_{\mathrm{MN}} = 21.5$ meV, observed for the C_{60} film grown by HWE at 250 °C, is probably the smallest reported so far for OFET mobility in organic transistors and is reflected also by a very reduced energetic disorder of $\sigma = 53.7$ meV. However, it is similar to the value of 50 meV determined by time of flight (ToF) measurements in MeLPPP conjugated polymers [51]. Normally, σ-values determined for the OFET mobility are somewhat larger than that for the ToF mobilities measured in the same material due to the interface effects in OFETs (surface traps, surface dipoles, etc.) [56]. In the present study an organic BCB non-polar gate isolator was used, so the interface effects are expected to be very weak compared to SiO_2. This circumstance combined with the optimized structure of C_{60} films grown by HWE technique can explain the significantly reduced energetic disorder in the C_{60} films.

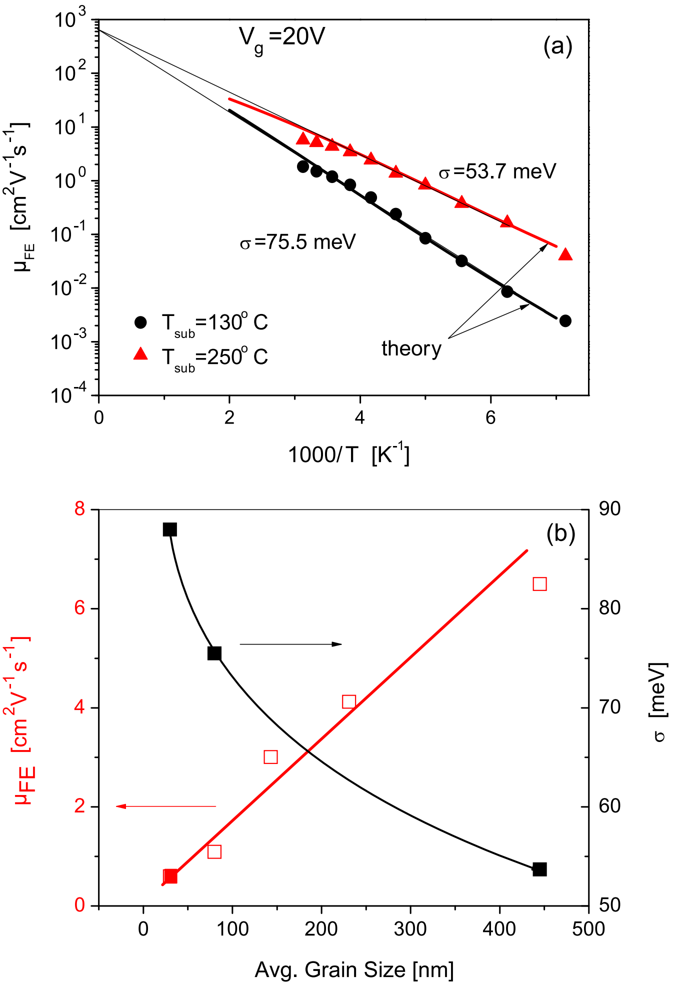

Fig. 8.19 (**a**) Temperature dependence of the FET mobility measured at constant $V_g = 20$ V in C_{60} films grown by HWE at $T_{\mathrm{sub}} = 130$ °C and 250 °C (*symbols*) and results of calculated temperature dependences by the EMA theory [31] (*bold curves*). Fitting experimental data with the theoretical description (Chap. 7) is shown by thin solid lines. (**b**) Average FET mobility in C_{60} films and width of the Gaussian DOS as a function of grain size in C_{60} films

8.9 Conclusion

In this chapter charge carrier mobilities are compared in the bulk of the fullerene films in diode structure by CELIV measurements and at the interface with an insulator by OFET analysis. A non-equilibrium mobility of photo-generated charge carriers were used in the CELIV technique, while a steady state mobility was measured in OFET. Much higher electron mobilities (>100 times) as compared to hole mobilities are observed. It is shown that the charge carrier mobility in fullerene films is strongly dependent on temperature, charge carrier concentration, electric field and structural properties of the C_{60} layers. The mobility values at low carrier concentrations are smaller and they follow a stronger Poole-Frenkel-type electric field dependence in agreement to the theory described in Chap. 7. The charge carrier mobility as a function of concentration at various temperatures is compared in the bulk of the film and in the channel of transistors, where much higher carrier concentrations can be reached. Arrhenius plots of the charge carrier mobility at various carrier concentrations demonstrate that the mobility data follow the Meyer-Neldel rule. It is shown that the Meyer-Neldel energy is similar in the bulk of the semiconductor and at the interface, suggesting similar levels of energetic disorder. However, the charge carrier mobilities differ significantly due to the carrier concentration difference in the different devices.

The electron mobility follows a Poole-Frenkel-type electric field dependence in fullerene diodes and field-effect transistors. Gill's law is observed in both types of device showing that activation energy for electron transport is larger at lower applied fields. Larger activation energy is required in diodes at lower carrier concentrations in comparison to OFETs. Gill's energy value in both devices $E_{\mathrm{Gill}} = 34$ meV is in a very good agreement with the observed Meyer-Neldel energy $E_{\mathrm{MN}} = 35$ meV.

The study of Meyer-Neldel behavior in OFETs at different applied lateral electric fields shows a change in the characteristic Meyer-Neldel energy, which is shifted from 35 meV $\rightarrow$ 32 meV by increasing the applied source-drain electric field. The experimental results are in excellent agreement with the predictions of the presented analytic model described in Chap. 7. The presented analytical model is superior to the previously suggested one as it allows a more accurate evaluation of important material parameters from experimental data measured at any electric field and does not require an extrapolation of experimental data to zero electric field.

Experimental observations of the Meyer-Neldel-type behavior in C_{60} films grown at different growth conditions are found to be in excellent agreement with the predictions of the Fishchuk's suggested theoretical model for organic semiconductors with a Gaussian DOS distribution. An amazing strong shift of the Meyer-Neldel (isokinetic) temperature T_0 (from $T_0 = 408\ \mathrm{K} \rightarrow 351\ \mathrm{K} \rightarrow 250\ \mathrm{K}$), was found in C_{60} films upon increasing the substrate temperature during film growth from room temperature [40] to $T_{\mathrm{sub}} = 130\ ^\circ\mathrm{C}$ and $T_{\mathrm{sub}} = 250\ ^\circ\mathrm{C}$, respectively, and this correlates with the change of the film morphology and, consequently, a change of the energetic disorder. An unusually small MNR energy of 21.5 meV was found for the C_{60} films grown at $T_{\mathrm{sub}} = 250\ ^\circ\mathrm{C}$ which correlates to a significantly reduced energetic disorder of $\sigma = 53.7$ meV and, consequently, a very high charge carrier mobility of 6.5 $\mathrm{cm}^2\ \mathrm{V}^{-1}\ \mathrm{s}^{-1}$ in these films. Finally, it should be mentioned that the Meyer-Neldel energy can be used as sensitive rating parameter, characterizing the quality of the active organic semiconductor layers independent of type and structure of electronic devices used.

References

1. M. Pope, C.E. Swenberg, *Electronic Processes in Organic Crystals* (Oxford University Press, New York, 1982)
2. A.R. Brown, C.P. Jarrett, D.M. de Leeuw, M. Matters, Synth. Met. **88**, 37 (1997)
3. G. Horowitz, R. Hajlaoui, P. Delannoy, J. Phys. III France **5**, 355 (1995)
4. S.F. Nelson, Y.-Y. Lin, D.J. Gundlach, T.N. Jackson, Appl. Phys. Lett. **72**, 1854 (1998)
5. I.N. Hulea et al., Nat. Mater. **5**, 982 (2006)
6. L. Torsi, A. Dodabalapur, L.J. Rothberg, A.W.P. Fung, H.E. Katz, Phys. Rev. B **57**, 2271 (1998)
7. R.J. Chesterfield, J.C. McKeen, Ch.R. Newman, C.D. Frisbie, P.C. Ewbank, K.R. Mann, L.L. Miller, J. Appl. Phys. **95**, 6396 (2004)
8. M.C.J.M. Vissenberg, M. Matters, Phys. Rev. B **57**, 12964 (1998)
9. W.A. Schoonveld, J. Wildeman, D. Fichou, P.A. Bobbert, B.J. Van Wees, T.M. Klapwijk, Nature (London) **404**, 977 (2000)
10. P.M. Borsenberger, Mol. Cryst. Liq. Cryst. **228**, 167 (1993)
11. V.A. Parsegian, *Van der Waals Forces: a Handbook for Biologists, Chemists, Engineers, and Physicists* (Cambridge University Press, Cambridge, 2006)
12. N. Mott, Electrons in glass. Nobel Lecture, Cavendish Laboratory, Cambridge, England, 8 December 1977
13. P.W. Anderson, Absence of diffusion in certain random lattices. Phys. Rev. **109**, 1492 (1958)
14. A.R. Brown, C.P. Jarrett, D.M. de Leeuw, M. Matters, Synth. Met. **88**, 37 (1997)
15. G. Horowitz, R. Hajlaoui, P. Delannoy, J. Phys. III France **5**, 355 (1995)
16. S.F. Nelson, Y.-Y. Lin, D.J. Gundlach, T.N. Jackson, Appl. Phys. Lett. **72**, 1854 (1998)
17. I.N. Hulea et al., Nat. Mater. **5**, 982 (2006)
18. L. Torsi, A. Dodabalapur, L.J. Rothberg, A.W.P. Fung, H.E. Katz, Phys. Rev. B **57**, 2271 (1998)
19. R.J. Chesterfield, J.C. McKeen, Ch.R. Newman, C.D. Frisbie, P.C. Ewbank, K.R. Mann, L.L. Miller, J. Appl. Phys. **95**, 6396 (2004)
20. M.C.J.M. Vissenberg, M. Matters, Phys. Rev. B **57**, 12964 (1998)
21. W.A. Schoonveld, J. Wildeman, D. Fichou, P.A. Bobbert, B.J. Van Wees, T.M. Klapwijk, Nature (London) **404**, 977 (2000)
22. P.V. Necliudov, M.S. Shur, D.J. Gundlach, T.N. Jackson Kannan Seshadri, C. Daniel Frisbie, Appl. Phys. Lett. **7**, 78 (2001)
23. H. Klauk, G. Schmid, W. Radlik, W. Weber, L. Zhou, C.D. Sheraw, J.A. Nichols, T.N. Jackson, Solid-State Electron. **47**, 297 (2003)
24. L. Wang, D. Fine, D. Basu, A. Dodabalapur, J. Appl. Phys. **101**, 054515 (2007)
25. W.D. Gill, J. Appl. Phys. **43**, 5033 (1972)
26. E.J. Meijer, M. Matters, P.T. Herwig, D.M. de Leeuw, T.M. Klapwijk, Appl. Phys. Lett. **23**, 76 (2000)
27. C.D. Dimitrakopoulos, P.R.L. Malenfant, Adv. Mater. **14**(2), 99 (2002)
28. E.J. Meijer, C. Tanase, P.W.M. Blom, E. Van Veenendaal, B.H. Huisman, D.M. De Leeuw, T.M. Klapwijk, Appl. Phys. Lett. **80**, 3838 (2002)
29. W. Meyer, H. Neldel, Z. Tech. Phys. (Leipzig) **18**, 588 (1937)
30. I.I. Fishchuk et al., Phys. Rev. B **76**, 045210 (2007)
31. I.I. Fishchuk, A. Kadachchuk, J. Ganoe, M. Ullah, H. Sitter, Th.B. Singh, N.S. Sariciftci, H. Bässler, Phys. Rev. B **81**, 045202 (2010)
32. J.C. Wang, Y.F. Chen, Appl. Phys. Lett. **73**, 948 (1998)
33. Th.B. Singh, N. Marjanovic, G.J. Matt, S. Günes, N.S. Sariciftci, A. Montaigne Ramil, A. Andreev, H. Sitter, R. Schwödiauer, S. Bauer, Org. Electron. **6**, 105 (2005)
34. T.D. Anthopoulos, B. Singh, N. Marjanovic, N.S. Sariciftci, A.M. Ramil, H. Sitter, Appl. Phys. Lett. **89**, 213504 (2006)
35. C. Tanase, E.J. Meijer, P.W.M. Blom, D.M. de Leeuw, Phys. Rev. Lett. **91**, 216601 (2003)
36. L. Li, G. Mellera, H. Kosina, Synth. Met. **157**, 243 (2007)

37. G. Horowitz, R. Hajlaoui, R. Bourguiga, M. Hajlaoui, Synth. Met. **101**, 401 (1999)
38. M. Shtein, J. Mapel, J.B. Benziger, S.R. Forrest, Appl. Phys. Lett. **81**, 268 (2002)
39. C. Tanase, E.J. Meijer, P.W.M. Blom, D.M. de Leeuw, Org. Electron. **4**, 33 (2003)
40. A. Pivrikas, M. Ullah, Th.B. Singh, C. Simbrunner, G. Matt, H. Sitter, N.S. Sariciftci, Org. Electron. **12**, 161–168 (2011)
41. M. Ullah, T.B. Singh, H. Sitter, N.S. Sariciftci, Appl. Phys. A **97**, 521 (2009)
42. G. Juska, K. Genevicius, K. Arlauskas, R. Osterbacka, H. Stubb, Phys. Rev. B **65**, 233208 (2002)
43. A. Palmaerts, L. Lutsen, T.J. Cleij, D. Vanderzande, A. Pivrikas, H. Neugebauer, N.S. Sariciftci, Polymer **50**, 5007 (2009)
44. H. Bässler, Phys. Status Solidi (b) **175**, 15 (1993)
45. A. Pivrikas, G. Juska, K. Arlauskas, M. Scharber, A. Mozer, N.S. Sariciftci, H. Stubb, R. Österbacka, Proc. SPIE **5938**, 59380N (2005)
46. G. Juška, G. Sliauzys, K. Genevicius, K. Arlauskas, A. Pivrikas, M. Scharber, G. Dennler, N.S. Sariciftci, R. Österbacka, Phys. Rev. B **74**, 115314 (2006)
47. G. Juška, K. Arlauskas, G. Sliauzys, A. Pivrikas, A.J. Mozer, N.S. Sariciftci, M. Scharber, R. Österbacka, Appl. Phys. Lett. **87**, 222110 (2005)
48. G. Juška, K. Genevicius, G. Sliauzys, A. Pivrikas, M. Scharber, R. Österbacka, J. Appl. Phys. **101**, 114505 (2007)
49. R. Österbacka, K. Genevicius, A. Pivrikas, G. Juška, K. Arlauskas, T. Kreouzis, D.D.C. Bradley, H. Stubb, Synth. Met. **139**, 811 (2003)
50. A.J. Mozer, Ph.D. Thesis. LIOS, Johannes Kepler University Linz, Austria
51. C.D. Dimitrakopoulos, D.J. Mascaro, Organic thin-film transistors, a review of recent advances. IBM J. Res. Dev. **45**, 11–27 (2001)
52. G. Horowitz, Organic thin film transistors: from theory to real devices. J. Mater. Res. **19**, 1946–1962 (2004)
53. B. Singh, N.S. Sariciftci, M. Jaiswal, R. Menon, in *Handbook of Organic Electronics and Photonics*, vol. 3, ed. by H.S. Nalwa (2008), pp. 153–176
54. R. Osterbacka, A. Pivrikas, G. Juska, K. Genevicius, K. Arlauskas, H. Stubb, Curr. Appl. Phys. **4**, 534 (2004)
55. A. Pivrikas, Charge transport and recombination in bulk-heterojunction solar cells. Doctoral Thesis, Åbo Akademi University (2006). ISBN 952-12-1784-3
56. M. Ullah, I.I. Fishchuk, A. Kadashchuk, P. Stadler, A. Pivrikas, C. Simbrunner, V.N. Poroshin, N.S. Sariciftci, H. Sitter, Appl. Phys. Lett. **96**, 213306-1 (2010)
57. H. Sitter, *Organic Nanostructures for Next Generation Devices: HWE Growth of Films of Conjugated Molecules* (Springer, Berlin, 2008)
58. M. Herman, H. Sitter, *Molecular Beam Epitaxy: Fundamentals and Current Status* (Springer, Berlin, 1996)

Part IV
Optical Properties

Chapter 9
Excited-State Dynamics and Laser Action in Epitaxial Organic Nanofibers

Francesco Quochi, Michele Saba, Andrea Mura, and Giovanni Bongiovanni

Abstract We present a review on the excited-state dynamics and nonlinear optical properties of *para*-sexiphenyl epitaxial nanofibers grown on muscovite mica and exhibiting amplified spontaneous emission and random lasing at low photoexcitation fluences. We also report on recent advances made with alternated epitaxy of *para*-sexiphenyl and sexithiophene.

9.1 Introduction

Solid-state organic semiconductors have long been investigated for their potential in photonics and optoelectronics applications [1]. Organic molecular crystals can benefit from excellent optical loss and carrier mobility figures, and, hence, offer technological advantages over thin-film disordered media based on either polymers or small molecules. Organic epitaxy is a powerful technique to grow highly ordered organic aggregates at crystalline surfaces. In fact, long-range epitaxial order could be successfully exploited to enhance optoelectronic properties of organic molecular thin films for device applications. An important example of organic epitaxy on inorganic substrates is represented by high-vacuum deposition of *para*-sexiphenyl (p-6P) and similar rod-like molecules on oriented muscovite mica [2] and KCl [3], which yields linear and crystalline nanofibers with extremely high surface-to-volume ratios, sub-wavelength cross-sectional dimensions, and lengths up to the millimeter scale [3–5]. These epitaxial nanofibers exhibit excellent photonic and optoelectronic properties: high photoluminescence efficiency [6], high in-fiber carrier mobility [7, 8], luminescence guidance [9], photoinduced spectral narrowing [10], Raman gain amplification [11], gain amplification of spontaneous emission [12, 13], and optically induced laser action [14–16]. Very recently, organic-organic heteroepitaxy of mixed p-6P/alpha-sexithiophene (6T) nanofibers with highly polarized blue, green and red emission has been successfully demonstrated [17], further broadening the range of potential applications of organic epitaxial nanofibers in photonics and optoelectronics.

F. Quochi (✉) · M. Saba · A. Mura · G. Bongiovanni
Dipartimento di Fisica, Università di Cagliari, 09042 Monserrato (CA), Italy
e-mail: francesco.quochi@dsf.unica.it

H. Sitter et al. (eds.), *Small Organic Molecules on Surfaces*,
Springer Series in Materials Science 173, DOI 10.1007/978-3-642-33848-9_9,

In this chapter, we will review the excited-state dynamics and photonic properties of p-6P and mixed 6T/p-6P nanofibers epitaxially grown on oriented muscovite mica by hot-wall epitaxy and organic molecular beam epitaxy. We will first present the results of transient photoluminescence and transient absorption spectroscopy of p-6P nanofibers, highlighting the interplay between bimolecular recombination, stimulated emission and photoinduced absorption. We will then discuss the occurrence of amplified spontaneous emission and random lasing in p-6P nanofibers. Potential applications of organic epitaxial nanofibers in photonics and sensing technologies will also be touched upon. Last, we will present recent results obtained in mixed 6T/p-6P nanofibers displaying high degree of epitaxial alignment, and highly polarized and broadband emission extending from the blue to the red.

9.2 Excited-State Dynamics and Random Lasing of Organic Media

Deep knowledge of the excited-state dynamics of a photoexcited material system is of fundamental importance for assessing the potential of the system for optoelectronic device applications. With relation to optical amplifiers and lasers, evaluating the lifetime of the excited state(s), as well as the strength of stimulated emission, is essential to determine the ability of the system to provide optical amplification. The so-called figure of merit for optical amplification can be defined as a quantity proportional to the $\sigma_{\mathrm{SE}} B_{\mathrm{SE}} \tau$ product, where σ_{SE} is the net stimulated-emission cross-section of the optical transition undergone by the excited system, B_{SE} is the net stimulated-emission bandwidth, and τ is the excited-state lifetime.

The excited-state lifetime is generally affected by linear and nonlinear, i.e., excitation-density dependent, nonradiative recombination processes. In fact, the shorter is the excited-state lifetime, the higher must be the excitation rate for the system to sustain a stationary optical gain. Bimolecular recombination is a well-known nonlinear deactivation process quenching the optical emission of crystalline semiconductors including highly ordered molecular crystals [18].

Time-resolved spectroscopy techniques such as transient photoluminescence and transient absorption are commonly used to investigate the excite-state dynamics of gain/ laser media upon photoexcitation. On the one hand, transient photoluminescence provides direct access to the temporal evolution of the population of the excited state; on the other hand, transient absorption measures the intensity of stimulated emission and absorption of the excited state during the photocycle of the system [19].

When a gain medium is inserted into an optical cavity, laser emission can occur only provided that the total optical phase acquired by the amplified light in one round trip be equal to a multiple integer of 2π. This oscillation condition does not only hold for a conventional (e.g., Fabry-Pérot) cavity, where feedback is provided by well-defined reflectors, but also for a random cavity, i.e., an optical cavity where closed loops for light amplification and laser oscillation are provided by optical

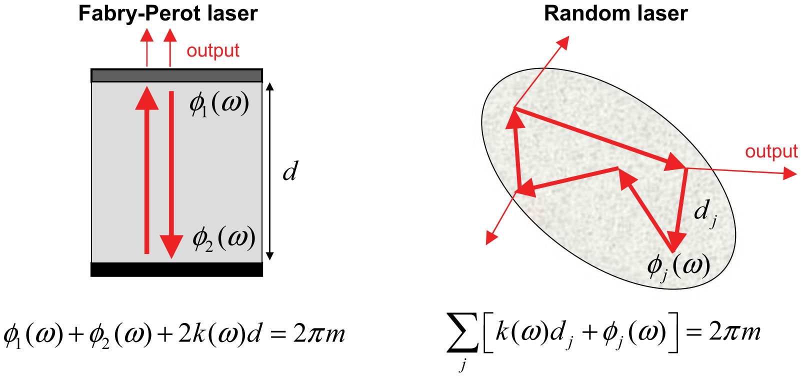

Fig. 9.1 Schematic representation of conventional (Fabry-Pérot) laser (*left*) and random laser (*right*). *Thick arrows* indicate the propagation direction of the light being amplified in the laser cavity or just exiting the cavity to form the output beam(s); $\Phi_j(\omega)$ is the phase jump undergone by the optical beam (of angular frequency ω) being reflected or scattered at jth mirror or scattering center; $k(\omega)$ is the light beam propagation constant; d_j is the path length covered by the light between subsequent reflections or scattering events, and m is an integer

scattering centers randomly distributed within the gain medium (Fig. 9.1). As a matter of fact, random lasing is currently an active field of research from both the experimental and theoretical point of view [20, 21]. Random lasing in organic media has been considered for applications in nanophotonics, sensing [22], and medical sciences as a potential tool for cancer diagnostics [23].

9.3 Growth and Characterization of *p*-6P Epitaxial Nanofibers

Para-sexiphenyl nanofiber films are grown on freshly cleaved, (001)-oriented muscovite mica by Hot-Wall Epitaxy [4] and Organic Molecular Beam Epitaxy [5]. In the hot-wall epitaxy technique, *p*-6P is purified by threefold sublimation under dynamic vacuum. The system is operated with a nominal base pressure during growth of about 9×10^{-6} mbar and the *p*-6P source temperature is set to the optimized value of 240 °C. The substrate temperature is varied between 90 and 180 °C, while the growth time is varied between 10 s and 120 min. Additional details can be found in [24, 25]. In the organic molecular beam epitaxy technique, sheets of muscovite mica are cleaved in air and are transferred immediately after cleavage into a high-vacuum apparatus (base pressure of 5×10^{-8} mbar). Before organic material is deposited, the samples are outgassed at a temperature of around 130 °C such that low energy electron diffraction shows the well-known hexagonal surface structure of clean mica with electric surface dipoles present. *Para*-sexiphenyl is deposited from a home-built Knudsen cell by vacuum sublimation; during the deposition the pressure inside the vacuum system rises to 2×10^{-7} mbar. Long *p*-6P needles grow for deposition rates of 0.1 Å/s and at substrate temperatures around 150 °C.

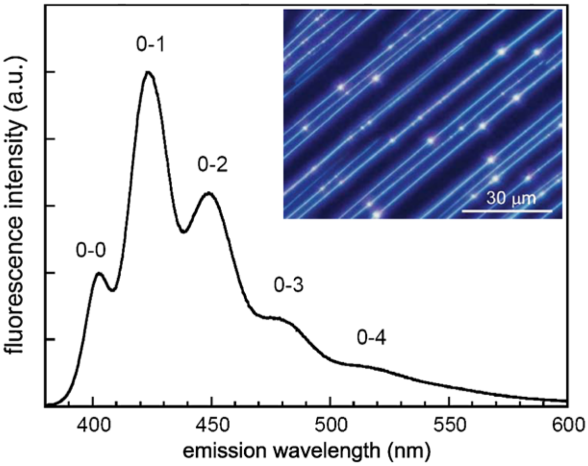

Fig. 9.2 Epifluorescence spectrum (*main panel*) and micrograph (*inset*) of an ensemble of *p*-6P nanofibers photoexcited by a Hg high-pressure in the 330–360 nm band. Emission bands originating from vibronic coupling with C–C stretching mode are labeled for clarity

Morphological characterization of the nanofibers is performed by scanning-probe atomic-force microscopy using Si-tip probes in tapping mode in air. Complementary optical characterization is carried out by cw epifluorescence measurements using an inverted microscope with a Hg high-pressure lamp as the excitation source.

9.3.1 Fluorescence Microscopy

Epifluorescence microscopy and microspectroscopy characterization techniques provide valuable information on the emission properties of nanofiber films. The inset of Fig. 9.2 shows an epifluorescence micrograph of an ensemble of nanofibers under UV illumination.

Large enhancement of fluorescence scattering into out-of-plane directions occurs at special positions on the nanofibers. These bright spots provide high-sensitivity detection of *p*-6P epifluorescence. Correlated optical microscopy and atomic-force microscopy data, which gives insight into the morphology of the strong optical scattering centers, are reported in Sect. 9.5.3. The main panel of Fig. 9.2 displays the room-temperature epifluorescence spectrum of photoexcited *p*-6P epitaxial nanofibers. The spectrum shows the typical features of an H-type molecular aggregate, that is, a weak electronic (0–0) transition and a more intense vibronic progression involving the C–C stretching mode.

9.3.2 Atomic-Force Microscopy

Topography studies of the surface morphology of films realized by hot-wall epitaxy at 130 °C substrate temperature with different growth times demonstrate that

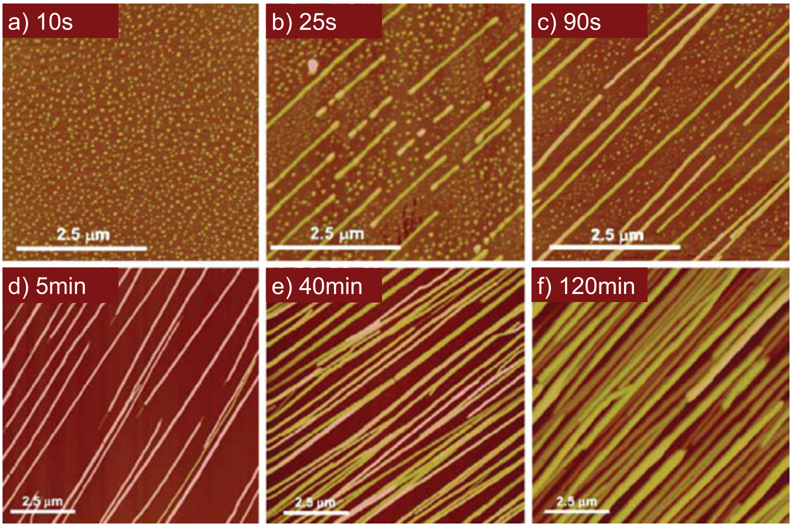

Fig. 9.3 AFM topography images of p-6P nanofiber films grown by hot-wall epitaxy on (001)-oriented muscovite mica for various deposition times. The growth temperature is 130 °C. The height scale is 0–50 nm in (**a**)–(**c**), 0–100 nm in (**d**), 0–220 nm in (**e**), and 0–700 nm in (**f**)

oriented and mutually parallel nanofibers are formed by progressive regrouping of individual crystallites originating at the early growth stages for deposition times $<$10–25 s [26]. For growth times longer than 5 min, only linear fibers are observed. Surface topographic images of films obtained with various growth times are shown in Fig. 9.3. For long ($>$40 min) deposition times, close-packed and interconnected nanofibers are realized.

X-ray diffraction studies demonstrated that p-6P nanocrystals packed in nanofibers are co-oriented and characterized by well-defined epitaxial relationships to the muscovite mica substrate: the long molecular axis of p-6P is nearly parallel to the mica surface plane and nearly perpendicular to the fiber axes [27]. Long-range azimuthal order is realized, which results in high optical anisotropy and high carrier mobility [4, 7].

Statistical analysis of topographic images reveals that the morphological parameters of nanofibers are strongly correlated to the growth time. Raising the growth time from 40 to 120 min. results in an increase of fiber mean height from ~110 to ~290 nm, while the mean base width increases from ~210 to ~350 nm. Deposition time turns out to be a knob to tune cross-sectional dimensions of nanofibers; cross-sectional size is in fact crucial to the attainment of optical waveguiding and amplification in nanofibers. In addition, topographic images show that nanofibers are characterized by the presence of breaks, resulting in fiber segmentation. Such breaks, ~50 to ~300 nm in width, occur at the end of the material growth process as a possible result of a surface thermal gradient during substrate cooling [5]. Breaks play a crucial role for the active photonic properties of nanofibers since they are re-

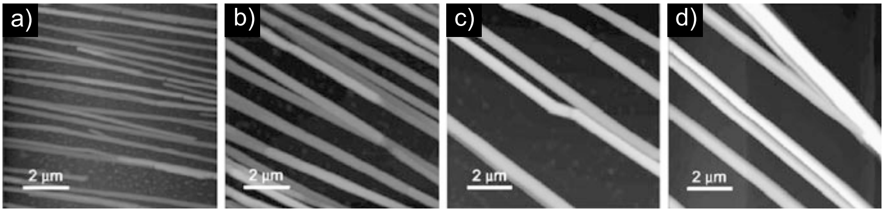

Fig. 9.4 Topographic images of the surface morphology of *p*-6P nanofiber films grown by hot-wall epitaxy on (001)-oriented muscovite mica at different substrate temperatures and with 60 min. Deposition time: (**a**) 90 °C; (**b**) 120 °C; (**c**) 150 °C; (**d**) 170 °C. The height scale is 0–500 nm

sponsible for the establishment of optical feedback along the nanofiber's axes and for light scattering into out-of-plane directions (see Sect. 9.5.3).

Substrate temperature is also an important growth parameter for tuning the morphological properties of nanofibers. In Fig. 9.4 are displayed topographic images of nanofiber films grown for 60 min by hot-wall epitaxy at different substrate temperatures. As temperature is raised from 90 to 170 °C, mean fiber height and cross-sectional area increase from $\sim$80 to $\sim$300 nm and from $\sim$0.05 to $\sim$0.3 μm^2, respectively, while the surface coverage (percentage of film surface covered by nanofibers) decreases from 70 to 20 %, approximately.

This behavior is consistent with Arrhenius dependences, from which one infers that nanofiber nucleation is a thermally activated process [28]. Activation energies range from a few tens to hundreds of meV, depending on whether hot-wall or beam deposition is used and on the morphological parameter being analyzed. Strong correlation is found between fiber morphology and substrate temperature during growth, and, hence, substrate temperature can also be used to control the photonic properties of nanofibers.

9.4 Excited-State Dynamics of *p*-6P Epitaxial Nanofibers

The potential of organic films for laser device technologies stems from the ability to achieve lasing thresholds compatible with indirect electrical pumping by unexpensive and convenient light sources. Lasing performance results from both extrinsic factors (i.e., optical confinement of lasing modes in the gain medium, propagation and feedback losses), and intrinsic gain performance of the active medium. The latter can be quantified by the figure of merit for optical amplification introduced in Sect. 9.2.

Nonlinear emission properties of *p*-6P epitaxial nanofibers are investigated by transient fluorescence spectroscopy using ultrashort ($\sim$150 fs) laser pulses delivered by an optical parametric amplifier running at 1 kHz repetition rate, allowing to tune the excitation wavelength across the 350–400 nm interval. The pump laser beam is focused to circular spots onto the nanofiber films over $\sim(1\text{–}3) \times 10^{-4}$ cm^2 areas, allowing to excite simultaneously tens of nanofibers with pulsed fluences up

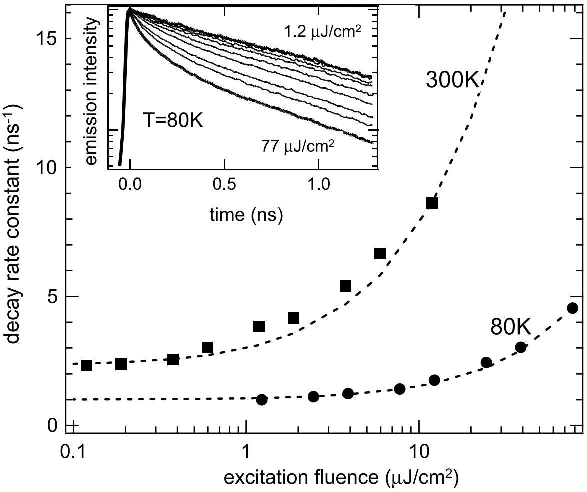

Fig. 9.5 Fluorescence decay rate constant of p-6P nanofibers excited by ultrafast pulses at 380 nm, at 300 K (*squares*) and 80 K (*circles*). *Dashed lines*: Calculated decay rate constant; the calculation includes both monomolecular and bimolecular recombination processes. *Inset*: Fluorescence decay traces measured at 80 K with pump pulsed fluence of 1.2, 2.5, 3.9, 7.8, 12, 25, 39, and 77 $\mu J/cm^2$

to 1 mJ/cm^2. In polarization-resolved experiments, the polarization of the optical emission is rotated using a retardation plate. For nonlinear emission experiments, the pump field polarization is set perpendicular to the axis of the nanofibers (parallel to the long axis of the p-6P molecules) for maximum optical absorption and the excitation fluence is varied using a variable density filter. A cold-finger cryostat fed with liquid air is used to vary the nanofiber lattice temperature in the 80–300 K range. Transient fluorescence is detected by a visible streak camera with $\sim$20 ps time resolution. Complementary transient absorption experiments measuring differential transmission ($\Delta T/T$) changes are performed using broadband pulses obtained by supercontinuum generation in a sapphire plate as the optical probe. The time delay between the pump and probe pulses is controlled by a motorized optical delay stage.

9.4.1 Transient Fluorescence Spectroscopy

Main results of time-resolved fluorescence studies are reported in Fig. 9.5, where fluorescence decay rate constant is plotted as a function of the pump pulsed fluence. Fluorescence decay traces taken at 80 K are drawn in the inset of Fig. 9.5 [16]. At high pump fluences, the excited-state decay dynamics is dominated by nonradiative, density–dependent processes ascribed to singlet-singlet (bimolecular) annihilations [18]. Bimolecular recombination strongly depends on lattice temperature. Upon fitting the initial $1/e$ decay times with the results of model simulations of the decay dynamics, bimolecular coefficient (κ_{SS}) is found to increase from 3×10^{-9}

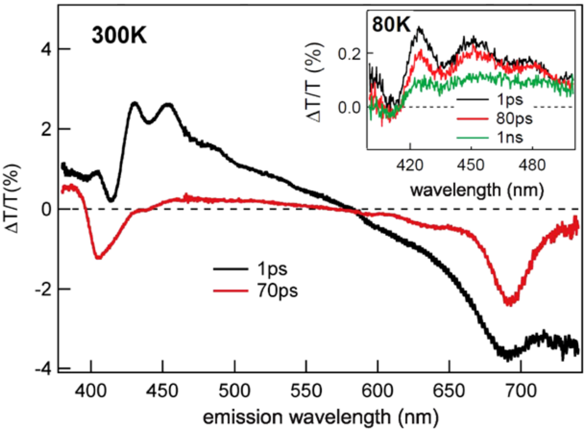

Fig. 9.6 Differential transmission spectra of p-6P epitaxial nanofibers excited by ultrafast pulses centered at 360 nm, for different lattice temperatures and probe-to-pump time delays. Pump pulsed fluence: 90 µJ/cm^2 (*main panel*); 10 µJ/cm^2 (*inset*)

to 4×10^{-8} cm^3/s when lattice temperature is increased from 80 to 300 K. The linear (monomolecular) recombination rate constant (k_0) also exhibits a temperature dependence, concomitantly increasing from 1×10^9 to 2.3×10^9 s^{-1}. At 80 K, bimolecular recombination kicks in for pump fluences of ∼2–4 µJ/cm^2, whereas the threshold goes down to 0.1 µJ/cm^2 at room temperature. The lattice temperature dependence of bimolecular recombination suggests that exciton migration is a thermally activated process [29]. Activation energy is possibly related to the presence of energetic disorder in p-6P nanostructured films [30].

9.4.2 Transient Absorption Spectroscopy

Excited-state photophysical processes such as stimulated emission and photoinduced absorption are studied by differential transmission measurements in transient pump-probe experiments. Transmission spectra taken for various pump-probe delays are shown in Fig. 9.6. At short delays (≤1 ps), the system response is characterized by broadband stimulated emission extending from the deep blue to the orange ($B_{SE} \sim 1$ eV) and exhibiting the vibronic progression of singlet excitons in p-6P crystalline nanofibers. The stimulated-emission cross-section is found to be $\sim 2 \times 10^{-16}$ cm^2, as estimated from $\Delta T/T$ signal amplitude at the 0-2 vibronic peak at zero time delay, assuming that primary photoexcitations are singlet excitons. On the long-wavelength side, the spectrum is dominated by photoinduced absorption of triplet excitons and polarons promptly excited by the pump pulses. At room temperature and high pump fluences (∼90 µJ/cm^2), stimulated emission decays rapidly due to singlet-singlet annihilations and a photoinduced absorption band arises near the optical gap of the material at ∼400 nm.

This long-lived photoinduced absorption band (with decay time >1 ns) is ascribed to intermolecular excitons with charge-transfer character and generated via singlet-singlet annihilations [13]. At cryogenic temperatures (80 K) and lower excitation fluences (∼10 µJ/cm^2), bimolecular recombination is strongly suppressed;

the excited-state lifetime (τ) increases up to $\sim$1 ns and the photoinduced absorption band associated to secondary charge-transfer excitons disappears (inset of Fig. 9.6).

Shortening of the excited-state lifetime is the primary effect of singlet-singlet annihilations. As a secondary effect, a nonlinear population of intermolecular, charge-transfer excitons is created, whose absorption spectrum overlaps with the gain spectrum of the singlet excitons. Combined effects of lifetime shortening, net-gain reduction and bandwidth shrinking by photoinduced absorption are detrimental to lasing action in nanofibers under cw excitation or long (nanosecond) pulsed excitation.

9.5 Optical Amplification and Laser Action in *p*-6P Epitaxial Nanofibers

Amplified spontaneous emission and lasing properties of *p*-6P epitaxial nanofibers are investigated by photoluminescence spectroscopy using $\sim$150 fs-long laser pulses with 360–392 nm central wavelength and 1 kHz repetition frequency. In polarization-resolved experiments, the polarization of the optical emission is rotated using a retardation plate. The optical emission is dispersed in a single grating spectrometer equipped with a liquid-N_2-cooled charge-coupled device allowing for high-sensitivity, time-integrated measurements. For microspectrographic measurements on individual nanofibers, the optical emission is excited through the back (substrate) surface and collected from the front surface using a microscope objective and focused onto the input slit of the spectrometer. Setting the spectrometer to zeroth-order diffraction and fully opening the input slit, fluorescing fibers covering the photoexcited area can be imaged with $\sim$2 μm spatial resolution. Tuning the spectrometer to first-order diffraction and narrowing the input slit, the emission of individual nanofibers aligned parallel to the input slit can be spectrally resolved.

9.5.1 Coherent Random Lasing vs. Amplified Spontaneous Emission

The evolution of the nanofiber emission spectrum for increasing pump pulsed fluence is shown in Fig. 9.7(a). The emission spectrum relates to tens of interconnected nanofibers and thus represents an ensemble-averaged response of nanofibers. When the pump fluence exceeds a threshold value Φ_{th}, resolution-limited peaks emerge from the spontaneous emission spectrum on the 0-1 vibronic band. Threshold fluences are position dependent and can vary from a few μJ/cm^2 to hundreds of μJ/cm^2. As pump fluence is much increased above threshold, the visibility of the narrow lines decreases until spectral narrowing of the vibronic peak dominates the system

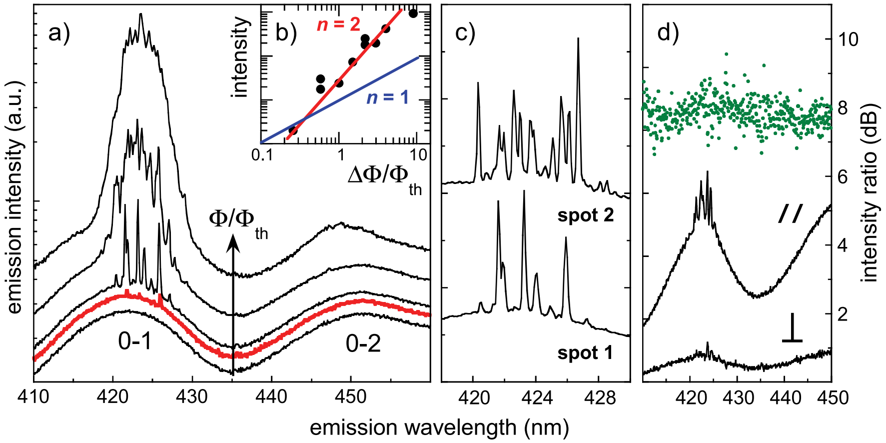

Fig. 9.7 (**a**) Room-temperature, time-integrated optical emission spectra of *p*-6P epitaxial nanofibers excited by subpicosecond pulses as a function of pump fluence: 0.8, 1.0, 1.6, 3.0, 10. Relative units refer to the Φ/Φ_{th} ratio, where Φ_{th} is lasing threshold fluence. (**b**) Time- and spectrally integrated intensity of nonlinear emission above lasing threshold. Linear and quadratic dependences are shown by *solid lines*. (**c**) Position sensitivity of lasing modes: emission spectra are taken in different positions of the pump laser spot on the film surface. (**d**) Polarization-resolved emission spectra, acquired upon polarization filtering of the emission along the direction parallel (//) and perpendicular (⊥) to the long molecular axis of *p*-6P. Spectral dependence of intensity ratio is displayed as *dots*

response. The narrow peaks denote the presence of coherent optical feedback (lasing) within the *p*-6P nanofiber films, whereas spectral narrowing of the 0-1 and 0-2 emission peaks indicates that amplified spontaneous emission occurs at the high pump levels. In Fig. 9.7(b), the emission intensity is plotted as a function of the normalized pump excess fluence, defined as $\Delta\Phi/\Phi_{\mathrm{th}} = (\Phi - \Phi_{\mathrm{th}})/\Phi_{\mathrm{th}}$. The signal intensity is spectrally integrated over the 0-1 band upon subtraction of the spontaneous emission contribution. The nonlinear dependence of the emission intensity on $\Delta\Phi/\Phi_{\mathrm{th}}$ (slope efficiency that increases with increasing pump fluence) is partially attributed to the fact that the number of coherent modes reaching threshold increases with raising pump excess fluence [14].

The spatial sensitivity of the spectrally narrow nonlinear emission of *p*-6P crystalline nanofibers is reported in Fig. 9.7(c). Different distributions of unequally spaced modes are realized in different positions of the excitation spot on the film surface, suggesting the occurrence of coherent random lasing [20, 21]. Moving the pump spots across the film surface results in the excitation coherent modes having different resonance wavelengths and optical losses; as a consequence, a strong variation in lasing threshold fluence is registered as the excited area is changed. As expected from the film structural anisotropy and epitaxial alignment, both linear and nonlinear optical emissions exhibit strong polarization anisotropy with intensity ratios as large as 10 dB (Fig. 9.7(d)).

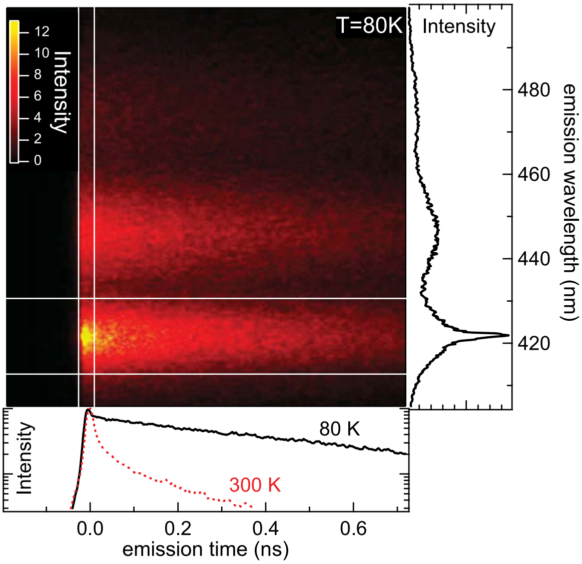

Fig. 9.8 Time-wavelength spectrogram of the fluorescence intensity of cryogenically cooled nanofibers, excited by subpicosecond pulses with 360 nm central wavelength. *Colors code* for intensity levels on an arbitrary unit scale. Pump pulsed fluence is 7 μJ/cm^2. *Vertical* (*horizontal*) *white lines* delimit the spectrogram region used for temporal (spectral) integration. *Right panel*: emission spectrum integrated in the first 30 ps after excitation pulse arrival. *Bottom panel*: Emission decay traces integrated over the 0-1 vibronic band of the p-6P emission. The *solid* (*dashed*) *line* depicts the time profile at 80(300) K

Substrate temperature used during growth has a big influence on the lasing threshold performance of p-6P epitaxial nanofibers. Increasing substrate temperature from 90 to 170 °C, mean lasing threshold, as measured in films grown by hot-wall epitaxy with 60 min deposition time, decreases from ~300 to ~50 μJ/cm^2. These findings are traced back to the thermally activated growth of p-6P epitaxial nanofibers; in fact, thermal activation of the cross-sectional size of nanofibers should result in strong temperature increase of the optical confinement factor of the guided optical emission. Therefore, substrate temperature does not only have an influence on the morphology of p-6P epitaxial nanofibers, but also allows for tuning their lasing properties.

9.5.2 Monomolecular Lasing

Nanofiber cooling to cryogenic temperatures makes it possible to circumvent bimolecular recombination and photoinduced absorption by charge-transfer excitons. Direct demonstration of occurrence of monomolecular lasing, that is, lasing in the linear recombination regime, is provided in Fig. 9.8, which reports the time-wavelength spectrogram of the transient emission intensity of nanofibers excited by subpicosecond pulses and detected by a picosecond streak camera. The spectral

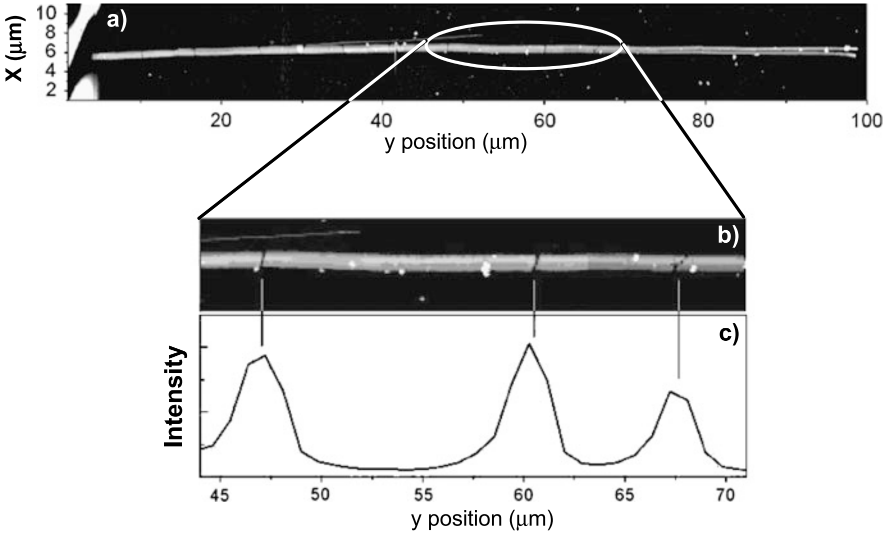

Fig. 9.9 (**a**) Topographic image of a p-6P epitaxial nanofiber exhibiting breaks. (**b**) Image of the indicated subsection of the nanofiber. (**c**) Lasing intensity profile relating to the same fiber segment as in (**b**). *Vertical marks* highlight the correspondence between the positions of breaks and those of optical scattering centers being the origin for coherent feedback and laser light outcoupling

profile (right panel) shows evidence of lasing emission on top of the 0-1 spontaneous emission band. The time profile analysis (bottom panel) shows clear evidence that at 80 K prompt laser emission decays rapidly, leaving the system with a population of singlet excitons undergoing monomolecular recombination with ∼1 ns decay time [16].

9.5.3 Microscopic Origin of Random Lasing

Isolated nanofibers exhibiting strong optical scattering centers give the opportunity to study one-dimensional random lasing in self-assembled epitaxial nanostructures. Emission spectra of isolated nanofibers grown by organic molecular beam epitaxy show that random lasing threshold is reached at both the 0-1 and 0-2 vibronic peaks. As expected for a single laser emitter, spontaneous emission saturates at the value reached at threshold [12]. Fluorescence clamping is not observed in fiber ensemble measurements, since not all the excited fibers reach lasing threshold (Fig. 9.7).

Correlated lasing measurements and atomic-force topographic measurements give insight into the origin of one-dimensional coherent feedback in individual p-6P nanofibers. Figure 9.9(a) shows the topographic image of a ∼100-µm-long, selected nanofiber. When the fiber morphology is compared to the lasing intensity profile on the same region (Figs. 9.9(b) and 9.9(c)), it clearly turns out that scattering of

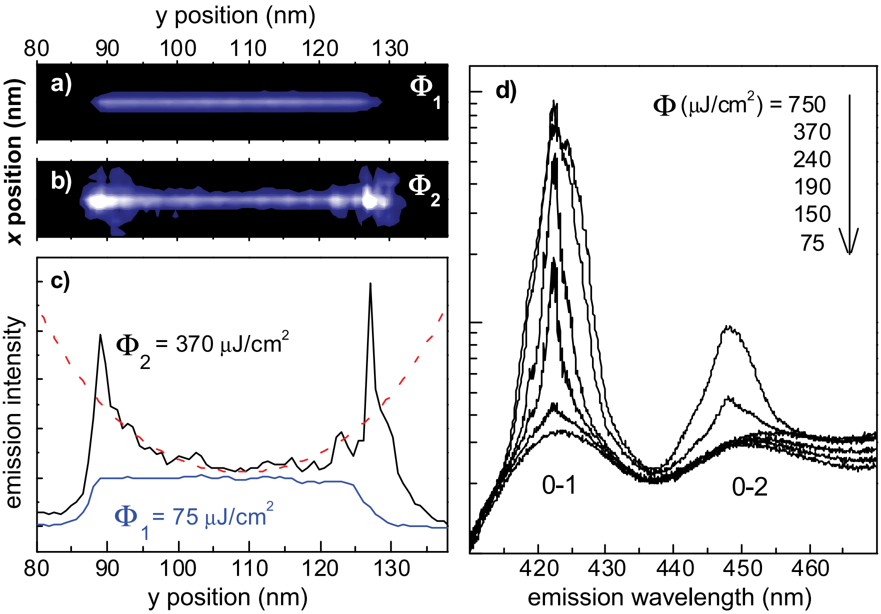

Fig. 9.10 (**a**, **b**) Time-integrated emission micrographs of an individual nanofiber excited by ultrafast laser pulses, for a pump pulsed fluence $\Phi_1 = 75$ (**a**) and $\Phi_2 = 370$ μJ/cm^2. (**c**) Spatial profiles of the emission intensity. The *dashed line* is the fit of a linear amplification function (see text) to the measured profile. (**d**) Emission spectra for different values of the excitation fluence. The spectra are spatially integrated over the nanofiber region

the guided lasing emission occurs at the fiber breaks. In fact, excellent correspondence is found between the positions of the bright lasing spots and those of the fiber breaks. These findings strongly suggest that back-reflections of the fiber waveguide modes at the fiber break interfaces are the main source of optical feedback along the nanofibers' axes. This interpretation of the experimental data in terms of one-dimensional coherent random lasing is in fact supported by calculations of the resonant optical modes of one-dimensionally disordered systems [15].

9.5.4 Guided Amplification of Spontaneous Emission

Determination of net optical gain in isolated fibers yields the optical amplification performance of *p*-6P epitaxial nanofiber waveguides. To this scope, nanofibers are required to display fairly uniform epifluorescence efficiency profiles and not to exhibit breaks with consequent strong optical scattering and feedback [12]. Singly selected fibers grown by organic molecular beam epitaxy are investigated.

The results obtained on a ~40 μm-long nanofiber are shown in Fig. 9.10. At low excitation levels, the emission micrograph of a selected nanofiber shows uniform emission intensity between the fiber tips (Fig. 9.10(a)). Increasing the pump fluence above a threshold value of ~100 μJ/cm^2 per pulse, enhancement of the emission intensity is detected near the fiber tips (Fig. 9.10(b)). The emission intensity increases continuously as the position approaches the tips, where the guided light is efficiently outcoupled (Fig. 9.10(c)).

Assuming linear amplification of spontaneous emission and uniform scattering efficiency across the fiber, the emission intensity profile can be fitted by the function $I_T(z) = I(z) + I(L - z)$, where $I(z) \sim [\exp(gz) - 1]/g$; z is the distance from a fiber tip, g the net modal gain coefficient, and L the fiber length.

The occurrence of amplified spontaneous emission is confirmed by the spectral analysis of the emission intensity above amplification threshold, which shows line narrowing of the emission towards the center of the vibronic bands (Fig. 9.10(d)), whereas spectral fringes relating to ~40 μm-long Fabry-Pérot resonator are not visible. Curve fitting of intensity profiles yields $g_1 \sim 1200$ cm^{-1} for the 0-1 emission band and $g_2 \sim 700$ cm^{-1} for the 0-2 emission band at the highest excitation fluence of 750 μJ/cm^2.

Overall, the results demonstrate that *p*-6P epitaxial nanofibers are able to guide and amplify their spontaneous emission with large amplification factors, and thus hold potential as optical nanoamplifiers at surfaces.

9.6 Photonic Sensing Using *p*-6P Epitaxial Nanofibers

Low-threshold random laser action could be exploited to achieve high photonic sensitivity to various agents; miniaturized random laser sources based on individual *p*-6P epitaxial nanofibers are thus be envisaged to enable new functionalities for next-generation technologies [22, 31].

Based on model simulations of the coherent optical response of a random medium [15], a typical *p*-6P epitaxial nanofiber with a length of ~100 μm and a dozen of thin (~200 nm) breaks is estimated to potentially display *attoliter* sensitivity to contamination by index matching fluids (Fig. 9.11(a)). Also, strain sensors with very large ($>10^3$) gauge factor and high dynamic range could be obtained by optical interrogation of single nanofibers aligned parallel to the strain axis (Figs. 9.11(b) and 9.11(c)).

Surface adsorption of molecular species in nanofibers assembled from suitably functionalized oligomers [32] could generate photonic chemosensing, e.g., by modulation of the effective refractive index of the nanofiber resonance modes. Photonic sensitivity could be further enhanced near lasing threshold, as demonstrated in recent reports [33, 34].

9.7 Sexiphenyl-Sexithiophene Heteroepitaxial Nanofibers

Tuning of laser emission wavelength of *p*-6P epitaxial nanofibers can possibly be achieved by crystal doping with long-wavelength emitting molecules. At relatively

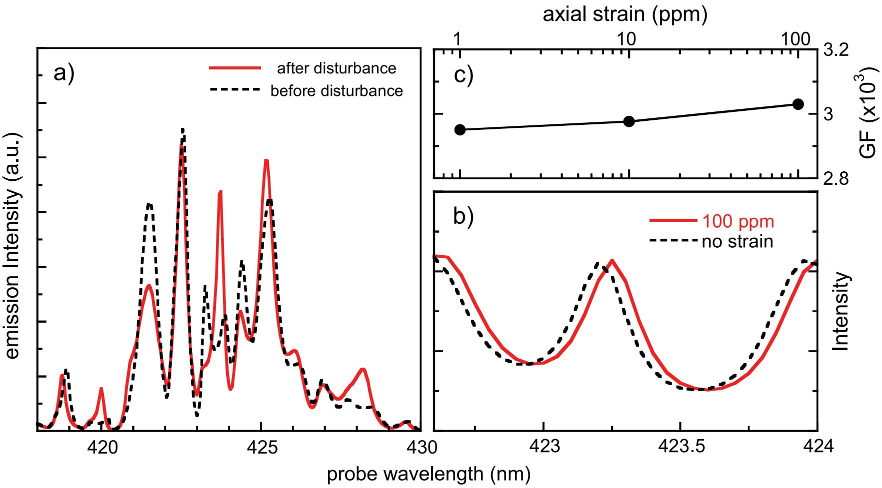

Fig. 9.11 Model calculations of the photonic sensitivity of a p-6P epitaxial nanofiber with one-dimensional random optical feedback. (**a**) Coherent emission spectrum before and after optical neutralization of a fiber break upon air-gap filling with index matching fluid. (**b**) Resonance wavelength shift in response to 100 ppm axial strain. (**c**) Strain gauge factor as a function of strain strength. Gauge factor (GF) is defined from the relation: $\Delta I/I$ (ppm) $= GF \cdot$ strain (ppm), where I is the optical emission intensity

low concentrations, dopant molecules can provide high cross-sections for stimulated emission and long population lifetimes, while their emission can be efficiently sensitized, hence allowing one to circumvent bimolecular recombination occurring in the p-6P crystalline host matrix.

In a recent approach, mixed p-6P/sexithiophene (6T) heteroepitaxial films are grown by hot-wall epitaxy on (001)-oriented muscovite mica to obtain nanofibers with tunable emission properties. Both p-6P and 6T are good model systems for heteroepitaxy and important oligomers for optoelectronic device applications. It has been demonstrated that both p-6P and 6T crystalline thin films can be used as organic templates to obtain highly crystalline organic-organic heterostructures in which p-6P and 6T molecules are both standing or parallel to the substrate [35, 36].

Templates of p-6P nanofibers grown on oriented muscovite mica can be used to obtain oriented and mutually parallel 6T/p-6P nanofibers whose emission color depends on the relative concentrations of the two components. A growth chamber equipped with two hot-wall epitaxy reactors for serial deposition of p-6P and 6T is used for these studies. The substrate is first exposed to the reactor with the p-6P source and then transferred to the 6T reactor; details can be found in [17]. When 6T is directly grown on muscovite, short nanofibers with red-orange fluorescence are yielded with several orientations, whereas 6T deposition on a template of p-6T nanofibers results in 6T/p-6P bilayer fibers which maintain the fiber template's orientation, with no 6T material being deposited in between adjacent p-6P fibers. This is clearly demonstrated by the epifluorescence micrographs shown in Fig. 9.12.

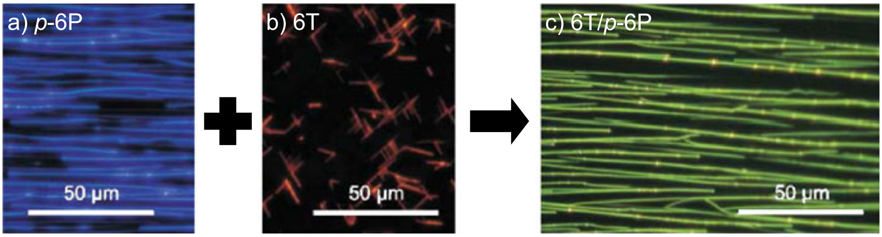

Fig. 9.12 Fluorescence micrographs of heteroepitaxial nanofibers grown on (001)-oriented muscovite mica by hot-wall epitaxy at 120 °C substrate temperature: (**a**) *p*-6P; (**b**) 6T; (**c**) bilayer of 6T (deposition time 90 min) on *p*-6P (deposition time 40 min). Epifluorescence is excited by UV lamp irradiation

Fig. 9.13 Fluorescence spectra of pure *p*-6P nanofibers (*blue line*) and 6T/*p*-6P bilayer nanofibers (*black line*). Fluorescence is excited by 370 nm laser pulses at 80 MHz repetition rate. *Green* and *red spectra* belong to interfacial (i) and bulk crystal (c) 6T in the bilayer sample. *Black dots* are the sum of 6T(i) and 6T(c) spectra

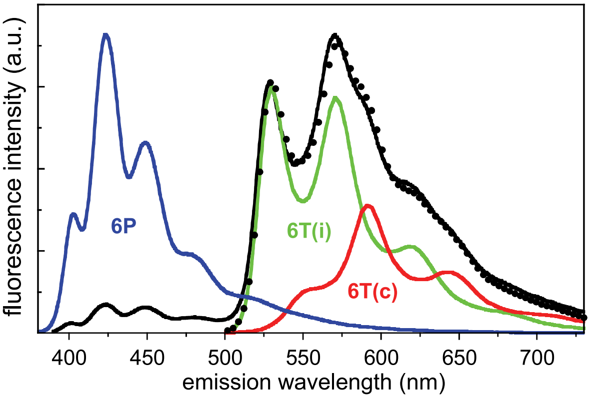

Green emitting fibers are obtained with a 6T deposition time of 5 s, corresponding to submonolayer coverage. In this limit, the 6T fluorescence spectrum is similar to that of a solvated 6T phase (green line spectrum labeled 6T(i) in Fig. 9.13).

Increasing 6T deposition time (and so the 6T-to-6P concentration ratio), oriented 6T crystalline fibers are deposited on top of *p*-6P templating fibers. Crystal phase emission, as obtained in pure 6T films, is shown as the red line labeled 6T(c) in Fig. 9.12. The overall emission spectrum of the 6T/*p*-6P bilayer nanofiber film grown with 40 min (*p*-6P) and 90 min (6T) deposition times (black line in Fig. 9.13) shows evidence of strong quenching of the *p*-6P emission. The interfacial, green emitting 6T sheet is highly emissive, its integrated intensity being comparable to that of the ~400-nm-thick 6T crystalline overlayer. The emission strengths of the interfacial and crystal components are determined by fitting a linear combination of the spectra of the two 6T phases to the total emission spectrum.

Quenching of *p*-6P emission is ascribed to efficient sensitization of 6T via resonance energy transfer [37]. The *p*-6P/6T material couple is thus inferred to display type-I alignment of electronic levels in the bilayer structure, which could allow for extending operation of *p*-6P epitaxial nanofiber lasers to 6T emission wavelengths in the green and in the red via resonance energy transfer from *p*-6P to 6T.

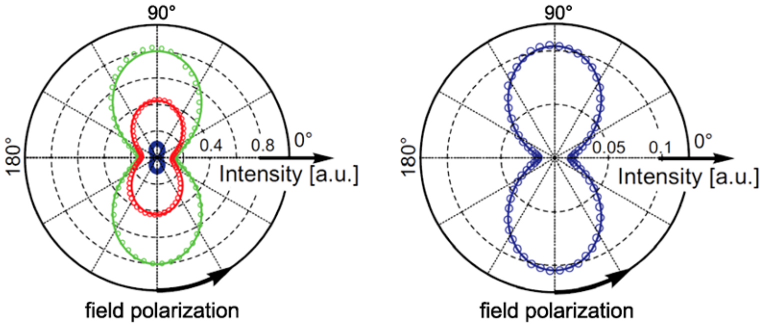

Fig. 9.14 Polar plots of the emission intensity of 6T/p-6P bilayer film versus analyzer polarization angle. *Dots*: experimental points; lines: fits of Malus' law function to the experimental data. *Blue*, *green* and *red colors* code for spectrally integrated emission intensity of p-6P, 6T(i) and 6T(c) material phases, respectively. A magnified view of p-6P intensity data is shown in the right panel for better visibility

Long-range azimuthal order is demonstrated in 6T/p-6P nanofibers by polarization-resolved fluorescence intensity measurements (Fig. 9.14). While the pump laser polarization is set parallel to the p-6P long molecular axis for maximum absorption, the collected fluorescence signal is analyzed by a rotating linear polarizer. For each angular position of the polarizer, the emission spectrum is acquired and decomposed in its p-6P (blue), interfacial 6T (green) and crystalline 6T (red) components. The integrated intensities of the three materials' components are then plotted versus polarizer rotation angle. The results fit quite well to Malus' law dependences for all the three materials' phases. In particular, optical emission dipoles of p-6P and 6T are found to be parallel over domains as large in area as $\sim$1 cm^2. These optical properties support the results X-ray diffraction studies, which determine the exact epitaxial relationships between the 6T/p-6P crystal phases and muscovite mica substrate [17].

In spite of the potential demonstrated by 6T/p-6P heteroepitaxial fibers on oriented muscovite mica for broadband laser emission, evidence of 6T lasing action in such nanostructures or in other epitaxial thin films is lacking yet.

9.8 Conclusion

We reviewed the excited-state dynamics and gain/lasing properties of p-6P epitaxial nanofibers grown by hot-wall epitaxy and organic molecular beam epitaxy on (001)-oriented muscovite mica. We presented the results of ultrafast transient photoluminescence and absorption experiments, which allowed for a quantitative account of the relevant photophysical processes occurring in the photoexcited nanofibers, namely, stimulated emission and excited-state absorption. We also reported on amplified spontaneous emission and coherent random lasing in ensembles of nanofibers, as well as in singly selected fibers, where waveguide amplification performance and coherent feedback mechanisms were investigated by microscopy and microspectroscopy techniques. After a brief discussion of potential applications of organic epitaxial nanofibers in photonic sensing, we concluded by showing recent results obtained in mixed 6T/p-6P heteroepitaxial nanofibers. In fact, the 6T/p-6P material system, combined with the potential of organic epitaxy techniques, is envisaged to bring to the future realization of nanoscale lasers operating in the blue, green and red spectral regions.

Acknowledgements The authors gratefully acknowledge scientific collaboration with F. Cordella, F. Floris, M. Marceddu, R. Orrù, A. Andreev, G. Hernandez-Sosa, N.S. Sariciftci, G. Schwabegger, C. Simbrunner, H. Sitter, M. Oehzelt, R. Resel, F. Balzer, V.G. Bordo and H.-G. Rubahn.

References

1. S.R. Forrest, M.E. Thompson, Introduction: organic electronics and optoelectronics. Chem. Rev. **107**, 923 (2007) and references therein
2. C. Simbrunner, D. Nabok, G. Hernandez-Sosa, M. Oehzelt, T. Djuric, R. Resel, L. Romaner, P. Puschnig, C. Ambrosch-Draxl, I. Salzmann, G. Schwabegger, I. Watzinger, H. Sitter, Epitaxy of rodlike organic molecules on sheet silicates—a growth model based on experiments and simulations. J. Am. Chem. Soc. **133**, 3056 (2011)
3. H. Yanagi, T. Morikawa, Self-waveguided blue light emission in p-sexiphenyl crystals epitaxially grown by mask-shadowing vapor deposition. Appl. Phys. Lett. **75**, 187 (1999)
4. A. Andreev, G. Matt, C.J. Brabec, H. Sitter, D. Badt, H. Seyringer, N.S. Sariciftci, Self-assembled structures of *para*-sexiphenyl grown by hot-wall epitaxy. Adv. Mater. **12**, 629 (2000)
5. F. Balzer, H.-G. Rubahn, Dipole-assisted self-assembly of light-emitting p-nP needles on mica. Appl. Phys. Lett. **79**, 3860 (2001)
6. J. Stampfl, S. Tasch, G. Leising, U. Sherf, Quantum efficiencies of electroluminescent poly(*para*-phenylenes). Synth. Met. **71**, 2125 (1995)
7. T. Birendra-Singh, G. Hernandez-Sosa, H. Neugebauer, A. Andreev, H. Sitter, N.S. Sariciftci, Electrical transport properties of hot wall epitaxially grown *para*-sexiphenyl nano-needles. Phys. Status Solidi (b) **243**, 3329 (2006)
8. J. Kjelstrup-Hansen, H.H. Henrichsen, P. Bøggild, H.-G. Rubahn, Electrical properties of a single p-hexaphenylene nanofiber. Thin Solid Films **515**, 827 (2006)
9. F. Balzer, V.G. Bordo, A.C. Simonsen, H.-G. Rubahn, Optical waveguiding in individual nanometer-scale organic fibers. Phys. Rev. B **67**, 115408 (2003)
10. H. Yanagi, T. Ohara, T. Morikawa, Self-waveguided gain-narrowing of blue light emission from epitaxially oriented p-sexiphenyl crystals. Adv. Mater. **13**, 1452 (2001)
11. H. Yanagi, A. Yoshiki, Stimulated resoance Raman scattering from epitaxially oriented crystals of bi-phenyl-capped thiophene. Appl. Phys. Lett. **84**, 4783 (2004)
12. F. Quochi, F. Cordella, A. Mura, G. Bongiovanni, F. Balzer, H.-G. Rubahn, Gain amplification and lasing properties of individual organic nanofibers. Appl. Phys. Lett. **88**, 041106 (2006)
13. F. Cordella, F. Quochi, M. Saba, A. Andreev, H. Sitter, N.S. Sariciftci, A. Mura, G. Bongiovanni, Optical gain performance of epitaxially grown *para*-sexiphenyl films. Adv. Mater. **19**, 2252 (2007)
14. F. Quochi, F. Cordella, R. Orrù, J.E. Communal, P. Verzeroli, A. Mura, G. Bongiovanni, A. Andreev, H. Sitter, N.S. Sariciftci, Random laser action in self-organized para-sexiphenyl nanofibers grown by hot-wall epitaxy. Appl. Phys. Lett. **84**, 4454 (2004)
15. F. Quochi, F. Cordella, A. Mura, G. Bongiovanni, F. Balzer, H.-G. Rubahn, One-dimensional random lasing in a single organic nanofiber. J. Phys. Chem. B **109**, 21690 (2005)

16. F. Quochi, M. Saba, F. Cordella, A. Gocalinska, R. Corpino, M. Marceddu, A. Anedda, A. Andreev, H. Sitter, N.S. Sariciftci, A. Mura, G. Bongiovanni, Temperature tuning of nonlinear exciton processes in self-assembled oligophenyl nanofibers under laser action. Adv. Mater. **20**, 3017 (2008)
17. C. Simbrunner, F. Quochi, G. Hernandez-Sosa, M. Oehzelt, R. Resel, G. Hesser, M. Arndt, M. Saba, A. Mura, G. Bongiovanni, H. Sitter, Organic–organic heteroepitaxy of red-, green-, and blue-emitting nanofibers. ACS Nano **4**, 6244 (2010)
18. M. Pope, C.E. Swenberg, *Electronic Processes in Organic Crystals and Polymers* (Oxford University Press, New York, 1999)
19. J. Shah, *Ultrafast Spectroscopy of Semiconductors and Semiconductor Nanostructures* (Springer, Berlin, 1999)
20. H. Cao, Lasing in random media. Waves Random Complex Media **13**, R1 (2003)
21. H. Cao, Review on latest developments in random lasers with coherent feedback. J. Phys. A, Math. Gen. **38**, 10497 (2005)
22. See, e.g., D.S. Wiersma, The smallest random laser. Nature **406**, 132 (2000)
23. R.C. Polson, Z.V. Vardeny, Random lasing in human tissues. Appl. Phys. Lett. **85**, 1289 (2004)
24. H. Plank, R. Resel, S. Purger, J. Keckes, A. Thierry, B. Lotz, A. Andreev, N.S. Sariciftci, H. Sitter, Heteroepitaxial growth of self-assembled highly ordered *para*-sexiphenyl films: a crystallographic study. Phys. Rev. B **64**, 235423 (2001)
25. A. Andreev, H. Sitter, C.J. Brabec, P. Hinterdorfer, G. Springholz, N.S. Sariciftci, Self-assembled growth of highly oriented para-sexiphenyl thin films. Synth. Met. **121**, 1379 (2001)
26. A. Andreev, F. Quochi, F. Cordella, A. Mura, G. Bongiovanni, H. Sitter, G. Hlawacek, C. Teichert, N.S. Sariciftci, Coherent random lasing in the deep blue from self-assembled organic nanofibers. J. Appl. Phys. **99**, 034305 (2006)
27. H. Plank, R. Resel, H. Sitter, A. Andreev, N.S. Sariciftci, G. Hlawacek, C. Teichert, A. Thierry, B. Lotz, Molecular alignments in sexiphenyl thin films epitaxially grown on muscovite. Thin Solid Films **443**, 108 (2003)
28. L. Kankate, F. Balzer, H. Niehus, H.-G. Rubahn, From clusters to fibers: parameters for discontinuous *para*-hexaphenylene thin film growth. J. Chem. Phys. **128**, 084709 (2008)
29. H. Wiesenhofer, E. Zojer, E.J.W. List, U. Scherf, J.-L. Brédas, D. Beljonne, Molecular origin of the temperature-dependent energy migration in a rigid-rod ladder-phenylene molecular host. Adv. Mater. **18**, 310 (2006)
30. A. Kadashchuk, A. Andreev, H. Sitter, N.S. Sariciftci, Y. Skryshevsky, Y. Piryatinski, I. Blonsky, D. Meissner, Aggregate states and energetic disorder in highly ordered nanostructures of *para*-sexiphenyl grown by hot wall epitaxy. Adv. Funct. Mater. **14**, 970 (2004)
31. D.S. Wiersma, S. Cavalieri, Light emission: a temperature-tunable random laser. Nature **414**, 708 (2001)
32. M. Schiek, A. Lützen, R. Koch, K. Al-Shamery, F. Balzer, R. Frese, H.-G. Rubahn, Nanofibers from functionalized para-phenylene molecules. Appl. Phys. Lett. **86**, 153107 (2005)
33. A. Rose, Z. Zhu, C.F. Madigan, T.M. Swager, V. Bulović, Sensitivity gains in chemosensing by lasing action in organic polymers. Nature **434**, 876 (2005)
34. R. Chen, B. Ling, X.W. Sun, H.D. Sun, Room temperature excitonic whispering gallery mode lasing from high-quality hexagonal ZnO microdisks. Adv. Mater. **23**, 2199 (2011)
35. M. Oehzelt, G. Koller, J. Ivanco, S. Berkebile, T. Haber, R. Resel, F. Netzer, M.G. Ramsey, Heteroepitaxy: p-sexiphenyl on uniaxially oriented α-sexithiophene. Adv. Mater. **18**, 2466 (2006)
36. G. Koller, S. Berkebile, J.R. Krenn, F.P. Netzer, M. Oehzelt, T. Haber, R. Resel, M.G. Ramsey, Heteroepitaxy of organic–organic nanostructures. Nano Lett. **6**, 1207 (2006)
37. B. Wieb Van Der Meer, G. Coker III, S.-Y. Simon Chen, *Resonance Energy Transfer: Theory and Data* (Wiley, New York, 1994)

Chapter 10
In-situ, Real-Time Investigation of Organic Thin Film Growth Using Reflectance Difference Spectroscopy

Lidong Sun and Peter Zeppenfeld

Abstract We review our recent work on the in-situ studies of organic thin films in ultra high vacuum (UHV) using reflectance difference spectroscopy (RDS). By monitoring in real time the evolution of the optical anisotropy of surfaces and the growing organic layers, the interface formation and subsequent growth behavior can be clearly revealed. At the same time, the influence of molecule-molecule and molecule-substrate interactions on the optical properties of the organic thin films can be explored. The assets of RDS as a versatile technique for real-time studies of organic thin film growth on inorganic substrates (metals, insulators and nano-structured templates) as well as organic–organic heteroepitaxial growth will be illustrated for selected examples.

10.1 Introduction

The intensive research carried out over the last decades concerning the physical properties of organic thin films has led to the development of several applications, such as organic light emitting diodes (OLEDs), organic solar cells, and organic field effect transistors (OFETs) [1–5]. The organic films required for these applications can be prepared by different techniques. However, it is well known that the optical properties of such films strongly depend on their crystal structure and morphology. For instance, a slight variation of the lattice parameter of the crystalline film may significantly affect the optical absorption and emission properties [6]. Therefore, in-situ analytical techniques which allow to probe the optical properties in conjunction with the thin film structure and morphology plays a key role in understanding the structure-properties relationship and its application in organic thin film devices. In fact, the morphology of organic thin films is determined by the delicate balance of the interactions between the molecules, and with the substrate [7]. On the other hand, the electronic structure and the splitting of the molecular and excitonic states

---

L. Sun (✉) · P. Zeppenfeld
Institute of Experimental Physics, Johannes-Kepler University Linz, Altenbergerstr. 69, 4040 Linz, Austria
e-mail: lidong.sun@jku.at

H. Sitter et al. (eds.), *Small Organic Molecules on Surfaces*,
Springer Series in Materials Science 173, DOI 10.1007/978-3-642-33848-9_10,

are strongly affected by these molecular interactions [6, 8]. Therefore, optical spectroscopies which probe the transitions between molecular electronic states directly sense the optical response of these key *interactions* and, hence, the influence of the growth morphology, crystal structure and thin film strain.

The optical properties of organic single crystals and thin films have been extensively studied both by experiment and theory, and a detailed understanding of the excitonic aspects has been achieved [9–19]. However, among the many studies, the research concerning the optical properties of ultra-thin films (from submonolayer coverage to several monolayers) is rather scarce despite its fundamental importance for the growth of thicker films. The reason is quite obvious: the study of ultra-thin films requires an extremely high optical sensitivity which is often lacking in conventional (linear) optical spectroscopy. On the other hand, compared with inorganic species, the adsorption and growth is more complex for organic molecules owing to their particular *internal* (*orientational*, *conformational* and *vibrational*) degrees of freedom especially during the initial stages of growth. This has challenged research based on surface science methods and concepts aiming at constructing adsorption phase diagrams of organic adlayers on various substrates [20–23]. The monitoring of the optical properties as a complement to the traditional surface science characterization methods is thus particularly attractive in the case of ultra-thin organic adlayers.

Reflectance difference spectroscopy (RDS), also called reflectance anisotropy spectroscopy (RAS), measures the difference in reflectance at normal incidence for light polarized along two orthogonal directions. RDS has been successfully used as a powerful technique for in-situ studies on semiconductors and metal surfaces. Recently, the method has also been applied to investigate the adsorption of organic molecules and the growth of organic thin films on metal, semiconductor and insulator substrates. The adsorption of a wide range of different types of organic molecule, including large aromatic molecules [24–42], small carboxylic acids [43–49], amino acids [50], DNA bases cytosine and cytidine 5′-monophosphate [51–53], single-stranded and double-stranded calf thymus DNA [54, 55], as well as spin-cast polymers [56] were subject to RDS investigations. In this review, we will concentrate on our recent applications of RDS to in-situ, real-time monitoring of the growth of organic thin films consisting of large aromatic molecules on single crystal metal and insulator substrates with well defined atomic structures obtained under UHV conditions. For a general introduction to RDS and its application to the investigation of organic molecule adsorption and organic thin film growth, several review and perspective papers can be recommended [8, 57–62].

10.2 Reflectance Difference Spectroscopy (RDS)/Reflectance Anisotropy Spectroscopy (RAS)

Reflectance difference spectroscopy (RDS), also termed reflectance anisotropy spectroscopy (RAS) is a non-destructive optical method, which measures the nor-

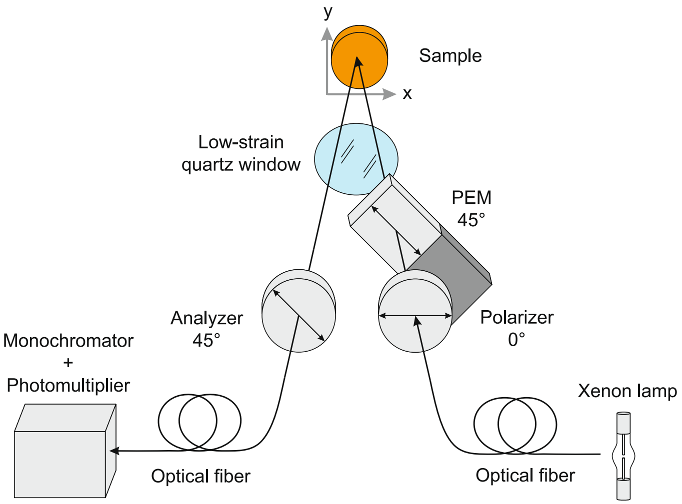

Fig. 10.1 Schematic setup of a PEM-based RD spectrometer

malized difference of the reflectance at near-normal incidence of light polarized along two perpendicular directions:

$$\frac{\Delta r}{r} = 2\frac{r_x - r_y}{r_x + r_y}, \tag{10.1}$$

where r_x and r_y denote the complex reflectivities along the two orthogonal in-plane polarization axes of the incident light beam. Due to the normalization, $\Delta r/r$ is independent of intensity fluctuations of the light source and the detection efficiencies.

The optical setup of a conventional RD spectrometer is schematically depicted in Fig. 10.1. The incident light beam, generated by a Xe lamp, is first linearly polarized by a polarizer. A photoelastic modulator (PEM) whose fast axis is rotated by 45° with respect to the initial polarization direction then introduces a periodic phase shift between the two orthogonal components of the electric field $\delta(t) = A\sin(\omega t)$, where A is the modulation amplitude and ω the modulation frequency which is usually around 50 kHz. After near-normal reflection from the sample, the polarization state of the reflected light beam is analyzed by a second polarizer (analyzer), also oriented at 45° relative to the initial polarization direction of the incident light beam. Finally, a monochromator and a photomultiplier are used to collect photons as a function of their energy in the spectral range between 1.5 and 5.5 eV.

The resulting intensity at the detector can be expressed as a series of harmonics:

$$I(t) = I_0 + I_\omega \sin\omega t + I_{2\omega}\sin 2\omega t + \cdots \tag{10.2}$$

Here I_0 is the *dc* component of the signal, and I_ω and $I_{2\omega}$ denote the *ac* components at the fundamental and the first harmonic of the excitation frequency of the PEM, respectively. The real and imaginary parts of $\Delta r/r$ can be extracted from the ac/dc ratios of the signal at these two frequencies. If, in particularly, one chooses $A = 137.79°$ where $J_0 = 0$ one obtains

$$\frac{I_{2\omega}}{2J_2(A)I_0} = \frac{\mathrm{Re}(\Delta r/r)}{1+|\Delta r/r|^2/4} \approx \mathrm{Re}\left(\frac{\Delta r}{r}\right) \tag{10.3}$$

$$\frac{I_{\omega}}{2J_1(A)I_0} = \frac{\mathrm{Im}(\Delta r/r)}{1+|\Delta r/r|^2/4} \approx \mathrm{Im}\left(\frac{\Delta r}{r}\right) \tag{10.4}$$

Here, J_n denotes the Bassel function of orders n. Therefore, the signal amplitudes of the second and first harmonics are directly proportional to the real and imaginary part of $\Delta r/r$, provided that the anisotropy $|\Delta r/r|$ is sufficiently small. This is typically the case on bare metal surfaces where $|\Delta r/r| \leq 10^{-2}$. However, organic films often exhibit a large optical anisotropy and the approximations in Eq. (10.3) and Eq. (10.4) do not hold anymore. Instead, the normalized difference of the reflected intensity:

$$\frac{\Delta R}{R} = 2\frac{|r_x|^2 - |r_y|^2}{|r_x|^2 + |r_y|^2} = \frac{I_{2\omega}}{J_2(A)I_0} \tag{10.5}$$

is often used as a measure of optical anisotropy of organic thin films [31]. Note that Eq. (10.5) is readily derived from Eq. (10.3) and Eq. (10.4) and holds irrespective of the amplitude of $|\Delta r/r|$.

Due to the normal incidence geometry, RDS is only sensitive to the in-plane optical anisotropy. For optically isotropic materials, such as cubic crystals, the anisotropic signal arises exclusively from a surface with a lower symmetry, such as the fcc (110) surfaces used as substrate in the experiments described below. In case of adsorbate layers and thin films grown on such an anisotropic surface, new features may be introduced into the RD spectra due to the intrinsic optical anisotropy of these overlayers. RDS is thus an extremely sensitive optical probe of the electronic and structural properties of surfaces, interfaces and thin films and has been used extensively to study semiconductor and metal surfaces [62].

The experiments described in this review have all been carried out in ultra high vacuum (UHV) chambers with a base pressure of 1×10^{-10} mbar. The substrates can be heated by electron beam bombardment from the backside and cooled down to temperatures below 15 K with a continuous flow liquid He cryostat. The clean surfaces were normally prepared by repeated cycles of Ar^+ ion sputtering and subsequent annealing. Organic molecules were evaporated from thoroughly degassed Knudsen cells. The deposition rate at the sample position was determined by a quartz microbalance prior to the actual growth experiments. To perform the in-situ RDS measurements, a reflectance difference spectrometer supplied by ISA Jobin Yvon [63, 64] was mounted in front of the UHV chamber. The light beam enters and exits the chamber through a low-strain quartz window (Bomco, Inc.). Under our measurement configuration, the x and y polarization directions (Eq. (10.1) and Eq. (10.5)) are parallel to the crystallographic $[1\bar{1}0]$ and $[001]$ axes of the substrate surfaces Cu(110) and $\mathrm{TiO}_2(110)$.

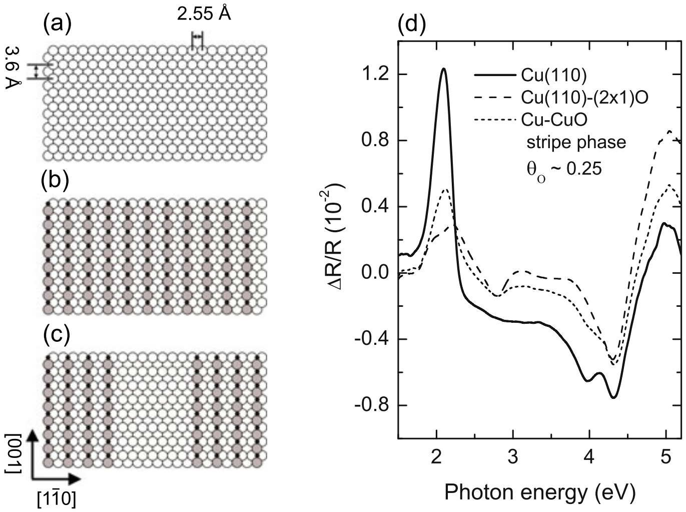

Fig. 10.2 Ball models of the surface atomic structure of Cu(110) (**a**), Cu(110)-(2 × 1)O (**b**), Cu-CuO stripe phase (**c**) and corresponding RD spectra (**d**). The Cu and oxygen atoms are represented by large and small black circles, respectively

10.3 Results and Discussion

In most of the examples discussed in this report, Cu(110), Cu(110)-(2 × 1)O, and the Cu-CuO stripe phase [65] were selected as substrates for organic thin film growth (see Fig. 10.2(a), (b) and (c), respectively). Cu(110) is terminated by densely packed Cu atomic rows that are oriented along the [1$\bar{1}$0] direction. Exposing Cu(110) to molecular oxygen leads to the formation of Cu(110)-(2 × 1)O reconstructed surface with a saturation coverage $\theta_O = 0.5$. The topmost layer consists of Cu-O chains running along the [001] direction with a spacing of two copper lattice distances $2a = 0.51$ nm along the [1$\bar{1}$0] direction. For lower oxygen doses ($\theta_O < 0.5$), the so-called Cu-CuO stripe phase is obtained which is composed of alternating strips of bare Cu(110) and Cu(110)-(2 × 1)O, respectively. All three substrates have an anisotropic surface atomic structure with unidirectional surface corrugation. Due to the different surface chemical termination, Cu(110) and Cu(110)-(2 × 1)O exhibit relatively strong and weak electronic interactions with organic adsorbates, respectively. As the Cu-CuO stripe phase consists of nano-domains of both Cu(110) and Cu(110)-(2 × 1)O areas. It plays a role as a more complex template for adsorption of organic molecules.

Figure 10.2(c) shows the RD spectra of clean Cu(110), Cu(110)-(2 × 1)O and the Cu-CuO stripe phase with an oxygen coverage of $\theta_O \simeq 0.25$, respectively. The RD spectrum of clean Cu(110) shows a pronounced peak at 2.1 eV which derives from three different contributions, namely electronic transitions between occupied- and unoccupied surface states localized at the $\bar{Y}$ point of the surface Brillouin zone, surface modified bulk interband and intraband transitions, respectively [66–72].

Fig. 10.3 Schematic of the *para*-sexiphenyl (*p*-6P) and pentacene molecules and the main intramolecular transitions

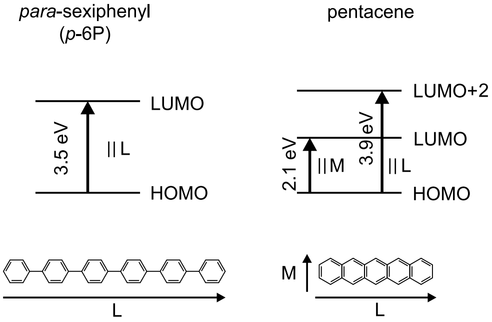

Among these contributions, the surface state related transition is the dominant one and is extremely sensitive to surface defects and adsorbates [71, 72]. It can thus be used as a sensitive measure of the density of surface defects and the adsorbates coverage. In addition, a negative peak at 4.3 eV and a positive peak around 5 eV are observed, which can be attributed to surface modified d-band transitions in the vicinity of the bulk critical point L [67, 69, 73]. Upon oxygen adsorption, the surface related RD signal at 2.1 eV decreases gradually and is completely quenched when the surface is fully covered by the (2×1)O phase [69]. With the formation of the Cu(110)-(2×1)O phase, the 2.1 eV peak of clean Cu(110) transforms into a weak double peak with maxima at 1.9 eV and 2.2 eV, corresponding to an oxygen induced surface state transition and the surface modified Cu bulk contribution, respectively [69]. Since the Cu-CuO stripe phase contains both Cu(110) and Cu(110)-(2×1)O areas, the corresponding RD spectrum is a linear superposition of the RD spectra of the clean and the fully (2×1)O reconstructed surface, respectively [74].

10.3.1 Organic–Inorganic Heteroepitaxy

In this section, we will illustrate the power of reflectance difference spectroscopy for monitoring the growth of organic thin films on metal and insulating substrates. The deposition of *p*-6P molecules on Cu(110) and its reconstructions induced by oxygen, namely, Cu(110)-(2×1)O and the Cu-CuO stripe phase will be used as an example to demonstrate the sensitivity of RDS to the optical anisotropy originating from organic molecules and its potential to monitor the growth on homogeneous surfaces as well as nano-structured surfaces such as the Cu-CuO stripe phase. The deposition of *p*-6P on $TiO_2(110)$ at elevated temperatures will be used to illustrate the capability of RDS to quantify the orientation of organic molecules, in particular, those buried at the organic–inorganic interface.

***p*-6P on Cu(110)**

Metal surfaces interact strongly with organic adsorbates. Consequently, the electronic structures of both the substrates and the organic molecules are significantly

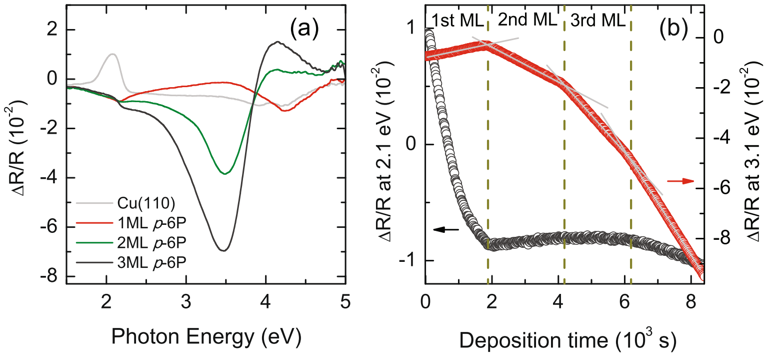

Fig. 10.4 (**a**) $\Delta R/R$ spectra of the clean Cu(110) surface and after deposition of various amounts of p-6P. (**b**) Variation of the $\Delta R/R$ intensity at 2.1 eV and 3.1 eV recorded as a function of the deposition time. All measurements were performed with the sample kept at room temperature [76]

modified at the interface. Therefore, to study the growth of organic thin films on metal substrates, particularly at the initial stage, it is important to measure *simultaneously* the attenuation of the intrinsic optical properties of the metal surface and the evolution of the optical anisotropy related to the intramolecular electronic transition of the adsorbed molecules.

To obtain an overview of the growth process, first, RD spectra are recorded as a function of the nominal thickness of the organic thin film. Based on the spectral lineshape including the sign and the energetic position of the characteristic RD features, information on the growth mode including morphology as well as the orientation and interactions of the constituting molecules can be deduced. In Fig. 10.4(a), selected RD spectra for different film thicknesses recorded during deposition of p-6P on Cu(110) are depicted. In the first monolayer, the p-6P molecules are in direct contact with the substrate and undergos a strong electronic interaction (hybridization) with the Cu(110) surface. As a consequence, the surface states related RD signal at 2.1 eV is completely quenched upon completion of the first p-6P monolayer. Moreover, the optical absorption related to the HOMO-LUMO transition of the p-6P molecule is also fully suppressed and the p-6P molecules are practically "invisible" to RDS. On the other hand, the electronic hybridization with the Cu(110) substrate is efficiently screened for p-6P molecules adsorbed in the second monolayer already. As a result, the RD signal at 3.5 eV, which is related to the HOMO-LUMO transition of p-6P (see Fig. 10.3), appears as soon as the second monolayer starts to grow. This is a quite general phenomenon for organic molecules deposited on metal surfaces: the intramolecular transition is quenched for the molecules in direct contact with the metal substrate and becomes active if only a single layer of molecules is buffered in between [37, 75, 76]. Upon further deposition, the RD signal at 3.5 eV grows monotonically to more negative values. As mentioned previously, the HOMO-LUMO transition dipole moment of a p-6P molecule is polarized along its long molecular axis. Therefore, the negative sign of the RD signal at 3.5 eV indicates that the long molecular axis of the p-6P molecules on the Cu(110) surface is oriented along the [001] direction of the substrate [37, 76]. Furthermore, the details of the spectral line shape around 3.5 eV varies as a function of the film thickness. This is due to the fact that the optical absorption of organic thin films depends strongly on its morphology as well as the arrangement and conformation of the constituting molecules.

In addition to the full range RD spectroscopic measurement, it is very helpful to record in real-time RD transients at characteristic photon energies during deposition so that the details of the surface kinetics and growth can be monitored in a dynamic way [44]. The data acquisition at a few selected energies is much faster than recording full RD spectra and thus allows sub-second temporal resolution. The energies can be chosen to match particular species or transitions whose evolution can thus be monitored in real time. For *p*-6P deposition on Cu(110), the RD signals at two photon energies are selected: (1) $E = 2.1$ eV, which is related to the surface states transition of Cu(110) and thus extremely sensitive to any kind of surface defects including organic adsorbates. It is used here to quantify the surface coverage of *p*-6P. (2) $E = 3.1$ eV, which is close to the excitation energy of the HOMO-LUMO transition of the *p*-6P molecule and thus reflects the optical properties of the growing thin film. It thus provides information concerning the molecular orientation and the thin film morphology. The evolution of the RD signals clearly shows that the growth of *p*-6P on Cu(110) follows a Stranski–Krastanov mode (Fig. 10.4(b)). The layer-by-layer growth up to the third monolayer is evidenced by the sharp kinks in the RD transient at $E = 3.1$ eV. These kinks separate regions with different but constant slopes. The perfect coincidence of the total quenching of the 2.1 eV signal with the onset of the rise of the RD signal at 3.1 eV demonstrates the complete wetting of the Cu(110) surface by a monolayer of *p*-6P [37, 76].

p-6P on Cu(110)-(2 × 1)O

Cu(110)-(2 × 1)O reconstructed surface can be prepared by exposing the Cu(110) surface to molecular oxygen at room temperature and subsequent annealing at 600 K. The surface is terminated by Cu-O rows running along the Cu[001] direction. On the Cu(110)-(2×1)O surface, the surface states of Cu(110) are completely quenched and the corresponding RD signal at 2.1 eV is no longer available for studying the adsorption of organic molecules. On the other hand, the Cu(110)-(2 × 1)O reconstructed surface is relatively inert in comparison to the bare Cu(110) substrate and interacts only weakly with organic molecules adsorbed on top of it. Consequently, the optical absorption of the molecules in the first monolayer is not completely suppressed but only slightly modified. The deposition of *p*-6P molecules on Cu(110)-(2 × 1)O can thus be followed by monitoring the evolution of the RD signal related to the intramolecular transition right from the beginning of the growth.

The RD transient at 3.3 eV recorded during the deposition of *p*-6P on the Cu(110)-(2 × 1)O surface at room temperature is shown in Fig. 10.5(a). The RD signal increases monotonically with increasing *p*-6P exposure. The positive sign of the RD signal at 3.3 eV indicates that the *p*-6P molecules adsorbed on the surface

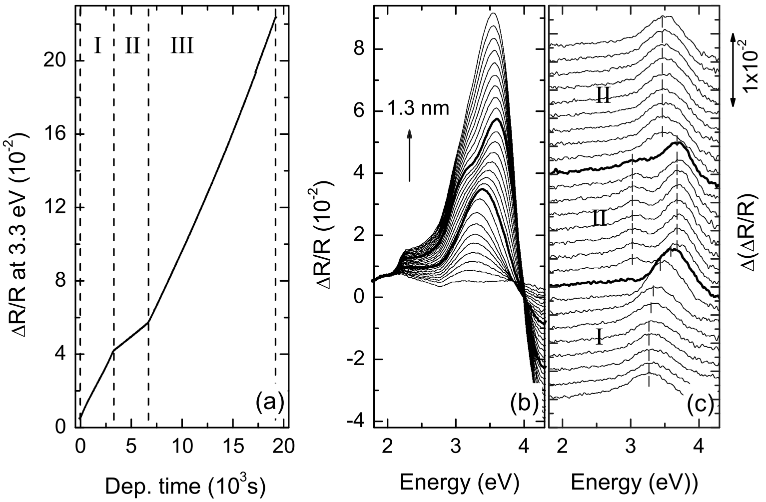

Fig. 10.5 (**a**) $\Delta R/R$ signal at 3.3 eV recorded during p-6P growth on the Cu(110)-(2 × 1)O surface at room temperature. The regions marked *I* and *II* correspond to the completion of the first and second monolayer, respectively. (**b**) $\Delta R/R$ spectra recorded from the bare Cu(110)-(2 × 1)O surface (*bottom line*) and after successive deposition of p-6P at room temperature. The p-6P coverage was increased in steps of 0.05 nm up to a final thickness of 1.3 nm. (**c**) Difference between subsequent $\Delta R/R$ spectra in (**b**) revealing the incremental changes of the optical properties. The *curves* corresponding to monolayer and bilayer completion (according to (**a**)) are highlighted by *thick lines* [77]

are exclusively oriented along the [001] direction of the Cu(110) substrate. The fact that the RD signal evolves in a step-wise fashion shows that the growth of p-6P on Cu(110)-(2 × 1)O follows a Stranski–Krastanov mode with the first two regions (I and II in Fig. 10.5) correspond to the growth of the first and second monolayer (ML) of lying p-6P molecules, respectively. The sudden change of the slope of the RD transient in between suggests an almost perfect layer-by-layer growth [77].

This particular shape of the $\Delta R/R$ transient at 3.3 eV displayed in Fig. 10.5(a) is due to the layer-wise evolution of the optical properties of the growing p-6P thin films, and reflects the sudden change of the molecule aggregation upon adding a new molecular layer. This can be seen in Fig. 10.5(b) which shows entire $\Delta R/R$ spectra for the bare Cu(110)-(2 × 1)O surface and after successive deposition of p-6P at room temperature up to a final thickness of 1.3 nm. According to the spectroscopic lineshape revealed in Fig. 10.5(b), the growth can be divided into three stages which coincide very nicely with those deduced from the RD transient at 3.3 eV shown in Fig. 10.5(a). This is even more evident in Fig. 10.5(c) where the *difference* between two subsequent $\Delta R/R$ spectra in Fig. 10.5(b) are plotted. These *difference* spectra $[\Delta(\Delta R/R)]$ thus reflect the incremental changes of the optical anisotropy of the p-6P film with each deposition step: (I) First monolayer: At the very beginning of the growth, the $\Delta R/R$ spectra are characterized by a growing single peak located at 3.3 eV. The peak position gradually shifts to higher energy when the nominal thickness increases from 0.35 nm to 0.45 nm. (II) Second monolayer: For film thicknesses between 0.45 nm and 0.85 nm, corresponding to the growth of the second monolayer, the $\Delta R/R$ spectra are characterized by a double peak with two maxima located at 3.2 and 3.6 eV, respectively. (III) 3D island formation: Beyond 0.85 nm, the spectra exhibit a single peak centered at 3.5 eV. This feature continues to grow with increasing *p*-6P coverage but no further abrupt change of the spectroscopic line shape is observed [77]. The $\Delta R/R$ signal eventually saturates when the film thickness becomes much larger than the optical penetration depth.

One of the most important observations in this study is that the spectral line shape is characteristic for each growth stage. This is due to the fact that the optical properties of organic molecules are strongly affected by the interactions with their surroundings, namely, the neighboring molecules as well as the underlying substrate. On the other hand, these molecular interactions crucially depend on the actual arrangement of the molecules within the thin film and its evolution especially during the initial stages of growth. This interplay between structure and optical properties allows one to characterize the structure in straight conjunction with the evolution of their optical properties [8, 77].

p-6P on Cu-CuO Stripe Phase

After discussing of the adsorption of *p*-6P on the bare and the fully (2 × 1)O reconstructed Cu(110) surface, respectively, we now consider the deposition of *p*-6P on the Cu-CuO stripe phases. One of the most interesting questions concerns the adsorption sequence on this one-dimensional template consisting of alternating Cu and CuO stripes with strong chemical contrast. Due to the fact that the surface states of Cu(110) still exist on the bare Cu areas but are completely quenched on the CuO stripes [74], the surface state related RD signal at 2.1 eV can be used to probe the adsorption of *p*-6P molecules on the Cu stripes. On the other hand, for submonolayer coverages, only those *p*-6P molecules which are adsorbed on the CuO stripes should contribute to the intramolecular transition related RD feature at 3.3 eV. Therefore, the RD signal at 3.3 eV can be used as an indicator for the adsorption of *p*-6P on the CuO stripes. The RD spectra recorded as a function of *p*-6P coverage on a Cu-CuO stripe phase with an oxygen coverage $\theta_{\mathrm{O}} = 0.25$ are presented in Fig. 10.6(a) and the corresponding RD intensities at 2.1 eV and 3.3 eV are plotted in Fig. 10.6(b). During adsorption of the first 0.125 ML of *p*-6P (stage I), neither the RD signal at 2.1 eV nor that at 3.5 eV shows any significant variation. This indicates that the *p*-6P molecules initially adsorb at the boundaries (step edges) between the Cu and the CuO stripes with their long molecular axis parallel to the [001] (i.e., the stripe) direction. Indeed, this is the only configuration for which the effect on both RD signals (surface state and molecular transitions) is minimized. Upon further deposition of *p*-6P (stage II) the RD signal at 2.1 eV decreases indicating that *p*-6P starts to adsorb on the bare Cu stripes. At a coverage of about 0.5 ML, the RD signal at 2.1 eV is completely quenched, whereas the RD intensity at 3.3 eV starts to increase significantly (stage III). Obviously, the Cu stripes are now fully covered with a single layer of *p*-6P and the newly deposited molecules are adsorbed on the CuO

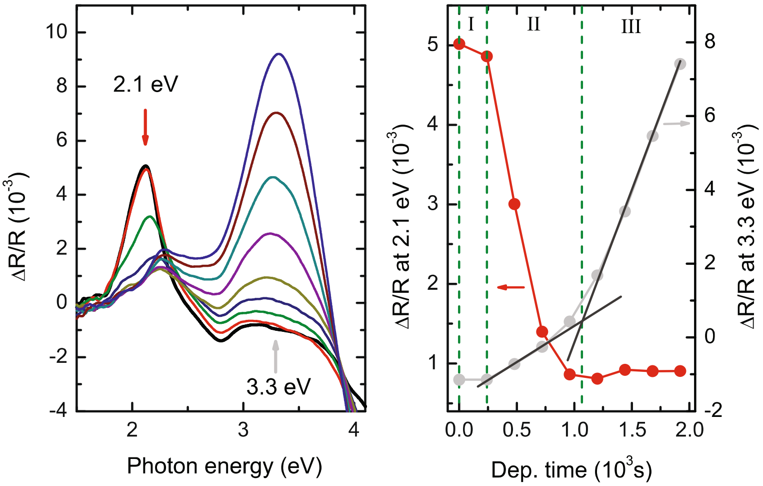

Fig. 10.6 (**a**) $\Delta R/R$ spectra recorded from the Cu-CuO stripe phase with an oxygen coverage $\theta_O = 0.25$ (*thick black line* at 2.1 eV) and after successive deposition of p-6P at room temperature. The p-6P coverage was increased in steps of 0.125 ML up to a final coverage of about 1 ML. (**b**) Variation of the $\Delta R/R$ intensity at 2.1 eV and 3.1 eV as a function of the p-6P deposition time. All measurements were performed with the sample kept at room temperature

stripes. Based on the sign and the amplitude of the RD signal at 3.3 eV, we can infer that the adsorption configuration of p-6P on the CuO stripes is the same as on the Cu(110)-(2 × 1)O surface (Fig. 10.5), i.e., the molecules are aligned along the [001] direction.

p-6P on TiO$_2$(110)

For the application of electronic and optical devices based on organic thin films, it is extremely relevant to know and eventually control the orientation of the organic molecules at the interface. The high sensitivity of RDS to the ordering and alignment of small amounts of organic molecules allows one not only to determine the azimuthal orientation of lying molecules (also shown in the previous sections) but also to discriminate between lying and near upright standing molecules [38]. In the following, we will discuss the interesting case of p-6P adsorbed on TiO$_2$(110) in which a wetting layer of lying molecules is subsequently covered by 3D islands consisting of near upright standing p-6P.

Figure 10.7(a) shows RD spectra ($\Delta R/R$) recorded after incremental p-6P deposition up to a nominal thickness of 6 nm at a substrate temperature of 380 K. The deposited amount of p-6P in each of the first 12 deposition steps corresponds to a nominal thickness of 0.1 nm. A final step of 4.8 nm of p-6P were deposited at 380 K to yield a total film thickness of 6 nm. For comparison, the RD spectrum of a p-6P film with the same thickness of 6 nm, but grown at room temperature (RT) is also

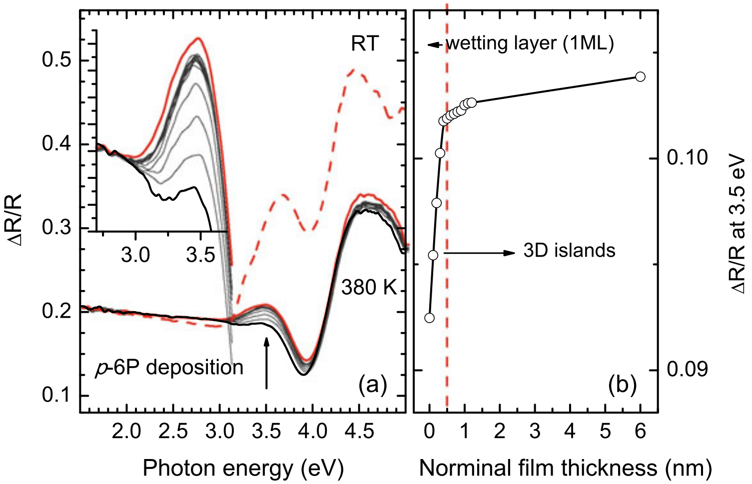

Fig. 10.7 (**a**) $\Delta R/R$ spectra recorded from the $TiO_2(110)$ surface (*thick black solid line*), after incremental deposition of 0.1 nm (*thin dark solid lines*) and one additional deposition step of 4.8 nm, (*thick red solid line*). The RD spectrum of a 6 nm, thick p-6P layer deposited at 300 K (*thick red dashed line*) is shown for comparison. The *inset* emphasizes the spectral evolution in the energy range around 3.5 eV. (**b**) The evolution of RD signal at 3.5 eV as a function of the nominal thickness of p-6P thin film during deposition at 380 K [78]

shown in Fig. 10.7. For the p-6P films with identical thickness of 6 nm, the optical anisotropy around 3.5 eV of the p-6P is much larger for the film grown at RT than for the one deposited at 380 K. This is due to the fact that in the film grown at RT, the p-6P molecules are lying, whereas the films deposited at 380 K mainly consists of upright standing molecules [38, 79].

To quantify the evolution of the thin film morphology, the RD intensity at 3.5 eV is plotted as a function of the nominal film thickness in Fig. 10.7b. During the initial stage of growth, the RD signal at 3.5 eV increases linearly up to a thickness of about 0.4 nm, which exactly corresponds to one monolayer of lying p-6P. The large optical anisotropy at 3.5 eV for the first monolayer results from the molecules in the first monolayer being uniaxially aligned along the [001] azimuth of $TiO_2(110)$ surface. Indeed, the line shape and amplitude of the RD spectra in this regime is identical to that obtained for growth at RT [38] and is due to a wetting monolayer of lying p-6P molecules. For further growth beyond the first monolayer, the incremental increase of the optical anisotropy as a function of the p-6P coverage becomes much smaller in the whole energy range of measurement. In particular, almost no change in the optical anisotropy is observed in the region around 3.5 eV. This result implies that the molecules grown on top of the lying monolayer do not display a strong in-plane anisotropy, which is expected for standing molecules [19, 38]. Of particular importance is the observation that no reduction of the anisotropy at 3.5 eV appears at any stage during the growth at elevated temperatures. Since the standing molecular layers are optically transparent around 3.5 eV [19], the optical anisotropy of the wetting layer is still accessible even when it is buried. If the molecules of the

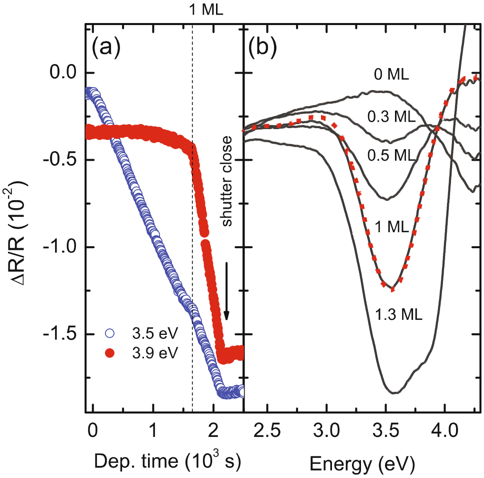

Fig. 10.8 (**a**) $\Delta R/R$ signals at 3.5 eV and 3.9 eV recorded at room temperature during the deposition of pentacene on one monolayer p-6P covered Cu(110) as a function of deposition time. (**b**) Corresponding RD spectra taken at different pentacene coverages indicated in monolayer (ML) units [80]

lying monolayer changed their orientation upon further growth, such as if they were incorporated into the film of upright molecules, the strong positive signal at 3.5 eV would significantly decrease in the subsequent RD spectra. As this is not the case, it can be concluded that the lying molecular monolayer does not dewet or significantly reorient upon the growth of layers of standing molecules on top of it [78].

10.3.2 Organic–Organic Heteroepitaxy on Metal Surface

Organic molecules can be distinguished by their characteristic optical response related to the specific intramolecular electronic transitions. This property can be used to investigate the growth of organic–organic heterostructures by monitoring the evolution of the characteristic optical transitions of each of the constituting molecules.

To fabricate p-6P/pentacene heterobilayers on Cu(110) and demonstrate their self-assembly properties, we deposited pentacene molecules on a well ordered p-6P monolayer on Cu(110). The RD spectrum of one monolayer p-6P covered Cu(110) is plotted in Fig. 10.8(b) (marked as 0 ML). Due to the strong electronic interaction between organic molecules and metal substrates, no characteristic absorption peak of p-6P can be observed in the RD spectrum recorded at this stage. During the subsequent pentacene deposition, RD signals at 3.5 eV and 3.9 eV were recorded as fingerprints of p-6P and pentacene (see Fig. 10.3), respectively. Interestingly, as soon as the deposition of *pentacene* is started, the negative RD signal at 3.5 eV, which is the signature of p-6P, spontaneously increases in amplitude, whereas the RD signal at 3.9 eV, i.e., the fingerprint of pentacene, remains unchanged (Fig. 10.8(a)). According to the previous discussion, the absence of an RD signature at 3.9 eV indicates that the deposited pentacene molecules are in direct contact with the Cu(110) substrate, whereas the increasing amplitude of the RD signal at 3.5 eV suggests that the p-6P molecules originally lying right on top of the substrate have been lifted up into the layer above. This situation continues until the amplitude of the negative peak at 3.9 eV starts to increase after 1650 seconds of pentacene deposition, indicating the completion of the first pentacene monolayer (Fig. 10.8(a)). The corresponding RD spectra recorded after different steps of pentacene deposition are shown in Fig. 10.8(b). Indeed, up to the completion of the first pentacene monolayer, only the RD signature of p-6P at 3.5 eV grows with pentacene coverage. When the pentacene coverage exceeds one monolayer, a shoulder at 3.9 eV appears which is contributed by the pentacene in excess of one monolayer. After desorbing the extra pentacene molecules by annealing at 400 K, a well ordered heterobilayer structure of p-6P/pentacene/Cu(110) is created. Moreover, based on the negative sign of the RD signals at 3.5 eV and 3.9 eV, one can conclude that both, the p-6P and the pentacene molecules are preferentially aligned along the $[1\bar{1}0]$ direction of the Cu(110) substrate [80].

RDS was also used to monitor the co-deposition of pentacene and p-6P on the Cu(110) surface. In this case, three RD transients at 2.1 eV, 3.5 eV and 3.9 eV were recorded simultaneously. As one can see from Fig. 10.9(a), the growth can be separated into three stages: (I) *The growth of the first monolayer composed of both, pentacene and p-6P molecules*. The RD signal at 2.1 eV decreases monotonically as a function of deposition time, indicating the increasing coverage of adsorbed molecules on the surface. At this stage the characteristic RD signals related to the molecular optical absorption are still absent, indicating that both pentacene and p-6P molecules adsorb directly on top of the Cu(110) surface. (II) *The formation of the p-6P/pentacene/Cu(110) bilayer structure*. As soon as the surface becomes fully covered (signalized by the complete quenching of the RD signal at 2.1 eV), the amplitude of the RD signal at 3.5 eV starts to increase while the RD signal at 3.9 eV stays constant. This observation reveals three characteristics: (a) all the pentacene molecules deposited during stage (II) diffuse into the first monolayer by exchanging with p-6P molecules; (b) the p-6P molecules being freshly deposited together with those being expelled from the first monolayer, accumulate in the second monolayer; (c) the p-6P molecules are oriented preferentially along the $[1\bar{1}0]$ direction of the substrate. (III) *The growth of excess p-6P and pentacene after completion of the p-6P/pentacene bilayer*. The onset of the increase of the RD signal at 3.9 eV is a sign of the completion of the pentacene/Cu(110) interface layer. All subsequently deposited molecules will be incorporated in the upper layers where they are optically active and thus give rise to a monotonous increase of the RD amplitudes at both, 3.5 and 3.9 eV. The RD spectra for coverages close to the bilayer completion are plotted in Fig. 10.9(b). The RD spectrum obtained after 1800 seconds of deposition corresponds to the completed p-6P/pentacene/Cu(110) bilayer and perfectly coincides with the characteristic spectrum obtained after subsequent deposition and shown in Fig. 10.8(b). The spectrum recorded after 2100 s deposition shows some excess p-6P and pentacene on top of the heterobilayer, which can be desorbed by heating to 400 K (dashed line in Fig. 10.9(b)) [80].

To investigate the kinetics of the inversion process, 0.7 ML of pentacene was deposited at low temperature (15 K) on top of a single monolayer of p-6P preadsorbed on the Cu(110) surface. Figure 10.10(a) shows the RD spectra recorded

Fig. 10.9 (**a**) $\Delta R/R$ signals at 2.1 eV, 3.5 eV and 3.9 eV recorded during the co-deposition at room temperature of p-6P and pentacene on Cu(110) as a function of deposition time. (**b**) $\Delta R/R$ spectra recorded from the bare Cu(110) surface and after successive co-deposition of p-6P and pentacene at room temperature (*solid lines*). The spectrum recorded after subsequent heating to 400 K is shown by the *dashed line* [80]

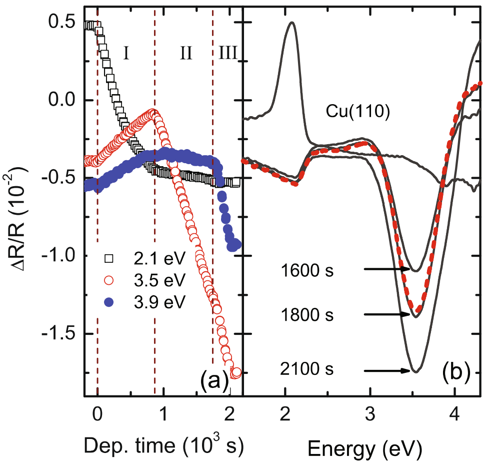

Fig. 10.10 $\Delta R/R$ spectra recorded after deposition at 15 K of 0.7 ML of pentacene on top of one monolayer of p-6P on Cu(110) (**a**), after heating the sample to 60 K and 130 K (**b**), and after further heating to 150 K, 170 K, 175 K, 180 K, 185 K and 200 K (**c**). As a reference, the $\Delta R/R$ spectrum of 1 ML of p-6P on Cu(110) is also plotted in (**a**). All $\Delta R/R$ spectra were recorded with the sample kept at 15 K [76]

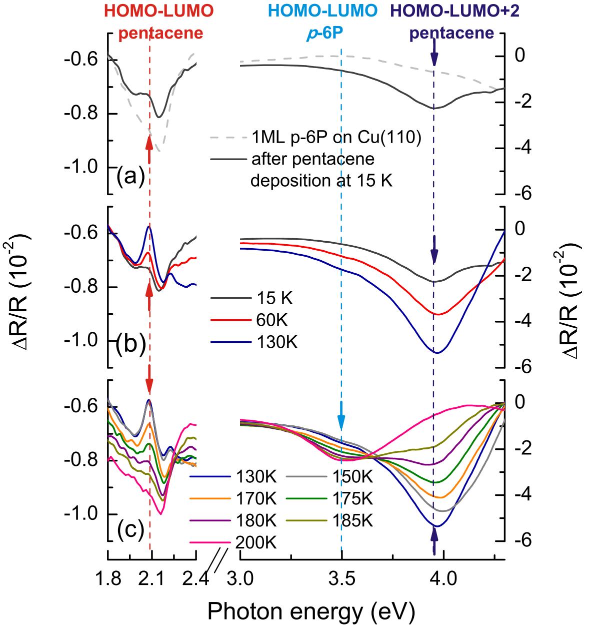

before and after the pentacene deposition. Upon pentacene deposition, new RD peaks appear at 2.1 eV and 3.9 eV, which are attributed to the HOMO-LUMO and HOMO-LUMO+2 transitions of pentacene (see Fig. 10.3), respectively. Compared to the RD spectrum recorded prior to pentacene deposition, the RD peaks at 2.1 eV and 3.9 eV possess a positive and a negative sign, respectively. Based on its energetic position, we can assign the RD peak at 2.1 eV to the HOMO-LUMO transition of the pentacene molecule [81, 82]. The opposite sign of the RD signal at 2.1 eV in comparison with the RD signal at 3.9 eV is due to the fact that the transition dipole

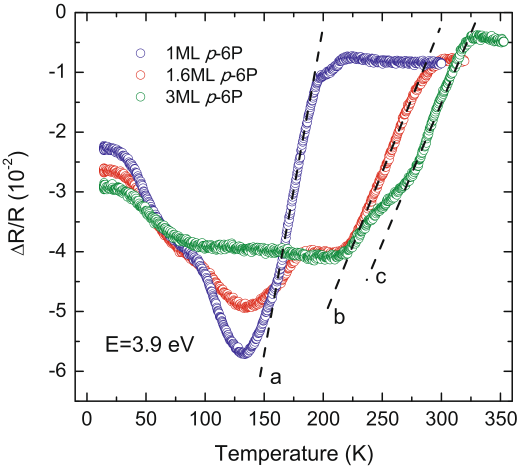

Fig. 10.11 $\Delta R/R$ signals at 3.9 eV recorded during heating of 0.7 ML pentacene on Cu(110) precovered by 1, 1.6 and 3 ML of *p*-6P, respectively. The initial deposition of pentacene on all three samples was performed at 15 K. The heating rate was 1 K/s [76]

moments of these two transitions are perpendicular to each other (see Fig. 10.3) [82]. From the sign of the RD signal originating from these two transitions, we conclude that the long molecular axis of the pentacene molecules now adsorbed on top of the *p*-6P layer is also preferentially aligned along the $[1\bar{1}0]$ direction of the substrate. Upon heating the sample to a temperature of 130 K, the amplitude of both RDS peaks at 2.1 eV and 3.9 eV rises monotonously (Fig. 10.10(b)). The increase of the pentacene related optical anisotropy indicates that the pentacene molecules which are still on top of *p*-6P layer improve their orientational order. Heating the sample further to temperatures above 170 K, both pentacene related RDS intensities at 2.1 eV and 3.9 eV start to decrease in amplitude, while the *p*-6P related RD signal at 3.5 eV starts to grow (Fig. 10.10(c)). This observation indicates the onset of the inversion process. This process is completed after heating the sample to 300 K when the pentacene related RD signals have vanished completely and the *p*-6P related peak at 3.5 eV has reached its saturation.

To study the kinetics of the inversion process as a function of the thickness of the *p*-6P buffer layer, 0.7 ML of pentacene were deposited at 15 K on Cu(110) precovered by 1 ML, 1.6 ML and 3 ML of *p*-6P, respectively. Subsequently, the samples were heated to elevated temperatures with a constant heating rate of 1 K/s. During the heating, the RD signal at 3.9 eV was monitored to probe the diffusion kinetics of the pentacene molecules (Fig. 10.11). Indeed, the attenuation of the negative RD peak at 3.9 eV (dashed lines labeled a, b and c in Fig. 10.11) reflects the diffusion of pentacene molecules from the top to the bottom of the *p*-6P layer. A clear shift of the onset of the inversion process to higher temperature is observed as the thickness of the *p*-6P buffer layer increases. This result demonstrates the step-wise increase of the kinetic barrier for the diffusion to the buried interface with each additional *p*-6P monolayer [80].

10.4 Conclusions and Future Perspectives

In this review, we reported our recent RDS studies on organic thin film growth on metal and insulator substrates. The method is extremely sensitive to the optical absorption related to the intramolecular transitions which allows monitoring the deposition of organic molecules on anisotropic surfaces in situ and in real time. The enhanced sensitivity originates from the anisotropic molecular electronic structure (intramolecular optical transitions) as well as the anisotropic molecular interactions (exciton states). The detection limit of the adsorbed organic molecules for RDS is well below 1 % of a monolayer of lying molecules. The success of RDS in the characterization of growth following the Stranski–Krastanov mode, which is generally encountered in organic thin film growth, lies in the strong influence of the molecular interactions to the optical properties of the organic thin film, giving rise to pronounced variations of the RD spectral line shapes. Concerning the deposition of organic molecules on bare metal surfaces, RDS is not only sensitive to the intramolecular transitions of the organic molecules and the related excitonic states but also to the intrinsic surface electronic structure of the substrate. This capability makes RDS a versatile technique for the investigation of organic thin film growth all the way, from the formation of organic/inorganic interface to the evolution of thicker films with specific morphology and structure.

Being an optical method, RDS is usually non-destructive and can be applied during film growth without inducing any noticeable damage or contamination. There are no restriction as to the environment, except that it is optically transparent. Therefore, RDS can be applied not only to the vacuum/solid but also liquid/solid interface and is thus excellently suited for monitoring the growth of organic thin films using wet processing.

As we have emphasized in this report, monitoring the spectral line shape during organic thin film growth can provide detailed information on the evolution of the morphology and structure of the growing thin film and the associated optical properties. Yet, there is room for further technical improvements of the RDS technique, in particular concerning acquisition speed and spatial resolution. Recently, we have developed a new type of RD spectrometer for fast spectroscopic measurement based on a rotating compensator design [83]. The instrument uses a 1024 element Si photodiode linear array for simultaneous multiwavelength detection. High-quality RD spectra covering a spectral range from 1.5 eV and 4.5 eV can thus be acquired within a few seconds. The RD spectrometer has been successfully applied for in-situ, real-time monitoring of the initial stages of *p*-6P thin film growth on Cu(110)-(2 × 1)O and its advantages for quantitative investigation of the growth and the concomitant evolution of the optical properties has been demonstrated [83]. Another promising extension of the RDS technique aims at the spatially resolved imaging of the optical anisotropy during organic thin film growth using Reflectance Difference Microscopy (RDM) [84, 85]. Due to the fact that the crystalline morphological structures of organic thin films are often so large that they can be well resolved by optical microscopy, RD microscopy will allow the direct correlation of the optical properties (RD spectroscopy) with the local morphology or individual crystallites.

Due to its superior sensitivity, RDS provides high-quality optical spectra from ultra-thin organic films whose crystalline structure differs from the their bulk counterparts. We have demonstrated that the corresponding optical spectra are indeed quite different from those of the molecular crystals. However, in order to establish the interrelationship between the optical spectra and crystalline structure, it is important to combine the RDS technique with other complementary experimental tools, such as scanning tunneling microscopy (STM), atomic force microscopy (AFM), low energy electron diffraction (LEED), and glancing incidence x-rag diffraction (GIXRD). Finally, a fundamental understanding of the correlation between optical properties and crystalline structure can only be achieved with the help of quantitative theoretical models and ab-initio calculations.

Acknowledgements We would like to thank the FWF for long term financial support. We would also like to acknowledge fruitful cooperations within the NFN ICFOF (Interface controlled and functionalized organic films).

References

1. C.D. Dimitrakopoulos, P.R.L. Malenfant, Adv. Mater. **14**, 99 (2002)
2. C.B. Gorman, Angew. Chem., Int. Ed. Engl. **41**, 4378 (2002)
3. S.R. Forrest, Nature **428**, 911 (2004)
4. C.R. Newman, C.D. Frisbie, D.A. da Silva Filho, J.-L. Brédas, P.C. Ewbank, K.R. Mann, Chem. Mater. **16**, 4436 (2004)
5. B. Geffroy, L.R. Philippe, P. Christophe, Polym. Int. **55**, 579 (2006)
6. M. Pope, C.E. Swenberg, *Electronic Processes in Organic Crystals and Polymers*, 2nd edn. (Oxford Scientific, Oxford, 1999)
7. R. Ruiz, D. Choudhary, B. Nickel, T. Toccoli, K.-C. Chang, A.C. Mayer, P. Clancy, J.M. Blakely, R.L. Headrick, S. Iannotta, G.G. Malliaras, Chem. Mater. **16**, 4497 (2004)
8. R. Forker, T. Fritz, Phys. Chem. Chem. Phys. **11**, 2142 (2009)
9. J. Cornil, D. Beljonne, J.-P. Calbert, J.-L. Brédas, Adv. Mater. **13**, 1053 (2001)
10. F.C. Spano, Annu. Rev. Phys. Chem. **57**, 217 (2006)
11. J. Gierschner, J. Cornil, H.-J. Egelhaaf, Adv. Mater. **19**, 173 (2007)
12. M. Muccini, M. Schneider, C. Taliani, M. Sokolowski, E. Umbach, D. Beljonne, J. Cornil, J.-L. Brédas, Phys. Rev. B **62**, 6296 (2000)
13. W. Gebauer, A. Langner, M. Schneider, M. Sokolowski, E. Umbach, Phys. Rev. B **69**, 125420 (2004)
14. A. Ruini, M.J. Caldas, G. Bussi, E. Molinari, Phys. Rev. Lett. **88**, 206403 (2002)
15. S. Tavazzi, D. Besana, A. Borghesi, F. Meinardi, A. Sassella, R. Tubino, Phys. Rev. B **65**, 205403 (2002)
16. K. Hummer, C. Ambrosch-Draxl, Phys. Rev. B **72**, 205205 (2005)
17. W. Gebauer, M. Sokolowski, E. Umbach, Chem. Phys. **227**, 33 (1998)
18. E. Umbach, W. Gebauer, A. Soukopp, M. Bäßler, M. Sokolowski, J. Lumin. **76/77**, 641 (1998)
19. E. Zojer, N. Koch, P. Puschnig, F. Meghdadi, A. Niko, R. Resel, C. Ambrosch-Draxl, M. Knupfer, J. Fink, J.L. Brédas, G. Leising, Phys. Rev. B **61**, 16538 (2000)
20. F. Schreiber, Prog. Surf. Sci. **65**, 151 (2003)
21. S. Barlow, R. Raval, Surf. Sci. Rep. **50**, 201 (2003)
22. F. Rosei, M. Schunack, Y. Naitoh, P. Jiang, A. Gourdon, E. Laegsgaard, I. Stensgaard, C. Joachim, F. Besenbacher, Prog. Surf. Sci. **71**, 95 (2003)
23. W. Schmidt, K. Seino, M. Preuss, A. Hermann, F. Ortmann, F. Bechstedt, Appl. Phys. A **85**, 387 (2006)

24. T.U. Kampen, U. Rossow, M. Schumann, S. Park, D.R.T. Zahn, J. Vac. Sci. Technol. B **18**, 2077 (2000)
25. C. Di Natale, C. Goletti, R. Paolesse, F. Della Sala, M. Drago, P. Chiaradia, P. Lugli, A. D'Amico, Appl. Phys. Lett. **77**, 3164 (2000)
26. A.M. Paraian, U. Rossow, S. Park, G. Salvan, M. Friedrich, T.U. Kampen, D.R.T. Zahn, J. Vac. Sci. Technol. B **19**, 1658 (2001)
27. C. Goletti, R. Paolesse, C. Di Natale, G. Bussetti, P. Chiaradia, A. Froiio, L. Valli, A. D'Amico, Surf. Sci. **501**, 31 (2002)
28. C. Goletti, G. Bussetti, P. Chiaradia, R. Paolesse, A. Froiio, E. Dalcanale, T. Berzina, C. Di Natale, A. D'Amico, Surf. Sci. **521**, L645 (2002)
29. C. Goletti, R. Paolesse, E. Dalcanale, T. Berzina, C. Di Natale, G. Bussetti, P. Chiaradia, A. Froiio, L. Cristofolini, M. Costa, A. D'Amico, Langmuir **18**, 6881 (2002)
30. C. Goletti, G. Bussetti, P. Chiaradia, A. Sassella, A. Borghesi, Appl. Phys. Lett. **83**, 4146 (2003)
31. C. Goletti, G. Bussetti, P. Chiaradia, A. Sassella, A. Borghesi, Org. Electron. **5**, 73 (2004)
32. C. Goletti, G. Bussetti, P. Chiaradia, A. Sassella, A. Borghesi, J. Phys. Condens. Matter **16**, S4393 (2004)
33. D. Monti, M. Venanzi, M. Russo, G. Bussetti, C. Goletti, M. Montalti, N. Zaccheroni, L. Prodi, R. Rella, M.G. Manera, G. Mancini, C. Di Natale, R. Paolesse, New J. Chem. **28**, 1123 (2004)
34. A. Sassella, M. Campione, M. Moret, A. Borghesi, C. Goletti, G. Bussetti, P. Chiaradia, Phys. Rev. B **71**, 201311R (2005)
35. A. Sassella, M. Campione, A. Papagni, C. Goletti, G. Bussetti, P. Chiaradia, V. Marcon, G. Raos, Chem. Phys. **325**, 193 (2006)
36. A. Sassella, A. Borghesi, M. Campione, S. Tavazzi, C. Goletti, G. Bussetti, P. Chiaradia, Appl. Phys. Lett. **89**, 261905 (2006)
37. Y. Hu, K. Maschek, L.D. Sun, M. Hohage, P. Zeppenfeld, Surf. Sci. **600**, 762 (2006)
38. L.D. Sun, M. Hohage, P. Zeppenfeld, S. Berkebile, G. Koller, F.P. Netzer, M.G. Ramsey, Appl. Phys. Lett. **88**, 121913 (2006)
39. G. Bussetti, C. Goletti, P. Chiaradia, A. Sassella, M. Campione, S. Tavazzi, A. Borghesi, Surf. Sci. **601**, 4488 (2007)
40. A. Sassella, M. Campione, L. Raimondo, S. Tavazzi, A. Borghesi, C. Goletti, G. Bussetti, P. Chiaradia, Surf. Sci. **601**, 2575 (2007)
41. M. Campione, A. Borghesi, M. Laicini, A. Sassella, C. Goletti, G. Bussetti, P. Chiaradia, J. Chem. Phys. **127**, 244703 (2007)
42. M. Scarselli, G. Ercolani, P. Castrucci, D. Monti, G. Bussetti, M. Russo, C. Goletti, P. Chiaradia, R. Paolesse, M. De Crescenzi, Surf. Sci. **601**, 2610 (2007)
43. B.G. Frederick, K.J. Kitching, N.V. Richardson, J. Chem. Soc. Faraday Trans. **91**, 3627 (1995)
44. B.G. Frederick, R.J. Cole, J.R. Power, C.C. Perry, Q. Chen, N.V. Richardson, P. Weightman, C. Verdozzi, D.R. Jennison, P.A. Schultz, M.P. Sears, Phys. Rev. B **58**, 10883 (1998)
45. B.G. Frederick, J.R. Power, R.J. Cole, C.C. Perry, Q. Chen, S. Haq, T. Bertrams, N.V. Richardson, P. Weightman, Phys. Rev. Lett. **80**, 4490 (1998)
46. C.C. Perry, B.G. Frederick, J.R. Power, R.J. Cole, S. Haq, Q. Chen, N.V. Richardson, P. Weightman, Surf. Sci. **427–428**, 446 (1999)
47. D.S. Martin, R.J. Cole, S. Haq, Phys. Rev. B **66**, 155427 (2002)
48. D.S. Martin, R.J. Cole, S. Haq, Surf. Sci. **539**, 171 (2003)
49. D.S. Martin, P. Weightman, Thin Solid Films **455–456**, 752 (2004)
50. R. LeParc, C.I. Smith, M.C. Cuquerella, R.L. Williams, D.G. Fernig, C. Edwards, D.S. Martin, P. Weightman, Langmuir **22**, 3413 (2006)
51. D.R.T. Zahn, S.D. Silaghi, C. Cobet, M. Friedrich, N. Esser, Phys. Status Solidi B **242**, 2671 (2005)
52. S.D. Silaghi, D.R.T. Zahn, Appl. Surf. Sci. **252**, 5462 (2006)
53. P. Weightman, G.J. Dolan, C.I. Smith, M.C. Cuquerella, N.J. Almond, T. Farrell, D.G. Fernig, C. Edwards, D.S. Martin, Phys. Rev. Lett. **96**, 086102 (2006)

54. M.C. Cuquerella, C.I. Smith, D.G. Fernig, C. Edwards, P. Weightman, Langmuir **23**, 2078 (2007)
55. C.I. Smith, A. Bowfield, M.C. Cuquerella, C.P. Mansley, T. Farrell, P. Harrison, D.S. Martin, D.G. Fernig, C. Edwards, J.E. Butler, R.J. Hamers, B. Sun, X. Wang, P. Weightman, Europhys. Lett. **85**, 18006 (2009)
56. E.K. Miller, K. Hingerl, C.J. Brabec, A.J. Heeger, N.S. Sariciftci, J. Chem. Phys. **113**, 789 (2000)
57. P. Chiaradia, R. Del Sole, Surf. Rev. Lett. **6**, 517 (1999)
58. Y. Borensztein, Surf. Rev. Lett. **7**, 399 (2000)
59. D.S. Martin, P. Weightman, Surf. Rev. Lett. **7**, 389 (2000)
60. G. Chiarotti, P. Chiaradia, F. Arciprete, C. Goletti, Appl. Surf. Sci. **175–176**, 777 (2001)
61. P. Weightman, Phys. Status Solidi A **188**, 1443 (2001)
62. P. Weightman, D.S. Martin, R.J. Cole, T. Farrell, Rep. Prog. Phys. **68**, 1251 (2005)
63. D.E. Aspnes, J.P. Harbison, A.A. Studna, L.T. Florez, J. Vac. Sci. Technol. A **6**, 1327 (1988)
64. O. Acher, B. Drévillon, Rev. Sci. Instrum. **63**, 5332 (1992)
65. K. Kern, H. Niehus, A. Schatz, P. Zeppenfeld, J. Goerge, G. Comsa, Phys. Rev. Lett. **67**, 855 (1991)
66. Ph. Hofmann, K.C. Rose, V. Fernandez, A.M. Bradshaw, W. Richter, Phys. Rev. Lett. **75**, 2039 (1995)
67. J.K. Hansen, J. Bremer, O. Hunderi, Surf. Sci. **418**, L58 (1998)
68. J. Bremer, J.K. Hansen, O. Hunderi, Appl. Surf. Sci. **142**, 286 (1999)
69. K. Stahrenberg, Th. Herrmann, N. Esser, W. Richter, Phys. Rev. B **61**, 3043 (2000)
70. D.S. Martin, A.M. Davarpanah, S.D. Barrett, P. Weightman, Phys. Rev. B **62**, 15417 (2000)
71. L.D. Sun, M. Hohage, P. Zeppenfeld, R.E. Balderas-Navarro, K. Hingerl, Phys. Rev. Lett. **90**, 106104 (2003)
72. L.D. Sun, M. Hohage, P. Zeppenfeld, R.E. Balderas-Navarro, Surf. Sci. **589**, 153 (2005)
73. L.D. Sun, M. Hohage, P. Zeppenfeld, R.E. Balderas-Navarro, K. Hingerl, Surf. Sci. **527**, L184 (2003)
74. L.D. Sun, R. Denk, M. Hohage, P. Zeppenfeld, Surf. Sci. **602**, L1 (2008)
75. R. Forker, D. Kasemann, Thomas Dienel, C. Wagner, R. Franke, K. Müllen, T. Fritz, Adv. Mater. **20**, 4450 (2008)
76. L.D. Sun, C.Y. Liu, D. Queteschiner, G. Weidlinger, P. Zeppenfeld, Chem. Phys. Phys. Chem. **13**, 13382 (2011)
77. L.D. Sun, M. Denk, R. Denk, M. Hohage, G. Weidlinger, P. Zeppenfeld, Chem. Phys. Phys. Chem. **12**, 14706 (2010)
78. L.D. Sun, S. Berkebile, G. Weidlinger, G. Koller, M. Hohage, F.P. Netzer, M.G. Ramsey, P. Zeppenfeld, Chem. phys. Phys. Chem. **12**, 3141 (2010)
79. R. Resel, M. Oehzelt, O. Lengyel, T. Haber, T.U. Schülli, A. Thierry, G. Hlawacek, C. Teichert, S. Berkebile, G. Koller, M.G. Ramsey, Surf. Sci. **600**, 4645 (2006)
80. L.D. Sun, C.Y. Liu, D. Queteschiner, P. Zeppenfeld, AIP Adv. **1**, 022112 (2011)
81. T.M. Halasinski, D.M. Hudgins, F. Salama, L.J. Allamandola, T. Bally, J. Phys. Chem. A **104**, 7484 (2000)
82. P. Sony, A. Shukla, Phys. Rev. B **75**, 155208 (2007)
83. C.G. Hu, L.D. Sun, J.M. Flores-Camacho, M. Hohage, C.Y. Liu, X.T. Hu, P. Zeppenfeld, Rev. Sci. Instrum. **81**, 043108 (2010)
84. J. Dick, P. Erichsen, J. Woolf, H.H. Rotermund, Surf. Sci. **462**, 90 (2000)
85. C. Punckt, F.S. Merkt, H.H. Rotermund, New J. Phys. **9**, 213 (2007)

Part V
Devices

Chapter 11
Dipole-Controlled Energy Level Alignment at Dielectric Interfaces in Organic Field-Effect Transistors

Philipp Stadler, Anna M. Track, Georg Koller, N. Serdar Sariciftci, and Michael G. Ramsey

Abstract In this section the energy level alignment at the semiconductor–dielectric interface in organic field-effect transistors is discussed. We focus at the comparison of pristine oxide structures with advanced organic interlayer structures. The interface is particularly interesting, since the performance of an organic field-effect transistor is significantly influenced by the energy level alignment. The study targets on an understanding of interfacial effects, hence complementary techniques are presented to investigate the interface. Most appropriately a combination of device analysis with a device-related photoemission spectroscopy study provides insight on the energy level alignment. Especially the role of commonly used organic interlayers is discussed, which enhance transistor performances. On organic–organic interfaces dipoles arise, which shift the relative positions of energy levels. Interestingly the magnitude and the direction of the shift is reflected in the device parameter analysis and in the corresponding photoemission spectra explaining the enhanced transistor performance.

11.1 Introduction

Organic field-effect transistors (OFETs) have gained a lot of interest in recent years for creating flexible, printable integrated circuits applying organic semiconductors [1–5]. The goal is to achieve high-performance device structures of organic

---

P. Stadler (✉) · N.S. Sariciftci
Physical Chemistry, Linz Institute for Organic Solar Cells (LIOS),
Johannes Kepler University of Linz, Altenbergerstrasse 69, 4040 Linz, Austria
e-mail: philipp.stadler@jku.at

A.M. Track · G. Koller · M.G. Ramsey
Surface and Interface Physics, Institute for Physics, Karl-Franzens University Graz,
Universitätsplatz 5, 8010 Graz, Austria

Present address:
A.M. Track
NXP Semiconductors Austria GmbH Styria, Mikronweg 1, 8101 Gratkorn, Austria

H. Sitter et al. (eds.), *Small Organic Molecules on Surfaces*,
Springer Series in Materials Science 173, DOI 10.1007/978-3-642-33848-9_11,

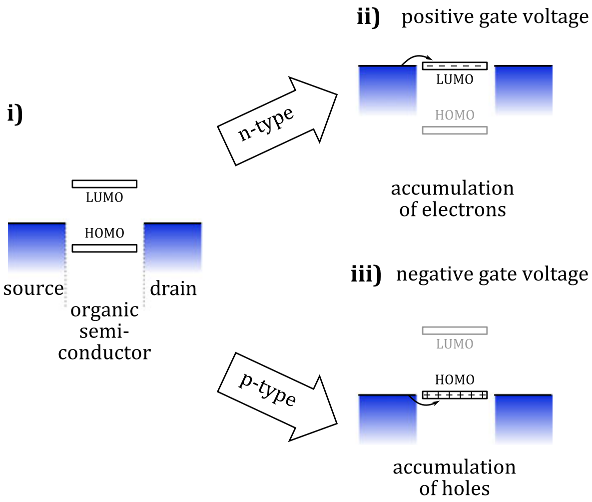

Fig. 11.1 Operation principle of OFETs depicted schematically in three stages: A conductive channel is formed by injecting charges (holes or electrons) to the initially intrinsic semiconductor as soon as a gate voltage is applied

field-effect transistors with operation frequencies in the MHz regime and low driving voltages between 1–10 V [6–8]. In state-of-the-art OFETs especially small π-conjugated molecules are performing well and a lot of optimized device structures are ready to take-off for integration in complex circuits [9, 10]. A closer look on the material aspect shows that organic small molecules have been optimized in terms of stability, their practical fabrication handling and their electrical properties such as morphology and charge carrier mobility [11, 12]. In previous chapters morphological issues have been addressed, especially the control of morphology is crucial for gaining high charge carrier mobilities for fast switching transistors [13–17]. Material research on dielectrics in OFETs is in progress as well. Field-effect devices require special dielectric materials, since they determine the magnitude of driving voltages, threshold voltages and limitations in switching speed [18, 19]. Ultra-thin dielectric layers exhibiting geometric capacitances in the range of several 100 $\text{nF}\,\text{cm}^{-2}$ are nowadays implemented to OFETs [20–22]. In particular metal oxides are proven to be useful.

This review article addresses interfacial effects. Apart from the pure material aspects OFETs are sensitive to the nature of the interface between the organic semiconductor and the dielectric. They are interface-driven devices, where mutual effects arise, which significantly influence the formation of the conductive channel and hence the overall device performance [23, 24]. Differently to inorganic semiconductors, one has to consider that organic small molecules are initially intrinsic. Figure 11.1 depicts right the operation principle in OFETs: Depending on which type of semiconductor is used, either electrons (ii) or holes (iii) are injected and accumulated at the semiconductor–dielectric interface. Charge injection is precisely controlled by the electrical-field applied to the gate electrode. Thus organic transistors operate in an accumulation regime.

Obviously the nature of the interface between organic semiconductor and dielectric plays a major role for the charge transport. As a matter of fact the primary goal is to design interfaces, where the energy level alignment is favorable for the formation of a conductive channel. Interestingly the combination of organic semiconductors with organic molecules leads to best performing transistors. The challenge is to understand the energy level alignment at organic–organic interfaces, which is profoundly discussed here. At least yet the golden rule for organics has not been found. In fact each family of organic semiconductor would behave different in combination with a certain dielectric surface.

11.2 Material and Structural Aspects in OFETs

In state-of-the-art OFETs usually hybrid or double layer dielectrics are applied [18, 19, 25]. Typical device structures are depicted in Fig. 11.2. Either silicon–silicondioxide or valve metals plus corresponding oxides lead to bottom-gated device structures.

The OFETs shown in Fig. 11.2, metal-oxide insulators are combined with thin, organic interlayers merging the advantages of different material classes. Metal oxides are nowadays implemented to inorganic norm integrated circuits e.g. MOSFETs and flash memory devices. Thin films in the range of 5–50 nm serve as excellent insulators with high breakdown fields (400–600 $\mathrm{V\,\mu m^{-1}}$) and high dielectric constants ($\epsilon > 6$). In combination with organic interlayers hybrid systems enhance the mentioned interface properties. Their role is considered as a passivating layer removing charge carrier traps from the oxide surface. Especially pristine oxides exhibit a high

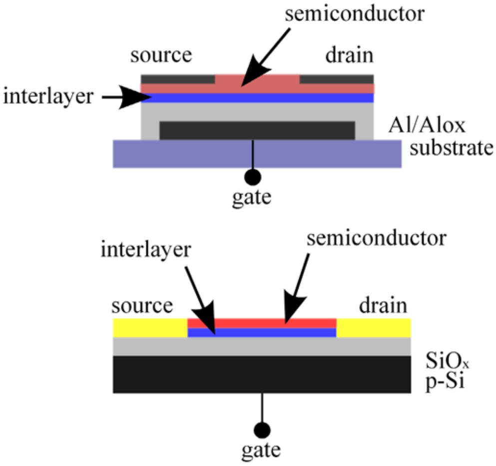

Fig. 11.2 Concepts used in literature of applied OFET structures. *Top*: Anodic grown oxide film on a valve metal (here aluminum) directly for a bottom-gate OFET structure. *Bottom*: Schematic of frequently adapted coplanar structured OFET using doped silicon as gate electrode (and as substrate) with thermally grown SiO_2 as insulator. Note in both cases the organic interlayer applied on top for a combined double layer or hybrid dielectric. The organic semiconductor is deposited on top of the interlayer forming a favorable interface. Figure courtesy of Stadler et al. [26]

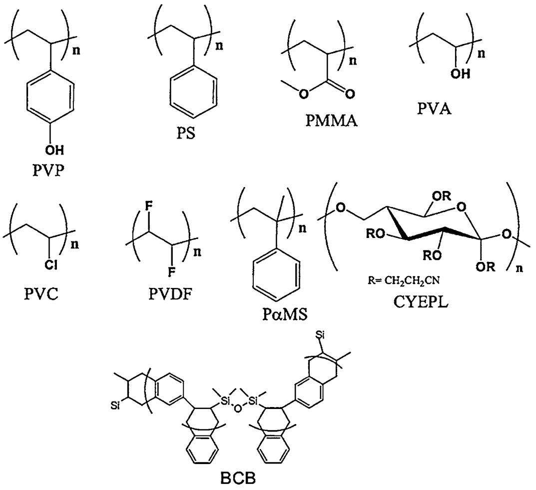

Fig. 11.3 Various polymers and resins used for high-performance OFETs. Figure courtesy of Singh et al. [28]

number of shallow traps, which interrupt the formation of a conductive channel [27]. The variety of organic material classes used as interlayers and active semiconductor layers opens almost an endless number of combinations.

The target is to find a matching organic–organic system, resulting in a systematic interface engineering [29–32]. However, empirical approaches to characterize interfaces are not sufficient, a deep understanding of organic–organic heterojunctions is required.

An excerpt of some typical, widely used examples for organic dielectric interlayer material classes, is suggested in the graphs below (Fig. 11.3). Classic polymers such as polystyrene (PS), bio-inspired polymers (Cypel) as well as molecular, cross-linkable resins (BCB) are implemented [33]. The latter class will be discussed in detail here in this review. An alternative approach to modify surfaces are covalently bonded functional molecules, which selectively attach to OH-terminated oxide surfaces and which form self-assembled monolayers (SAMs). Using the right surfactants surface properties can be changed for a more favorable alignment for the organic semiconductor. This technique reduces the organic interlayer to monolayers for ultra-thin devices. A number of candidates with different anchoring functional groups are shown in Fig. 11.4.

On the semiconductor side, typically molecules such as oligoacenes and oligothiophenes plus derivatives are used as hole-conductors (Fig. 11.5). Electron transport in systems with high electron affinity is found in fullerenes, functionalized perylenebisimides and perfluorinated π-conjugated molecules.

11.3 Organic Interlayers in OFETs

Zhang et al. [35] demonstrate with an empiric OFET study the influence of the organic interlayer on the device performance of OFETs. Systematically the impact of

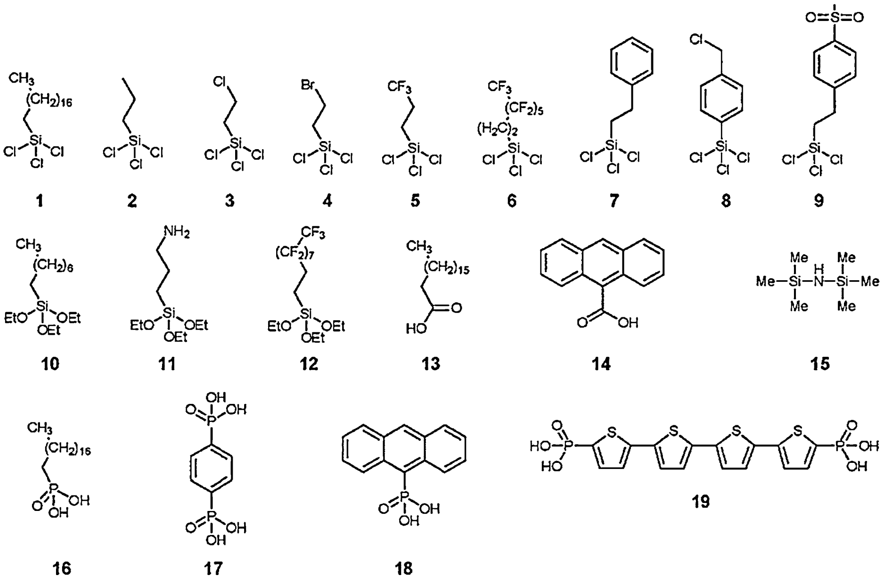

Fig. 11.4 Examples for SAM-molecules with different anchoring functionalized groups: Trichlorosilanes (*1–9*), triethoxysilanes (*10–12*), carboxylic acids (*13*,*14*), hexamethyl-disilazane (HMDS, *15*) and phosphonic acids (*16–19*). The most commonly used compound *1* is known as OTS (octadecyl-trichlorosilane). Figure courtesy of Miozzo et al. [19]

the organic interlayer on the performance has been studied by applying a structure as introduced in Fig. 11.2 (i). As seen in the Fig. 11.6 the current–voltage characteristics change significantly by varying the organic interlayer (T1–T4). The shape as well as the onset—the threshold voltage—are different for each interlayer. BCB (T1) exhibits the best performance, seen in graph (f). The question here arises: what is actually the driving force for the significant changes?

The system BCB–C_{60} turns out to perform very well when compared to other, widely used interlayers such as PMMA, PS or OTS. BCB used as organic interlayer enhances remarkably device performances of various n-type semiconductors [36–38]. Additional advantages for applying BCB are the thermal stability, which is in particular important for the growth of small molecules at higher temperatures beyond 100 °C, and the dielectric function, which remains constant over a wide frequency and temperature range [14]. Both characteristic properties can be read out from the graph presented in Fig. 11.7.

OFETs combining C_{60} with BCB have shown high mobilities and good performances in integrated circuits [6]. In addition, C_{60}'s unique symmetry and stability in ambient conditions allows probing with spectroscopic techniques. In the following we compare alumina and BCB as hybrid dielectric system. They have been widely used in organic electronics [2, 21, 36]. For a complementary study on the role of the BCB interlayer OFETs with and without the cross-linkable resin are character-

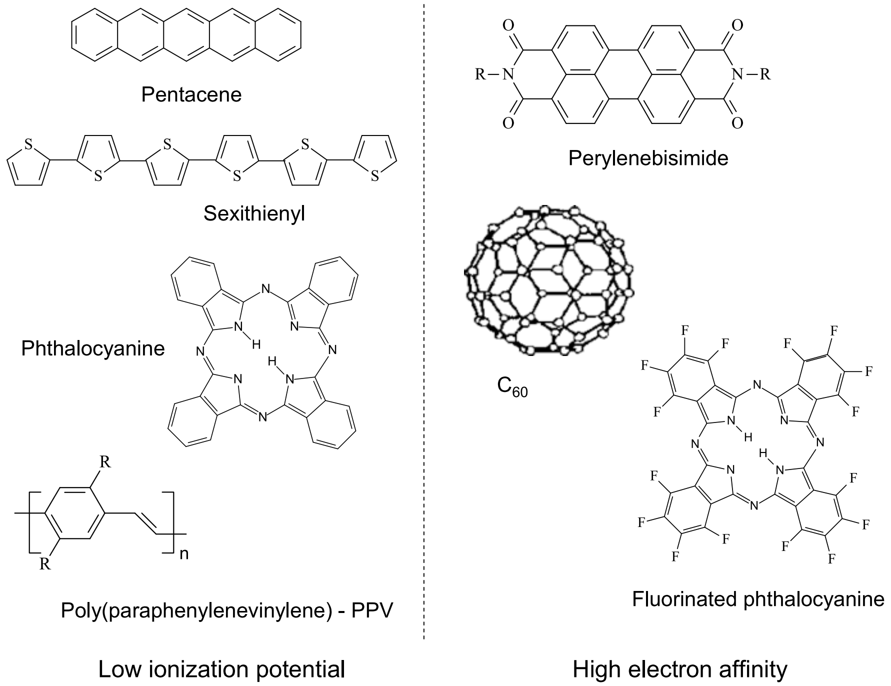

Fig. 11.5 Examples electron-dense organic p-type semiconductors (*left*) and electron-poor molecular systems for n-type transport. Figure courtesy of Cornil et al. [34]

ized. The corresponding device structures are depicted in Fig. 11.8, which serve as a model system discussed in the next chapter.

11.4 Threshold Voltage as Interface Parameter

In OFETs the threshold voltage represents *the* interface parameter per se. Hence for the threshold analysis the performance characteristics of both transistors with and without BCB is plotted in Fig. 11.9. The black line represents the device with BCB and the red line is assigned to the device without BCB. The onset in the current—the threshold—is actually shifted to higher voltages without BCB, seen in the linear plot in the inset. Consequently the latter structure operates at higher driving voltages, which acts as persistent burden. In addition by removing BCB the on/off ratio is reduced and hysteresis arises. All these issues are negative aspects in view of transistor circuit analysis.

A direct measure of the role of the interlayer in an OFET is consequently the threshold voltage U_{th}, which is considered as *the* interface parameter. Different groups have empirically proven influences of e.g. of the organic interlayer to the

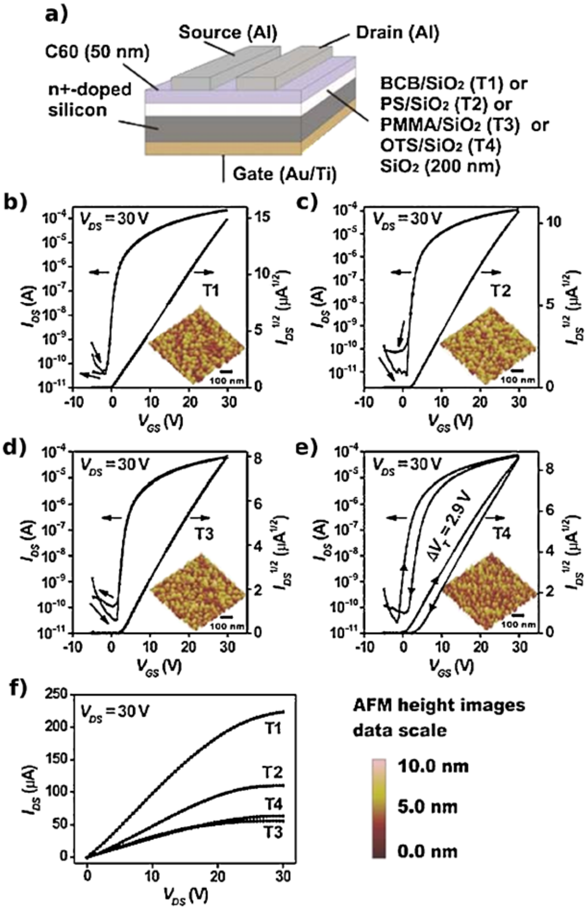

Fig. 11.6 Different current–voltage characteristics of C_{60}-based FET with four different interlayers. The device threshold and the absolute current value is influenced by the organic interlayer. Within the interlayers discussed here the combination BCB–C_{60} is obviously the best choice. Figure courtesy of Zhang et al. [35]

threshold voltages [27, 40–43]. The threshold voltage U_{th} represents by definition the gate voltage at which charge carriers are injected from the source electrode. In case of n-type organic semiconductors, the LUMO is then close to the Fermi potential of the electrode (Fig. 11.10).

The parameter extraction has to be performed with care, since OFETs often represent non-ideal systems. Contact resistances at the electrode–organic interface are influencing the source–drain characteristics and consequently the threshold voltage [44]. In order to work around these effects and for determining a reliable value for the onset in the transfer characteristics, the second derivative (SD) method is applied. The presented model system particularly exhibits low contact effects and optimized thin-film dielectrics, which itself approaches ideality [45–47]. A sketch in Fig. 11.11 below actually demonstrates an example for extraction. The threshold is defined at the inflection point in the transfer curve, which is read out from he second derivative. The plot exhibits then a maximum at the onset (indicated in the

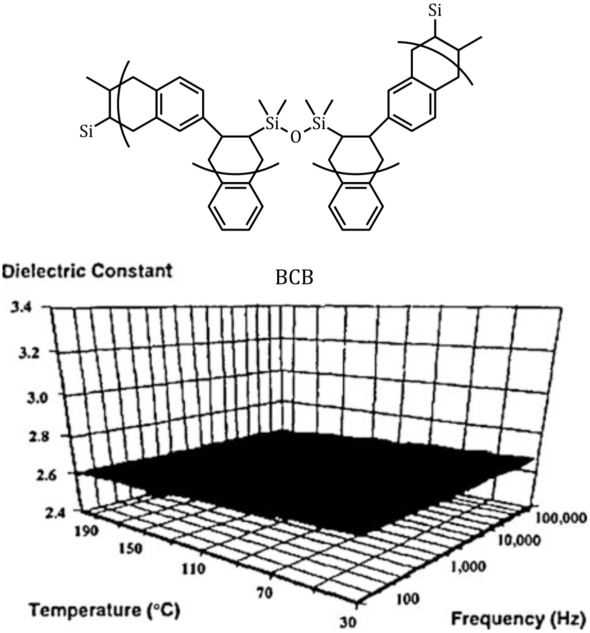

Fig. 11.7 *Top*: The structure of cross-linked benzocyclobutene derivative (Cyclotene, Dow Chemicals, $\epsilon = 2.6$) is shown. Underneath the dielectric function of a thin film is plotted as function of temperature and frequency. Figure courtesy of Mills et al. [39]

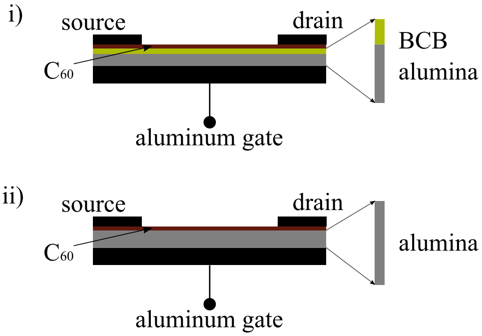

Fig. 11.8 Schematic of complementary model systems: C_{60}-based FET structures using hybrid dielectric with alumina/BCB (i) and pristine oxide (ii). Figure courtesy of Stadler et al. [26]

graph). The SD method has been derived from a MOSFET analysis [48]. However, its reliability has been demonstrated in OFET systems too [49].

Coming back to the initial Fig. 11.9 the threshold voltage is extracted from both curves. The result is plotted in Fig. 11.12, where the peak maximum is found at 0–0.1 V for the BCB device, whereas for the reference structure without BCB interlayer the maximum arises around 0.7 V. Obviously the shift in threshold voltage ΔU_{th} is 0.6 V, which is significant. It indicated that the energy levels at the interface align differently: BCB pushes the LUMO, already close to the Fermi level of the electrode, while on the pristine oxide a potential offset is found [50].

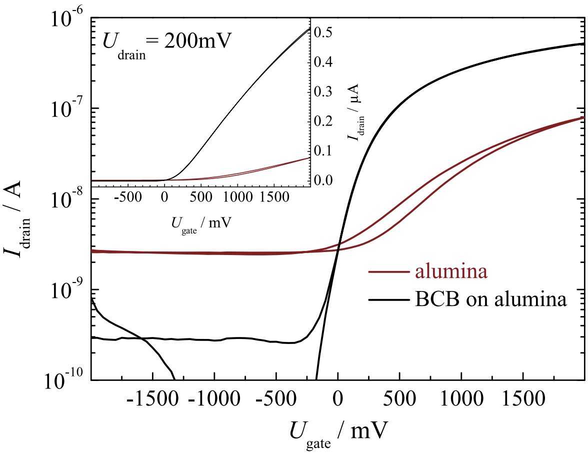

Fig. 11.9 Comparative OFET transfer characteristics with (*black*) and without (*red*) BCB in semilogarithmic and linear plot (*inset*). The performance drops in terms of lower on/off ratio, arising of hysteresis and apparently higher onset (threshold) for accumulation in case of missing BCB interlayer. Figure courtesy of Stadler et al. [26]

11.5 The Role of the Dielectric Interlayer in OFETs

Seen in the threshold voltage analysis the energy levels of the organic semiconductor at the interface is determined exclusively by the alignment at the interface. Thus the channel region in an OFET is reflected by a simple metal-insulator-semiconductor (MIS) structure. The gate electrode serves as a reference metal for the Fermi potential, followed by the insulator (hybrid dielectric) and the semiconductor. The energy diagram is depicted in Fig. 11.13, starting with the gate metal left-hand side followed by metal-oxide, organic interlayer and finally the organic semiconductor.

Indicated in the schematic pure material parameters are defined, such as the electron affinity (*EA*), the ionization potential (*IP*) and work functions ϕ of metals and metal oxide. Undefined parameters are actually found at interfaces, where the energy level alignment is controlled by dipoles [51–53]. They are indicated in the vacuum-level offset (Δ). The magnitude is determined by the nature of the interface. As shown in the diagram the role of the organic interlayers is assigned to tune energy levels of the semiconductor to more favorable positions compared to pristine oxide surfaces. This obviously happens, as indicated by the arrow in the

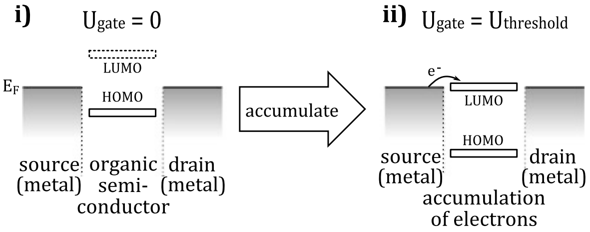

Fig. 11.10 (i) OFET at zero potential. The LUMO is indicated, the Fermi level for C_{60} is within the gap. In (ii) the situation is depicted after applying the threshold potential. Per definition now the LUMO converges the Fermi potential from the electrode. Charge injection from source is energetically enabled and the semiconductor can accumulate with electrons

Fig. 11.11 Threshold voltage extraction applying the second derivative method. The *top graph* is the transfer characteristics, at the inflection point the second derivative (*bottom*) renders a maximum. The peak is a good estimate for the threshold voltage. Figure courtesy of Stadler et al. [26]

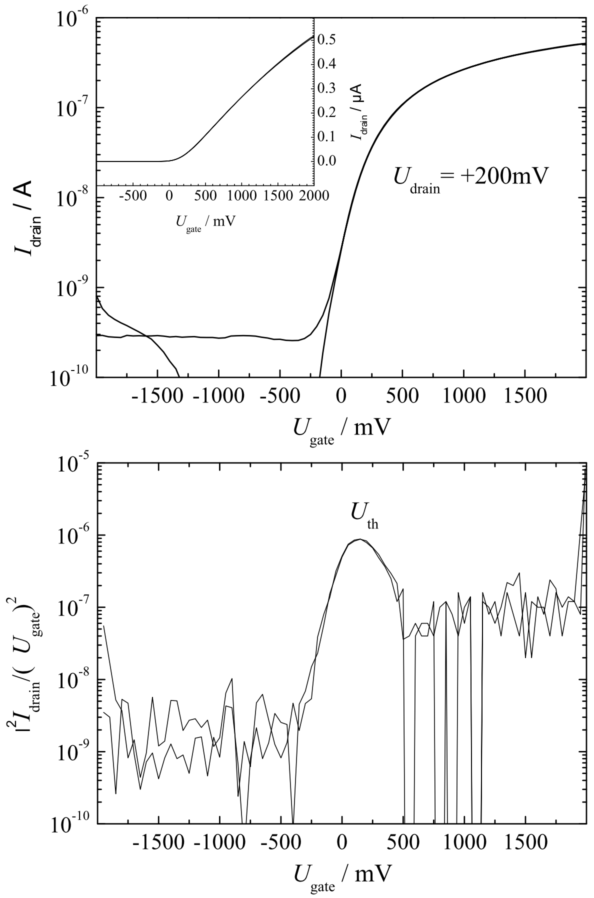

Fig. 11.12 Second derivative of plot in Fig. 11.9. The active role of the BCB is visible by the distinct shift of the peak maximum from around 0.7 V down to 0.1 V. Figure courtesy of Stadler et al. [26]

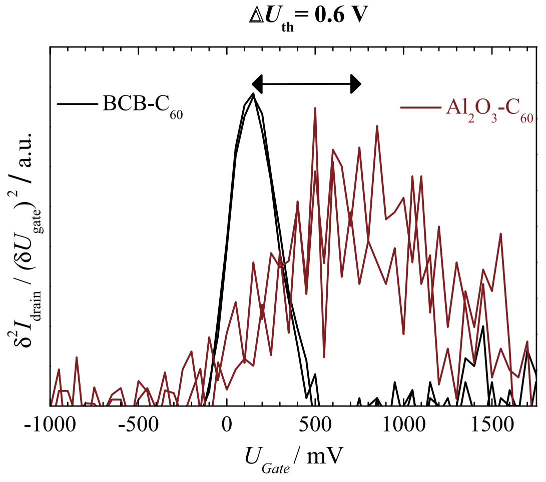

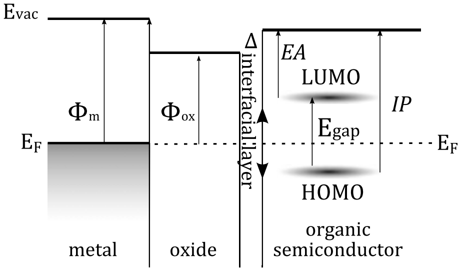

Fig. 11.13 Schematic energy diagram of an metal–insulator–semiconductor (MIS) structure with an organic interlayer between the metal–oxide and the organic semiconductors. The dipole controls the position relative to the gate metal. Figure courtesy of Stadler et al. [26]

schematic the interlayer either pushes HOMO or LUMO close to the Fermi level. Depending whether n-type or p-type organic semiconductors are used, the matching interlayer would drive the threshold voltage to a position close to the Fermi level. Consequently in ideal systems the threshold voltage should be close to 0 V. A good example for such a dipole-controlled alignment is seen in case of C_{60}–BCB, which obviously pushes the LUMO close to the Fermi potential visible in the threshold potential around 0 V.

11.6 Photoemission Spectroscopy on Transistor-Related Structure

In light of the energy diagram the substantial issue is now to seize origin and magnitude of dipoles at interfaces involving organic thin films. Here OFETs may only provide an indirect insight to interfaces, which can be shielded by parasitic, competitive device effects. There is need for a complementary technique, which provides direct access to interface properties. A solution is apparently to apply photoemission spectroscopy (PES).

The advantage is its surface sensitivity, which ranges between 10–30 Å, depending on the excitation source. Few layer films of organic π-conjugated small molecules actually correspond to the mean-free-path of electrons. In several contributions shown before growth and characterization of organic ultra-thin films is presented in great detail.

Device-related photoemission spectroscopy is particulary challenging, since layers cannot be directly grown in-situ in the PES vacuum system. BCB for instance is solution processed, alumina is grown electrochemically. For a cross-check a reference spectrum of C_{60}, which has been exposed to air (Fig. 11.14), is presented. As the UV-source He(I)-lamp excites at 21.2 eV, a heavy p-doped silicon(110) waver serves as reference substrate. The spectral features conform to literature data on in-situ deposited organic films [55]. The fingerprint DOS of C_{60} is clearly identified. The ionization potential *IP* of the thin solid film is determined at 6.5 eV [56], which is derived by adding the work function and the distance from the Fermi energy to the maximum of the HOMO. The corresponding energy levels are illustrated in the energy diagram in Fig. 11.15.

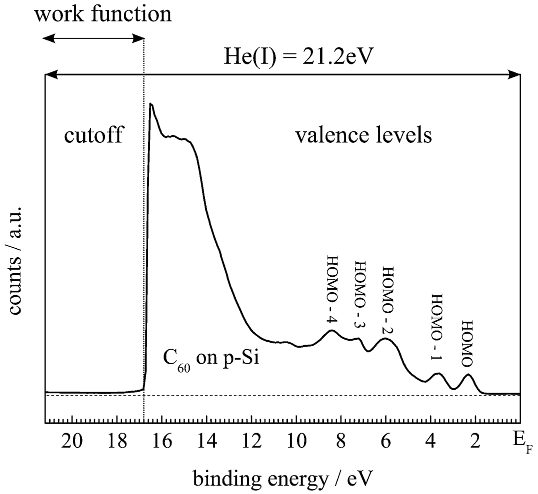

Fig. 11.14 UPS spectra of ex-situ vacuum-prepared C_{60} on p-Si. The DOS is identified and labeled in the graph. Their quality are comparable to in-situ vacuum-prepared samples from e.g. Sakamoto et al. [54]. Valence levels and work function obtained by a metal substrate as well as the excitation energy are indicated. Figure courtesy of Stadler et al. [26]

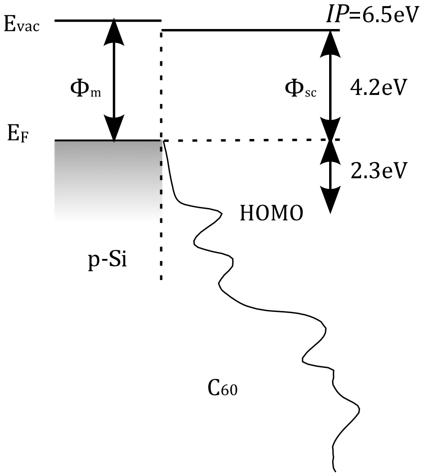

Fig. 11.15 Energy diagram of p-Si-C_{60} structure. From the peak of the HOMO to the vacuum level the ionization potential *IP* is derived. The HOMO actually is found 2.3 eV below the Fermi edge. Figure courtesy of Stadler et al. [26]

Instead of well-defined substrates the uppermost layer of C_{60} has to be probed in an adopted OFET channel for the desired interface study. The source–drain electrodes are not needed, a simple MIS structure with ultra-thin C_{60} models the channel in the corresponding OFET structure, see Fig. 11.16. As substrates aluminum-alumina w/o BCB is applied. A cross-section of the discussed sample is depicted in Fig. 11.17 revealing the investigated interface: alumina–BCB and BCB–C_{60}. Almost the shape of the fullerene molecule is visible in the electron transmission.

A direct comparison of samples with and without BCB are directly investigated applying PES. Now the valence levels (0–8 eV BE) and the electron cut-off (16–21.2 eV BE) are plotted in Fig. 11.18. Qualitatively minor changes are observed. The features in the valence levels are smeared out a bit on alumina, on BCB they

Fig. 11.16 Sample structure for device-related PES. The role of BCB is investigated by copying the transistor structure from Fig. 11.8 without source–drain contacts

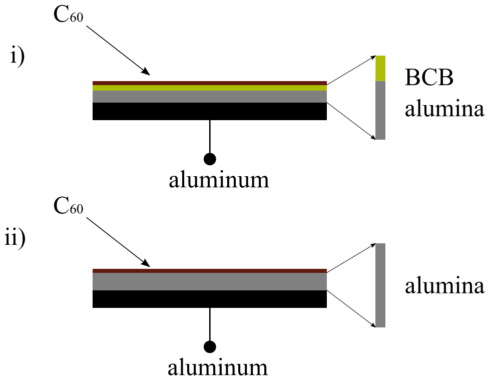

Fig. 11.17 Corresponding TEM picture of thin C_{60} layer on BCB from Fig. 11.16 (i). The TEM cross-section resolves the interfaces of fullerene–BCB and BCB–alumina. Note the thickness indicated by the *scale*. The C_{60} layer diameter is 20–30 Å within the discussed sensitivity range of the PES experiment. Figure courtesy of Stadler et al. [26]

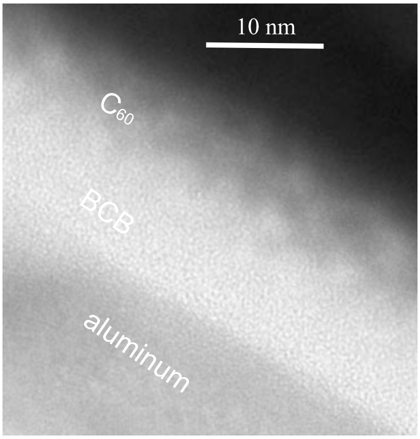

Fig. 11.18 Spectra revealing the DOS of C_{60} on BCB (*black line*) and pristine alumina (Al_2O_3, *red line*). The features are well defined. A dipole by 0.6 eV controls the position of the entire spectrum relative to the gate reference metal (E_F). Figure courtesy of Stadler et al. [50]

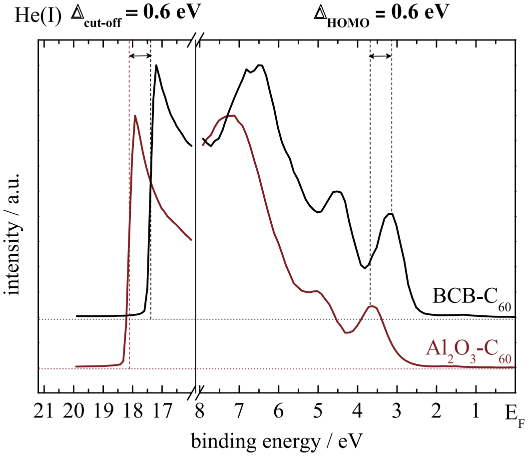

Fig. 11.19 Energy diagram of alumina–C_{60} and alumina–BCB–C_{60} as measured by PES. Note that all DOS spectra are experimental results by a careful layer-by-layer analysis. As indicated BCB actually shifts C_{60} levels upwards back to a situation as found at e.g. p-Si 11.14. The dipole at the organic–organic interface is reduced, compared to the offset between metal–C_{60} the valence levels differ by 0.6 eV. Figure courtesy of Stadler et al. [26]

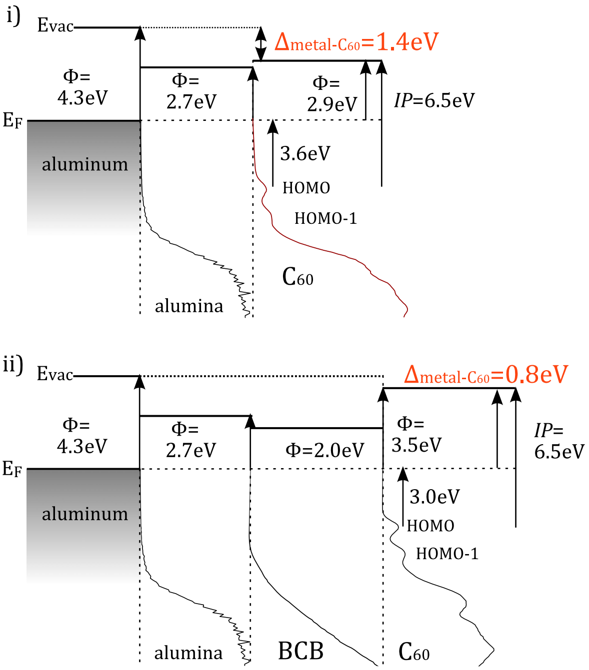

are better defined. Anyhow these effects are almost negligible compared to the significant change induced by BCB. The entire spectrum shifts by 0.6 eV towards the Fermi energy. The changes are concomitantly found for the valence features as well as for low kinetic energy electrons in the cut-off and seen identically in the threshold analysis in Fig. 11.12 before.

The energy level analysis is completed by measuring all interfaces involved, starting with alumina, BCB and finally C_{60}. The results are illustrated in the MIS energy diagram, all values are gained from the device-related PES. As discussed earlier the valence levels of each component are measured, the energy offset shows a significant drop in the vacuum level for aluminum–C_{60} in the structure without BCB interlayer. The dipole Δ is labeled in Fig. 11.19. Interestingly at the oxide–organic semiconductor interface the vacuum levels align, which leads finally to the huge potential drop from C_{60} to the reference metal of 1.4 eV. The changes induced by the BCB unveil the role of BCB, seen in Fig. 11.19, where actually a dipole-controlled alignment is found. Compared to the oxide–organic interface the energy offset is huge, but consequently the potential drop with respect to the metal is decreased by 0.6 eV (marked red in the graph). The basic role of BCB is to shift the relative position of the C_{60}-DOS with respect to gate. Both PES and threshold voltage shift are in good agreement reducing the dipole (and voltage) by 0.6 eV (or V). The role of the organic interlayer is to compensate the disadvantageous vacuum-level offset formed on the pristine oxide structure. It re-establishes the situation found for the case with p-Si and C_{60}.

11.7 Discussion

Both results, OFETs threshold voltage and transistor-related PES experiment demonstrate a complementary technique to understand organic interfaces. The role of organic interlayers in OFETs is interpreted to be more than just a passivation layer. In fact the results show that an organic interlayer changes the energy level alignment of the corresponding organic semiconductor significantly. The experiments point out their inherent *active* role.

Instead of vacuum-level alignment a dipole is formed at the organic–organic interface, which finally drives the energy levels of the organic semiconductor to a position close to the Fermi level. The built-in potential is to some extend compensated. A similar alignment is for instance found on metals or silicon substrates [54, 55, 57]. Though the model system BCB–C_{60} studied in detail here does not represent organic interfaces in general, the aspect of dipole-controlled alignment is widely accepted in the literature [58]. Organic interface dipoles can be significant, and in light of the complementary OFET results, a shift by 0.6 V as detected for BCB has a deep impact on the device performance. Hence a lot of attention has recently been paid to interface engineering with organic interlayers in organic electronics device studies. A closer look to the oxide-only structure allows a number of conclusions as well. On the contrary to BCB, on pristine alumina rather vacuum-level alignment is found, at least the energy offset at the interface is low compared to the organic–organic system. Consequently the energy drop found between metal–metal oxide is passed on to the organic semiconductor leading finally to a large offset in the vacuum level by 1.4 eV. In the field-effect transistor the offset is then revealed by the increased threshold voltage, since the inherent built-in potential can only be compensated by applying gate voltage. Similar effects have been presented for a number of pristine oxide OFET structures, where significant threshold potentials arise [27]. These support the assumption of a vacuum-level alignment on oxide–organic semiconductor interfaces.

11.8 Conclusion and Outlook

A sound theory on organic interlayer's relating their magnitudes of introduced dipoles and their influence on device performances is yet not found. Most of commonly used interlayers are presented in rather empirical studies. In various contributions interface effects on device performances are reduced to surface traps or surface passivation. The authors believe that such consideration are in agreement with the dipole-controlled alignment uncovered by a device-related photoemission study. Pristine oxide surfaces due to OH-termination indeed introduce trapped states in the organic semiconductors. Negative charges at the interface are present, which push the energy levels of the semiconductor downwards and away from the Fermi energy. In OFETs they have to be compensated by the gate voltage, thus leading to increased and unwanted threshold potentials. Device-related photoemission can help to understand the interaction at organic–organic interfaces. Still suspense as regards the magnitude and polarity of the dipole is a real problem. An approach to model and systematically analyze organic interfaces might be derived from donor–acceptor studies in bulk-heterojunction solar cells [59, 60]. Depending on the system the interlayer either acts as quasi-donor or acceptor, which becomes apparent by the threshold voltage. At least from the experimental data, the dipoles formed at heterojunctions are similar to interactions on π-conjugated systems. Therefore interface studies could be expanded for photo-induced effects on OFET interfaces for a better understanding.

11.9 Summary

The contribution discusses the complex nature of organic interfaces, which are key-components in organic electronic devices. Especially in OFETs the formation of a conductive channel is sensitive to mutual, interfacial effects. The variety of organic interfacial or dielectric layers has increased during the past years, at the same time the development of small π-conjugated molecules has yielded in an enormous amount of systems. Practically a number of combinations result in good performing organic field-effect transistors, which in the end will be implemented to complex, organic integrated circuits.

In this article interfacial effect in view of the complex energy level alignment is investigated. The question arises of why organic interlayers enhance transistor performances compared to devices with pristine oxide. For gaining information about energy levels at the interface, complementary techniques are applied, one based on a systematic analysis of the threshold voltages in OFETs, one involving device-related photoemission spectroscopy. In detail, an oxide–organic interface is compared to an organic–organic interface using the model system alumina–C_{60} and BCB–C_{60}. The device analysis show clear results from both interfaces: as soon as BCB is applied, the threshold voltage is lowered from previous 0.7 V almost to 0 V.

A similar effect is found for the complementary photoemission study, where actually BCB induces a shift in the same magnitude resulting in a different energy level alignment at the interface. Interestingly the entire spectrum is shifted concomitantly, both valence features and secondary electron cut-off exhibit the same result. The quality of the spectra is not affected by the different interfaces.

The spectral data together with the device parameters provide valuable information about the organic–organic and the organic–oxide system. On the one hand, huge dipoles control the energy level alignment at the interface. They compensate built-in fields and consequently move valence levels to more favorable positions for creating a conducting channel in the OFET. On the other hand, at oxide–organic interfaces almost vacuum-level alignment is observed, therefore the compensation of built-in fields has to be performed by applying gate voltage resulting in the disadvantageous huge threshold potential. Similar effects on oxide–organic interfaces have been reported by several groups in the literature. The authors believe that exactly the findings presented here can help to understand organic interface system and to tailor organic electronic devices to higher performances.

Still little is known about the energy level alignment at organic–organic interfaces. From empirical studies general pathways for high-performance systems have been demonstrated, and parameters are defined which may be considered for further development.

References

1. H. Klauk, U. Zschieschang, J. Pflaum, M. Halik, Ultralow-power organic complementary circuits. Nature **445**(7129), 745–748 (2007). doi:10.1038/nature05533. http://www.ncbi.nlm.nih.gov/pubmed/17301788
2. H. Klauk, U. Zschieschang, M. Halik, Low-voltage organic thin-film transistors with large transconductance. J. Appl. Phys. **102**(7), 074514 (2007). doi:10.1063/1.2794702. http://link.aip.org/link/JAPIAU/v102/i7/p074514/s1&Agg=doi
3. K. Myny, S. Steudel, S. Smout, P. Vicca, F. Furthner, B. van der Putten, a.K. Tripathi, G.H. Gelinck, J. Genoe, W. Dehaene, Organic RFID transponder chip with data rate compatible with electronic product coding. Org. Electron. **11**(7), 1176–1179 (2010). doi:10.1016/j.orgel.2010.04.013. http://linkinghub.elsevier.com/retrieve/pii/S1566119910001308
4. K. Suganuma, S. Watanabe, T. Gotou, K. Ueno, Fabrication of transparent and flexible organic field-effect transistors with solution-processed graphene source–drain and gate electrodes. Appl. Phys. Express **4**(2), 021603 (2011). doi:10.1143/APEX.4.021603. http://apex.jsap.jp/link?APEX/4/021603/
5. T. Sekitani, T. Someya, Stretchable, large-area organic electronics. Adv. Mater. **22**(20), 2228–2246 (2010). doi:10.1002/adma.200904054. http://www.ncbi.nlm.nih.gov/pubmed/20229571
6. T.D. Anthopoulos, T.B. Singh, N. Marjanovic, N.S. Sariciftci, A. Montaigne Ramil, H. Sitter, M. Coelle, D.M. de Leeuw, High performance n-channel organic field-effect transistors and ring oscillators based on C60 fullerene films. Appl. Phys. Lett. **89**(21), 213504 (2006). doi:10.1063/1.2387892. http://link.aip.org/link/APPLAB/v89/i21/p213504/s1&Agg=doi
7. T. Yokota, T. Nakagawa, T. Sekitani, Y. Noguchi, K. Fukuda, U. Zschieschang, H. Klauk, K. Takeuchi, M. Takamiya, T. Sakurai, T. Someya, Control of threshold voltage in low-voltage organic complementary inverter circuits with floating gate structures. Appl. Phys. Lett. **98**(19), 193302 (2011). doi:10.1063/1.3589967. http://link.aip.org/link/APPLAB/v98/i19/p193302/s1&Agg=doi
8. T. Sekitani, T. Yokota, U. Zschieschang, H. Klauk, S. Bauer, K. Takeuchi, M. Takamiya, T. Sakurai, T. Someya, Organic nonvolatile memory transistors for flexible sensor arrays. Science **326**(5959), 1516–1519 (2009). doi:10.1126/science.1179963. http://www.ncbi.nlm.nih.gov/pubmed/20007895
9. J.C. Ribierre, K. Takaishi, T. Muto, T. Aoyama, Flexible organic field-effect transistors and complementary inverters based on a solution-processable quinoidal oligothiophene derivative. Opt. Mater. **33**(9), 1415–1418 (2011). doi:10.1016/j.optmat.2011.03.015. http://linkinghub.elsevier.com/retrieve/pii/S0925346711001364
10. U. Zschieschang, F. Ante, T. Yamamoto, K. Takimiya, H. Kuwabara, M. Ikeda, T. Sekitani, T. Someya, K. Kern, H. Klauk, Flexible low-voltage organic transistors and circuits based on a high-mobility organic semiconductor with good air stability. Adv. Mater. **22**(9), 982–985 (2010). doi:10.1002/adma.200902740. http://www.ncbi.nlm.nih.gov/pubmed/20217824

11. T. Sakanoue, M. Yahiro, C. Adachi, H. Uchiuzou, T. Takahashi, A. Toshimitsu, Ambipolar light-emitting organic field-effect transistors using a wide-band-gap blue-emitting small molecule. Appl. Phys. Lett. **90**(17), 171118 (2007). doi:10.1063/1.2734389. http://link.aip.org/link/APPLAB/v90/i17/p171118/s1&Agg=doi
12. A. Huebler, F. Doetz, H. Kempa, H.E. Katz, M. Bartzsch, N. Brandt, I. Hennig, U. Fuegmann, S. Vaidyanathan, J. Granstrom, Ring oscillator fabricated completely by means of mass-printing technologies. Org. Electron. **8**(5), 480–486 (2007). doi:10.1016/j.orgel.2007.02.009. http://linkinghub.elsevier.com/retrieve/pii/S1566119907000365
13. M. Mas-Torrent, C. Rovira, Novel small molecules for organic field-effect transistors: towards processability and high performance. Chem. Soc. Rev. **37**(4), 827–838 (2008). doi:10.1039/b614393h. http://www.ncbi.nlm.nih.gov/pubmed/18362986
14. M. Ullah, I.I. Fishchuk, A. Kadashchuk, P. Stadler, A. Pivrikas, C. Simbrunner, V.N. Poroshin, N.S. Sariciftci, H. Sitter, Dependence of Meyer Neldel energy on energetic disorder in organic field effect transistors. Appl. Phys. Lett. **96**(21), 213306 (2010). doi:10.1063/1.3435477. http://link.aip.org/link/APPLAB/v96/i21/p213306/s1&Agg=doi
15. M. Ullah, A. Pivrikas, I.I. Fishchuk, A. Kadashchuk, P. Stadler, C. Simbrunner, N.S. Sariciftci, H. Sitter, Effect of source–drain electric field on the Meyer–Neldel energy in organic field effect transistors. Appl. Phys. Lett. **98**(22), 223301 (2011). doi:10.1063/1.3584131. http://link.aip.org/link/APPLAB/v98/i22/p223301/s1&Agg=doi
16. A. Pivrikas, M. Ullah, H. Sitter, N.S. Sariciftci, Electric field dependent activation energy of electron transport in fullerene diodes and field effect transistors: Gill's law. Appl. Phys. Lett. **98**(9), 092114 (2011). doi:10.1063/1.3557503. http://link.aip.org/link/APPLAB/v98/i9/p092114/s1&Agg=doi
17. A. Pivrikas, M. Ullah, T.B. Singh, C. Simbrunner, G.J. Matt, H. Sitter, N.S. Sariciftci, Meyer–Neldel rule for charge carrier transport in fullerene devices: a comparative study. Org. Electron. **12**(1), 161–168 (2011). doi:10.1016/j.orgel.2010.10.014. http://linkinghub.elsevier.com/retrieve/pii/S1566119910003393
18. Y.M. Park, J. Daniel, M. Heeney, A. Salleo, Room-temperature fabrication of ultrathin oxide gate dielectrics for low-voltage operation of organic field-effect transistors. Adv. Mater. **23**(8), 971–974 (2011). doi:10.1002/adma.201003641. http://www.ncbi.nlm.nih.gov/pubmed/21341309
19. L. Miozzo, A. Yassar, G. Horowitz, Surface engineering for high performance organic electronic devices: the chemical approach. J. Mater. Chem. **20**(13), 2513 (2010). doi:10.1039/b922385a
20. H. Klauk, M. Halik, U. Zschieschang, F. Eder, D. Rohde, G. Schmid, C. Dehm, Flexible organic complementary circuits. IEEE Trans. Electron Devices **52**(4), 618–622 (2005). doi:10.1109/TED.2005.844739. http://ieeexplore.ieee.org/lpdocs/epic03/wrapper.htm?arnumber=1408167
21. A. Jedaa, M. Burkhardt, U. Zschieschang, H. Klauk, D. Habich, G. Schmid, M. Halik, The impact of self-assembled monolayer thickness in hybrid gate dielectrics for organic thin-film transistors. Org. Electron. **10**(8), 1442–1447 (2009). doi:10.1016/j.orgel.2009.08.006. http://linkinghub.elsevier.com/retrieve/pii/S1566119909002262
22. E.C.P. Smits, S.G.J. Mathijssen, P.a. van Hal, S. Setayesh, T.C.T. Geuns, K.a.H.a. Mutsaers, E. Cantatore, H.J. Wondergem, O. Werzer, R. Resel, M. Kemerink, S. Kirchmeyer, A.M. Muzafarov, S.a. Ponomarenko, B. de Boer, P.W.M. Blom, D.M. de Leeuw, Bottom-up organic integrated circuits. Nature **455**(7215), 956–959 (2008). doi:10.1038/nature07320. http://www.nature.com/doifinder/10.1038/nature07320
23. M.F. Calhoun, J. Sanchez, D. Olaya, M.E. Gershenson, V. Podzorov, Electronic functionalization of the surface of organic semiconductors with self-assembled monolayers. Nat. Mater. **7**(1), 84–89 (2008). doi:10.1038/nmat2059. http://www.ncbi.nlm.nih.gov/pubmed/18026107
24. N. Björklund, F.S. Pettersson, D. Tobjörk, R. Österbacka, Controlling the turn-on-voltage in low-voltage Al2O3 organic transistors with mixed self-assembled monolayers. Synth. Met. **161**(9–10), 743–747 (2011). doi:10.1016/j.synthmet.2011.01.024. http://linkinghub.elsevier.com/retrieve/pii/S0379677911000385

25. U. Zschieschang, M. Halik, H. Klauk, Microcontact-printed self-assembled monolayers as ultrathin gate dielectrics in organic thin-film transistors and complementary circuits. Langmuir **24**(5), 1665–1669 (2008). doi:10.1021/la703818d. http://www.ncbi.nlm.nih.gov/pubmed/18198917
26. P. Stadler, Interfacial Effects in an Organic Semiconductor Heterojunction. Dissertation, Johannes Kepler University Linz, 2011
27. L.-l. Chua, J. Zaumseil, J.-f. Chang, E.C. Ou, General observation of n-type field-effect behaviour in organic semiconductors. Nature **434**(March), 194–199 (2005). doi:10.1038/nature03293.1
28. T.B. Singh, N.S. Sariciftci, Progress in plastic electronics devices. Annu. Rev. Mater. Res. **36**(1), 199–230 (2006). doi:10.1146/annurev.matsci.36.022805.094757. http://arjournals.annualreviews.org/doi/abs/10.1146/annurev.matsci.36.022805.094757
29. Y. Don Park, J.A. Lim, H.S. Lee, K. Cho, Interface engineering in organic transistors. Mater. Today **10**(3), 46–54 (2007). ISSN 1369-7021. http://www.sciencedirect.com/science/article/pii/S1369702107700196
30. H. Ma, H.-L. Yip, F. Huang, A.K.-Y. Jen, Interface engineering for organic electronics. Adv. Funct. Mater. **20**(9), 1371–1388 (2010). doi:10.1002/adfm.200902236. http://dx.doi.org/10.1002/adfm.200902236
31. a. Wang, I. Kymissis, V. Bulovic, a.I. Akinwande, Engineering density of semiconductor–dielectric interface states to modulate threshold voltage in OFETs. IEEE Trans. Electron Devices **53**(1), 9–13 (2006). doi:10.1109/TED.2005.860633. http://ieeexplore.ieee.org/lpdocs/epic03/wrapper.htm?arnumber=1561539
32. X. Sun, C.-a. Di, Y. Liu, Engineering of the dielectric–semiconductor interface in organic field-effect transistors. J. Mater. Chem. **20**(13), 2599 (2010). doi:10.1039/b921449f. http://xlink.rsc.org/?DOI=b921449f
33. Y. Noh, H. Sirringhaus, Ultra-thin polymer gate dielectrics for top-gate polymer field-effect transistors. Org. Electron. **10**(1), 174–180 (2009). doi:10.1016/j.orgel.2008.10.021. http://linkinghub.elsevier.com/retrieve/pii/S1566119908002127
34. J. Cornil, J.-L. Brédas, J. Zaumseil, H. Sirringhaus, Ambipolar transport in organic conjugated materials. Adv. Mater. **19**(14), 1791–1799 (2007). doi:10.1002/adma.200602922. http://doi.wiley.com/10.1002/adma.200602922
35. X.-H. Zhang, B. Domercq, B. Kippelen, High-performance and electrically stable C60 organic field-effect transistors. Appl. Phys. Lett. **91**(9), 092114 (2007). doi:10.1063/1.2778472. http://link.aip.org/link/APPLAB/v91/i9/p092114/s1&Agg=doi
36. X.-H. Zhang, B. Kippelen, Low-voltage C60 organic field-effect transistors with high mobility and low contact resistance. Appl. Phys. Lett. **93**(13), 133305 (2008). doi:10.1063/1.2993349. http://link.aip.org/link/APPLAB/v93/i13/p133305/s1&Agg=doi
37. H. Sirringhaus, Device physics of solution-processed organic field-effect transistors. Adv. Mater. **17**(20), 2411–2425 (2005). doi:10.1002/adma.200501152. http://doi.wiley.com/10.1002/adma.200501152
38. F. Todescato, R. Capelli, F. Dinelli, M. Murgia, N. Camaioni, M. Yang, R. Bozio, M. Muccini, Correlation between dielectric/organic interface properties and key electrical parameters in PPV-based OFETs. J. Phys. Chem. B **112**(33), 10130 (2008). doi:10.1021/jp8012255
39. M.E. Mills, P. Townsend, D. Castillo, S. Martin, A. Achen, Benzocyclobutene (DVS-BCB) polymer as an interlayer dielectric (ILD) material. Microelectron. Eng. **33**(1–4), 327–334 (1997). doi:10.1016/S0167-9317(96)00061-5. http://linkinghub.elsevier.com/retrieve/pii/S0167931796000615
40. W. Ou-Yang, M. Weis, D. Taguchi, X. Chen, T. Manaka, M. Iwamoto, Modeling of threshold voltage in pentacene organic field-effect transistors. J. Appl. Phys. **107**(12), 124506 (2010). doi:10.1063/1.3449078. http://link.aip.org/link/JAPIAU/v107/i12/p124506/s1&Agg=doi
41. W. Ou-Yang, X. Chen, M. Weis, T. Manaka, M. Iwamoto, Tuning of threshold voltage in organic field-effect transistor by dipole monolayer. Jpn. J. Appl. Phys. **49**(4), 04-04 (2010). doi:10.1143/JJAP.49.04DK04. http://jjap.jsap.jp/link?JJAP/49/04DK04/

42. a. Deman, J. Tardy, PMMA–TaO bilayer gate dielectric for low operating voltage organic FETs. Org. Electron. **6**(2), 78–84 (2005). doi:10.1016/j.orgel.2005.03.002. http://linkinghub.elsevier.com/retrieve/pii/S1566119905000108
43. K.P. Pernstich, S. Haas, D. Oberhoff, C. Goldmann, D.J. Gundlach, B. Batlogg, a.N. Rashid, G. Schitter, Threshold voltage shift in organic field effect transistors by dipole monolayers on the gate insulator. J. Appl. Phys. **96**(11), 6431 (2004). doi:10.1063/1.1810205. http://link.aip.org/link/JAPIAU/v96/i11/p6431/s1&Agg=doi
44. H. Klauk, Contact resistance in organic thin film transistors. Solid-State Electron. **47**(2), 297–301 (2003). doi:10.1016/S0038-1101(02)00210-1. http://linkinghub.elsevier.com/retrieve/pii/S0038110102002101
45. T.B. Singh, N. Marjanovic, G.J. Matt, S. Günes, N.S. Sariciftci, A. Montaigne Ramil, A. Andreev, H. Sitter, R. Schwödiauer, S. Bauer, High-mobility-channel organic field-effect transistors based on epitaxially grown C films. Org. Electron. **6**(3), 105–110 (2005). doi:10.1016/j.orgel.2005.03.006. http://linkinghub.elsevier.com/retrieve/pii/S1566119905000145
46. T.B. Singh, N.S. Sariciftci, H. Yang, L. Yang, B. Plochberger, H. Sitter, Correlation of crystalline and structural properties of C60 thin films grown at various temperature with charge carrier mobility. Appl. Phys. Lett. **90**(21), 213512 (2007). doi:10.1063/1.2743386. http://link.aip.org/link/APPLAB/v90/i21/p213512/s1&Agg=doi
47. L.-L. Chua, P.K.H. Ho, H. Sirringhaus, R.H. Friend, High-stability ultrathin spin-on benzocyclobutene gate dielectric for polymer field-effect transistors. Appl. Phys. Lett. **84**(17), 3400 (2004). doi:10.1063/1.1710716. http://link.aip.org/link/APPLAB/v84/i17/p3400/s1&Agg=doi
48. A. Ortiz-Conde, F.J. Garcia Sanchez, J.J. Liou, A. Cerdeira, M. Estrada, Y. Yue, A review of recent MOSFET threshold voltage extraction methods. Microelectron. Reliab. **42**(4–5), 583–596 (2002). doi:10.1016/S0026-2714(02)00027-6. http://linkinghub.elsevier.com/retrieve/pii/S0026271402000276
49. D. Boudinet, G. Le Blevennec, C. Serbutoviez, J.-M. Verilhac, H. Yan, G. Horowitz, Contact resistance and threshold voltage extraction in n-channel organic thin film transistors on plastic substrates. J. Appl. Phys. **105**(8), 084510 (2009). doi:10.1063/1.3110021. http://link.aip.org/link/JAPIAU/v105/i8/p084510/s1&Agg=doi
50. P. Stadler, A.M. Track, M. Ullah, H. Sitter, G.J. Matt, G. Koller, T.B. Singh, H. Neugebauer, N.S. Sariciftci, M.G. Ramsey, The role of the dielectric interface in organic transistors: a combined device and photoemission study. Org. Electron. **11**(2), 207–211 (2010). doi:10.1016/j.orgel.2009.10.017. http://linkinghub.elsevier.com/retrieve/pii/S1566119909003085
51. G. Heimel, I. Salzmann, S. Duhm, J.A.P. Rabe, N. Koch, Intrinsic surface dipoles control the energy levels of conjugated polymers. Adv. Funct. Mater. **19**(24), 3874–3879 (2009). doi:10.1002/adfm.200901025. http://doi.wiley.com/10.1002/adfm.200901025
52. A. Rajagopal, C.I. Wu, A. Kahn, Energy level offset at organic semiconductor heterojunctions. J. Appl. Phys. **83**(5), 2649 (1998). doi:10.1063/1.367027. http://link.aip.org/link/JAPIAU/v83/i5/p2649/s1&Agg=doi
53. H. Vázquez, W. Gao, F. Flores, A. Kahn, Energy level alignment at organic heterojunctions: role of the charge neutrality level. Phys. Rev. B **71**(4), 1–4 (2005). doi:10.1103/PhysRevB.71.041306. http://link.aps.org/doi/10.1103/PhysRevB.71.041306
54. K. Sakamoto, Electronic structure of K-doped C60 monolayer films adsorbed on Si(0 0 1)-(2x1) and Si(1 1 1)-(7x7) surfaces. Surf. Sci. **499**(1), 63–72 (2002). doi:10.1016/S0039-6028(01)01794-0. http://linkinghub.elsevier.com/retrieve/pii/S0039602801017940
55. C. Cepek, P. Schiavuta, M. Sancrotti, M. Pedio, Photoemission study of C 60 / Si (111) adsorption as a function of coverage and annealing temperature. Phys. Rev. B **60**(3), 2068–2073 (1999). doi:10.1103/PhysRevB.60.2068. http://link.aps.org/doi/10.1103/PhysRevB.60.2068
56. M.W. Ruckman, B. Xia, S.L. Qiu, Adsorption of C60 on Ta(110): photoemission and C K-edge studies. Phys. Rev. B **48**(20), 15457 (1993)
57. S.J. Chase, W.S. Bacsa, M.G. Mitch, L.J. Pilione, J.S. Lannin, Surface-enhanced Raman scattering and photoemission of C60 on noble-metal surfaces. Phys. Rev. B **46**(12), 7873–7877 (1992)

58. J. Ivanco, F.P. Netzer, M.G. Ramsey, On validity of the Schottky–Mott rule in organic semiconductors: sexithiophene on various substrates. J. Appl. Phys. **101**(10), 103712 (2007). doi:10.1063/1.2734879. http://link.aip.org/link/JAPIAU/v101/i10/p103712/s1&Agg=doi
59. W. Osikowicz, M.P. de Jong, W.R. Salaneck, Formation of the interfacial dipole at organic-organic interfaces: C60/Polymer interfaces. Adv. Mater. **19**(23), 4213–4217 (2007). doi:10.1002/adma.200700622. http://doi.wiley.com/10.1002/adma.200700622
60. S. Braun, W. Osikowicz, Y. Wang, W.R. Salaneck, Energy level alignment regimes at hybrid organic–organic and inorganic–organic interfaces. Org. Electron. **8**(1), 14–20 (2007). doi: 10.1016/j.orgel.2006.10.006. http://linkinghub.elsevier.com/retrieve/pii/S156611990600142X

Chapter 12
Natural Materials for Organic Electronics

**Mihai Irimia-Vladu, Eric D. Głowacki, N. Serdar Sariciftci,
and Siegfried Bauer**

Abstract Biological materials in organic electronics stand for low-cost production of biocompatible, biodegradable, and sustainable electronic devices. In this chapter, we discuss such materials and their implementation in the fabrication of electronic circuits. We briefly introduce applications of such biocompatible and biodegradable materials for interfacing electronics with living tissue. Research on bio-organic materials may ultimately result in establishing robust, environmentally safe, "green electronics" alternatives.

12.1 Introduction

Organic electronics research began to look at highly unusual material platforms for biodegradable and biocompatible, even metabolizable, low-cost products which may ultimately be used in daily life applications, including (1) home appliances and portable devices, (2) microchips for biomedical implants, (3) electronics for low-cost, large-volume, "throwaway" applications useful in packaging, plastic bags, disposable dishware, to name a few [1–5].

In this chapter, we will briefly discuss the use of unusual materials in organic electronics. We have divided the chapter according to the typical device architecture used in electronics. We first start with substrates—the actual basis of any electronic device fabrication; we then discuss smoothening layers—useful in the planarization of rough substrates; followed by dielectrics—necessary in transistors but also in

---

M. Irimia-Vladu · E.D. Głowacki · N.S. Sariciftci
Physical Chemistry, Linz Institute for Organic Solar Cells, Johannes Kepler University Linz,
Altenbergerstraße 69, 4040 Linz, Austria

M. Irimia-Vladu · S. Bauer
Department of Soft Matter Physics, Johannes Kepler University Linz, Altenbergerstraße 69, 4040
Linz, Austria

M. Irimia-Vladu (✉)
Division of Surface Technologies and Photonics, Department of Materials, Joanneum Research
Forschungsgesellschaft mbH, Franz-Pichler Strasse Nr. 30, 8160 Weiz, Austria
e-mail: Mihai.Irimia-Vladu@joanneum.at

H. Sitter et al. (eds.), *Small Organic Molecules on Surfaces*,
Springer Series in Materials Science 173, DOI 10.1007/978-3-642-33848-9_12,

packaging; semiconductors—charge transport materials in amplifiers and circuits; and contact electrodes—used as contacts in transistors, solar cells, photodiodes, and as interconnects between circuit elements.

Highly uncommon materials in electronics, such as paper, leather, silk, hard gelatine, natural resin shellac and also degradable plastics were recently introduced as substrates in the fabrication of organic electronic devices [6–10]. Smoothening of such substrates is often essential before device fabrication, since most of these substrates are inherently rough. We discuss polydimethylsiloxane (PDMS), a soft elastomer frequently employed in food industry and also in biomedicine (due to its biocompatibility) as cosmetic implant; as well as shellac, an ancient natural resin produced by the female lac beetle-used extensively in the past for wood finishing and electrical insulation [11–14] as smoothening layers.

As biodegradable and biocompatible dielectrics, we describe natural silk and natural deoxyribonucleic acid (DNA) in their processible forms [15, 16]. We further introduce small molecule nucleobases (adenine, guanine, cytosine, and thymine), the inner constituents of DNAs and RNAs, easily processable by vacuum evaporation. Nucleobases have excellent film forming properties; they are good insulators with low dielectric losses and high dielectric strength. Besides nucleobases, we also mention the use of molecules in the sugar family (glucose, lactose, or sucrose) as dielectrics [10].

While it seems easy to identify biological insulators, only few bio-originating semiconductors (e.g. chlorophyll, beta-carotene indigo and tyrian purple) have been identified to be useful in organic electronics [10, 17, 18]. Many synthetic "bio-inspired" semiconductors within the indigo and anthraquinone families derived from their naturally occurring counterparts show interesting charge transport properties. Indigo and its derivatives for example have shown electron and hole mobility close to the state-of-the-art level [19, 20].

Conductive electrodes are probably the most underdeveloped branch in this emerging field of bio-electronics [21]. Intense effort has been done only in the past couple of years to extend the biocompatible conductive polymers database [22–27] towards contact electrodes, as briefly reviewed in this chapter.

The purpose of this book chapter is not only to show recent advancements and pathways, but also to suggest key avenues that may be followed in order to establish a self-standing branch "environmentally friendly organic electronics".

12.2 Natural Substrates & Smoothening Layers

12.2.1 Natural Substrates

In the initial stages of development, organic electronics devices were fabricated exclusively on glass or silicon substrates. Successive steps were pursued for the fabrication on flexible (i.e. PET, PEN) as well as stretchable substrates [28–30]. Currently, new research efforts focus on the investigation of highly unusual substrates

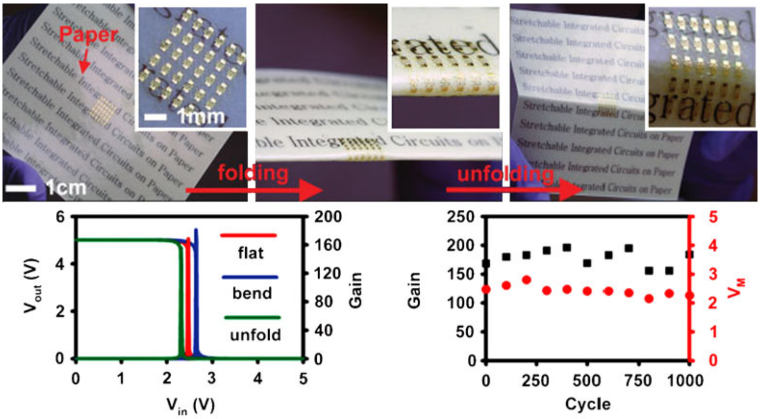

Fig. 12.1 (*top*) Photographs of CMOS inverters fabricated on paper substrate in flat (*left*), folded (*center*) and unfolded (*right*) states; (*bottom left*) Voltage transfer curve and (*bottom right*) cycling test gain in *black* type and threshold voltage in *red*, of the inverter measured in the flat states after multiple folding/unfolding cycles. From D.-H. Kim, Y.-S. Kim, J. Wu, Z. Liu, J. Song, H.-S. Kim, Y.Y. Huang, K.-C. Hwang and J.A. Rogers, Ultrathin silicon circuits with strain-isolation layers and mesh layouts for high-performance electronics on fabric, vinyl, leather, and paper, Adv. Mater. **21**, 3703–3707 (2009). Copyright Wiley-VCH Verlag GmbH & Co. KGaA. Reproduced with permission

(e.g. silk, fabric, hot-pressed cotton-fiber paper, leather, degradable polymers and even metabolizable/edible substrates) [6, 8–10, 31–33], which will be highlighted in the following.

Paper clearly is an interesting choice for the fabrication of electronic circuits: it is low cost, widely available, and biodegradable [6, 8, 33–40]. Arguably one major problem of paper is its rough surface. This deficiency can be circumvented by smoothening layers which render the rough surface of the paper substrate to a level of acceptable smoothness suitable for an easy deposition of metal electrodes and/or active layers. Polydimethylsiloxane (PDMS) is widely employed for smoothening purposes, mostly due to its excellent adhesive features [11]. The strong covalent bonds formed between the –OH groups of PDMS and the surface of the paper prevents adhesive failure, while concomitantly providing stress isolation during stretching and/or bending deformations of the substrate. This concept is illustrated in Fig. 12.1 where the strains in the metal layer of the interconnects and in the silicon of the active islands were reduced to less than 0.5 % of the applied strain, leading to no deterioration of the inverter gain measured after 1000 strain cycles [38].

In a recent report, a hybrid paper substrate was fabricated by embedding natural discrete cellulose fibers into an ionic resin that allowed paper to exhibit a large permanent electric charge. In such a configuration, the paper was shown to play two roles (substrate and gate dielectric) in the fabrication of low-cost, disposable, non-volatile memory elements. The performance achieved with such a device illus-

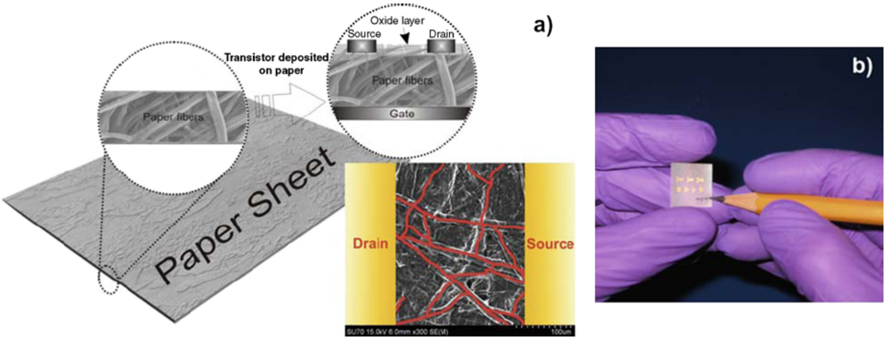

Fig. 12.2 (**a**) Schematic of the device structure, showing different layers. The device is fabricated by integration of natural discrete cellulose fibers functioning simultaneously as dielectric and substrate. The fibers are embedded in an ionic resin, giving the hybrid system a large permanent electric charge ($\sim 1\ \mathrm{mC\,m^{-2}}$). (**b**) Photograph of the paper-based memory device. From R. Martins, P. Barquinha, L. Pereira, N. Correira, G. Goncalves, I. Fereira and E. Fortunato, Selective floating gate non-volatile paper memory transistor, Phys. Status Solidi RRL **9**, 308–310 (2009). Copyright Wiley-VCH Verlag GmbH & Co. KGaA. Reproduced with permission

trated in Fig. 12.2: writing times less than 0.1 ms, operating voltage ∼5 V, cycling endurance greater than 10^7 and charge retention time in excess of 1.5 years [36].

Thermochromic display was successfully demonstrated on an ultrathin, flat and lightweight Xerox 32 lb Glossy Photo paper substrate. In Fig. 12.3, electrically conductive wires serve as heaters for the thermochromic ink patterned on the opposite side of the paper sheet. The heat produced by the wires generated a change in shade of the thermochromic ink, making the printed text visible [8].

Electrowetting displays on paper were demonstrated in [40]. The stimulus behind this investigation was to make the e-paper "look-and-feel" like classic ink on paper. The group investigated three types of paper: Glassine, Kromekote and Sappi, the main characteristics of them are displayed in Table 12.1. The initial roughness of the paper influences both the contact angle of the liquid droplet and the contact angle vs. applied voltage characteristics of the electrowetting structure. Demonstration of the electrowetting effect on paper is illustrated in Fig. 12.4, where the contact angle of the aqueous solution droplet was changed with the applied voltage. Given its inherent high smoothness, the Sappi paper displayed the best performance among the investigated paper grades, allowing contact angle modulations of ∼90°, a value required in e-paper applications.

Xerox paper has been used as a flexible substrate for the development of conductive lines drawn by a rollerball pen. Figure 12.5a–e shows conductive electronic artwork on Xerox paper. The lines are drawn by a silver-ink filled rollerball pen with a ball diameter of 960 μm for writing conductive text [34]. In the example shown, conductive text was easily printed on paper, having features of ∼650 μm wide.

Paper was also used as a substrate for large area monolithic photovoltaic arrays. Figure 12.6a–d shows lines of ∼20 μm thick conductive polymer, poly(3,4-ethylenedioxythiophene) patterned by oxidative chemical vapor deposition (oCVD)

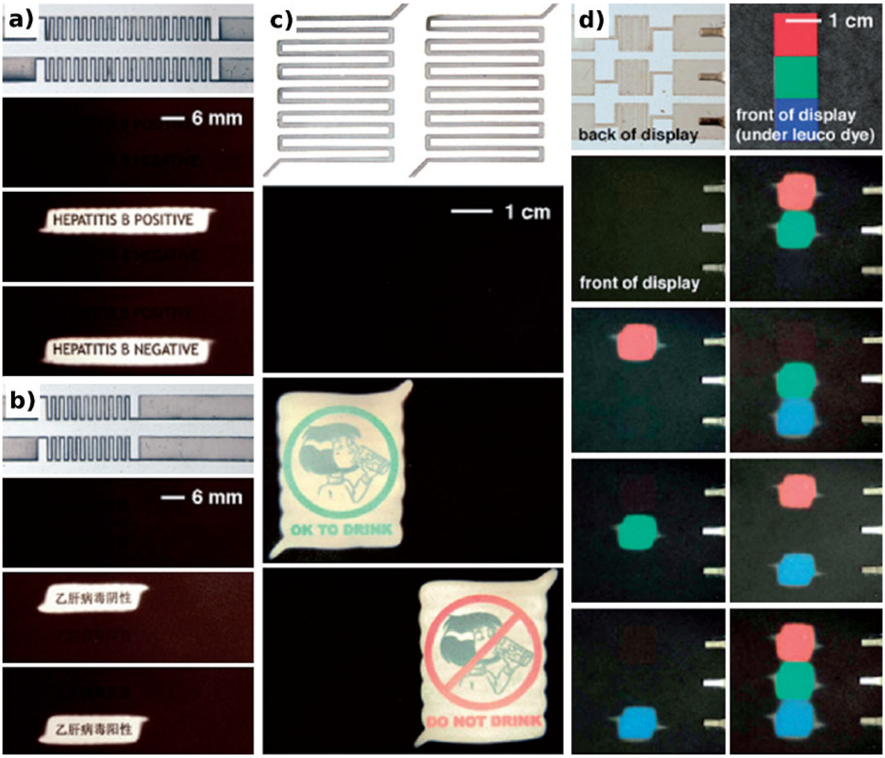

Fig. 12.3 Simple textual displays indicators fabricated on Xerox 32 lb, 1.5 mm thick photo paper substrates with 50-mm thick layer of thermochromic ink patterned on one side and 100 % Zn metallic wires on the non-ink side as heating elements. (**a**–**b**) Example of displays showing the result of a hepatitis B test (positive vs. negative) in English and Chinese characters. The English message is activated by passing a current of ~140 mA through one of the two heating elements of wire resistance, 26 Ω; the Chinese message is activated by passing current of ~160 mA, wire resistance, 15 Ω. (**c**) A display meant to communication messages to populations with high illiteracy or to populations where multiple languages are used that indicates safe vs. unsafe drinking water using pictures; current, 300 mA, wire resistance, 15 Ω. (**d**) A three-color, *red-green-blue* (RGB) shutter display with the back side of the display comprising three heating elements, one behind each color. Reproduced with permission from The Royal Society of Chemistry, Reference [8]: A.C. Siegel, S.T. Phillips, B.J. Wiley, G.M. Whitesides, Thin, lightweight, foldable thermochromic displays on paper, Lab on Chip **9**, 2775–2781 (2009)

on various substrates including paper, instead on the traditional transparent conductive electrode, ITO. The advantage of the oCVD is given by the dryness of the printing process, eliminating the undesired wettability or surface tension issues normally occurring when printing on rough surfaces such as paper. The performance of the array of 250 OPV cells (0.1 cm × 0.3 cm each) fabricated on paper compares favorably with the performance of the respective cells built on glass substrates [35]. Advantageously, the paper-built array could be folded and creased without substantial loss of performance. In addition, by applying a thin film encapsulation layer on

Table 12.1 Properties of Glassine, Kromekote, and Sappi papers

Material property	Glassine	Kromekote	Sappi
Thickness (μm)	45	235	180
Basis weight (g/m^2)	48	212	167
Specific volume (m^3/g)	9.37×10^{-7}	1.11×10^{-6}	1.08×10^{-6}
Water contact angle (deg)	44.5	80.4	105.7

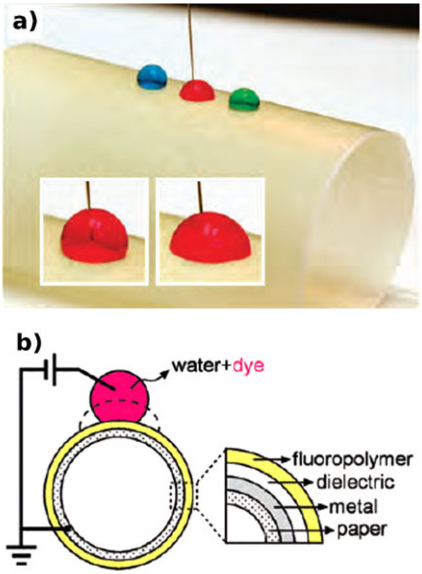

Fig. 12.4 (**a**) A schematic of the electrowetting process on a rolled glassine paper substrate showing the typical operation principle: high contact angle (i.e. of the *blue and green water blobs*, when no voltage is applied) vs. low contact angle generated in the *red droplet* after passing an experimental voltage. (**b**) Schematic of the structure, consisting of a ground electrode, a dielectric layer, and a fluoropolymer top layer on paper substrate. Reprinted with permission from D.Y. Kim, A.J. Steckl, Electrowetting on paper for electronic paper display, Appl. Mater. Interf. **2**(11), 3318–3323 (2010). Copyright (2010) American Chemical Society

top of the OPV array, the respective monolithic circuit could be even operated when immersed in water.

Not only paper, many other unconventional substrates (i.e. silk, leather, vinyl, fabric, etc.) were recently employed in organic electronics [3, 7, 9, 38, 41]. Electronics developed on bioresorbable silk fibroin substrates to interface with living tissue were demonstrated [41]. An image of an electrode array fabricated on silk substrate and wrapped onto a glass hemisphere is displayed in Fig. 12.7. The silk substrate supporting the meshed devices is biocompatible and fully resorbs when introduced inside living tissue. In addition, the silk substrate allows a spontaneous,

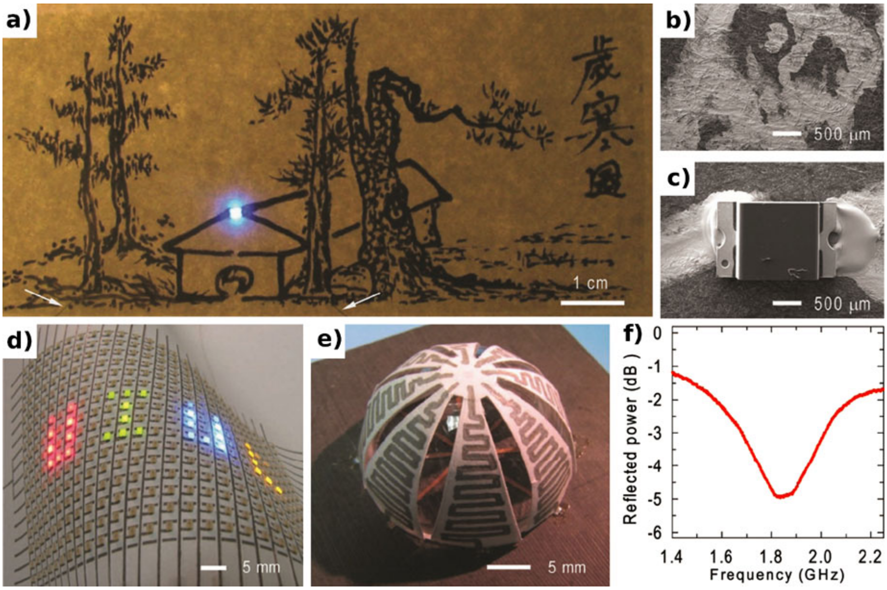

Fig. 12.5 (**a**) Photograph of conductive electronic artwork drawn on Xerox paper. The lines are created by a silver-ink filled rollerball pen. (**b**) SEM image at the root of the tree, revealing the continuous silver network (**c**) SEM image of the LED chip, adhered to the paper substrate with the conductive silver interconnects. (**d**) Photograph of a display on Xerox paper substrate, containing a LED array. (**e**) Photograph of the 3D antenna, fabricated by drawing conductive silver lines on a sticky paper. (**f**) Recorded reflected power of the 3D antenna as a function of frequency. From A. Russo, B.Y. Ahn, J.J. Adams, E.B. Duoss, J.T. Bernhard, J.A. Lewis, Pen-on-paper flexible electronics, Adv. Mater. **23**, 3426–3430 (2011). Copyright Wiley-VCH Verlag GmbH & Co. KGaA. Reproduced with permission

conformal wrapping process (driven by capillary forces) of the supporting circuit at the biotic/abiotic interface.

Fully bioresorbable, biocompatible and biodegradable substrates based on poly(L-lactide-co-glycolide), PLGA, hard gelatine, shellac or even caramelized sugar were employed in the fabrication of OFETs [2, 10, 31], the chosen materials are easy to process and low cost. As shown in Fig. 12.8a, PLGA substrates allow the fabrication of biodegradable electronics without necessitating a smoothening layer. Ecoflex is a fully biodegradable plastic foil, fabricated from starch and polylactic acid (commercially available at BASF) for plastic bags, food packaging and nursery foils. The biodegradability tests made by BASF showed that Ecoflex degrades completely in bio-compost within half a year. Hard gelatine is another example of a fully biocompatible and biodegradable substrate; currently these capsules are mainly used in pharmaceutics industry, as carrier capsule for oral drug delivery. Hard gelatine is easily manufactured from collagen of animal residues (i.e. skins and bones) with various additions of chemicals that play the role of plasticizers, preservatives, colors and even flavors. Shellac is an example of a fully natural substrate recently employed for the fabrication of OFETs and circuits [19]. Shellac is

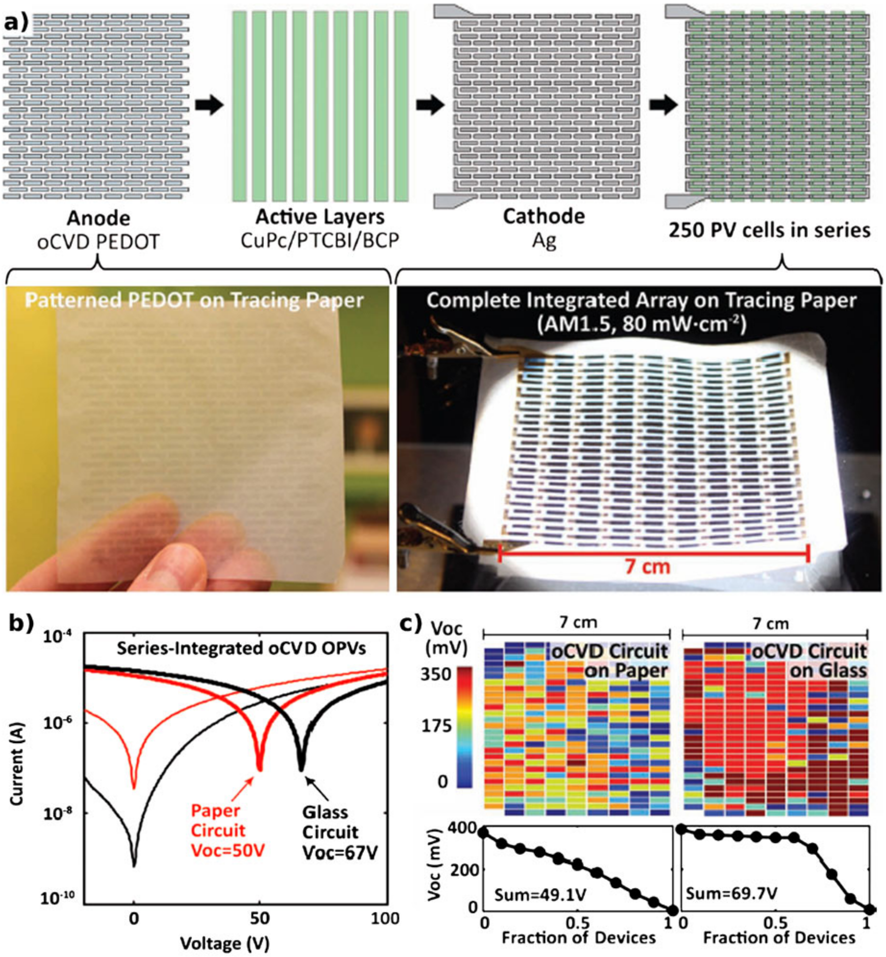

Fig. 12.6 (**a**) Schematic of the fabrication steps (*top*) and photograph (*bottom*) of an array of 250-cell series-integrated photovoltaic cells on paper substrate. (**b**) Current–voltage characteristics for series-integrated photovoltaic arrays. The conducting electrodes are vapor-patterned by oCVD technique. Comparison curves are recorded for the PV array built on paper substrate (*red*) and glass (*black*) in dark (*thin line*) and under illumination conditions (*bold line*) of AM1.5, 80 mW/cm^2). (**c**) Spatial map of the open-circuit voltages of each cell across the respective 50 cm^2 array. The *lower graphs* present the cumulative fraction of devices producing at or below a given voltage. From M.C. Barr, J.A. Rowehl, R.R. Lunt, J. Xu, A. Wang, C.M. Boyce, S.G. Im, V. Bulovic, K.K. Gleason, Direct, monolithic integration of organic photovoltaic circuits on unmodified paper, Adv. Mater. **23**, 3500–3505 (2011). Copyright Wiley-VCH Verlag GmbH & Co. KGaA. Reproduced with permission

produced by female lac beetles, and is harvested from trees in India and Thailand. Nevertheless, the chemical composition of shellac has been long ago determined, and nowadays shellac can be industrially produced in a multitude of grades [42]. Its

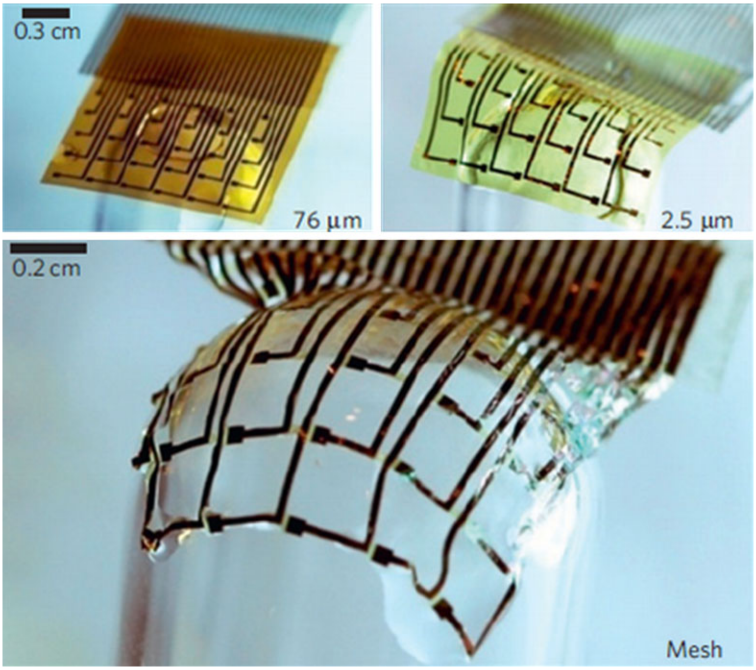

Fig. 12.7 Photograph of a 30 Au electrode array developed on sheets of various thicknesses (76 µm and 2.5 µm) (*top two panels*) and mesh (2.5 µm) (*bottom panel*). The conformable contact to a glass hemisphere is increasing with decreasing sheet thicknesses and with introduction of the mesh layout on bioresorbable silk supports. Reprinted by permission from Macmillan Publishers Ltd: Nature Materials, D.H. Kim, J. Viventi, J.J. Amsden, J. Xiao, L. Vigeland, Y.S. Kim, J.A. Blanco, B. Panilaitis, E.S. Frechette, D. Contreras, D.L. Kaplan, F.G. Omenetto, Y. Huang, K.C. Hwang, M.R. Zakin, B. Litt, J.A. Rogers, Dissolvable films of silk fibroin for ultrathin conformal bio-integrated electronics, Nature Mater. **9**, 511–517 (2010), copyright (2010)

excellent surface properties (its smoothness rivaling that of typical glass slides), recommends shellac as a preferable substrate for the development of high-performance organic electronics devices. Examples of electronics built on edible hard gelatine capsule, Ecoflex, and shellac are presented in Fig. 12.8b–d [10, 19].

Silk-based, conformal, adhesive, edible food sensors were recently developed based on wireless passive antennas across multiple frequency regions (MHz, GHz, THz) of the electromagnetic spectrum [43]. The resonant response of the antennas, conformally attached to food objects was monitored during the spoilage process. In an example showed in Fig. 12.9, the ripening of bananas and adulteration of cheese is assessed by measuring the resonant frequency response of the RFID-like sensors attached to their surface.

The research summarized in this section shows that application engineers can choose among a wide variety of unusual materials for electronic device design and development, coming closer to a view of electronics anywhere.

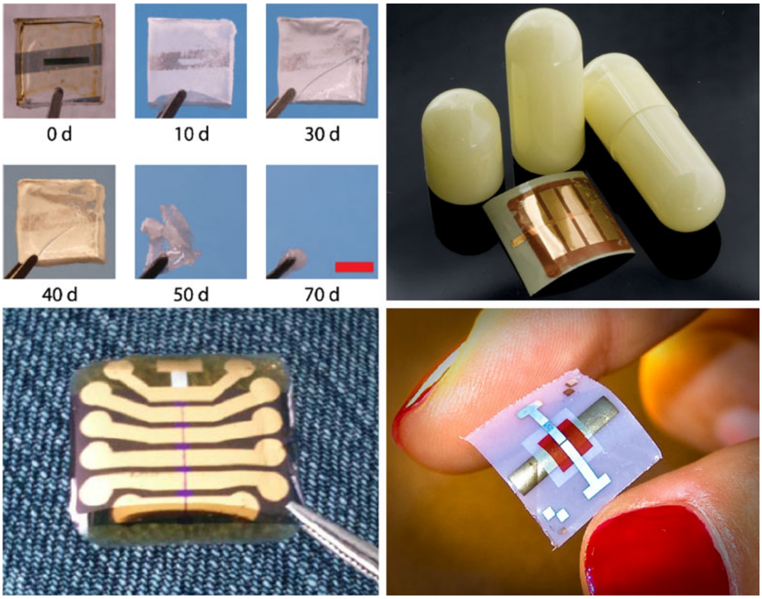

Fig. 12.8 (*Top left*) Photographs of the PLGA substrate at various stages of degradation (numbers represent days of exposure to citrate buffer). The device lost its optical transparency after about 10 days but maintained its integrity for the first 40 days; it fully resorbed after 70 days of exposure. From C.J. Bettinger and Z. Bao, Organic thin film transistors fabricated on resorbable biomaterial substrates, Adv. Mater. **22**, 651–655 (2010). Copyright Wiley-VCH Verlag GmbH & Co. KGaA. Reproduced with permission. (*Bottom left*) Photograph of organic field effect transistors fully fabricated from natural materials (Shellac substrate, tetratetracontane passivated aluminum oxide gate, indigo semiconductor and gold source and drain electrodes). From M. Irimia-Vladu, E.D. Glowacki, P.A. Troshin, G. Schwabegger, L. Leonat, D.K. Susarova, O. Krystal, M. Ullah, Y. Kanbur, M.A. Bodea, V.F. Razumov, H. Sitter, S. Bauer, N.S. Sariciftci, Indigo, a natural pigment for high-performance ambipolar organic field effect transistors and circuits, Adv. Mater. **24**(3), 375–380 (2012). Copyright Wiley-VCH Verlag GmbH & Co. KGaA. Reproduced with permission. (*Top right*) Organic field effect transistors fabricated on edible hard gelatine capsule. The device consists of gold gate, source and drain electrodes, adenine for gate dielectric and indanthrene brilliant orange RS for the semiconductor material. Adapted from Organic Electronics, 11, M. Irimia-Vladu, P.A. Troshin, M. Reisinger, G. Schwabegger, M. Ullah, R. Schwoediauer, A. Mumyatov, M. Bodea, J.W. Fergus, V. Razumov, H. Sitter, S. Bauer, N.S. Sariciftci, Environmentally sustainable organic field effect transistors, Org. Electron. **11**, 1974–1990 (2010). Copyright (2010), with permission from Elsevier. (*Bottom right*) Organic field effect transistor fabricated on biodegradable Ecoflex (BASF) plastic foil. The transistor consists of aluminum gate, source, and drain electrodes, adenine dielectric (*white square*) and cosmetic color perylene diimide semiconductor (*red square*). Adapted from M. Irimia-Vladu, P.A. Troshin, M. Reisinger, L. Shmygleva, Y. Kanbur, G. Schwabegger, M. Bodea, R. Schwoediauer, A. Mumyatov, J.W. Fergus, V. Razumov, H. Sitter, N.S. Sariciftci, S. Bauer, Biocompatible and biodegradable materials for organic field effect transistors, Adv. Funct. Mat. **20**(23), 4069–4076 (2010). Copyright Wiley-VCH Verlag GmbH & Co. KGaA. Reproduced with permission

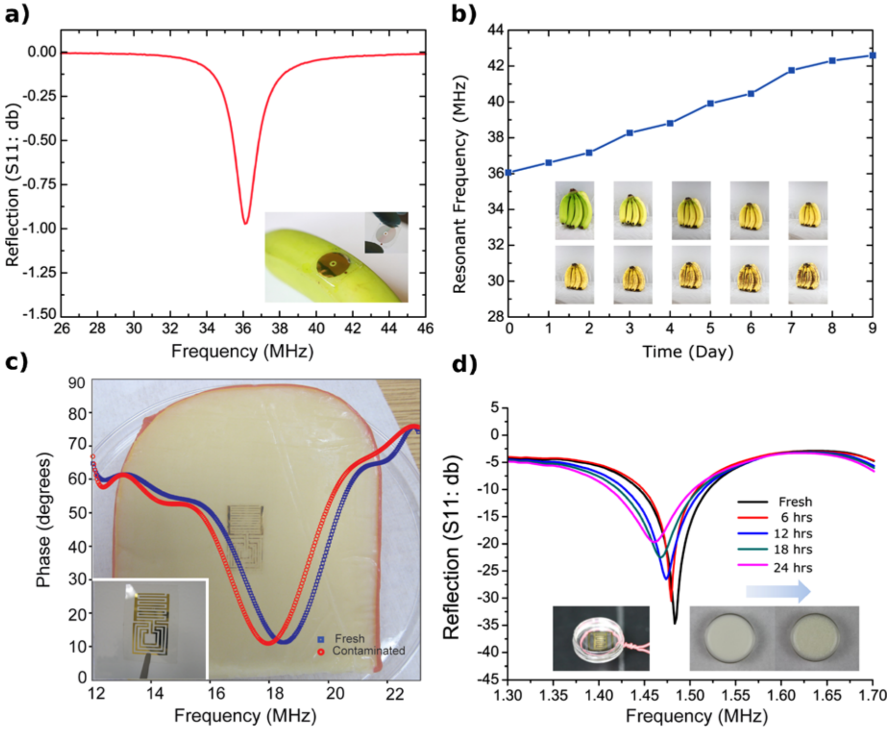

Fig. 12.9 Conformal silk antennas operating at radio and microwave frequency for food adulteration monitoring. (**a**) Measured reflection spectra of a silk RFID-like antenna attached to a banana skin. (**b**) Measured time-dependent resonant frequencies of the silk antenna while the banana ripened over 9 days. (**c**) Measured frequency-dependent impedance phase angle of a silk sensor applied to a slice of cheese (*blue curve*) to detect bacterial contamination (*red curve*). The *inset* shows a magnified view of the device. (**d**) Measured frequency responses of a silk sensor applied to a plastic container filled with milk during spoilage. From H. Tao, M.A. Brenckle, M. Yang, J. Zhang, M. Liu, S.M. Siebert, R.D. Averitt, M.S. Mannoor, M.C. McAlpine, J.A. Rogers, D.L. Kaplan, F.G. Omenetto, Silk-based conformal, adhesive, edible food sensors, Adv. Mater. **24**, 1067–1072 (2012). Copyright Wiley-VCH Verlag GmbH & Co. KGaA. Reproduced with permission

12.2.2 Natural Smoothening Layers

Due to its excellent surface forming properties, PDMS was employed not only as a substrate but also as smoothening layer for applications in organic electronics [9, 11, 38] and biomedical research [44]. The main attractive feature of PDMS is its biocompatibility that made it a reference material when used in vitro for biocompatibility and inflammatory response, as well as in vivo studies. Rosolic acid and shellac are two other examples of compounds that occur naturally, yet are easy and cheap to manufacture synthetically [12, 13]. Both materials are readily soluble in ethyl alcohol and form very smooth films on wide range of surfaces. As an example, the rough substrate surfaces of Ecoflex (BASF) or hard gelatine could be substantially smoothened to a root-mean square roughness below 10 nm when spin coated with a 0.1 g/ml rosolic acid solution in ethanol [10]. Drop-cast and spin-coated shellac films form smooth and uniform substrates. The root-mean-square roughness of a 0.5 mm thick drop-cast shellac substrate was only 0.5 nm, those of a 250 nm thick spin-coated shellac film had a root-mean-square roughness of only 0.35 nm, rivaling with the smoothness of glass slides [19].

12.3 Natural Dielectrics & Semiconductors

12.3.1 Natural Dielectrics

DNA is one of the most fascinating molecules of life, which has inspired many research teams looking for technical applications in photonics and organic electronics. Organic light-emitting diodes (OLEDs), and nonlinear opto-electrical modulators based on deoxyribonucleic acid (DNA) were developed [45–48]. DNA thin films were implemented as effective electron blocking layers in organic light-emitting diodes (i.e. BioLEDs) [46] with a significant enhancement of luminance and luminous efficiency. Figure 12.10 shows the comparison between devices made with DNA BioLEDs and control devices using common polymers such as polymethyl methacrylate or polyvinyl carbazole.

Solution processed DNA, as well as vacuum processed nucleobases (adenine, guanine, thymine and cytosine) also found use in gate dielectrics for organic field effect transistors [2, 10, 49, 50]. An advantage of the simple nucleobases instead of the full strands of solubilized DNA is the high purity obtained in the former materials that are amenable to rigorous cleaning through train sublimation. All four nucleobases display good dielectric properties with large breakdown fields from $\sim$1 MV/cm to $\sim$3.5 MV/cm. Vacuum processed nucleobases allowed for the fabrication of high-performance field effect transistors. Interestingly, despite the inherent roughness, reaching even root-mean-square (rms) values of 65 nm, the transfer and output characteristics of most nucleobase OFETs were hysteresis-free [2, 10]. Unexpectedly, the best film forming nucleobase (i.e. guanine) displayed hysteresis in the transfer characteristics, as shown in Fig. 12.11a, whereas the nucleobase that showed the highest tendency for crystallization resulting in inherently rough films (i.e. thymine), generated hysteresis-free OFETs. Moreover, the field effect mobility of the thymine-based devices was superior to the ones with guanine (Fig. 12.11b). These observations are somehow surprising and illustrate the complexity of mobility issues in OFETs [51]. Dielectrics from the sugar family were also employed for the fabrication of organic field effect transistors [2, 10]. Sucrose, glucose and lactose can be processed in aqueous solvents and have comparable film forming dielectric characteristics to poly vinyl alcohol (PVA). Dielectric properties of the investigated natural dielectrics are summarized in Table 12.2.

The brief presentation of natural dielectrics shows that nature offers a wealth of materials that may be useful in organic electronic devices, providing for biocompatible, biodegradable and eventually bioimplantable and bioresorbable applications.

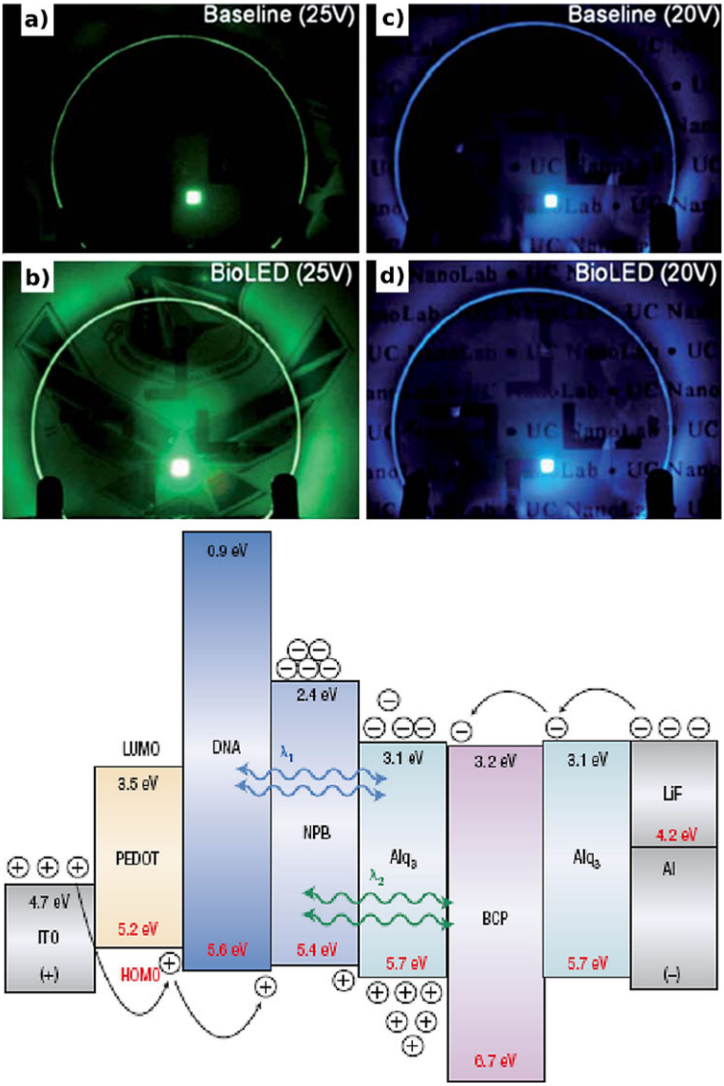

Fig. 12.10 (Photographs **a**–**d**) Luminous performance of green and blue LEDs. Comparison between green AlQ3 LEDs at 25 V: (**a**) baseline of green Alq3 OLED and (**b**) green Alq3 BioLED with DNA electron blocking layer. Comparison between blue NPB LEDs working at 20 V: (**c**) baseline blue NPB OLED and (**d**) blue NPB BioLED with DNA electron blocking layer. The DNA-based BioLEDs were as much as 10 times more efficient and 30 times brighter than their OLED counterparts. Reprinted with permission from J.A. Hagen, W. Li, A.J. Steckl and J.G. Grote, *Appl. Phys. Lett.*, **88**, 171109 (2006). Copyright (2006), American Institute of Physics. (*Bottom Schematic*) Energy-level diagrams for the blue-emitting (NPB) and green-emitting (Alq3) BioLEDs, Hole and electron injection occurs from PEDOT and LiF layers, respectively; the transport through the layers of the device is indicated schematically; $\lambda 1$ and $\lambda 2$ represent blue and green emission, respectively. Reprinted by permission from Macmillan Publishers Ltd: Nature Photonics A.J. Steckl, DNA, a new material for photonics?, Nature Phot. **1**, 3–5 (2007), copyright (2007)

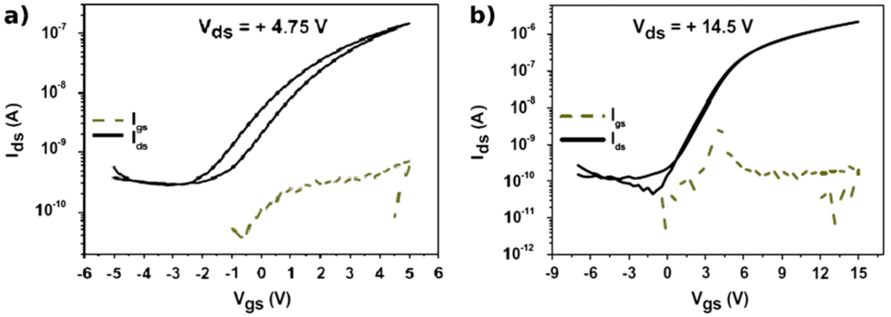

Fig. 12.11 Transfer characteristics of organic field effect transistors with C_{60} semiconductor and (**a**) guanine gate dielectric; capacitance per area, $C_{0d} = 9.25$ nF/cm^2, field effect mobility $\mu = 0.1$ cm^2/V s. (**b**) Inorganic–organic aluminum oxide and thymine gate dielectric; Capacitance per area C_{0d}, 23.6 nF/cm^2, field effect mobility $\mu = 0.5$ cm^2/V s. The occurrence of higher mobility for the device having a much higher roughness of the gate dielectric is surprising and yet unclear. Reprinted from Organic Electronics, 11, M. Irimia-Vladu, P.A. Troshin, M. Reisinger, G. Schwabegger, M. Ullah, R. Schwoediauer, A. Mumyatov, M. Bodea, J.W. Fergus, V. Razumov, H. Sitter, S. Bauer, N.S. Sariciftci, Environmentally sustainable organic field effect transistors, Org. Electron. **11**, 1974–1990 (2010), Copyright (2010), with permission from Elsevier

Table 12.2 Dielectric properties of investigated natural dielectrics. Reprinted from M. Irimia-Vladu, P.A. Troshin, M. Reisinger, G. Schwabegger, M. Ullah, R. Schwoediauer, A. Mumyatov, M. Bodea, J.W. Fergus, V. Razumov, H. Sitter, S. Bauer, N.S. Sariciftci, Environmentally sustainable organic field effect transistors, Org. Electron. **11**, 1974–1990 (2010), Copyright (2010), with permission from Elsevier

Material	Dielectric constant (at 1 kHz)	Breakdown field (MV/cm)	Loss tangent (at 100 mHz)
Adenine	~3.8	~1.5	~4 × 10^{-3}
Cytosine	~4.6	~3.4	~5 × 10^{-3}
Guanine	~4.3	~3.5	~7 × 10^{-3}
Thymine	~2.4	~0.9	~1 × 10^{-2}
Glucose	~6.3	~1.5	~5 × 10^{-2}
Lactose	~6.5	~4.5	~2 × 10^{-2}
PVA	~6.1	~2	~4 × 10^{-2}
AlOx	~9	~3.5	~4 × 10^{-3}

12.3.2 Unipolar and Ambipolar Natural Semiconductors

Conjugated organic molecules are present in nature, constituting many natural pigments. Past reports of chlorophyll and beta-carotene semiconductors also stimulated research in optical, nonlinear optical, and fluorescence applications of such materials [52–55]. Nevertheless, the pool of natural semiconductors for organic electronics applications remained limited until recently. However, a closer look at natural semiconductors showed performance on par with top of the class synthetic semiconductors [19, 20]. Indigo is a naturally occurring compound, a highly prized pigment in antiquity, traditionally extracted from plants of *Indigofera* genus [56]. 6,6′-dibromoindigo, the main component of tyrian purple, another valued dye in antiquity, has been originally extracted from sea snails [57]. These two natural compounds, as well as other "nature-inspired" indigoids showed surprisingly good ambipolar charge transport properties, which make them potential candidate materials for sustainable OFET, OLED and photovoltaic applications.

Carotenoids

Carotenoids are oligo-olefins with varying chain lengths of sp^2-hybridized carbons, making them analogous to polyacetylene. Carotenoid pigments are responsible for the color of many natural systems, such as flowers, fruits, and vegetables [58]. The archetypical carotenoid, β-carotene, was first reported in 1831 when crystals of the material were extracted from carrots [59]. Interest into β-carotene and related products research arose because of its presumed anti-aging and heart-disease prevention properties [60]. Initial steps into the implementation of β-carotene as semiconductor in organic electronics revealed modest performance in OFETs [55]. β-carotene processed from chloroform was used as semiconductor channel for organic field effect transistors with glucose as gate dielectric. Although the semiconductor mobilities surpassed 1×10^{-4} $cm^2/V\,s$ practical application is hampered by the propensity for oxidation of the carotenoid backbone [2]. β-carotene/fullerene bulk heterojunction type devices have been reported though photocurrents produced by such devices were low.

Indigoids

Indigo and its dibromo analog, 6,6′-dibromoindigo, or tyrian purple, are the oldest blue and purple dyes. Indigo is a dye extracted from *indigofera tinctoria* and *isatis tinctoria* plants, which were cultivated for at least 4000 years in China, India and Egypt for coloring textiles [56]. Tyrian purple, in contrast, is of animal origin, being produced from certain types of shellfish. The synthetic production of indigo was initiated in 1882, but the low reaction yield made the process not competitive with natural-origin indigo [61]. It was not until the reaction pathway improvement in 1887 that synthetic indigo has become the most industrially produced dye, with the coloring of cotton yarn for blue jeans industry producing the highest demand. Indigo is also a biocompatible and low toxicity compound, its soluble salt form being accepted as food colorant both in the United States and the European Union [56]. Tyrian purple was the most prized dye in antiquity, being known as *royal purple*, *shellfish purple* or *purple of the ancients* [57]. Both molecules are highly planar and have strong intra- and intermolecular hydrogen bonding. Each indigo molecule is hydrogen bonded to four neighbors. The strength of intermolecular interactions reinforcing π-stacking and crystalline-order rationalizes why such small molecules

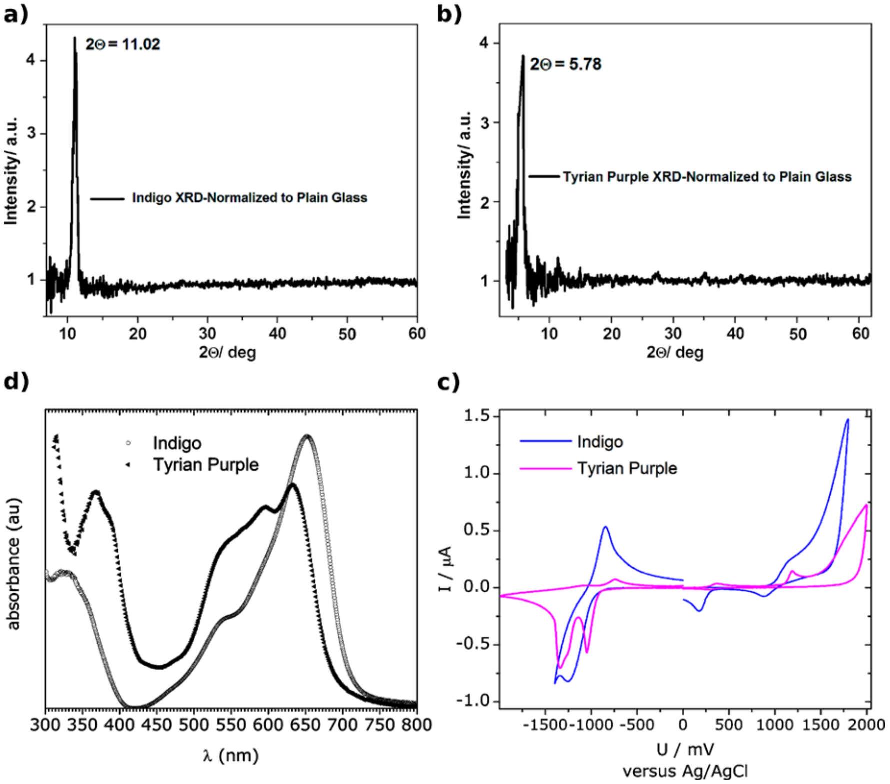

Fig. 12.12 X-ray difractogram of thin films (100 nm thick) of (**a**) indigo and (**b**) tyrian purple showing the occurrence of crystalline texture with a single preferential orientation in the growth direction when the films are grown on substrates that support the crystallinity, i.e. polyethylene, polystyrene or tetratetracontane. (**c**) UV-vis. Absorption of the indigo (*empty symbol*) and tyrian purple (*filled symbol*). (**d**) Cyclic voltammogram of indigo (*blue line*) and tyrian purple (*red line*) showing the similar behavior of both materials: reversible two-electron oxidation and reduction electrochemistry. From the cyclic voltammograms and the onset of absorption of the two materials, the band gaps are estimated to be 1.7 eV and 1.8 eV for indigo and tyrian purple, respectively

with limited conjugation prove to be good charge transporters. Both indigo and tyrian purple material were recently employed in the fabrication of ambipolar organic field effect transistors and inverters that showed performance on-par with the top reports for synthetic organic semiconductors.

Indigo and tyrian purple are easily sublimable and form highly crystalline films. XRD of these vacuum processed thin films yielded a single diffraction peak centered at ∼11.06 degrees for indigo and ∼5.72 degrees for tyrian purple (Fig. 12.12a–b), indicating a crystalline texture with a single preferential orientation in the growth direction. For both materials, cyclic voltammetry scans of thin films in acetonitrile show a reversible two-electron reduction and reversible two-electron oxidation pattern. The HOMO and LUMO levels evaluated from CV are shown in Table 12.3. The

Table 12.3 The HOMO and LUMO levels of indigo and tyrian purple estimated from cyclic voltammetry and optical absorption

Material	HOMO (eV)	LUMO (eV)	E_g (CV)	E_g (optical)	Mobility
Indigo	−5.5	−3.8	1.7	1.7	$\mu_e = 1 \times 10^{-2}$ $\mu_h = 1 \times 10^{-2}$
Tyrian purple	−5.8	−4.0	1.8	1.8	$\mu_e = 0.3$ $\mu_h = 0.3$

energy gap of indigo and tyrian purple estimated from both cyclic voltammetry and onset of absorption of the UV-Vis spectra (Fig. 12.12c–d) is ~1.7 eV and ~1.8 eV, respectively. The reversible oxidation and reduction of these molecules suggest the possibility pf ambipolar charge transport, while the low band gap implies that electrons and holes could be injected from a single metal electrode. A demonstration of ambipolar transport in indigo-based OFETs fabricated on natural resin shellac substrate is shown in Fig. 12.13a–c. The measured field effect mobilities for electron and holes are well balanced (~1×10^{-2} cm^2/V s). Similarly, ambipolar charge transport in OFETs with tyrian purple channel is depicted in Fig. 12.13d–e. The field effect mobilities of electrons and holes are, as in the case of indigo, high and well balanced, both being equal to 0.3 cm^2/V s [62]. The performance of a complementary type inverter fabricated with indigo and tyrian purple channels, with a single type of contact electrodes (i.e., gold) is depicted in Fig. 12.14a–d. The measured gain at low operating voltage of the inverters is 110 in the first and 105 in the third quadrant for indigo; 255 in the first and 285 in the third quadrant for tyrian purple. The deep LUMO level of tyrian purple (being situated at ~−4.0 eV) makes tyrian purple stable against oxygen degradation when measured in air [63]. Diode devices with tyrian purple showed no degradation after at least one month of continued operation in air.

12.4 Biocompatible & Biodegradable Electrodes

The development of electronic devices interfacing with living tissue paves ways for applications of electronics in biomedicine to improve diagnosis and treatment [64]. So far, state-of-the-art implantable devices consist of microfabricated arrays of electrodes on silicon substrates. These electrode microarrays are invasive and susceptible to produce tissue damage. They are not only non-conformable to the nonplanar shape of the organs, they are also rigid and bulky and therefore not susceptible for miniaturization. Arrays of metal electrodes on soft, biocompatible plastic substrates provide alternative routes much better suited for contact with living tissue. Polyimide, polydimethylsiloxane and parylene C were explored as substrates for the fabrication of such thin, conformable electronics with thicknesses in the range of 10 µm to 100 µm [21–27].

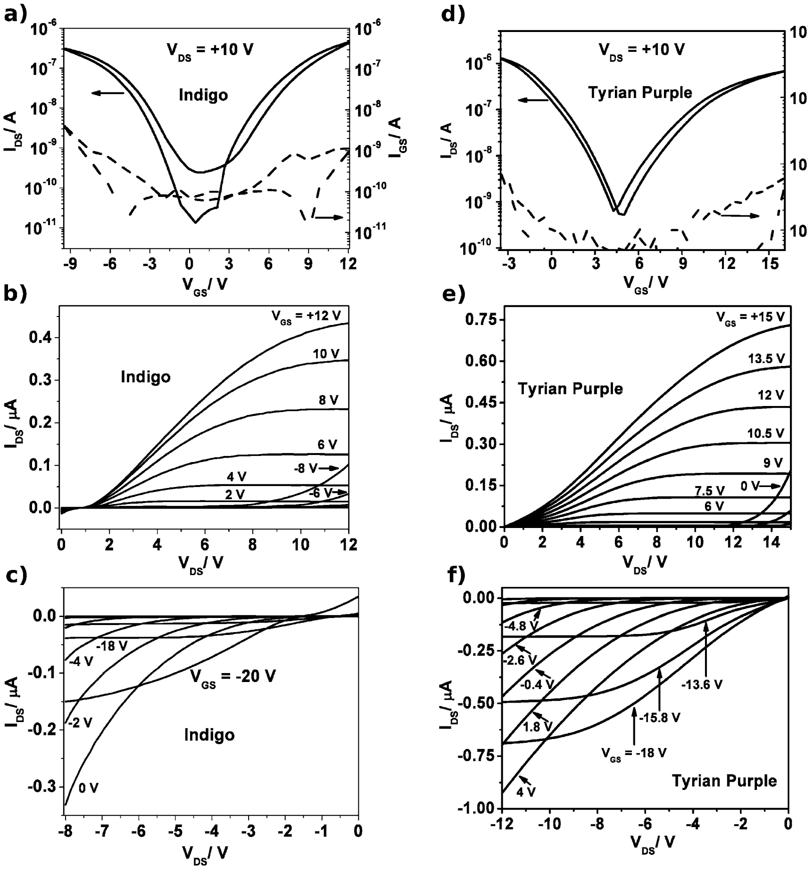

Fig. 12.13 (**a**–**c**) Transfer and output characteristics of organic field effect transistors fabricated on shellac substrates with aluminum oxide and tetratetracontane inorganic–organic gate dielectric and indigo semiconductor. The OFET devices have balanced electron and hole mobilities of $\sim 1 \times 10^{-2}$ cm^2/V s. Adapted from M. Irimia-Vladu, E.D. Glowacki, P.A. Troshin, G. Schwabegger, L. Leonat, D.K. Susarova, O. Krystal, M. Ullah, Y. Kanbur, M.A. Bodea, V.F. Razumov, H. Sitter, S. Bauer, N.S. Sariciftci, Indigo, a natural pigment for high-performance ambipolar organic field effect transistors and circuits, Adv. Mater. **24**(3), 375–380 (2012). Copyright Wiley-VCH Verlag GmbH & Co. KGaA. Reproduced with permission. (**d**–**e**) Transfer and output characteristics of organic field effect transistors fabricated on glass substrates with aluminum oxide and polyethylene inorganic–organic gate dielectric and tyrian purple semiconductor. Electron mobility 0.03 cm^2/V s and hole mobility of $\sim$0.2 cm^2/V s. Adapted from E.D. Glowacki, L.N. Leonat, G. Voss, M. Badea, Z. Bozkurt, M. Irimia-Vladu, S. Bauer, N.S. Sariciftci, Ambipolar field effect transistors and inverters with the natural material tyrian purple, AIP Advances **4**, 042132 (2011); used in accordance with the Creative Commons Attribution 3.0 Unported License

In a recent report, thin gold electrodes were sandwiched between two 1.2 µm thick layers of polyimide, subsequently transferred on silk films that helped handling the conductive electrode array [41]. Not only improving the processibility of biocompatible gold electrodes was intensely explored, but also the implementation of

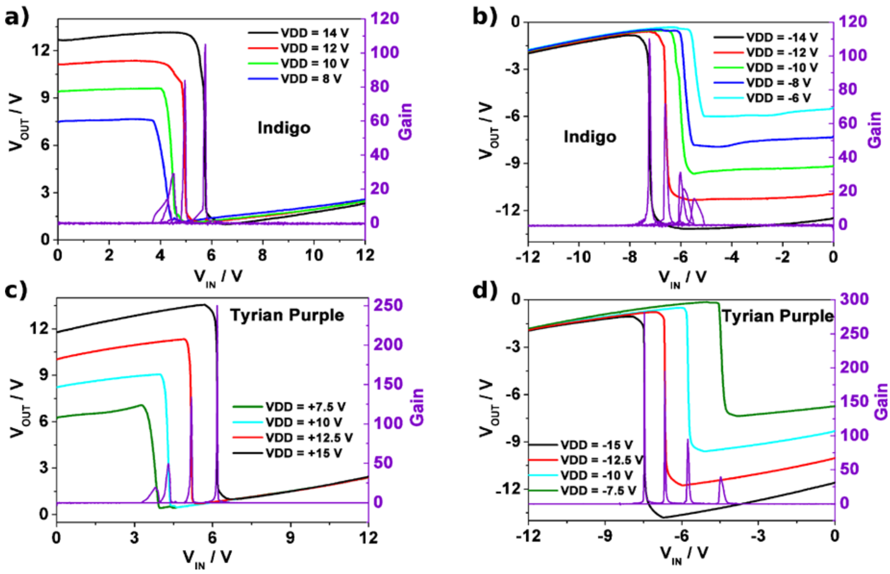

Fig. 12.14 Complementary-like voltage inverter characteristics measured in quasi steady state for indigo: (**a**) in the first quadrant and (**b**) in the third quadrant. The respective voltage gain is displayed on the *right axes*. Reproduced from M. Irimia-Vladu, E.D. Glowacki, P.A. Troshin, G. Schwabegger, L. Leonat, D.K. Susarova, O. Krystal, M. Ullah, Y. Kanbur, M.A. Bodea, V.F. Razumov, H. Sitter, S. Bauer, N.S. Sariciftci, Indigo, a natural pigment for high-performance ambipolar organic field effect transistors and circuits, Adv. Mater. **24**(3), 375–380 (2012). Copyright Wiley-VCH Verlag GmbH & Co. KGaA. Reproduced with permission. Complementary-like voltage inverter characteristics measured in quasi steady state for tyrian purple: (**c**) in the first quadrant and (**d**) in the third quadrant. The voltage gain as high as 255 to 285 displayed on the *right axes* is among the highest reported to date for a single ambipolar material with a single type of contact electrodes. Reproduced from E.D. Glowacki, L.N. Leonat, G. Voss, M. Badea, Z. Bozkurt, M. Irimia-Vladu, S. Bauer, N.S. Sariciftci, Ambipolar field effect transistors and inverters with the natural material tyrian purple, AIP Advances **4**, 042132 (2011); used in accordance with the Creative Commons Attribution 3.0 Unported License

alternative biocompatible materials, i.e. conductive polymer electrodes [21, 65, 66]. Compared to gold, conductive polymer electrodes reduce the reaction of the body to the foreign object invasion and enable recordings for longer times. More-over, by lowering the electrical impedance at the interface with living tissue (presumably because of the ability of the polymers to conduct ions), the conductive polymer electrodes were shown to significantly improve the quality of electric signals [67].

Water-based isotropically conducting adhesives were introduced for applications with electrical interconnects and printed circuits for ultralow-cost flexible/foldable printed electronics [26]. Hybrid electronic and photonic devices emerged by employing n- and p-type silicon nanowires coated with porphyrins. The photonic functions were supported by the high light sensitivity of porphyrins, in order to detect incident light and implement complementary photoconductors at the nanometer scale level [22].

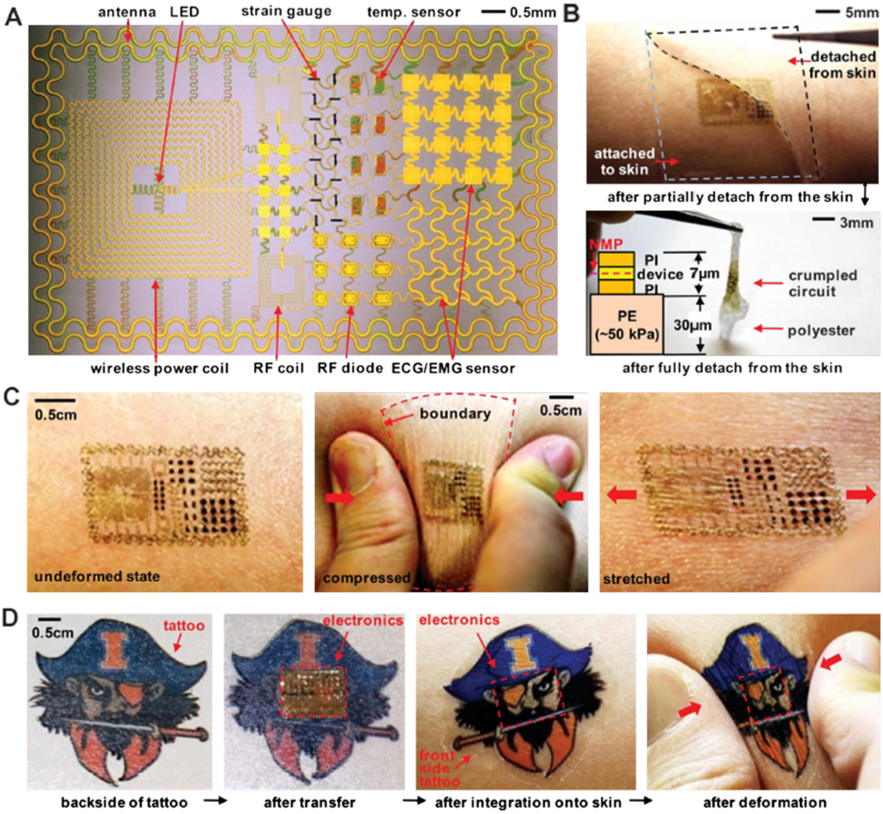

Fig. 12.15 (**A**) photograph of complex circuit for multifunctional electronics with physical properties matched to the human epidermis. The circuit contains an antenna, a LED, a strain gauge, a temperature sensor, wireless power coils, radio frequency coils, as well as sensors monitoring the brain and the heart functions (electroencephalograms, EEG and electrocardiograms, ECGs). The circuit is mounted on a sacrificial, biocompatible and water-soluble film of PVA and transferred face-down onto the skin. Following the dissolution of the sacrificial substrate, the device remains conformally attached to the skin through van der Waals forces alone. (**B**) Epidermal electronics being peeled away from the skin: partially (*top*) and fully (*bottom*). The *inset of the top figure* shows a cross-sectional illustration of the structure, with the neutral mechanical plane (NMP) defined by a *red dashed line*. (**C**) and (**D**) Multifunctional and commercial epidermal electronics transferred on skin in various stretched, released and compressed states. From D.-H. Kim, N. Lu, R. Ma, Y.-S. Kim, R.-H. Kim, S. Wang, J. Wu, S.M. Won, H. Tao, A. Islam, K.J. Yu, T. Kim, R. Chowdhury, M. Ying, L. Xu, M. Li, H.-J. Chung, H. Keum, M. McCormick, P. Liu, Y.-W. Zhang, F.G. Omenetto, Y. Huang, T. Coleman, J.A. Rogers, Epidermal electronics, Science **333**, 838–843 (2011). Reprinted with permission from American Association for the Advancement of Science (AAAS)

An ample study of electronic systems was reported that achieved thicknesses, effective elastic moduli, bending stiffnesses, as well as areal mass densities matching closely with the respective values of human epidermis. The conformable devices could be transferred to skin in a fashion mechanically invisible to the user.

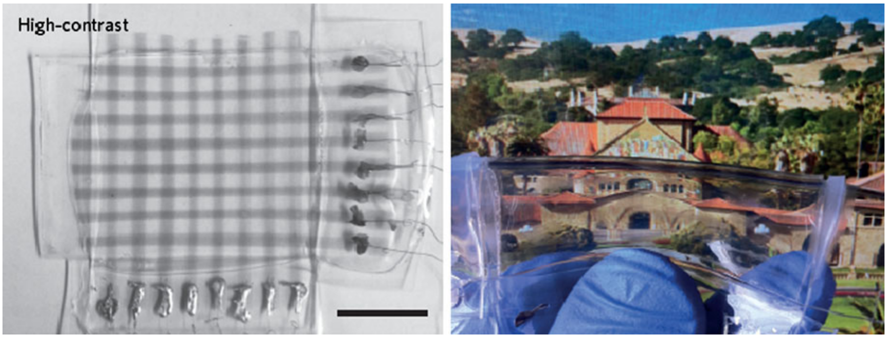

Fig. 12.16 (*Left*) Photographs showing the characteristics of a 64-pixel array of compressible pressure sensors. The lines of the nanotubes are visible (*scale bar*, 1 cm). (*Right*) Photograph of the same device reversibly adhered to a backlit liquid-crystal display. The device is being deformed by hand. Reprinted by permission from Macmillan Publishers Ltd: Nature Nanotechnology, D.J. Lipomi, M. Vosgueritchian, B.C.-K. Tee, S.L. Hellstrom, J.A. Lee, C.H. Fox, Z. Bao, Skin–like pressure and strain sensors based on transparent elastic films of carbon nanotubes, Nature Nanotech. **6**, 788–792 (2011), copyright (2011)

Figure 12.15 shows the transfer of such a device fabricated on water-soluble PVA substrate onto the skin, in a similar way a tattoo is applied. The structure could be subsequently stretched and compressed without destroying its integrity or function.

Transparent, conducting spray-deposited films of single-walled carbon nanotube-based thin films were developed in a recent study [68]. The deposited films could be stretched by applying strain along each axis, followed by releasing the strain. This repeated stretch-release process generated spring-like structures in the nanotubes that could uptake strains of up to 150 % while displaying conductivities as high as 2,200 S/cm in the stretched state (Fig. 12.16a–b). The same principle was employed to render nanotube films in electrode arrays of transparent, stretchable capacitors with applicability as pressure and strain sensors.

12.5 Conclusion

In summary, this chapter has briefly highlighted recent advances in the use of highly unconventional materials for organic electronics. Today we can choose among a wide range of diverse materials for creating new electronic functionalities, coming closer to a vision of a sustainable electronics world. Of course, there is still a long way to go until we can use electronics everywhere. Nature remains a huge reservoir of inspiration for material scientists since it holds still unrevealed secrets.

References

1. C.J. Bettinger, Z. Bao, Polym. Int. **59**, 563–567 (2010)

2. M. Irimia-Vladu, P.A. Troshin, M. Reisinger, L. Shmygleva, Y. Kanbur, G. Schwabegger, M. Bodea, R. Schwödiauer, A. Mumyatov, J.W. Fergus, V. Razumov, H. Sitter, N.S. Sariciftci, S. Bauer, Adv. Funct. Mater. **20**, 4069–4076 (2010)
3. D. Többjork, R. Österbacka, Adv. Mater. **23**, 1935–1961 (2011)
4. D. Benett, S. Kim, J. Mater. Sci. **46**, 4723–4740 (2011)
5. K. Svennersten, K.C. Larsson, M. Berggren, A. Richter-Dahlfors, Biochim. Biophys. Acta **1810**, 276–285 (2011)
6. B. Lamprecht, R. Thünauer, M. Osterman, G. Jakopic, G. Leising, Phys. Status Solidi A **202**(5), R50–R52 (2009)
7. V. Benfenati, S. Toffanin, R. Capelli, L.M.A. Camassa, S. Ferroni, D.L. Kaplan, F.G. Omenetto, M. Muccini, R. Zamboni, Biomaterials **31**, 7883–7891 (2010)
8. A.C. Siegel, S.T. Phillips, B.J. Wiley, G.M. Whitesides, Lab Chip **9**, 2775–2781 (2009)
9. D.H. Kim, Y.S. Kim, J. Amsden, B. Panilaitis, D.L. Kaplan, F.G. Omenetto, M.R. Zakin, J.A. Rogers, Appl. Phys. Lett. **95**, 133701 (2009)
10. M. Irimia-Vladu, P.A. Troshin, M. Reisinger, G. Schwabegger, M. Ullah, R. Schwödiauer, A. Mumyatov, M. Bodea, J.W. Fergus, V. Razumov, H. Sitter, S. Bauer, N.S. Sariciftci, Org. Electron. **11**, 1974–1990 (2010)
11. R. Boehm, R.J. Narayan, R. Aggarwal, N.A. Montiero-Riviere, S.P. Lacour, J. Miner. Met. Mater. Soc. **61**(9), 53–58 (2009)
12. R. Foresti, M. Hoque, D. Monti, C.J. Green, R. Motterlini, J. Pharmacol. Exp. Ther. **312**, 686–693 (2005)
13. H. Weinberger, W.M. Howlett Gardner, Ind. Eng. Chem. **30**, 454–458 (1938)
14. S.S. Srivastava, D.D. Puri, Nature **183**, 37–38 (1959)
15. R. Capelli, J.J. Amsden, G. Generali, S. Toffanin, V. Benfenati, M. Muccini, D.L. Kaplan, F.G. Omenetto, R. Zamboni, Org. Electron. **12**, 1146–1151 (2011)
16. Y.W. Kwon, C.H. Lee, D.H. Choi, J.I. Jin, J. Mater. Chem. **19**, 1353–1380 (2009)
17. P.V. Kamat, J.P. Chauvet, R.W. Fessenden, J. Phys. Chem. **90**, 1389–1394 (1986)
18. R.R. Burch, Y.H. Dong, C. Fincher, M. Goldfinger, P.E. Rouviere, Synth. Met. **146**, 43–46 (2004)
19. M. Irimia-Vladu, E.D. Glowacki, P.A. Troshin, G. Schwabegger, L. Leonat, D.K. Susarova, O. Krystal, M. Ullah, Y. Kanbur, M.A. Bodea, V.F. Razumov, H. Sitter, S. Bauer, N.S. Sariciftci, Adv. Mater. **24**(3), 375–380 (2012)
20. E.D. Glowacki, L.N. Leonat, G. Voss, M. Badea, Z. Bozkurt, M. Irimia-Vladu, S. Bauer, N.S. Sariciftci, AIP Adv. **4**, 042132 (2011)
21. A.N. Zelikin, D.M. Lynn, J. Farhadi, I. Martin, V. Shastri, R. Langer, Angew. Chem., Int. Ed. Engl. **41**, 141–144 (2002)
22. S.J. Choi, Y.C. Lee, M.L. Seol, J.H. Ahn, S. Kim, D.I. Moon, J.W. Han, S. Mann, J.W. Yang, Y.K. Choi, Adv. Mater. **23**, 3979–3983 (2011)
23. G. Corbelli, C. Ghisleri, M. Marelli, P. Milani, L. Ravagnan, Adv. Mater. **23**, 4504–4508 (2011)
24. S. Huang, L. Li, Z. Yang, L. Zhang, H. Saiyin, T. Chen, H. Peng, Adv. Mater. **23**, 4707–4710 (2011)
25. D. Khodagholy, T. Doublet, M. Gurfinkel, P. Quilichini, E. Ismailova, P. Leleux, T. Herve, S. Sanaur, C. Bernard, G.G. Malliaras, Adv. Mater. **23**, H268–H272 (2011)
26. C. Yang, W. Lin, Z. Li, R. Zhang, H. Wen, B. Gao, G. Chen, P. Gao, M.M.F. Yuen, C.P. Wong, Adv. Funct. Mater. **11**, 4582–4588 (2011)
27. D.H. Kim, N. Lu, R. Ma, Y.S. Kim, R.H. Kim, S. Wang, J. Wu, S.M. Won, H. Tao, A. Islam, K.J. Yu, T. Kim, R. Chowdhury, M. Ying, L. Xu, M. Li, H.J. Chung, H. Keum, M. McCormick, P. Liu, Y.W. Zhang, F.G. Omenetto, Y. Huang, T. Coleman, J.A. Rogers, Science **333**, 838–843 (2011)
28. Y.L. Loo, T. Someya, K.W. Baldwin, Z. Bao, P. Ho, A. Dodabalapur, H.E. Katz, J.A. Rogers, Proc. Natl. Acad. Sci. USA **99**, 10252–10256 (2002)

29. N. Stutzmann, R.H. Friend, H. Sirringhaus, Science **299**, 1881–1884 (2003)
30. S.P. Lacour, J. Jones, S. Wagner, T. Li, Z. Suo, Proc. IEEE **23**(8), 1459–1466 (2005)
31. C.J. Bettinger, Z. Bao, Adv. Mater. **22**, 651–655 (2010)
32. F. Eder, H. Klauk, M. Halik, U. Zschieschang, G. Schmid, C. Dehm, Appl. Phys. Lett. **84**(14), 2673–2675 (2004)
33. U. Zschieschang, T. Yamamoto, K. Takimiya, H. Kuwabara, M. Ikeda, T. Sekitani, T. Someya, H. Klauk, Adv. Mater. **23**, 654–658 (2011)
34. A. Russo, B.Y. Ahn, J.J. Adams, E.B. Duoss, J.T. Bernhard, J.A. Lewis, Adv. Mater. **23**, 3426–3430 (2011)
35. M.C. Barr, J.A. Rowehl, R.R. Lunt, J. Xu, A. Wang, C.M. Boyce, S.G. Im, V. Bulovic, K.K. Gleason, Adv. Mater. **23**, 3500–3505 (2011)
36. R. Martins, P. Barquinha, L. Pereira, N. Correira, G. Goncalves, I. Fereira, E. Fortunato, Phys. Status Solidi **9**, 308–310 (2009)
37. A.C. Siegel, S.T. Phillips, M.D. Dickey, N. Lu, Z. Suo, G.M. Whitesides, Adv. Funct. Mater. **20**, 28–35 (2010)
38. D.H. Kim, Y.S. Kim, J. Wu, Z. Liu, J. Song, H.S. Kim, Y.Y. Huang, K.C. Hwang, J.A. Rogers, Adv. Mater. **21**, 3703–3707 (2009)
39. H. You, A.J. Steckl, Appl. Phys. Lett. **97**, 023514 (2010)
40. D.Y. Kim, A.J. Steckl, Appl. Mater. Interfaces **2**(11), 3318–3323 (2010)
41. D.H. Kim, J. Viventi, J.J. Amsden, J. Xiao, L. Vigeland, Y.S. Kim, J.A. Blanco, B. Panilaitis, E.S. Frechette, D. Contreras, D.L. Kaplan, F.G. Omenetto, Y. Huang, K.C. Hwang, M.R. Zakin, B. Litt, J.A. Rogers, Nat. Mater. **9**, 511–518 (2010)
42. H. Weinberger, W.M. Howlett Gardner, Ind. Eng. Chem. **30**, 454–458 (1938)
43. H. Tao, M.A. Brenckle, M. Yang, J. Zhang, M. Liu, S.M. Siebert, R.D. Averitt, M.S. Mannoor, M.C. McAlpine, J.A. Rogers, D.L. Kaplan, F.G. Omenetto, Adv. Mater. **24**, 1067–1072 (2012)
44. M.C. Belanger, Y. Marois, J. Biomed. Mater. Res. **58**, 467–477 (2001)
45. Y.W. Kwon, C.H. Lee, D.H. Choi, J.I. Jin, J. Mater. Chem. **19**, 1353–1380 (2009)
46. J.A. Hagen, W. Li, A.J. Steckl, J.G. Grote, Appl. Phys. Lett. **88**, 171109 (2006)
47. X. Dong, Y. Shi, W. Huang, P. Chen, L.J. Li, Adv. Mater. **22**, 1649–1653 (2010)
48. P. Lin, X. Luo, I.M. Hsing, F. Yan, Adv. Mater. **23**, 4035–4040 (2011)
49. B. Singh, N.S. Sariciftci, J. Grote, J.G. Hopkins, J. Appl. Phys. **100**, 024514 (2006)
50. P. Stadler, K. Oppelt, B. Singh, J. Grote, R. Schwödiauer, S. Bauer, H. Piglmayer-Brezina, D. Bauerle, N.S. Sariciftci, Org. Electron. **8**, 648–654 (2007)
51. S.E. Fritz, T.W. Kelley, C.D. Frisbie, Appl. Phys. Lett. **109**, 10574–10577 (2005)
52. P. Karrer, C.H. Eugster, Helv. Chim. Acta **33**, 1952–1954 (1950)
53. P.V. Kamat, J.P. Chauvet, R.W. Fessenden, J. Phys. Chem. **90**, 1389–1394 (1986)
54. E. Ehrenfreund, D. Moses, A.J. Heeger, J. Cornil, J.L. Bredas, Chem. Phys. Lett. **196**, 84–90 (1992)
55. R.R. Burch, Y.H. Dong, C. Fincher, M. Goldfinger, P.E. Rouviere, Synth. Met. **146**, 43–46 (2004)
56. E. Steingruber, in *Ullmann's Encycl. Ind. Chem.*, vol. 1–9 (Wiley/VCH, Weinheim, 2004)
57. C.J. Cooksey, Molecules **6**, 736–769 (2001)
58. J.A. Olson, N.I. Krinsky, FASEB J. **9**, 1547–1550 (1995)
59. H. Wachenroder, Geiger's Magaz. Pharm. **33**, 144–172 (1831)
60. G.S. Omenn, Annu. Rev. Public Health **19**, 73–99 (1998)
61. A. Baeyer, V. Drewsen, Ber. Deut. Chem. Ges. **15**, 2856–2864 (1882)
62. Y. Kanbur, M. Irimia-Vladu, E.D. Glowacki, G. Voss, M. Baumgartner, G. Schwabegger, L. Leonat, M. Ullah, H. Sarica, S. Erten-Ela, R. Schwödiauer, H. Sitter, Z. Küçükyavuz, S. Bauer, N.S. Sariciftci, Org. Electron. **13**, 919–924 (2012)
63. T.D. Anthopoulos, G.C. Anyfantis, G.C. Papavassiliou, D.M. de Leeuw, Appl. Phys. Lett. **90**, 122105 (2007)
64. J.S. Perlmutter, J.W. Mink, Annu. Rev. Neurosci. **29**, 229 (2006)

65. G.G. Wallace, S.E. Moulton, G.M. Clark, Science **324**, 185–186 (2009)
66. M. Asplund, T. Nyberg, O. Inganas, Polym. Chem. **1**, 1374–1391 (2010)
67. K.A. Ludwig, J.D. Uram, J. Yang, D.C. Martin, D.R. Kipke, J. Neural Eng. **3**, 59–70 (2006)
68. D.J. Lipomi, M. Vosgueritchian, B.C.K. Tee, S.L. Hellstrom, J.A. Lee, C.H. Fox, Z. Bao, Nat. Nanotechnol. **6**, 788–792 (2011)

Index

H. Sitter et al. (eds.), *Small Organic Molecules on Surfaces*,
Springer Series in Materials Science 173, DOI 10.1007/978-3-642-33848-9,